Computational Fluid Dynamics
Analysis of Jet Engine Test Facilities

Jordan Gilmore, BE (Hons)

A thesis presented for the degree of Doctor of Philosophy

in

Mechanical Engineering at the University of Canterbury, Christchurch, New Zealand

2011

For all those who have helped along the way

Abstract

This thesis investigates the application of CFD techniques to the aerodynamic analysis of a U-shaped JETC. Investigations were carried out to determine the flow patterns present at a number of locations within the structure of a full U-shaped JETC. The CFD solutions produced in these investigations used recommendations from the literature in the set-up of the CFD solver, and provided the computational component towards problem-specific validation of the CFD techniques used.

A structured series of CFD-aided investigation and design processes were then performed. These processes were based around a series of analyses that evaluated the influence of a number of cell parameters in terms of cell airflow efficiency and velocity distortion. Four cell components; the inlet and exhaust stack baffle arrangements, the turning-vanes, the rear of the working section and augmenter entrance, and the lower exhaust stack, including the BB, were investigated in individual analyses. Throughout the investigations the value of CFD as a design tool was constantly assessed.

Overall, the findings suggest that aerodynamic optimisation of the baffle arrangements would provide the greatest gains to cell airflow efficiency. As some cells contain as many as three baffle arrangements, the potential increases made to cell airflow capacity are sizable. Through implementing the findings of the baffle arrangement investigations, static pressure loss across the five-row baseline arrangement was reduced by 79%.

For low levels of velocity distortion in the upstream region of the working section, the need to design the inlet stack baffles in the turning-vane arrangement was highlighted. Mid-baffle vane alignment, consistent flow channels, and sufficiently low chord to gap ratios should be incorporated into a turning-vane design to maximise flow uniformity. The need for the baffle and vane components to combine with the geometry of the cell to limit adverse pressure gradients was found as a requirement to minimise inner corner separation, and the downstream threat it creates to a safe testing environment.

CFD proved to be a valuable analysis tool throughout the investigations performed in this thesis. The number of design iterations analysed, and the detail of data that could be extracted, significantly exceeded what could have been achieved through an isolated experimental testing programme.

Table of Contents

List of Figures

List of Tables

List of Abbreviations

BB	Blast Basket
BC	Boundary Condition
BL	Boundary Layer
BPR	Bypass Ratio
CAA	Civil Aviation Authority
CHCEC	Christchurch Engine Centre
CFD	Computational Fluid Dynamics
DACQ	Data Acquisition
DES	Detached Eddy Simulation
DNS	Direct Numerical Simulation
FOD	Foreign Object Damage
FSM	Fractional Step Method
IAE	International Aero Engines
ICAO	International Civil Aeronautics Organization
JBD	Jet Blast Deflector
JETC	Jet Engine Test Cell
LES	Large Eddy Simulation
LE	Leading Edge
MRO	Maintenance, Repair and Overhaul
MFR	Mass Flow Rate
MTC	Master Test Cell
MUSCL	Monotone Upstream-Centred Schemes for Conservation Laws
NITA	Non-Iterative Time Advancement
NS	Navier-Stokes
OLB	Object Limitation Boundary
PDE	Partial Differential Equation
Pe	Peclet Number
Pr	Prandtl Number
PISO	Pressure Implicit Splitting of Operators
R&D	Research and Design
RANS	Reynolds Averaged Navier-Stokes
Re	Reynolds Number
RNG	Renormalization-Group

RSM	Reynolds Stress Model
SA	Spalart-Allmaras
SFS	Resolved Sub-Filter Scales
SGS	Sub-Grid Scales
SST	Shear-Stress-Transport
SIMPLE	Semi-Implicit Method for Pressure Linked Equations
TI	Turbulence Intensity
TLS	Turbulence Length Scale

List of Symbols

C_2	Porous-jump coefficient	m^{-1}
d_h	Hydraulic diameter	m
D_i	Engine inlet face diameter	m
E	Specific Energy	Jkg^{-1}
H	Height (ground plane to centre of engine inlet face)	m
i	Internal energy	Jkg^{-1}
k	Turbulent kinetic energy	m^2s^{-2}
k'_{Re}	Low Re pressure loss correction factor	
K	Pressure loss coefficient	
K_S	Roughness height	m
p	Pressure	Pa
S	Source term	
t	Time	S
T	Temperature	K
u	Velocity component in x-direction	ms^{-1}
u_{avg}	Average velocity	ms^{-1}
u_{max}	Maximum velocity	ms^{-1}
u_{min}	Minimum velocity	ms^{-1}
$\vec{u}$	Velocity vector	ms^{-1}
v	Velocity component in y-direction	ms^{-1}
v_{dist}	Velocity distortion	
Vi	Main-Stream Velocity	
Vo	Engine Inlet Velocity	ms^{-1}
w	Velocity component in z-direction	ms^{-1}
α	Permeability	s^{-1}
β	Porosity	
Γ	Diffusion coefficient	
Δm	Thickness of Medium	m
η	Orifice roughness value	
κ	Conductivity	$Wm^{-1}K^{-1}$
λ	Second viscosity	Pa·s
μ	Dynamic viscosity	Pa·s
ρ	Density	kgm^{-3}

ς	Orifice geometry value	
τ	Shear stress	Pa
υ	Velocity normal to a porous face	ms^{-1}
φ	General fluid property	
Ω	Ramp elevation angle	°
p	Pressure	Pa
Φ	Dissipation term	

1 Project Overview and Motivation

This section discusses the impetus behind the initiation of this project and the subjects covered within. In the latter part of this section the scope of the investigations that were performed is presented, along with a brief discussion of the layout of this thesis.

1.1 Formulation and Impetus of Project

The formulation of this project was born out of the relationship between the University of Canterbury (UoC) and the Christchurch Engine Centre (CHCEC) during a final year undergraduate project in 2005 (Agmen, Bosworth, Gilmore, & Hager, 2005). The work carried out in that project performed an aerodynamic analysis of the (at the time) new Jet Engine Test Cell (JETC) at the CHCEC base in Christchurch, New Zealand.

The work performed by (Agmen et al., 2005) aimed to introduce and investigate the use of Computational Fluid Dynamics (CFD) techniques to the analysis of the CHCEC JETC. Such techniques had not been employed previously by the cell designers, CENCO, or by the engineers in the alliance formed by Air New Zealand and Pratt & Whitney in the creation of the CHCEC.

Upon completion of the work performed by (Agmen et al., 2005), a desire was shown by both the Mechanical Engineering Department at the UoC and the CHCEC to develop the findings of the final year project, and the general application of CFD techniques to the analysis of JETCs. This project was therefore born out of the desire to create an ongoing relationship between the two parties that would utilise the academic resources of the UoC in combination with the full-scale 'real-world' test bed that the CHCEC offered.

1.2 The Christchurch Engine Centre

The CHCEC is situated at Christchurch International Airport with the main administration facilities located alongside the domestic terminal. The company provides maintenance, repair, overhaul (MRO) and testing facilities for a range of aircraft engines. These include the Rolls-Royce Dart, Pratt & Whitney JT8-STD, and JT8-200 amongst others. An additional facility was completed at 115/117 Orchard Road in 2005, also within the vicinity of the airport.

The 2005 development of the Orchard Road site was performed to expand CHCECs capabilities to include the International Aero Engines' (IAE) V2500 range of engines. Figure 1 shows the A1 version of the IAE V2500, which comes in a number of thrust ratings, between 23000lbf and 33000lbf, and two mounting configurations (IAE, 2011). This range of engines is fitted to the national airlines fleet of Airbus', and the construction of the new CHCEC facility allowed locally-based MRO, saving costs for the company.

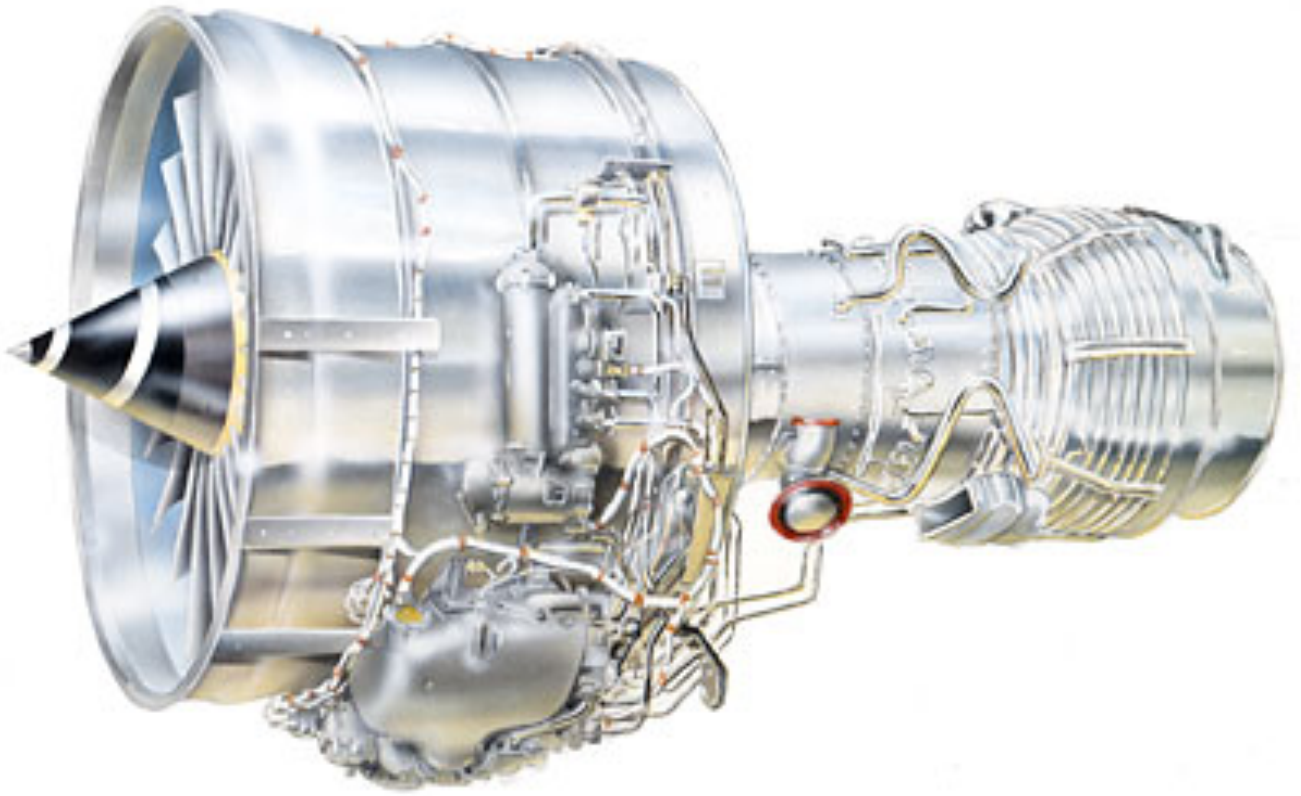

Figure 1 IAE V2500-A1 Jet Engine (Source: Rolls-Royce Website)

The Orchard Road CHCEC facilities comprise two main sections, each housed in its own building. The first is the maintenance and service section that carries out overhaul, rebuild, and inspection programmes. The second is the testing facility, the building for which is based around the CHCEC #1 test cell (referred to as the 'CHCEC test cell' from this point on). Accompanying facilities within the building include the preparation area and control room used to view and control engines whilst in the test chamber.

1.3 Jet Engine Test Cells

Prior to commercial use, jet engines are subject to performance and safety testing. To conduct off-wing testing JETCs are used. A JETC is a fully enclosed structure in which a jet engine is mounted

and operated in airflow similar to that experienced when in service. A jet engine generates thrust by accelerating airflow through its internal structure. During testing a large rate of airflow is developed in the test cell. A flow structure develops in which a number of flow patterns and features are present. There are a small number of test cell designs currently in use, all of which have been developed to achieve steady, balanced, and repeatable airflow conditions.

The three airflow criteria mentioned above are a basic safety standard. To predict and prevent problems, the industry monitors the performance over time, aka 'trending', of each and every engine in commercial service. Through performance monitoring, the condition of an engine can be assessed in an operational state. As engines are tested both before and after MRO treatment, performance trending becomes an important asset. The trended performance data gives information on the quality of the MRO treatment, and gives an indication of any potential problems that may have been introduced prior to re-installation on the aircraft. Likewise, after an engine has suffered damage, a repair can be assessed by comparing pre-incident data with post-repair data. This gives information on the completeness, safety, and reliability of the repair.

For trended performance data to be of value, repeatable test conditions must be provided. As such, the airflow in JETCs needs to be steady, consistent and repeatable. MRO treatment of each engine is not always carried out at the same JETC over their commercial lifespan. To ensure test conditions remain repeatable over a number of individual cells, a process of correlation and certification takes place. For each in-service engine make and model, a Master Test Cell (MTC) is assigned. To achieve MTC status, testing needs to be performed and analysed using what it termed a 'gold-plate' engine. A 'gold-plate' engine is an engine that has known performance characteristics as a result of testing in another MTC facility. A MTC can receive such status only when the known performance characteristics from the 'gold-plate' engine can be replicated in the new facilities testing environment (and accurately controlled and monitored with the new facilities analysis systems). In the case of the IAE V2500 series of engines, the CHCEC test cell has been given MTC status.

A MTC acts as the benchmark for all other test cells to be performance tested, and is thus required to conform to stricter performance guidelines than other JETCs. Therefore, the nature of the airflow characteristics and patterns within a MTC, such as that at the CHCEC, need to be well understood. Measurable airflow characteristics of each 'standard' cell are compared with the MTC, and a maximum deviation limit for each is imposed, below which the cell will be certified for testing. Correction factors are applied to correct engine test data so cell-to-cell comparisons are possible.

During engine testing a number of engine and cell characteristics are measured and recorded. To monitor engine performance; thrust, fuel flow properties, shaft speeds, internal engine pressures/temperatures, and actuator control locations are measured. Comparisons are made between relevant measurements to create meaningful performance parameters. Examples of these include the ratio of engine entrance and exhaust pressures, and comparison of fan speed to engine thrust.

During all testing ambient conditions and airflow parameters within the cell are monitored as an assurance repeatable test conditions are maintained. Air temperature, humidity, and pressure are measured. Corrections are then made to the collected engine data so all comparisons made during performance trending are under ‘standard day’ conditions. ‘Standard day’ conditions are a set of reference values for air temperature, density and pressure set by the International Civil Aeronautics Organization (ICAO).

1.3.1 Types of Jet Engine Test Cell

Across the industry there is some variation in JETC design, but the majority of cells fall into one (or a combination) of the two following categories; those with vertically orientated inlet and exhaust planes (‘straight-through' cells), and those with horizontally orientated inlet and exhaust plane designs (U-shaped cells).

The CHCEC test cell is U-shaped in design as shown in Figure 2. The test cell itself consists of the structures labelled ‘Inlet Stack’ and ‘Exhaust Stack’ along with a number of components that directly link the two, including that labelled as ‘Working Section’. The components of the test cell are discussed in more detail in following sections.

‘Straight-through’ cells are more commonly used with older turbo-fan and jet engines that produce lower levels of thrust. U-shaped cells have become more common with the higher thrust modern engines now in use (Flynn, 2008). ‘Straight-through’ cells require a larger footprint compared to U-shaped cells to accommodate the inlet depression and exhaust plumes. Greater airspace above U-shaped cells is required for the same reason.

An L-shaped cell (also called a J-shaped cell) is an example of a design that combines both ‘straight-through' and U-shaped design components, with the inlet stack orientated as in the former, and the exhaust stack orientated as in latter. There are a number of less used designs that contain

more complex flow paths. One example is the 'folded inlet' design that turns the airflow through a number of orientations prior to entry to the working section. The 'folded inlet' design has such benefits as increased accessibility to the working section (or 'engine test chamber') and lower sensitivity to side wind conditions (Ballough, 2002).

Figure 2 External Layout of a U-Shaped JETC (Source: CHCEC Website)

1.3.2 'Large-Scale' Jet Engine Test Cell Design Factors

In designing a JETC a large number of factors need to be considered, and can be roughly broken down into two groups. The first group of factors relate to internal test cell aerodynamics. These factors determine the flow quality and characteristics internally within the test cell, and are discussed in detail in Section 1.3.3. The second group are 'large-scale' factors that relate to the overall size and location of the JETC and its proposed site. This group includes:

- Above airspace restrictions;
- Size of engine to be tested and the flow-rate generated;
- Potential for testing of larger engines at a future date;
- Prevailing wind direction and speed;
- Access for installation and removal of engines;

- Site footprint restrictions;
- Location relative to related facilities;
- Acoustic effects on the surrounding areas;
- Structural strength; and
- Cost.

1.3.2.1 Airspace Restrictions

Airspace restrictions apply due to the location of many test cells, and the nature of the industry that they service. As with the CHCEC, many JETCs are located within the vicinity of airports. The logic in doing so in terms of reduction of transport costs and convenience are obvious. JETCs are therefore often located below flight paths of aircraft in the above airspace. The state of the airflow exiting U- and L-shaped JETCs creates large vertical exhaust plumes that have the potential to interfere with air traffic overhead.

In the case of the CHCEC, the efflux velocities are restricted by the local obstacle limitation boundary (OLB). As discussed by (Bosworth, 2005), the OLB for the site of the CHCEC is 45m above ground level. Local Civil Aviation Authority (CAA) regulations state that if efflux velocities above 4.3ms^{-1} are detected above the OLB notification to the CAA must be given.

1.3.3 'Internal' Jet Engine Test Cell Design Factors

As mentioned in Section 1.3.2, there are a number of internal factors that need to be considered when designing a JETC. This section starts the discussion of these by presenting the airflow path within a U-shaped JETC during engine testing conditions. Section 1.4 continues the discussion by defining common test cell performance parameters and introducing known test cell airflow problems that these parameters are used to detect and prevent.

1.3.3.1 Airflow Path within a Jet Engine Test Cell

Figure 3 shows a simplified airflow diagram for a U-shaped JETC. For a U-shaped test cell the air path originates in the atmosphere surrounding the inlet stack. When the engine is running, air is drawn through the inlet stack. The inlet stack contains a number of baffles to reduce noise emission (Doelling & Bolt, 1961). The air is turned at right angles into a horizontal direction with the assistance of a turning-vane arrangement.

Prior to entry into the working section, debris and large eddies are removed via Foreign Object Damage (FOD) and turbulence screens. Depending on cell size and design, an additional set of baffles may be in place prior to the working section. An example of this in practice can be seen at the General Electric test facility in Peebles.

The working section of the cell is generally feature-free up to the engine inlet face. At the plane of the engine inlet (shown in Figure 3) the airflow splits into two paths. One path passes through the engine, and the other passes around the engine, between the engine body and the test cell walls.

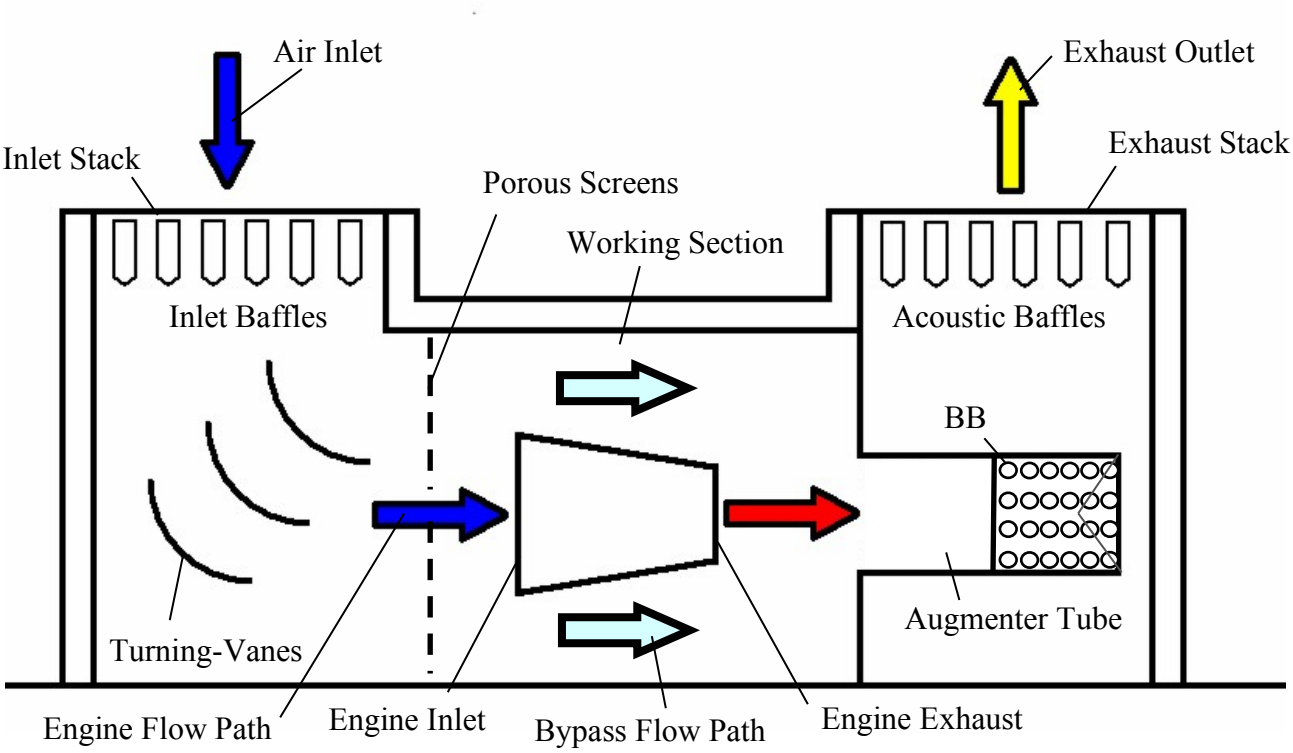

Figure 3 Airflow Paths through a U-shaped JETC

Drawn in by the depression created by the engine's fan and first stage compressor, the engine airflow is encapsulated in what is termed the 'inlet stream-tube'. The two-dimensional bounds of an inlet stream-tube are illustrated in Figure 4 by the green lines that encapsulate all streamlines entering the engine inlet.

After the airflow enters the engine, it is split into two further paths, an engine bypass flow and a combustion flow. The engine bypass flow bypasses the combustion process in the core of the engine. This flow is pumped (by the inlet fan) between the core of the engine and the engine cowling to the engine bypass exhaust face (shown in Figure 4). The combustion flow is drawn through the core of the engine and is compressed, combusted, and exhausted through the engine

core exhaust face (shown in Figure 4). The overall flow exiting the engine is therefore made up from components of both the engine bypass and core flows.

The portion of flow that passes between the engine and the test cell walls, termed the cell bypass flow, is drawn past the engine inlet and remixes with the engine exhaust downstream. The mechanism drawing the cell bypass flow past the engine inlet is the entrainment effect.

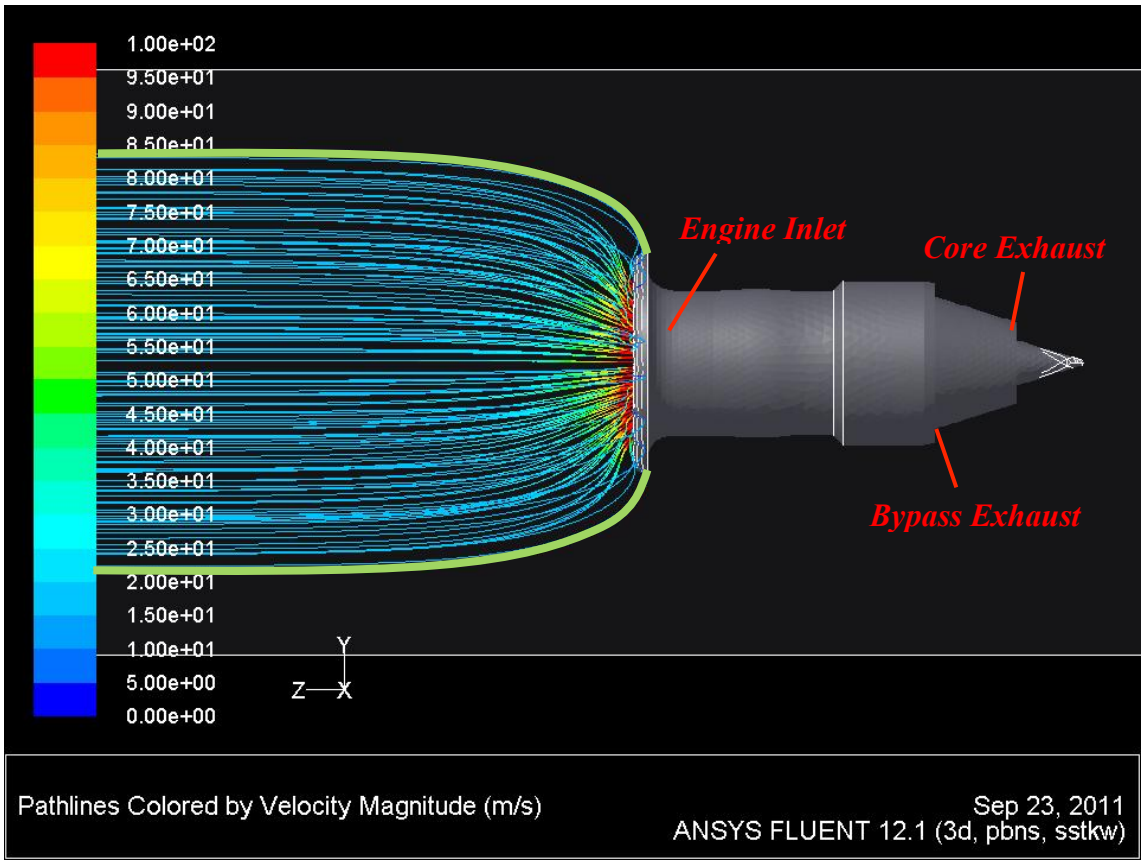

Figure 4 Profile of an Engine Inlet Stream-Tube

The entrainment effect occurs when momentum is transferred, via turbulent mixing, from the high velocity flow of the engine exhausts to the comparatively low velocity of the bypass flow (Massey, 2001).

The recombined engine and cell bypass flows enter an augmenter tube (shown on the right hand side of Figure 5). For the design shown in Figure 5, the airflow is then abruptly dispersed and reoriented in blast basket (BB). In the example of Figure 5 the BB is a perforated extension of the augmenter tube that terminates with a forward-facing cone.

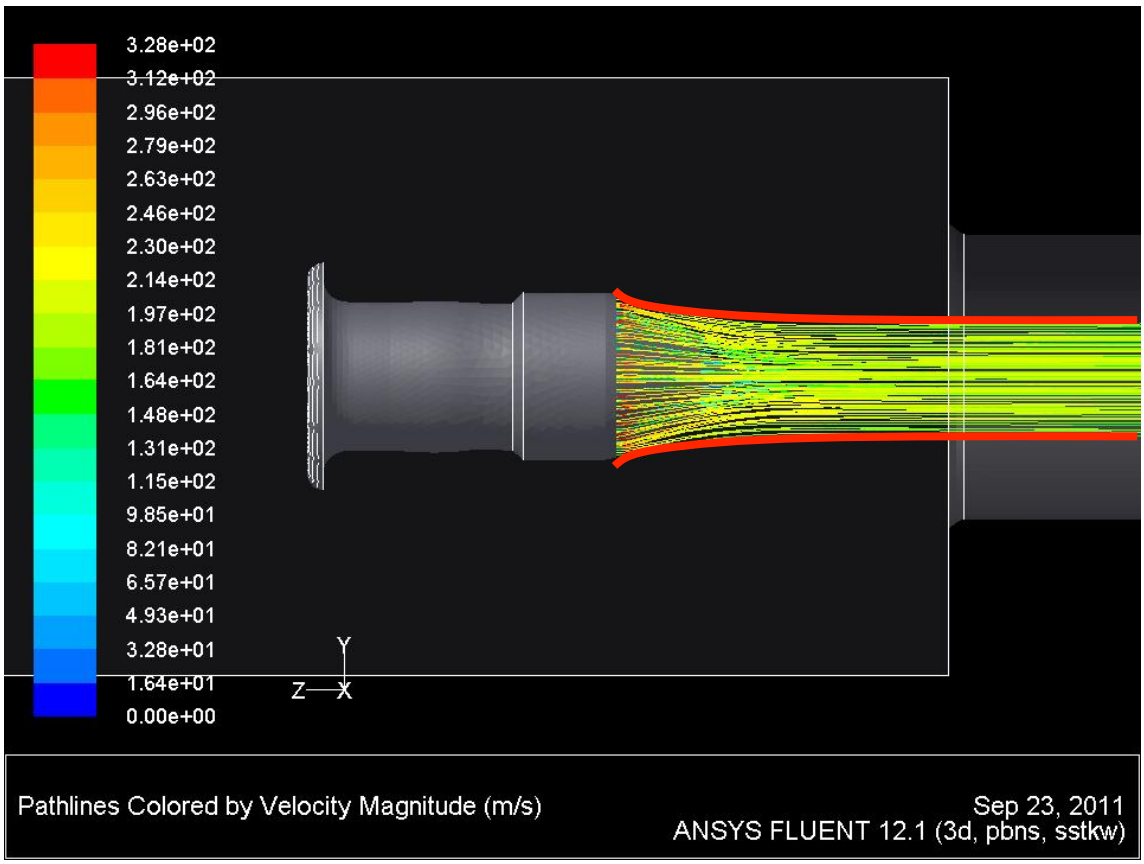

Figure 5 Profile of an Engine Exhaust Stream-Tube

Through contact with the exhaust stack surfaces, and momentum transfer with re-orientated exhaust stack flow, the airflow exiting the BB is forced vertically upwards. The airflow passes through a further set of acoustic baffles before being expelled into the atmosphere.

There are a number of other mechanisms that can be used in place of the BB and exhaust stack combination to exhaust gases from the working section of a JETC. If surrounding space allows, the augmenter tube can be designed to eject the test cell air directly into the surrounding atmosphere with no further treatment or redirection. This requires the facility to possess a significant clear area downstream of the augmenter exhaust.

An external jet blast deflector (JBD) is sometimes used downstream of the augmenter exhaust face. A JBD is often not little more than an angled ramp (at 45° – 60°), and primarily work to redirect the exhausted flow in a more vertical direction. A JBD has the advantage of limiting the amount of clear area required downstream of the augmenter exhaust. JBDs come in many forms, from stationary to fully adjustable and automated units with cooling systems installed. The construction materials can vary from simple concrete, to metal or fibreglass.

1.3.3.2 Features of a Jet Engine Test Cell Working Section

Upstream of the engine inlet the working section of a test cell is generally featureless to ensure consistent airflow enters the engine. However, downstream of the engine face there are a number of objects which come in contact with the airflow. Most JETCs, including that at the CHCEC, have wall- and ceiling-mounted fixtures such as lighting, cameras, and ladders that protrude into the cell. In some cases the features are recessed into the walls. When not recessed they can protrude up to 500mm as shown in Figure 6. Substantial piping and nozzles for fire suppression systems is a feature that is always present.

To transport an engine into a cell a number of methods are employed. The most common method, as utilised at the CHCEC, uses a monorail system that enters via a door located in a sidewall of the cell (Flynn, 2008). Generally the monorail enters the cell perpendicular to the wall, and turns 90° before placing the engine in a thrust-bed.

The thrust-bed performs a number of functions including; supporting the engine, measuring thrust produced, supporting fuel, power and compressed air supply lines, and as an interface for the data acquisition (DACQ) system. The requirements of the thrust-bed mean that the structure is significant, and creates a large blockage between the ceiling of the cell and the engine.

To access the engine when installed in the cell, retractable work platforms are used. At the CHCEC the work platforms are raised from the base of the cell and are then retracted during testing. Guardrails are installed for safety purposes which, when the platform is retracted, can protrude from the floor by up to 1m.

1.4 Jet Engine Test Cell Measures of Performance and Problem Identification

In order to measure the performance of a JETC there are two main parameters that are analysed, velocity distortion upstream of the engine inlet face and the cell bypass ratio (BPR). Velocity distortion and cell BPR are discussed in detail in Section 1.4.1 and Section 1.4.2 respectively. These performance parameters are an important tool for a test engineer. They enable potential cell problems such as vortex formation, exhaust re-ingestion, and side-wind sensitivity to be predicted.

1.4.1 Velocity Distortion

Velocity distortion is a measurement of the quality and consistency of airflow over a given plane. In a JETC scenario velocity distortion, as a percentage, is calculated using Eq. 1.1 applied over a plane orientated perpendicular to the cell walls in the upstream portion of the working section.

$$v_{dist} = \frac{u_{\max} - u_{\min}}{u_{avg}} \times 100 \qquad \text{Eq. 1.1}$$

Most commonly dynamic pressure readings are simultaneously taken at a number of points 5-10m (2-3 bell-mouth diameters) upstream of the engine inlet face. The pressure data are converted into velocity data, upon which Eq. 1.1 is applied. Alternatively velocity readings can be taken directly via an anemometer.

There are a number of anemometer technique variations that can be used including thermal, cup-vane, and winged arrangements. The number and arrangement of the data extraction points vary from analysis to analysis, but a common arrangement uses 25 data extraction points spread across five columns and five rows.

In order for a test cell to be certified for use, velocity distortion must be less than a specified value (e.g. 15-30%). If a cell produces a higher distortion value than desired, the innermost nine points on the collection plane are often analysed individually and the certification re-evaluated (Flynn, 2008).

1.4.2 Cell Bypass Ratio

Cell BPR (as a percentage) is a measure of the way the two airflow paths in the working section are distributed. As a percentage, the cell BPR is calculated using Eq. 1.2 and measurements of the engine and cell mass flow rates (MFRs).

$$CellBPR = \frac{MFR_{cell} - MFR_{engine}}{MFR_{engine}} \times 100\% \qquad \text{Eq. 1.2}$$

Figure 6 Wall Mounted Working Section Features and Thrust-Bed

The same engine being tested in the same test cell will generate a different cell BPR for each thrust level it is tested at. The cell BPR that test engineers use to analyse cell performance is taken under maximum thrust conditions. At maximum thrust the cell is under its maximum 'aerodynamic strain', and thus is likely to show unwanted flow pattern problems more readily.

Caution needs to be taken to ensure that the cell BPR is not confused with the engine BPR, which is defined in Eq. 1.3.

$$EngineBPR = \frac{MFR_{inletfan} - MFR_{core}}{MFR_{core}} \times 100\% \qquad \text{Eq. 1.3}$$

The engine BPR is the MFR ratio of air entering the engine inlet face, but bypassing the core, to the MFR of air entering the engine inlet face, and passing through the core. The engine BPR is used to measure performance of an engine, and is in no way used as a test cell performance parameter.

During operation, the magnitude of the static pressure loss created by internal cell components (i.e. inlet stack lip, acoustic baffles, turning-vanes, porous media, working section features, augmenter transition, augmenter, BB, and exhaust stack etc.) all contribute to the achievable cell BPR. The higher the cell pressure losses are, the lower the cell BPR is. The consequences of not maintaining a sufficient cell BPR can be severe. An accepted industry minimum for cell BPR, below which testing could prove problematic without the inclusion of additional airflow aids, is 80% (Clarke, 2000). A general rule in relation to cell BPR is, the higher that can be achieved, the safer the test environment.

Unacceptable levels of velocity distortion and cell BPR can indicate a number of problems pertaining to the quality and safety of the engine test environment. Section 1.4.3 through Section 1.4.5 discuss a number of potential cell problems, and indicate how prevention or detection of these problems can be determined by monitoring the velocity distortion and cell BPR.

1.4.3 Inlet Vortices

Inlet suction operation near a solid surface is often associated with the presence of vortex behaviour (Shin, Cheng, Greitzer, & Tan, 1986). The structure of the vortex is anchored to a point on the solid surface and stretches to the inlet suction face. When operating a jet engine over a ground plane, as in a JETC scenario, the criteria required to set up inlet vortex phenomena can be created. Inlet

vortex generation and ingestion by gas turbine engines can cause a number of problems including FOD, blade erosion, compressor surge, and compressor stall (Shin, Greitzer, Cheng, Tan, & Shippee, 1986).

In relation to jet engines there are a number of factors that contribute to the formation of inlet vortices including; engine thrust level, engine inlet diameter, distance of the engine inlet from a solid surface, ambient vorticity, and the direction of atmospheric flow relative to the engine centreline (Jermy & Ho, 2008).

Two mechanisms have been identified as being responsible for inlet vortex formation. The first mechanism is the amplification of upstream vorticity (De Siervi, Viguer, Greitzer, & Tan, 1982). The second mechanism can be formed without the presence of upstream vorticity, and occurs due to a variation in circulation along the inlet face. Variation in circulation along a face occurs in such cases as a jet in a cross wind (Shin, Greitzer et al., 1986). Only the first mechanism is relevant when discussing vortex formation in a fully enclosed JETC, and is the focus of the remaining discussion.

For vortex formation (induced by the amplification of upstream vorticity) to occur in a JETC, several conditions must be met (De Siervi et al., 1982; Kline, 1953). Firstly, there must be a vertical component of upstream vorticity. In a test cell, the presence and extent of upstream vorticity can be detected through monitoring velocity distortion data taken across an analysis plane perpendicular to the cell flow. Secondly, the inlet stream-tube from the engine must intersect with a solid surface. If the second condition is satisfied, it is then possible for a third condition to be met, where a stagnation point is generated on the solid surface. This stagnation point provides a site at which a potential vortex can be anchored.

In order for the second and third conditions to be met, four independent factors are considered; engine inlet diameter (*Di*), distance of the inlet from a solid surface (*H*), the main-stream velocity (*Vi*), and the engine inlet velocity (*Vo*). The first and second factors can be combined in a ratio which is termed the ‘distance threshold’ (*H/Di*). The third and fourth factors can be combined as a ratio that is termed the ‘blow-away velocity’ (*Vi/Vo*). These two ratios are often combined in a plot of *H/Di* against *Vi/Vo* (Jermy & Ho, 2008). Figure 7 shows such a plot with experimental data collected by (Glenny & Pyestock, 1970; Liu, Greitzer, & Tan, 1985; Nakayama & Jones, 1996; Ridder & Samuelsson, 1982; Ruehr, 1975; Shin, Greitzer et al., 1986).

A line determining a threshold can be fitted between the point where no vortex is present, and the point where a vortex has formed. From Figure 7 it is seen that for a given ‘distance threshold’, the ‘blow-away velocity’ needs to be below a certain value for a vortex to form. If the ‘blow-away velocity’ is too high, the vortex structure is blown away.

1.4.3.1 Inlet Vortices on a Runway

Due to the large size of the inlet face on modern high bypass jet engines, vortex formation problems have arisen with low-slung engine mountings and the associated limited engine-ground clearance. The combination of a large inlet face diameter (*Di*) and comparatively limited ground clearance (*H*) have lead to inlet vortices being generated on airport runways during taxiing and reverse thrust operation (Motycka & Walter, 1975). When an on-wing engine ingests an inlet vortex, the vortex anchor point is generally the runway surface.

In a runway situation, when an engine ingests a vortex, damage can occur in a number of ways. Small particles can be lifted in the pressure field of the vortex and ingested into the engine (Glenny & Pyestock, 1970). If this occurs repeatedly over a period of time, a heightened rate of fan blade erosion results. The low-pressure field of the vortex can be of such a magnitude that portions of loose runway material can be ingested. Particles large enough to put an engine immediately out of service are capable of being lifted and ingested into the engine. There is also the potential for engine compressor surge and/or stall as the rate of air entering the engine varies and the correct oxygen-to-fuel ratio is disrupted.

1.4.3.2 Inlet Vortices in a Test Cell

The presence of vortex behaviour is often not visible. When an inlet vortex is formed in a JETC this causes additional problems. Engine performance data will often show fluctuations in fan speed and thrust levels. Trending of engine performance may then lead to false conclusions about the state of the engine under examination, as the cause of the fluctuations will not be readily apparent. In high humidity conditions, a vortex may become visible as the moisture in the air condenses within the vortex as seen in Figure 8.

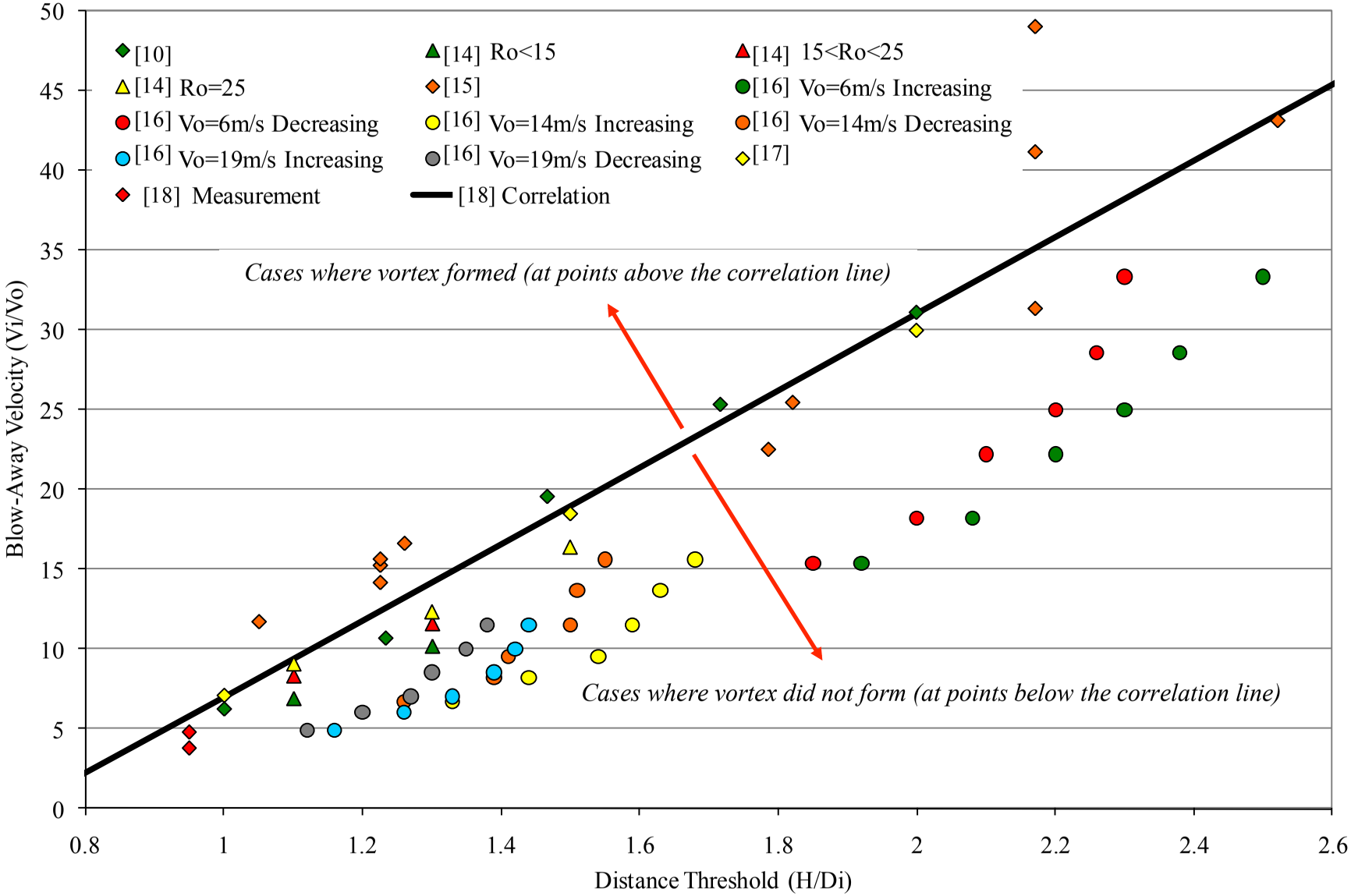

Figure 7 Collation of Experimental Data Establishing Vortex/No-Vortex Threshold

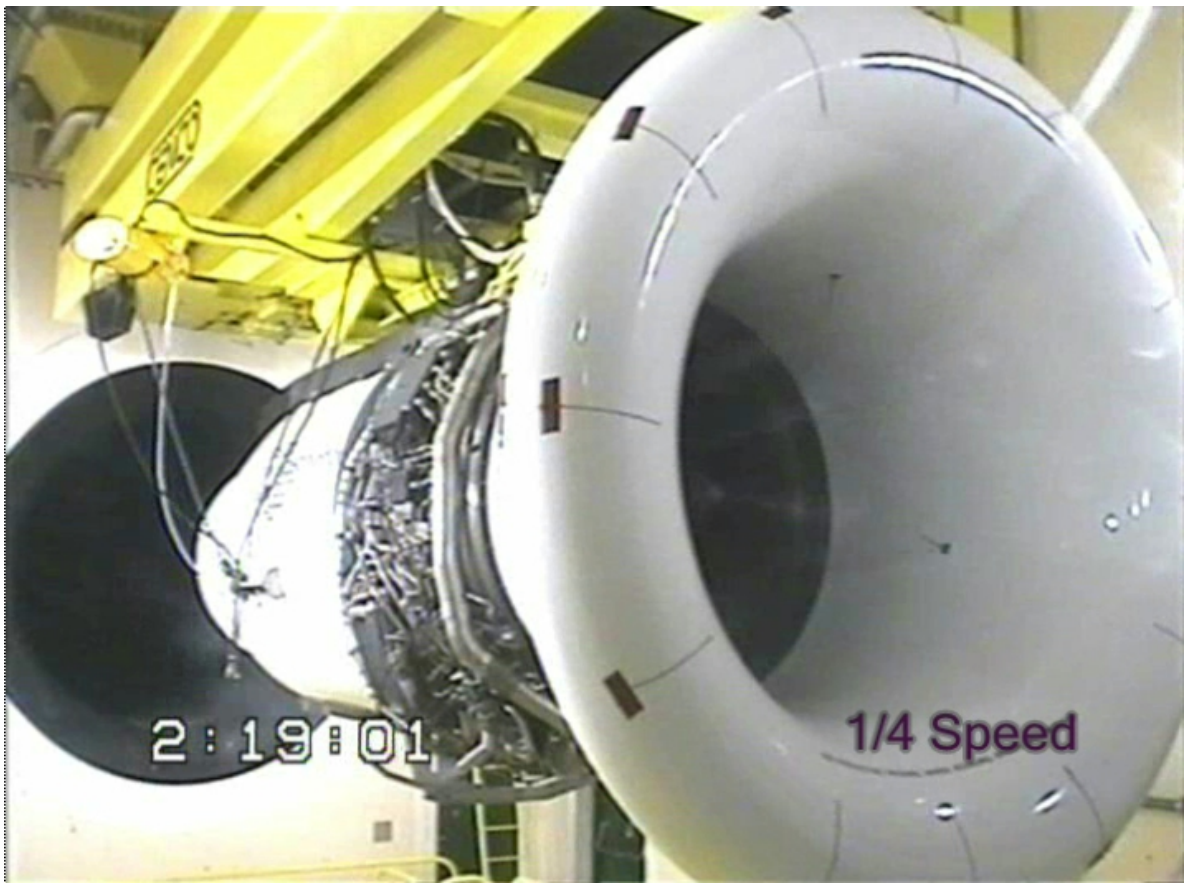

Figure 8 Inlet Vortex Production during Engine Testing in a JETC

In a JETC the large number of solid surfaces within the vicinity of the engine inlet face provides multiple options for vortex anchor points. In addition, the cross-sectional area of a test cell limits the amount of flow that can bypass the engine. An insufficient amount of cell bypass flow can be detected through monitoring of the cell BPR. Limiting the cell bypass flow leads to low values of 'blow-away velocity', and results in heightened vortex potential.

1.1.1.1 Vortex Avoidance Strategies

To avoid particle ingestion via inlet vortex in a runway scenario there are a number of methods that have been trialled experimentally. Such methods include the use of 'blow-away jet debris guards', and mechanical barriers (Glenny & Pyestock, 1970). (Glenny & Pyestock, 1970) also discusses modifications to operational techniques by progressive throttle application. This avoids the potential of generating a low 'blow-away velocities' scenario, occurring when an engine is run at full throttle on a stationary, or nearly stationary, aircraft. The strategy adopted worldwide however is to keep runways well swept, thus removing any potential material that could be ingested.

In JETCs the most common method of vortex avoidance is to retain high cell BPRs. As mentioned in Section 1.4.2, cell BPRs less than 80% are generally considered too low to test an engine safely (Clarke, 2000). In cells with low BPR, the engine inlet stream-tube expands more significantly towards the working walls than in a high BPR cell. The consequence of the more prominent stream-tube expansion is the potential for the stream-tube to intersect a solid surface within the working section. If such a scenario occurs, the criterion for a vortex anchor point to form is created.
The exact pressure losses, and therefore cell BPR, for a test cell are not often fully determined until construction of the cell is complete, although scale modelling can provide loss predictions. Correlation and certification runs are then used as the first real test of the achievable cell BPR. If problems are detected as being present during correlation and certification, retrofit solutions are then sought as a remedy.

The overall geometry of the cell and the location and size of protruding fittings cannot be easily modified to increase cell BPR. Retrofit solutions therefore concentrate on reducing and/or removing upstream vorticity and inlet vortex anchor points. To reduce and/or remove upstream vorticity, a common practice is to install blockages upstream of the engine inlet. An example of such a treatment is seen in Figure 9.

The cell shown in Figure 9 initially had a vertical velocity distortion with velocities in the upper section of the cell exceeding those in the lower section. Blocking plates were added to provide an additional pressure loss in the upper section of the cell to equalise the velocity profile. A slight horizontal distortion was also present, and resulted in the offset placement of the uppermost blocking plate.

Even with minimal upstream vorticity, operation of a low BPR cell with no additional airflow treatment is deemed risky. The increased thrust and larger inlet face diameters of newly developed engines mean existing facilities are at times aerodynamically strained, and a cell BPR of 80% cannot be achieved. In cases where an undesirably low cell BPR is present, airflow ramps are often employed. The use of airflow ramps in test cells is a patented design idea by United Technologies Corporation (UTC). With the use of an inlet ramp, engines can safely be tested with BPRs as low as 40% (Clarke, 2000).

Airflow ramps are installed along the ceiling, floor and/or walls of the working section. The ramps are located in the stream-wise direction within the vicinity of the engine inlet face. The upstream face of the ramp provides an angular redirection of the airflow into the engine inlet as shown in Figure 10. The

effect created is that of a ‘picture frame’. By redirecting the airflow away from the solid surfaces, an inlet vortex anchor point is unable to form.

Figure 9 Blocking Plates Mounted on the a FOD Screen, viewed from Downstream (top), and Upstream (bottom)

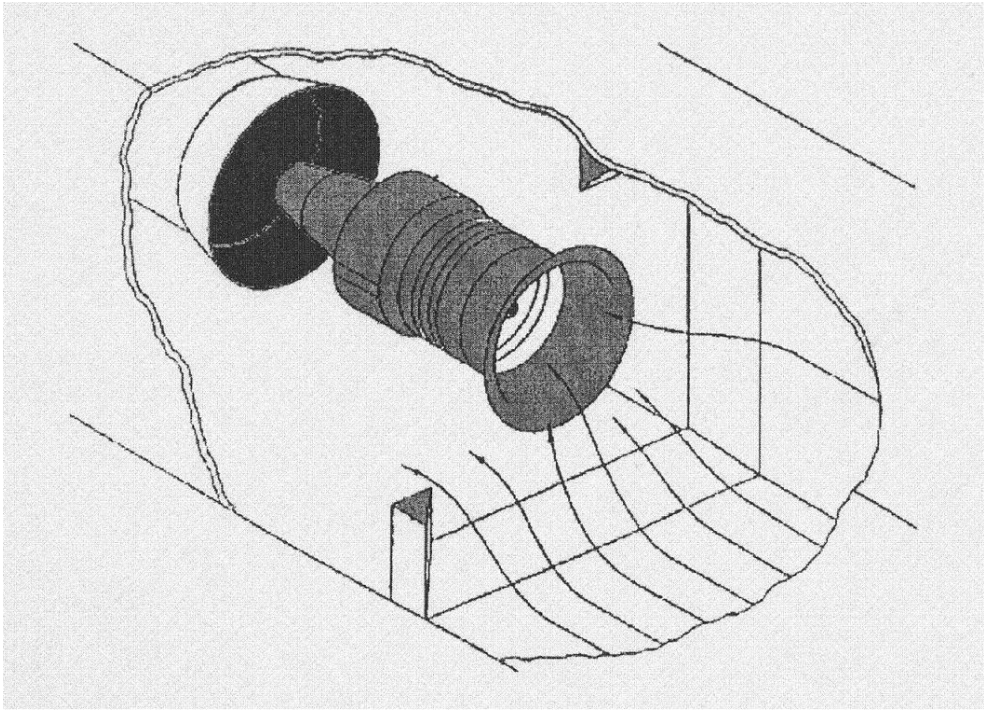

Figure 10 Test Cell Working Section with Inlet Ramp (Source: (2000))

Figure 11 Working Section with Ceiling Mounted Inlet Ramp

Test cell airflow ramps come in various forms. If a vortex is known to be forming during testing, and the surface where it is anchored to can be identified, a ramp applied along a single side of the cell is

employed. These ramps are often placed along the ceiling of the cell, as in the example shown in Figure 11 (Clarke, 2005). The suspected cause of vortex formation along the ceilings of cells, in comparison to the walls or floor, is the large obstruction of the roof-mounted thrust-bed and the rapid growth of the ceiling boundary layer (BL).

Alternatively, a full cell ramp can be fitted against all four surfaces of the cell floor, ceiling, and walls. This removes the possibility of a vortex forming from any of the working section surfaces, and is most often used as a preventative measure.

1.4.4 Internal Exhaust Re-Ingestion

Internal exhaust re-ingestion occurs when the cell BPR is so low that the depression created at the engine inlet fan causes some of the exhausted engine gases to re-circulate and re-enter the engine inlet face (Sapp, 1978). This is undesirable as the chemical makeup of the airflow entering the engine (now containing a portion of combustion by-products that lack oxygen and are at high temperature) is inconsistent. Lack of consistency in the engine airflow causes combustion fluctuations. These fluctuations mean performance trending cannot be accurately performed.

1.4.5 Side-Wind Sensitivity

During testing, the effect of atmospheric wind can disrupt the performance of a test cell. The effect of atmospheric wind on testing will be dependent on both its direction and velocity. When a component of the atmospheric wind flows perpendicular to the lengthwise axis of the cell, a side-wind condition is created. A majority of test cells have atmospheric condition limitations, outside of which engine testing does not take place. These limitations are put in place to ensure trend monitoring is performed in a consistent environment as well as to protect the engine under examination.

Heightened velocity distortion and the generation of vorticity can occur during high velocity side-wind conditions. The vorticity has the potential to be magnified by the suction at the engine inlet face (as discussed in Section 1.4.1) and create a condition where an inlet vortex forms. Wind velocity, wind direction, cell orientation, inlet stack height, inlet stack ‘lip’ profile, the presence of side-wind dampening devices, and internal test cell components upstream of the engine are only some of the factors influencing velocity distortion and generation of vorticity in a side-wind condition.

1.5 Current Jet Engine Test Cell Design Practices

The development of new test cell designs, and tuning of current designs, is limited. This is partly due to the lack of an appropriate analysis tool to efficiently analyse and design various concepts. In addition, the industry is naturally conservative and therefore reluctant to modify designs that have had a good track record. However, engines themselves are changing rapidly, and the requirements of off-the-wing test environments are changing with them.

Currently test cell designers utilise three main sources of information. Firstly, is full-scale and scale model data that contribute a significant amount of information. Secondly, is the knowledge gained through operational and testing experience of engineers. Thirdly, are one-dimensional pressure loss calculations that supplement this work by providing rough predictions of cell static pressure loss.

Scale modelling, whilst currently an extremely valuable investigative tool in JETC design, uses scaled gas turbine engines and as a result is an expensive process. One-dimensional pressure loss calculations provide no information on the flow structure developed within a cell. This means that problematic flow features are in many cases not identified during the design stage.
To attain a given cell BPR, cell designers often simply alter the cell geometry and features of current designs. Larger engine MFRs lead to larger cell cross-sections that contain cell components that balance pressure loss against acoustic and turbulence treatment.

The limited amount of pre-construction data allows potential problem areas to go undetected until operation of the cell commences. Problem-solving modifications to the constructed cell are then made retrospective of initial full-scale testing. The same design techniques are applied during the problem solving phase, leading to ‘trial and error’ solutions being developed.

Airflow ‘solutions’ implemented retrospective of the initial construction often detrimentally affect aerodynamic efficiency. Figure 9, and the related discussion in Section 1.4.3.3, is an example of this. Aerodynamic efficiency also suffers when cell and component designs are not thoroughly investigated and ‘fine-tuned’.

1.6 Computational Fluid Dynamics

CFD is the numerical simulation of systems that incorporate fluids in either a static, or most commonly, dynamic state. CFD incorporates the three different disciplines of physics, mathematics, and computer science. The physics aspect brings the governing conditions of fluid flow and heat transfer. These conditions can be described through mathematical equations, usually expressed in partial differential form, that are then converted and solved using the programming languages and software packages of computer scientists (Tu, Yeoh, & Liu, 2008). Development of CFD was seen as early as the late 1920's, but application into R&D fields was not seen until the 1960's (Chung, 2002).

To assist engineers in design and problem-solving tasks, experimental or theoretical disciplines have traditionally been employed. With the advent of high-powered digital computing, CFD has emerged as a viable third accompanying option. The three investigative alternatives are strongly linked, both in terms of their development and supplementing each other in real-world application. The future development of CFD relies on the inputs from both of the other disciplines. This comes in the form of verification of mathematical and computational code by the theoretical discipline, and validation of the CFD solutions through comparison with experimental work. It is important to note that the three disciplines work well to complement each other, and should not be viewed as replacements or competitors to one another.

As a research tool CFD is employed to gain greater understanding of the physical events and processes that are present in fluid flows in and around objects of engineering interest. Many of the flows of engineering interest have non-linear characteristics, and as such, a full understanding cannot be provided through analytical methods alone. This provides the motivation to use numerical methods.

The numerical methods of CFD are analogous to 'wind tunnel testing', and effectively provide the results of a 'numerical experiment' (Tu et al., 2008). The depth of data that can be collected from a 'numerical experiment' is far greater than can be achieved through its physical counterpart. The ease at which a large number of designs can be tested, and the relative compactness of the 'experimental' equipment, affirm the value of CFD.

1.7 Project Scope

1.7.1 Development of the Project Scope

The overview of test cell design practices presented in Section 1.5 discusses an industry and scenario that would strongly benefit from the application of the CFD techniques discussed in Section 1.6. This situation was recognised by the CHCEC and the UoC, and led to the formation of a final year undergraduate project in 2005 (Agmen et al., 2005). The work of (Agmen et al., 2005) showed the substantial merit of applying CFD in the JETC industry, and thus led to the formation of this postgraduate project.

Section 2 will discuss the development of CFD as an analytical technique. It will show that a number of assumptions, approximations, and models are used to turn the physical principles that CFD is based on, into a useful analytical tool. To achieve this, a problem-specific validation is required to obtain quantitatively accurate CFD solutions.

Performing a problem-specific validation of CFD techniques to JETC analyses was identified as the primary goal in the formation of this project. This goal led to the formation of objectives that planned to significantly utilise the CHCEC test-bed to generate experimental validation data for the CFD techniques developed at the UoC.

Experimental data are of importance in establishing quantitatively valid CFD solutions for two reasons. Firstly, the data provides accurate physical parameters to be used as inputs into the CFD models. Secondly, the experimental data is used to validate the accuracy of the CFD techniques once applied, and a solution developed.

Unfortunately, due to a number of circumstances, the gathering full-scale experimental data was unable to be performed within this project. Likewise, the opportunity to gather data from a scale modelling experimental effort was unable to be achieved, and as such, the project goals were reassessed.

Whilst the full problem-specific validation process was unable to be performed as intended, a significant contribution towards it could be achieved. A sound validation process involves both experimental and computational contributions. Recognising this, the new objective was formed of

producing the computational contributions, through which later experimental work could be quantitatively validated against.

Recommendations from the literature, along with solid reasoning, and engineering knowledge were therefore applied to generate CFD solutions that could be qualitatively analysed in performing the second objective of the project. This second objective was to perform a number of detailed qualitative analyses which would give a greater understanding of the flow patterns developed in an operational JETC.

Once the understanding of the flow patterns was developed satisfactorily the third objective of the project aimed at improving JETC performance characteristics. This was achieved through employing a CFD-aided design processes based on the techniques developed in the earlier objectives. The performance characteristic that was the main focus of the design and development efforts was cell airflow efficiency. Cell airflow efficiency was defined as the mass flow rate of air passing through the cell under a certain engine thrust condition. The greater the mass flow rate produced, the more efficient the cell was deemed in regards to airflow. The secondary focus of the design and development effort was to reduce velocity distortion in the upstream region of the working section. The benefits in achieving both of these were discussed in Section 1.4.

Through applying consistent CFD techniques throughout the design processes, both quantitatively comparative and qualitative analyses could be performed with confidence. Through utilising CFD techniques throughout the design process, the technique of CFD itself could be analysed as a problem solving and design tool. This subsequently became the fourth objective of the project. Section 1.7.2 discusses the layout of this thesis, showing how the revised goals of this project were achieved.

1.7.2 Thesis Layout

Each internal component of a JETC performs its own specific task. Acoustic baffles are used for pressure wave suppression, turning-vanes to rotate airflow through a desired angle, the working section houses a testing environment, and the augmenter and BB are used to extract and dissipate flow into the exhaust stack.

The research reported in this thesis analyses a number of major cell components individually. Through doing this an understanding of the flow patterns produced as a result of cell components interaction with the airflow was achieved. Once this basic understanding was obtained, the design of the components was analysed, and alterations were made in CFD-aided investigation and design processes. To drive the design process, the cell performance parameters of cell BPR and velocity distortion were used. These parameters formed a benchmark to monitor the success of the design iterations throughout the design process.

Section 1.7.2.1 through Section 1.7.2.6 discuss the thesis layout and details on how the above-mentioned goals were achieved.

1.7.2.1 Computational Fluid Dynamics – Investigations Tool

Throughout this project the primary investigative tool was CFD. As such, Section 2 provides a background in the development of CFD. Section 2.2 shows how the governing physics equations are transformed into a useful analysis tool. Areas where assumption, estimation, and modelling are used in the development of CFD techniques are demonstrated. These are presented in an effort to illustrate the nature in which CFD solutions are produced, and more importantly how they should be interpreted.

Section 2.3 then discusses the process required in setting up and performing a CFD calculation. In the process of doing so there are a number of decisions that need to be made. These decisions are almost always dependent on the problem being analysed. As such, Section 2.3 and Section 2.4 discuss some of the choices that a CFD analyst has available.

The remainder of the thesis is presented in a manner that follows the natural internal airflow path through a JETC during operation. This flow path starts with the acoustic baffle arrangement in the inlet stack, followed by the turning-vane arrangement, the working section, the augmenter entrance, the BB, and the exhaust stack.

1.7.2.2 Acoustic Baffles

Section 3 investigates the acoustic baffle arrangements. These arrangements are present in the inlet and exhaust stacks of a U-shaped JETC. Baffle arrangements normally contain in excess of 30 individual

baffles distributed in a structured pattern. The baffles, in combination, act to dampen pressure wave emissions created through engine testing.

In Section 3 a standard baffle design is assessed through a CFD analysis. The primary flow features in the arrangement are identified. A CFD-aided design process is then performed. The driving force behind the design process was increased cell BPR, and the benefits that such an improvement would bring.

1.7.2.3 Turning-Vane Arrangement

Downstream of the baffle arrangement is the turning-vane arrangement, which is investigated in Section 4. This investigation contained several steps. Firstly, a validation analysis, using externally sourced experimental data, was performed to determine the validity of the techniques used in the analysis of the CHCEC turning-vanes by (Agmen et al., 2005).

Secondly, the main body of Section 4 then investigates a standard turning-vane arrangement through CFD analysis. Flow patterns in and around the arrangement are identified along with areas of potential flow distortion and inefficiency. A CFD-aided design process was then performed. The primary driving force behind the design process was decreased velocity distortion downstream of the arrangement.

1.7.2.4 Working Section and Augmenter Transition

Downstream of the turning-vane arrangement is the working section. Section 5 initially gains an understanding of the flow patterns that develop when a jet placed upstream of an abruptly contracting square-to-circular duct.

An investigation is then carried out to establish how the components in the rear of the working section, being the engine and augmenter tube, interact to vary the flow patterns and cell BPR. A similar analysis is then performed to determine the influence working section cross-sectional shape had on flow patterns in the rear of the working section.

A CFD-aided design process is then performed to develop the proposal of a ‘retrofitable’ rear cell ramp. The design of the ramp, as a cell efficiency aid in currently built cells, is computationally analysed, and the original design tuned through consultation with the CFD solutions generated.

1.7.2.5 Lower Exhaust Stack

Downstream of the working section is the augmenter tube, BB and exhaust stack. Section 6 investigates the interaction of these three components. Initially a thorough understanding of the flow patterns exiting the BB and being re-orientated in the lower exhaust stack is achieved through CFD analysis.

The interaction of the BB and lower exhaust stack was then analysed by adjusting the BB geometry, and then the location of the BBs relative stream-wise location within the exhaust stack. Findings were made in relation to heightened cell BPR through the BB relocation, and attempts were then made to replicate these gains through the employment of ‘retrofitable’ devices for current cells.

Finally, several BB design iterations were developed in order to promote a more efficient flow pattern by isolating the lower exhaust stack. The driving force behind the lower stack isolation design process was an increase in cell BPR.

1.7.2.6 Conclusions

The summaries of findings for Section 2 through Section 6 are presented at the end of each of the respective chapters. The summaries of findings for Section 2 through Section 6 are presented at the end of each of the respective chapters. Section 7 then concludes this thesis by collating all the findings made, and presenting a relevant discussion of the topics covered. Particular mention is made in Section 7 of how the respective sections in this thesis contributed to the original goals of the project. A discussion of areas worthy of future research efforts is presented as Section 7.1.

2 Investigative Tool - Computational Fluid Dynamics

The major investigative tool used throughout this thesis is CFD. This section is provided as an introduction to CFD concepts, terminology, and limitations. The considerations required when employing CFD during an analysis are also discussed. This section is not intended as an all-encompassing description of CFD and the relevant methods and techniques included. It should however be viewed as a background overview of CFD for a novice. Particular focus is placed on the parameters applicable to the work carried in this thesis.

Section 2.1 gives a brief and general overview of what CFD is, how CFD has been developed as a solution technique, and the steps required in performing a CFD analysis. Section 2.1 does not discuss any particular aspect of CFD in detail in an effort to enhance the continuity and flow of the overview. Instead, extensive reference is made to Section 2.2 through Section 2.4 where more detailed discussions of relevant CFD aspects are presented.

2.1 Overview of Computational Fluid Dynamics

CFD is a branch of fluid mechanics. Fluid mechanics encompasses fluids in both static and dynamic state. As the name implies, CFD is primarily concerned with the dynamic state, and predicts flow fields through the utilisation of numerical methods and algorithms.

Fluid dynamics is governed by three fundamental principles, being that energy, momentum, and mass are conserved (Currie, 2003). The most common way to express these principles in fluid dynamics is in the form of partial differential equations (PDEs), the development of which is shown in Section 2.2.1 through Section 2.2.3. These PDEs can be related to one another through the equations of state, discussed in Section 2.2.4 (Versteeg & Malalasekera, 2007).

For a Newtonian fluid, the PDEs developed through the conservation of momentum principle form the Navies-Stokes (NS) equations, discussed in Section 2.2.5. The NS equations, energy conservation PDE, and the equations of state form the governing equations for the motion of a Newtonian fluid, as presented in 2.2.6 (Currie, 2003).

Numerical methods are often required to solve the PDEs in the governing equations due to their mathematical complexity. Numerical methods, as employed in CFD, are used to give approximate, but accurate solutions, to complex problems. As such, CFD does not produce exact analytical solutions, but instead produce very close approximations that fall within 'reasonable' margins of error. In engineering applications these close approximations are in the vast majority of cases adequate.

There are a number of forms of CFD, based on how the turbulence in the flow under investigation is treated. Of the available forms, Direct Numerical Simulation (DNS) generates the most accurate results, as it computes all turbulent fluctuations within the flow being analysed (Fluent, 2006). Turbulent flows however are very complex, as is discussed in Section 2.4.1, and significant computational expense is required to pick up small length scales and the rapid transient fluctuations of a turbulent flow. This results in DNS having prohibitive computational expense for many flows of engineering interest and industrial flow problems. The application of DNS is thus limited in practice to flows of low-moderate Reynolds Number (Re) (Wesseling, 2001).

As the vast majority of flows of engineering interest are turbulent, and the current lack of sufficient computing hardware means DNS is not a currently viable option, an alternative method for resolving the turbulence is required (Versteeg & Malalasekera, 2007). Turbulence models have been created to do so by using mathematical models to predict the effects of turbulence, as discussed in Section 2.4.

The process of developing a CFD solution can be broken down into three main steps. Pre-processing, solving, and post-processing. Pre-processing, discussed in more detail in Section 2.3.1, entails carrying out the following tasks (Versteeg & Malalasekera, 2007):

- Defining the geometry of the problem;
- Sub-dividing the geometrical domain into smaller pieces, creating a grid of cells making up the computational domain (meshing); and
- Allocating appropriate conditions at the bounding faces of the computational domain (boundary condition (BC) assignment).

Solving, as discussed in Section 2.3.2, initially involves setting up the solver. Decisions need to be made in regards to selection of the discretisation and linearisation schemes, turbulence model, solution initialisation, pressure-velocity coupling, how porous media will be treated, and the parameters used to

monitor solver performance. Solving then involves the application of a numerical method to generate a numerical flow solution. To do so the following steps are performed (Versteeg & Malalasekera, 2007);

1. The flow variables are approximated;
2. The approximations are substituted into the governing equations which are then discretised; and
3. The resulting set of algebraic equations is then numerically solved.

There are three streams of numerical technique that can be employed in generating a solution; finite element, finite difference, finite volume, and spectral methods. These methods are discussed in more detail in Section 2.3.2.

Post-processing then takes the data, which has been generated in numerical form, and presents it in a manner from which analysis can take place. There are many methods of presenting CFD solutions, the most useful of which will be dependent on the analysis being performed. A number of examples are presented as part of the investigations in the remainder of this thesis.

The remainder of Section 2 is dedicated to an elaborated discussion of the aspects covered in the brief CFD overview above.

2.2 Development of the Governing Equations of Fluid Flow for a Newtonian Fluid

As discussed in Section 2.1, fluid dynamics is governed by three fundamental principles relating to the conservation of mass, momentum and energy. The first principle, being that the mass of the fluid is conserved, is known as ‘continuity’. The second principle, being that momentum is conserved (or that the rate of change of momentum equals the sum of the forces on a fluid particle), is known as ‘Newton’s Second Law’. The third principle, being that energy is conserved (or that the rate of change of energy is equal to the sum of the rate of heat addition to, and the rate of work done on, a fluid particle), is known as the ‘First Law of Thermodynamics’.

For the derivation of the governing equations a small particle of fluid, as shown in Figure 12, needs to be considered.

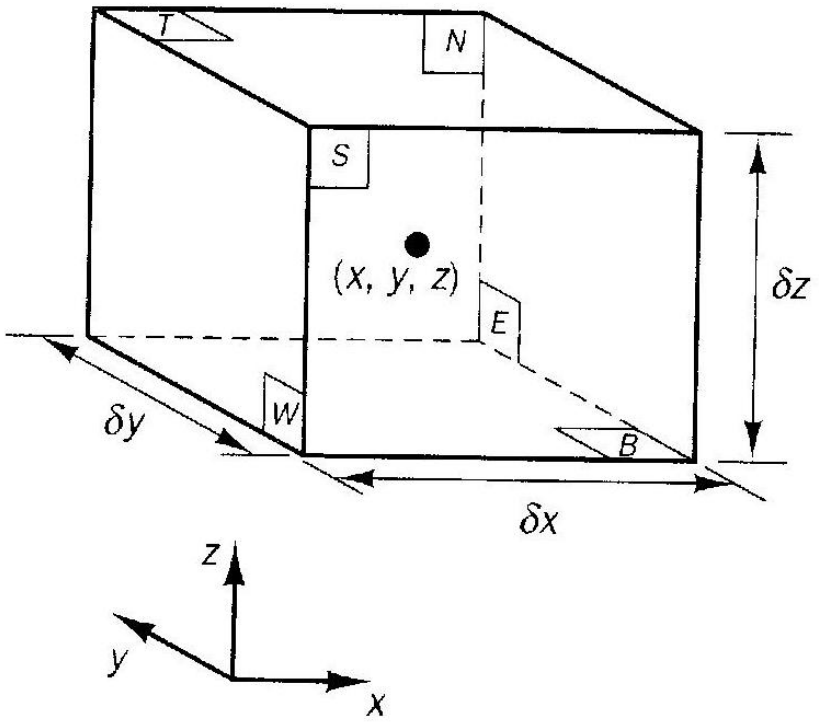

Figure 12 Fluid Particle with associated Notation for Derivation of Governing Equations (Source: (Versteeg & Malalasekera, 2007))

2.2.1 Continuity

Continuity deals with the conservation of mass. The mass balance for the fluid particle shown in Figure 12 is,

Rate of increase of mass in the fluid particle = Net rate of flow of mass into the particle

When all the terms of the mass balance are arranged, the equation takes the form of Eq. 2.1. u, v, and w are x, y, and z velocity components respectively, ρ is density, and t is time.

$$\frac{\partial \rho}{\partial t} + \frac{\partial (\rho u)}{\partial x} + \frac{\partial (\rho v)}{\partial y} + \frac{\partial (\rho w)}{\partial z} = 0 \qquad \text{Eq. 2.1}$$

Eq. 2.1 can be written more compactly as Eq. 2.2 by using the velocity vector, $\vec{u}$.

$$\frac{\partial \rho}{\partial t} + \nabla \bullet \left(\rho \vec{u}\right) = 0 \qquad \text{Eq. 2.2}$$

Eq. 2.2 is the unsteady, three-dimensional continuity equation at a point in a compressible fluid (Versteeg & Malalasekera, 2007). Commonly, incompressible flows are encountered in engineering problems. In such problems Eq. 2.2 simplifies to Eq. 2.3 as density remains constant over time.

$$\nabla \bullet \left(\vec{u}\right) = 0 \qquad \text{Eq. 2.3}$$

2.2.2 Newton's Second Law

Newton's Second Law deals with the conservation of momentum, and states that,

Rate of increase of momentum of a fluid particle = Sum of forces on the fluid particle

The forces on a fluid particle can be broken down into surface forces (pressure and viscous) and body forces (gravitational, Coriolis and electromagnetic). For the fluid particle of Figure 12, the total surface force in the x-direction per unit volume on the fluid is represented by Eq. 2.4.

$$\frac{\partial\left(-p + \tau_{xx}\right)}{\partial x} + \frac{\partial \tau_{yx}}{\partial y} + \frac{\partial \tau_{zx}}{\partial z} \qquad \text{Eq. 2.4}$$

p corresponds to pressure and τ_{ij} is the viscous force acting in the j-direction on the surface normal to the i-direction. Setting the rate of change of x-momentum of the fluid particle to the total force in the x-direction, gives the x-component of the momentum equation (Eq. 2.5). The contribution of the body forces is included as the source term, S_{Mx}.

$$\frac{\partial\left(\rho u\right)}{\partial t} = \frac{\partial\left(-p + \tau_{xx}\right)}{\partial x} + \frac{\partial \tau_{yx}}{\partial y} + \frac{\partial \tau_{zx}}{\partial z} + S_{Mx} \qquad \text{Eq. 2.5}$$

The y- and z-components of the momentum equation are formed in a similar way, and are shown as Eq. 2.6 and Eq. 2.7 respectively. S_{My} and S_{Mz} are the contributions of the body forces in the y- and z-components of the momentum equation.

$$\frac{\partial(\rho v)}{\partial t} = \frac{\partial \tau_{xy}}{\partial x} + \frac{\partial(-p + \tau_{yy})}{\partial y} + \frac{\partial \tau_{zy}}{\partial z} + S_{My} \qquad \text{Eq. 2.6}$$

$$\frac{\partial(\rho w)}{\partial t} = \frac{\partial \tau_{xz}}{\partial x} + \frac{\partial \tau_{yz}}{\partial y} + \frac{\partial(-p + \tau_{zz})}{\partial z} + S_{Mz} \qquad \text{Eq. 2.7}$$

2.2.3 First Law of Thermodynamics

The First Law of Thermodynamics deals with the conservation of energy, and is expressed by,

Rate of increase of energy of a fluid particle =
Net rate of heat addition to the fluid particle + Net rate of work done on the fluid particle

Using the fluid particle of Figure 12, the energy equation takes the form of Eq. 2.8 (Versteeg & Malalasekera, 2007). E, κ, T, and S_E represent the specific energy, conductivity, local temperature and the potential energy source term respectively.

$$\rho \frac{DE}{Dt} = -\nabla \bullet (\rho \vec{u}) + \begin{bmatrix} \frac{\partial(u\tau_{xx})}{\partial x} + \frac{\partial(u\tau_{yx})}{\partial y} + \frac{\partial(u\tau_{zx})}{\partial z} + \\ \frac{\partial(v\tau_{xy})}{\partial x} + \frac{\partial(v\tau_{yy})}{\partial y} + \frac{\partial(v\tau_{zy})}{\partial z} + \\ \frac{\partial(w\tau_{xz})}{\partial x} + \frac{\partial(w\tau_{yz})}{\partial y} + \frac{\partial(w\tau_{zz})}{\partial z} \end{bmatrix} + \nabla \bullet (\kappa \nabla T) + S_E \qquad \text{Eq. 2.8}$$

2.2.4 Equations of State

The five equations, Eq. 2.2, Eq. 2.5, Eq. 2.6, Eq. 2.7, and Eq. 2.8, describe the motion of a fluid in three-dimensions. There are a number of unknowns present throughout these equations. By making the valid assumption that the fluid is in thermodynamic equilibrium, four of the variables, ρ, p, i (internal energy), and T, can be related as shown in Eq. 2.9, the compressible form of the equations of state.

$$\rho = \rho(p,T) \qquad T = T(i,p) \qquad \text{Eq. 2.9}$$

The thermodynamic equilibrium assumption reduces the thermodynamic state variables to two, ρ and T. The equations of state provide a link between energy equation and the mass and momentum equations during the computation of a compressible flow problem (Versteeg & Malalasekera, 2007).

2.2.5 Formation of the Navier-Stokes Equations

Viscous stress components provide more unknowns in the equations of motion. In a Newtonian fluid viscous stresses are proportional to the rates of deformation (Currie, 2003). To link the stresses to deformations, constants of proportionality are used. The constants are dynamic viscosity, μ, and the second viscosity, λ.

Taking into account that viscous stresses can be equated to rates of deformation with the inclusion of a constant of proportionality, the x, y, and z components of the momentum equation (Eq. 2.5, Eq. 2.6, and Eq. 2.7) can be re-written as Eq. 2.10, Eq. 2.11, and Eq. 2.12, the forming the NS equations.

$$\frac{\partial(\rho u)}{\partial t} + \nabla \bullet (\rho u \vec{u}) = -\frac{\partial p}{\partial x} + \nabla \bullet (\mu \nabla u) + S_{Mx} \qquad \text{Eq. 2.10}$$

$$\frac{\partial(\rho v)}{\partial t} + \nabla \bullet (\rho v \vec{u}) = -\frac{\partial p}{\partial y} + \nabla \bullet (\mu \nabla v) + S_{My} \qquad \text{Eq. 2.11}$$

$$\frac{\partial(\rho w)}{\partial t} + \nabla \bullet (\rho w \vec{u}) = -\frac{\partial p}{\partial z} + \nabla \bullet (\mu \nabla w) + S_{Mz} \qquad \text{Eq. 2.12}$$

In a similar way, when the Newtonian model is used for viscous stresses, the energy equation (Eq. 2.8), can be re-written in terms of internal energy, i, as shown in Eq. 2.13. Φ is a dissipation function and represents deformation work performed on the particle that is converted to internal energy and heat, and S_i is the internal energy source term.

$$\frac{\partial(\rho i)}{\partial t} + \nabla \bullet (\rho i \vec{u}) = -p \nabla \bullet (\vec{u}) + \nabla \bullet (\kappa \nabla T) + \Phi + S_i \qquad \text{Eq. 2.13}$$

2.2.6 Collating the Governing Equations

Table 1 collates the governing equations, in a conservative form, for the flow of a compressible Newtonian fluid.

Table 1 Governing Equations of flow for a Compressible Newtonian Fluid

Continuity	$\frac{\partial \rho}{\partial t} + \nabla \bullet \left(\rho \vec{u}\right) = 0$
x-momentum	$\frac{\partial \left(\rho u\right)}{\partial t} + \nabla \bullet \left(\rho u \vec{u}\right) = -\frac{\partial p}{\partial x} + \nabla \bullet \left(\mu \nabla u\right) + S_{Mx}$
y-momentum	$\frac{\partial \left(\rho v\right)}{\partial t} + \nabla \bullet \left(\rho v \vec{u}\right) = -\frac{\partial p}{\partial y} + \nabla \bullet \left(\mu \nabla v\right) + S_{My}$
z-momentum	$\frac{\partial \left(\rho w\right)}{\partial t} + \nabla \bullet \left(\rho w \vec{u}\right) = -\frac{\partial p}{\partial z} + \nabla \bullet \left(\mu \nabla w\right) + S_{Mz}$
Energy	$\frac{\partial \left(\rho i\right)}{\partial t} + \nabla \bullet \left(\rho i \vec{u}\right) = -p \nabla \bullet \left(\vec{u}\right) + \nabla \bullet \left(\kappa \nabla T\right) + \Phi + S_i$
Equations of State	$\rho = \rho\left(p, T\right)$ and $T = T\left(i, p\right)$

The equations in Table 1 are comparable in form to one another. Eq. 2.14 presents the form of the equations for a general variable φ.

$$\frac{\partial \left(\rho \varphi\right)}{\partial t} + \nabla \bullet \left(\rho \varphi \vec{u}\right) = \nabla \bullet \left(\Gamma \nabla \varphi\right) + S_{\varphi} \qquad \text{Eq. 2.14}$$

Γ represents the diffusion coefficient, and Eq. 2.14 is termed the 'transport equation' for property φ, and translates to,

Rate of increase of φ of fluid element + Net rate of flow of φ out of fluid element =
Rate of increase of φ due to diffusion + Rate of increase of φ due to sources

The equations contained within Table 1 therefore become transport equations for the various properties of each equation (i.e. u for the x-momentum equation). For CFD to be a useful tool, these transport equations need to be solved for velocity, pressure, density and temperature throughout the flow field. As discussed in Section 2.1, this cannot be done analytically in a majority of practical applications due

to the computational complexity. As a result, numerical methods are employed. Numerical methods are discussed further in relation to the solving process in Section 2.3.2.

2.3 Producing a Computational Fluid Dynamics Solution

This section elaborates on the discussion presented in Section 2.1 to provide more details of the considerations and decisions that are made in generating a CFD solution. Included in this section is mention of the commercial software packages that were used in the investigations of this thesis. The discussion is presented in two sections relating to the first two of three steps needed to generate a CFD solution, being pre-processing (Section 2.3.1), and solving (Section 2.3.2).

2.3.1 Pre-processing

Pre-processing firstly involves defining the geometry of the problem to be solved by creating a computational domain. Secondly, the computational domain is sub-divided into smaller pieces via a process of 'meshing'. Thirdly, bounding faces of the computational domain are assigned appropriate types of properties depending on the physical qualities they represent (e.g. walls, symmetry faces, pressure inlets etc.).

2.3.1.1 Creating the Computational Domain

During creation of the computational domain consideration is given to the remainder of the pre-processing tasks and the objectives of the CFD analysis. When creating the computational domain, unnecessary geometry features are removed in the process of 'geometry simplification'. By simplifying the geometry the computational expense in the subsequent stages of generating a solution is reduced. Depending on the computational resources available and the problem complexity, it is often necessary to simplify the problem geometry in order to simply perform an analysis.

During geometry simplification several factors are considered. Firstly, the impact of simplification on the flow solution is identified. If the simplification is unlikely to affect the final flow regime, the feature can be removed. Secondly, the available computing resources are identified. With the resources available, is it likely a suitable mesh for the given geometry and flow complexity can be created, stored, and solved? If there is a requirement to reduce the geometrical complexity of a given problem

due to lack of computational resources, each possible simplification needs to be considered in terms of the impact it will have on the accuracy of the solution.

Throughout the work of this thesis the commercial software package of SolidWorks was employed for generating the computational domains to be investigated.

2.3.1.2 Meshing

After defining the problem geometry the computational domain is sub-divided via the process of meshing. The result of the sub-division is a mesh of two- or three-dimensional cells that when combined represent the geometry of the computational domain.

In either two- or three-dimensions there are two types of mesh structure that can be used; structured or unstructured. Both mesh structures have advantages and disadvantages. Applying the appropriate mesh structure enables a mesh independent, time efficient, and accurate solution to be generated (Fluent, 2006).

In structured meshes all mesh points have an equal number of adjacent elements. This gives the mesh a consistent geometric regularity. Figure 13 shows sections of structured two and three-dimensional meshes. In most structured two-dimensional meshes, each mesh element has four nodes, and four edges. A typical three-dimensional structured mesh volume is defined by eight nodes and six quadrilateral faces.

When using a structured mesh, the non-uniform mesh in ‘physical space’ is transformed into a uniform rectangular mesh in ‘computational space’. The numerical methods applied in solving the flow problem are made over the uniform rectangular mesh. The results are then transferred back on to the corresponding points in ‘physical space’(Nijdam, 2007).

The advantages of using a structured mesh include; faster more robust computations, lower memory usage, higher degree of mesh control, and greater accuracy because the grid is often flow aligned. A flow aligned mesh reduces numerical diffusion. Numerical diffusion, in the case of CFD, is the result of discretising a continuous fluid system, and can lead in solution inaccuracy. In addition, structured

mesh elements and volumes support a larger amount of skewness before the solution is detrimentally affected (Fluent, 2006; Nijdam, 2007).

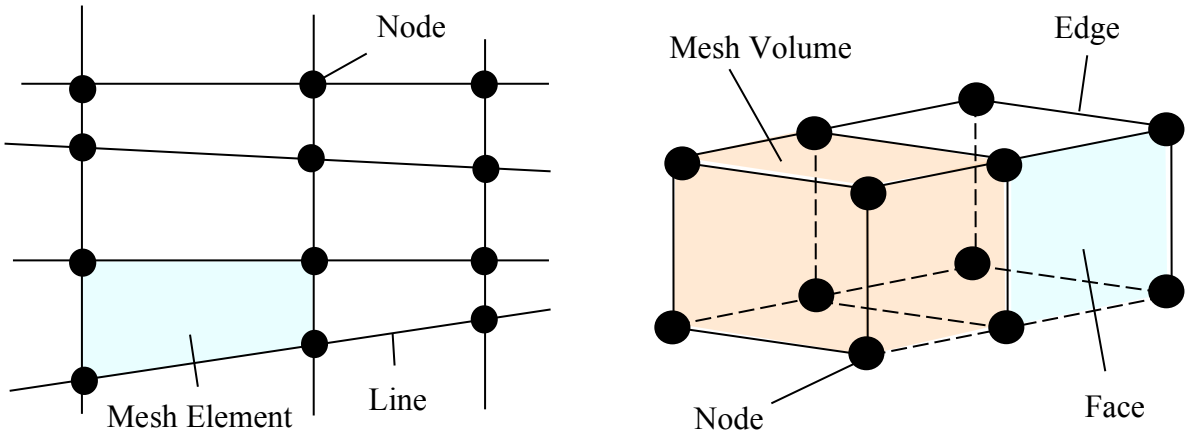

Figure 13 Structured Two-Dimensional Mesh (left), and Structured Hexagonal Three-Dimensional Mesh (right)

The disadvantages of a structured mesh are that they are often cumbersome, and need a lot of experience and time to set up on complex geometries. The increase in computational efficiency the structured mesh gives can be offset by extended meshing times.

In an unstructured mesh the mesh elements or volumes are placed in the computational domain in an irregular fashion. In the two-dimensional unstructured case, there is no restriction on the number of adjacent mesh elements meeting at a point. Likewise, in the three-dimensional case, there is no restriction placed on the number of adjacent mesh volumes meeting along an edge (Nijdam, 2007; Versteeg & Malalasekera, 2007). Figure 14 shows unstructured two and three-dimensional meshes.

Unstructured meshes are faster to set up on complex geometries as they are more flexibly applied. During solution an unstructured mesh is simpler to adapt. However, greater memory is required for storing an unstructured mesh due to the amount of connectivity information required. Additionally, less control is given to the user during the meshing process. Unstructured mesh elements and volumes do not distort well, and thus need to be isotropic (Nijdam, 2007).

Figure 15 demonstrates a practical application of structured and unstructured meshes. It is possible to use a number of different element and volume types in unstructured meshes. Two-dimensional meshes

of triangular and quadrilateral elements are possible, as are three-dimensional meshes of tetrahedral and hexagonal volumes. Meshes with multiple element or volume types are referred to as hybrid meshes. Applying a hybrid mesh allows enhanced mesh resolution in required areas, whilst utilising efficient use of computational storage in other areas of the computational domain.

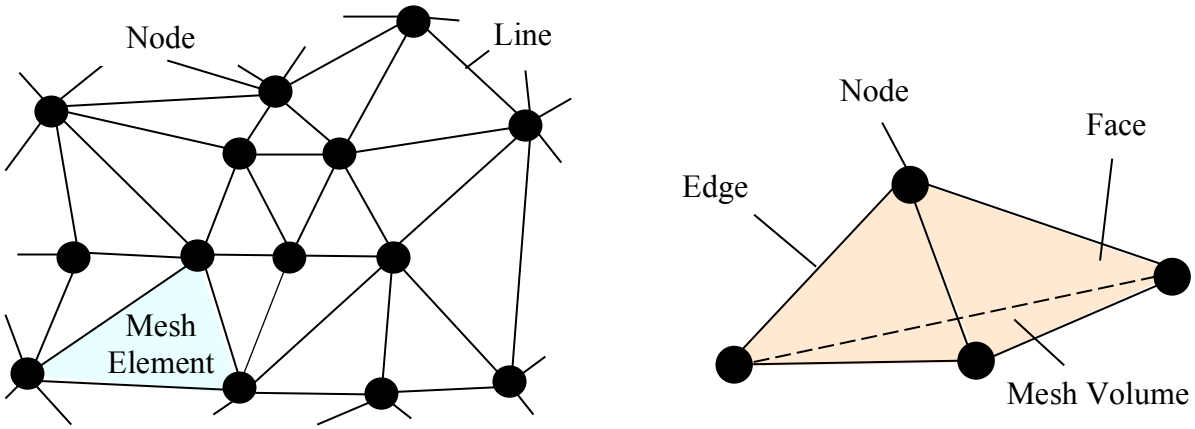

Figure 14 Unstructured Two-Dimensional Mesh (left) and Unstructured Tetrahedral Three-Dimensional Mesh (right)

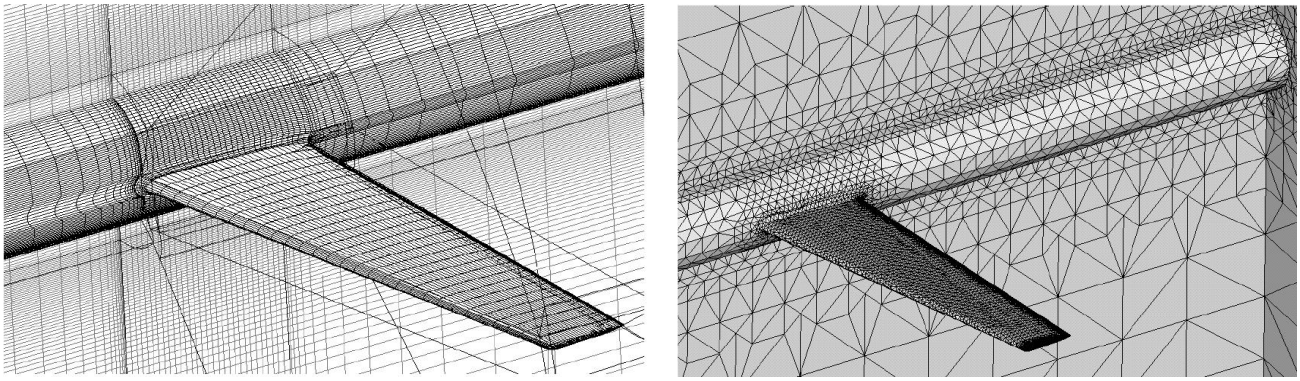

Figure 15 Structured (left) and Unstructured (right) Meshes of a Wing Test Structure (Source: ANSYS)

The commercial software package of Gambit was used for meshing the computational domains in the work of this thesis. Prior to meshing, the given problem was evaluated for the type of flow features that were likely to develop in the solution. The computational domain was then separated into zones that defined the boundaries of the likely flow features.

In zones where the likely flow pattern was not complex, and the zone geometry allowed, structured elements were used. In zones where the likely flow patterns were complex or unknown, unstructured elements were used. Size functions were used to grow the mesh element or volume size away from

zones of complex flows and small geometries. Small growth rates of 1-10% were employed to retain mesh continuity and avoid distortion of individual elements. Skewness checks were performed prior to solution to evaluate element and volume distortion prior to solving.

Throughout the investigations of this thesis, all meshes and meshing techniques were subject to a mesh independence check prior to the main body of the analysis. The first mesh iteration was developed using the process described above. The initial mesh was then solved using the BCs and solver settings to be employed in the main body of the analysis.

The solution generated was analysed and compared to the initial mesh structure. Zones of high flow complexity and large parameter gradients were identified. If required, zones of high mesh density were realigned to coincide with the complex flow features in the solution. This process was repeated until the mesh density distribution was adequate. Once the mesh density distribution was established, meshes of finer and/or coarser global density were developed and comparative solutions produced.

The original objective of the relevant analysis was then considered in defining one or more 'mesh independence parameters'. The solutions across the range of global mesh densities were then compared for variation in the 'mesh independence parameters'. The mesh density employed in the main body of the analysis was then selected based on where the 'mesh independence parameters' failed to deviate by a defined amount between subsequent solutions.

2.3.2 Solving

The commercial software package of Fluent was used throughout the investigations of this thesis to perform the CFD solving tasks. As discussed in Section 2.1, solving a CFD problem involves the application of numerical methods. Finite element, finite difference, and spectral methods were mentioned as the three streams of discretisation technique that could be employed. Fluent employs a finite volume method, being similar to both finite difference and finite element methods. The main difference between the various numerical methods is the smallest building block present in the solution space. The smallest building blocks of the three above-mentioned methods are presented in Table 2.

Through whichever stream of discretisation technique is employed, a number of discretisation schemes can be used. Each of the various schemes are a set of rules for calculating the gradient or derivative of a

property from discrete values at known points (W. H. Ho, 2009). Discretisation schemes are discussed in Section 2.3.2.1 in more detail.

Table 2 Smallest Building Blocks of Discretisation Techniques (Source: (W. H. Ho, 2009))

Technique	*Smallest Building Block*
Finite Volume Method	Volume surrounding node
Finite Element Method	Element connecting two or more nodes
Finite Difference Method	The node itself

Prior to executing the solving process, a number of other settings need to be assigned. One of the most important decisions in terms of solution accuracy is the selection of an appropriate turbulence model. The importance of selecting a turbulence model, and the need to understand the limitations of the various options available, dictate a relatively detailed discussion. Such a discussion is presented later in Section 2.4.

For incompressible flows pressure does not appear explicitly in the discretised continuity equation. As such, a pressure-velocity coupling needs to be used. These are discussed in more detail in Section 2.3.2.2.

When dealing with fine porous features, the computational expense in modelling the flow patterns through each pore is too high to achieve, and often not of particular interest. In order to account for porous media as part of a larger computational domain with acceptable computational expense, the use of porous models are used. The application of these, and the information required to set these up are discussed in Section 2.3.2.3.

In order to start the solution process an initial estimate of the solution needs to be provided. Prescribing this estimate is called ‘solution initialisation’, and is discussed in Section 2.3.2.4. When the solution process is being performed, solution monitors need to be used to judge the quality of the solution produced, as well as when the iterative solution process is converging upon a near constant solution for the flow domain. A discussion of these monitors, along with convergence criteria is presented in Section 2.3.2.5.

2.3.2.1 Discretisation Schemes

In Fluent the following discretisation schemes are available, with only those marked with a '*' applicable to the turbulence models relevant to this thesis (Fluent, 2006):

- First-Order Upwind*;
- Second-Order Upwind*;
- Power Law*;
- QUICK*;
- Third-Order MUSCL*;
- Central Differencing;
- Bounded Central Differencing;
- Low Diffusion Second-Order; and
- Modified HRIC.

The discretisation schemes that are of relevance to this thesis are discussed in more detail below. For more information on the other schemes listed above, the reader is directed to (Fluent, 2006).

In the first-order upwind scheme the cell-centre values are assumed to be the cell average values. The face values of the cell are set equal to the cell-centre value of the immediate upstream cell, as the names implies (Fluent, 2006; Versteeg & Malalasekera, 2007).

The second-order upwind scheme provides a potential accuracy improvement, at the cost of increased computing time, by using a more complex method of calculating the face value from upstream cells. The more complex method employs a 'multidimensional linear reconstruction approach' which uses input from two upstream cells adjacent to the cell face (Fluent, 2006).

The power law scheme employs a one-dimensional convection-diffusion equation, which when integrated has a Peclet number (Pe) dependence. The Pe number dependence dictates the relative contributions of convection and diffusion to the face value. If there is no flow movement, then Pe is zero, and a face value based purely on diffusion is calculated. If the Pe is large (nearing one) the face value becomes closely equal to the upstream cell-centre value. In such a case the power law scheme

becomes nearly equivalent to the first-order upwind scheme, but requires more computational expense (Fluent, 2006).

The QUICK scheme is based on weighted averages from both the second-order upwind scheme and second-order central differencing scheme. In a similar way that the power law scheme has Pe dependence, the QUICK scheme in Fluent uses a solution-dependent variable to dictate the relative weightings. With the variable tending towards zero the central differencing scheme heavily dictates the face value. When tending towards one the second-order upwind scheme heavily dictates the face value. The QUICK scheme is typically more accurate on structured grids aligned with the flow direction. In Fluent, for regions of the computational domain that contain non-structured meshes, the QUICK scheme reverts to second-order upwind scheme (Fluent, 2006).

The third-order MUSCL (Monotone Upstream-Centred Schemes for Conservation Laws) scheme, like the QUICK scheme, blends the central differencing scheme and second-order upwind schemes using a weighted average. The scheme potentially reduces numerical diffusion and therefore improves the spatial accuracy for all type of meshes. However, it is hampered by the lack of a flux limiter which means undershoots or overshoots can occur at discontinuities in the flow-field (Fluent, 2006; Versteeg & Malalasekera, 2007).

2.3.2.2 Pressure-Velocity Coupling

Through solving the equations presented in Table 1, a velocity field for the flow domain can be resolved. This is possible as a velocity component is present in each of the momentum equations. In addition, all three velocity components are present in the continuity equation. This leaves the three momentum equations and the continuity equation coupled.

A pressure gradient term is also present in all the momentum equations. However, a transport equation for pressure is not present. The pressure gradient for the solution is generally not known beforehand, and in most cases is to be investigated through solution of the equations in Table 1.

When the flow is compressible, the continuity equation and energy equation can be used as the transport equations for ρ and T, respectively. Through the equations of state, discussed in Section 2.2.4, the pressure can be determined.

When the flow is incompressible, the constant density of the flow medium is no longer linked to the pressure. In this situation an iterative solution strategy is applied. If the correct pressure field is applied to the momentum equations, the resulting velocity field should satisfy the continuity equation (Versteeg & Malalasekera, 2007). There are a number of iterative algorithms that have been developed to achieve a pressure-velocity coupling. The selection of which method is most appropriate depends on the nature of the flow being analysed. In Fluent the following coupling schemes are available:

- SIMPLE;
- SIMPLE-C;
- PISO; and
- Fractional Step Method (FSM).

The FSM is only applicable to Non-Iterative Time Advancement (NITA) models which were not employed in the research of this thesis. The reader is referred to (Fluent, 2006) for a discussion of the FSM.

The SIMPLE (Semi-Implicit Method for Pressure Lined Equations) algorithm first approximates the velocity field by solving the momentum equations. The pressure gradient is then determined using the pressure field from the previous iteration (or the initial guess after the first iteration). From these two sources of information a revised pressure field is calculated. The velocities are corrected from the initial approximation resulting in a new set of conservative fluxes (Fluent, 2006).

The SIMPLE-C coupling varies from the SIMPLE algorithm by altering one of the terms used in the equation determining the face flux correction. The benefit of SIMPLE-C over SIMPLE lies in the increased rate of convergence when the pressure-velocity coupling is the limiting factor. As it is often the case that parameters other than this coupling limit convergence, SIMPLE and SIMPLE-C in many instances perform in a comparative manner (Fluent, 2006).

The PISO (Pressure Implicit Splitting of Operators) coupling, as with SIMPLE-C, was developed as a variation of the SIMPLE algorithm. The PISO coupling provides skewness and neighbour corrections for the SIMPLE algorithm. The PISO coupling is recommended in Fluent for ‘transient flow calculations, especially when you want to use a large time step’, as this is what it was initially

developed for (Fluent, 2006; Versteeg & Malalasekera, 2007). It is also recommended for steady state flows with meshes of high skewness (Fluent, 2006). (Wesseling, 2001), who remarks on a study of the three above-mentioned couplings by (Raithby & Van Doormaal, 1984), suggests that variants of the SIMPLE method (with include SIMPLE-C and PISO) do not essentially give any improvement of solution efficiency or robustness.

2.3.2.3 Treatment of Porous Media in Computational Fluid Dynamics

When a porous medium is part of a larger CFD investigation, it is almost always computationally inefficient or impossible to generate a solution for the detailed flow that develops in and around the porous structure. In the example of a JETC, the overall length of the building, including inlet and exhaust stacks, can exceed 110m, and the height can exceed 30m. The FOD screen within such a cell will be constructed of wires approximately 1mm in diameter.

To mesh and solve for the flow within such small and highly repeated features in a full JETC computational domain would require extremely large computational resources. The specific flow patterns that develop around the pores of the porous media are not of great importance in most, if not all, JETC analyses. The influence of porous media on the overall flow in terms of pressure loss and cell MFR is of importance. The influence of the porous media on the overall flow can be calculated using pressure loss calculations in the form of porous media models (Fluent, 2006).

In Fluent the treatment of porous media (that is not physically modelled) is dealt with by using the porous media model. For a thin-membrane porous medium, such as a wire screen or perforated plate, a one-dimensional simplification of the porous media model, called a porous-jump, is applied (Fluent, 2006). A porous-jump is assigned as a BC across a face defined within the computational domain. A porous-jump is preferentially used over the full porous media model when possible due to its robustness and better convergence properties.

In the porous-jump model, the pressure loss over the membrane is defined over a finite thickness using a combination of Darcy's Law and an inertial loss term as shown in Eq. 2.15 (Fluent, 2006). The bracketed left hand term represents the contribution from Darcy's Law, and the bracketed right hand term represents the inertial loss contribution. C_2 is the pressure jump coefficient, v is the velocity normal to the porous face, and Δm is the thickness of the medium.

$$\Delta p = -\left(\frac{\mu}{\alpha}\upsilon + C_2 \frac{1}{2}\rho\upsilon^2\right)\Delta m \qquad \text{Eq. 2.15}$$

α, C_2, and Δm need to be determined for each porous medium being modelled. When modelling the materials used in the construction of porous media encountered in a JETC, you can eliminate the permeability term, α, and use the inertial loss term alone (Fluent, 2006). This can be done by retaining the 'default' Fluent value for α and employed without error (Bosworth, 2005; Fluent, 2006).

Δm is easily measured and/or defined. C_2 can be measured experimentally with accuracy. When applying CFD to a given analysis, it is often the desired choice as it provides an alternative to experimental analysis. Thus, experimentally measuring C_2 each time a new porous medium is encountered is undesirable. An alternative approach is to predict C_2 through a mathematically defined correlation. Two such approaches, using the correlations of Brundrett (Brundrett, 1993) and Idelchik (Idelchik & Fried, 1986) are presented below.

(Brundrett, 1993) established a general correlation for the pressure loss through woven wire meshes for flows in the Re range of 1.0E-04 to 1.0E04. The work of (Groth & Johanssson, 1988; Munson, 1988; Shubauer, Spangenburg, & Klebanoff, 1948) used (Brundrett, 1993) to establish a new correlation that is shown as Eq. 2.16.

$$K = \left(\frac{1-\beta^2}{\beta^2}\right)\left(\frac{7.0}{\mathrm{Re}} + \frac{0.9}{\log(\mathrm{Re}+1.25)} + 0.05\log(\mathrm{Re})\right) \qquad \text{Eq. 2.16}$$

β is the porosity of the medium. K is the pressure loss coefficient, and relates to the pressure jump coefficient, C_2, by Eq. 2.17.

$$C_2 = \frac{K}{\Delta m} \qquad \text{Eq. 2.17}$$

(Brundrett, 1993) indicates Eq. 2.17 can be applied to incompressible and uniform flows normal to the porous medium. (Idelchik & Fried, 1986) also provides a correlation for wire screens, shown as Eq. 2.18.

$$K = 1.3(1-\beta) + \left(\frac{1}{\beta} - 1\right)^2 k'_{\mathrm{Re}} \qquad \text{Eq. 2.18}$$

k'_{Re} is a tabulated value from (Idelchik & Fried, 1986), and provides a low Re correction for screens with a wire Re below 1.0E03. (Idelchik & Fried, 1986) states Eq. 2.18 is applicable across all Re.

In addition to the correlation of Eq. 2.18 for wire screens, (Idelchik & Fried, 1986) also developed a correlation for K for a thick perforated plate, as shown in Eq. 2.19.

$$K = \left[\left(0.5 + \varsigma\sqrt{1-\beta}\right) \times (1-\beta) + (1-\beta)^2 + \eta\frac{\Delta m}{d_h}\right] \times \frac{1}{\beta^2} \qquad \text{Eq. 2.19}$$

ς and η are tabulated values reflecting the geometry and inner wall roughness of each individual orifice. Δm is the porous medium thickness, and d_h, the hydraulic diameter, is defined by Eq. 2.20.

$$d_h = \frac{4 \times Area_{Orifice}}{Perimeter_{Orifice}} \qquad \text{Eq. 2.20}$$

(Idelchik & Fried, 1986) indicates Eq. 2.20 can be applied to incompressible and uniform flows normal to the porous medium with Re above 1.0E05.

2.3.2.4 Solution Initialisation

The first step in the solution process of a CFD model is solution initialisation. When a solution is initialized, an initial estimate, or guess, for the flow solution is defined. It is important to adequately initialize the solution in such a way that the correct final solution can be attained. (Fluent, 2006) provides the following example to demonstrate the importance of adequate initialization.

'A real-life supersonic wind tunnel will not 'start' if the back pressure is simply lowered to its operating value; the flow will choke at the tunnel throat and will not transition to supersonic. The same holds true for a numerical simulation: the flow must be initialized to a supersonic flow or it will simply choke and remain subsonic.'

A solution can be initialised across an entire flow field with identical values, or defined specifically in individual zones. In the investigations of this thesis the use of zones was utilised extensively. The zones were created during the meshing process in Gambit, which also provides basic geometry creation capability. A technique of 'patching' individual initial solutions in each zone throughout the computational domain was then performed in Fluent immediately prior to running the solution process.

2.3.2.5 Monitors of Solution Performance

The iterative numerical methods employed in CFD mean certain parameters need to be monitored during the solution process. Monitoring these parameters helps ascertain whether a converged solution is being approached. These parameters also give some indication in regards to the quality of the set-up of the computational model, solver settings, and solution initialisation.

In assessing the convergence of a solution, the parameters that are monitored will reflect the amount each solution produced, by the iterative numerical method, varies from the previous iteration. These parameters are known as 'residuals'. The residuals that will be of interest during solution will be dependent on the solver settings and choice of turbulence model that is being used. The residuals effectively reflect the equations that are being solved during each iteration of the solution process.

There are a number of considerations made when forming convergence criterion or criteria. In Fluent the 'default' convergence criterion is when all residuals (scaled in relation to the residuals of the first solution iteration) reach a value of less than 1.0E-03. By adjusting this value the criterion can be made more or less stringent. If the value is lowered a more stringent agreement between subsequent solution iterations is required before being judged 'converged', and vice-versa.

The monitoring of the convergence criteria needs to be made in regard of a number of factors, including the accuracy of the initial estimate during initialisation. In addition it is also worth monitoring relevant integrated parameters to the flow problem under-investigation to ensure that the convergence of residuals is reflected by the convergence of these parameters. (Fluent, 2006) provides an elaborated discussion on judging convergence.

2.4 Turbulence and Turbulence Modelling

The discussion of Section 2.1 indicated that in a vast majority of flows of engineering interest turbulent behaviour is present. This section discusses turbulence, why the need to model it arises, and the methods that are employed to do so.

2.4.1 Turbulence in Computational Fluid Dynamics

Laminar flows, which are smooth and in which the fluid layers slide in an ordered fashion past each other, can be solved correctly using the continuity, momentum, and energy equations presented in Table 1. When the Re of the flow increases past a critical value, termed Re_{crit}, a transition from laminar to turbulent behaviour occurs.

A turbulent flow exhibits irregular, chaotic and randomly fluctuating velocity and pressure components and becomes intrinsically unsteady (Francis, 1975; Versteeg & Malalasekera, 2007). For accurate CFD solutions to be generated, the velocity components present in the governing equations need to consider the flows transient nature.

There is extreme computational expense in generating a Direct Numerical Solution (DNS) of turbulent behaviour down to the smallest scales that are present (Wesseling, 2001). As such, one of two alternate approaches is taken. The first approach models the effects of turbulence through consideration of a limited number of the turbulence properties. The second approach considers only the larger scale turbulence, whilst the smaller scale turbulence is filtered out. Section 2.4.2 discusses these approaches, in relation to CFD application, in greater detail.

2.4.2 Turbulence Models

Turbulence models are mathematical models that approximate the physical behaviour of turbulent flows (Wilcox, 1998). By employing turbulence models the use of the full time-dependent NS equations, as in DNS, along with the significant computational expense can be avoided. Turbulence models in commercial software packages generally fall into one of two categories, Reynolds Averaged Navier-Stokes (RANS), or Large Eddy Simulation (LES).

In RANS methods the NS equations presented in Table 1 are time-averaged. The time-averaging leads to additional terms appearing in the equations of Table 1. These additional terms are called Reynolds stresses, and thus the revised set of governing equations is termed the RANS equations. The RANS equations are shown below as Eq. 2.21 and Eq. 2.22.

$$\frac{\partial \rho}{\partial t} + \frac{\partial}{\partial x_i}\left(\rho u_i\right) = 0 \qquad \text{Eq. 2.21}$$

$$\frac{\partial}{\partial t}\left(\rho u_i\right) + \frac{\partial}{\partial x_j}\left(\rho u_i u_j\right) = -\frac{\partial p}{\partial x_i} + \frac{\partial}{\partial x_j}\left[\mu\left(\frac{\partial u_i}{\partial x_j} + \frac{\partial u_j}{\partial x_i} - \frac{2}{3}\delta_{ij}\frac{\partial u_l}{\partial x_l}\right)\right] + \frac{\partial}{\partial x_j}\left(-\rho\overline{u_i' u_j'}\right) = 0 \qquad \text{Eq. 2.22}$$

These equations are similar to the instantaneous NS equations other than the addition of an extra term that represents the effects of turbulence, termed the Reynolds stresses (Fluent, 2006). This term is the last bracketed term in Eq. 2.22.

The system of the RANS equations has becomes open with the inclusion of the Reynolds stresses term. In this system there are now not enough equations available to solve for all unknowns. An issue of closure therefore arises. The Reynolds stresses component therefore must be modelled in some way so that Eq. 2.21 and Eq. 2.22 can be closed. The modelling process is carried out through creating transport equations for various turbulent quantities (Wilcox, 1998).

A number of different closure methods, focussing on various different turbulence quantities, have been successfully and unsuccessfully attempted. Section 2.4.3 discusses a number of the closure methods that are in common use in commercial CFD software.

In LES space-averaging of the turbulence is applied (Abbott & Dasco, 1989). LES simulates the larger scale turbulence explicitly in an unsteady simulation (Wesseling, 2001). The resolution of the mesh dictates the exact scale of the turbulence that is simulated, with only eddies larger than the size of mesh cells being accounted for. The smaller scale turbulence is removed through a filtering process (Sagaut, 2006). The size of the turbulence that is filtered out is determined the scale of the filter applied.

Filtering out smaller scale turbulence leads to the need to model the unresolved scales in some manner. To do so the unresolved scales are defined as being either 'resolved sub-filter scales' (SFS) or 'sub-grid scales' (SGS). SFS are not filtered out entirely, but their effects are dampened by the filter. SGS are filtered out entirely.

SFS are repaired through a filter reconstruction process. The effects of SGS are accounted for by models that fall into one or both of two possible classes, functional or structural. Some examples and discussion of several proposed models can be found in (Smagorinsky, 1963), (Germano, Piomelli, Moin, & Cabot, 1991), (Lilly, 1992), and (Meneveau, Lund, & Cabot, 1996).

LES, whilst far less computationally expensive than DNS, still requires substantial computational requirements. RANS methods require substantially less computational requirements than LES, albeit at the cost of potential accuracy improvements. Although still computationally too expensive for many CFD investigations, Detached Eddy Simulation (DES) does provide a method of compromise between the two. DES utilises the accuracy of LES in the main body of the flow, whilst applying RANS methods close to the walls (W. H. Ho, 2009).

2.4.3 Reynolds Averaged Navier-Stokes Models

RANS models are the approach of choice for many CFD investigations as they sit near the limit at what is computationally achievable when analysing engineering problems. The computational expense and the available hardware become a limiting factor on CFD solution accuracy. Therefore the applicability of the various turbulence models needs to be understood prior to performing a CFD analysis and interpreting the results produced.

This section discusses the applicability and relative accuracy of popular RANS model in use. A summary of the strengths and weaknesses of the respective models is presented in Table 3 later in the section.

Fluent was used as the solver for the investigations of this thesis. Within Fluent the following RANS models are available (Fluent, 2006).

- Spalart-Allmaras (SA);

- k-ε and variations (Standard, Renormalization-group (RNG), and Realizable);
- k-ω;
- k-ω Shear-Stress-Transport (SST); and
- Reynolds Stress Model (RSM).

Section 2.4.3.1 through Section 2.4.3.6 discusses these models in more detail to give an overview of their relative capability and restrictions. In Section 2.4.3.1 through Section 2.4.3.6 a number of equations are used to discuss the RANS closure models. These equations are developed for the purpose of identifying closure constants that are needed to complete the closure process.

A vast majority of these terms are only discussed within this section, where they are defined, and have not been included in this thesis' list of symbols, as they are not of relevance at any point outside of this section. In addition, the terms α and β, which have been defined previously as permeability and porosity respectively, are used in a different context solely in Section 2.4.3.1 through Section 2.4.3.6.

2.4.3.1 Spalart-Allmaras Model

As mentioned in Section 2.4.2, a closure problem arises in the RANS equations due to the presence of the turbulent Reynolds stresses term. Joseph Boussinesq made the first steps towards modelling these stresses by relating them to the mean flow and introducing a new proportionality constant, turbulence viscosity (μ_t). This allowed the Reynolds stresses to be found by augmenting the molecular viscosity with μ_t. The Spalart-Allmaras model along with the two-equation k-ε and k-ω models (discussed in the following sections) all apply the Boussinesq hypothesis when closing the RANS equations, and simply offer direct methods of calculating μ_t.

The SA model, initially presented in (Spalart, 1992), is the computationally least expensive turbulent model available in Fluent. This is a result of only one turbulence transport equation, kinematic turbulent viscosity, being solved. The model was primarily developed for the aerospace industry for application in wall-bounded flows and flows with mild separation (STAR-CCM, 2011).

(Fluent, 2006) suggests that the SA model 'is the best choice for relatively crude simulations on coarse meshes where accurate turbulent flow computations are not critical'. (Fluent, 2006) also provides a cautionary note on the SA models application to complex flows, as its suitability is yet unknown.

(STAR-CCM, 2011) notes that the SA model provides inaccurate results for spreading rates of plane and round jets, of particular relevance to this thesis. (Wilcox, 1998) suggests that no one-equation turbulence model will ever be universally applicable.

2.4.3.2 Standard *k*-*ε* Model

The *k*-*ε* model, along with the *k*-*ω* and *k*-*ω* SST models, is a two-equation model. The standard *k*-*ε* model is one of the most widely used two-equation methods of modelling turbulence (Wilcox, 1998). The mechanisms that cause the creation and destruction of the turbulent kinetic energy, *k*, are the focus of the transport equations which close the set of governing equations.

In derivation of the *k*-*ε* model, the assumption is made that flow is fully turbulent, and is thus only applicable to such flow regimes (Fluent, 2006). *k*, and its rate of dissipation, *ε*, are substituted into the general form of the transport equation presented earlier as Eq. 2.14. *k* is used to define the turbulence velocity scale, and *ε* is used to define the turbulence length scale (TLS). After algebraic manipulation, the *k* and *ε* transport equations take the form of Eq. 2.23 and Eq. 2.24 respectively (Fluent, 2006).

$$\frac{\partial}{\partial t}(\rho k)+\frac{\partial}{\partial x_i}(\rho k u_i)=\frac{\partial}{\partial x_j}\left[\left(\mu+\frac{\mu_t}{\sigma_k}\right)\frac{\partial k}{\partial x_j}\right]+G_k+G_b-\rho\varepsilon-Y_M+S_k \qquad \text{Eq. 2.23}$$

$$\frac{\partial}{\partial t}(\rho\varepsilon)+\frac{\partial}{\partial x_i}(\rho\varepsilon u_i)=\frac{\partial}{\partial x_j}\left[\left(\mu+\frac{\mu_t}{\sigma_\varepsilon}\right)\frac{\partial \varepsilon}{\partial x_j}\right]+C_{1\varepsilon}\frac{\varepsilon}{k}(G_k+C_{3\varepsilon}G_b)-C_{2\varepsilon}\rho\frac{\varepsilon^2}{k}+S_E \qquad \text{Eq. 2.24}$$

G_k and G_b represent generation terms for *k* due to mean velocity gradients and buoyancy. Y_M contributes to the overall dissipation rate (and is only applicable to high Mach number flows) and S_k /S_ε are source terms. μ_t is the turbulent viscosity, and σ_k and σ_ε are the turbulent Prandtl numbers (Pr) for *k* and *ε*. $C_{1\varepsilon}$, $C_{2\varepsilon}$, and C_μ, together with σ_k, and σ_ε form the closure constants.

The most common closure constants used when applying the *k*-*ε* model, are shown below. These values were experimentally derived by (Launder & Spalding, 1972), and can be modified to user defined values in Fluent.

$$C_{1\varepsilon} = 1.44\,,\ C_{2\varepsilon} = 1.92\,,\ C_{\mu} = 0.09\,,\ \sigma_k = 1.0\,,\ \sigma_{\varepsilon} = 1.3$$

Using this set of constants (Abbott & Dasco, 1989) indicates that the *k-ε* model has 'successfully simulated a number of real, fluid flow problems in two- and three-dimensions'. Specific examples are given for abrupt pipe expansions, flow around obstacles and side-discharge into a channel. (Versteeg & Malalasekera, 2007) indicates that the *k-ε* model is well established and is the most widely validated turbulence model, which has proven excellent performance for many industrial flows. Some problems areas for the *k-ε* model discussed by (Versteeg & Malalasekera, 2007) are in unconfined flows, swirling flows, flows with curved boundary layers, rotating flows and fully developed flows in non-circular ducts. (Wilcox, 1998) states that the *k-ε* model has been employed with only mixed success, a limiting factor for its lack of general applicability being its poor accuracy in flows with adverse pressure gradients.

2.4.3.3 *k-ε* Model Variations

There are a number of variants of the *k-ε* model. Two of the more common are the RNG and 'realizable' models (Fluent, 2006; Versteeg & Malalasekera, 2007). The RNG *k-ε* model was derived using a statistical technique called renormalization group (RNG) theory. There is an additional term in the ε equation and provides an analytical formula for the closure constants σ_k and σ_{ε}.

The RNG variation of the *k-ε* model performs better in swirling flow calculations, and those with regions of low Re (Fluent, 2006). (Yakhot, Thangam, Gatski, Orszag, & Speziale, 1991) presents the development of the model, and reports very good accuracy in flows over backward facing steps. (Versteeg & Malalasekera, 2007) notes, that compared to the standard *k-ε* model, the RNG model comparatively lacks widespread validation.

The 'realizable' *k-ε* model provides a new transport equation for ε. In addition a new formulation for μ_t is present. (Fluent, 2006) suggests the 'realizable' *k-ε* model is superior to the standard *k-ε* model in flows exhibiting strong streamline curvature, vortices, and rotation. (Fluent, 2006) continues by stating that the 'realizable' variation will outperform both of standard and RNG *k-ε* models in separated flows, and in flows with complex secondary flow features. (Fluent, 2006) also notes however, that only

limited accuracy is achieved when the computational domain contains both rotating and stationary fluid zones.

2.4.3.4 *k-ω* Model

There are a number of ways of defining the TLS, ε, as used in the *k-ε* model, being just one example. A popular alternate approach is the use of ω, which is regarded as 'the rate of dissipation per unit turbulent kinetic energy' by (Speziale, 1990; Wilcox, 1988; Wilcox & Rubesin, 1980), although has been identified differently in other papers (Wilcox, 1998). Using the above definition, ω takes the form of Eq. 2.25.

$$\omega = \frac{\varepsilon}{k} \qquad \text{Eq. 2.25}$$

Through algebraic manipulation, the transport equations for k and ω become Eq. 2.26 and Eq. 2.27 (Fluent, 2006).

$$\frac{\partial}{\partial t}(\rho k) + \frac{\partial}{\partial x_i}(\rho k u_i) = \frac{\partial}{\partial x_j}\left[\left(\mu + \frac{\mu_t}{\sigma_k}\right)\frac{\partial k}{\partial x_j}\right] + G_k - Y_k + S_k \qquad \text{Eq. 2.26}$$

$$\frac{\partial}{\partial t}(\rho \omega) + \frac{\partial}{\partial x_i}(\rho \omega u_i) = \frac{\partial}{\partial x_j}\left[\left(\mu + \frac{\mu_t}{\sigma_\omega}\right)\frac{\partial \omega}{\partial x_j}\right] + G_\omega - Y_\omega + S_\omega \qquad \text{Eq. 2.27}$$

σ_ω represents the turbulent Pr number for ω, and S_ω is a source term. The following discussion relating to the expansion of terms in Eq. 2.26 and Eq. 2.27 is presented in order to identify the closure constants. G_ω represents the generation of ω, and is expanded to the form of Eq. 2.28.

$$G_\omega = \alpha \frac{\omega}{k} G_k \qquad \text{Eq. 2.28}$$

α can be expanded to the following form.

$$\alpha = \frac{\alpha_\infty}{\alpha^*}\left(\frac{\alpha_0 + \mathrm{Re}_t / R_\omega}{1 + \mathrm{Re}_t / R_\omega}\right) \qquad \text{Eq. 2.29}$$

α_∞, α_0, and R_ω are closure constants. Re_t is defined later in Eqs. 2.32, and α^* acts as a dampening function for μ_t, which takes the form of Eq. 2.30.

$$\mu_t = \alpha^* \frac{\rho k}{\omega} \qquad \text{Eq. 2.30}$$

α^* can be expanded to the form of Eq. 2.31.

$$\alpha^* = \alpha_\infty^* \left(\frac{\alpha_0^* + \mathrm{Re}_t / R_k}{1 + \mathrm{Re}_t / R_k}\right) \qquad \text{Eq. 2.31}$$

α_∞^* and R_k are closure constants. Re_t and α_0^* can be expanded in the following manner.

$$\mathrm{Re}_t = \frac{\rho k}{\mu \omega} \qquad \alpha_0^* = \frac{\beta_i}{3} \qquad \text{Eqs. 2.32}$$

β_i is a closure constant. Y_k and Y_ω, of Eq. 2.26 and Eq. 2.27, represent the dissipation of k and ω respectively. Y_k expands to the form of Eq. 2.33.

$$Y_k = \rho \beta^* f_{\beta^*} k \omega \qquad \text{Eq. 2.33}$$

Where,

$$\beta^* = \beta_i^* \left[1 + \zeta^* F(M_t)\right] \qquad \beta_i^* = \beta_\infty^* \left(\frac{4/15 + \left(\mathrm{Re}_t / R_\beta\right)^4}{1 + \left(\mathrm{Re}_t / R_\beta\right)^4}\right) \qquad \text{Eqs. 2.34}$$

$F(M_t)$ is a compressibility function, and ζ^*, β_∞^*, and R_β are closure constants. f_{β^*} is a piecewise function, with its value being dependent on local value of ω and the spatial rate of change of both k and ω. Y_ω expands to the form of Eq. 2.35.

$$Y_\omega = \rho\beta f_\beta \omega^2 \qquad \text{Eq. 2.35}$$

In which,

$$f_\beta = \frac{1+70X_\omega}{1+80X_\omega} \qquad X_\omega = \left|\frac{\Omega_{ij}\Omega_{jk}S_{ki}}{(\beta_\infty * \omega)^3}\right|$$

$$\Omega_{ij} = \frac{1}{2}\left(\frac{\delta u_i}{\delta x_j} - \frac{\delta u_j}{\delta x_i}\right) \qquad \beta = \beta_i\left[1 - \frac{\beta_i *}{\beta_i}\xi * F(M_t)\right] \qquad \text{Eqs. 2.36}$$

S_{ki} is a strain tensor. The form of the *k-ω* model used in Fluent is that presented by (Wilcox, 1988), which uses the closure constants shown below (Fluent, 2006). Fluent allows user definition of these constants.

$$\alpha_\infty * = 1.0,\ \alpha_\infty = 0.52,\ \alpha_0 = 1/9,\ \beta_\infty * = 0.09,\ \beta_i = 0.072,\ R_\beta = 8.0,\ R_k = 6.0,\ R_\omega = 2.95,\ \zeta * = 1.5,$$
$$M_{t0} = 0.25,\ \sigma_k = 2.0, \text{ and } \sigma_\omega = 2.0$$

(Wilcox, 1998) discusses several advantages the *k-ω* model has over the *k-ε* model; very good accuracy for two-dimensional boundary layers with adverse or favourable pressure gradients, agreement with measured properties in re-circulating flows, and reproduction of more subtle features of *k* near solid boundaries. (Fluent, 2006) adds that the *k-ω* model also provides close agreement in flow regimes for far wakes, mixing layers, as well as plane, round and radial jets. (Wilcox, 1998) indicates that the relative accuracy for the *k-ω* and *k-ε* model is similar in the case of plane jets, although a weakness of the *k-ω* model over the *k-ε* model is its sensitivity to free-stream BCs in shear flows.

2.4.3.5 *k-ω* Shear-Stress-Transport Model

The *k-ω* SST model of (F. R. Menter, 1993; F. R. Menter, 1994) takes advantage of the accurate attributes of both the *k-ε* and the *k-ω* models. To combine the models a blending function is used to alter the effect of each turbulence model as a function of the distance from the nearest wall. The transport equations for the *k-ω* SST model are shown below as Eq. 2.37 and Eq. 2.38 (Fluent, 2006).

$$\frac{\partial}{\partial t}(\rho k)+\frac{\partial}{\partial x_i}(\rho k u_i)=\frac{\partial}{\partial x_j}\left[\left(\mu+\frac{\mu_t}{\sigma_k}\right)\frac{\partial k}{\partial x_j}\right]+G_k-Y_k+S_k \qquad \text{Eq. 2.37}$$

$$\frac{\partial}{\partial t}(\rho \omega)+\frac{\partial}{\partial x_i}(\rho \omega u_i)=\frac{\partial}{\partial x_j}\left[\left(\mu+\frac{\mu_t}{\sigma_\omega}\right)\frac{\partial \omega}{\partial x_j}\right]+G_\omega-Y_\omega+D_\omega+S_\omega \qquad \text{Eq. 2.38}$$

The equations are of a similar form to those of Eq. 2.26 and Eq. 2.27 for the *k-ω* model. The differences lie in the inclusion of a damped cross-diffusion derivative term (D_ω) being incorporated into the ω equation, and modified definitions of μ_t, σ_k, and σ_ω to account for transport of turbulent shear-stress.

The following discussion presents the expansion of terms in Eq. 2.37 and Eq. 2.38 that were not discussed in relation to the *k-ω* in Section 2.4.3.4. These equations are presented primarily in order to identify the new closure constants of the *k-ω* SST model. The modified definition of μ_t is shown in Eq. 2.39.

$$\mu_t=\frac{\rho k}{\omega}\frac{1}{\omega_{\max}\left[\frac{1}{\alpha^*},\frac{\Omega F_2}{\alpha_1 \omega}\right]} \qquad \text{Eq. 2.39}$$

where,

$$\Omega \equiv \sqrt{2\Omega_{ij}\Omega_{ij}} \qquad \text{Eq. 2.40}$$

α_1 is a closure constant and F_2 is a blending function. Ω is the mean rate of rotation tensor. The modified definitions of σ_k, and σ_ω are shown as Eq. 2.41 and Eq. 2.42 respectively.

$$\sigma_k=\frac{1}{F_1/\sigma_{k,1}+(1-F_1)/\sigma_{k,2}} \qquad \text{Eq. 2.41}$$

$$\sigma_\omega = \frac{1}{F_1 / \sigma_{\omega,1} + (1 - F_1) / \sigma_{\omega,2}} \qquad \text{Eq. 2.42}$$

$\sigma_{k,1}$, $\sigma_{k,2}$, $\sigma_{\omega,1}$, and $\sigma_{\omega,2}$ are closure constants. F_1 is a blending function, and along with F_2 is defined below in Eq. 2.43 and Eq. 2.45.

$$F_1 = \tanh\left(\Phi_1^4\right) \qquad \text{Eq. 2.43}$$

where,

$$\Phi_1 = \min\left[\max\left(\frac{\sqrt{k}}{0.09\omega y^2}, \frac{500\mu}{\rho y^2 \omega}\right), \frac{4\rho k}{\sigma_{\omega,2} D_\omega^+ y^2}\right] \qquad \text{Eq. 2.44}$$

$$F_2 = \tanh\left(\Phi_2^2\right) \qquad \text{Eq. 2.45}$$

where,

$$\Phi_2 = \max\left[2\frac{\sqrt{k}}{0.09\omega y^2}, \frac{500\mu}{\rho y^2 \omega}\right] \qquad \text{Eq. 2.46}$$

y is the distance to the closest surface. D_ω^+ is the positive portion of the cross-diffusion (D_ω), defined in Eq. 2.47.

$$D_\omega = 2(1 - F_1)\rho\sigma_{\omega,2}\frac{1}{\omega}\frac{\partial k}{\partial x_j}\frac{\partial \omega}{\partial x_j} \qquad \text{Eq. 2.47}$$

The definition of G_ω in Eq. 2.38 differs from that in the k-ω model (Eq. 2.27), as shown in Eq. 2.48.

$$G_\omega = \frac{\alpha}{\nu_t} G_k \qquad \text{Eq. 2.48}$$

v_t is turbulent kinematic viscosity. α_∞ also differs from the *k-ω* model, in which it defined as a constant. For the *k-ω* SST model α_∞ is defined by Eq. 2.49.

$$\alpha_\infty = F_1\alpha_{\infty,1} + (1 - F_1)\alpha_{\infty,2} \qquad \text{Eq. 2.49}$$

where,

$$\alpha_{\infty,1} = \frac{\beta_{i,1}}{\beta^*_\infty} - \frac{\kappa^2}{\sigma_{\omega,1}\sqrt{\beta^*_\infty}} \qquad \text{Eq. 2.50}$$

$$\alpha_{\infty,2} = \frac{\beta_{i,2}}{\beta^*_\infty} - \frac{\kappa^2}{\sigma_{\omega,2}\sqrt{\beta^*_\infty}} \qquad \text{Eq. 2.51}$$

$\beta_{i,1}$, $\beta_{i,2}$, and κ are closure constants. In the *k-ω* SST model, the Y_ω from the *k-ω* model (Eq. 2.38) becomes Eq. 2.52, as f_β becomes equal to 1.

$$Y_\omega = \rho\beta\omega^2 \qquad \text{Eq. 2.52}$$

β in the *k-ω* model is constant, but in the *k-ω* SST model is blended as shown in Eq. 2.53.

$$\beta_i = F_1\beta_{i,1} + (1 - F_1)\beta_{i,2} \qquad \text{Eq. 2.53}$$

The transport equations of the *k-ω* SST model require the closure constants given below in addition to those already defined in the Section 2.4.3.4. In Fluent the value of the constants used are those generated and discussed in (F. R. Menter 1994). The values for the constants defined at the end of Section 2.4.3.4, for the *k-ω* model, remain in use for the *k-ω* SST model.

$\sigma_{k,1} = 1.176$, $\sigma_{\omega,1} = 2.0$, $\sigma_{k,2} = 1.0$, $\sigma_{\omega,2} = 1.168$, $\alpha_1 = 0.31$, $\beta_{i,1} = 0.075$, $\beta_{i,2} = 0.0828$, $\kappa = 0.41$

The result of the blending functions defined in Eq. 2.47, Eq. 2.49, and Eq. 2.53 is that near the wall the *k-ω* model is solely activated, and in the turbulent free stream the *k-ε* model is solely activated.

Between the near wall and free stream regions the blending function adds and scales contributions from both turbulence models.

(Fluent, 2006) indicates that the *k-ω* SST model is more accurate for a wider range of flows than the standard *k-ω* model, including problems with separated flows. (CFD-Online, 2011) indicates the 'very popular' nature of the *k-ω* SST model is a successful combination of positive attributes from the two contributing models (discussed in Section 2.4.3.2 and Section 2.4.3.4). (CFD-Online, 2011) also specifically indicates that users of the *k-ω* SST model 'report good behaviour in adverse pressure gradients and separating flow'.

(F. R. Menter, Kuntz, & Langtry, 2003) provides a good summary of the capabilities of the *k-ω* SST model and current advances being made. (F. R. Menter et al., 2003) makes reference to (Obi, Aoki, & Masuda, 1993) who presents a comparison of the *k-ε* model and *k-ω* SST model with experimental results in an asymmetric diffuser. The SST model is seen to give significantly better separation prediction accuracy, although slower recovery than observed experimentally. In (Obi et al., 1993) the *k-ε* model produced a more accurate recovery rate in the separation region, but (F. R. Menter et al., 2003) describes this improved accuracy more of an 'artefact of the under predicted separation' than a genuine improvement.

2.4.3.6 Reynolds Stress Turbulence Model

In the two-equation RANS models presented above, solution accuracy problems emerge in flows that contain complex strain fields or significant body forces (Versteeg & Malalasekera, 2007). The two-equation models assume the local turbulence state can be approximated by *k* and the dissipation term, which under the above mentioned conditions is inadequate (Mankbadi, Habashi, & Hafez, 1995; Versteeg & Malalasekera, 2007). This is a result of the Reynolds stresses (the stress tensors in a fluid due to the random turbulent fluctuations in the fluid momentum), being inadequately represented by the extended Boussinesq relationship (Davidson, 2004; Versteeg & Malalasekera, 2007).

First it is important to remember where the Reynolds stresses first originated. If we recall the discussion of Section 2.4.2, and the RANS equations (Eq. 2.21 and Eq. 2.22), the Reynolds stresses appeared as a result of the 'Reynolds averaging' process. The appearance of the Reynolds stresses,

which are not present in the instantaneous NS equations, meant that the RANS equations were unable to be closed.

Instead of using the Boussinesq relationship, which has been the link between the RANS equations and the previous turbulence models discussed, the RSM takes a more direct approach and makes an attempt at representing the Reynolds stresses by emulating the physics in the energy cascade of the turbulence – a complex task. The RSM does so by working with a new system of transport equations involving Reynolds stresses. There are a number of different ways in which the RSM can be executed.

The transport equation for the Reynolds stresses takes the following form.

Local Time Derivative + Convection = – Turbulent Diffusion
+ Molecular Diffusion – Stress Production – Buoyancy Production + Pressure Strain
– Dissipation + Production by Rotation + User defined source term

Mathematically the terms are in the form of Eq. 2.54.

$$\frac{\partial}{\partial t}\left(\rho\overline{u_i'u_j'}\right)+\frac{\partial}{\partial x_k}\left(\rho u_k\overline{u_i'u_j'}\right)=-\frac{\partial}{\partial x_k}\left[\rho\overline{u_i'u_j'u_k'}+\overline{p\left(\delta_{kj}u_i'+\delta_{ik}u_j'\right)}\right]$$

$$+\frac{\partial}{\partial x_k}\left[\mu\frac{\partial}{\partial x_k}\left(\overline{u_i'u_j'}\right)\right]-\rho\left(\overline{u_i'u_k'}\frac{\partial u_j}{\partial x_k}+\overline{u_j'u_k'}\frac{\partial u_i}{\partial x_k}\right)-\rho\beta\left(g_i\overline{u_j'\theta}+g_j\overline{u_i'\theta}\right)+\overline{p\left(\frac{\partial u_i'}{\partial x_j}+\frac{\partial u_j'}{\partial x_i}\right)}$$

$$-2\mu\overline{\frac{\partial u_i'}{\partial x_k}\frac{\partial u_j'}{\partial x_k}}-2\rho\Omega_k\left(\overline{u_j'u_m'}\varepsilon_{ikm}+\overline{u_i'u_m'}\varepsilon_{jkm}\right)+S_{user} \qquad \text{Eq. 2.54}$$

In order to get a solvable form of the equation the turbulent diffusion, buoyancy production, pressure strain, and dissipation terms all need to be approximated via modelling. This means that an exact solution for the Reynolds stresses is still not achieved (Versteeg & Malalasekera, 2007), and (Mankbadi et al., 1995).

It will be left to the reader to investigate the modelling of each of the above mentioned components in more detail. For the purposes of the investigations carried out in this thesis the form of the RSM used was that of (Launder, G. J. Reece, & Rodi, 1975), (Gibson & Launder, 1978), and (Launder, 1989b).

For use in this thesis the following models were used for the above mentioned components. The specific derivation and form of each of the models will be left for the reader to investigate within the references given. In modelling the turbulent diffusion the model developed by (Daly & Harlow, 1970) and then (Lein & Leschziner, 1994) was utilised. To model pressure strain the work of (Gibson & Launder, 1978), (Fu, Launder, & Leschziner, 1987), (Launder, 1989b), and (Launder, 1989a). Dissipation rate was modelled using the work of (Sarkar & Balakrishnan, 1990), and a discussion of how buoyancy effects on turbulence were modelled can be found in (Fluent, 2006).

Due to the number of transport equations that need to be solved, the RSM is computationally far more expensive than the two-equation models. In addition, (Fluent, 2006) notes that due to the strong coupling between the Reynolds stresses and the mean flow result in an increase in iterations for a converged solution compared to the k-ε and k-ω models.

A discussion of the merits of the RSM in practice is presented below. (Davidson, 2004) suggests that the complexity involved in modelling the turbulent energy cascade makes the RSM of only limited value in an engineering context. (Fluent, 2006) notes that due to the closure approximations employed, accuracy is limited in many flow scenarios to a level comparable, or below that of the more basic, and computationally far less expensive two-equation models. However, (Fluent, 2006) also adds, 'the RSM is a must when the flow features of interest are the result of anisotropy in the Reynolds stresses. Among the examples are cyclone flows, highly swirling flows in combustors, rotating flow passages, and the stress-induced secondary flows in ducts.'

(Versteeg & Malalasekera, 2007) notes that the RSM is potentially the most generally applicable of all models discussed in Section 2.4.3.2 through Section 2.4.3.6, and provides a very accurate calculation of mean flow properties. The extreme increase in computing cost, comparative lack of validation, and no better than equal performance to the k-ε model in a number of flow regimes (including axis-symmetric jets and unconfined re-circulating flows) are suggested as the RSMs relative disadvantages.

(Mankbadi et al., 1995) also discusses the results of RSM application to a variety of flow scenarios. (Mankbadi et al., 1995) argues that the prediction of wall jets, turbulence driven secondary flow, and strain rates formed by wall curvature exceeded that of the two-equation k-ε model. Although round jets, swirl, and the spreading of weak shear flows only achieved comparable accuracy with the increase computational expense. Lack of universal applicability in practice is noted as one of the RSM weaknesses.

Table 3 summarises the relative strengths and weaknesses of each of the turbulence models discussed.

Table 3 Summary of Turbulence Models

Model	*Advantages*	*Disadvantages*
Spalart-Allmaras	1. Computationally inexpensive 2. Examples of performing well in: a. Wall bounded flows b. Flows with mild separation c. Flows where accurate turbulence computations are not required	1. Limited range of applicability 2. Examples of performing poorly in: a. Complex flows b. Spreading rates of jets
Standard *k*-*ε*	1. Most wide validated turbulence model 2. Excellent performer in a range of industrial flows 3. Computationally inexpensive compared to RSM 4. Examples of performing well in: a. Abrupt pipe expansions b. Flows around obstacles c. Side-discharge into channels d. Plane jets	1. Computationally more expensive than SA model 2. Examples of performing poorly in: a. Some unconfined flow b. Flows with large extra strain c. Rotating flows d. Fully developed flows in non-circular ducts e. Adverse pressure gradients
k-*ε* RNG	1. Outperforms standard *k*-*ε* model in swirling, low Re flows 2. Slightly more widely applicable than standard *k*-*ε* model 3. Examples of performing well in: a. Backward facing steps	1. Not widely validated 2. More susceptible to instability in steady state solutions compared to standard *k*-*ε* model 3. Shares some of the standard *k*-*ε* model weaknesses 4. Slightly more computationally expensive than the standard *k*-*ε* model

k-ε Realizable	1. Outperforms standard *k-ε* model in flows with strong streamline curvature, vortices, and rotation 2. Outperforms standard *k-ε* and *k-ε* RNG model in separated flows, and in flows with complex secondary flow features	1. Not widely validated 2. Limited accuracy in domains containing both rotating and stationary fluid zones 3. Shares some of the standard *k-ε* model weaknesses 4. Slightly more computationally expensive than the standard *k-ε* model
k-ω	1. Comparable accuracy to standard *k-ε* model in plane jets 2. Outperforms *k-ε* model in free-shear flows 3. Computationally inexpensive compared to RSM 4. Examples of performing well in: a. Separation points b. Far wakes c. Mixing layers d. Plane, round and circular jets	1. Computationally more expensive than SA model 2. Results dependent of the assumed free stream value of *ω* 3. Sensitive to free-stream BCs compared to *k-ε* model 4. Examples of performing poorly in: a. External aerodynamic problems
k-ω SST	1. Contains positive attributes of both *k-ε* and *k-ω* models 2. Less sensitive to free stream assumptions than the *k-ω* model 3. Near wall performance better than the *k-ε* model 4. More widely applicable than both the *k-ε* and *k-ω* models 5. Computationally inexpensive compared to RSM 6. Examples of performing well in: a. Adverse pressure gradients	1. Computationally more expensive than SA model 2. Poor predictor of interactions of turbulent stresses compared to RSM 3. Less accurate prediction of recovery rate compared to *k-ε* model

	b. Separation points	
RSM	1. Potentially the most generally applicable model 2. Predicts mean flow properties well 3. Performs better than the *k*-ε model in flows with wall jets, turbulence driven secondary flow, strain rates formed by wall curvature 4. Examples of performing well in: a. Cyclones b. High swirl combustion flows c. Rotating flow passages d. Stress induced secondary duct flow	1. In practice is not as generally applicable as its potential suggests 2. Significantly higher computational expense than one- and two-equation models 3. Not widely validated 4. Performs no better than *k*-ε model in a number of flow regimes including axis-symmetric jets, unconfined re-circulation, spreading of weak shear flows and jets

3 Baffle Arrangements - Cell Efficiency

3.1 Background Information

Running a jet engine in either an operational or testing state generates a significant amount of noise. Far-field noise can reach levels in excess of 90dBA in military cells (Kodres, 2000; D. R. Schmidt, 1987). JETCs are in most cases located near airports where building and population densities are high. Local governing authorities often restrict the noise levels allowed to impact on surrounding areas. Acoustic treatments are required to minimise the noise related impact. Some examples of noise reduction technologies in JETCs can be found in (Corce, 1990; Dickman, Hehlnann, Hoelmert, & Freuler, 1984; Huff, 2007; Kodres, 2000).

Noise disturbances are created through pressure waves generated in both the audible range (20-20000Hz, (Caldarelli & Campanella, 2003)) and the infrasound range (<20Hz) (Huff, 2007). Infrasound waves can be problematic as they have the potential to result in human discomfort and vibration of structures and fittings (Flynn, 2008; Moller & Pedersen, 2004). Inlet and exhaust stack baffles are used in a vast majority of JETCs to protect against excessive noise levels. Depending on the cell size and the type of engines being tested, additional baffles are at times included in the fore-region of the working section.

A baffle arrangement consists of a number of individual baffles located in a structured fashion as shown in Figure 16. In individual baffle arrangements, the number of baffles will vary. Generally there will be between three and nine rows of baffles. The inlet stack of the CHCEC is an example of the former, and the exhaust stack at the CENCO cell in Hanover is an example of the latter. Each row normally consists of six to ten individual baffles. This is determined by both the cell and baffle dimensions.

Most commonly, baffles are arranged so that each second row of baffles is aligned in the stream-wise direction. The intermediate rows are aligned with the spaces between successive baffles in the rows both above and below. This is shown in the typical baffle arrangement of Figure 16.

In most cases, all baffles within a single arrangement will be identical. Each individual baffle consists of three sections as shown in Figure 16; the upstream face, the body, and the downstream face. The width of the individual baffle design is noted by (Doelling & Bolt, 1961) as being the major determining factor on the frequency of sound suppressed by the arrangement.

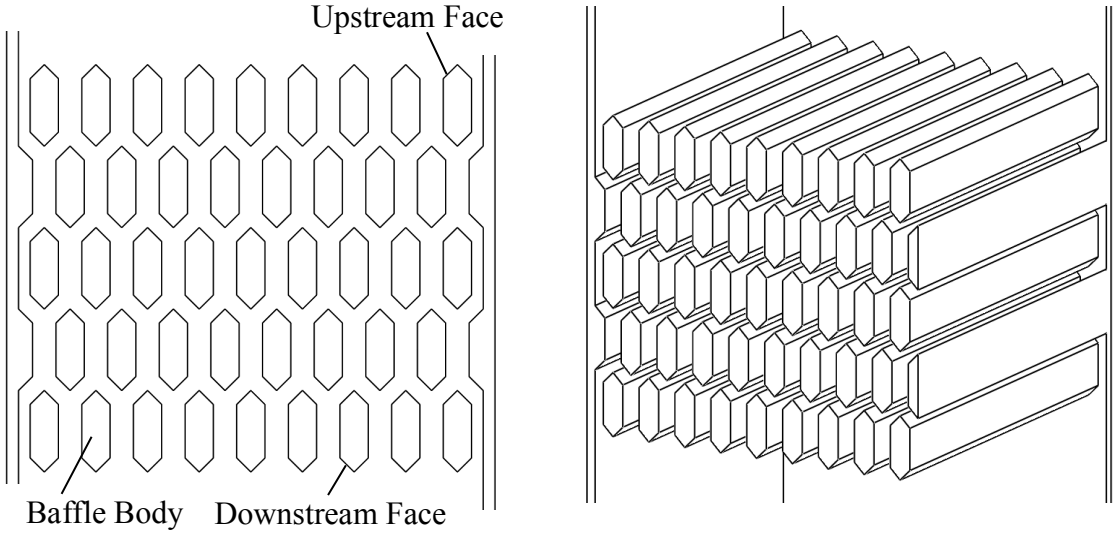

Figure 16 Typical Acoustic Baffle Arrangement in an Inlet or Exhaust Stack

As with all flow obstructions, a static pressure drop occurs across a baffle arrangement during operational conditions. The aerodynamic performance of a baffle arrangement therefore contributes to the achievable cell BPR and overall cell efficiency. Ideally, adequate acoustic dampening of a baffle arrangement will be achieved with minimum static pressure loss. This allows a higher cell BPR to be generated, leading to safer test conditions and greater cell capacity.

3.2 Baffle Analysis Methodology

An investigation into the aerodynamic efficiency of a typical JETC baffle arrangement was performed. The broader aim of the investigation was to analyse the application of CFD techniques to a region of a JETC under operational conditions. This aim hoped to more specifically achieve the following objectives:

- To apply recommendations from the literature along with sound reasoning and engineering knowledge to set up and generate CFD solutions;
- To gain an understanding of the flow patterns and features through and around a typical JETC baffle arrangement;
- To provide computational solutions to contribute one of the two aspects required for problem-specific validation of the techniques used;
- To qualitatively assess the accuracy of computational solutions produced for physical realism;
- To conduct a CFD-aided design process as an assessment of CFDs capability as a design tool; and

- To use increased cell BPR, and the associated benefits it brings, as the driving force behind the design process.

The remainder of this section discusses the methodology employed to achieve these objectives.

Firstly, a baseline baffle arrangement was chosen. The selection and details of the arrangement is discussed in Section 3.2.1. A computational domain was then generated to represent the baseline arrangement, the detail of which is discussed in Section 3.2.2.1. Through consultation with the literature and reasoning, the selection of the required CFD solver settings was made. These are discussed in Section 3.2.2.2 and Section 3.2.2.3. The computational domain of the baseline arrangement was then meshed. A mesh independence check was then performed using the solver settings discussed in Section 3.2.2.2 and Section 3.2.2.3. The development of the mesh and the performance of the mesh independence check are presented in Section 3.2.2.4.

A solution to the baseline arrangement was then generated. The findings made are presented in Section 3.3.1. Using the settings and meshing techniques developed in Section 3.2.2.1 through Section 3.2.2.4, a CFD-aided design process was then performed.

This design process was performed with the aim of enhancing aerodynamic efficiency through the baffle arrangement. In an effort to retain the acoustic properties of the baseline arrangement, a set of restrictions were placed upon the design process. These restrictions are discussed in Section 3.3.2. The implementation and development of the design process itself is presented in Section 3.3.3 through 3.3.9. Section 3.4 then concludes the investigation with a summary of the findings made.

3.2.1 Baseline Baffle Arrangement

With the intention that the findings of this section would contribute towards problem-specific JETC validation, an entire baffle arrangement within a cell stack was chosen for the baseline design. The width of the stack was selected to be of a square cross-section. The choice of a square cross-section was based on the use of a common industry design. The CHCEC cell, the CENCO cell in Hanover, and the General Electric cell in Peebles are some examples of this design employed in practice.

The width of the stack was set at 10m in diameter. Again, this was chosen for compatibility with examples seen in industry. The CHCEC cell, with inlet and exhaust stack widths of slightly less than 7.0m, is considered ‘small’ by industry standards (Flynn, 2008). The CENCO cell in Hanover,

which was investigated for use in testing the General Electric GE90 series of engines, the largest engines in aviation history with a fan diameter of 3.12m, has an exhaust stack approximately 13.0m in width. The 10m stack width chosen was therefore representative of a ‘mid-sized’ cell.

In choosing the structure of the baseline baffle arrangement, attempts were made where appropriate to incorporate features of the CHCEC inlet stack. The stack of the CHCEC uses three full rows of baffles. This was increased to five rows during this analysis. The decision to do so was based on two factors. Firstly, the arrangement of the CHCEC stack contains relatively few rows compared to other industry examples. An increase in baffle rows therefore provided wider applicability of the results. Secondly, it was thought that the flow characteristics of a repeated baffle pattern may require more than three rows to develop. A three row design could therefore have restricted the extent of the investigation.

Nine evenly spaced full baffles were used per row, in alignment with the CHCEC. For similar reasoning, and to align with industry convention, each successive row of baffles was offset from the previous by 180°. For the offset pattern to be used, the second and fourth rows contained eight full baffles and two half baffles. This is illustrated in Figure 17, which includes labels used for reference in following sections. The leading edge (LE) and trailing edge (TE) of each adjacent row was placed in stream-wise alignment.

3.2.2 Computational Settings

3.2.2.1 Computational Domain

The decision was made to model the baseline arrangement in a two-dimensional computational domain. This enabled a significant reduction in computational expense. However, doing so meant that the solution produced would not account for any interactions between the baffles and the sidewalls that they would be mounted on in reality. The interpretation of the results produced therefore needed to be made with this in mind.

The design of the individual baffles in the baseline arrangement was selected to be ‘basic’ so that a CFD-aided design process could be performed and analysed. An effort was made to keep the relative proportions of the baffles similar to those of the inlet stack at the CHCEC cell. As shown in Figure 17, the individual baffles were 1750mm in length and 600mm in width. The upstream and downstream faces were tapered at 45° to a centrally located point as shown in Figure 18.

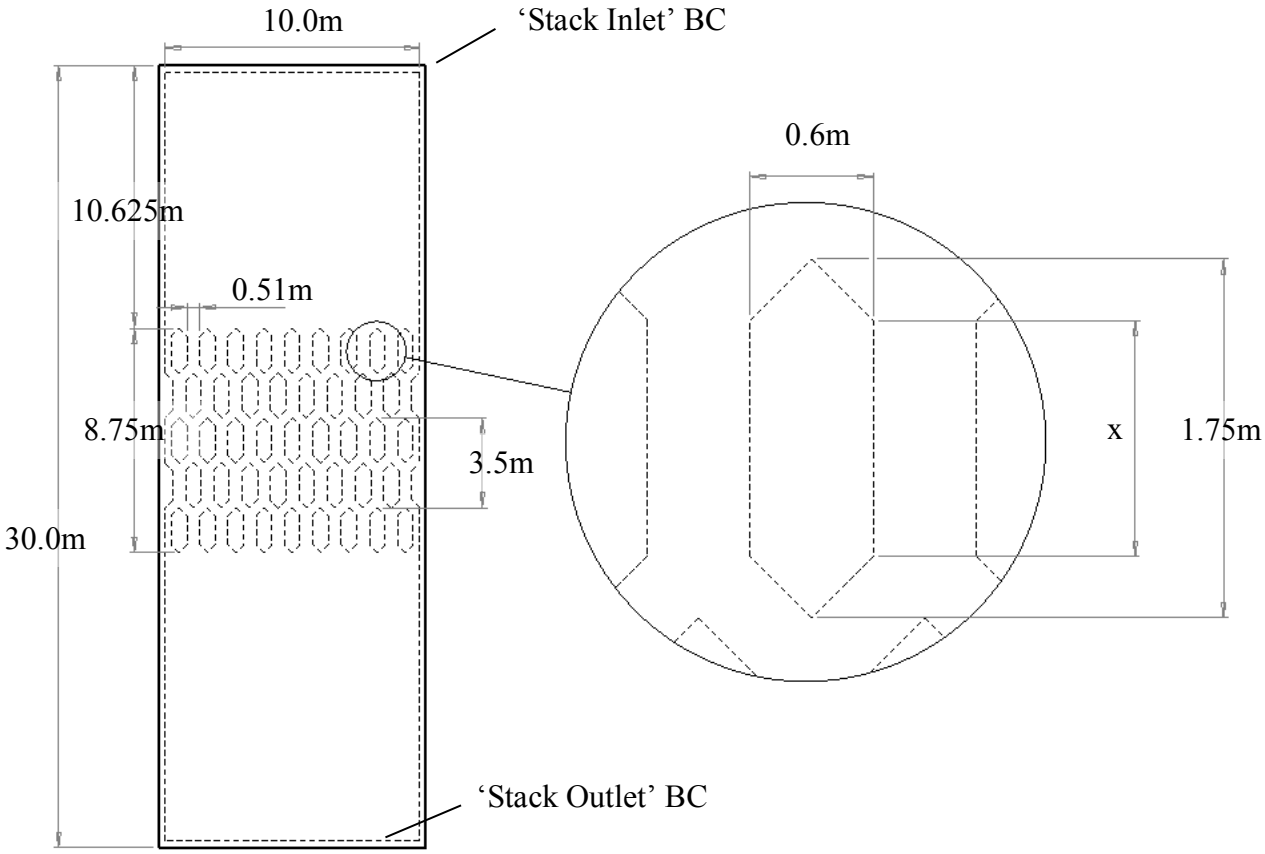

Figure 17 Geometry of Baseline Baffle Arrangement

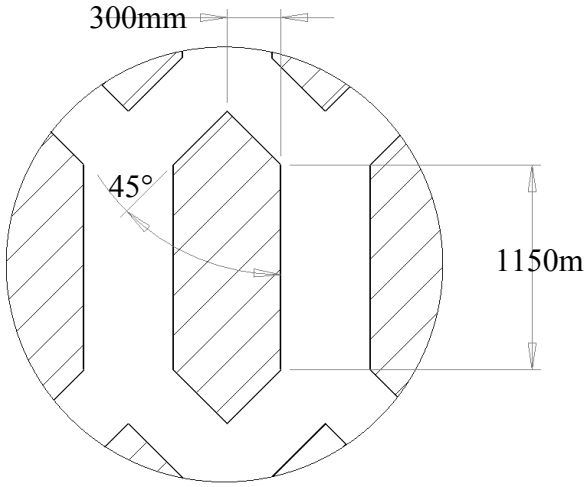

Figure 18 Geometry of Individual Baffle in the Baseline Arrangement

The width of the stack and formation of the baffle arrangement were assigned the dimensions as per the discussion of Section 3.2.1. The computational domain was extended evenly upstream and downstream of the baffle arrangement to be 30m in overall length. As shown in Figure 17, this effectively represented an extended inlet or exhaust stack condition. In practice many cells have the

inlet and exhaust baffle arrangements aligned with the inlet and exit planes of their respective stacks. This was avoided to maintain a more general applicability of the results. This also allowed the baffle flow patterns to be isolated from other flow features, so a more focused investigation could be performed.

'Stack Inlet' and 'Stack Outlet' BCs were assigned at the upstream and downstream extent of the domain. The distance of slightly greater than 10m between the baffle arrangement and the BCs was incorporated to allow the flow features of baffle arrangement to develop with minimum impediment.

3.2.2.2 Solver Settings

The fluid modelled within the computational domain was air, with constant density, specific heat, thermal conductivity, and viscosity. Compressibility effects were consciously not accounted for. The maximum velocity through the most restricted portion of the solution was predicted to be relatively low at 50-55ms^{-1}. This enabled the energy equation to be removed during solution, decreasing computational expense.

The CHCEC cell was used for reference when setting the wall roughness BCs within the domain. The CHCEC baffles are constructed of painted metal, and the stack walls are smoothened concrete. Access to the CHCEC was not able to be attained to assess whether a measurable roughness was present. Analysis of independent (of CHCEC) and comparable painted metal and smoothed concrete surfaces confirmed that if access had be gained, a measurable roughness was not likely to be present due to the smooth nature of both finishes.

Using the recommendations of (Fluent, 2006), a wall roughness height (K_S) of 0m was applied to all solid surfaces represented in the computational domain. Although the K_S of 0m could not be verified with direct measurements, the same value was used throughout the analysis process. This meant that if any erroneous effects were generated (which it is not thought likely), they would be consistently present throughout the solutions and would therefore have negligible impact on the comparative analysis performed.

A first-order spatial discretisation scheme was used. This was chosen based on a number of factors. With the lack of problem-specific validation data for comparison, any analysis that was conducted would be limited to quantitatively comparative and qualitative techniques. Higher-order schemes

could have potentially provided accuracy improvements. However, problem-specific validation of such was unable to be tested. As such, when interpreting the solution produced, no more certainty or confidence could have been attributed to the findings whether a first- or higher-order solver was used. With this consideration, the 'unvalidatable' potential of a higher-order scheme was decided against in preference to a first-order scheme. The first-order scheme was able to provide a usable benefit in the form of decreased computational expense.

A steady-state solver was used as no areas of transient flow were predicted. Solution convergence using a steady-state solver was unable to be achieved in several instances. A solution method of applying a transient solver over a number of time steps was employed in such cases. This solution procedure is recommended by (Fluent, 2006). The transient solver was employed with 0.01s time steps over a 2.00s solution period. All 'initially transient' solutions reached a time independent solution within the 2.00s period.

The exact nature of the flow pattern within the domain was unknown prior to analysis. However, due to the expanding channel created between the downstream faces of adjacent baffles, the potential for adverse pressure gradients and separation needed to be accounted for. This was of particular importance when selecting a turbulence model. The SA model was discounted due to its lack of general applicability (STAR-CCM, 2011; Wilcox, 1998). Of the two-equation models, the *k-ω* SST model is reported by (CFD-Online, 2011; Fluent, 2006) to be more widely applicable, than the contributing *k-ε* and *k-*ω models. In addition, (Obi et al., 1993) showed in a study of a asymmetrical diffuser that the *k-ω* SST model outperformed the *k-ε* model in prediction of separation points. Although it was noted that wake recovery lengths were over-predicted.

The reduction of the computational domain to two-dimensions meant the increased computational expense of the RSM could be accommodated. However, the discussions of (Mankbadi et al., 1995; Versteeg & Malalasekera, 2007) suggest that the scenarios where the RSM exceeds the performance of the two-equation models did not align with this investigation. Although the accuracy of the RSM is discussed by (Versteeg & Malalasekera, 2007) as being comparable to the *k-ε* model in a range of flow regimes, the substantial increase in computational expense made it a poorer option in this case. As such, it was deemed the *k-ω* SST model was most applicable to this investigation. In applying the *k-ω* SST model, the likely over prediction of wake length was considered when analysing the solutions.

A SIMPLE pressure-velocity coupling was used. The choice of coupling was based on the discussion of (Raithby & Van Doormaal, 1984) which suggested that developments of the SIMPLE coupling, SIMPLE-C and PISO being the available options, did not provide notable improvements in solution efficiency or robustness.

To assess solution convergence, the residuals of continuity, x and y velocity, k, and ω were monitored. The convergence criterion for the solution was based on the residuals, scaled in relation those produced in the first solution iteration, dropping below a value of 5.0E-04.

The average velocity at the 'Stack Out' BC was also monitored throughout the solution process. A further convergence criterion was added, stating that the 'Stack Out' average velocity needed to be oscillating within $0.05 ms^{-1}$ of a constant value. In doing so it was assured that the flow rate through the domain was not transient or 'divergent' in nature.

3.2.2.3 Boundary Conditions

The 'Stack Inlet' and 'Stack Outlet' BCs, shown in Figure 17, were used to drive airflow through the domain. In a real-world scenario, the airflow from upstream of the baffle arrangement would be drawn in from the atmosphere, at 0Pa static gauge pressure, via the depression created at the engine inlet. The static pressure immediately downstream of the baffle arrangement would be expected to be below 0Pa, resulting from the upstream propagation of the engine inlet depression.

Experimental test cell data were unable to be gathered to accurately set the BCs. As such, focus was placed on generating a realistic airflow velocity through the domain by assigning 'artificial' upstream and downstream BCs in combination.

Both (Idelchik & Fried, 1986) and (Massey, 2001) discuss the pressure loss coefficient, a measure of flow efficiency, as being a function of Re for a bluff body. The Re is defined below as Eq. 3.1.

$$\mathrm{Re} = \frac{\rho u w_b}{\mu} \qquad \text{Eq. 3.1}$$

For application relevant to this investigation, w_b represents the baffle width and u represents the mainstream velocity. The fluid properties ρ and μ remain constant throughout this investigation, as compressibility effects were not being accounted for. For the scenario modelled the Re, and

therefore the pressure loss coefficient of the baffles, was dependent on u alone. The use of 'artificial' BCs to generate a given u was therefore deemed justified for the purpose of calculating flow efficiency through baffle arrangements in this investigation.

Taking the above discussion into account, the 'Stack Outlet' was modelled as a pressure outlet with a static pressure of 0Pa. The 'Stack Inlet' was modelled as a velocity inlet. Through review of (Agmen et al., 2005), the velocity at the 'Stack Inlet' was set at $20ms^{-1}$, as being a realistic value that would be expected in the inlet stack of an operational JETC.

As a check of the realism of these BCs, the following scenario was considered. For a test cell with a square cross-sectioned inlet stack and working section of 10m in width, a MFR of $2440kgs^{-1}$ would be developed with a uniform velocity at the inlet stack face of $20ms^{-1}$. Three jet engines were then selected as being at the 'small', 'medium', and 'large' end of the aviation scale. These engines were the IAE V2500, the Rolls-Royce Trent 500, and the General Electric GE90, which produce approximate MFRs of $400kgs^{-1}$, $860kgs^{-1}$, and $1350kgs^{-1}$ respectively (Cantwell, 2011 - Downloaded ; MTU, 2011; Rolls-Royce, 2009). A cell MFR of $2440kgs^{-1}$ would represent a cell BPR of 510%, 183%, and 81% for the V2500, Trent 500, and GE90 respectively.

For the 'small' V2500 this is unrealistically excessive. For the 'mid-sized' Trent 500 this value is realistic, and would represent a safe testing environment (Clarke, 2000). For the 'large' GE90, the value is realistic, but bordering on an unsafe test environment due to the low cell BPR. Thus, the $20ms^{-1}$ inlet velocity at the 'Stack Inlet' was deemed to realistically represent the MFR developed by the size of engine likely to be tested in the size of cell modelled.

In setting the turbulence BCs at the 'Stack Inlet' the following was considered. The geometry of the stack in the computational domain was extended both upstream and downstream of the baffle arrangement so a non-specific inlet or exhaust stack condition was created. In assigning the turbulence BCs the same was done. Upstream of a baffle arrangement in an inlet stack is the external atmosphere. Upstream of a baffle arrangement in an exhaust stack is the lower exhaust stack and BB. Considering the geometry of the lower exhaust stack and BB it would be expected substantial mixing and turbulence would be present, a radically different state to that upstream of the inlet stack.

The turbulence at the 'Stack Inlet' BC was consciously set to replicate neither the inlet or exhaust stack cases specifically. As such, the generality of the findings was retained. The turbulence BCs were therefore set in an effort to replicate a physical wind tunnel test environment. The turbulence

intensity (TI) was set at 1%, reflective of a working section in general purpose wind tunnel with no specific features for high level turbulence suppression. The inlet TLS was set based on the maximum length scale that can be produced in a fully developed duct flow (Fluent, 2006). (Fluent, 2006) defines this maximum TLS as being 7% of the duct width, corresponding to 0.7m in the current case.

3.2.2.4 Mesh and Mesh Independence

To control the use of element types, the computational domain was broken into the following zones, which are also illustrated in Figure 19:

- Upstream of baffle arrangement;
- Baffle body channels;
- Inter-baffle rows; and
- Downstream of baffle arrangement.

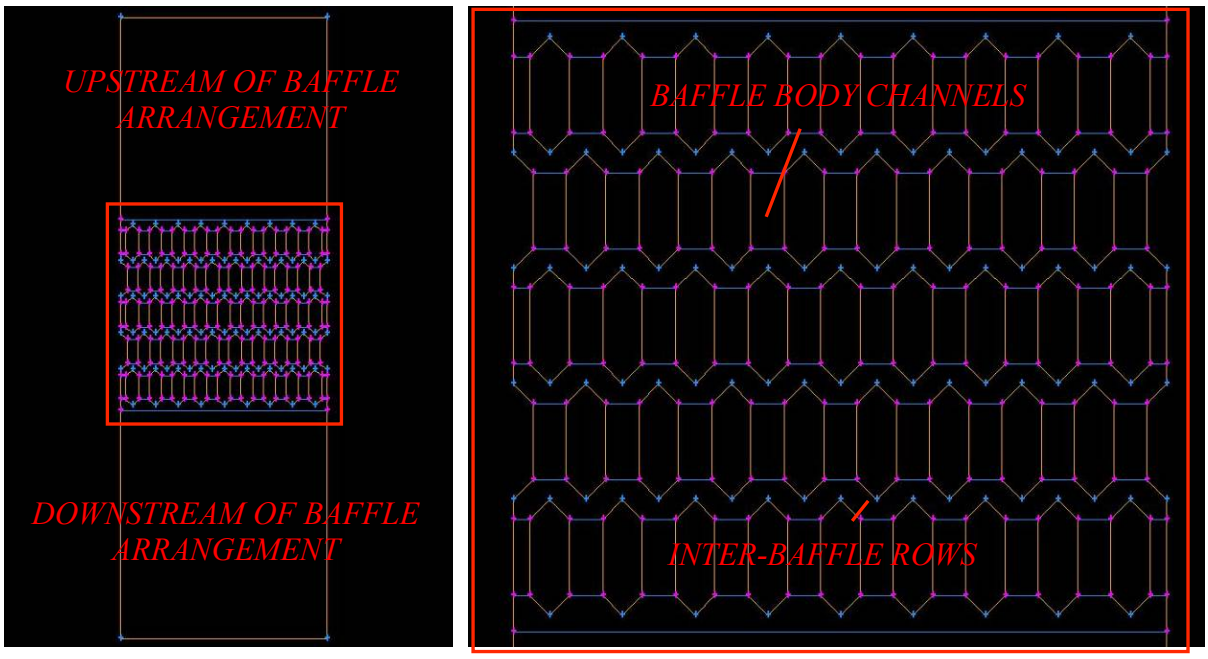

Figure 19 Zones within the Computational Domain used for Mesh Control

In the zones upstream and downstream of the baffle arrangement, structured quad elements were used. In these regions the airflow was predicted to be aligned with the inlet stack walls. Quad elements perform well when they can be applied in such flow scenarios (Fluent, 2006). This also enabled the benefit of efficient stacking to be utilised, which led to a lower computational requirement.

The geometry of each baffle body channel was rectangular and located downstream of a converging duct. The flow patterns in these regions were predicted to be simple, and in alignment with the baffle body walls. Applying the above-mentioned reasoning, quad elements were also used in the baffle body channels.

The inter-baffle rows were predicted to contain areas of flow complexity. In addition, the geometry of the inter-baffle rows was irregular but repetitive. This meant structured quad elements could not be applied without high levels of skewness. Triangular elements are suited to these applications, and as such were applied in the inter-baffle rows (Fluent, 2006). Figure 20 shows the element types and element density distribution used in the computational domain.

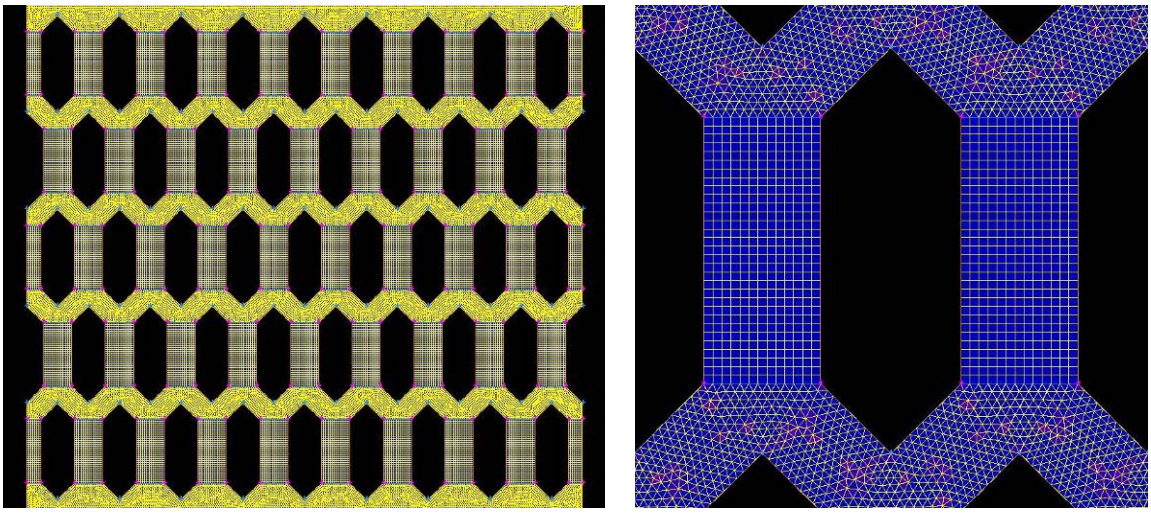

Figure 20 Element Types and Element Density Distribution in the Computational Domain

The computational domain was initially meshed using 5.90E04 elements. A computational solution was generated using the solver settings and BCs described in Section 3.2.2.2 and Section 3.2.2.3.

Further meshes containing 8.01E04, 1.15E05, 1.43E05, 1.86E05, 2.05E05, and 2.40E05 elements were developed. Computational solutions were generated following the development of each mesh. Figure 21 shows a comparison of flow patterns between the solutions developed with meshes of 2.05E05 and 2.40E05 elements.

Figure 21 shows that qualitatively no discernable differences are present between the solutions produced with meshes of 2.05E05 and 2.40E05 elements. Figure 21a shows that in both solutions localised areas of low velocity are present at the tip of the upstream face, and downstream of the

intersection between the baffle body and downstream face. Localised areas of high velocity are seen in both solutions at the intersection of the upstream face and baffle body.

Figure 21b shows that the realignment of flow in the baffle body channels is replicated in both solutions. Importantly, Figure 21c shows separation behaviour is generated at the intersection of the baffle body and downstream face in both solutions. The profile of the separation region can be seen to be qualitatively identical in the solutions produced with 2.05E05 and 2.40E05 elements.

The presence of separation in this region, which is effectively a two-dimensional diffuser, has been experimentally observed in a number of previous studies, including those of (Buice & Eaton, 2000) and (Cherry, Elkins, & Eaton, 2008). Detection of the separations presence contributes a level of qualitative validation to the computational settings discussed in Section 3.2.2.

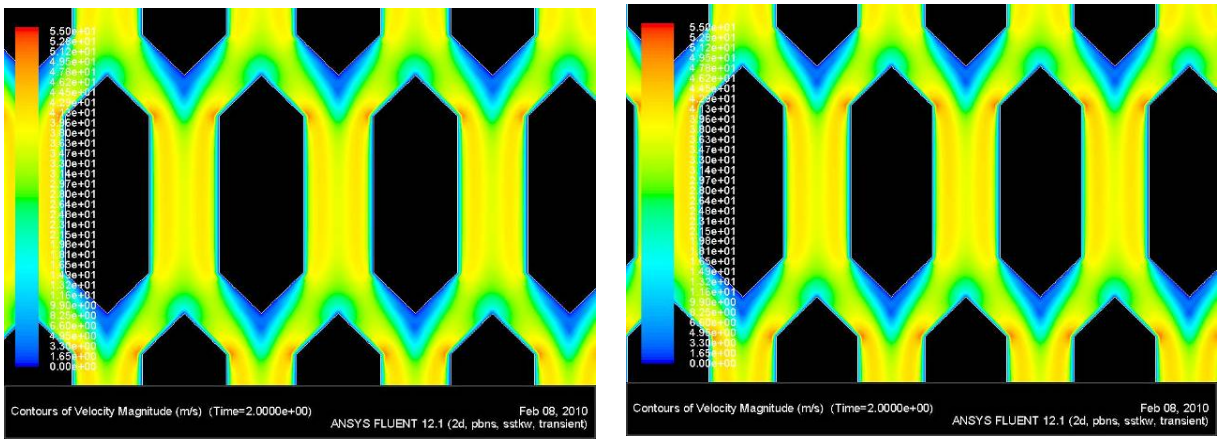

a.

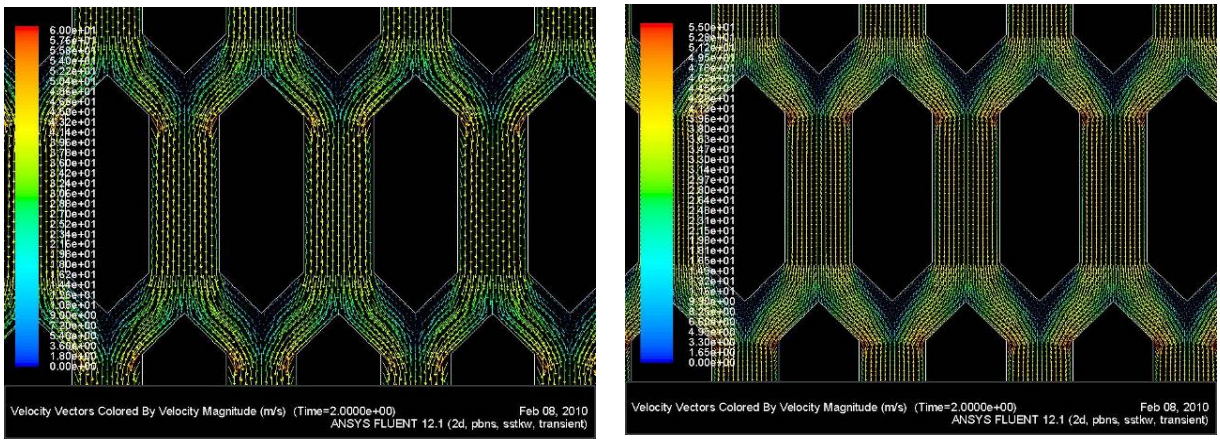

b.

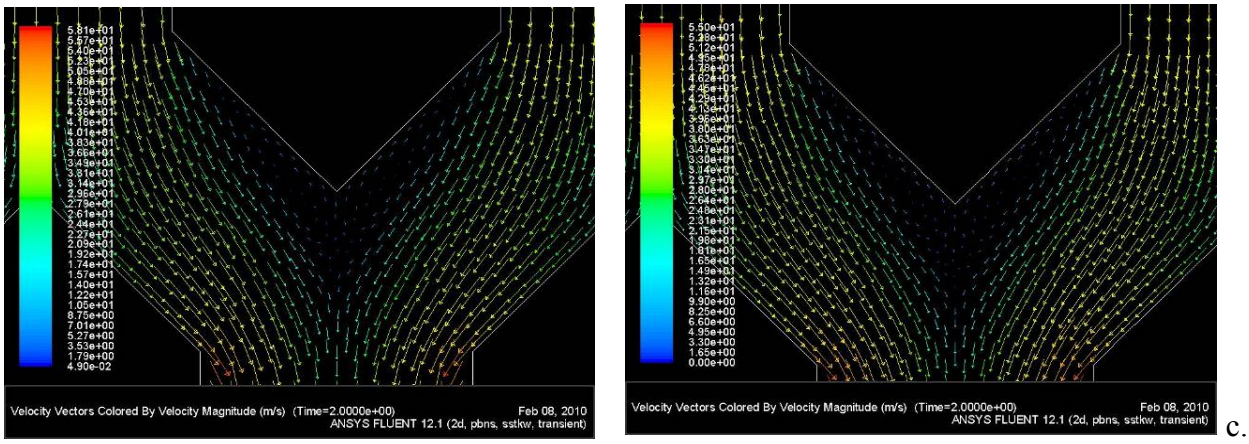

c.

Figure 21 Flow Patterns Surrounding (a/b) and Below (c) Baffles in Solutions generated using Meshes of 2.05E05 (left) and 2.40E05 Elements (right)

Cell MFR was chosen as the determining quantitative parameter in mesh independence. Cell MFR is used regularly in the JETC industry to define cell efficiency through calculation of cell BPR. For the purposes of checking mesh independence a pressure difference across the 'Stack Inlet' and 'Stack Outlet' BCs was prescribed.

The pressure difference used was found through a trial and error process. A pressure difference was prescribed and a solution generated. The flow rate through the computational domain was then calculated from the solution, and the pressure difference at the BCs altered. This process was performed until the prescribed pressure difference generated an equivalent MFR of ~2000kgs^{-1} in the computational domain meshed with 5.90E04 elements. An arbitrary (but realistic) cell depth of 10.0m was assigned to the two-dimensional computational domain for the purpose of MFR calculation. An identical pressure difference was applied across all domains in the mesh independence checking procedure. Figure 22 compares the MFRs calculated for each solution produced.

Figure 22 shows the absolute variation in cell MFR between the 2.05E05 element and 2.40E05 element solutions was less than 1.0%. In consideration of this, and the above-mentioned qualitative agreement, a mesh of 2.40E05 elements was deemed to be of adequate density to achieve the aims of the baffle arrangement investigation.

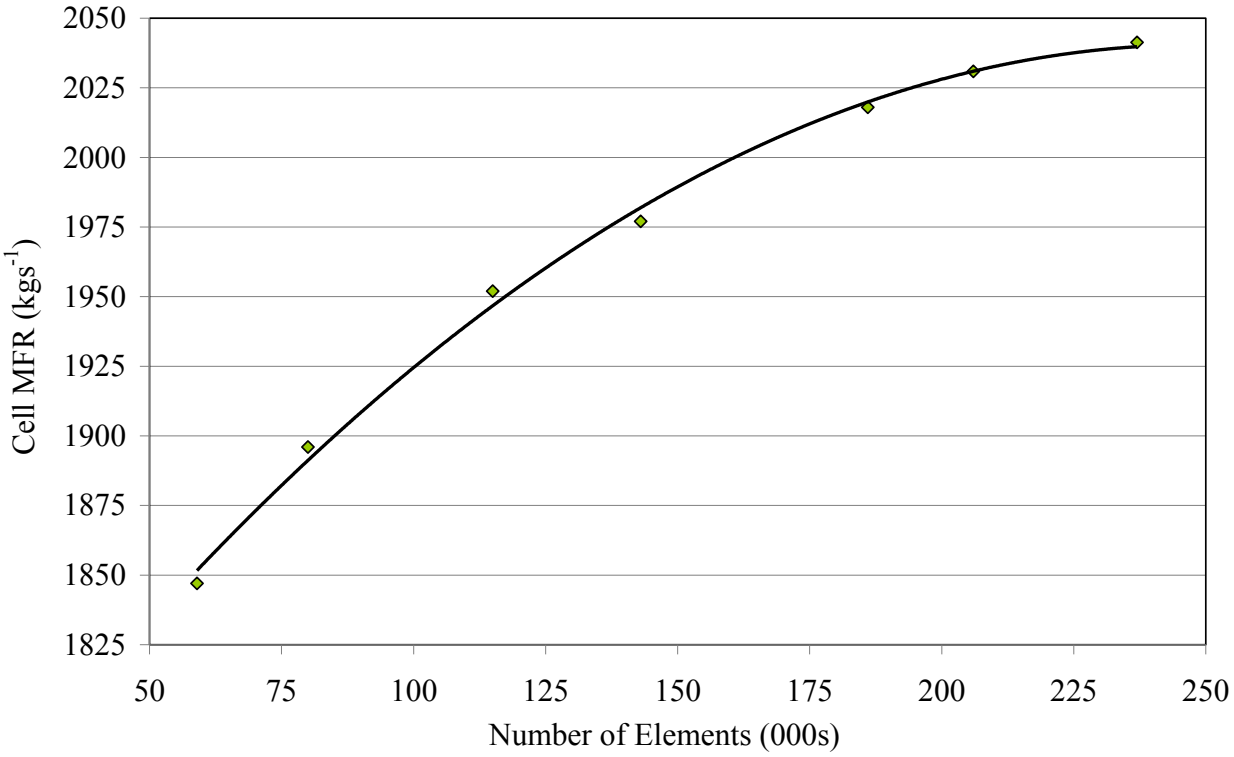

Figure 22 Cell MFR Variation with Number of Elements in the Baseline Baffle Arrangement

3.3 Results

This section presents the results of the baffle arrangement investigation. The analysis of the baseline arrangement is presented in Section 3.3.1. The design process, performed with the aim of flow efficiency improvements, is then presented in Section 3.3.2 through Section 3.3.9.

3.3.1 Baseline Design

The flow patterns briefly discussed in the mesh independence check of Section 3.2.2.4 are elaborated upon in this section. Figure 23 shows the flow pattern around a section of baffles within the baseline arrangement. Separation can be seen to be present downstream of all baffles. A detailed view of the separation structure is shown in Figure 24. An adverse pressure gradient can be seen in Figure 25 at the sharp change in direction at the intersection of the baffle body and the downstream face. This adverse pressure gradient is the driving force behind the separation (Francis, 1975).

To find the cause of the adverse pressure gradient, the baffle arrangement geometry is analysed. Between adjacent baffle bodies, in the baffle body channels, the flow can be seen to be confined to a 500mm wide passage. Downstream of the baffle body the channels expand to 1100mm along the

length of the downstream face. As a result, a diffuser effect is created. Both (Francis, 1975) and (Massey, 2001) discuss adverse pressure gradients being formed in diffuser scenarios.

It is also noted by (Francis, 1975) and (Massey, 2001) that in conical diffusers separation can only be avoided with extremely small taper angles, of less than 6°. With a taper angle of 45°, the presence of separation should therefore be expected for the comparable scenario of the baseline solution.

Figure 26 compares lines of 'zero stream-wise velocity' between the baseline solution and experimental data of (Cherry et al., 2008). The experimental data of (Cherry et al., 2008) was produced with an asymmetric diffuser. A number of qualitative similarities are present between the two results. Firstly, the initiation of the 'zero stream-wise velocity' lines in both figures occurs at a distance downstream of the initial solid boundary change in direction. Secondly, the initial growth of the 'zero stream-wise velocity' lines is closely aligned with the stream-wise flow direction in both examples. Thirdly, both 'zero stream-wise velocity' lines then tend towards a gradual and near liner growth away from the solid boundary until the termination of the diffuser.

Two notable qualitative differences are present in the comparison of Figure 26. Firstly, the 'zero stream-wise velocity' line in the baseline solution shows a change in direction after its initial growth in the stream-wise direction. Secondly, after the change in direction the line in the baseline solution becomes significantly offset from the stream-wise flow. This differs from the experimental result of (Cherry et al., 2008), which shows a continual growth away from the solid surface along a majority of the diffuser length.

Several reasons are suggested for these differences. Firstly and most importantly, as shown by Figure 25, the static pressure field is in the baseline solution is affected by the downstream row of baffles. This static pressure field augments the flow pattern in the separation region. Secondly, the experimental work of (Cherry et al., 2008) is performed on a diffuser with a significantly lower taper angle than used on the baseline baffles. Thirdly, the work of (Cherry et al., 2008) is performed on an asymmetric diffuser, compared to the effective symmetric diffuser in the baseline solution.

The structure of baffle arrangement was then analysed in relation to its influence on the downstream face separation regions. After the above-mentioned expansion of the flow channel, the flow path is then seen to contract along the upstream face in the following row of baffles. The flow pattern through the expansion followed by a contraction is presented in Figure 23 and Figure 24.

Comparison can be made with Figure 27 and Figure 28 which show the channel expansion below the lowermost baffle row. Being the lowermost baffle row, the initial expansion of the channel geometry is devoid of a following contraction.

Without the immediate channel contraction, the separation zone is seen to be significantly increased. Figure 29 can be compared with Figure 25 to show how the static pressure variation is altered through the lack of a downstream convergence. Figure 29 shows that the adverse pressure gradient forming the separation is not significantly affected by the following contraction. However, the opposing pressure gradient that limits the separations downstream propagation has been removed. This is more clearly illustrated in Figure 30 which shows the static pressure variation through, and below, the three lowermost baffle rows.

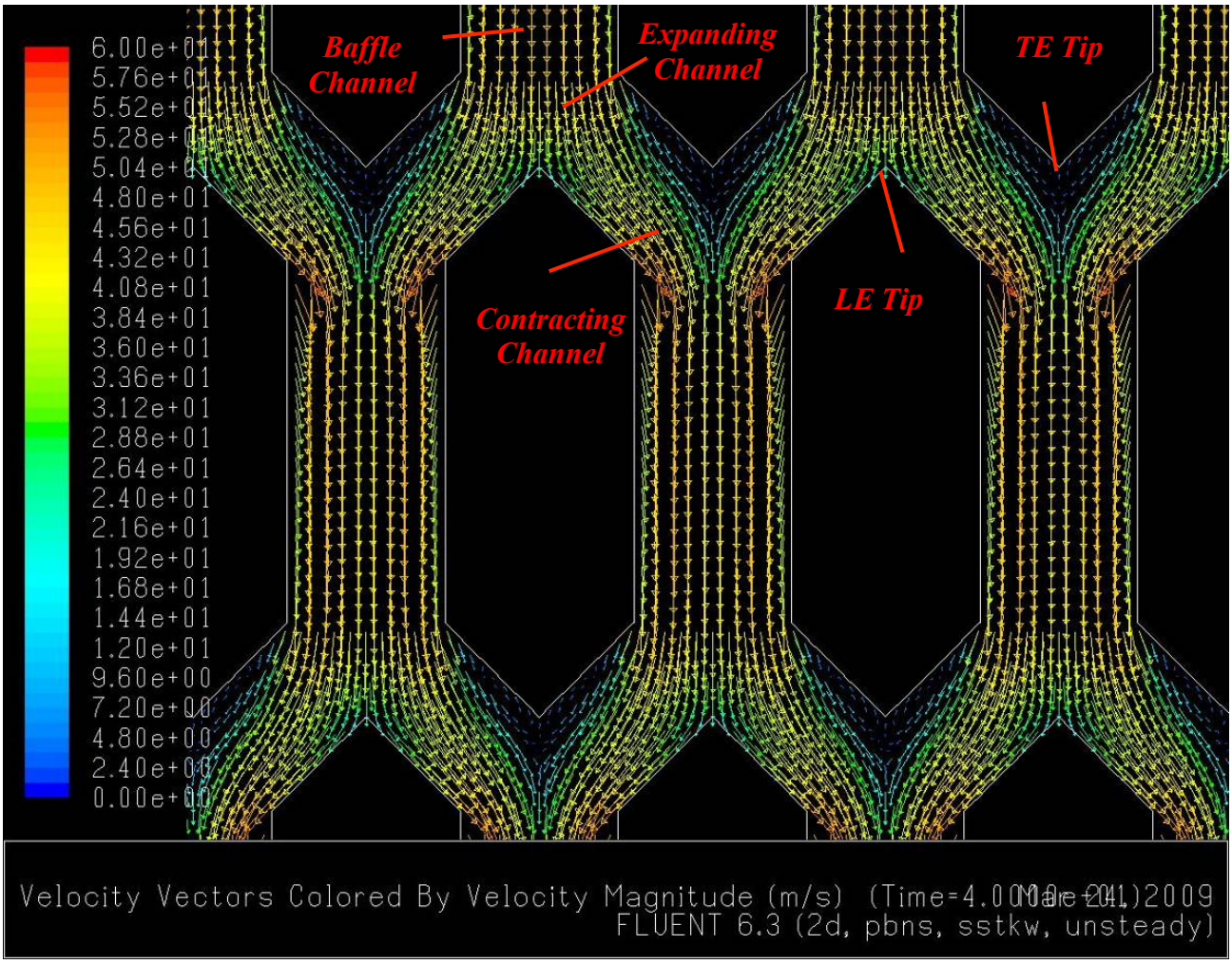

Figure 23 Flow Pattern through the Baseline Baffle Arrangement

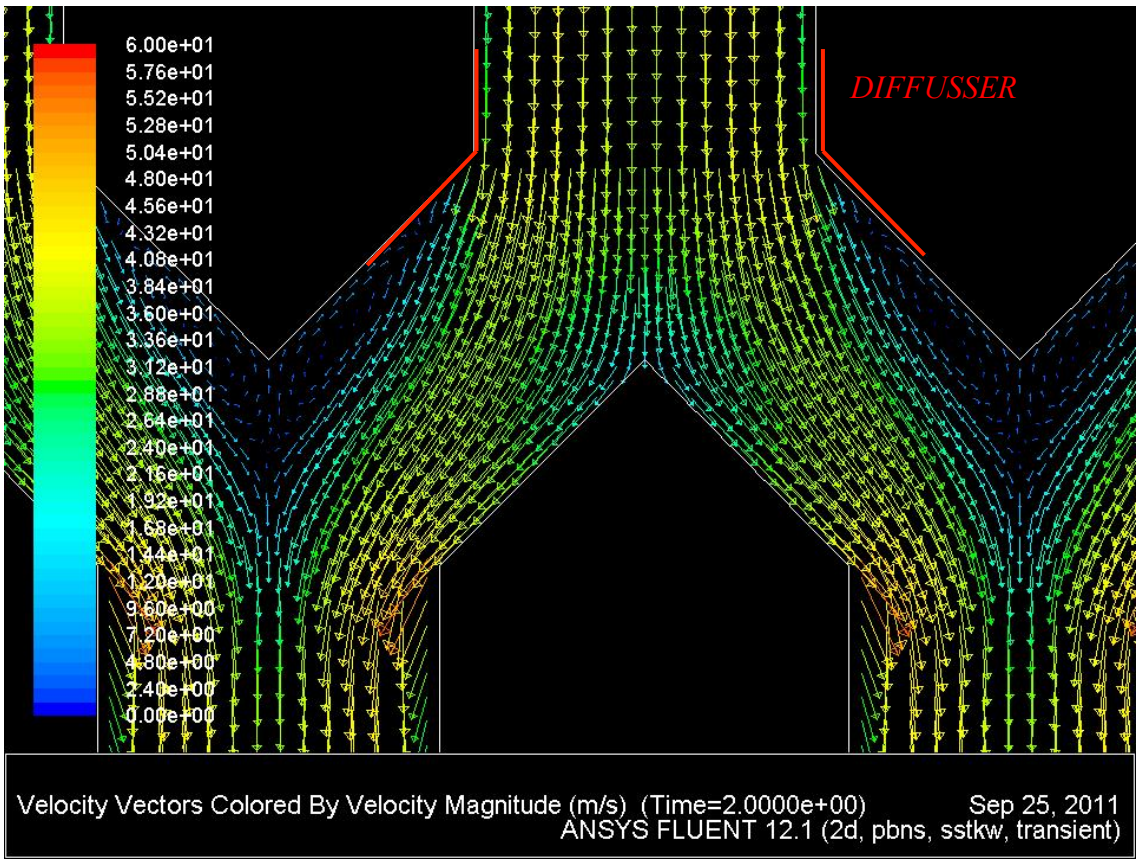

Figure 24 Separation Structure in the Baseline Baffle Arrangement

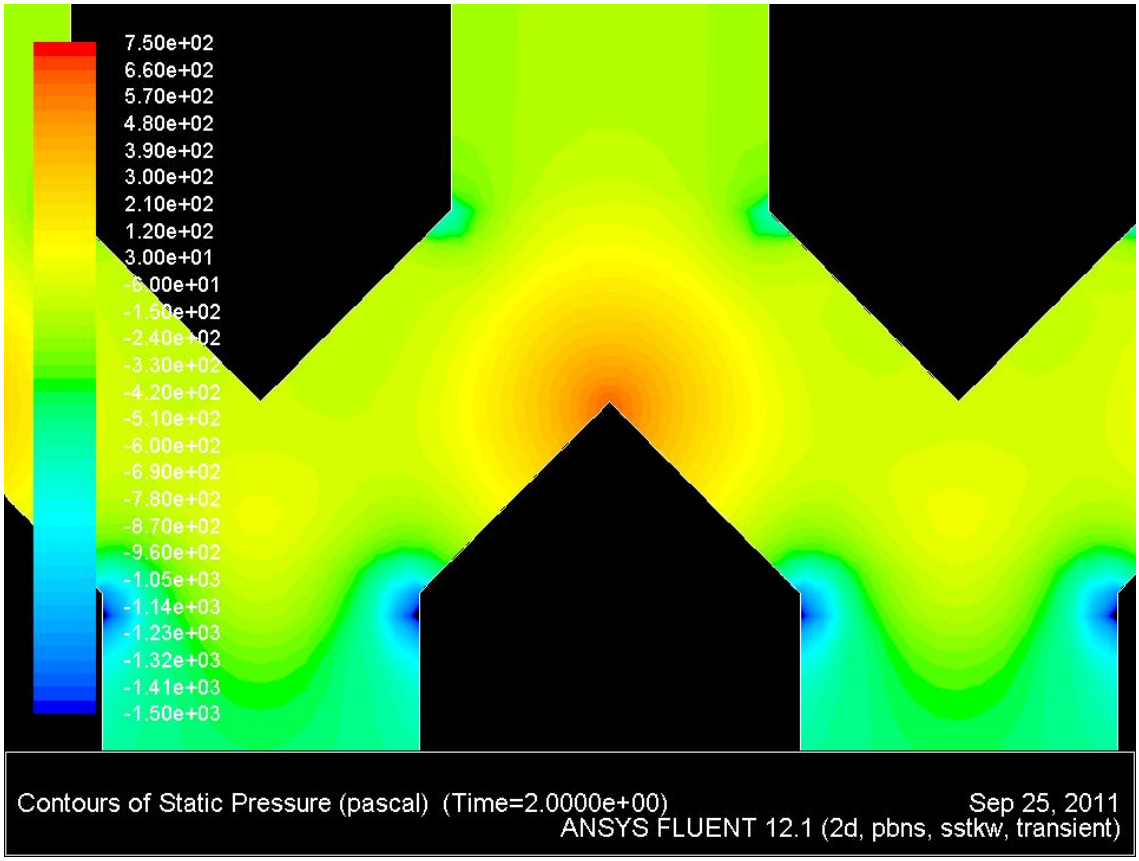

Figure 25 Static Pressure Distribution in the Baseline Baffle Arrangement

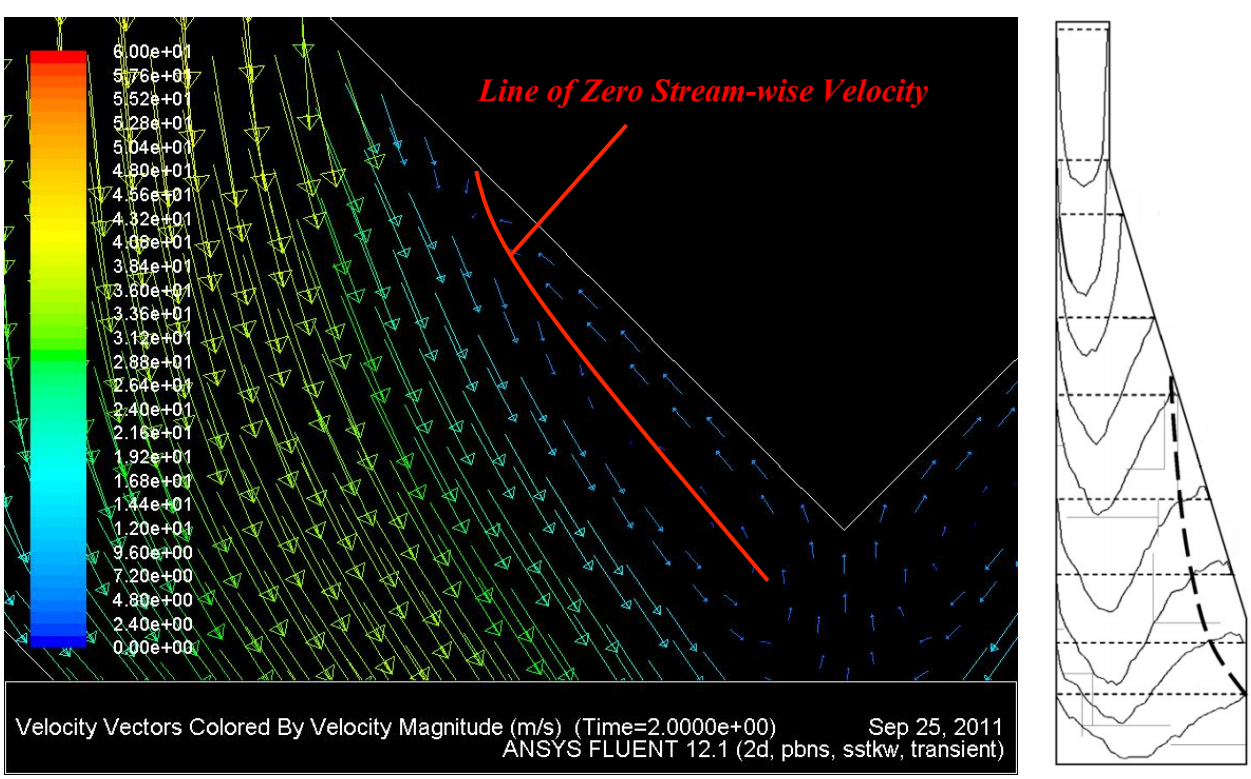

Figure 26 Comparison of Zero Stream-Wise Velocity Lines in the Baseline Arrangement Solution (left) and in Experimental Results (right) (Source of experimental results: (Cherry et al., 2008))

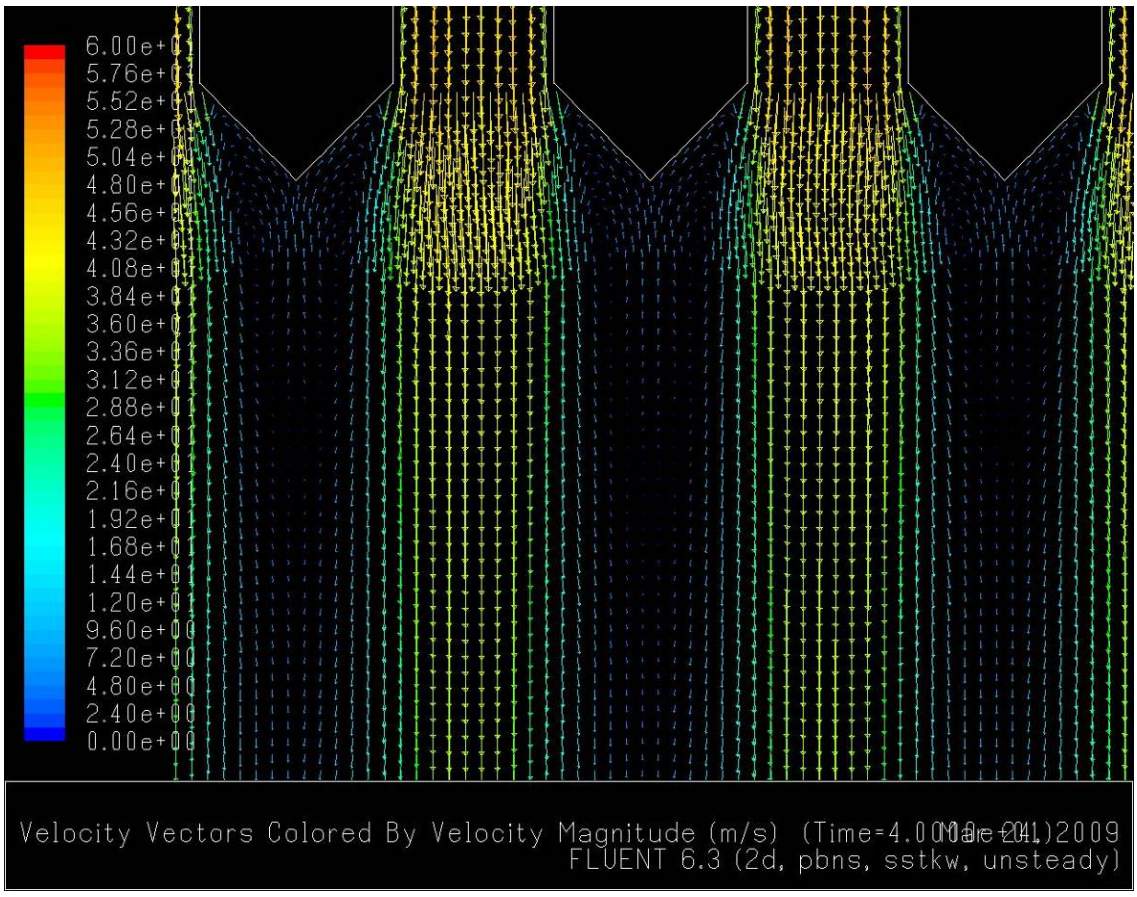

Figure 27 Separation Structure below the Lowermost Baffle Row in the Baseline Baffle Arrangement

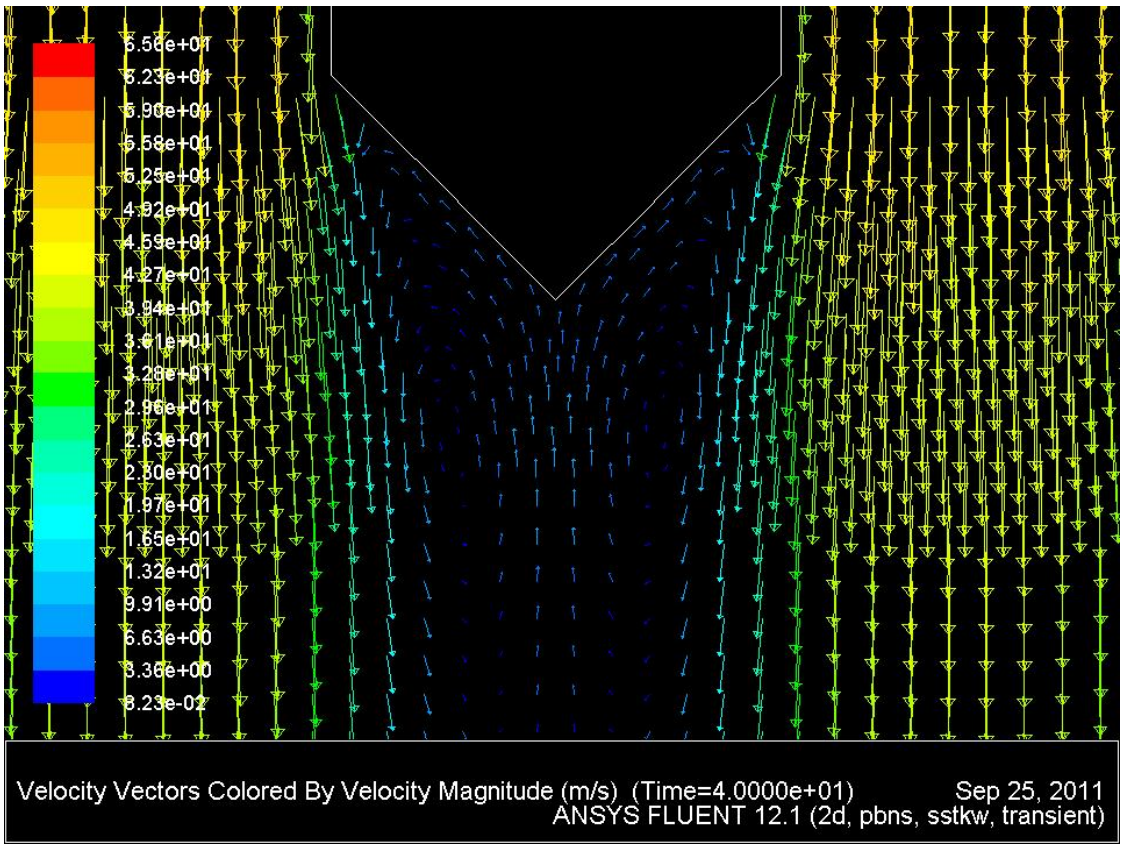

Figure 28 Detail of Separation below Baffle in the Lowermost Row in the Baseline Baffle Arrangement

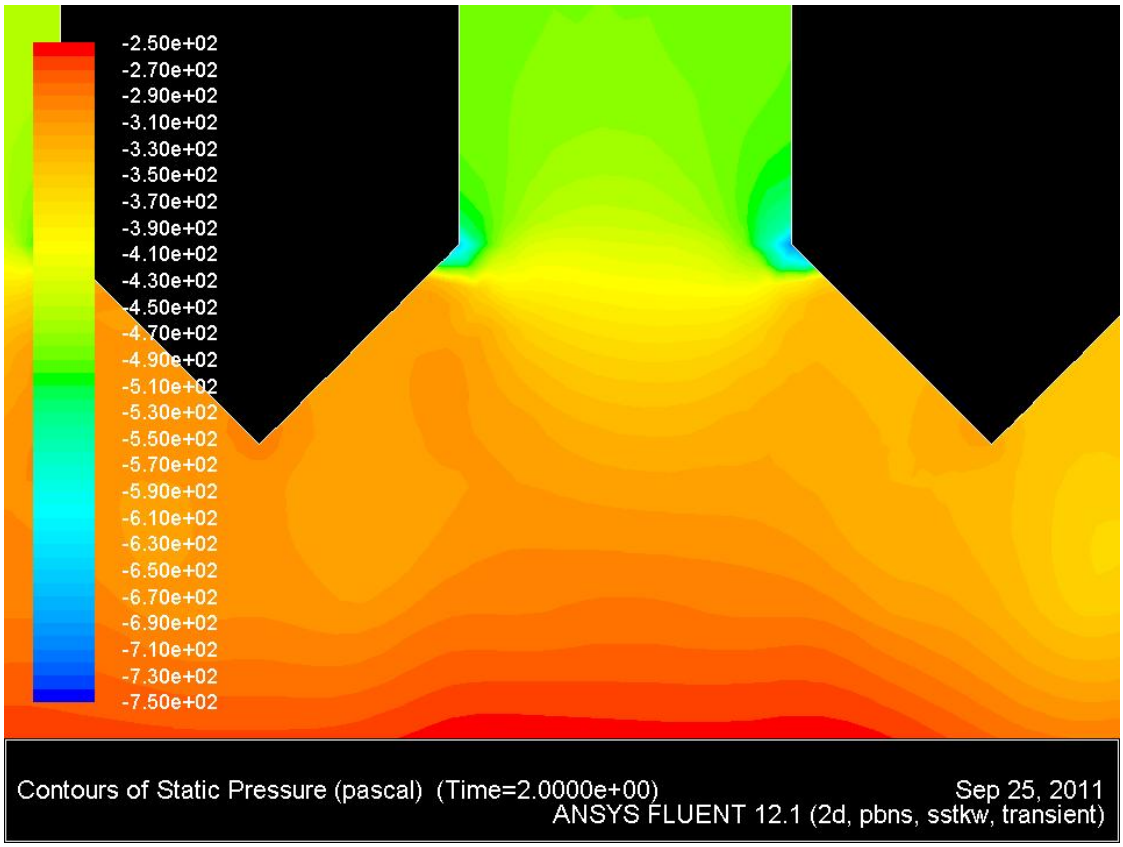

Figure 29 Static Pressure Distribution below the Lowermost Baffle Row in the Baseline Baffle Arrangement

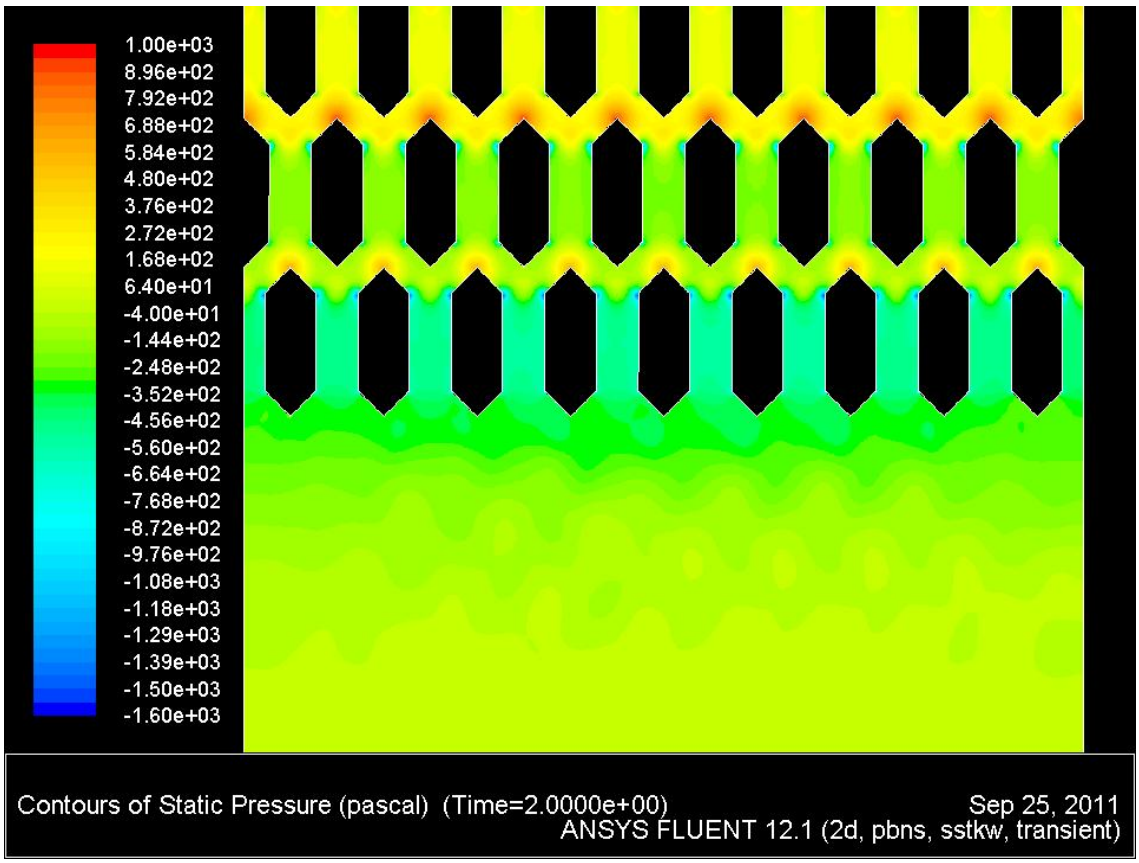

Figure 30 Static Pressure Distribution in Lower Portion of the Baseline Baffle Arrangement

It should be noted that (Obi et al., 1993) did experimentally show that the flow recovery downstream of a asymmetric diffuser was over-predicted by the *k-ω* SST turbulence model. Figure 31 shows the findings of (Obi et al., 1993), in which the development of a velocity profile downstream of a asymmetric diffuser is presented for both experimental and computational analyses.

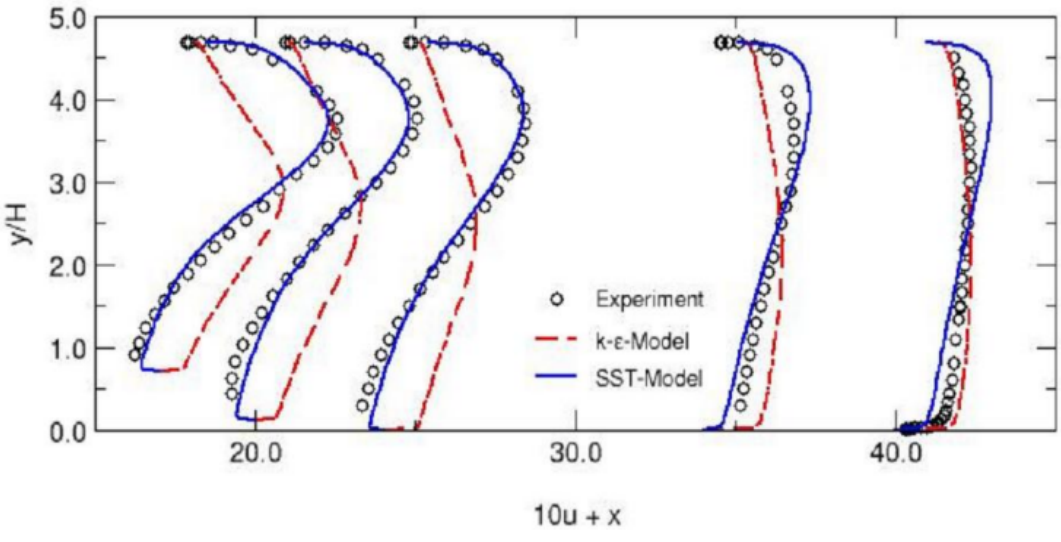

Figure 31 Experimental-Computational Comparison of Velocity Profiles showing Flow Recovery Downstream of an Asymmetric Diffuser (Source: (Obi et al., 1993))

With an understanding of the flow patterns developed in the baseline arrangement, a design process was performed with the goal of improving the aerodynamic efficiency. The results of this design process are presented in Section 3.3.3 through Section 3.3.9. Section 3.3.2 firstly discusses some limitations put on the design process in an effort to restrict deviation away from the acoustic performance of the baseline solution during the design process.

As a measure of aerodynamic efficiency in the design process, static pressure loss was used. This was initially calculated for the baseline solution. The static pressure loss across each design iteration was then scaled in relation to that of the baseline solution before comparison.

To calculate the static pressure loss, the average static pressure at the 'Stack Outlet' was deducted from that at the 'Stack Inlet'. The 'Stack Outlet' static pressure was fixed at 0Pa through the BC assignment, so the pressure loss 'calculated' was in practice a reading taken from the 'Stack Inlet'.

The progressive static pressure drop through the baseline arrangement is shown in Figure 32. It can be seen that the comparison of static pressure at the upstream and downstream BCs would account for the pressure loss as a result of wall friction along the extended stack.

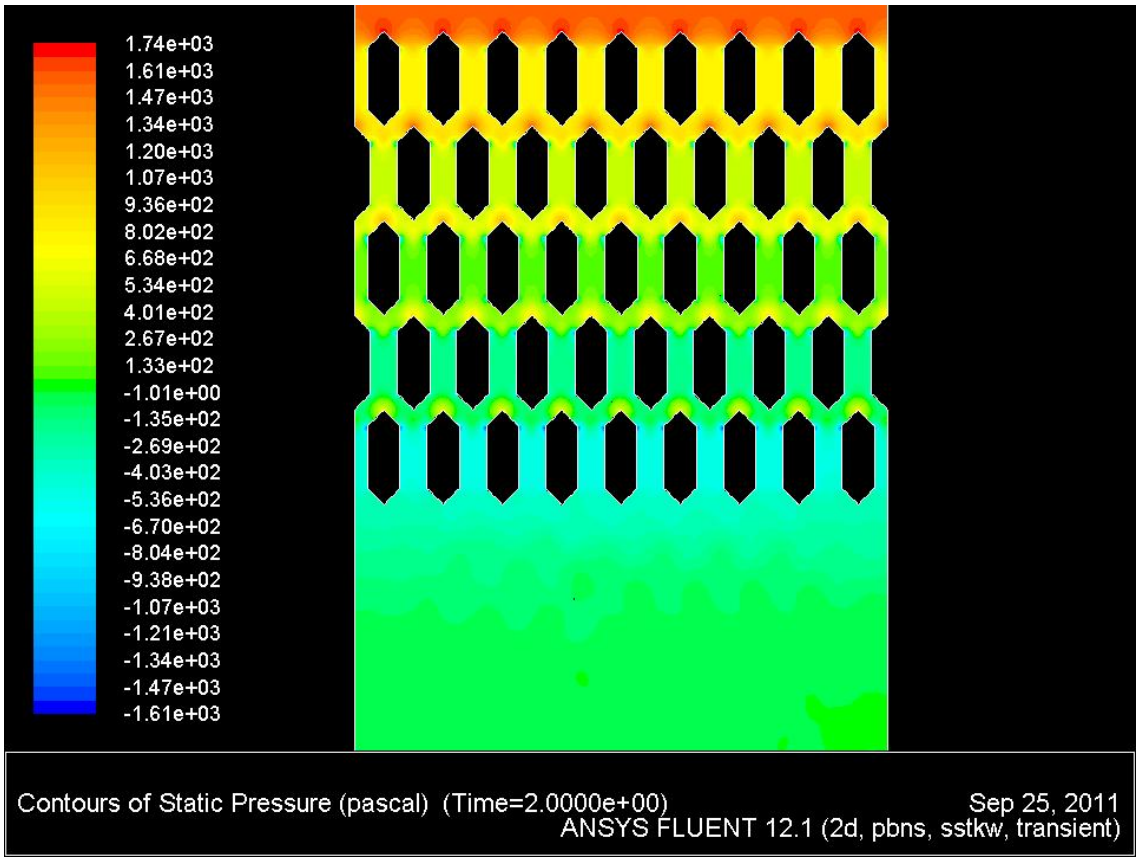

Figure 32 Static Pressure Drop through the Baseline Baffle Arrangement

The use of consistent stack geometry throughout the design process, along with the use of a consistence practice for calculating the pressure loss, negated any negative affects this would cause. In the following sections of this investigation it is noted that the terms ‘decreased pressure loss’ and ‘increased efficiency’ are used interchangeably.

3.3.2 Restrictions of the Baffle Design Process

A design process was performed to assess the potential for improved aerodynamic efficiency through the baseline baffle arrangement. To restrict deviation away from the baseline arrangements acoustic properties, restrictions were placed on the modifications that could be made during the design process. The restrictions related to both the baffle arrangement and the individual baffle design. The baffle arrangement restrictions are listed below:

- Five rows of baffles were to be used;
- The baffle-baffle spacing along each row was to remain constant;
- The LE of baffles in each successive row was fixed 1750mm downstream of the LE of baffles in the previous row;
- The second and fourth rows were fixed to align 180° offset from the first, third and fifth rows; and
- Nine full baffles were to be used in the first, third and fifth rows; the second and fourth rows were to be made up of eight full baffles, and two half baffles.

The design of the individual baffles was restricted by the following:

- Each baffle was to be symmetric about a stream-wise centreline to maintain a consistent flow structure across the arrangement;
- Each baffle was to be 600mm thick at its widest point to retain the frequency dampened by the arrangement (Doelling & Bolt, 1961);
- The body of the baffle (distance ‘x’ in Figure 17) was limited to a minimum of 500mm in length to restrict significant variation in the constrained channel length; and
- The overall length of the baffles was fixed at 1750mm to maintain comparable contact area with the airflow.

3.3.3 30° Tapered Downstream Face

(Cherry et al., 2008) found that diffuser airflow exhibits a high degree of geometric sensitivity. As previously mentioned, (Francis, 1975) and (Massey, 2001) discussed that with low taper angles, separation, and the associated losses, can be avoided. The comparison made with the experimental work of (Cherry et al., 2008) in Figure 26 showed that the immediate downstream contraction aided in the reduction of the upstream separation through the development of an opposing pressure gradient. As such, the reduction and eventual removal of separation from the baseline solution was thought to be achievable with taper angles greater than 6°, mentioned by (Francis, 1975) and (Massey, 2001) as being the upper limit to avoid separation in a circular diffuser.

In an effort to reduce separation downstream of the baffle body, the 45° taper angle on the downstream face was reduced to 30° in the development of a new domain. This design change is shown in Figure 33.

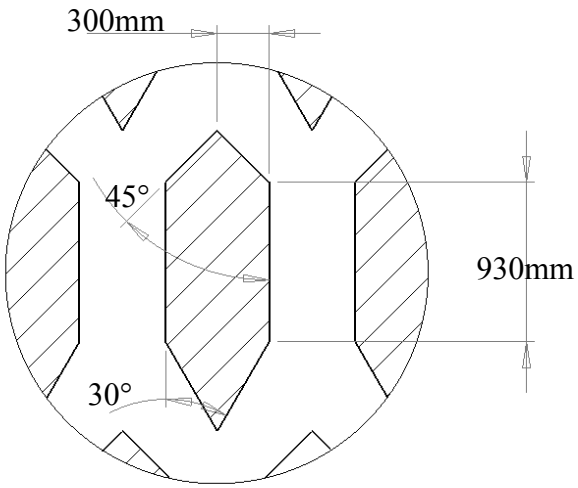

Figure 33 Baffle Design utilising 45°/30° Tapered Upstream/Downstream Faces

Figure 34 shows the reduction in adverse pressure gradient downstream of the intersection of the baffle body and the downstream face as a result of the taper angle reduction. Figure 35 shows the subsequent reduction in separation when compared with the baseline solution. The reduction in separation was accompanied by a 26% drop in static pressure loss.

A similar effect was observed experimentally by (Cherry et al., 2008). Separation was less readily formed with a reduction in taper angle. Figure 34 shows a negative trade-off of a lower taper angle on the downstream face was a slight increase in static pressure build-up at the LE. In addition, a

more significant low pressure zone formed at the intersection of the upstream face and the baffle body.

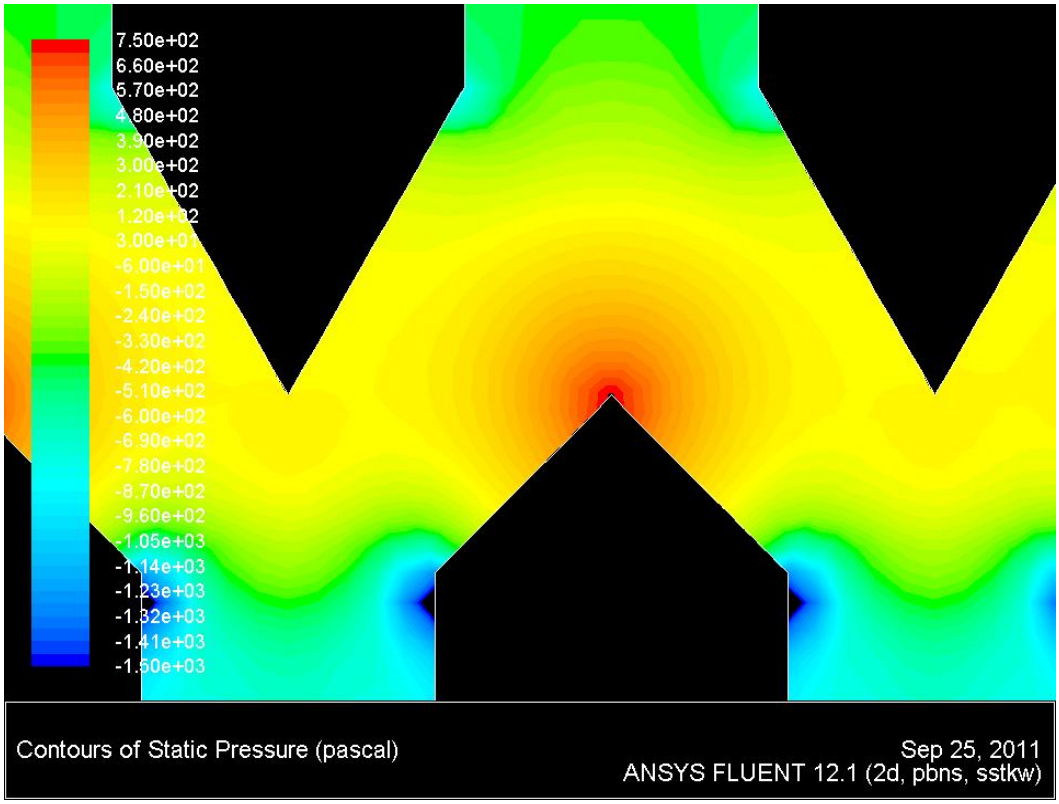

Figure 34 Static Pressure in the Baffle Arrangement using the design of Figure 33

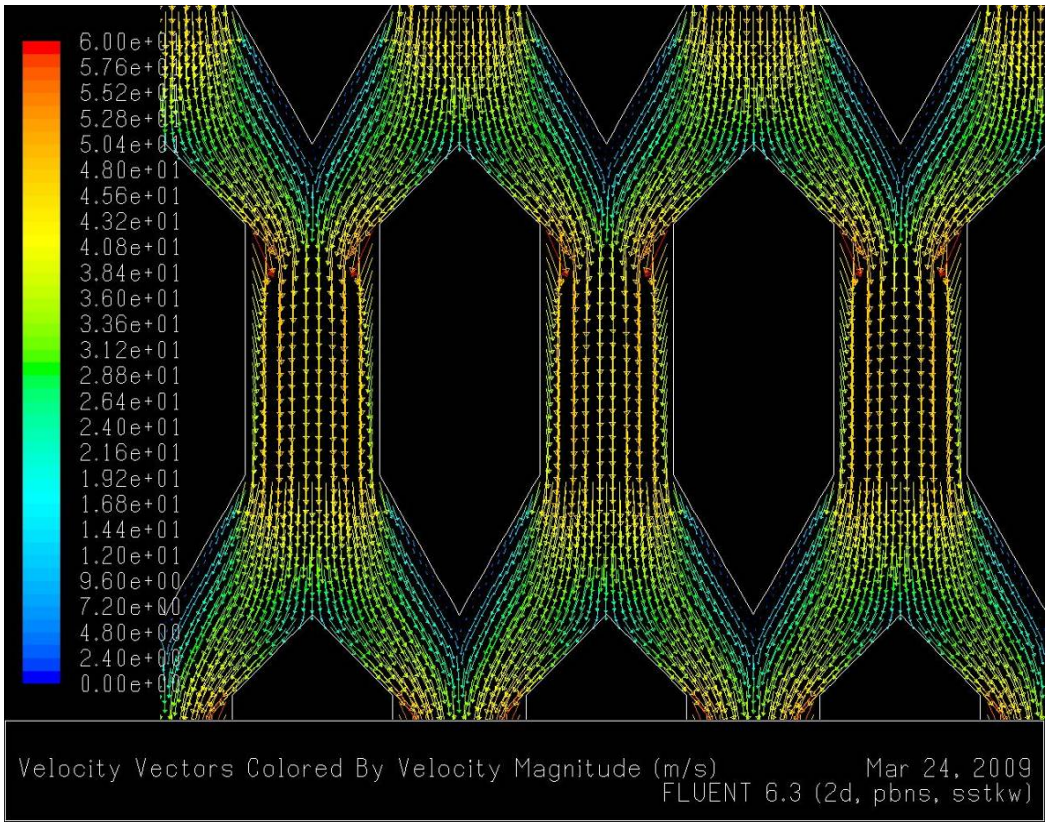

Figure 35 Flow Pattern in the Baffle Arrangement using the design of Figure 33

3.3.4 Semi-Circular Upstream Face

In an effort to reduce the concentration of low static pressure at the intersection of the upstream face and baffle body, the upstream face was modified to a semi-circular profile as shown in Figure 36. The semi-circular face was designed to have a diameter matching that of the baffle body width. In doing so a tangential intersection between the upstream face and the baffle body was formed, thus creating a more gradual change in direction.

To further investigate the findings made in Section 3.3.3, the semi-circular upstream face was combined with downstream faces tapering at 45°, 30°, and 20° in individual domains.

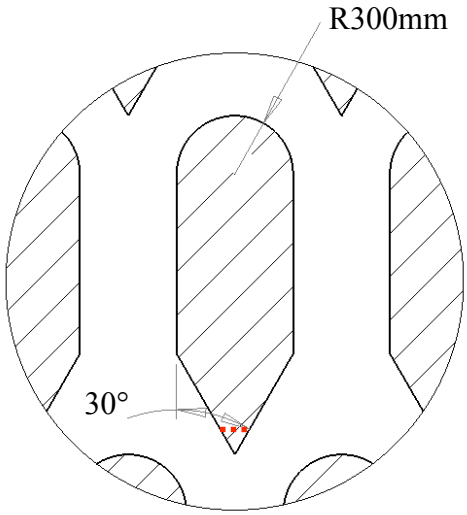

Figure 36 Baffle Design utilising a Semi-Circular Upstream Face and 30° Tapered Downstream Face

Figure 37 shows how the static pressure distribution was altered through the inclusion of a semi-circular upstream face. The areas of concentrated low pressure in Figure 34 have been removed. These areas are replaced with a less severe and more even distribution of low pressure. As a trade-off, a more significant build-up of static pressure is seen at the revised 'blunt' LE.

Figure 38a shows the flow pattern in the separation region using a 45° downstream taper. A significant reduction in the size of the separation can be seen in comparison with the baseline solution. With this reduction in separation, a 26% decrease in static pressure loss was achieved over the baseline arrangement, exactly matching that observed with a decrease in downstream taper angle in Section 3.3.3.

Reviewing the revised geometry, the inclusion of a semi-circular face can be seen to create a more significant flow contraction between itself and the adjacent downstream face of the upstream baffles due to the presence of the curvature. This can be seen when comparing Figure 33 with Figure 36. In Figure 37 it appears that this more significant contraction combines with the increase in static pressure build-up at the LE to create an opposing pressure gradient that propagates upstream.

This opposing pressure gradient interacts with the separation region and results in the reduction of its extent in the stream-wise direction. So, although achieving efficiency gains matching those seen in Section 3.3.3, slightly different mechanisms were used in doing so. With a downstream taper of 30° (coupled with a semi-circular upstream face) the static pressure loss across the arrangement dropped by 58% over the baseline solution. This equated to a 44% improvement over the two design iterations discussed immediately above.

With a downstream taper angle of 20°, the static pressure loss across was reduced by a further 30%, giving an overall efficiency improvement over the baseline solution of 71%. Figure 38 shows the significant increase in flow efficiency is the result of further reduction, and then removal, of the downstream separation. Figure 39, when compared with Figure 37, shows this was achieved via reduction of the adverse pressure at the intersection of the baffle body and downstream face.

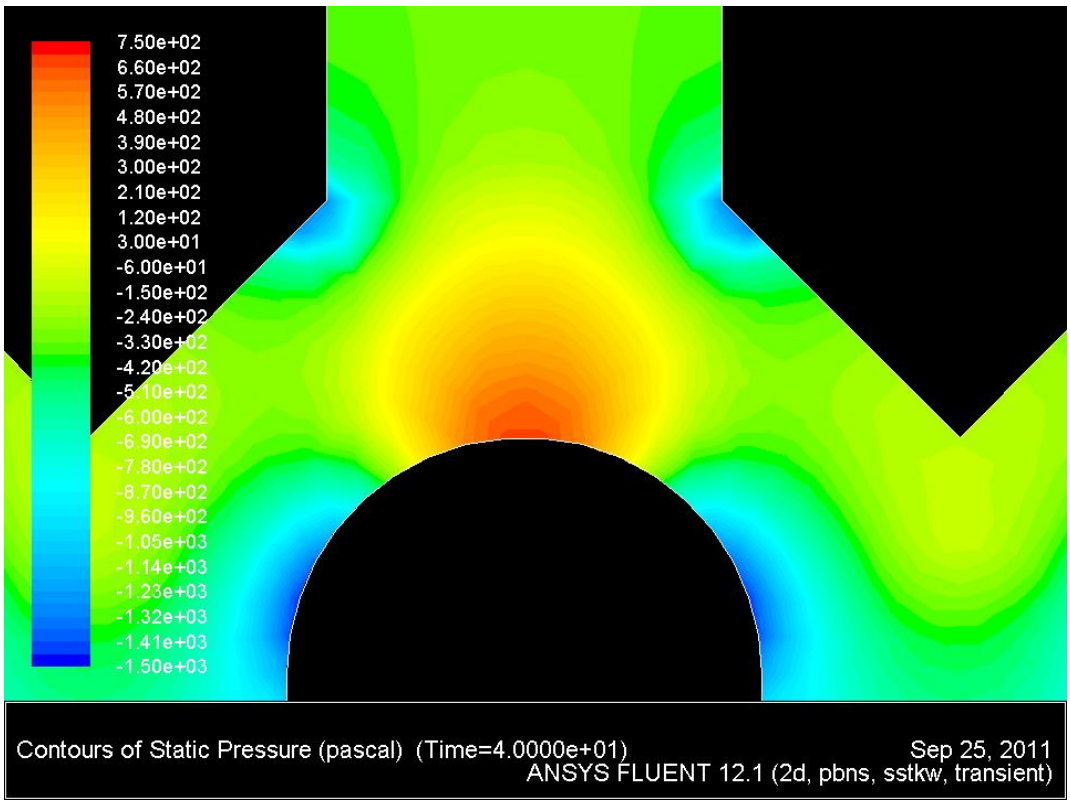

Figure 37 Static Pressure Distribution in the Baffle Arrangement using the design of Figure 36 (with a 45° Tapering Downstream Face)

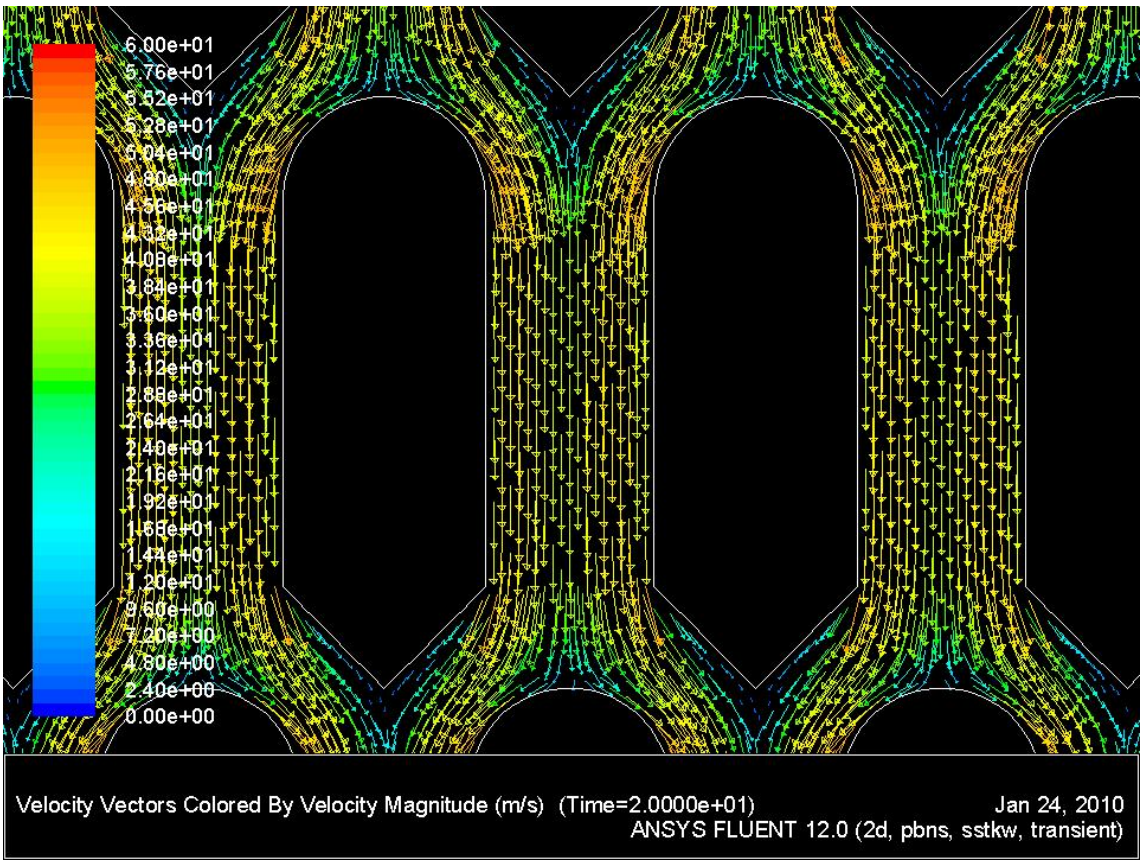
6.00e+01
5.76e+01
5.52e+01
5.28e+01
5.04e+01
4.80e+01
4.56e+01
4.32e+01
4.08e+01
3.84e+01
3.60e+01
3.36e+01
3.12e+01
2.88e+01
2.64e+01
2.40e+01
2.16e+01
1.92e+01
1.68e+01
1.44e+01
1.20e+01
9.60e+00
7.20e+00
4.80e+00
2.40e+00
0.00e+00
Velocity Vectors Colored By Velocity Magnitude (m/s) (Time=2.0000e+01)
Jan 24, 2010
ANSYS FLUENT 12.0 (2d, pbns, sstkw, transient)
a.

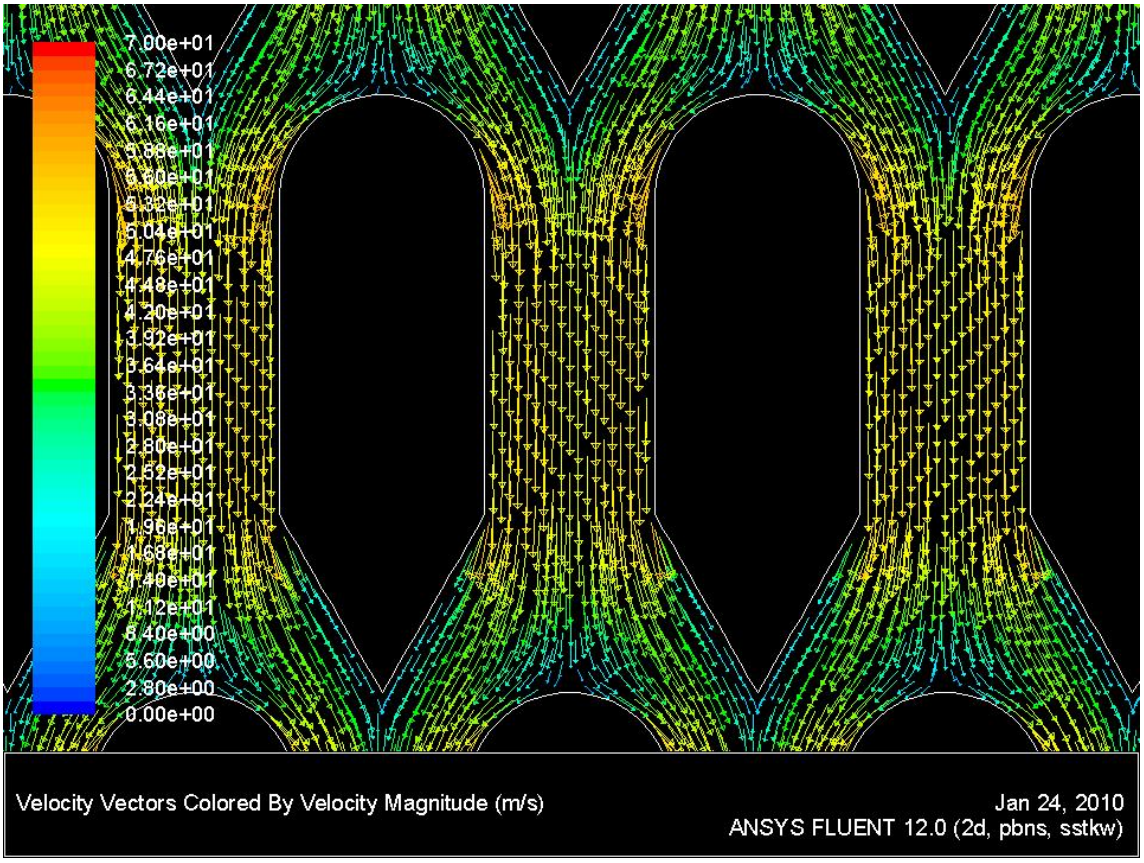
7.00e+01
6.72e+01
6.44e+01
6.16e+01
5.88e+01
5.60e+01
5.32e+01
5.04e+01
4.76e+01
4.48e+01
4.20e+01
3.92e+01
3.64e+01
3.36e+01
3.08e+01
2.80e+01
2.52e+01
2.24e+01
1.96e+01
1.68e+01
1.40e+01
1.12e+01
8.40e+00
5.60e+00
2.80e+00
0.00e+00
Velocity Vectors Colored By Velocity Magnitude (m/s)
Jan 24, 2010
ANSYS FLUENT 12.0 (2d, pbns, sstkw)
b.

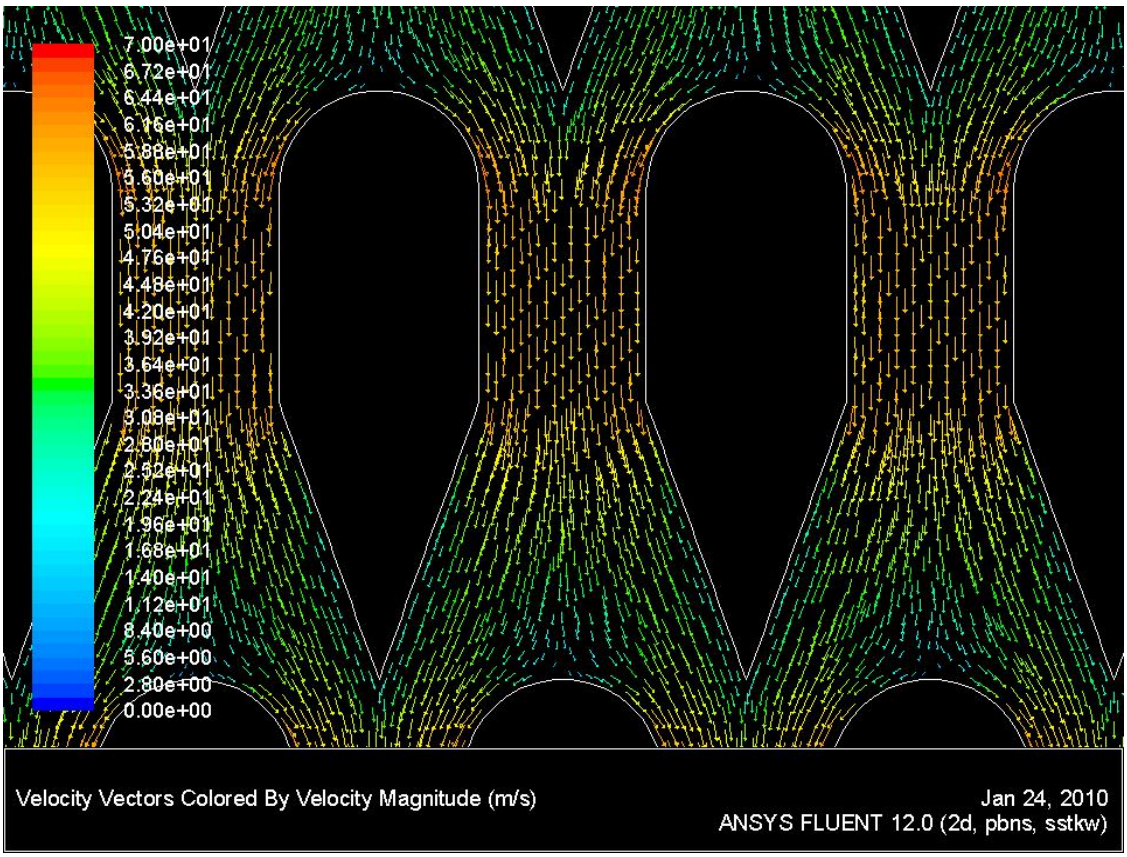

c.

Figure 38 Flow Pattern in the Baffle Arrangement using the design of Figure 36 with Downstream Faces Tapering at 45° (a), 30° (b), and 20° (c)

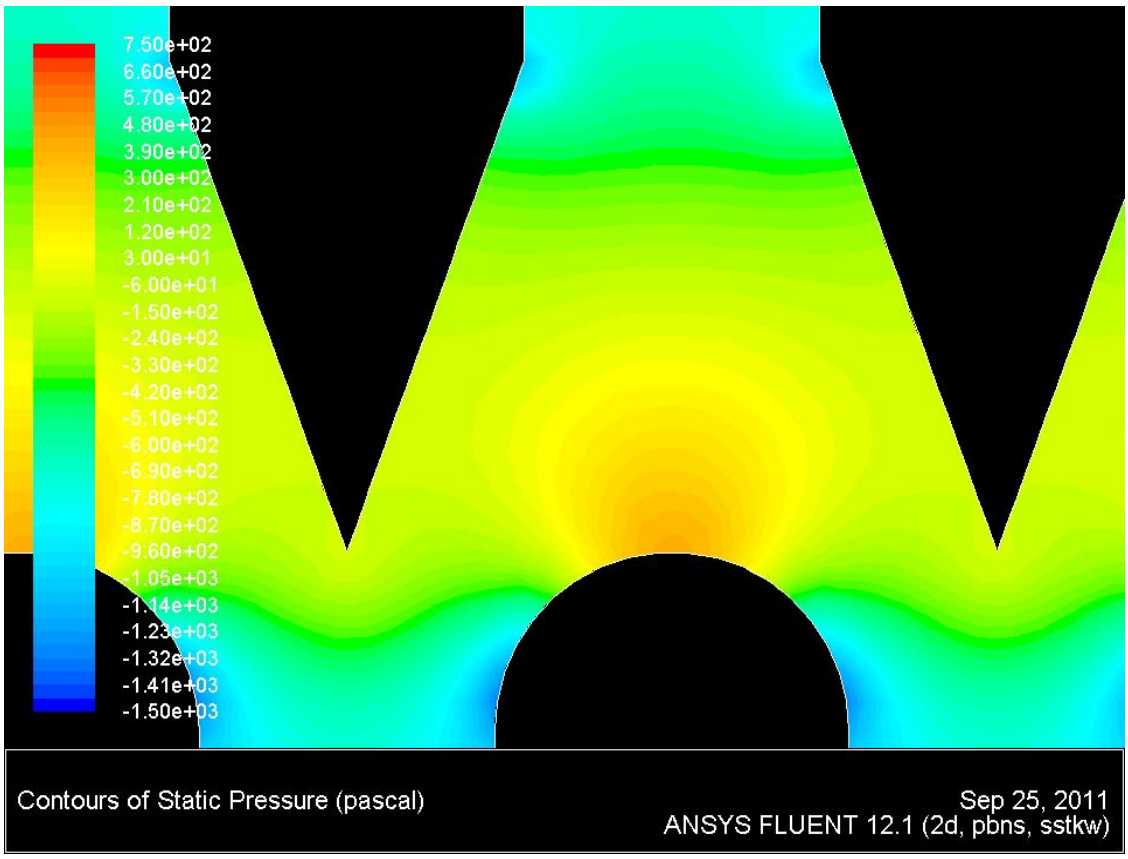

Figure 39 Static Pressure Distribution in the Baffle Arrangement using the design of Figure 36 (with a Downstream Face Tapering at 20°)

3.3.5 Smoothing Downstream Intersection

Both Section 3.3.3 and Section 3.3.4 showed that a reduction in downstream face taper angle significantly improved flow efficiency. However, the decrease in taper angle resulted in a significant reduction in baffle body length. The shorter the baffle body length is made, the further the acoustic performance departs from that of the baseline arrangement.

In an effort to retain a longer baffle body length, whilst decreasing the abruptness of the intersection of the baffle body with the downstream face, a radius linking the two was incorporated. This is shown in shown in Figure 40.

The semi-circular upstream face was retained from Section 3.3.4, and coupled with a 30° tapering downstream face. A 1m radius was used to link the baffle body and the downstream face. A solution to this domain was created and provided direct comparisons with the solutions presented in Figure 38b and Figure 38c.

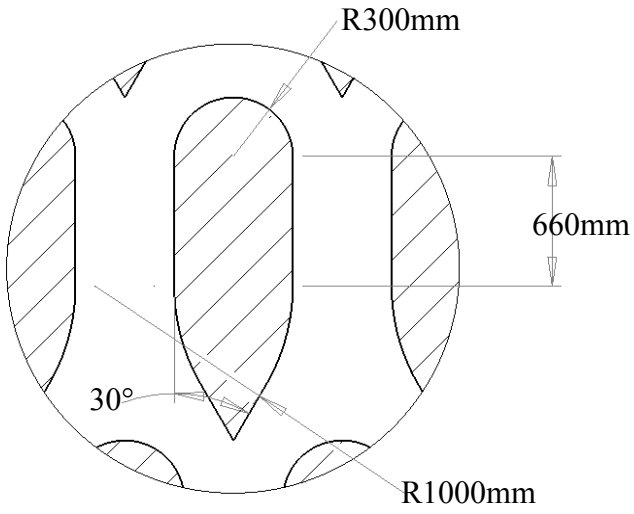

Figure 40 Baffle Design utilising a Semi-Circular Upstream Face and 30° Tapered Downstream Face with 1m Radius

Figure 41 shows the flow profile around a baffle with a smoothed downstream intersection. Separation has been successfully removed. This qualitative result was comparable to that achieved using a 20° downstream taper angle without a smoothing radius. The static pressure drop across the baffle arrangement was 73.1% lower than that calculated in the baseline solution, a 10% decrease over the 20° tapered solution.

Whilst the increase in efficiency over the non-radius 20° design was only moderate in comparison with other gains made previously, the increase was able to be achieved whilst retaining a longer baffle body length. Therefore, the original goal of the design modification was achieved.

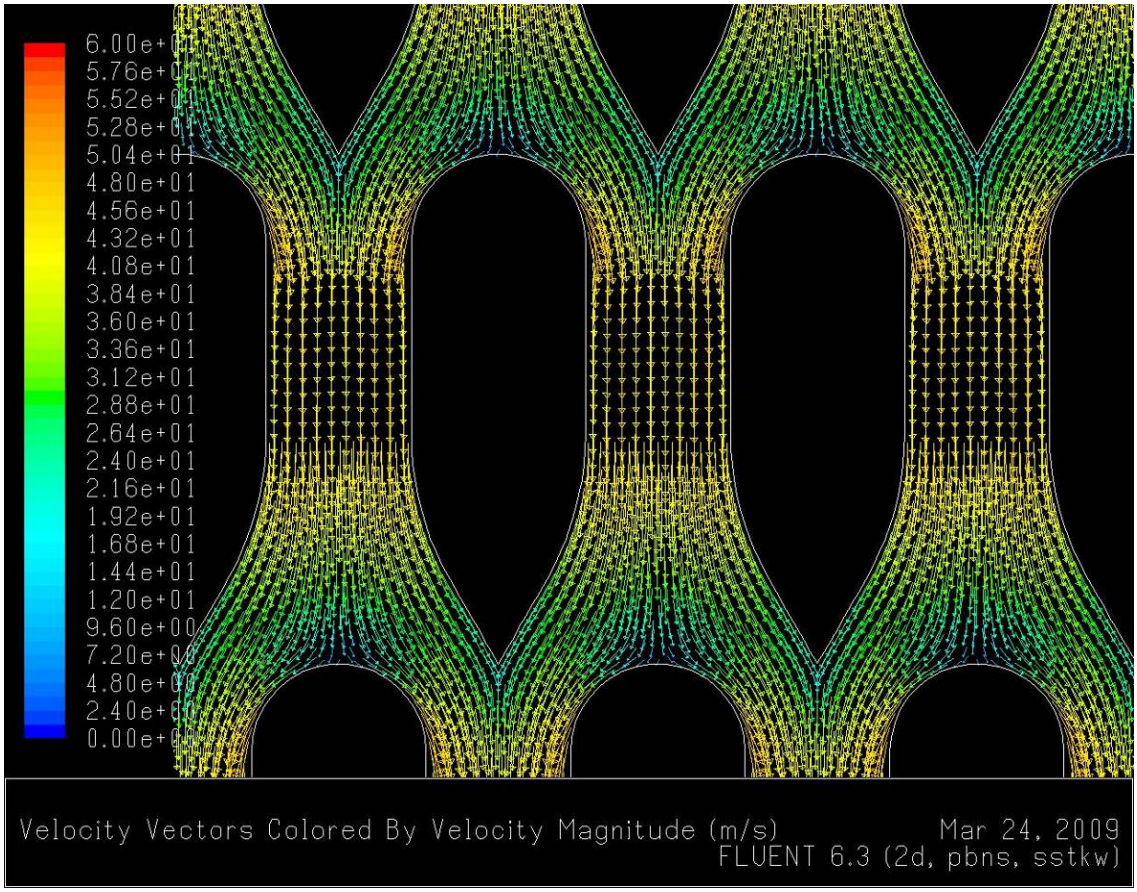

Figure 41 Flow Pattern in the Baffle Arrangement using the design of Figure 40

3.3.6 Clipped Trailing Edge

The design presented in Section 3.3.5 successfully achieved the aims that were set. However, to do so incorporated a radius feature that would likely add substantial expense during construction. As a 'simpler', and therefore theoretically more easily and cheaply constructed alternative, a 'clipped' TE design was developed in an effort to achieve the same efficiency gains through lower construction costs.

This design retained the semi-circular upstream face and baffle body length of the previous design iteration. However, a 20° taper on the downstream face was used. This was achieved within the restrictions outlined in Section 3.3.2 by 'clipping' the TE, as indicated by the line overlaid in Figure 36.

Figure 42 shows the flow profile around a baffle with a 'clipped' TE. No separation was present adjacent to the downstream face. However, a new separation zone was created downstream of the clipped face. The single separation zone was significantly smaller than the two separation zones seen either side of the downstream face in the baseline solution. This was supported by a 45% decrease in static pressure loss when compared.

However, when compared with other design iterations utilising a semi-circular upstream face, the design proved inferior to all others with the exception of one, being that utilising a 45° downstream face. It should also be noted that the baffle design presented in this section closely resembles that used in the inlet stack of the CHCEC.

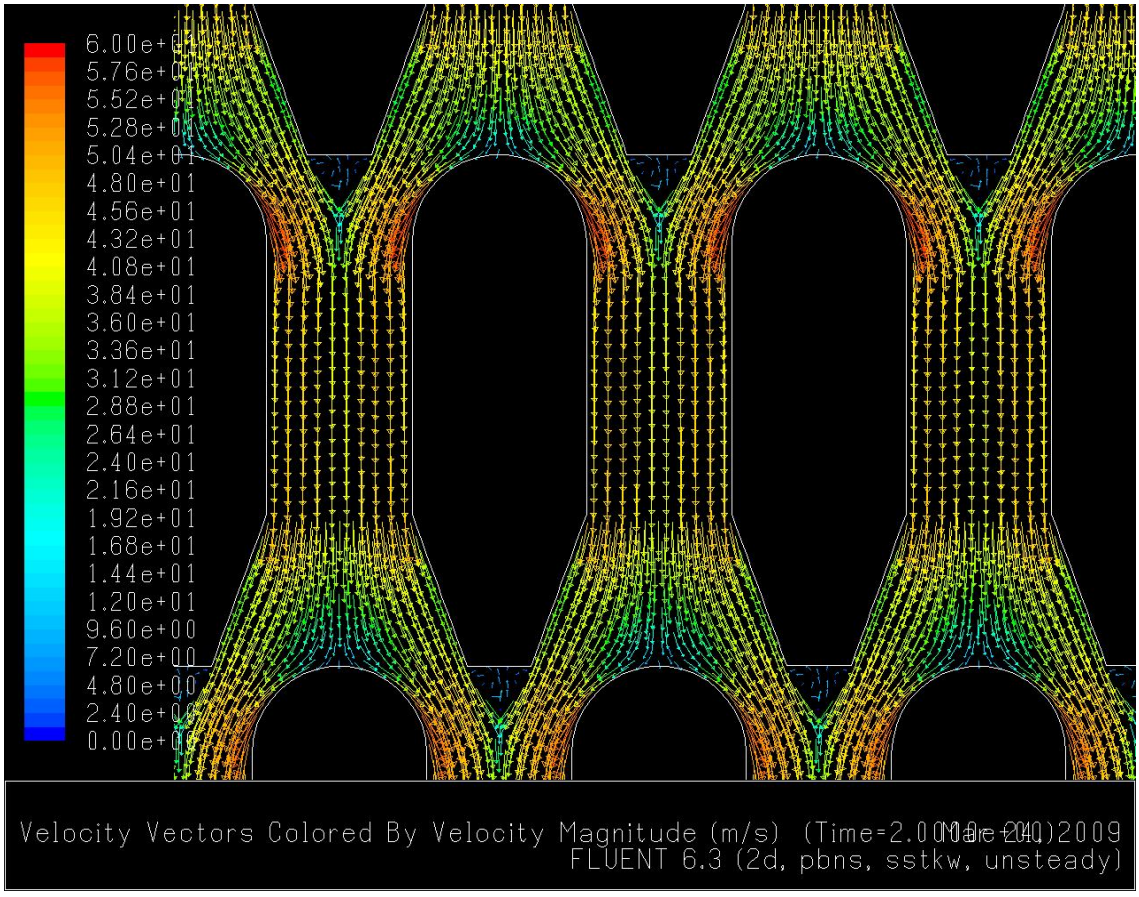

Figure 42 Flow Pattern in the Baffle Arrangement using the design of Figure 36 (with a 'Clipped' TE)

3.3.7 Multi-Radius Downstream Face

The smoothed design of Section 3.3.5 removed the downstream separation as desired. An additional reverse radius of 2000m was applied to the tapering tail. This is shown in Figure 43. The additional radius was incorporated in an effort to aid in the realignment of the flow streams from either side of

the baffles. In theory this would reduce losses associated with the transfer of momentum between the combining streams. The radius of the reverse curvature was limited by the design restriction for minimum baffle body length of 500mm.

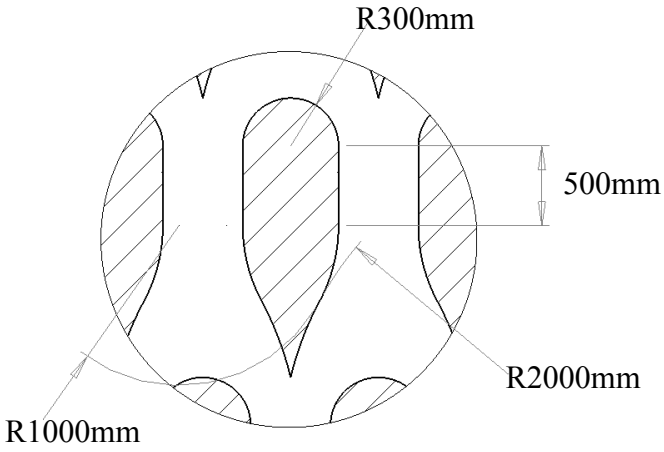

Figure 43 Baffle Design utilising a Semi-Circular Upstream Face and a Multiple Radii Downstream Face

Figure 44 shows the flow pattern developed. Pressure losses at the TE were lessened as the flows were aligned to near parallel prior to re-joining. This is shown in Figure 45 by the decrease in static pressure at the TE. The static pressure drop across the arrangement was calculated to be a 76% lower than in the baseline solution. This corresponded to a 9% increase in efficiency when compared to the design of Section 3.3.5.

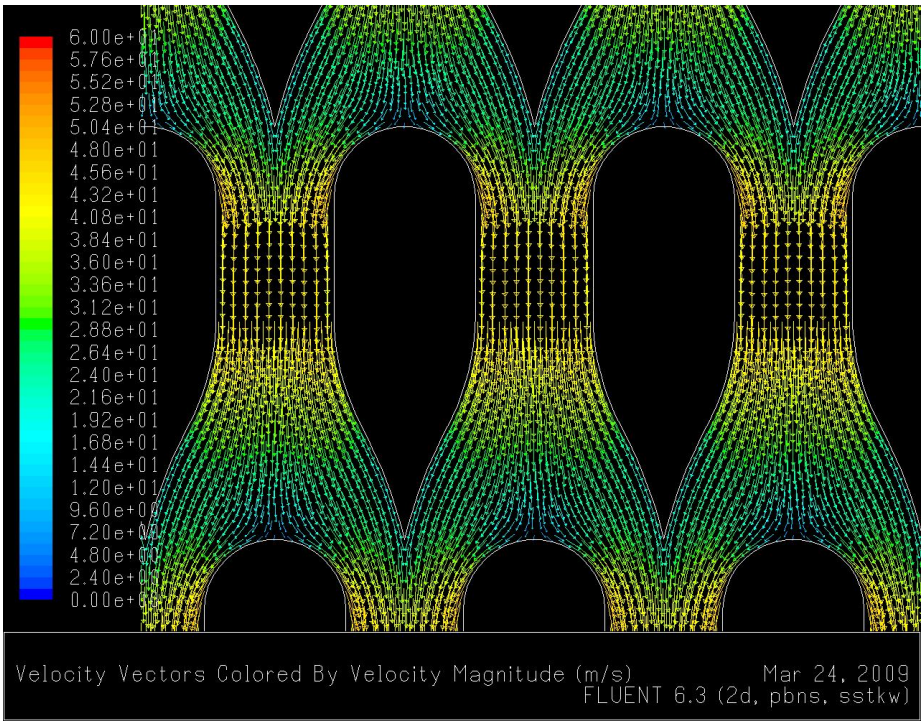

Figure 44 Flow Pattern in the Baffle Arrangement using the design of Figure 43

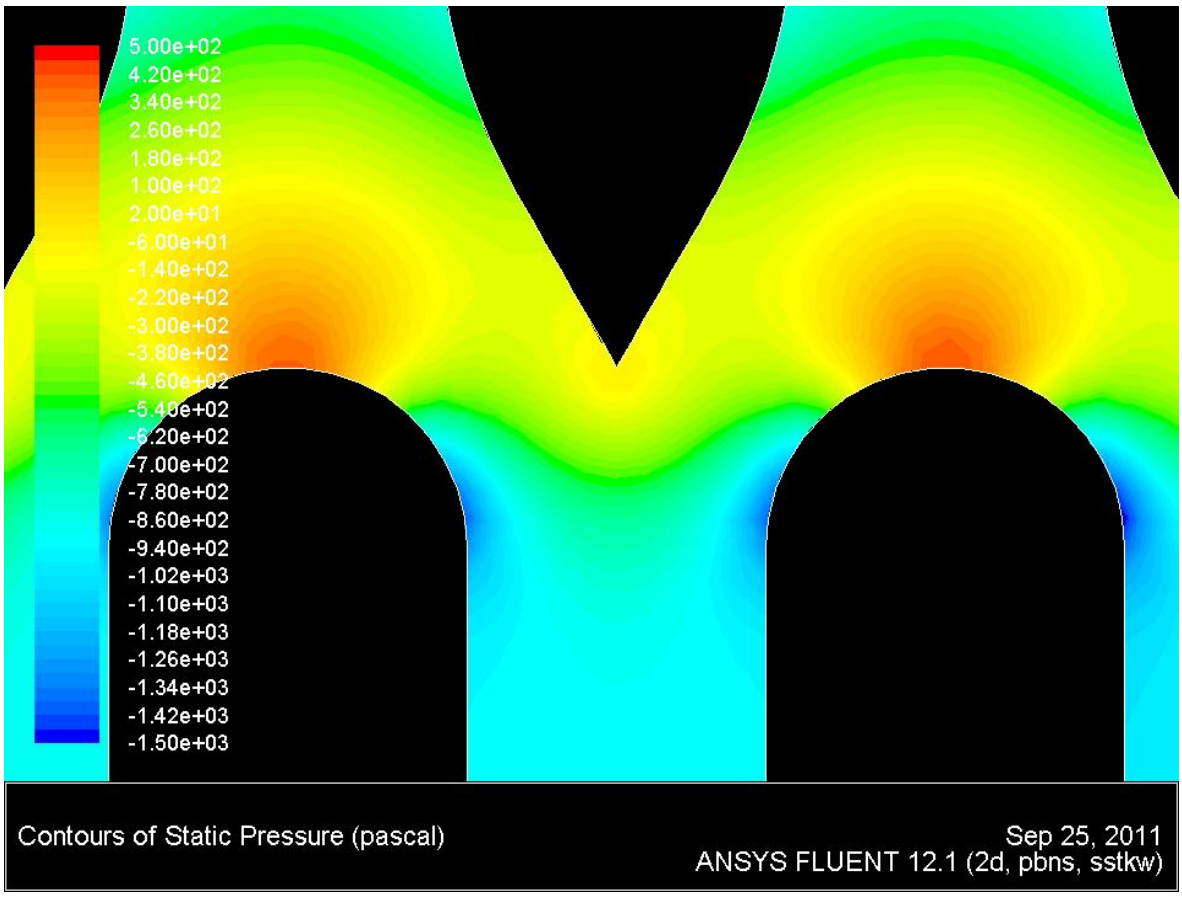

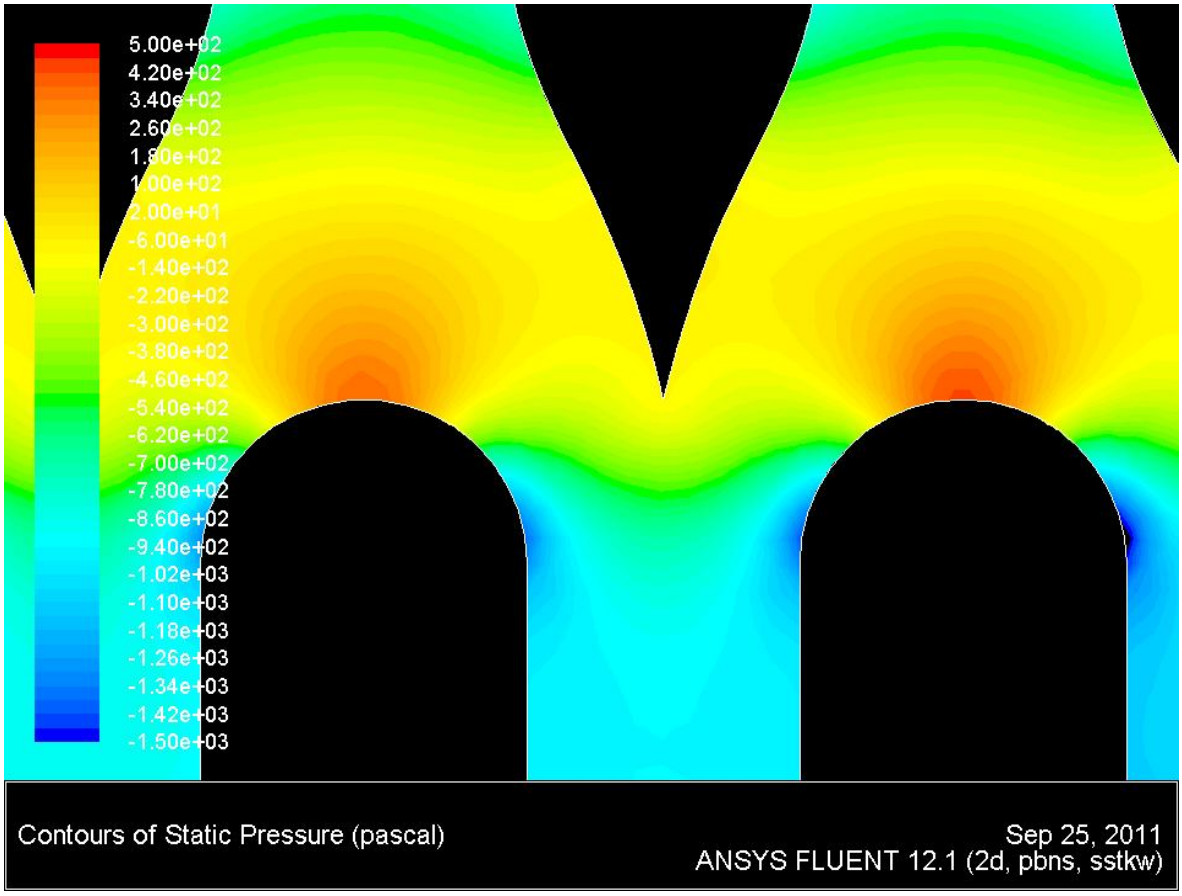

Figure 45 Static Pressure Distribution in the Baffle Arrangement using the design of Figure 40 (top) and Figure 43 (bottom)

3.3.8 Smoothed Upstream Face Intersection

Section 3.3.3 through Section 3.3.7 showed that significant gains in flow efficiency could be achieved through alteration of the downstream face. Through all solutions presented in Section 3.3.4 through Section 3.3.7, which have incorporated a consistent upstream face design, the flow patterns and pressure distribution around the upstream face have been largely ignored. However, through all solutions presented in Section 3.3.4 through Section 3.3.7, a notable static pressure build-up at the 'blunt' LE is observed.

The semi-circular upstream face was initially incorporated to reduce the concentrated region of low static pressure at the intersection of the upstream face with the baffle body. This was achieved, but resulted in the above-mentioned increase in static pressure at the LE. In Section 3.3.3 it was suggested that the opposing pressure gradient, created as a result of this pressure build-up, was in part responsible for the decrease in downstream face separation.

However, development of the downstream face alone in Section 3.3.5 through Section 3.3.7 showed a significant reduction in the adverse pressure gradient at the intersection of the downstream face and baffle body. This is clearly illustrated when comparing Figure 46, showing the pressure distribution through the previous design iteration, with Figure 25, the baseline solution.

As such, the need for the opposing pressure gradient, created by the build-up of static pressure on the semi-circular upstream face, as a means of downstream face separation reduction may have been negated.

In this section an alternative upstream face design was sought in which the improvements seen through incorporating the semi-circular face could be achieved at the same time as reducing the LE static pressure build-up. To do so, a 45° tapering upstream face was utilised, along with a 300mm radius linking it to the baffle body. This is shown in Figure 47.

The smoothing radius allowed a less abrupt direction change between the upstream face and baffle body, a feature retained from the semi-circular face designs. This was combined with a 30° tapering downstream face so comparisons could be made with solutions of both Section 3.3.3 and Section 3.3.4.

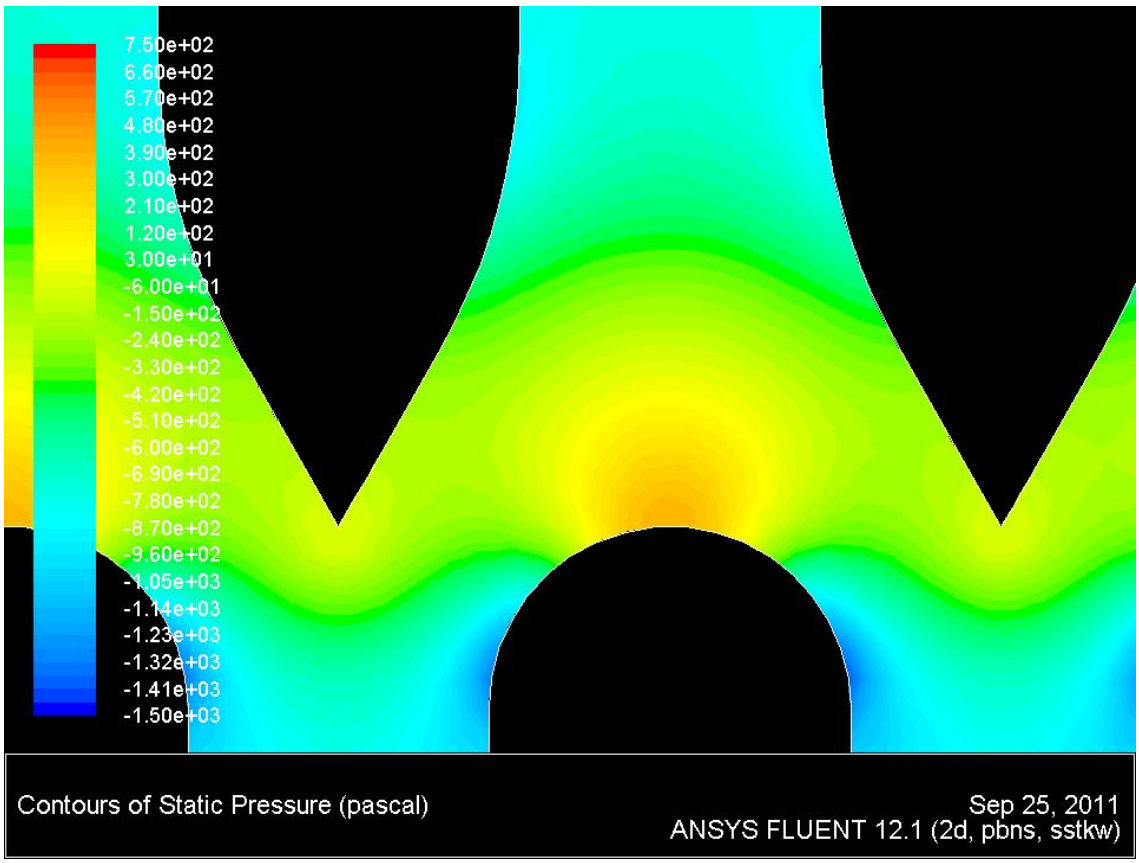

Figure 46 Static Pressure Distribution in the Baffle Arrangement using the design of Figure 43

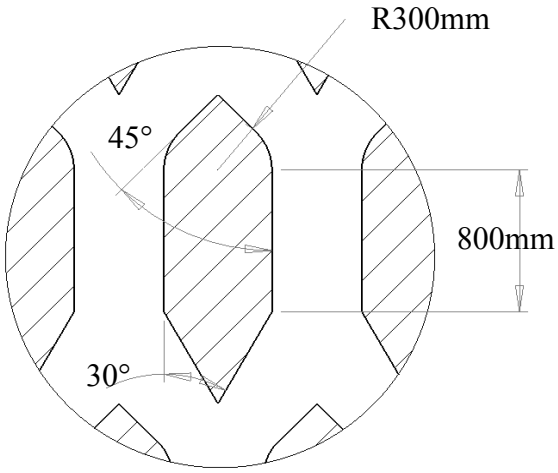

Figure 47 Baffle Design utilising a 45° Upstream Face Taper with 300mm Radius and a 30° Tapered Downstream Face

Figure 48b shows the static pressure profile around the design of Figure 47. The magnitude of the high static pressure at the leading edge was notably reduced when compared to the semi-circular upstream face solution of Figure 48a. In Figure 48b the low static pressure at the intersection of the upstream face and baffle body was substantially reduced when compared with Figure 34, using a simple tapered face, and comparable with that of Figure 39, using the semi-circular face.

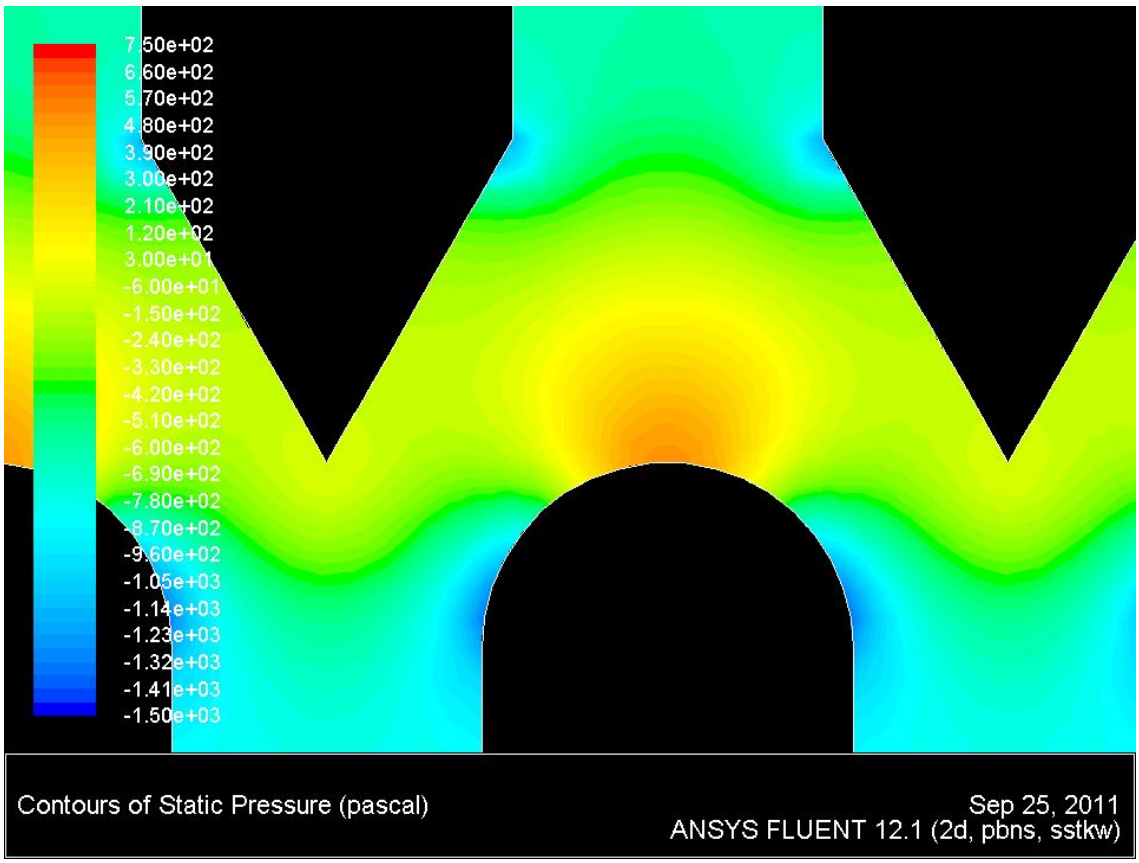

a.

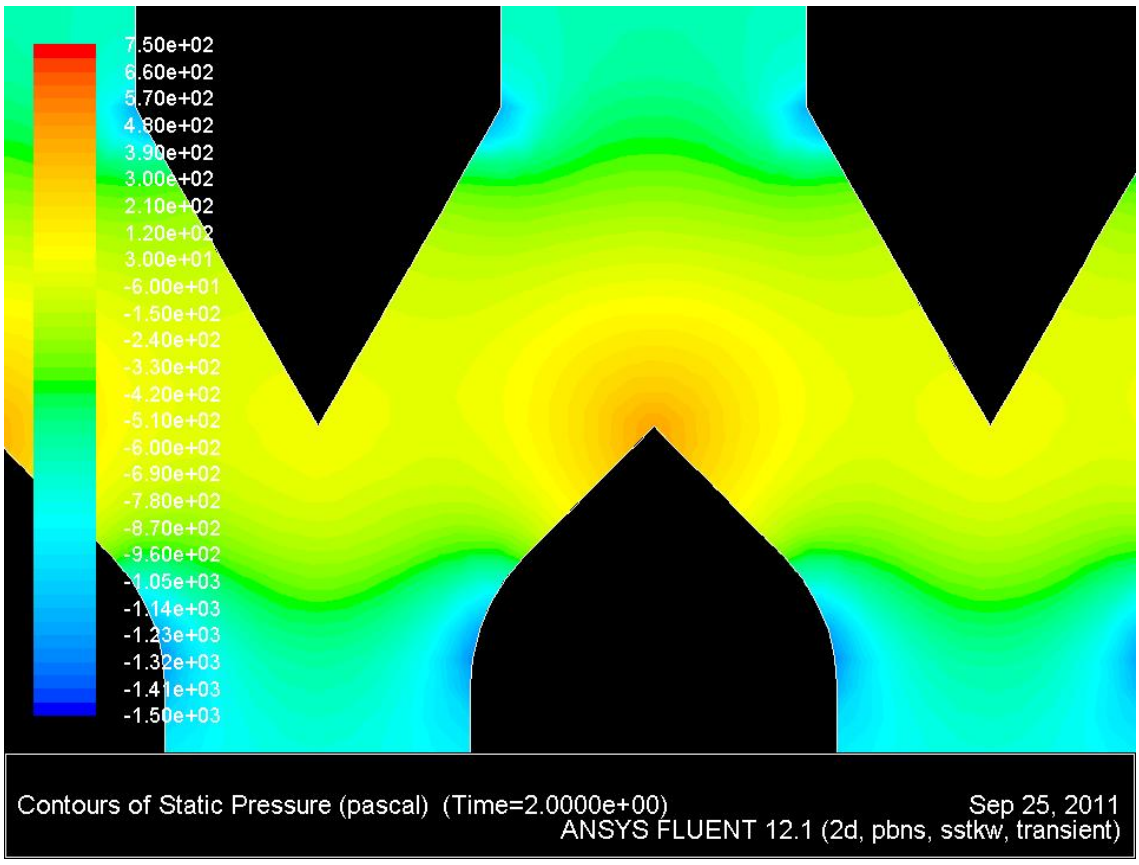

b.

Figure 48 Static Pressure Distribution in the Baffle Arrangement using the design of Figure 36 (a) and Figure 47 (b)

Figure 49 compares the flow between the three upstream face designs of Figure 33, Figure 36, and Figure 47, which all incorporate 30° downstream tapers. Figure 49c shows that separation is not present as a result of the adverse pressure gradient seen in Figure 48b at the intersection of the baffle body and downstream face. However, a region of slightly lower velocity along the downstream face is seen in Figure 49c when compared with Figure 49b.

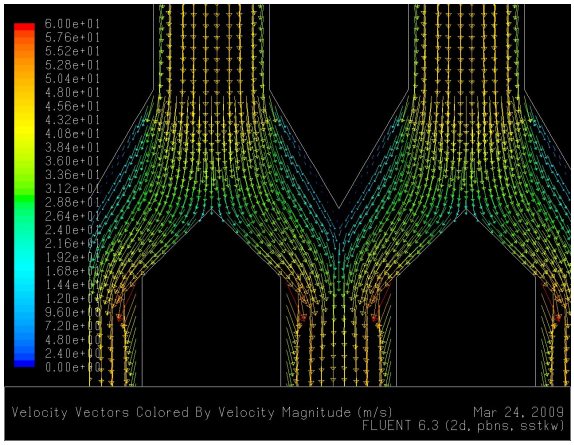

a.

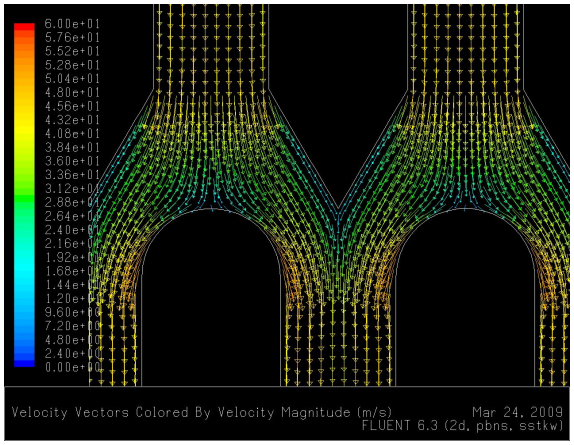

b.

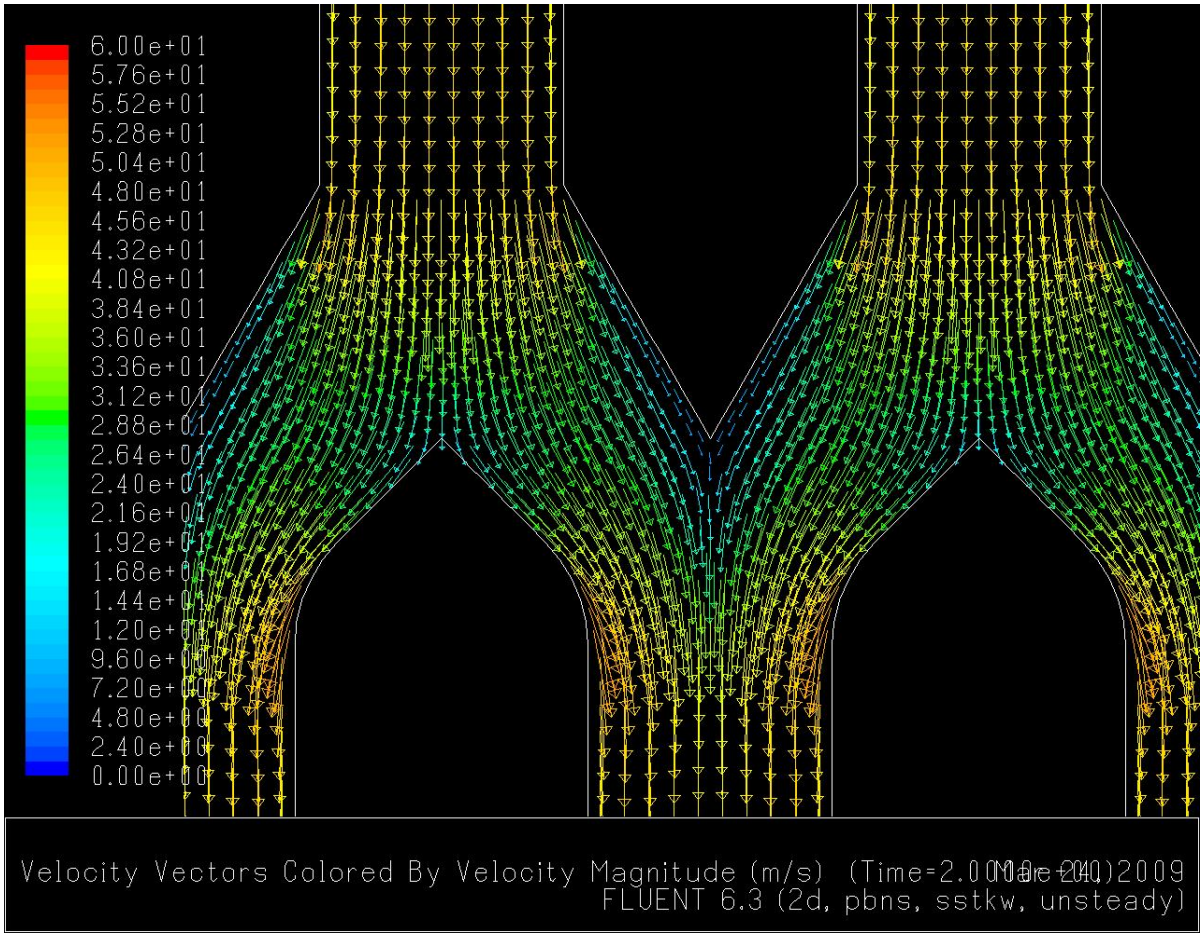

c.

Figure 49 Flow Pattern in the Baffle Arrangement using the design of Figure 33 (a), Figure 36 (b), and Figure 47 (c)

Comparison of the solutions in Figure 48 suggests this is a result of the reduction in the size of the pressure build-up when the 'blunt' LE is replaced with a 'sharp' LE. This shows that an upstream influence, as a result of an opposing pressure gradient formed by the static pressure build-up on the semi-circular face, is present.

The static pressure drop across the design of Figure 47 was 63% less than calculated in baseline solution. This corresponds to a 50% decrease in static pressure drop over the design of Figure 33, and a 10% decrease over the design of Figure 36.

3.3.9 Combination Design

The findings of Section 3.3.1 through Section 3.3.8 were incorporated into a final design. The design elements, showing the greatest increases in flow efficiency were combined. This was done by combining the 45° upstream face of the baseline design, with the upstream smoothing treatment of Figure 47, and the multi-radius downstream smoothing treatment of Figure 43.

Figure 50 and Figure 51 show the static pressure distribution and flow pattern around the combined baffle design. Comparisons with results in the preceding sections show that no negative effects were generated as a result of the combination in design elements.

In comparison with the baseline solution, the combined element design achieved the following:

1. A significant reduction in the adverse pressure gradient at the intersection of the baffle body and the downstream face;
2. A significant reduction in the concentrated area of low static pressure at the intersection of the upstream face and the baffle body; and
3. A significant decrease in the static pressure build-up at the LE.

The combination of these qualitative observations resulted in a static pressure loss that was 79% lower than in the baseline solution. Figure 52 is provided as a direct comparison with Figure 28, showing the wake downstream of the lowermost row of baffles. Even in the absence of a downstream contraction, the combined element design is seen to be free of separation along the downstream face.

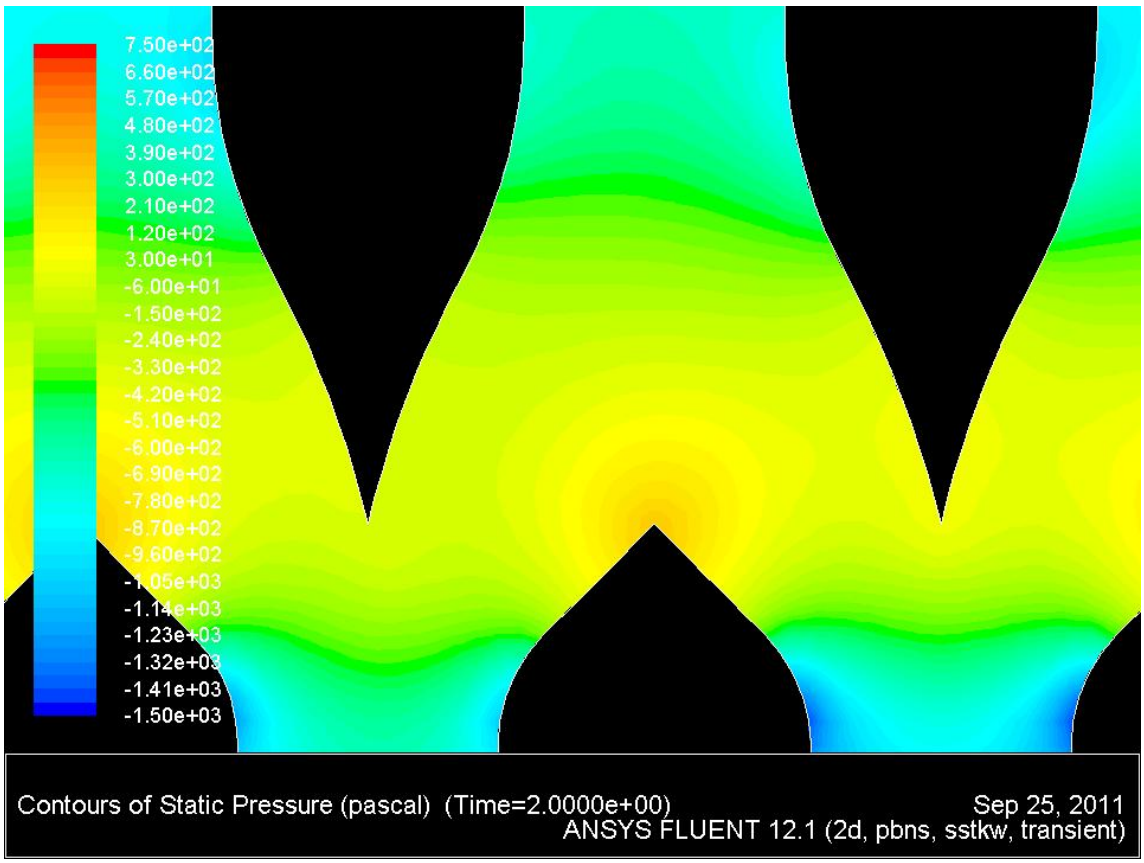

Figure 50 Static Pressure Distribution in the Baffle Arrangement using the Combined Element Baffle Design

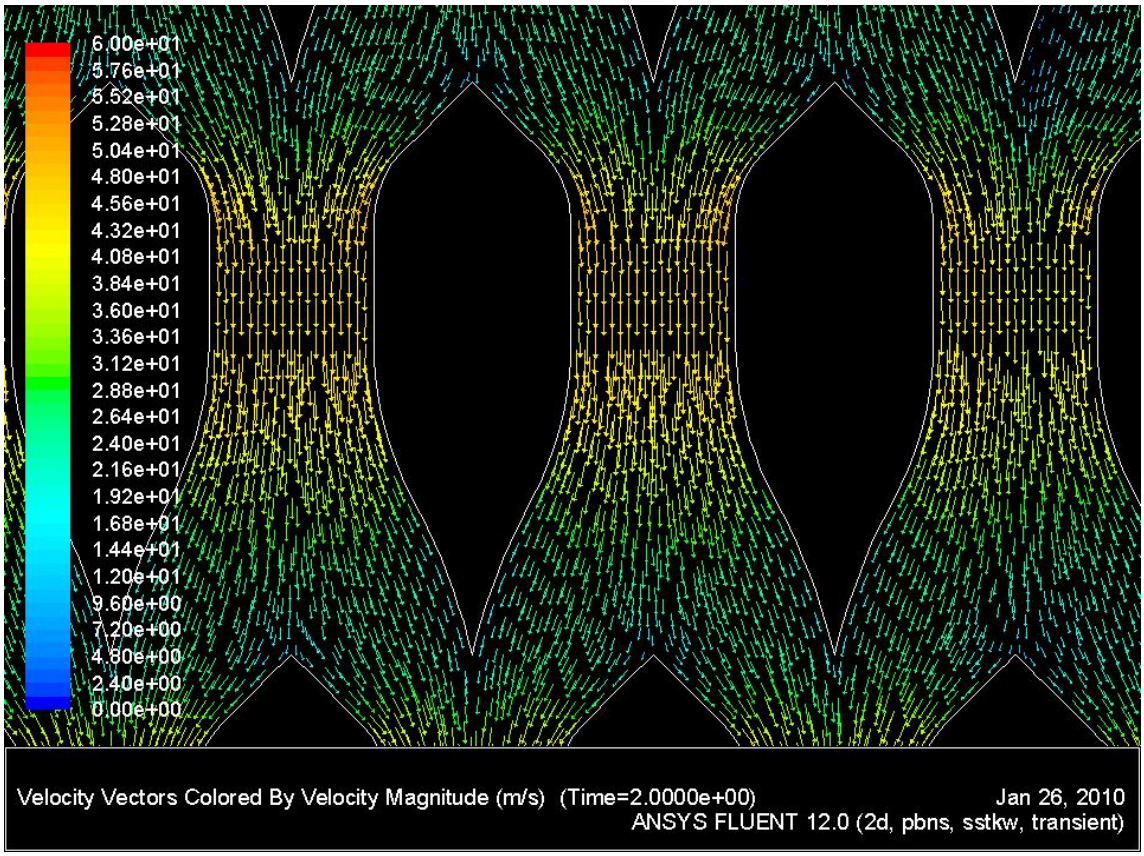

Figure 51 Flow Pattern in the Baffle Arrangement using the Combined Element Baffle Design

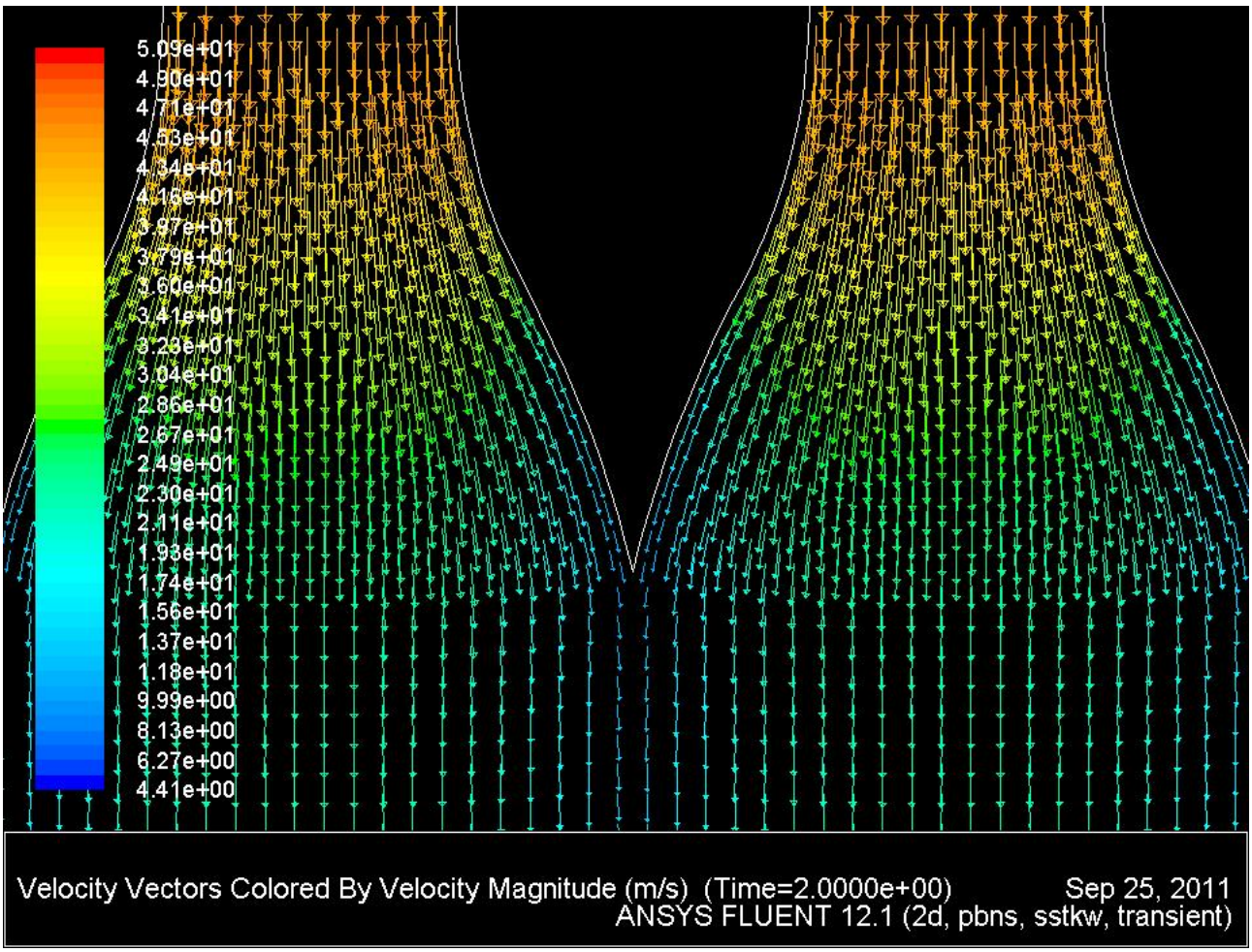

Figure 52 Detail of Separation below Baffle in the Lowermost Row using the Combined Element Baffle Design

Figure 53 and Figure 54 compare the velocity profile of the baseline and combined element designs at distances of 0.625m and 5.625m downstream of the lowermost baffle row. Figure 53 shows a significant difference in the wake propagation 0.625m downstream. The baseline arrangement shows a substantial variation across the width of the domain, and this is reflected by a velocity distortion of 171%. This compares with 34% using the combined element design.

Figure 54 shows that by 5.65m downstream, the baffle wakes have equalised substantially. The velocity distortions of 42% and 23% for the respective baseline and combined element solutions reflect this. Although substantially equalised, a notable variation is still present.

Figure 55 compares the static pressure drop of all design iterations in relation to that of the baseline solution.

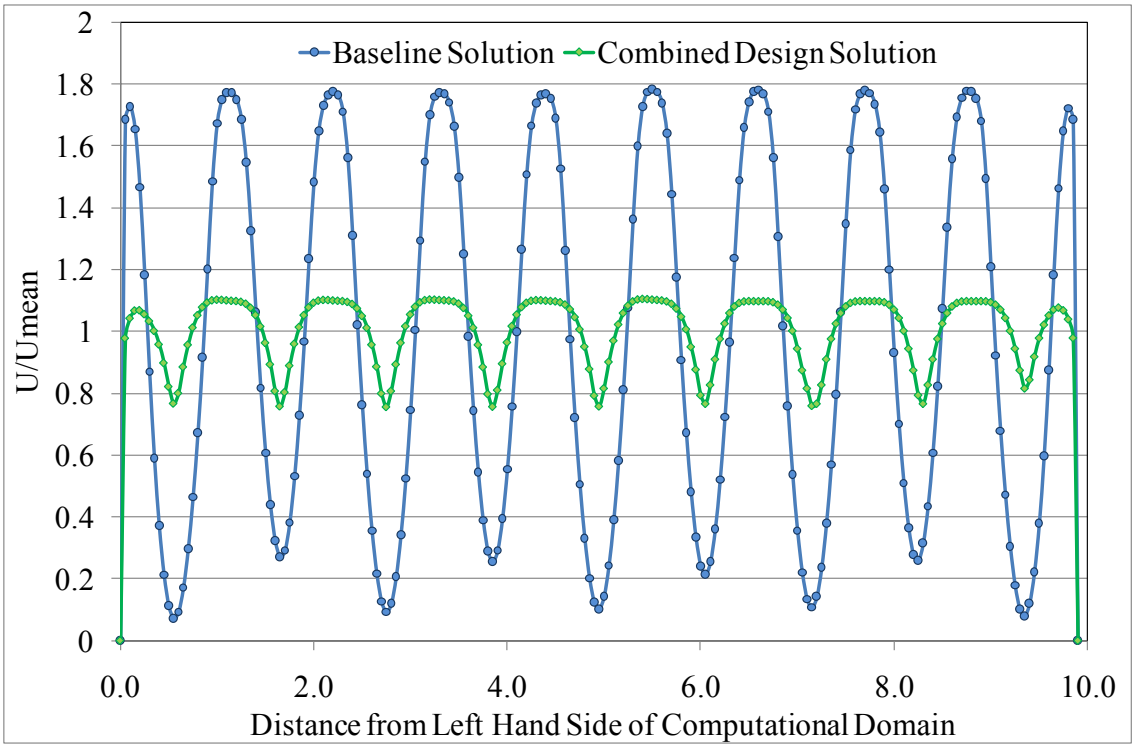

Figure 53 Velocity Profile across the Computational Domain 0.625m Downstream of the Baffle Arrangement

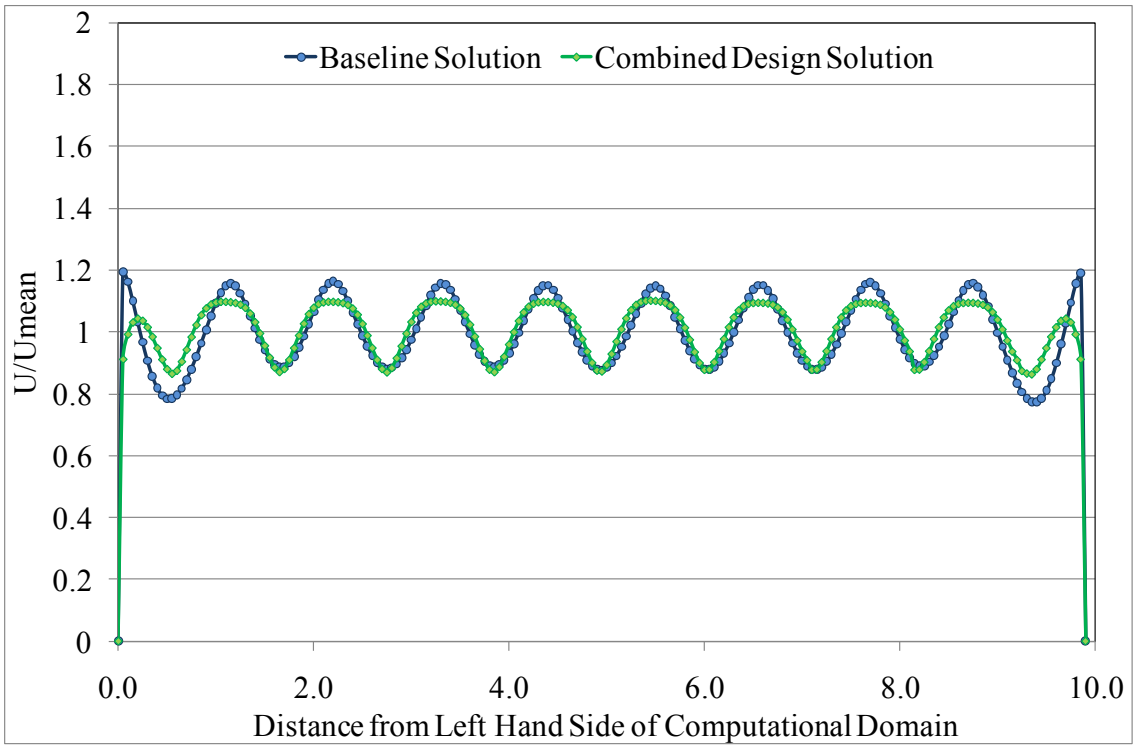

c.

Figure 54 Velocity Profile across the Computational Domain 5.625m Downstream of the Baffle Arrangement

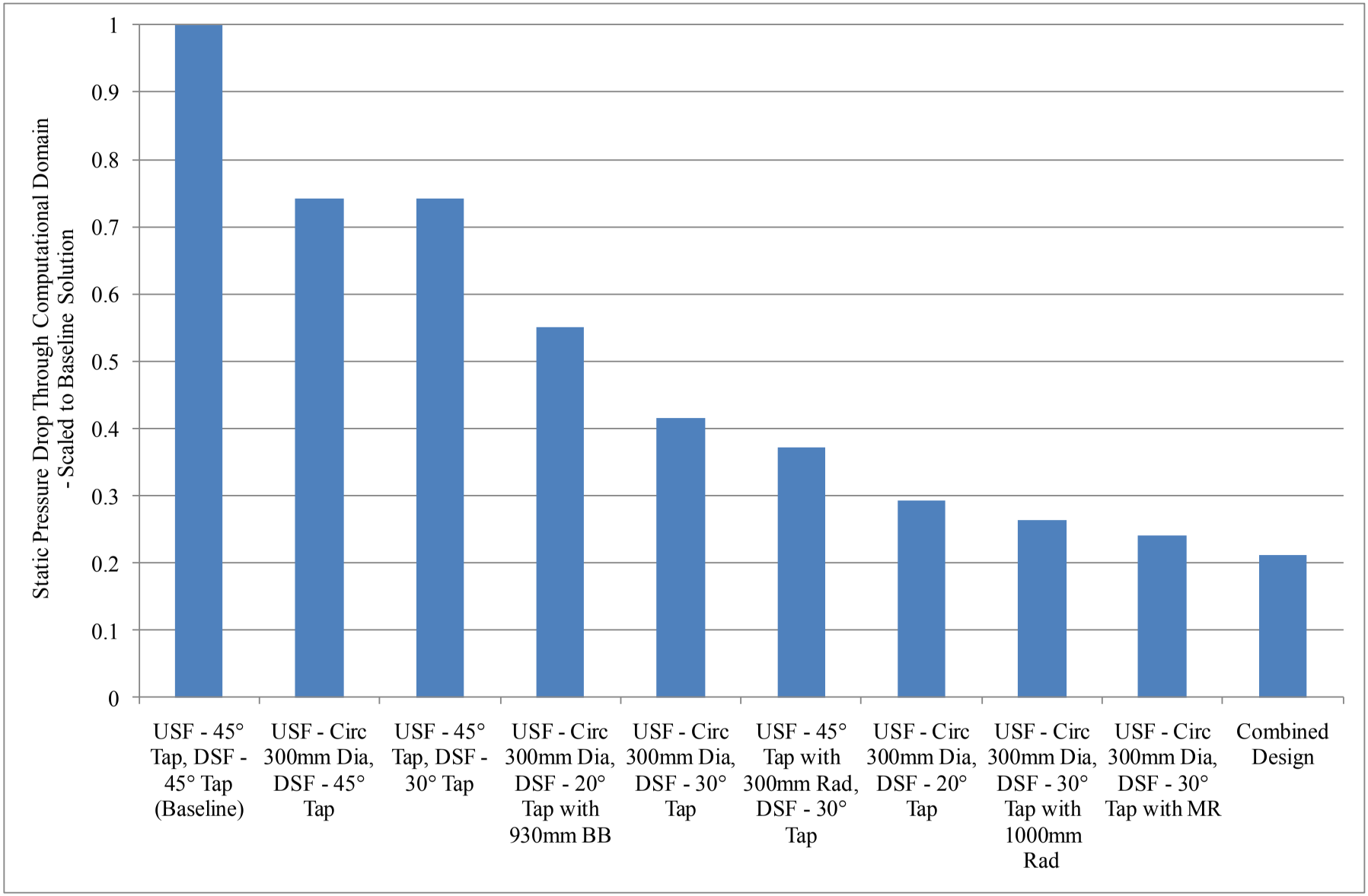

Figure 55 Scaled Static Pressure Loss through all Baffle Arrangements Investigated in Section 3 (USF = Upstream Face, DSF = Downstream Face, Tap = Taper, Circ = Circular, Dia = Diameter, Rad = Radius, MR = Multi-Radii, BB = Baffle Body)

3.4 Summary of Findings

A CFD analysis was performed on a JETC baffle arrangement in this section. Initially, a baseline baffle arrangement was modelled to gain an understanding of the flow patterns under conditions comparable to that of a JETC in an operational state.

In the baseline solution an adverse pressure gradient was found to cause separation along both sides of the downstream face in every baffle within the arrangement. The cause of the adverse pressure gradient was found to be the diffuser scenario created by the diverging flow channels between adjacent baffles.

Separation in a diffuser has been experimentally observed in a number of studies, including those of (Buice & Eaton, 2000) and (Cherry et al., 2008). The computational solution of the baseline arrangement was compared with the experimental work of (Cherry et al., 2008). A line of 'zero stream-wise velocity' from one of the separation regions within the baffle arrangement was compared alongside the asymmetric diffuser case of (Cherry et al., 2008). Similarities were seen between the two studies. In particular, both showed a stream-wise direction of the initial growth of the line away from the diffuser wall, and then a gradual, near linear, growth of the line away from the diffuser wall along the remaining length of the taper. However, several dissimilar properties were also observed. It is suggested that these differences could be attributed to the presence of downstream flow features, a greater taper angle, and a fully symmetric diffuser in the computational case.

Separation from a baffle within the arrangement was compared with a baffle in the lower-most row. Significant differences were seen. Within the arrangement, opposing pressure gradients formed on the LE of the upstream face of the downstream baffle. This opposing pressure gradient then combined with a following channel convergence to significantly reduce the size of the separation produced.

Downstream of the arrangement, none of these 'separation interference' features were present. Below the lower-most baffle row separation developed and dissipated in an unaffected manner. The wakes resulting from the separation propagated downstream for a significant length. The work of (Obi et al., 1993) showed that the k-ω SST turbulence model that was used in this investigation, does have a tendency to over-predict wake recovery length. Therefore, the above findings need to be made in consideration of this fact, and strict quantitative statements cannot be confidently made.

A CFD-aided design process was then performed to enhance the aerodynamic performance of the baffle arrangement as a whole. A number of design restrictions were placed on the design process to maintain comparability with the baseline solution, in both an aerodynamic and acoustic sense. The work of (Francis, 1975), (Massey, 2001), and (Cherry et al., 2008) suggested that the flow pattern through a diffuser is sensitive to the geometry of the bounding surfaces, and that a decrease in taper angle would lead to a reduction in the level of separation generated, and the associated pressure losses.

The first design iteration imposed a smaller 30° taper angle of the downstream face of the baseline arrangement, which was initially set at 45°. This resulted in a 26% drop in static pressure loss across the arrangement when compared with the baseline solution. A negative trade-off was a slight build-up in static pressure on the LE of the baffles within the arrangement. Additionally, a significant low-pressure zone formed at the intersection of the upstream faces and the baffle bodies throughout.

Initially, a solution was sought to remedy the low-pressure zone formed at the intersection of the upstream face and the baffle body. The proposed solution incorporated a semi-circular upstream face in place of the 45° tapered face in the baseline design. The theory behind the design change was that the tangential meeting of the semi-circular face with the baffle body would remove the sudden change in direction that the tapered upstream face and baffle body created.

This change was successful in dispersing the low-pressure region and lessening the minimum static pressure present. However, the change resulted in a further increase in static pressure build-up on the now ‘blunt’ LE. Observation of pressure plots suggested that this opposing pressure build-up aided in the reduction of the upstream separation. This assistance was the result of the opposing pressure field augmenting the adverse pressure gradient that was driving the separation behaviour.

When the semi-circular upstream face was combined with a tapering 45° downstream face, a 26% drop in static pressure loss across the arrangement was achieved. This figure exactly matched that achieved with the prior decrease in the downstream taper angle. When the semi-circular upstream face was combined with 30° and 20° tapering downstream faces, significant reductions in static pressure losses occurred: a 58% drop in the case of the 30° taper, and a 71% drop in the case of the 20° taper, compared to the baseline arrangement.

In the 30° and 20° tapering downstream faces solutions, downstream face separation had been completely removed. In the texts of both (Francis, 1975) and (Massey, 2001) it is suggested that in a circular diffuser, with no downstream assistance, separation removal cannot be achieved with taper angles greater than 6°. Likewise, for the case of a planar diffuser, separation at taper angles of 10° has been experimentally observed and reported in numerous pieces of literature, two examples being (Buice & Eaton, 2000) and (El-Behery & Hamed, 2011).

(El-Behery & Hamed, 2011) also discusses the merits of various turbulence models in the CFD prediction of such diffuser separation. The findings indicated that of the models discussed within this thesis, the *k-ω* SST and standard *k-ω* variants predicted a number of parameters of the flow behaviour most accurately, including in locating the point of separation. The RSM and *k-ε* models were noted by (El-Behery & Hamed, 2011) as being poor performers in a comparative flow scenario.

The experimental work on planar diffusers by (Torblom, Lindgren, & Johansson, 2009) detected separation behaviour in a planar diffuser tapering at a lesser angle of 8.5°. When the above-mentioned examples are considered alongside the findings in this section the following is found. The impact of a gradually introduced taper, an opposing pressure gradient, and adjacent downstream contraction has on the diffuser separation behaviour is significant.

To have full confidence in the above statement experimental validation of a comparative baffle arrangement and similar diffuser geometry has to be performed. This becomes most evident when analysing Figure 52. In Figure 52 the opposing pressure gradient and adjacent downstream contraction are not present. This left only the gradually introduced taper to limit separation occurring on the downstream face, tapered at 30°. Separation was not observed in Figure 52 indicating that the gradually introduced taper alone removed the conditions for separation to occur. When this is considered alongside the findings in the experimental works mentioned above, the question of solution accuracy has to be asked, the answer to which cannot be given without case specific experimental validation work being performed.

Whilst a sizable reduction in taper angle was shown to remove separation, the reduction in taper angles severely shortened the length of the baffle body which would affect the acoustic dampening capacity of the arrangement. A design was then sought that could retain the lower static pressure losses without such a significant reduction in baffle body length.

Two designs were proposed in an attempt to achieve this. The first design utilised a 30° tapering downstream face, with a 1m radius linking it to the baffle body. This design showed a larger drop in static pressure loss than any of the previous design iterations: 73% lower than the baseline arrangement. The design maintained the separation of the free flow pattern.

The second design was developed to retain the removal of separation, achieved through a 20° downstream taper, whilst retaining a lengthened baffle body. This was achieved through 'clipping' the TE, so that the overall baffle length would not fall outside the design parameters. Whilst a 45% drop in static pressure loss was achieved over the baseline arrangement, this design performed poorly compared with the majority of the others tested. Separation along the downstream face was avoided. However, a smaller yet still substantial new area of separation and circulation formed immediately downstream of the 'clipped' TE.

The study then sought to enhance these positive findings by including a radiused intersection between the baffle body and the downstream face. At the TE of each baffle of this design, airflow from streams on either side of the baffle meets and recombines. It was found that at this point, an area of slightly increased static pressure was present in the flow domain. This indicated an area of flow inefficiency. To reduce this inefficiency, a second radius curving in the opposing direction, was added to the downstream face. This second radius 'sharpened' the point of the TE, and aimed to more closely realign the respective flows prior to recombining. This design change had the desired effect. A further drop in static pressure loss was calculated. This equated to a level 76% less than the baseline solution.

The opposing pressure gradient at the LE was earlier seen to reduce the size and losses associated with downstream face separation. However, the substantial improvement in the flow patterns through the downstream face modifications were thought to make the advantages of the opposing pressure gradient negligible. Therefore, focus was shifted to reducing the static pressure build-up on the 'blunt' leading edge of the semi-circular face.

To retain the positive attribute of reduced low-velocity regions at the intersection of the upstream face and the baffle body, a tapered upstream face was combined with a 0.3m radius linking it to the baffle body. When combined with a 30° tapering downstream face, static pressure loss across the arrangement decreased by 50% for the tapered upstream face and 10% for the semi-circular upstream face. This equated to a 63% drop compared with the baseline solution.

The positive findings made through the investigations of the section were combined into a final design iteration. A 45° tapering upstream face was combined with a 0.3m radius at the upstream intersection of the baffle body. The downstream face joined the baffle body with a 1.0m radius curve. The downstream face also contained the 0.5m reverse curvature radius to realign flow at the TE. In combination these design features created a significant drop in static pressure loss of 79% over the baseline solution. Downstream of the combined element and baseline arrangements a significant variation in velocity distortion was noted. This was particularly evident at a distance of 0.625m downstream of the arrangements TE. However, by 5.625m downstream, the variation was significantly reduced.

Although a costing analysis was not performed, it is the opinion of the author that the greatest gains in efficiency, when traded-off against potential manufacturing expense, occurred with a semi-circular upstream face and a downstream face with a taper angle of 30°. The combination of these two design features significantly reduced pressure loss when compared with either of the features employed individually. Further modification to the baseline arrangement beyond this point provided comparatively small gains for the predicted investment required to produce.

4 Turning-Vane Arrangement - Velocity Distortion

4.1 Background Information

A number of JETC's in operation across the industry, including the CHCEC, are U-shaped in design. The airflow in a U-shaped cell is re-orientated 180° between entry and exhaust. The airflow re-orientation is performed in two 90° stages. The first stage is performed in a turning-vane arrangement at the base of the inlet stack. Turning-vane arrangements are incorporated to avoid large pressure losses (Pope & Rae, 1984). Figure 56 shows the turning-vane arrangement at the CHCEC test cell.

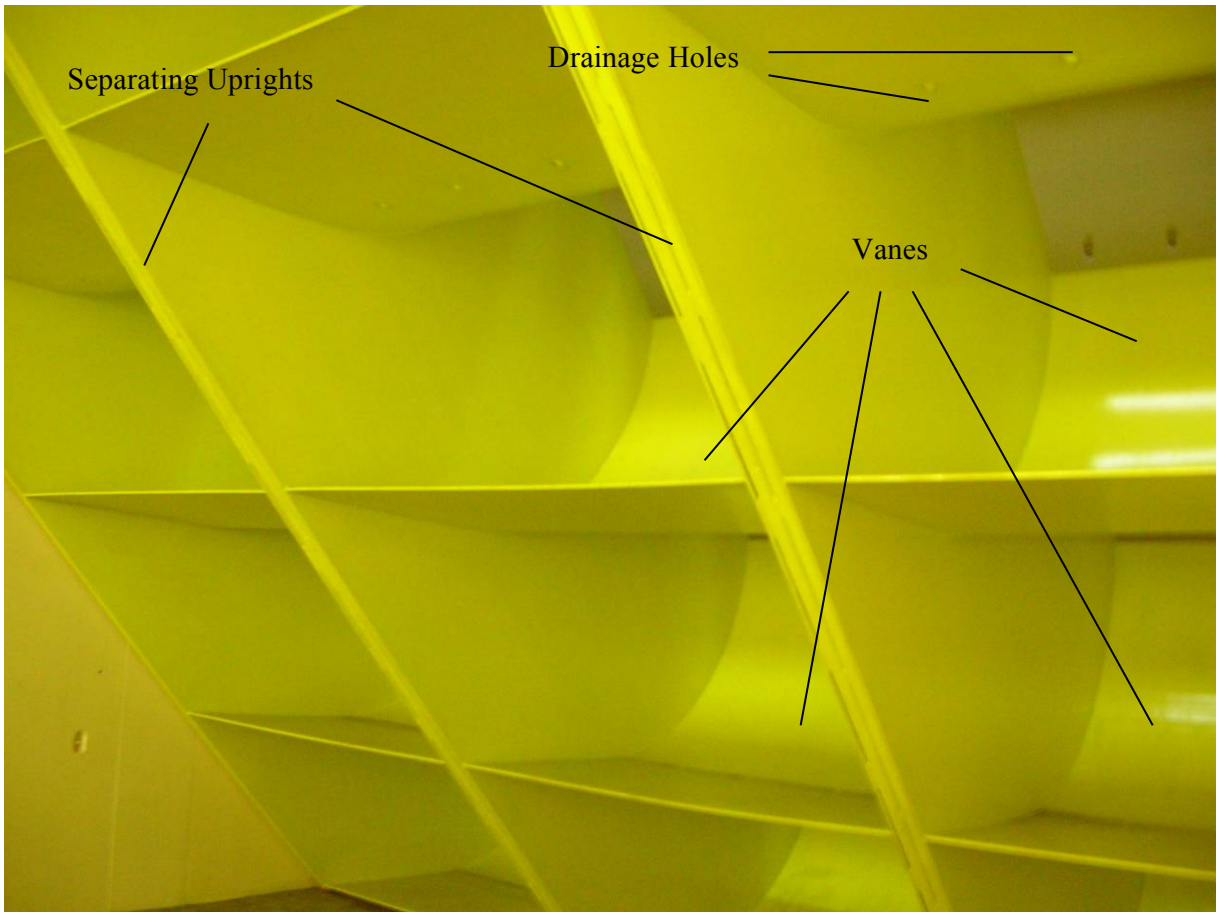

Figure 56 CHCEC Turning-Vane Arrangement

4.1.1 Turning-Vanes In Jet Engine Test Cells

In a test cell a turning-vane arrangement consists of an individual vane design that is repeated a number of times throughout a full vane structure. The vanes are constructed of rolled sections of flat plate, 2-5mm thick. The individual turning-vanes are arranged in a number of rows. Each row is

located and supported by separating-uprights. The separating-uprights provide structural support and alignment for the individual vanes in addition to assisting in the maintenance of horizontal flow uniformity. The separating-uprights angle forwards, allowing each successive row of vanes to be within view of the upstream flow as shown in Figure 56.

In a test cell scenario, airflow is drawn from the atmosphere by the depression at the engine inlet. The airflow enters the turning-vane from above, corresponding to the top edge in the example of Figure 56. The airflow is re-orientated by ~90° in the arrangement, and exits in a near horizontal state, corresponding to left edge of Figure 56. The number of rows and columns in a vane arrangement varies from cell to cell, along with the lean angle of the separating uprights. As an example of this, the CHCEC cell uses six rows of vanes, whilst the CENCO cell in Hanover uses twelve.

4.1.2 Interaction of Acoustic Baffles and Turning-Vanes

Immediately upstream of the turning-vane arrangement in a U-shaped JETC are acoustic baffles. The orientation of a baffle arrangement can take one of two forms. With the length of the baffles running either parallel, as shown in Figure 57, or perpendicular to the main-stream flow in the working section.

When the lower row of baffles is located closely above the uppermost row of vanes, airflow disruptions can be created due to the interaction of the two components (Agmen et al., 2005). Wakes are created downstream of each baffle. This was shown in the investigation presented in Section 3. The wakes create pockets of low velocity flow which can impinge upon the turning-vane arrangement. When an adverse interaction is created between the wakes and the vane arrangement, a flow disturbance can result. This flow disturbance is then transmitted downstream, causing heightened velocity distortion in the upstream region of the working section.

During certification the CHCEC cell suffered from unacceptably high levels of velocity distortion (Flynn, 2008). (Agmen et al., 2005) computed a significant amount of interaction between the baffle wakes and the turning-vane arrangement, and suggested this as one of the possible causes of the distortion.

4.1.3 Problems Downstream of Test Cell Turning-Vane Arrangements

In a turning-vane arrangement there is potential for portions of the airflow to separate and circulate. Separation and circulation are commonly found on the underside of the inner corner, and below each row of vanes. Both of these features were observed in the analysis of (Agmen et al., 2005). The likely cause of the under-vane separation is thought to be that the number of vanes is insufficient for the MFR being turned through the corner.

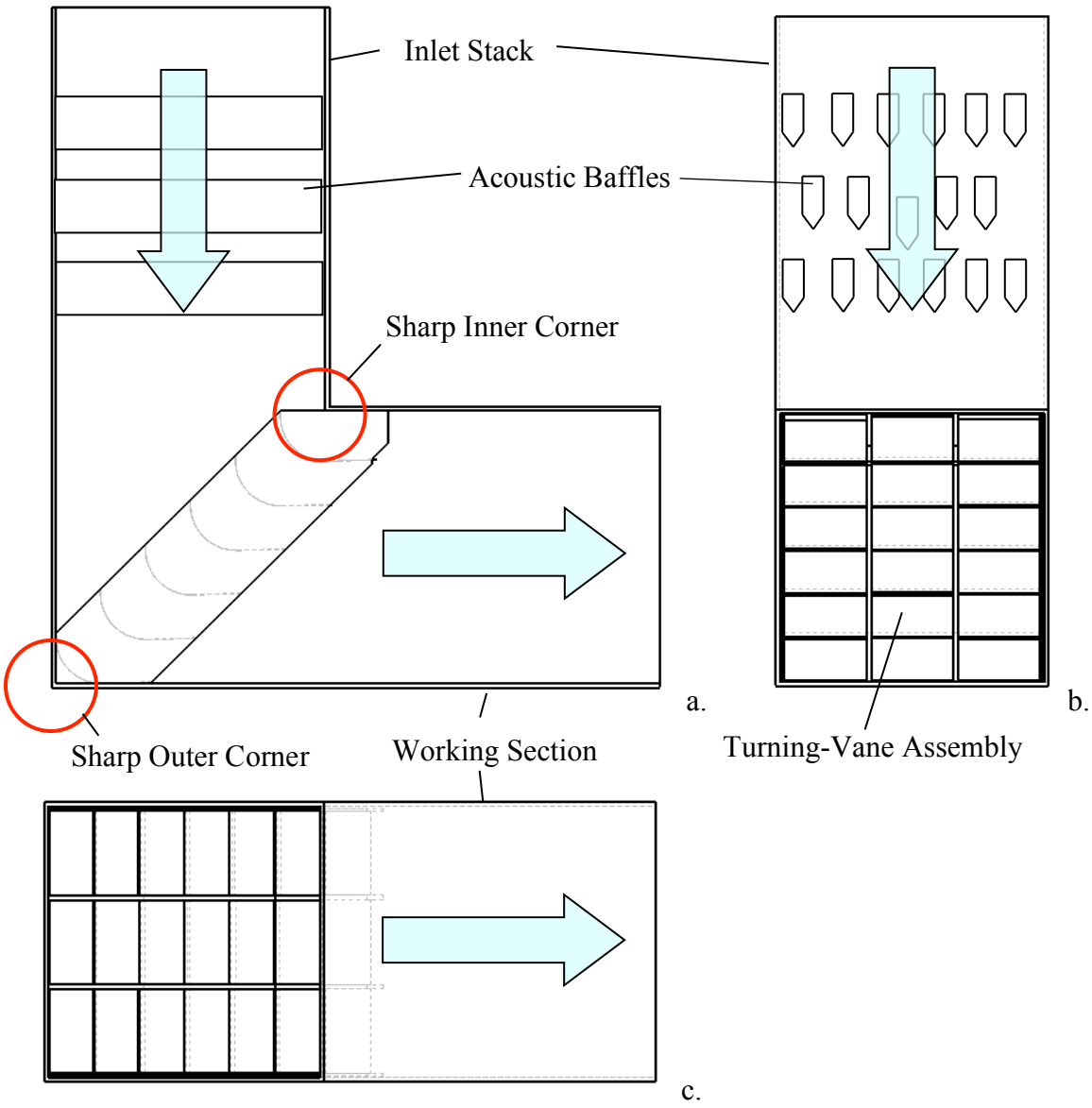

Figure 57 Side Elevation (a), End Elevation (b), and Plan View (with baffles removed) (c) of an Inlet Stack and Turning-Vane Arrangement

The presence of separation and circulation upstream of the engine affects operation in two ways. Firstly, separation from the inner corner creates a low velocity zone on the roof of the working section. The low velocity zone has the potential to extend downstream towards the engine inlet face.

The probability of vortex formation is heightened because of the increased potential of a stagnation point forming adjacent to the low velocity zone.

Secondly, separation also contributes to increased velocity distortion. The level of additional disturbance is dependent on the size of the separation and working section settling area. Velocity distortion is a determining factor in cell certification, and any adverse effects introduced by the turning-vane arrangement need to be considered.

4.1.4 Wind Tunnel Corner Design

Experimental wind tunnels share many features with JETCs. Wind tunnels are designed to ensure a desired MFR of air passes through the working section in an 'undisturbed' state. In a JETC the engine generates the airflow. In a wind tunnel a fan generates the airflow (Pope & Rae, 1984).

The airflow at the entrance to a wind tunnel working section is ideally aligned with the tunnel walls and contains low levels of velocity distortion and turbulence (Pope & Rae, 1984). The following guidelines were put together by (Pope & Rae, 1984) and (Pankhurst & Holder, 1952) for the design of wind tunnel corner areas. The guidelines predominantly deal with airflow efficiency, but also include airflow quality-related recommendations:

- Rounded corner bends provide superior efficiency to right-angled bends;
- If the flow needs to be rotated by 180°, the use of two 90° steps reduces pressure losses and airflow distortion;
- Both flat-plate and aerofoil vane profiles have been employed successfully;
- Recent trends have seen predominant use of thin flat-plate vanes for multiple reasons;
- For flat-plate vanes, a circle quadrant with extended tangential extension 'fins' on the LE and TE is the recommended design;
- The addition of LE and TE fins does not affect efficiency and provides assistance during manufacture and installation;
- For vanes of all thickness, airflow efficiency is greatest when the angle of incidence at the LE (θ in Figure 58a) is between 0° and 5°;
- Pressure losses are smallest when R/D and W/D (Figure 58a) are largest;
- With vanes of all cross-sections, a gap-chord ratio (see Figure 58b) of 1:3 or below should be used;

- Vanes in larger cross-sectional areas of the tunnel experience fewer pressure losses due to the lower velocity airflow;
- Provisions should be included in the tunnel design to adjust the vanes in a rotational manner after installation; and
- Vanes placed immediately upstream of the working section should have small chord lengths so that disturbances generated will decay quickly.

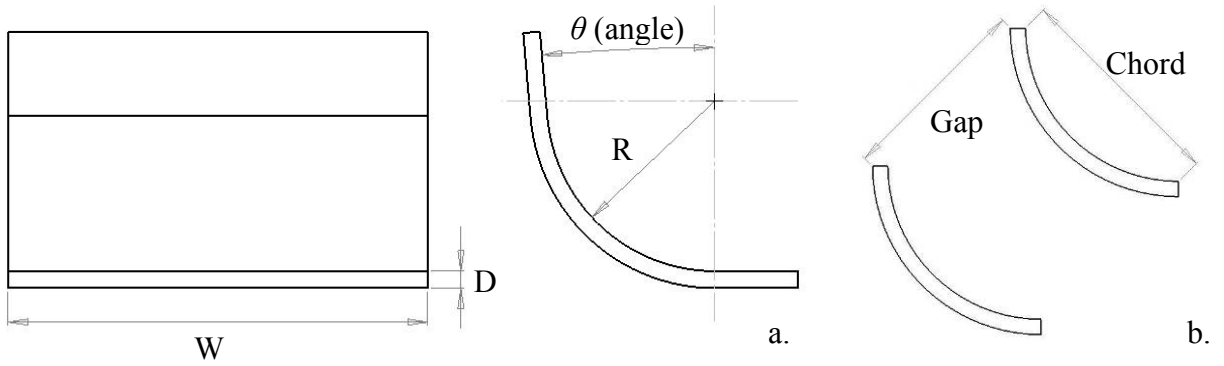

Figure 58 Front and Side Elevation of a Wind Tunnel Turning-Vane (a), and Side Elevation of Two Successive Turning-Vanes (b)

4.2 Turning-Vane Analysis Methodology

An investigation of the turning-vane arrangement in a JETC was performed. The broader aim of the investigation was to analyse the application of CFD techniques to a region of JETC under operational conditions. This aim hoped to more specifically achieve the following objectives:

- To investigate the validity of the CFD techniques used in the turning-vane analysis of (Agmen et al., 2005);
- To set up and generate a CFD solution of the flow patterns through and around a JETC turning-vane arrangement;
- To provide the CHCEC with information on the performance of their vane arrangement;
- To provide computational solutions to contribute one of the two parts required for a problem-specific validation of the techniques used;
- To qualitatively assess the accuracy of computational solutions for physical realism;
- To conduct a CFD-aided design process as an assessment of the capability of CFD as a investigation and design tool; and
- Use decreased velocity distortion, and the associated benefits it provides, as the driving force behind the design process.

The remainder of this section discusses the methodology employed to achieve these objectives.

One of the objectives of the investigation was to gain an understanding of the flow through the turning-vane arrangement of the CHCEC cell. As such the geometry of the CHCEC cell was used to create a baseline turning-vane arrangement. The details of the arrangement are discussed in Section 4.2.1. A computational domain was created to replicate the baseline design upon which a CFD analysis could be performed. The generation of the computational domain is discussed in Section 4.2.2.1.

This investigation also sought to validate the techniques used by (Agmen et al., 2005). To do so, the solver settings used by (Agmen et al., 2005) were initially retained. These are discussed in Section 4.2.2.2, and are followed by a discussion of the boundary conditions used in Section 4.2.2.3. The baseline arrangement was then meshed, and a mesh independence check performed. These are discussed in Section 4.2.2.4.

Prior to the main body of the analysis, a validation check was performed to evaluate the accuracy of the techniques used by (Agmen et al., 2005). A discussion of the validation case, the computational setup, and analysis of the validation results are presented in Section 4.2.3.

Following the validation analysis, a solution to the baseline vane arrangement was generated. The findings are discussed in Section 4.3.1. An investigation and design process was then performed with the primary objective of decreasing velocity distortion downstream of the arrangement. The work of the CFD-aided investigations performed to achieve this objective is presented in Section 4.3.5 through Section 4.3.8. Section 4.4 then concludes the investigation with a summary of the findings.

4.2.1 Baseline Design – Christchurch Engine Centre Cell

As discussed above, the geometry of the CHCEC cell was used in the creation of the baseline arrangement for the turning-vane investigation. This allowed the objective of providing CHCEC with information regarding their vane arrangement to be achieved. In addition, the CHCEC cell was seen as an appropriate baseline arrangement for the remaining objectives in the investigation for the following reasons:

- Many of the CHCEC cell features are present in other industry examples;

- In the CHCEC cell there is limited distance between the baffles and turning-vane arrangements, providing an ideal test bed for an analysis of the interaction between the two components;
- The initial study by (Agmen et al., 2005) indicated that separation likely occurs under each row of turning-vanes in the CHCEC cell; and
- The two above-mentioned points made the CHCEC cell an ideal candidate to perform a velocity distortion driven design process on.

The inlet stack of the CHCEC cell is a vertically orientated hollow concrete shaft, 12.3m in height, and 6.7m wide with a square cross-section. The inlet stack houses an acoustic baffle arrangement and six rows of turning-vanes.

In the baffle arrangement, all individual baffles are identical. The cross-sectional profile of the baffle arrangement is shown in Figure 59. Figure 59 contains labelling for reference later in this section. Each baffle is 1630mm long and 375mm wide. They utilise a semi-circular upstream face and a tapering downstream face.

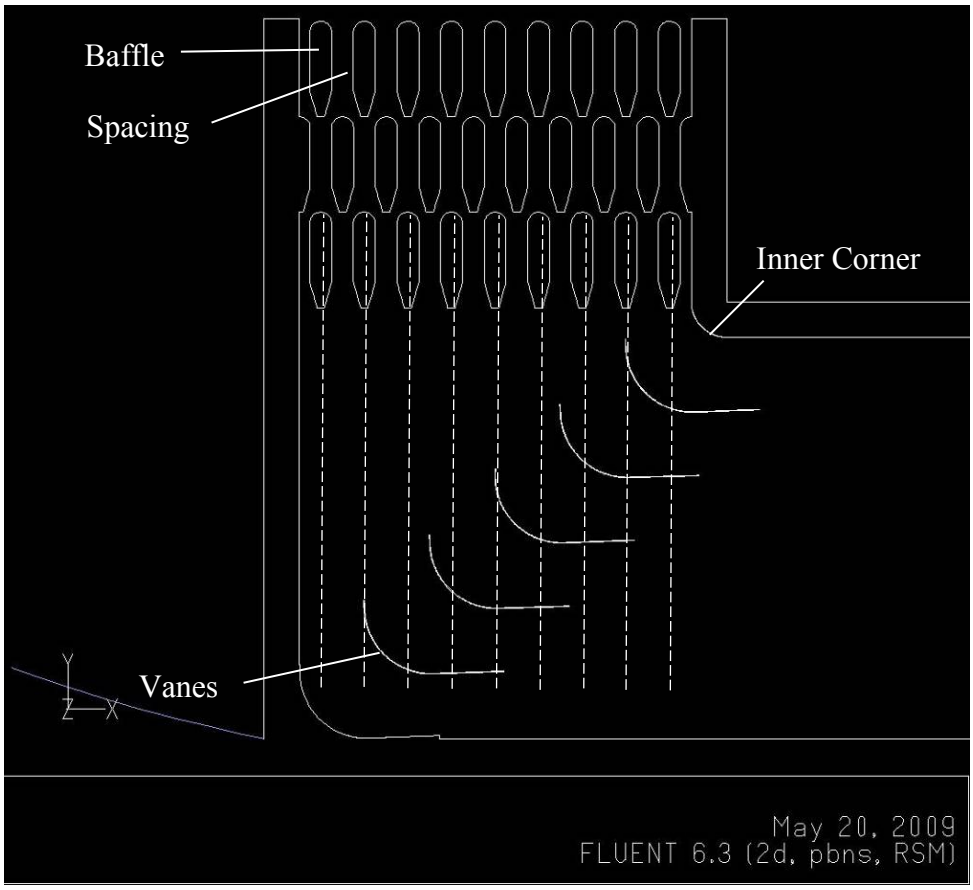

Figure 59 Alignment between Baffle and Turning-Vane Arrangements in the CHCEC Cell

The tapering downstream face narrows to 125mm over the downstream 442.5mm of the baffle, giving a 'clipped' appearance. A similar design was tested in the analysis of Section 3. In terms of aerodynamic efficiency, the design performed poorly, rating seventh out of ten in terms of flow efficiency.

The layout of the CHCEC baffle arrangement is also shown in Figure 59. The LE of the uppermost baffle row is aligned with the lip of the inlet stack. The TE of each baffle is aligned with the LE of the downstream baffle. The lengthwise direction of the baffles runs perpendicular to the main body of flow in the working section.

This was the only baffle alignment scenario considered in the investigations of this section. This decision was made to allow a more focused and thorough investigation of the CHCEC alignment to be conducted. In doing so, the design process and investigations would be directly applicable to the CHCEC cell if future modifications were to be considered.

In the CHCEC cell the uppermost row of vanes is located 500mm below the lowermost row of baffles. As shown in Figure 59, the baffle-vane alignment varies across the span of the inlet stack. The first (uppermost), third, and fifth row of vanes are aligned with baffles in the lower row. The second, fourth and sixth (lowermost) row of vanes are aligned with baffles in the centre row. The sixth row of vanes is thus located adjacent to the inlet stack wall.

Vane Positioning in CHCEC Cell

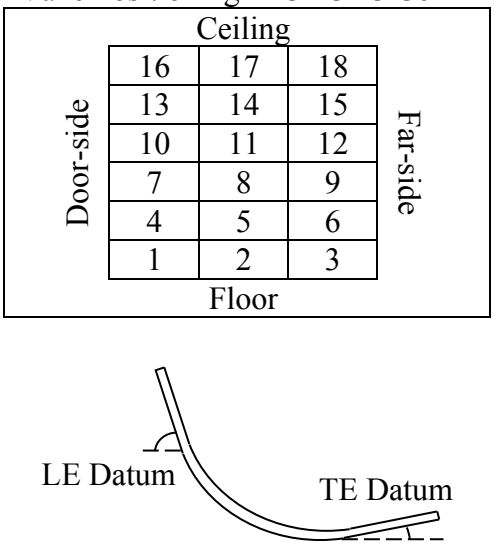

							Avg.
		LE and TE Angles (°)					
LE	16	87.5	17	91.9	18	89.3	89.6
TE		2.2		2.3		1.8	2.1
LE	13	87.4	14	91.5	15	87.8	88.9
TE		1.5		1.2		2.0	1.6
LE	10	91.1	11	89.8	12	90.1	90.3
TE		2.2		1.5		1.4	1.7
LE	7	88.1	8	88.5	9	88.7	88.4
TE		1.7		2.3		1.7	1.9
LE	4	87.6	5	87.3	6	88.4	87.8
TE		2.0		1.2		1.4	1.5
LE	1	89.7	2	88.9	3	89.4	89.3
TE		2.1		2.0		2.2	2.1
TE	Overall Avg.						89.1
LE							1.8

Figure 60 LE and TE Angles of the Turning-Vane Arrangement in the CHCEC Cell

In the CHCEC cell the radius of each vane is 1153mm, and has a TE extension 1200mm in length. Each row of vanes is divided into three sections by separating-uprights. The LE and TE angles

differ between each vane. This is the result of inaccuracies introduced during construction. The 'as-built' LE and TE angles of each vane within the CHCEC arrangement are presented in Figure 60. The inner corner, at the intersection of the inlet stack and working section, is rounded at a constant radius of 600mm.

4.2.2 Computational Settings

4.2.2.1 Computational Domain

(Salter, 1952) described the generation of vortices, near the side wall of a turning-vane in a square duct, as an inevitable occurrence unless provision is made to limit their formation. This indicates that a three-dimensional flow pattern would be expected across the width of a turning-vane arrangement. It is also noted that the corner vortices dissipate towards the centreline of the tunnel. (Salter, 1952) states that the three-dimensional corner flow becomes two-dimensional by the centre of the duct. The rate of the vortex dissipation is noted as being dependent on the uniformity of the vane geometry and the pitch/chord ratio.

In designing a test cell, the vanes within the turning-vane arrangement will possess uniformity due to the desire to generate a uniform velocity profile upstream of the engine inlet face. Figure 60 shows that, through construction, the ideal uniformity is often lost in practice.

The two above-mentioned factors were considered alongside the objectives of the investigation. The majority of the objectives were based around validating the prediction of, and then decreasing, velocity distortion. In Section 1.4.1, it was discussed that in real-world practice, velocity distortion is calculated over a geometrically limited plane. This plane does not account for the full flow effects near the cell walls. As such, it was thought that it would be unlikely that these three-dimensional effects would register in the measurements taken over the restricted distortion plane in reality. In addition, a lack of provision by the JETC industry, to reduce the intrusion of sidewall vortices, suggested to the author that test cells are not significantly affected by their presence.

It was deemed a two-dimensional computational domain would accurately achieve the aims of the analysis. Doing so effectively meant the vane arrangement was modelled to be of infinite width. In interpreting the findings of the investigations of this section, it needs to be acknowledged that the results will not be applicable to the near wall regions of a real-world stack.

The geometry of the baffle and vane arrangements discussed in Section 4.2.1, were transferred to a two-dimensional domain. In doing so, the three-dimensional variation in vane geometry at the CHCEC was unable to be accounted for. The average LE and TE angles (shown in Figure 60) were therefore applied to all vanes within the domain. This practice aligned with the method employed by (Agmen et al., 2005).

The domain was extended through to the top of the inlet stack and into the surrounding atmosphere. This is shown in Figure 61. This was done to ensure that flow profile entering the turning-vane arrangement would account for any effects created by the inlet stack lip, and the effects downstream interaction with the baffle arrangement.

The computational domain was extended from the 'Atmospheric Inlet' BC, through the inlet stack and fore-region of the working section. The height of the working section was set at 6.858m to align with the CHCEC cell. The working section was extended 20m downstream of the outer stack wall, and terminated with a 'Working Section Outlet' BC. The 'Working Section Outlet' was set at a location relative to the outer stack wall so it would be closely aligned with the inlet face of an IAE V2500 being tested in the CHCEC cell.

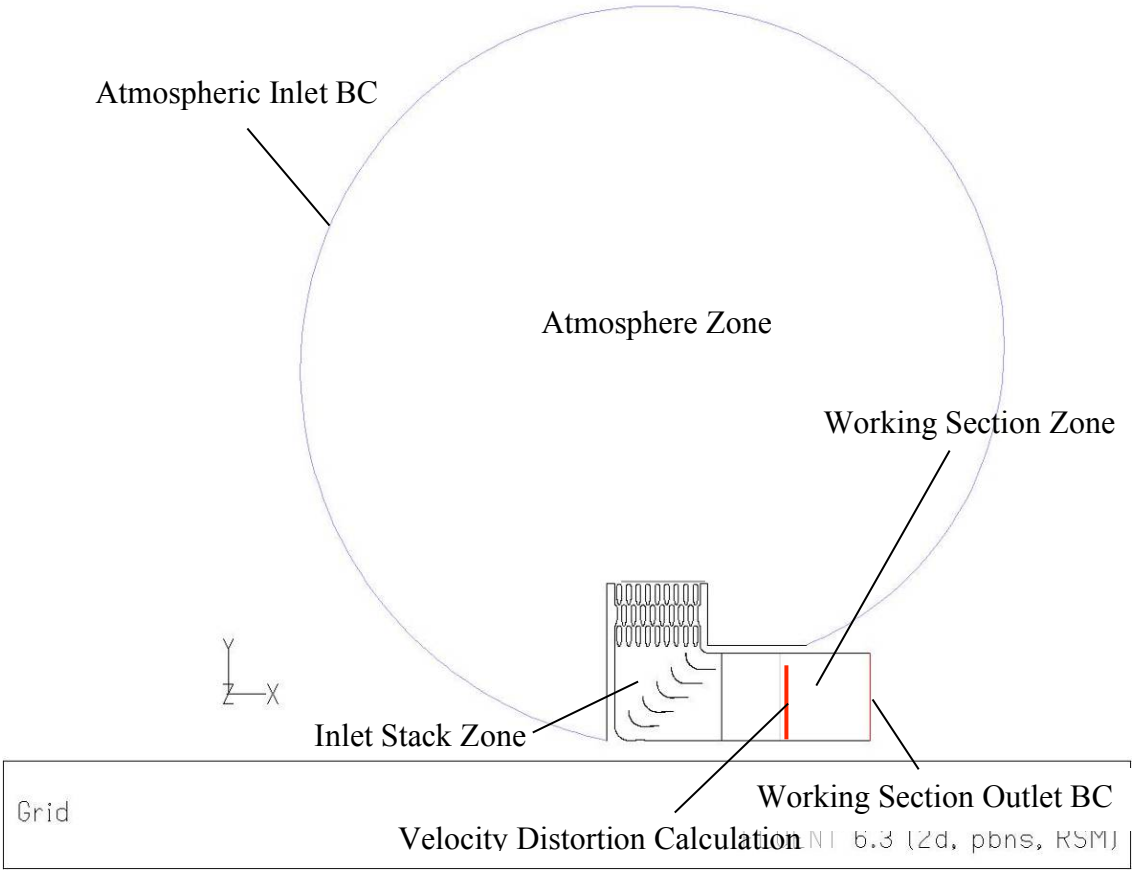

Figure 61 Computational Domain, BC Locations, and Meshing Zones used in the Turning-Vane Investigation

4.2.2.2 Solver Settings

To achieve the goal of validating the methods used by (Agmen et al., 2005), the solver settings from that analysis were initially retained. The fluid modelled within the computational domain was air, with constant density, specific heat, thermal conductivity, and viscosity. The effects of compressibility were not accounted for. The maximum predicted velocity was expected to occur through the channels in the baffle arrangement. The velocity in these channels, with a realistic cell MFR, was not predicted to exceed $55ms^{-1}$. The decision by (Agmen et al., 2005) to discount compressibility effects appeared justified.

The turning-vanes in the CHCEC cell are constructed of the same painted metal as the inlet baffles. As per the discussion of Section 3.2.2.2, a K_S of 0m was applied to the surfaces in the domain representing both the baffle and turning-vanes. Likewise, the working section walls are constructed and finished in a similar manner to the inlet stack walls at the CHCEC. Both have a smoothed concrete surface. As such, surfaces in the domain representing the inlet stack and working section walls were modelled with a K_S of 0m as well.

A second-order spatial discretisation scheme was applied to maintain consistency with (Agmen et al., 2005). In (Agmen et al., 2005) a transient solver was used as the potential for transient flow patterns wanted to be accounted for. However, no transient effects were detected during the solution process. As such, a steady-state solver was applied for the investigation of this section. Solution monitors and convergence criteria, both of which are discussed later in this section, were chosen to ensure that any tendency towards transient behaviour would be detected through the solution process.

The turbulence model used by (Agmen et al., 2005) was the RSM. For validation purposes, the RSM was retained for this investigation. The potential benefit of the RSM in the turning-vane analysis is its claimed good level of accuracy in prediction of flows in rotating ducts (Fluent, 2006). The reduction of the domain to two-dimensions meant the additional computational expense could be accommodated.

In (Agmen et al., 2005) the PISO pressure-velocity coupling was used. The selection of this coupling was based on its appropriateness to transient solvers (Fluent, 2006; Versteeg & Malalasekera, 2007). This benefit of the PISO coupling could not be utilised with the steady-state solver of this investigation. However, in the domain under investigation, small geometries (i.e. the

vane thickness) existed within a much larger domain. Such a scenario leads to the potential for high levels of skewness to occur during meshing. (Fluent, 2006) suggests that the PISO coupling is also beneficial in such scenarios, even when coupled with a steady-state solver. As such, the PISO coupling was retained for this investigation.

To assess solution convergence, the residuals of continuity, x and y velocity, k, ε, and the four applicable Reynolds stresses (for a two-dimensional domain) were monitored. The convergence criterion for the solution was based on these residuals, scaled in relation to those produced in the first solution iteration, dropping below a value of 1.0E-04.
This convergence criterion was set to a stricter degree than in the analysis of Section 3. This was done in an effort to more stringently assess the presence of transient effects in the solution should they appear. As in Section 3, the average velocity at the outlet BC was also monitored. A further convergence criterion was applied. This criterion stated that the average velocity needed to oscillate within 0.05ms^{-1} about a constant value.

4.2.2.3 Boundary Conditions

In the work of (Agmen et al., 2005), the BCs were set via a pressure drop between the 'Atmospheric Inlet' and the 'Working Section Outlet'. The 'Atmospheric Inlet' was modelled with a 0Pa total pressure, and the 'Working Section Outlet' with a -1000Pa static pressure. In retrospect, it is seen that the velocities these BCs produced within the domain were higher than would be realistically be expected in a cell of the CHCECs size.

At the 'Working Section Outlet' the average velocity across the BC was calculated at approximately 25ms^{-1}. A uniform velocity of 25ms^{-1} across the CHCEC working section would equate to a MFR of approximately 1510kgs^{-1}. A mid thrust-level IAE V2500, as the CHCEC cell was designed to test, produces an air MFR of 400kgs^{-1} under maximum thrust conditions (MTU, 2011). This would correspond to a cell BPR of more than 275% using the BCs of (Agmen et al., 2005). This value is higher than realistic.

As such, the BCs were re-considered for the investigation of this section. The setting of the 'Atmospheric Inlet' by (Agmen et al., 2005) seemed to be a fair representation of a real-world state. The total pressure of 0Pa indicated that the air being drawn into the domain was coming from a near stationary state. The physical extent of the 'Atmospheric Inlet' and the solution of (Agmen et al., 2005) suggested this assumption was accurate.

As such, the 'Working Section Outlet' BC was revised. The assignment of the BC as a pressure outlet was deemed to be an accurate representation of the driving force behind a real-world test cell. This force being the depression created at the engine inlet face.

The observation of vortex activity in the CHCEC during early certification testing, as shown in Figure 8, suggested the engine inlet stream-tube rapidly extended to the cell boundaries during engine run conditions. This was supported by the findings of (Agmen et al., 2005). As such, applying the 'Working Section Outlet' BC over the height of the cell, as opposed to a smaller region representing the engine face, was deemed appropriate.

Unfortunately, as test cell data were unable to be obtained, the following process was employed to set the 'Working Section Outlet' BC. A realistic cell BPR was selected, 150% (Clarke, 2000). Using a realistic engine MFR, 400kgs^{-1}, a cell MFR was calculated, 1000kgs^{-1} (MTU, 2011). The assumption of incompressibility was applied. The cross-sectional area of the CHCEC working section was calculated at 49.4m^2. A uniform cross-sectional cell velocity of 16.5ms^{-1} was then calculated to reflect the above-mentioned cell MFR of 1000kgs^{-1}.

Prior to the main body of the analysis, the static pressure at the 'Working Section Outlet' was incrementally increased in 100Pa steps from the -1000Pa employed by (Agmen et al., 2005). A solution was obtained for each incremental change, and the average velocity at the 'Working Section Outlet' calculated. With a static pressure at the BC of -500Pa, an average velocity of 17.4ms^{-1} was calculated. This value satisfactorily agreed to within 5.5% of the 16.5ms^{-1} velocity. The 'Working Section Outlet' BC was therefore set at a static pressure of -500Pa for the main body of the analysis, and was deemed to accurately represent a realistic cell flow.

No side-wind conditions were accounted for in the investigation. As mentioned above, the findings of (Agmen et al., 2005) agreed that the air entering the domain would be in a near static state. As such, turbulence at the 'Atmospheric Inlet' was modelled with a low TI of 1%, and a TLS of 0.1m to reflect this. It was also deemed that the extent of the computational domain upstream of the turning-vane arrangement would assist in rectifying any inaccuracies of the turbulence levels employed at the BC. The baffle arrangement, immediately upstream of the vanes, was expected to be the major contributor in defining the turbulence profile at the inlet to the vane arrangement. If side-wind conditions were to be accounted for, the paper of (Roth, 2000) is suggested as a starting point for determining an atmospheric turbulence profile.

4.2.2.4 Mesh and Mesh Independence

The computational domain described in Section 4.2.2.1 was broken down into three zones to control the meshing process. The three zones are shown in Figure 61, labelled as the 'Working Section', 'Inlet Stack', and 'Atmosphere'.

A BL function was used to grow mesh elements away from the inner corner and turning-vane walls. Outside of the BL function, the 'Inlet Stack' was meshed with triangular elements. Triangular elements were used as a majority of the flow patterns in the region were not known, and areas of flow complexity predicted. Triangular elements were also used in the 'Atmosphere' region due to its irregular shape, and to accommodate the significant growth away from the stack inlet.

In the 'Working Section' the flow was predicted to align with the inlet stack walls over a majority of the zone. As such, quad elements were used to utilise their staking efficiency and performance when aligned with the flow (Fluent, 2006). The computational domain of the baseline arrangement was initially meshed using 3.1E05 elements. Figure 62 shows the variation in mesh density and the element types used.

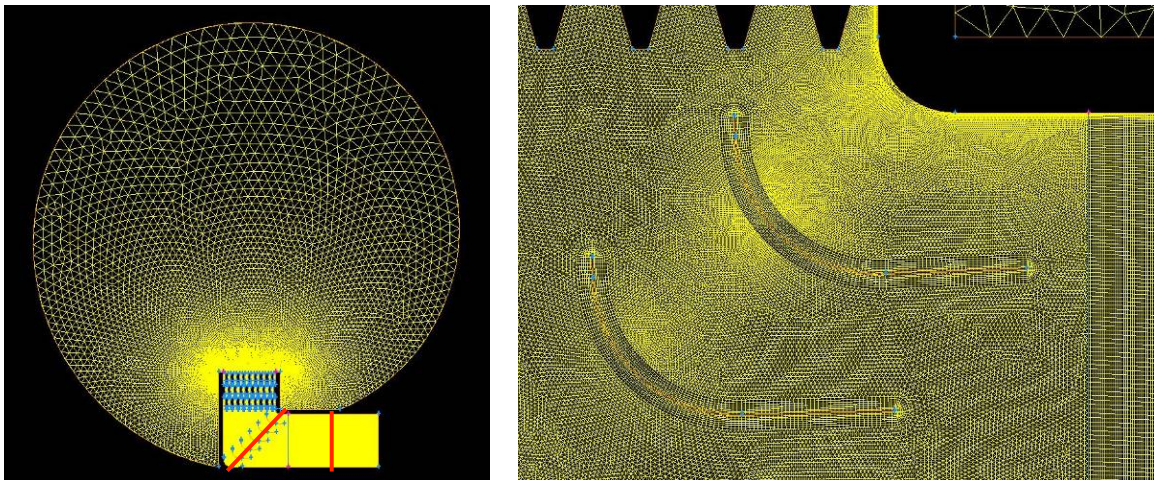

Figure 62 Element Types and Element Density Distribution in the Computational Domain

A solution using the solver setting and BCs described in Section 4.2.2.2 and Section 4.2.2.3 was generated. The density distribution of Figure 62 was retained, and the domain was re-meshed in two further iterations with an increase in elements numbers to 3.5E05 and 5.0E05 respectively. A solution was produced for each mesh.

Figure 63 compares velocity magnitude across the solutions generated. Qualitatively, a separation zone of similar size can be seen to develop in each of the solutions below the inner corner and under all turning-vanes. Figure 64 shows a more detailed view of the inner corner separation. In all three solutions the point of separation is located in an identical position, and the separation profile follows the same path.

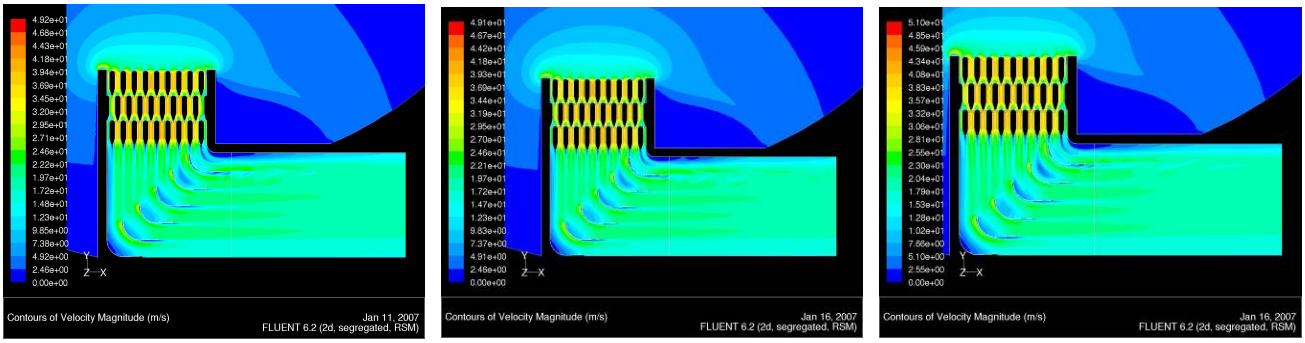

Figure 63 a-c Velocity Magnitude Plots produced in Computational Solutions using Meshes of 3.1E05 (left), 3.5E05 (middle), and 5.0E05 Elements (right)

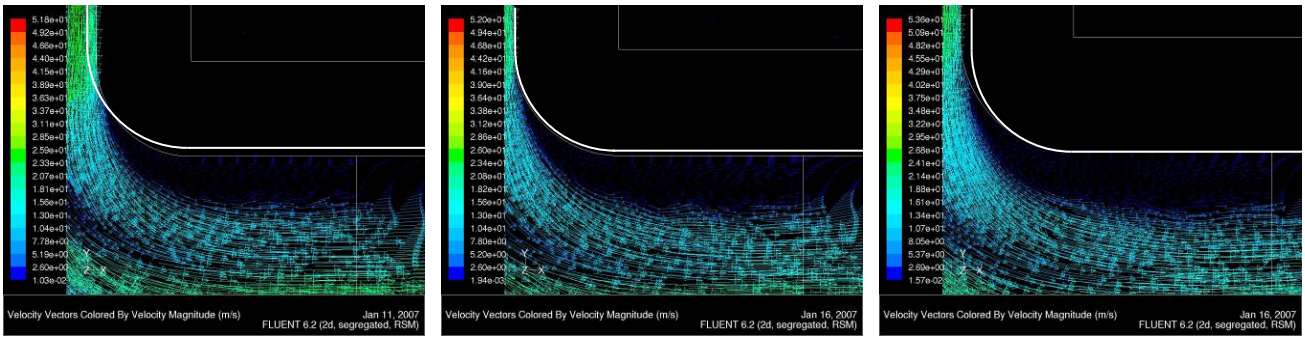

Figure 64 a-c Velocity Vectors produced in Computational Solutions using Meshes of 3.1E05 (left), 3.5E05 (middle), and 5.0E05 Elements (right)

Figure 65 presents the velocity profile at two locations within the three generated solutions. The location of the velocity profiles is marked in red in Figure 62 with vertical and diagonal red lines. Figure 65 shows that the variation in mesh density only marginally affects the flow patterns. Every feature of the velocity profile is clearly identified in each solution. It was deemed that the presence, size, and location of the significant flow features in the solutions were not mesh dependent, and as such, a mesh of 3.1E05 elements was retained for the main body of the analysis.

4.2.3 Validation of Computational Settings

A validation check of the computational settings outlined in Section 4.2.2 was performed. Section 4.2.3.1 describes the test case that was chosen and gives an overview of the experimental work that

was conducted. Section 4.2.3.2 outlines the computational setup used in the validation checks, and is followed by a comparison of the experimental and computational solutions in Section 4.2.3.3.

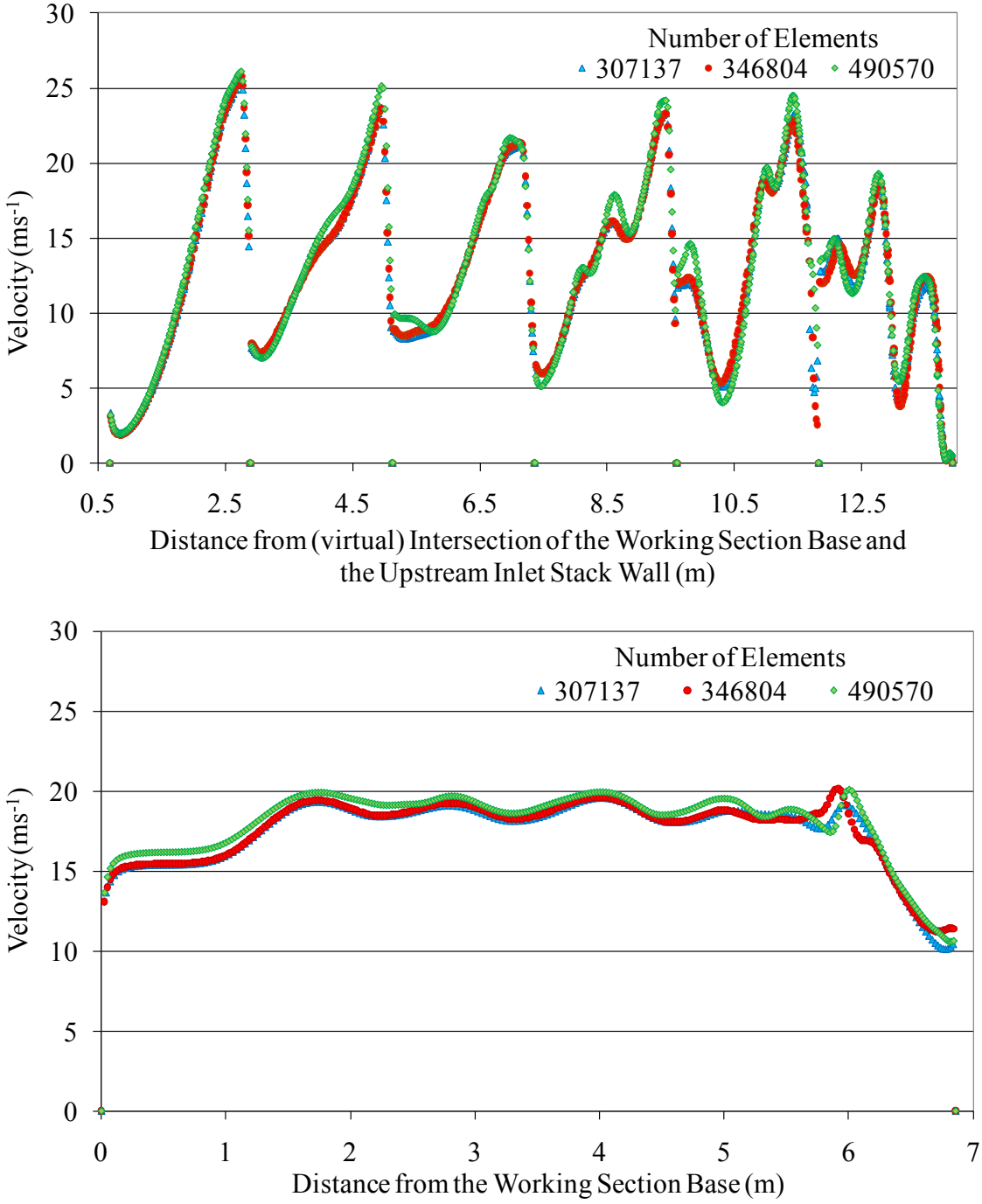

Figure 65 Velocity Profile Variation with Number of Elements along the Diagonal (top) and Vertical (bottom) lines marked in Figure 62

4.2.3.1 Turning-Vane Validation Test Case

The experimental data of (Johl, Passmore, & Render, 2007) was used to perform a validation check of the settings discussed in Section 4.2.2. (Johl et al., 2007) performed an experimental

investigation of the performance of thin, circular arc, turning-vanes in relation to the performance of a wind tunnel in the Aeronautical and Automotive Engineering department at Loughborough University in the United Kingdom.

(Johl et al., 2007) initially performed an analysis of both three- and four-vane arrangements in a test module. The same experimental techniques were then applied to the analysis of a 28-vane arrangement (using thicker vanes of otherwise identical individual properties) in an operational wind tunnel. The validation performed in this section focuses on comparisons with the three- and four-vane test module results. This was done as the 28-vane wind tunnel arrangement incorporated both upstream and downstream tapering sections, a scenario less representative of a JETC corner.

The geometry of the individual turning-vanes used in (Johl et al., 2007) is shown in Figure 66. The vanes share many features with those in the CHCEC arrangement. A vane radius of 245mm is coupled to a TE extension of 165mm. The LE of the vanes was also angled to be slightly open to oncoming flow.

The geometry of the test module is shown in Figure 67a. Two turning-vane arrangements were investigated within the test module. The first used a three-vane design with a constant s/c of 0.237, and the second used a four-vane design with a constant s/c of 0.190.

In (Johl et al., 2007) pressure data were collected via a pitot-probe traverse along lines A-A, B-B, and C-C, shown in Figure 67a. Both vane arrangements were tested using flows of Re 5.74E05, with Re being calculated based on chord length.

4.2.3.2 Computational Settings

Two computational domains were created to resemble the test model of (Johl et al., 2007), with three- and four- vane arrangements in place. The three-vane domain is shown in Figure 67b. The domains were meshed using the same mesh density distribution and element types as discussed in Section 4.2.2.4. The solvers were set up using the settings discussed in Section 4.2.2.2.

Although not mentioned by (Johl et al., 2007), it was assumed that the flow was driven from the entrance of the module, as opposed to being drawn through from the exit.

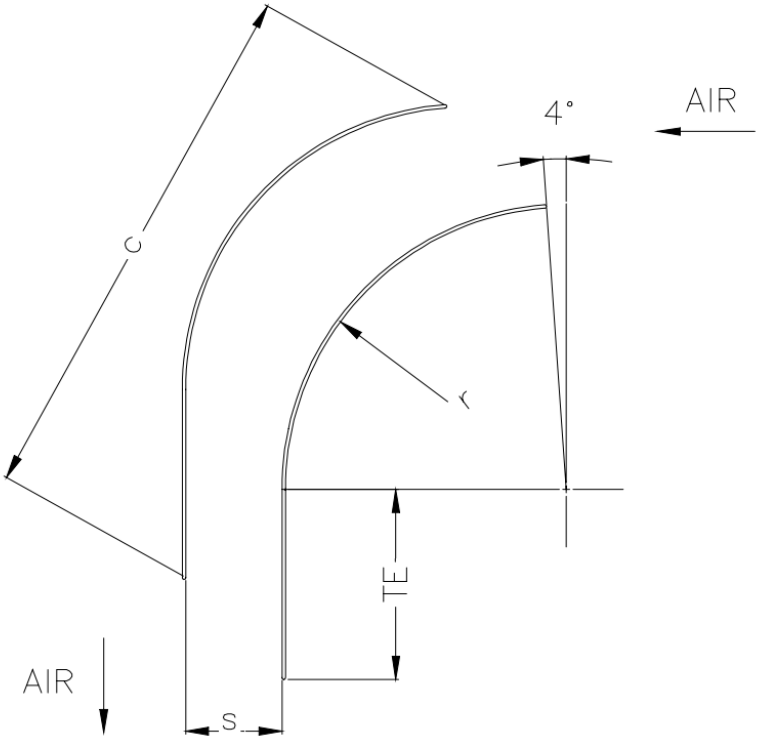

Figure 66 Profile of Individual Vanes used in the work of (Johl et al., 2007)

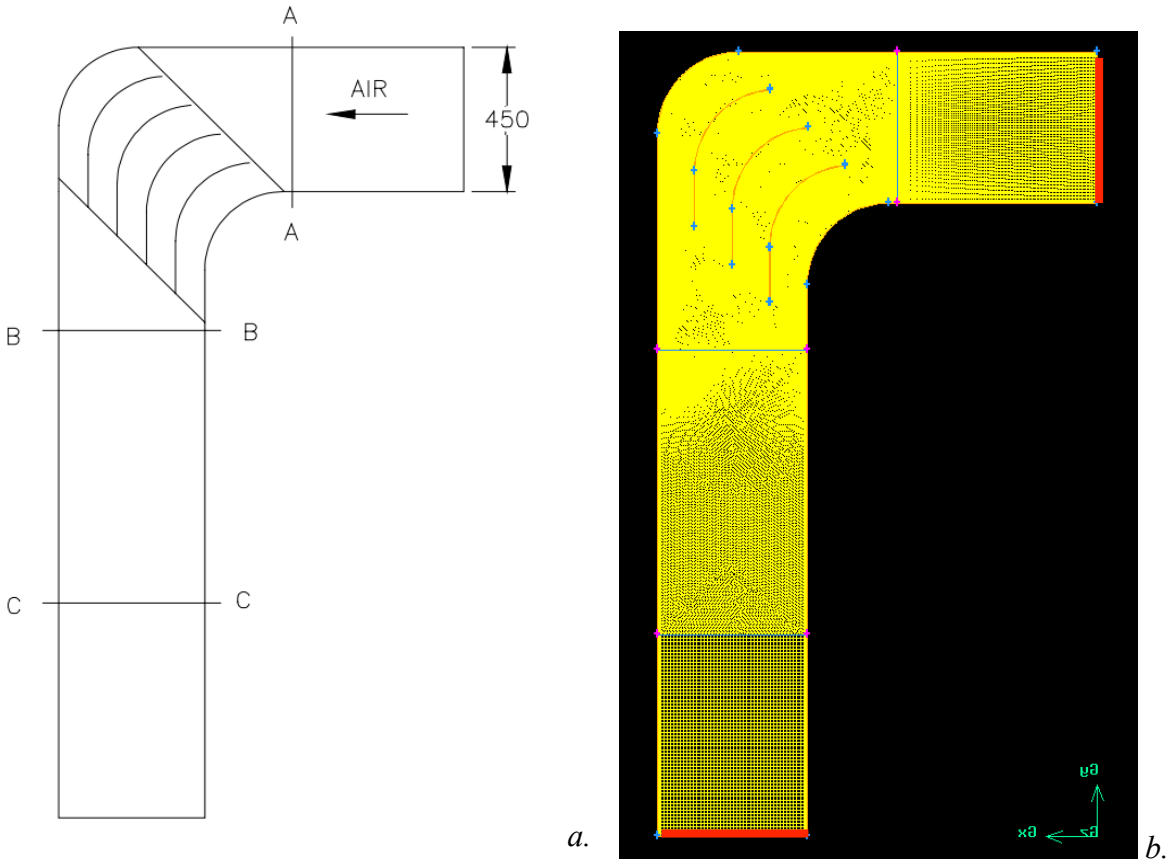

Figure 67 Four-Vane Test Module Geometry used by (Johl et al., 2007) (a), and Three-Vane Test Module Computational Domain (b)

As such, the inlet BCs, indicated with a vertical red line in Figure 67b, were assigned a constant velocity profile to generate a flow of Re 5.74E05. The outlet BCs, indicated with a horizontal red line in Figure 67b, were set as a pressure outlet, exhausting to the atmosphere at a static pressure of 0Pa.

The specific turbulence conditions at the module inlet were not discussed by (Johl et al., 2007). As such, turbulence was assigned based on estimates after considering the description of the experimental setup. The test module described in (Johl et al., 2007) appears to reflect a basic wind tunnel arrangement. As such, it was assumed that the upstream flow was in a fully developed state. (Fluent, 2006) states that the maximum TLS in a fully developed duct flow can be approximated as 7% of the duct width. As such, a TLS of 0.0315m was assigned.

From examples given in (Fluent, 2006) and (Pope & Rae, 1984), TIs of well below 1.0% can be achieved in modern low-turbulence wind tunnels. This is backed up by the discussion of (Johl et al., 2007), indicating that TI of 0.1% is achieved in the Loughborough tunnel. However, modern low-turbulence wind tunnels utilise multiple turbulence reduction screens and significant changes in the cross-sectional area. Neither of these appear to be present in the test module of (Johl et al., 2007). Therefore, a moderately low 1% TI was applied for the validation analysis.

4.2.3.3 Comparison of Experimental and Computational Data

The computational velocity profiles, as a proportion of mean stream velocity, are shown in comparison with the experimental profiles of (Johl et al., 2007) in Figure 68 through Figure 71. In general, a good level of agreement is achieved. The main areas of deviation are discussed below.

Figure 68 through Figure 71 show an under-prediction of the BL thickness downstream of the inner bend in all solutions. This is not seen consistently downstream of the outer bend. Along B-B the poorest prediction of minimum wake velocity is seen downstream of the outermost vane in Figure 68. The experimental result show the minimum velocity occurs 0.10m from the outside bend. This compares to 0.11m in the computational solution, a deviation equivalent to 2.2% of the module width.

The magnitude of the minimum wake velocity was most poorly predicted downstream of the outermost vane in the four-vane module. This is seen in Figure 70. A minimum velocity of 90% of the free stream value was measured experimentally, compared with 96% computationally. The

trends in Figure 68 and Figure 70 suggest that the rate of wake recovery is computationally being slightly over-predicted.

In Figure 69, there is moderate disagreement downstream of the inner bend where the computational result predicts notably greater velocity than the experimental value. Whilst an under-prediction of the computational BL thickness has been acknowledged above, comparison of Figure 69 and Figure 71 suggests that the experimental velocity profile downstream of the inner bend in Figure 69 may be erroneous.

Figure 68 also shows an inconsistency between the computational and experimental results downstream of the outer corner. Qualitatively observation of the solutions however showed no obvious erroneous flow features developed that reflect this inconsistency.

Overall, the computational accuracy was observed as being greatest near the inner bend of the module. The location and magnitude of all wakes were represented with at least moderate accuracy in the computational solutions. Some variation between the experimental and computational results showed that quantitative parameters should be extracted from the solutions with caution.

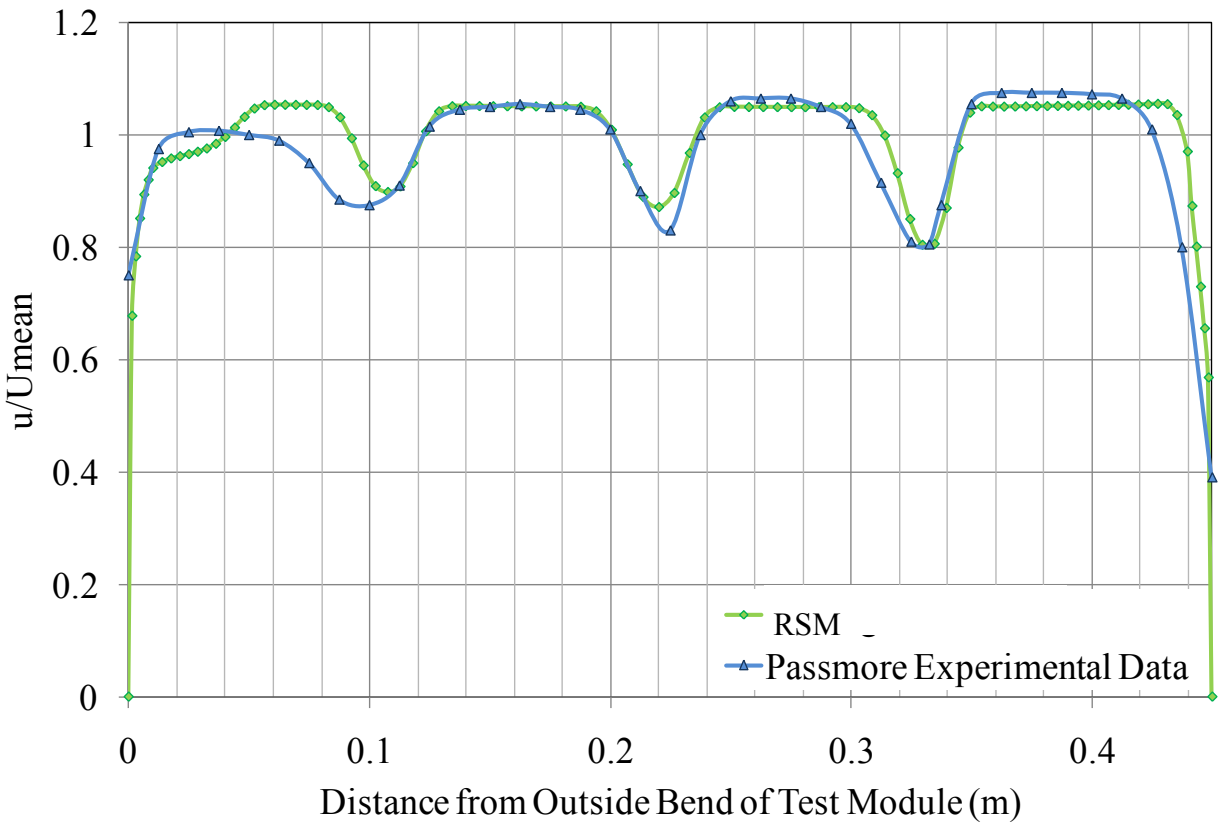

Figure 68 Velocity Profiles comparing Experimental Data of (Johl et al., 2007) with a Computational Solution along the B-B line in the Three-Vane Test Module

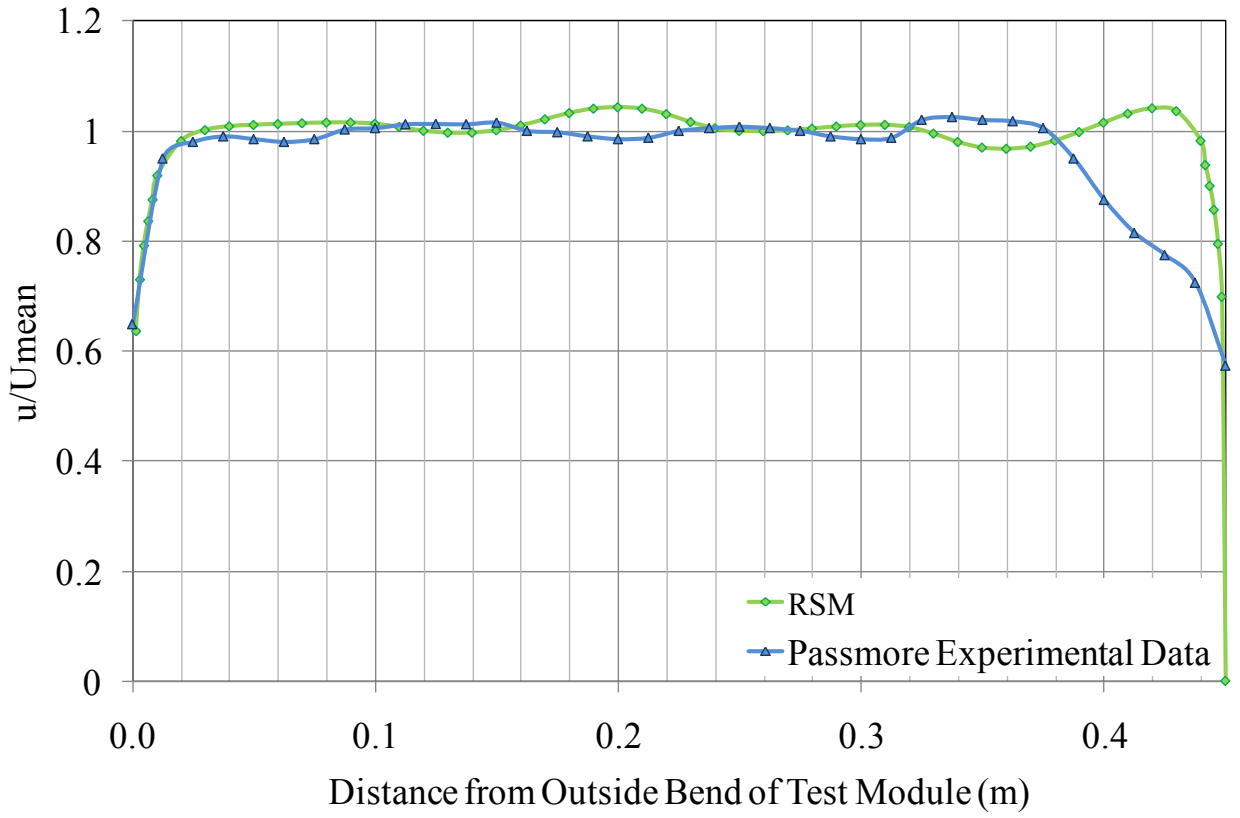

Figure 69 Velocity Profiles comparing Experimental Data of (Johl et al., 2007) with a Computational Solution along the C-C line in the Three-Vane Test Module

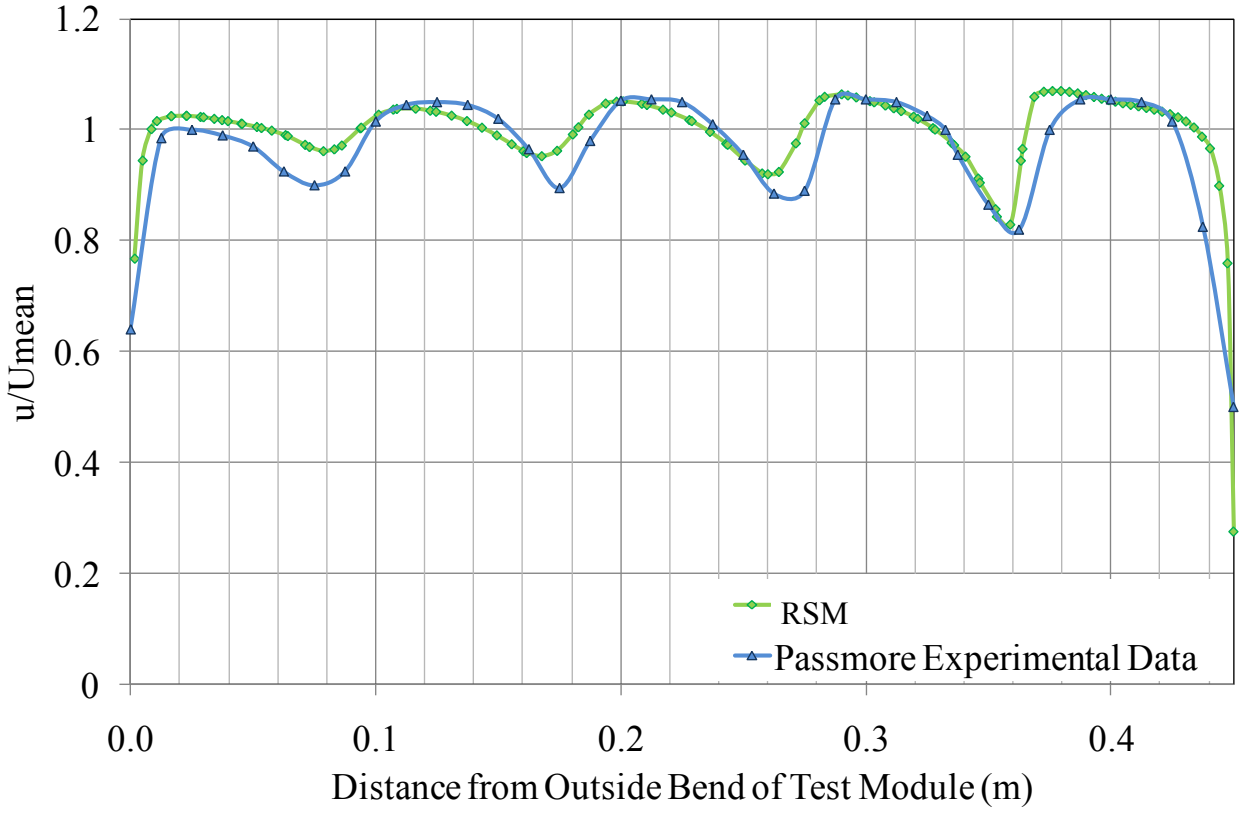

Figure 70 Velocity Profiles comparing Experimental Data of (Johl et al., 2007) with a Computational Solution along the B-B line in the Four-Vane Test Module

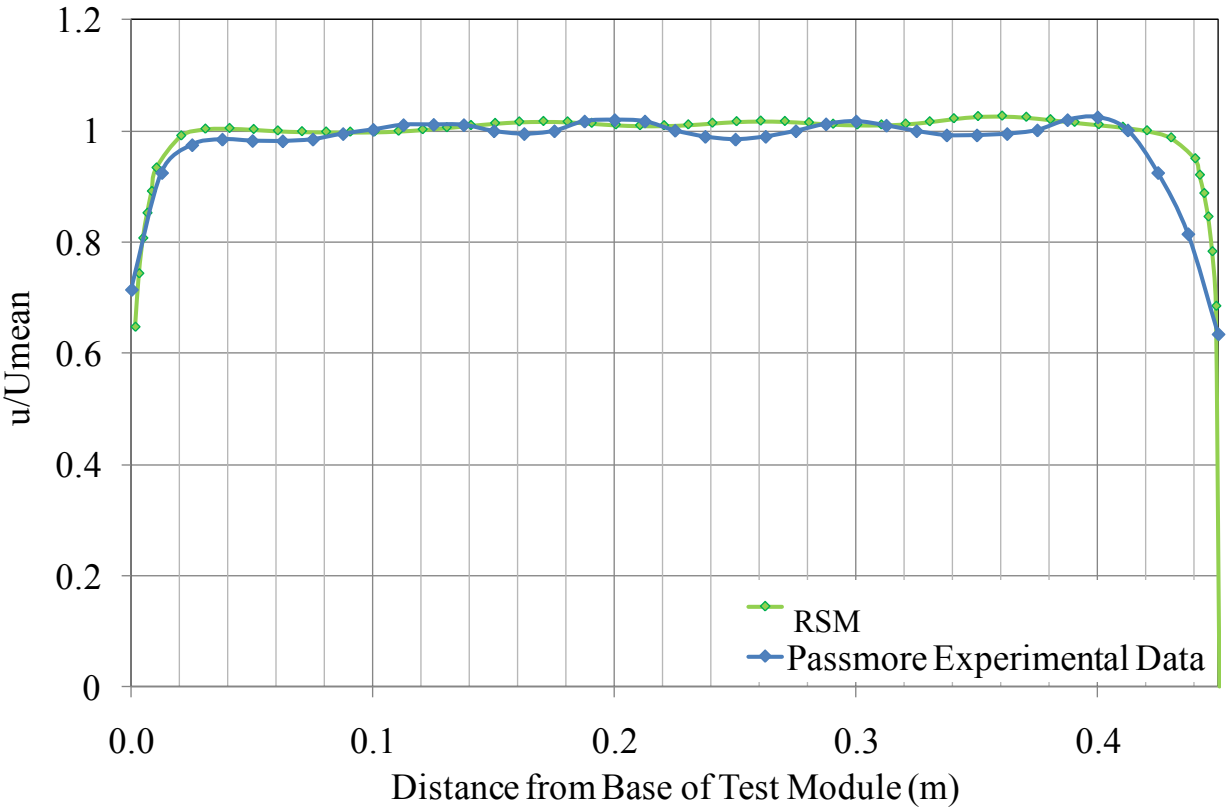

Figure 71 Velocity Profiles comparing Experimental Data of (Johl et al., 2007) with a Computational Solution along the C-C line in the Four-Vane Test Module

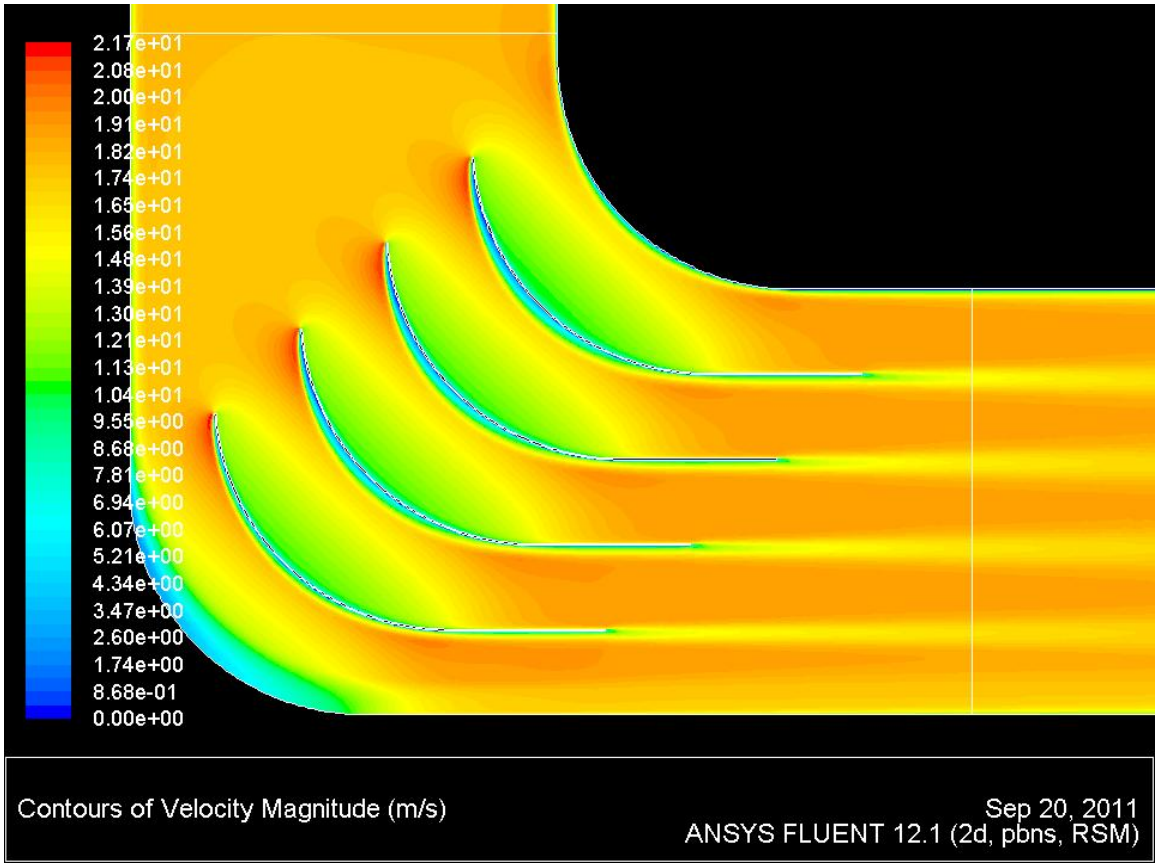

Figure 72 Velocity Magnitude in the Four-Vane Test Module

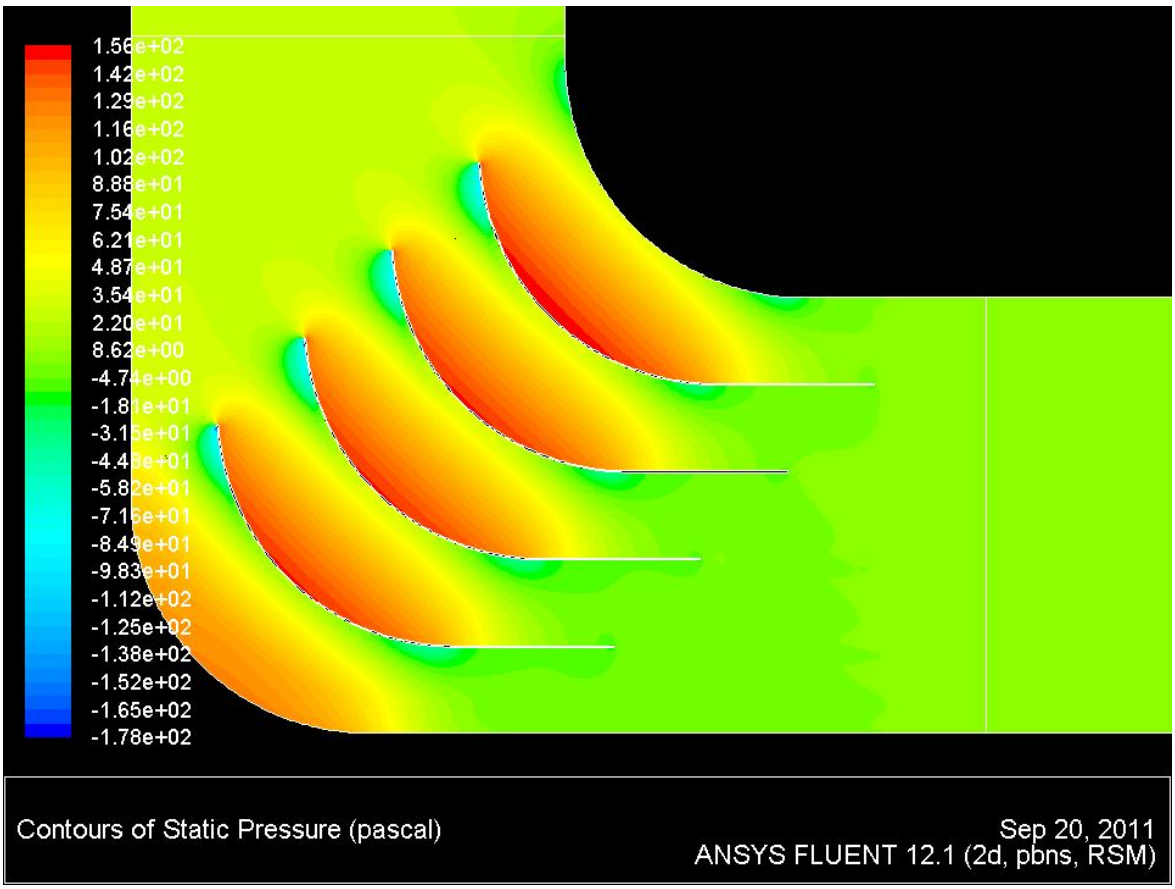

Figure 73 Static Pressure Distribution in the Four-Vane Test Module

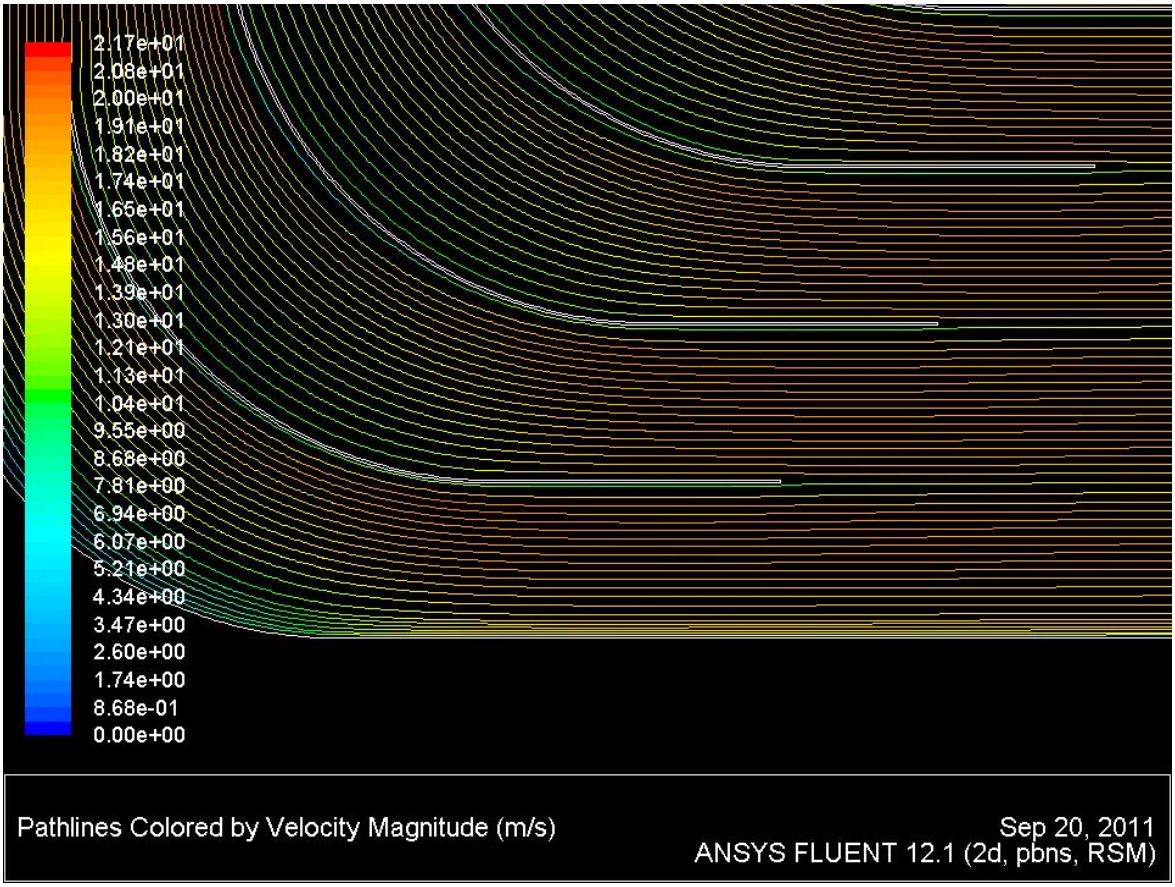

Figure 74 Streamlines near the Base of the Four-Vane Test Module

However, accurate qualitative assessments can be made with confidence. The qualitative flow patterns produced in the computational solution can be considered to be reflective of realistic flow behaviours. It was deemed the experimental-computational agreement attained, would allow the objectives of the main body of this investigation to be achieved through applying the techniques used in this validation process.

4.3 Results

The findings and development of the turning-vane design process are presented in this section. To achieve the objectives outlined in Section 4.2, both qualitative and quantitatively comparative methods were employed. For the quantitatively comparative analysis, a measure of flow quality was required. Velocity distortion, discussed and defined in Section 1.4.1, was chosen as it is a defining property in the JETC industry of cell airflow quality.

The line over which data was extracted for the velocity distortion calculation is marked in red Figure 61. This line was 11.85m downstream of the outer inlet stack wall, and corresponded to the location of the data extraction plane used during the cell certification process at the CHCEC. Data points within 1m of the cell walls were not considered in order to maintain consistency with real-world practice (Flynn, 2008; Kennedy, 2008).

4.3.1 Baseline Design – Christchurch Engine Centre Cell

The flow patterns discussed in the mesh independence check of Section 4.2.2.4 are elaborated upon in this section. Figure 75 through Figure 81 present the solution generated using the baseline turning-vane arrangement.

As seen in Figure 75, the downstream face of the innermost baffle tapers away from the inner corner. This creates an expansion in the flow channel next to the stack wall, immediately upstream of the inner corner. A second expansion occurs 500mm downstream of the first, between the uppermost vane and the inner corner of the cell. This can be seen in Figure 76 and Figure 78. The two channel expansions combine with the change in direction of the inner corner. This combination leads to the creation of an adverse pressure gradient and a separation zone that can be seen in Figure 77 and Figure 78 respectively.

The presence of separation at the inner corner can be troublesome in a JETC scenario. A low velocity region downstream follows the separation zone created. This is seen in Figure 75. With the

presence of the low velocity region, the potential for inlet vortex formation increases. This is a result of the increased ease at which an anchor point can form due to the reduction in the 'blow-away' velocity, as discussed in Section 1.4.3. Such inlet vortex behaviour occurred along the ceiling of the CHCEC cell during certification, (Figure 8). Modifications to the cell have been made subsequent to the discovery of the vortex so future vortex generation is avoided.

In the baseline solution, a separation/low-velocity zone is also created below each turning-vane. This can be seen in Figure 79. This zone is also a result of an adverse pressure gradient as shown in Figure 80. The cause of the adverse pressure gradient in the case of the turning-vanes is the change in direction of the solid bodies bounding the flow channel.

Below the 'clipped' TE of each baffle, a wake region forms as shown in Figure 81. The wakes contain small areas of circulation immediately downstream. The continuation of the low velocity wake streams can be seen in Figure 76, Figure 78, and Figure 81. Figure 81 shows a majority of the wakes produced by the lower row of baffles interact with the vane arrangement. The upper vanes, due to their closer relative location, are most greatly affected.

Figure 78 and Figure 81 show the disturbance created by the intersection of the baffle wakes with the vanes. The wake from the baffle adjacent to the inner corner aids in the development of separation in that region. Inconsistencies in the flow patterns between successive rows of vanes are also created.

The velocity distortion was calculated to be 23.6% in the baseline solution. Figure 82 plots the velocity profile along the velocity distortion line. The peaks and troughs between 1.5m above the base of the cell and the top of the plot compare qualitatively with the experimental patterns produced by (Johl et al., 2007).

The velocity of flow near the base of the cell is lower than would be expected if the flow had been turned through an even 90°. Figure 83 plots the vertical velocity component of the flow along an extended velocity distortion line. The extended velocity distortion line runs from the base to the roof of the cell. The velocities at all points along the plot are positive. This indicated that an upward velocity component was present across the entire height of the working section flow. An undesirable over-rotation of the flow through the turning-vane arrangement therefore has occurred. The over-rotation can be more subtlety detected in the velocity vectors downstream of the upper turning-vanes in Figure 78.

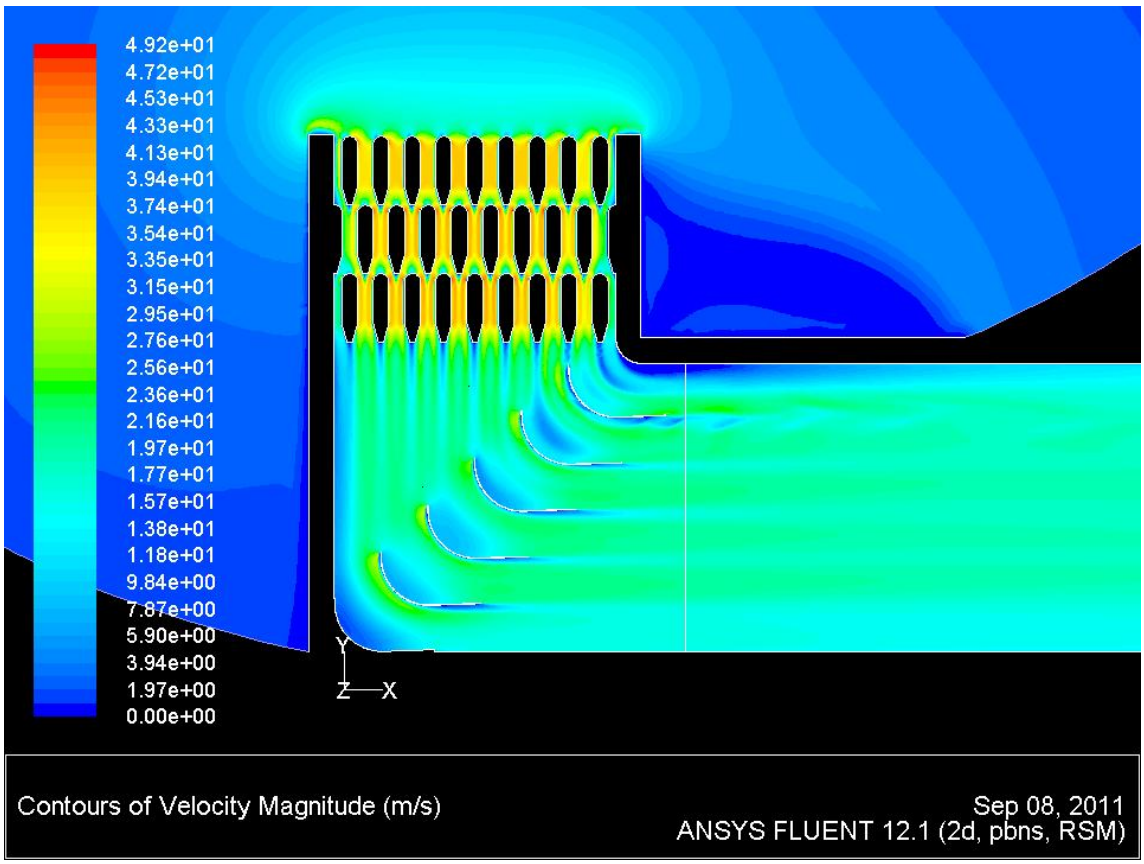

Figure 75 Velocity Magnitude in the Baseline Turning-Vane Arrangement

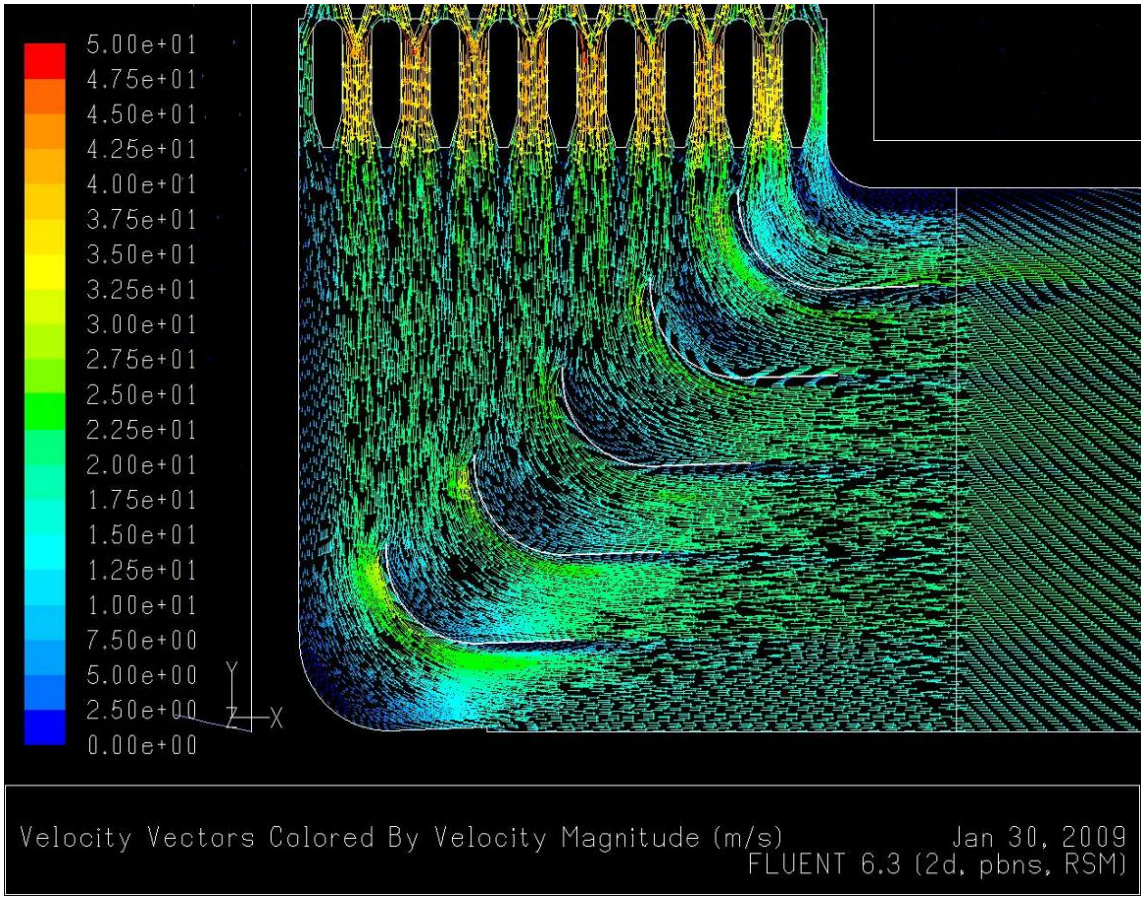

Figure 76 Flow Patterns in the Baseline Turning-Vane Arrangement

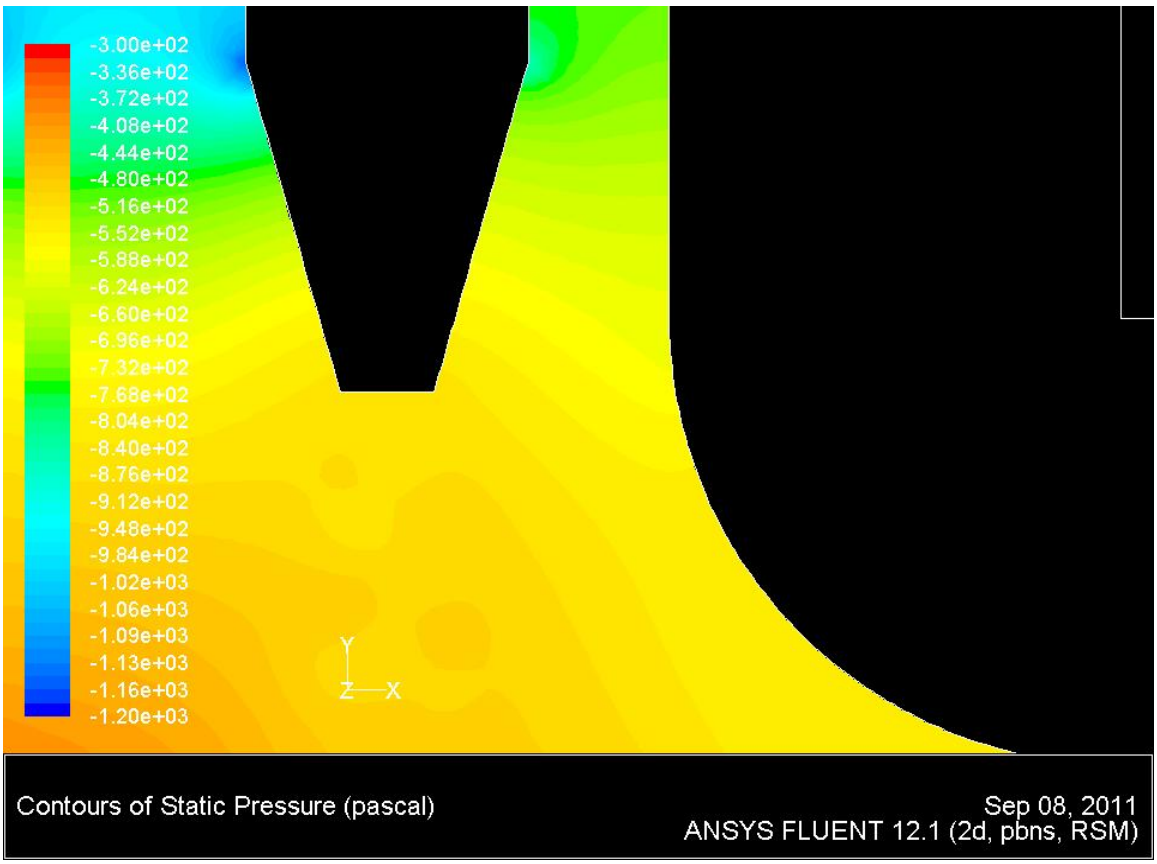

Figure 77 Static Pressure Distribution at the Inner Corner in the Baseline Turning-Vane Arrangement

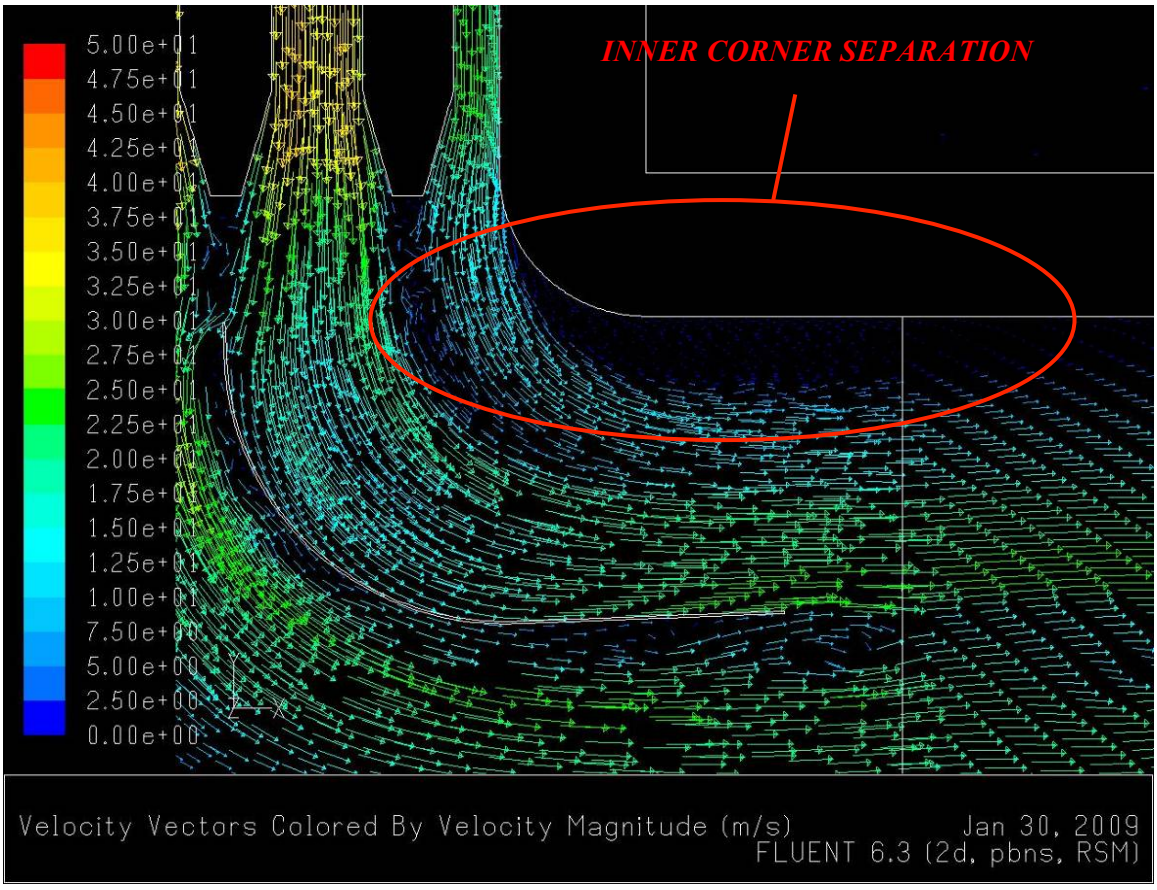

Figure 78 Flow Pattern near the Inner Corner in the Baseline Turning-Vane Arrangement

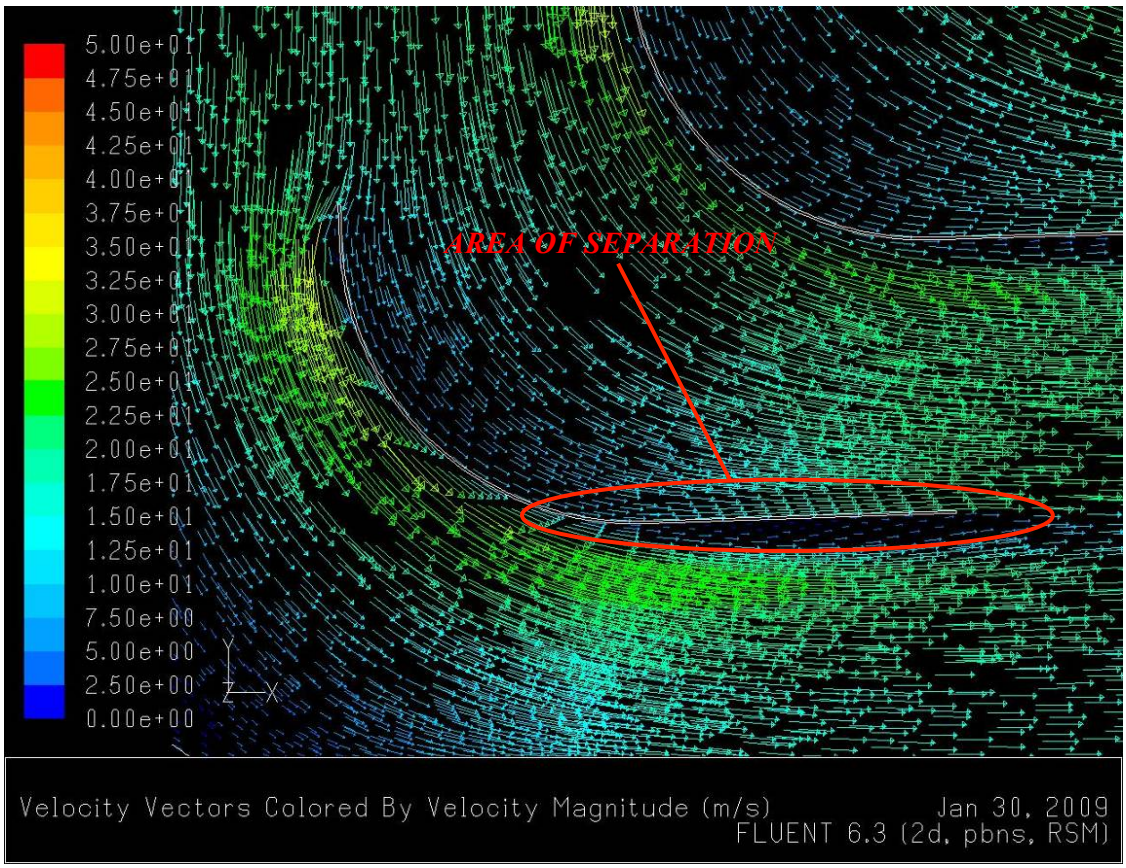

Figure 79 Flow Pattern around a Turning-Vane in the Baseline Turning-Vane Arrangement

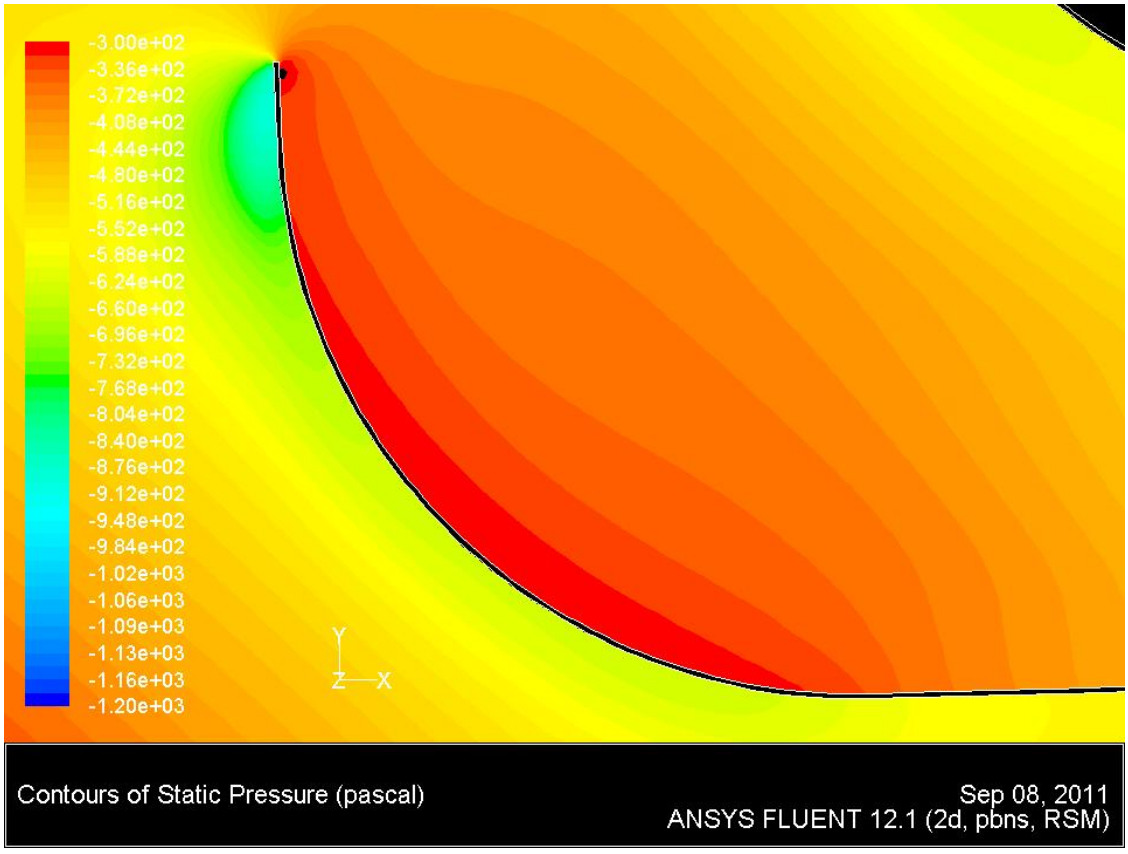

Figure 80 Static Pressure Variation around a Turning-Vane in the Baseline Turning-Vane Arrangement

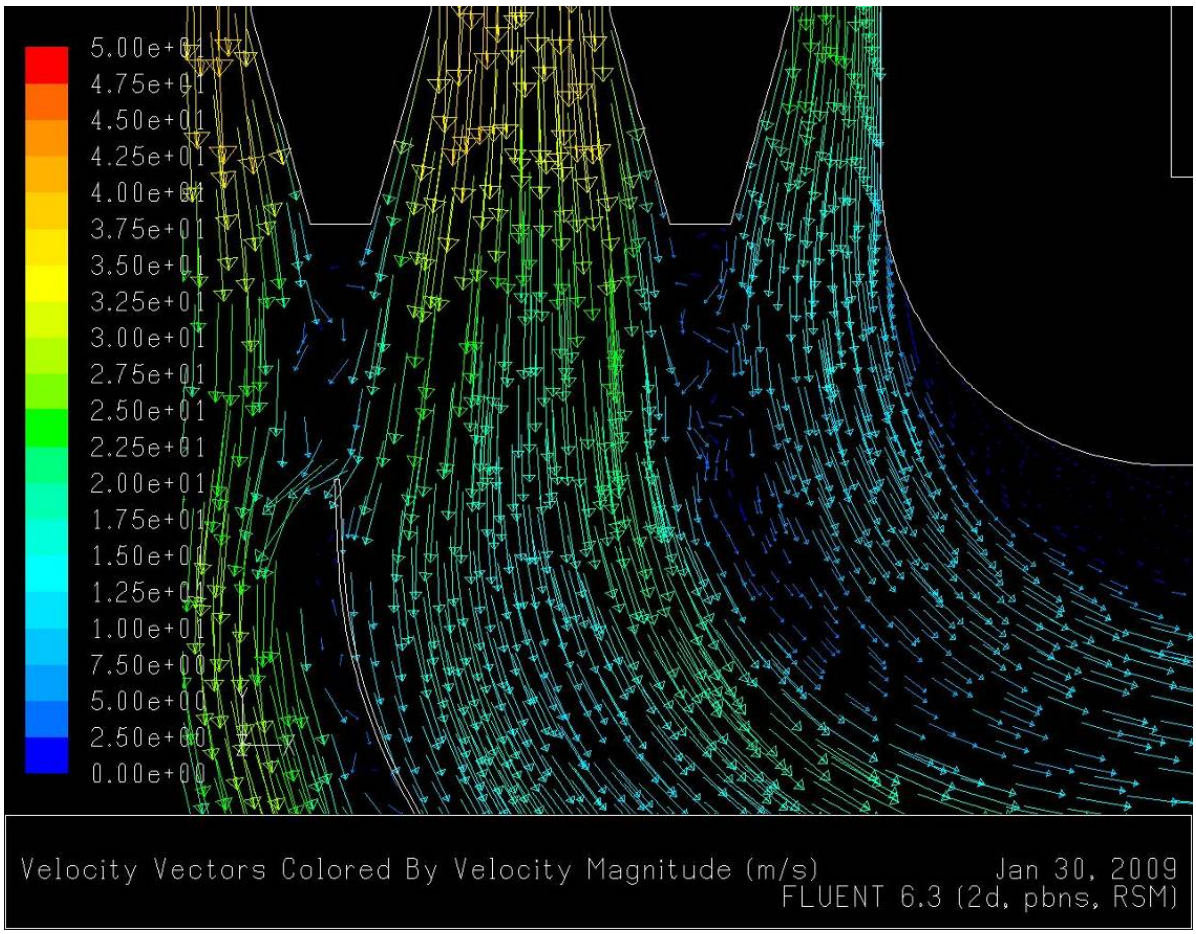

Figure 81 Interaction of the Baffle Arrangement Wake with the Turning-Vanes in the Baseline Turning-Vane Arrangement

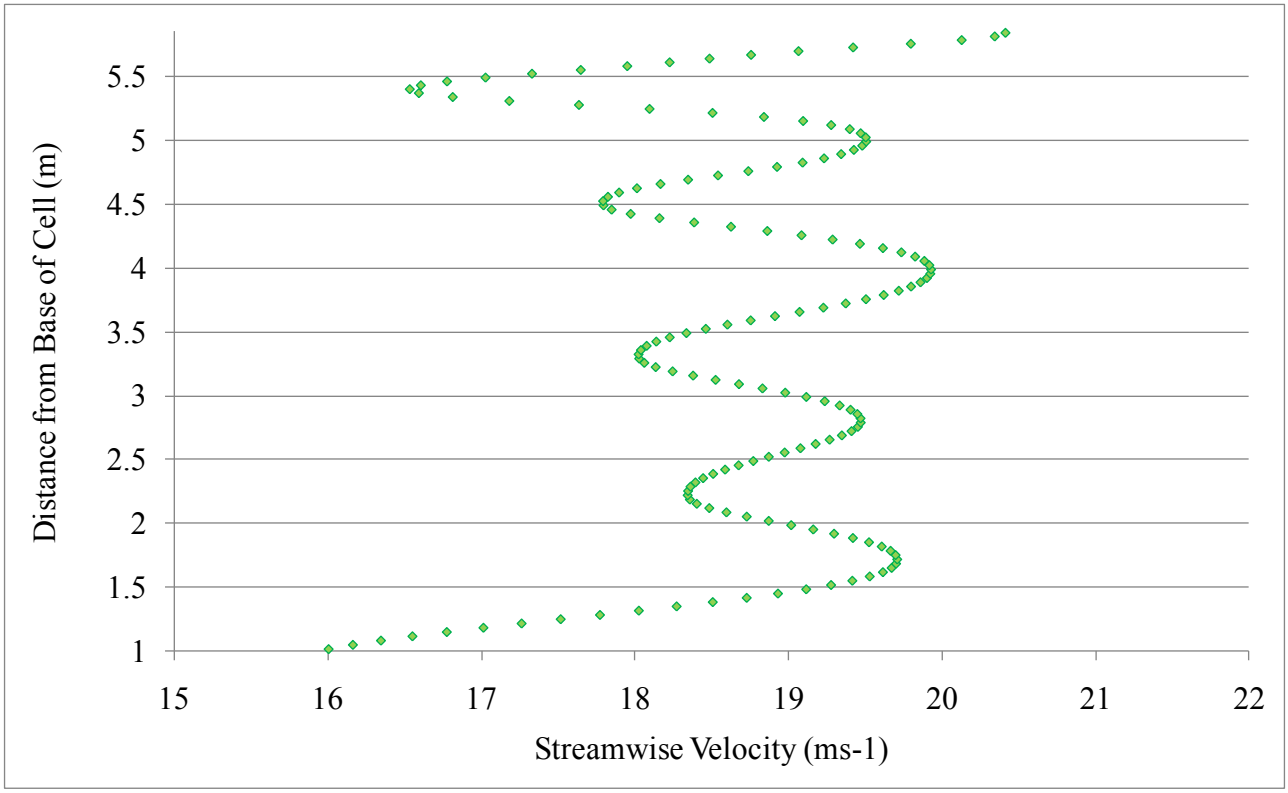

Figure 82 Stream-Wise Velocity Profile in the Baseline Turning-Vane Arrangement

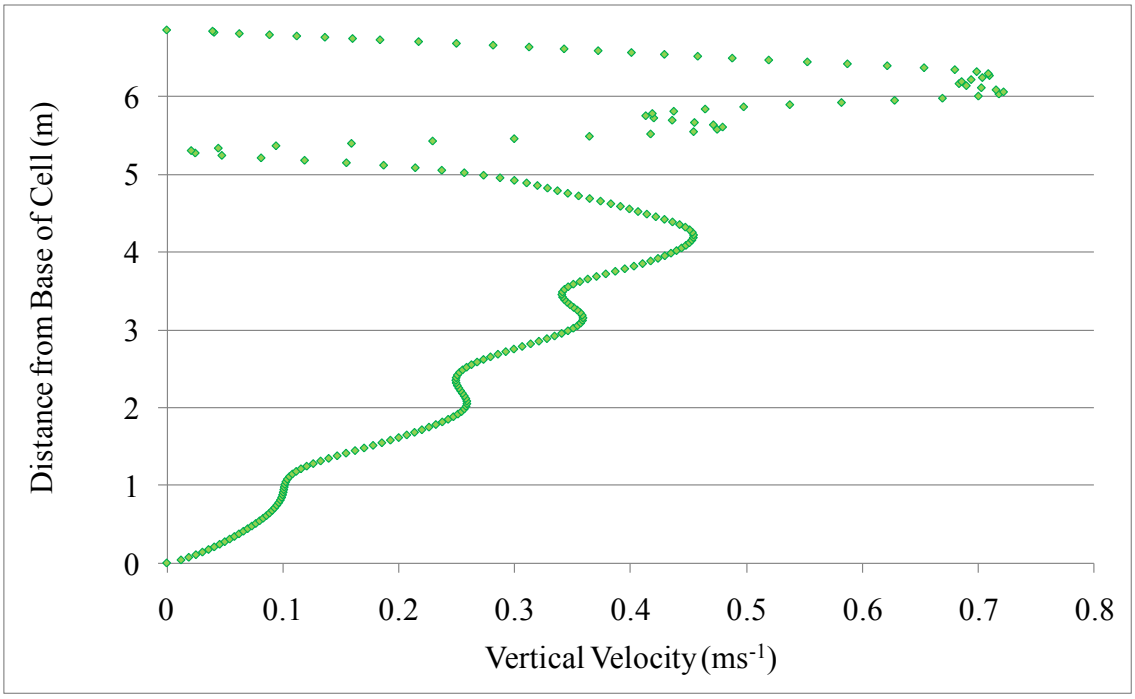

Figure 83 Vertical Velocity Profile along an Extended Velocity Distortion Line in the Baseline Turning-Vane Arrangement

The following sections present the investigation and design processes performed to improve velocity distortion downstream of the vane-arrangement. An important feature of this investigation was to analyse the interaction between the vane arrangement and the upstream baffles. To ensure a consistent flow pattern was entering the vane arrangement, the baffle arrangement was kept constant throughout a majority of the investigation.

4.3.2 Baffle-Aligned Arrangements

In Section 4.3.1 it was found that the flow patterns through the turning-vane arrangement of the baseline solution were partially dependent on the alignment with the upstream baffle arrangement. This finding aligns with the three-dimensional analysis performed by (Agmen et al., 2005). An investigation was therefore performed to determine the dependency of the quality of flow downstream of the vane arrangement on the baffle-vane alignment.

As described in Section 4.2.1, the turning-vanes in the baseline domain are arranged to align with baffles in both the lower and middle rows of the baffle arrangement. As such, the wakes produced downstream of the baffle arrangement interacted differently at different positions within the vane arrangement. This was shown in Figure 76.

To provide a more consistent flow entering the turning-vane arrangement, computational domains were created in which each row of turning-vanes was aligned directly downstream of a column of baffles from the lowermost row. To achieve this alignment without altering the baffle arrangement, the number of vanes needed to be adjusted. As such, domains with five- and nine-vane arrangements were developed. For the five-vane case, a vane was aligned with every second baffle on the lower row. In the nine-vane case, a vane was aligned with every baffle on the lower row. Figure 84 shows the two baffle-aligned domains created.

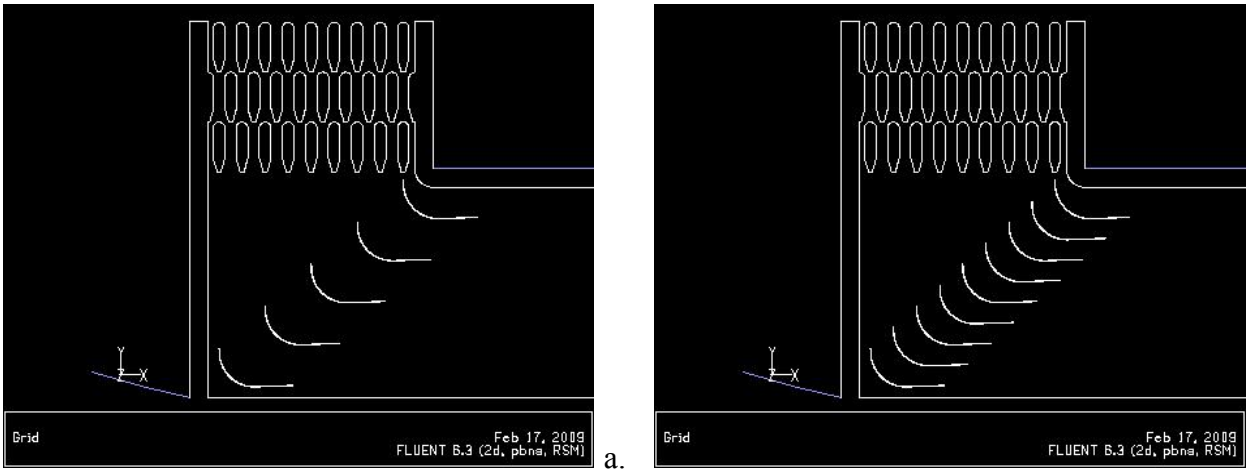

a. b.

Figure 84 Computation Domains of Baffle-Aligned Five- (a) and Nine-Vane (b) Arrangements

Solutions were generated for each domain. Figure 85 shows the flow pattern of the five-vane baffle-aligned solution. The five-vane arrangement performed poorly compared with the baseline design in four specific areas.

Firstly, a significant increase in the size of the separation originating at the inner corner was observed. By aligning the uppermost vane with the innermost baffle on the lower row, an increased diffuser scenario was created. This increase in the diffuser effect can be seen by comparing Figure 84a and Figure 61.

Secondly, the outer corner was exposed by the vane re-alignment as shown in shown in Figure 85. This resulted in the flow around the outer corner becoming very unstructured and messy. This is shown in Figure 86. Thirdly, and of most interest to the baffle-vane alignment investigation, was the generation of a low velocity ‘pocket’ on the inner side of the second uppermost vane. Figure 85 clearly shows the wake downstream of the above baffle propagating, and adversely interacting with the turning-vane flow. A more detailed view of the flow pattern in the low velocity pocket is shown in Figure 87.

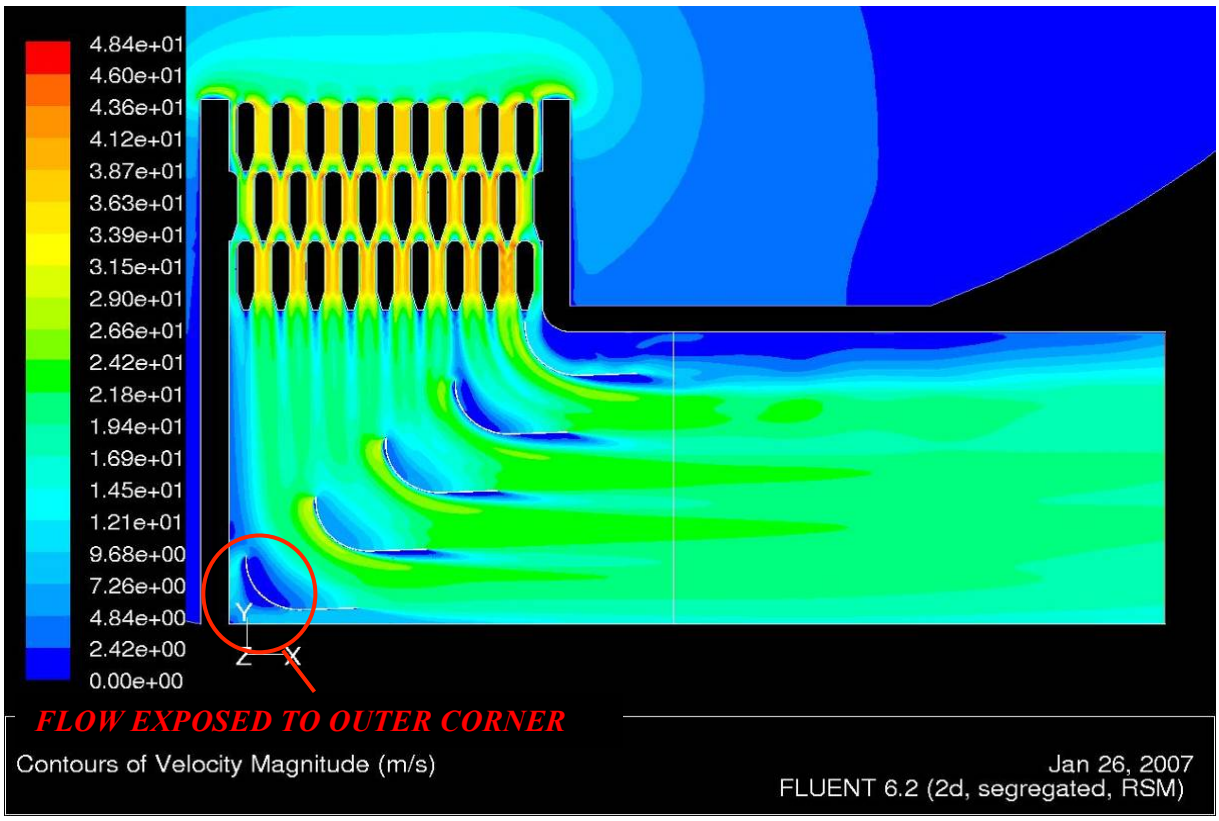

Figure 85 Velocity Magnitude in the Five-Vane Baffle-Aligned Arrangement

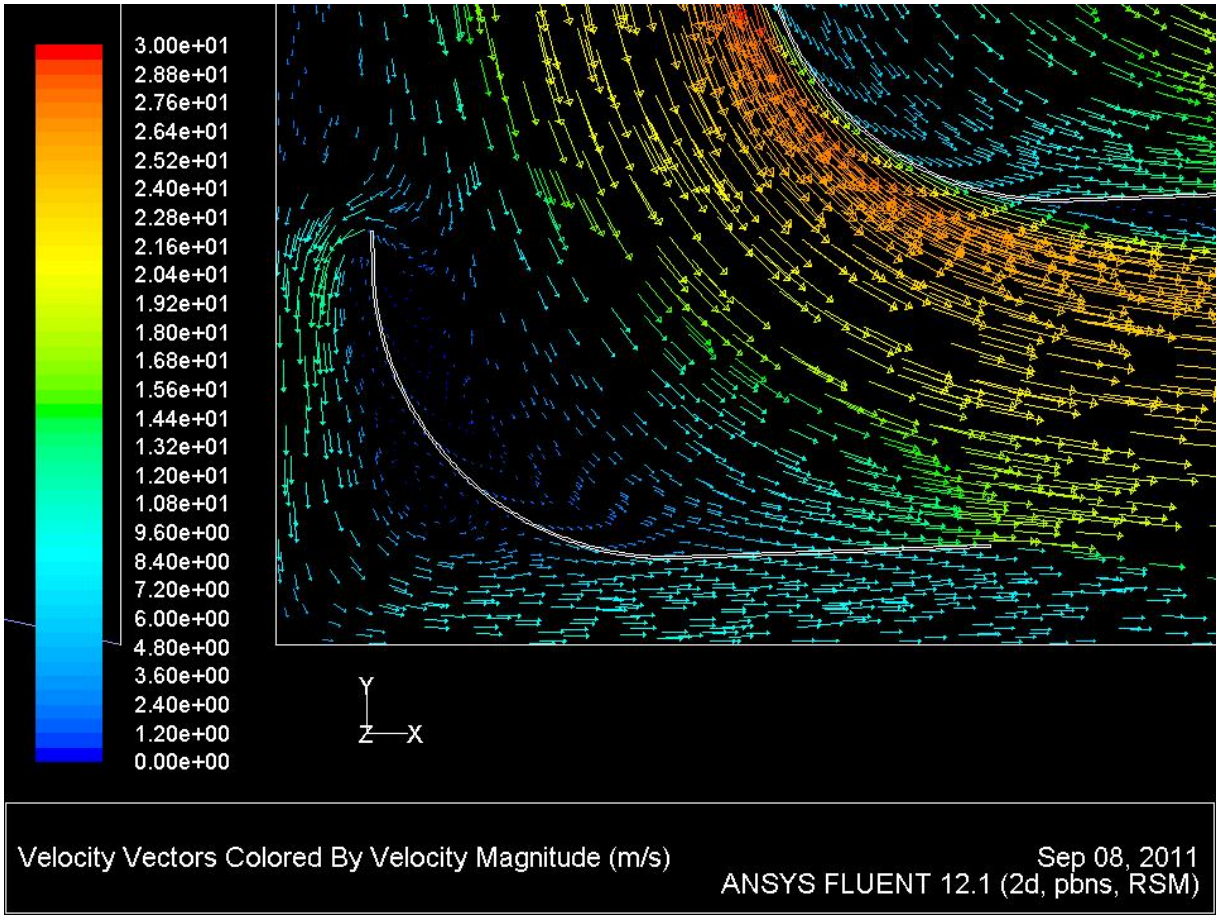

Figure 86 Exposed Outer Corner in the Five-Vane Baffle-Aligned Arrangement

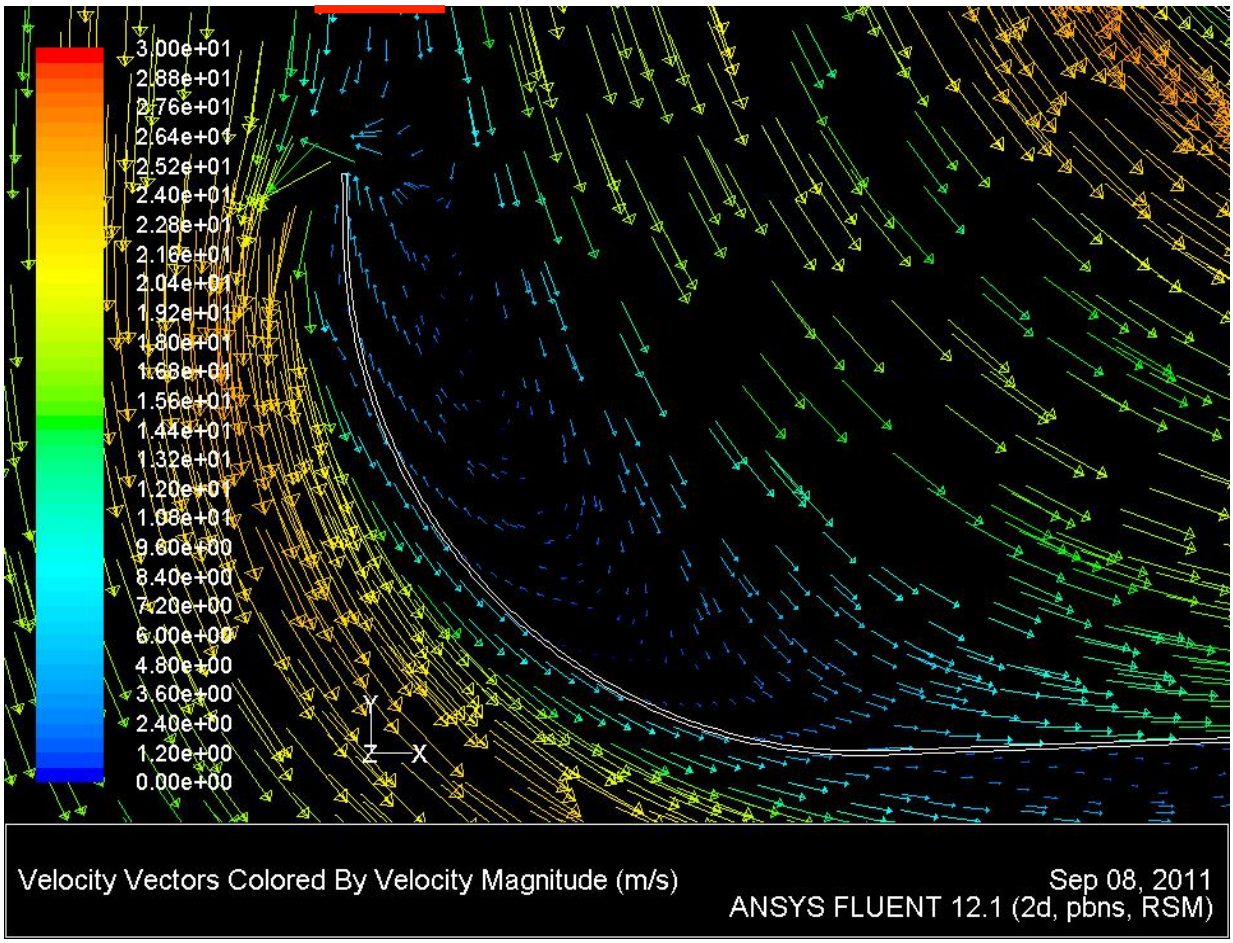

Figure 87 Low Velocity 'Pocket' Adjacent to Uppermost Turning-Vane in the Five-Vane Baffle-Aligned Arrangement

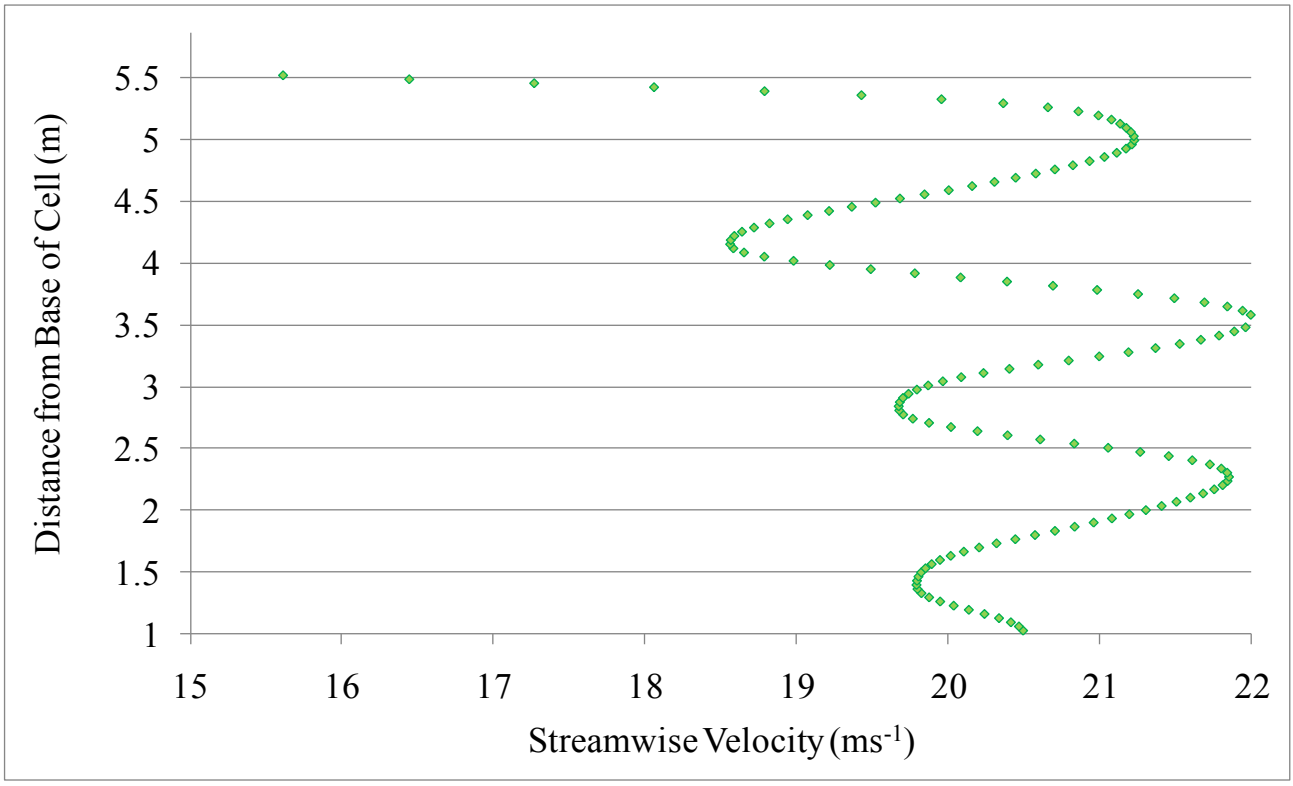

Figure 88 Stream-Wise Velocity Profile in the Five-Vane Baffle-Aligned Arrangement

Fourthly, the size and magnitude of the low velocity region on the underside of each vane increased. The amount of flow that each vane was required to 'turn' was 16% greater on average than the baseline arrangement due to the reduction in vane numbers. As such, the five-vane arrangement possessed less 'turning power'. A velocity distortion of 69.2% was calculated for the five-vane arrangement, a significant increase over the baseline solution. Figure 88 shows that the low velocity flow downstream of the increased separation was the major contributing factor to the heightened value of velocity distortion.

Figure 89 shows the flow patterns within the nine-vane baffle-aligned solution. Velocity distortion was calculated to be 7.8%, and on this basis the nine-vane arrangement provided flow quality far superior to the baseline solution. However, the velocity distortion figure is slightly misleading due to the range over which the calculation is made. The velocity distortion profile is shown in Figure 90, and when compared with Figure 89, it can be seen that the significant low velocity region at the top of the cell falls outside the velocity distortion calculation boundary.

Only one of the four areas of poor flow quality noted in the five-vane baffle-aligned solution was improved upon in the nine-vane solution, to a level that exceeded that of the baseline solution. The nine-vane baffle-aligned arrangement provided a reduction in the under-vane low velocity compared with both the baseline and five-vane arrangements. This, combined with the comparatively smooth profile of Figure 90 and inter-vane flow patterns in Figure 91, showed the benefits to downstream flow quality with an increase in vane numbers in the arrangement.

(Pope & Rae, 1984) suggests that downstream flow quality can be improved with an improvement to the gap-chord ratio in a wind tunnel. This appears to be the case in this JETC scenario, where the gap-chord ratio was decreased from 0.59 to 0.32 in the five- and nine- vane arrangements. The gap-chord ratio of the baseline design was 0.49. The recommendations assembled in Section 4.1.4, from the work of (Pope & Rae, 1984) and (Pankhurst & Holder, 1952), suggested that a gap-chord ratio of below 1/3 should be used in the design of wind-tunnel corner sections. Only the nine-vane design falls within this recommendation.

The three other areas of poor flow quality - the large area of inner corner separation, the messy flow outer corner flow, and the negative interaction between the second uppermost vane and its aligned baffle, all remained present in the nine-vane baffle-aligned solution.

Overall, it was not felt that a full understanding of the interaction a result of the baffle-vane alignment was obtained through the investigation of this section. As such, the work of Section 4.3.3 was performed to develop the understanding further.

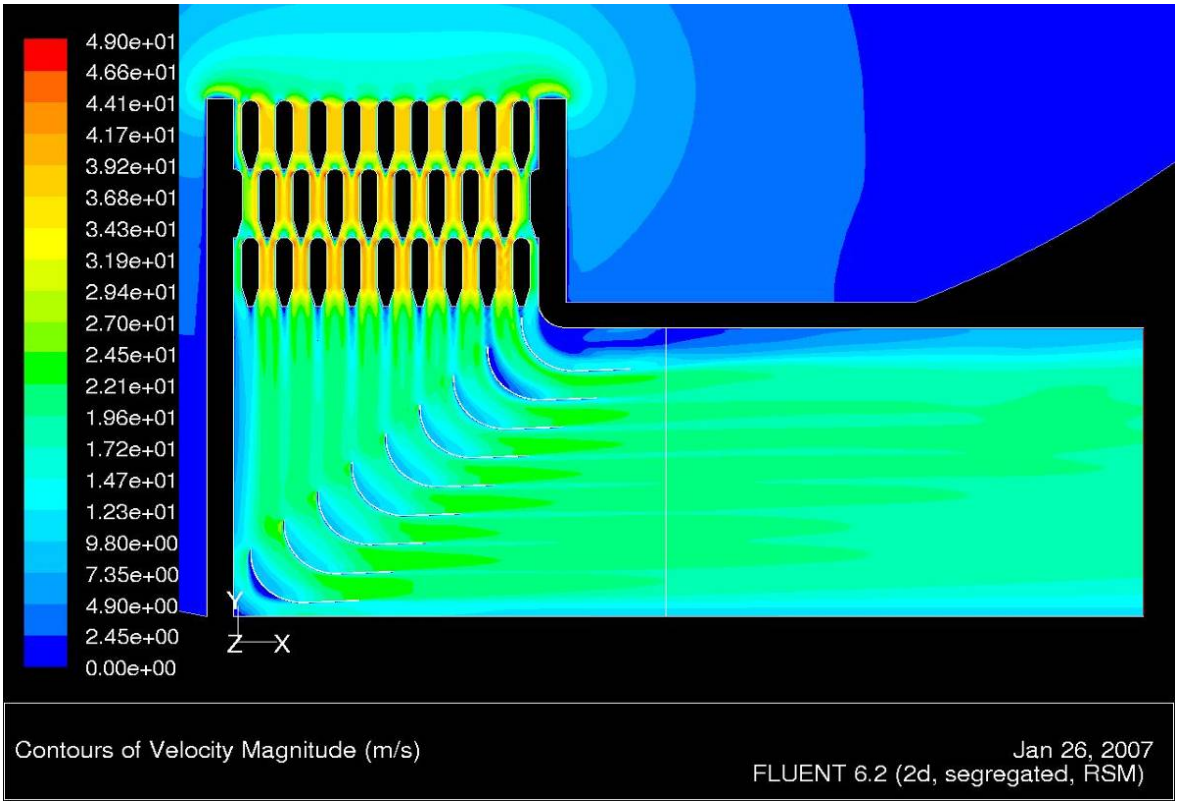

Figure 89 Velocity Magnitude in the Nine-Vane Baffle-Aligned Arrangement

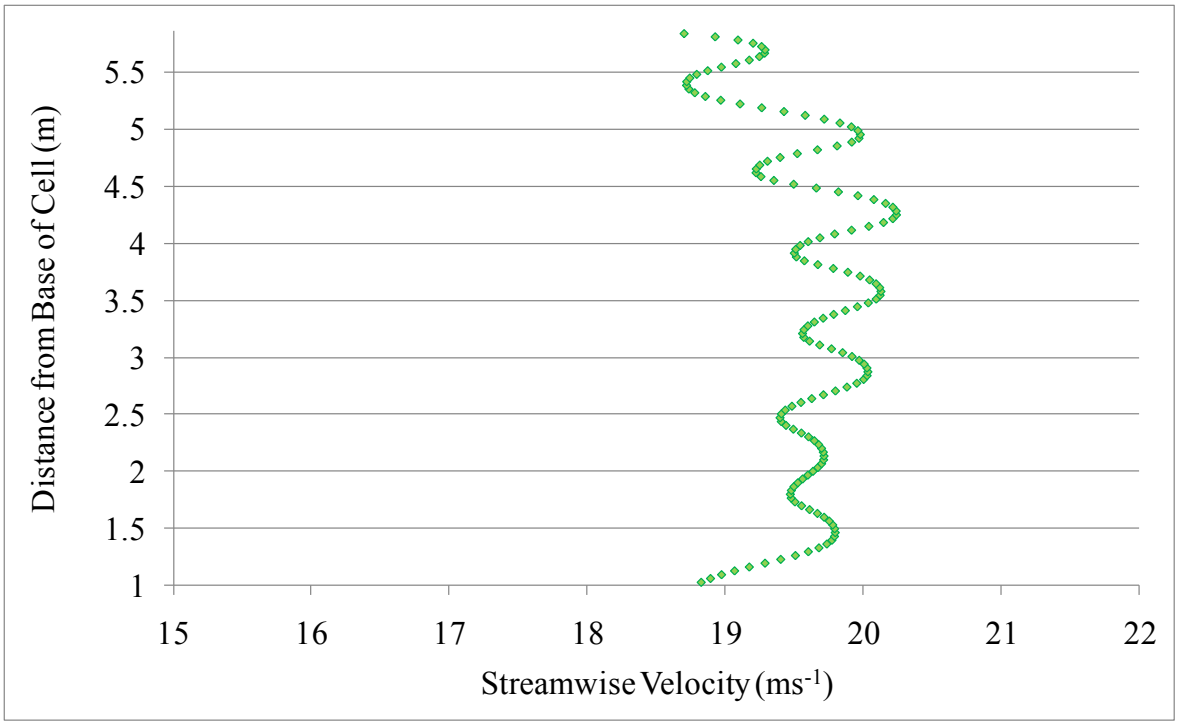

Figure 90 Stream-Wise Velocity Profile in the Nine-Vane Baffle-Aligned Arrangement

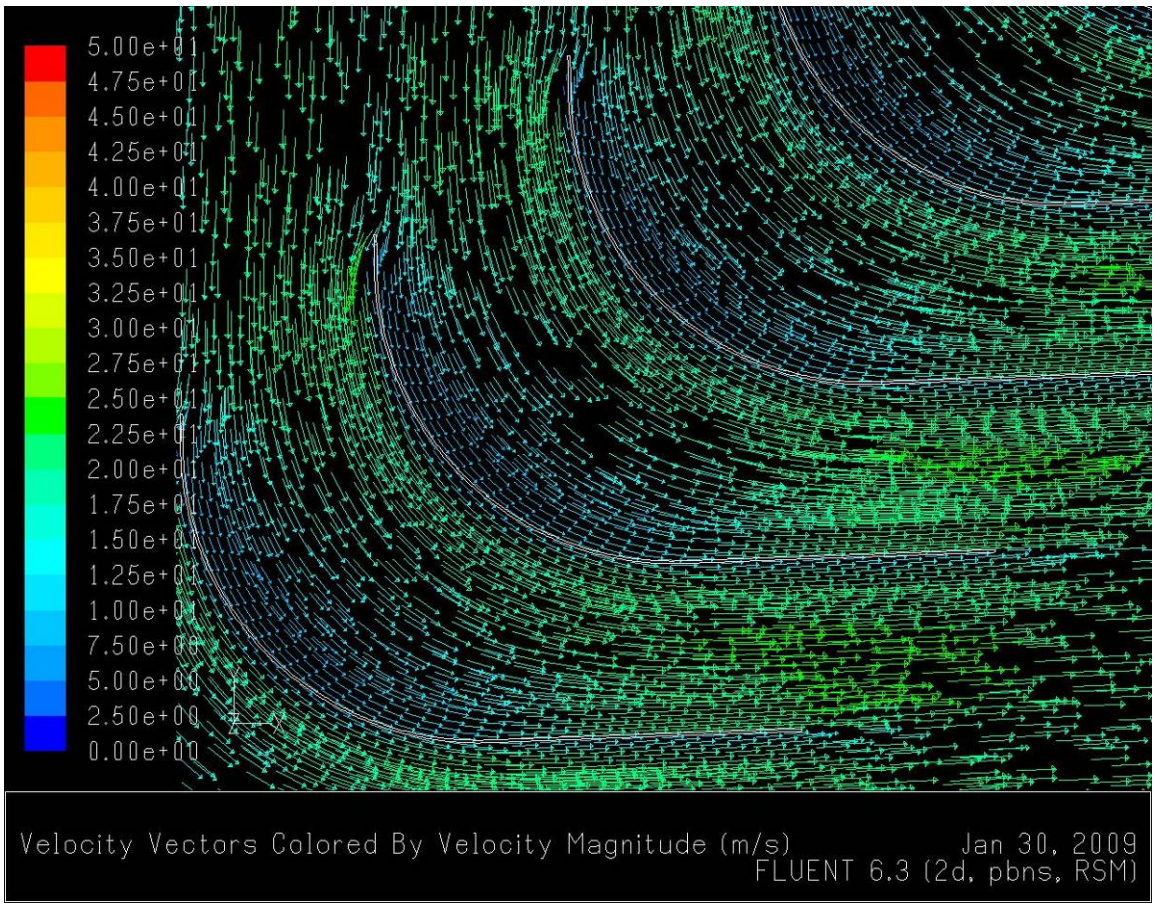

Figure 91 Flow Pattern around a Turing-Vane in the Nine-Vane Baffle-Aligned Arrangement

4.3.3 Mid-Baffle-Aligned Arrangements

The five- and nine-vane arrangements of Section 4.3.2 were modified to align each vane with a baffle from the middle row (180° offset from the lower row) in the creation of two further computational domains. Figure 92 shows the two domains. As each vane row was aligned with a baffle in the middle row, the vanes were aligned with the channels between baffles in the lower row. Therefore, vanes with this alignment are referred to as 'mid-baffle-aligned' from this point on.

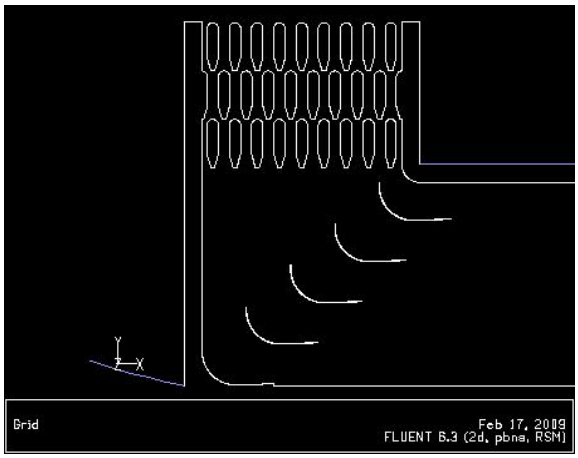

a.

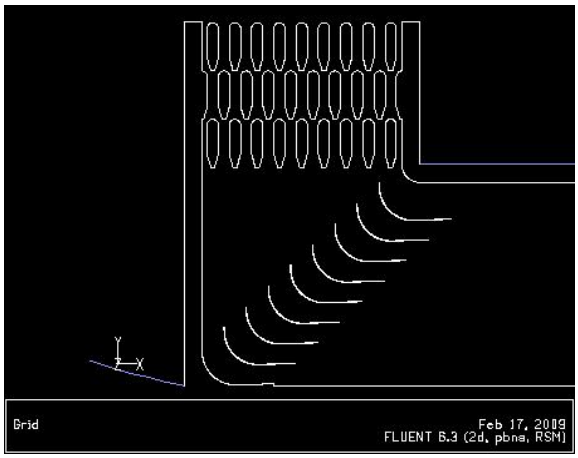

b.

Figure 92 Computation Domains of Mid-Baffle-Aligned Five- (a) and Nine-Vane (b) Arrangements

The flow pattern of five-vane mid-baffle-aligned arrangement is shown in Figure 93. A velocity distortion of 16.7% was calculated, a significant reduction over the comparable five-vane baffle-aligned design. A plot of the velocity profile along the velocity distortion line is shown in Figure 94.

The higher quality flow exiting the vane arrangement (represented by the reduction in velocity distortion) is a result of two areas of particular flow pattern improvement. As expected, the first was in the region of the inner corner, where the separation zone was reduced to a level comparable with the baseline arrangement, where the same alignment for the uppermost baffle was present.

The second area was in the reduction of the low velocity region under each turning-vane. Comparison of Figure 85 and Figure 93 shows that the size of the under-vane low velocity region is reduced below all baffles. The magnitude of the minimum velocities within each of the regions is not so substantial in the mid-baffle-aligned case.

Two other areas within the mid-baffle-aligned solution show flow pattern improvements, although the impact on the lowered velocity distortion is not as readily apparent. The first is the isolation of the outer corner, as in the baseline arrangement. The second is the interaction of the baffle wakes with the vane arrangement. A vector plot of the flow around the second uppermost vane is shown in Figure 95 as a direct comparison with Figure 87. Both graphics are marked with a red line that indicates where the most prominent wake from the above baffle arrangement enters.

Figure 87 shows a low velocity ‘pocket’ adjacent to the vane that is not evident in Figure 95. Comparison of these graphics with Figure 85 and Figure 93 show that this low velocity ‘pocket’, although likely to be aerodynamically ‘inefficient’, does not propagate downstream to a great degree. This is likely due to two factors. The first is the over-rotation of flow in the vane arrangements, as discussed in Section 4.3.1. The second is the slight flow channel contraction between adjacent vanes due to the elevated TE angle, the TE extensions, and the slope of the vane arrangement.

Figure 87 and Figure 95 also show that the velocity near the backside of the vanes varies between the solutions. The baffle wake of the vane-aligned solution in Figure 87 creates a low velocity flow along the length of the backside of the vane in contrast to that of the mid-vane aligned solution in Figure 95.

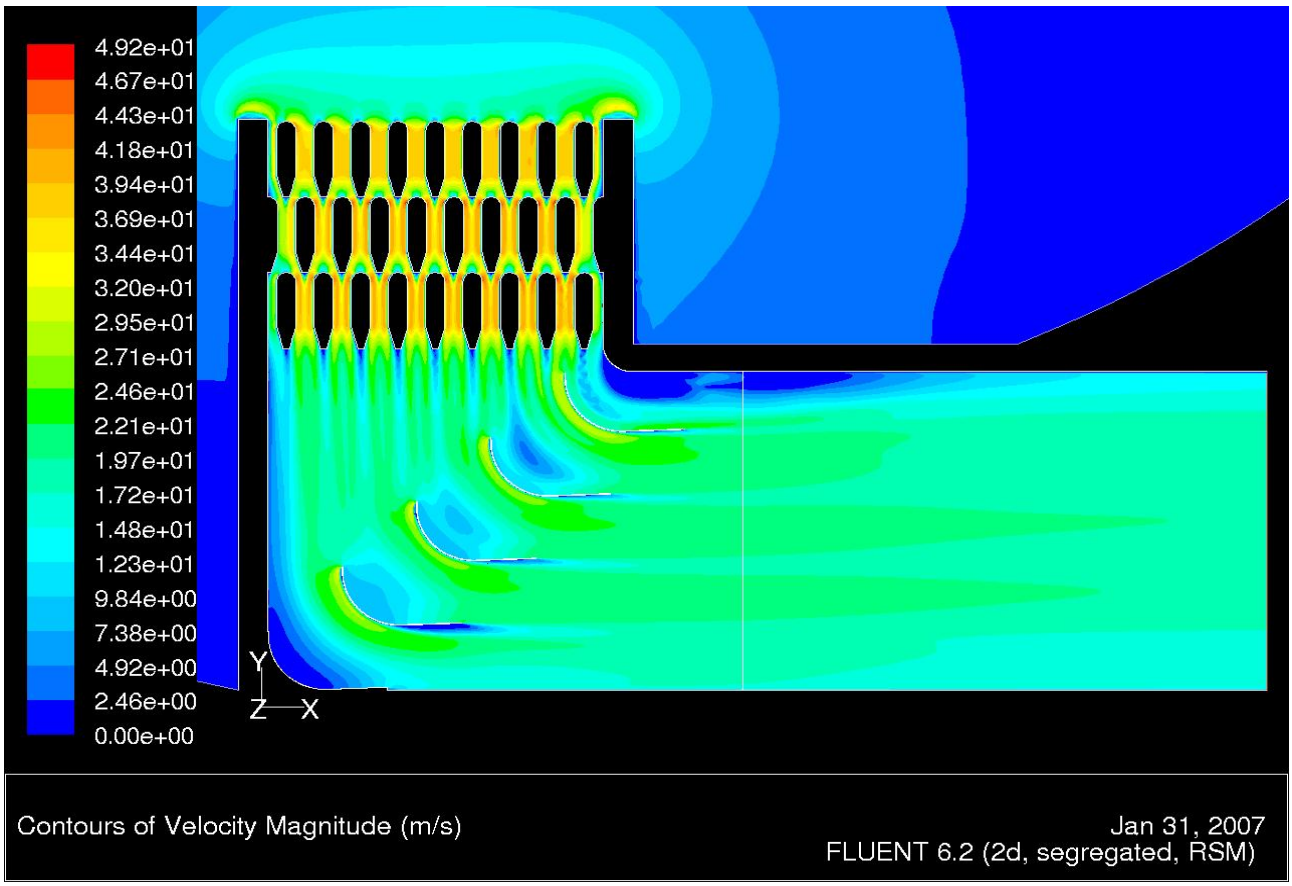

Figure 93 Velocity Magnitude in the Five-Vane Mid-Baffle-Aligned Arrangement

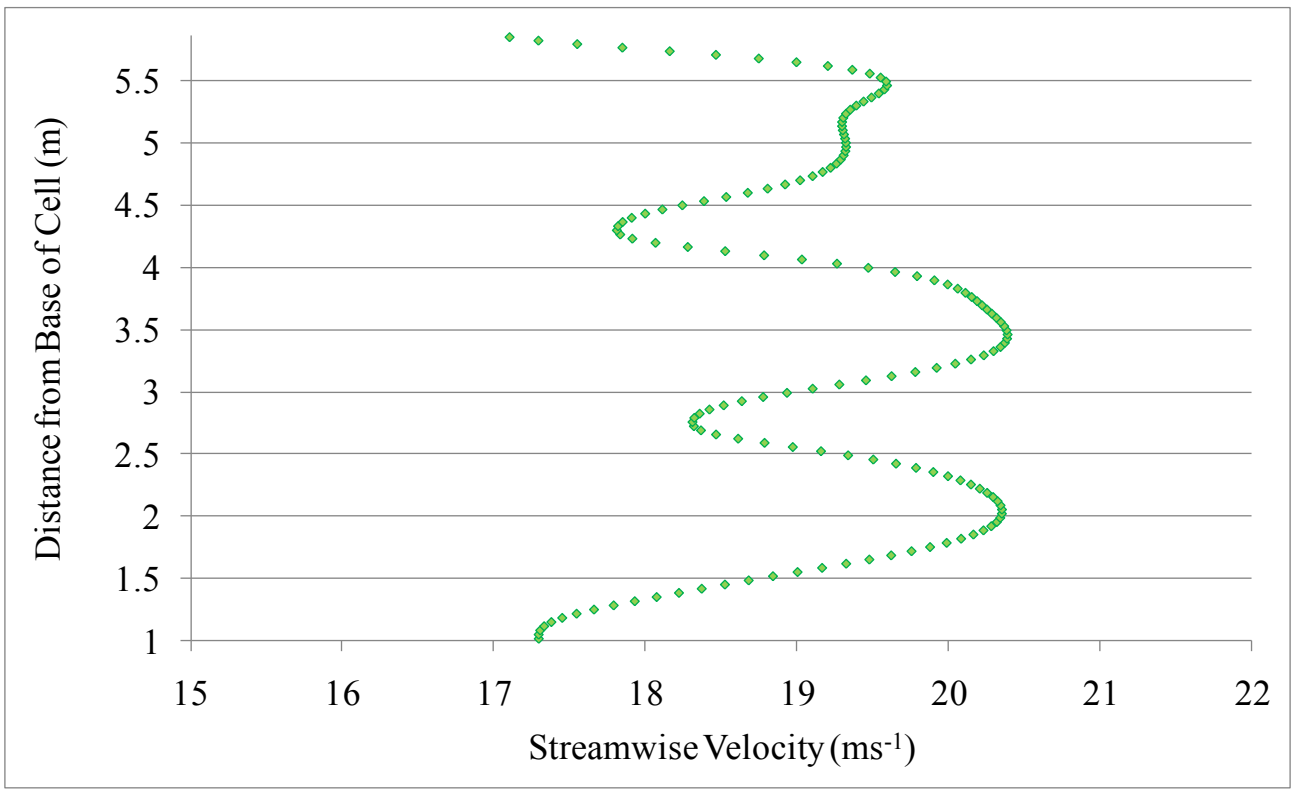

Figure 94 Stream-Wise Velocity Profile in the Five-Vane Mid-Baffle-Aligned Arrangement

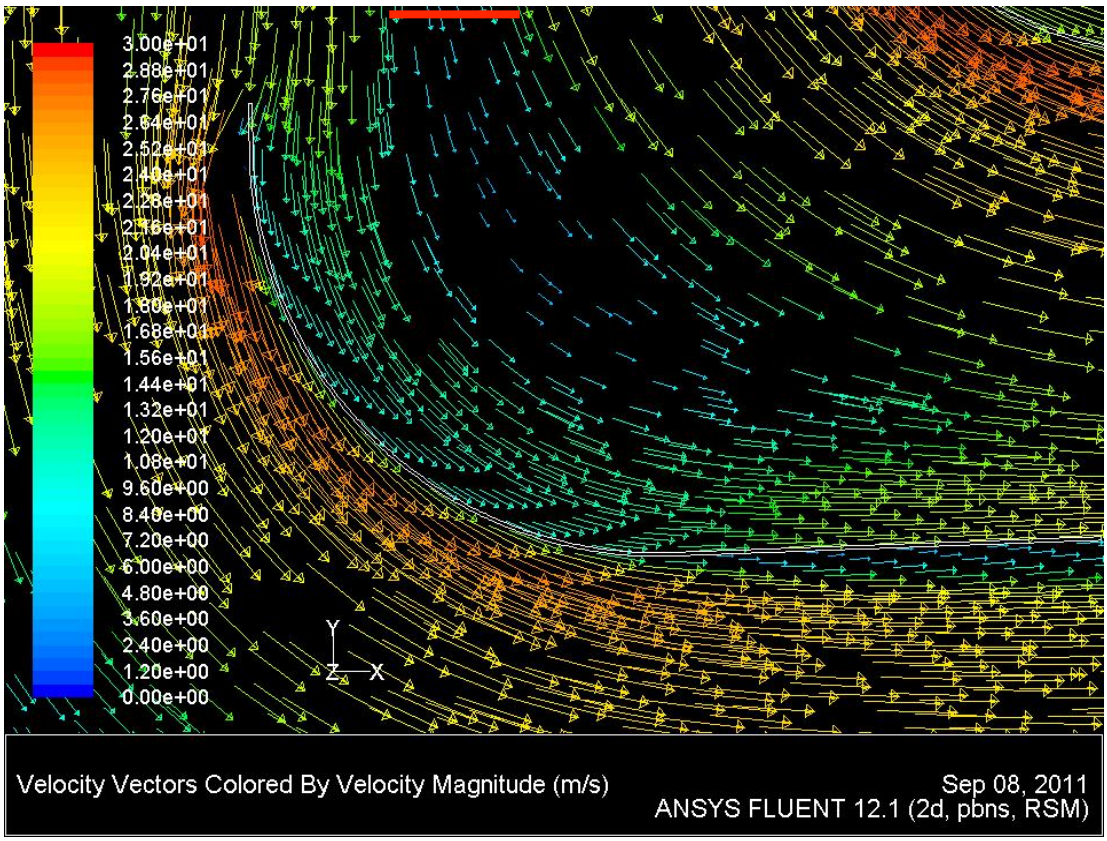

Figure 95 Flow Pattern around Turning-Vane in the Five-Vane Mid-Baffle-Aligned Arrangement

Figure 96 presents the flow pattern of the nine-vane mid-baffle-aligned solution. Qualitatively, a more consistent and higher quality flow was generated compared with all previous arrangements. Separation at the inner corner and low velocity under the vanes was most notably improved over the nine-vane baffle-aligned solution of Figure 89. As in the five-vane mid-baffle-aligned case, the isolation of the outer corner produced a more consistent flow pattern. The more consistent flow in the outer corner was replicated throughout the vane arrangement. Comparison of Figure 89 and Figure 96 shows that aligning the vanes mid-baffle produced a slightly larger low velocity region between adjacent vanes, which is compensated for by a heightening of the minimum velocities within the regions.

Quantitatively, the calculated velocity distortion of 12.3% does not entirely reflect the qualitative analysis. The velocity profile of the distortion calculation is shown in Figure 97. Comparisons of Figure 97 with Figure 89, Figure 90, and Figure 96 show that the velocity distortion of the baffle-aligned nine-vane solution was decreased by the influence of the separation zone at the roof of the cell.

The experimental work of (Johl et al., 2007) shows that logically, in the absence of significant separation at the inner corner, the highest streamline velocity on the velocity distortion plane should

be observed slightly above the height of the uppermost vanes TE, as is the case in Figure 97. The velocity distortion of the baffle-aligned case (Figure 90) was influenced by the separation zone at the roof of the cell (seen in Figure 89) in a way that produces u_{max} at a location slightly above the height of the third uppermost vane TE. As a result, the value of u_{max} is reduced along with the velocity distortion value, reflecting more an artefact of a negative upstream flow pattern as opposed to a genuine design improvement.

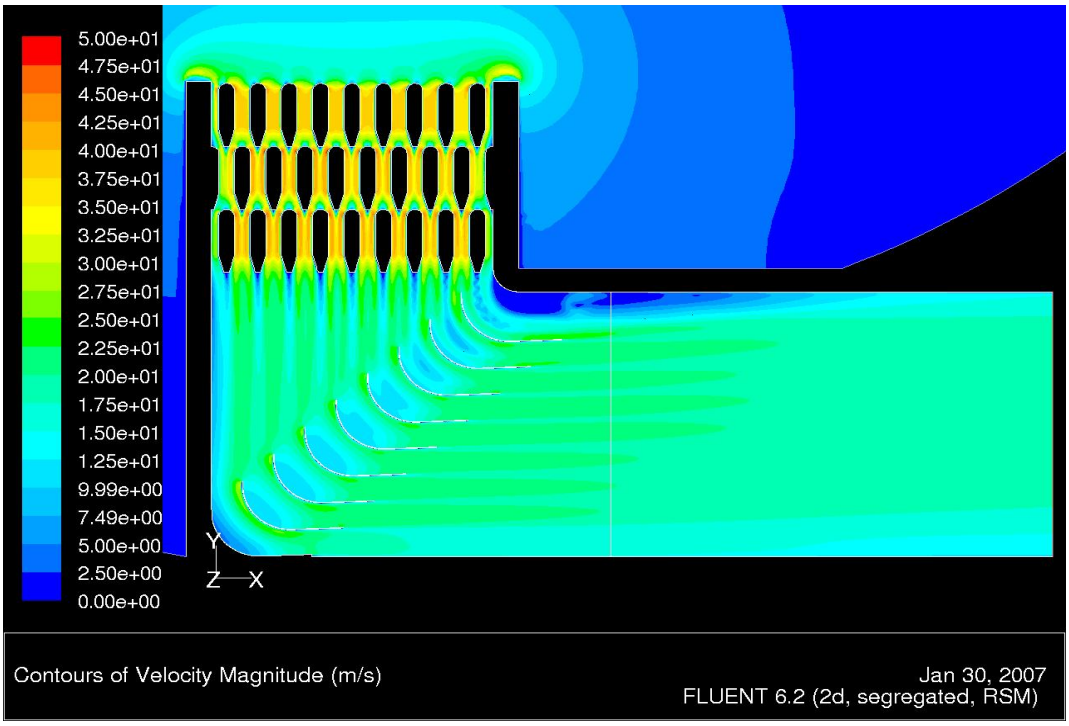

Figure 96 Velocity Magnitude in the Nine-Vane Mid-Baffle-Aligned Arrangement

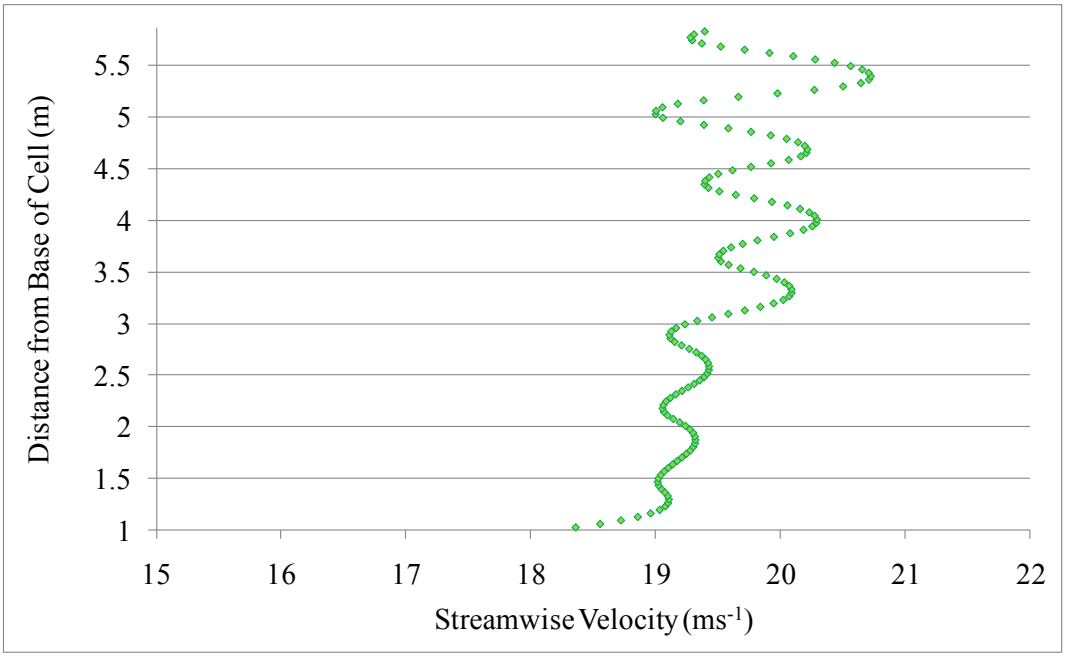

Figure 97 Stream-Wise Velocity Profile in the Nine-Vane Mid-Baffle-Aligned Arrangement

4.3.4 Trailing Edge Extension Length Variation

In Figure 83 of Section 4.3.1 it was seen that a positive vertical velocity component was generated in the baseline solution. This represented an over-rotation of the flow by the vane arrangement. The positively-angled TE along with the 1200mm long TE extensions were determined as the likely sources of the flow over-rotation. This section investigates the influence of TE extension length in relation to the over-rotation and flow quality downstream of the vane arrangement.

Answers to two specific questions were sought in this investigation. With a positive TE angle, how much directional change in the exiting flow would be seen with a variation in TE length? And, could the same quality of flow be retained with a lower material investment in the TE extensions? To answer these questions a series of computational domains were created using the baseline geometry as a starting point.

Individual domains with TE extension lengths of 600mm, 900mm, 1500mm, and 1800mm were generated and solutions obtained for each. When combined with the baseline solution a data set of five TE length designs, increasing in 300mm increments, from 600mm to 1800mm was generated.

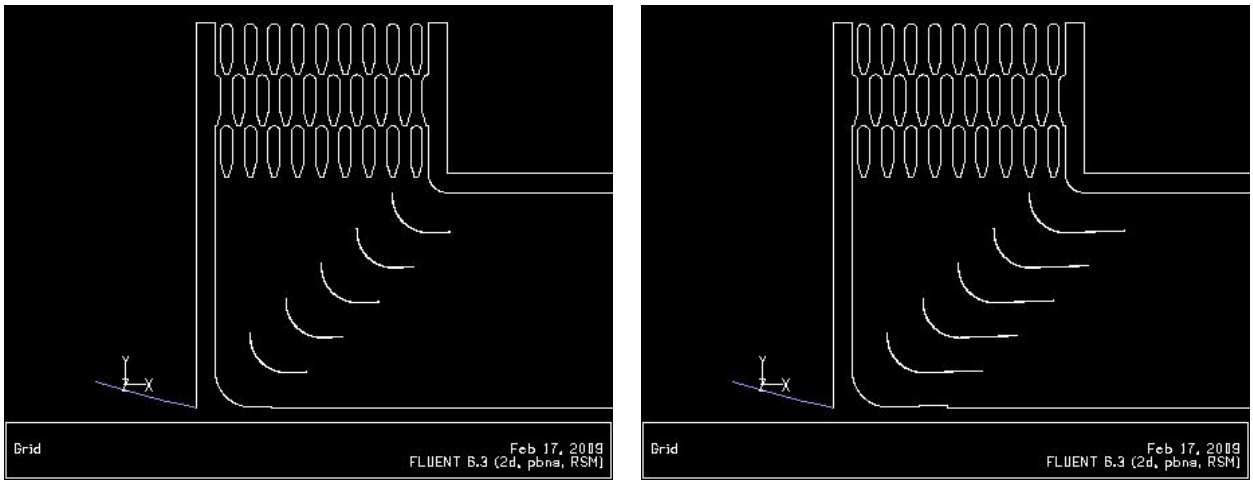

Figure 98 Computation Domains using 600mm (left), and 1800mm (right) TE Extension Lengths

Figure 99 presents the solutions for the TE length variations. Figure 99, in combination with Figure 75, show that as extension length was increased, a transient flow pattern, originating from the underside of the upper turning-vane, was produced. A vortex-shedding motion was seen to propagate downstream. As extension length was increased, the frequency of the shedding motion decreased, but the size of the shed low velocity pockets increased.

It should be noted that in solving the 1500mm and 1800mm TE length cases, the convergence criterion discussed in Section 4.2.2.2, and in particular continuity, was unable to be met. This confirmed that the solutions were showing a tendency towards transient behaviour. Figure 100 shows mass imbalance in the shedding region below the uppermost vane in the 1800mm TE length solution as being the cause of the non-convergence. Figure 101 shows the mass imbalance is isolated to the region below the uppermost vane. It was deemed that the remainder of the solution within the domain could therefore be discussed with confidence of accuracy.

The transient nature of the solutions led to inconsistencies in the quantitative analysis of the velocity distortion calculations. Extension lengths of 600mm, 900mm, 1500mm, and 1800mm produced velocity distortions of 30.2%, 35.1%, 25.7%, and 42.3% respectively.

Figure 102 presents the velocity profiles along a limited velocity distortion line that was isolated from shedding flow patterns. The limited distortion line ran from 1.0m to 4.5m above the base of the cell. Over this limited velocity distortion line the 600mm, 900mm, 1200mm, 1500mm, and 1800mm TE length solutions produced distortions of 10.6%, 14.3%, 20.0%, 23.7%, and 26.4% respectively. Figure 103 shows that these values represent a near linear increase in distortion with TE length.

Figure 99 shows that the under-vane low velocity regions increase in size, but decrease in intensity, with an increase in TE length. Figure 102 and Figure 103 suggest that the smaller, but more intense low velocity zones produce lower levels of distortion at the downstream location of the distortion line.

Qualitatively, the size of the inner corner separation zone decreased with an increase in extension length as can be seen in Figure 99. Figure 104 suggests that this is a result of an increase in over-rotation with an increase in TE length. With a greater over-rotation, transfer of momentum between the higher velocity flow and the flow in the separation region likely occurs.

An alternate option to increasing the length of the TE length, which was not considered as part of the investigations, would be to increase the TE angle. Theoretically this would increase the ‘turning power’ of the vane arrangement and increase the positive vertical velocity component of the exiting flow. Although not considered part of this investigation because it was beyond the time resource available, it is believed that merit would lie in future efforts analysing the TE angle variable alongside the findings presented in this work.

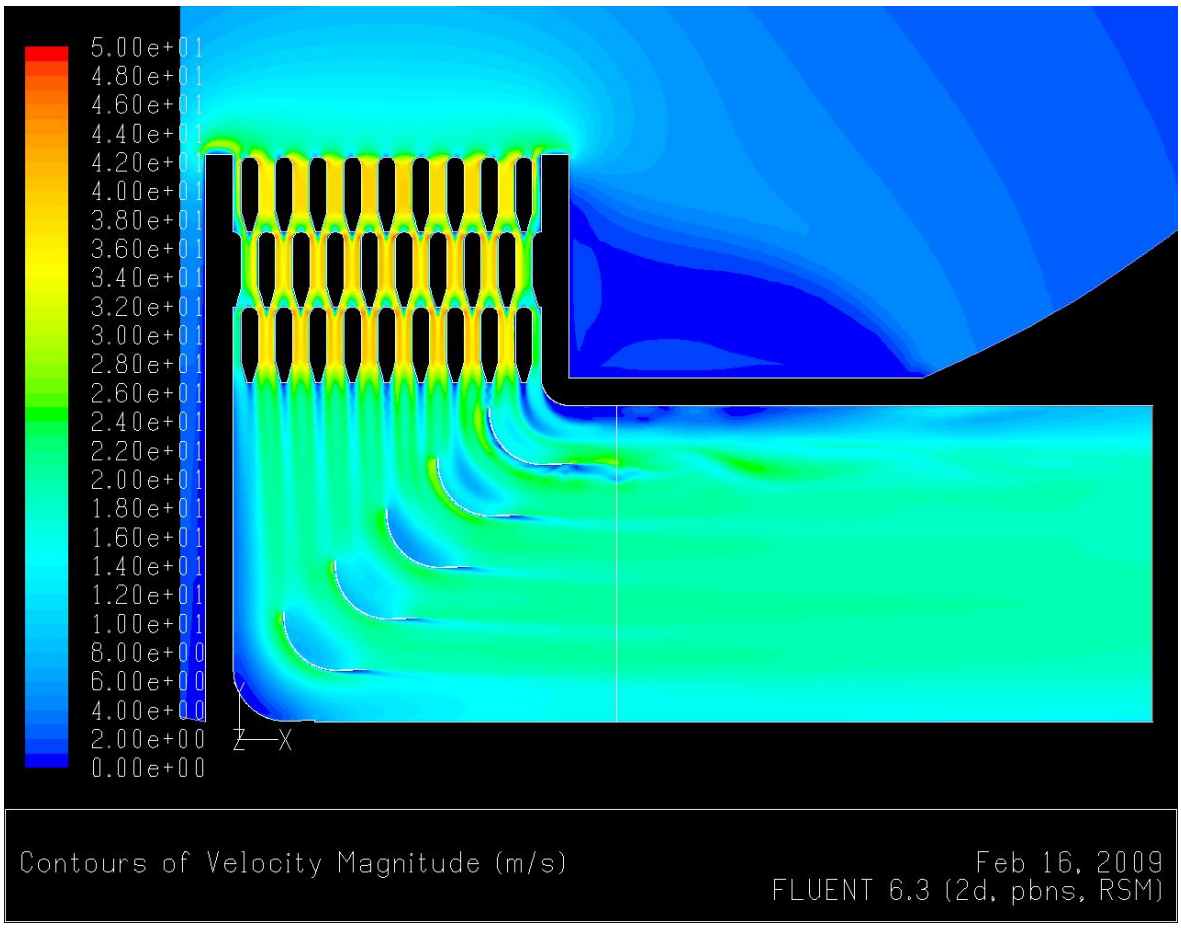
5.00e+01
4.80e+01
4.60e+01
4.40e+01
4.20e+01
4.00e+01
3.80e+01
3.60e+01
3.40e+01
3.20e+01
3.00e+01
2.80e+01
2.60e+01
2.40e+01
2.20e+01
2.00e+01
1.80e+01
1.60e+01
1.40e+01
1.20e+01
1.00e+01
8.00e+00
6.00e+00
4.00e+00
2.00e+00
0.00e+00
Y
Z
X
Contours of Velocity Magnitude (m/s)
Feb 16, 2009
FLUENT 6.3 (2d, pbns, RSM)

a.

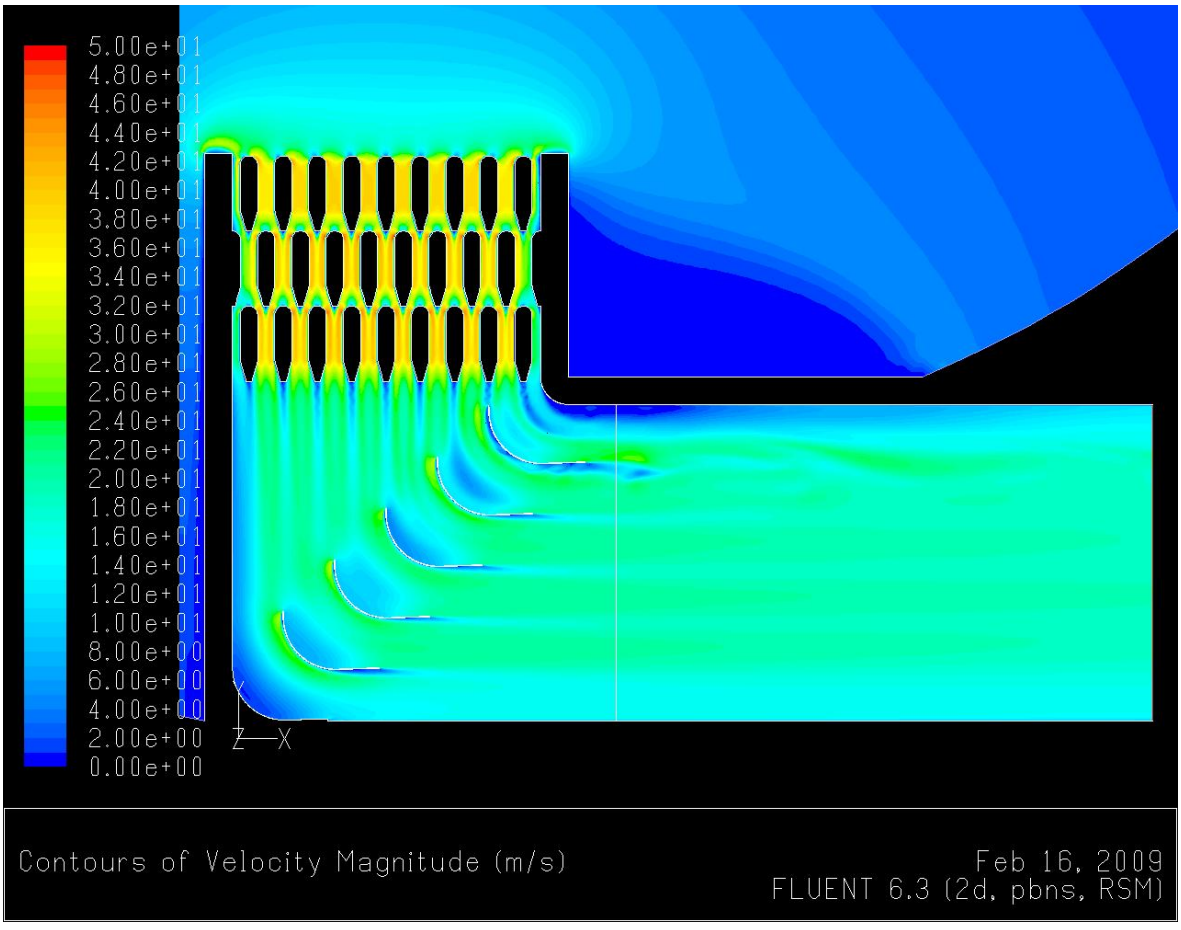
5.00e+01
4.80e+01
4.60e+01
4.40e+01
4.20e+01
4.00e+01
3.80e+01
3.60e+01
3.40e+01
3.20e+01
3.00e+01
2.80e+01
2.60e+01
2.40e+01
2.20e+01
2.00e+01
1.80e+01
1.60e+01
1.40e+01
1.20e+01
1.00e+01
8.00e+00
6.00e+00
4.00e+00
2.00e+00
0.00e+00
Y
Z
X
Contours of Velocity Magnitude (m/s)
Feb 16, 2009
FLUENT 6.3 (2d, pbns, RSM)

b.

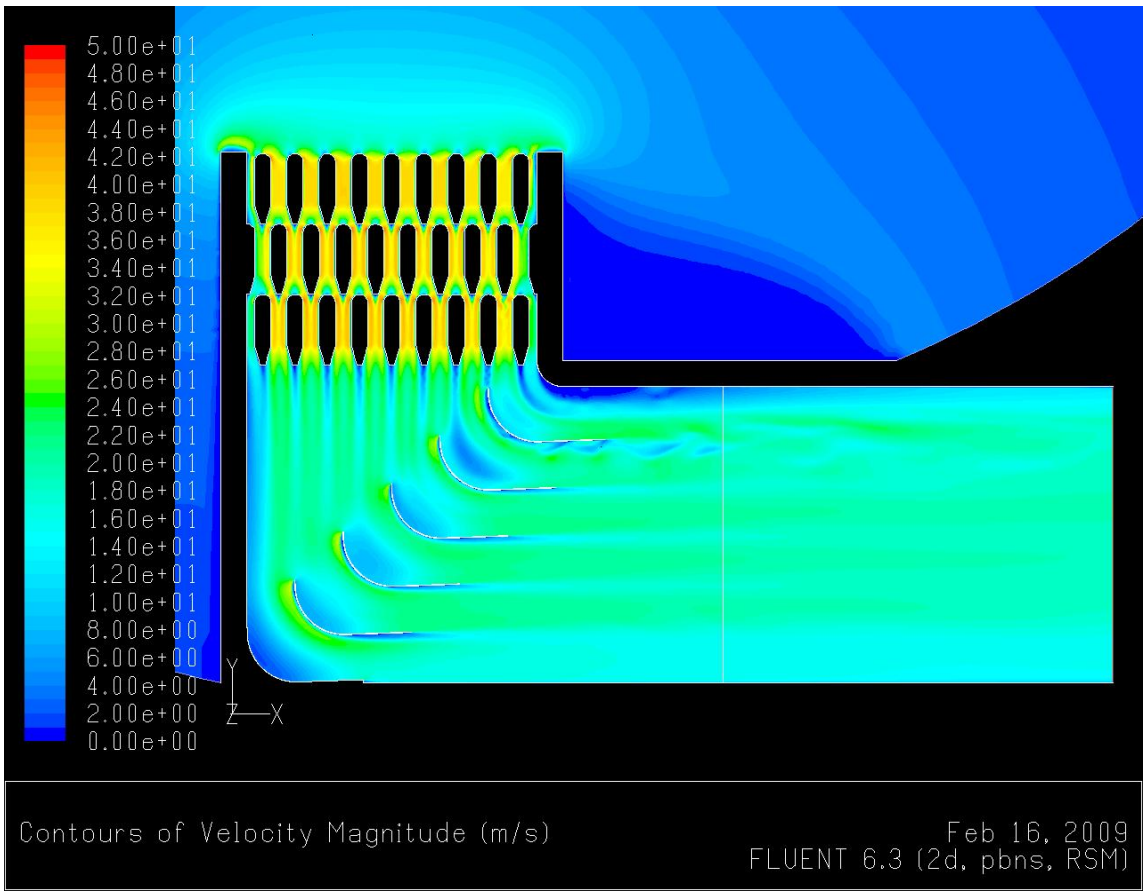

c.

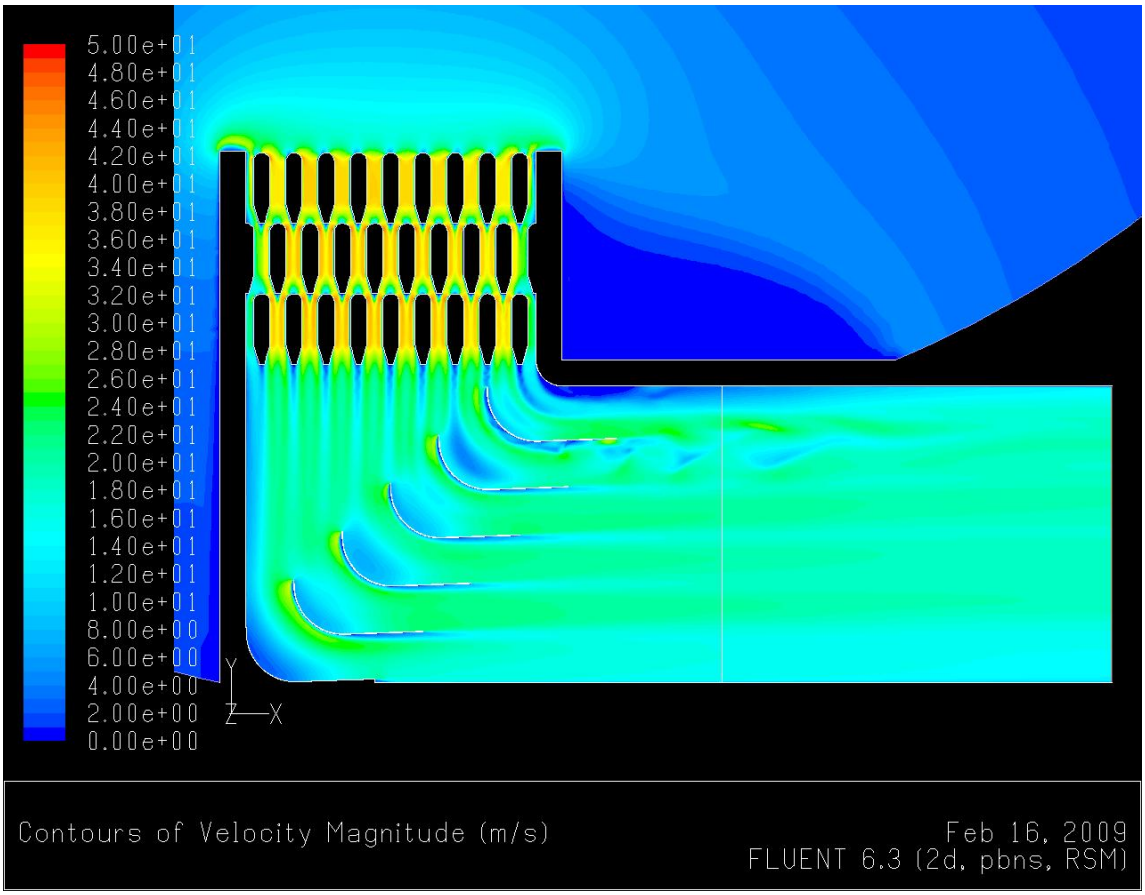

d.

Figure 99 Velocity Magnitude with of 600mm (a), 900mm (b), 1500mm (c), and 1800mm (d) TE Lengths

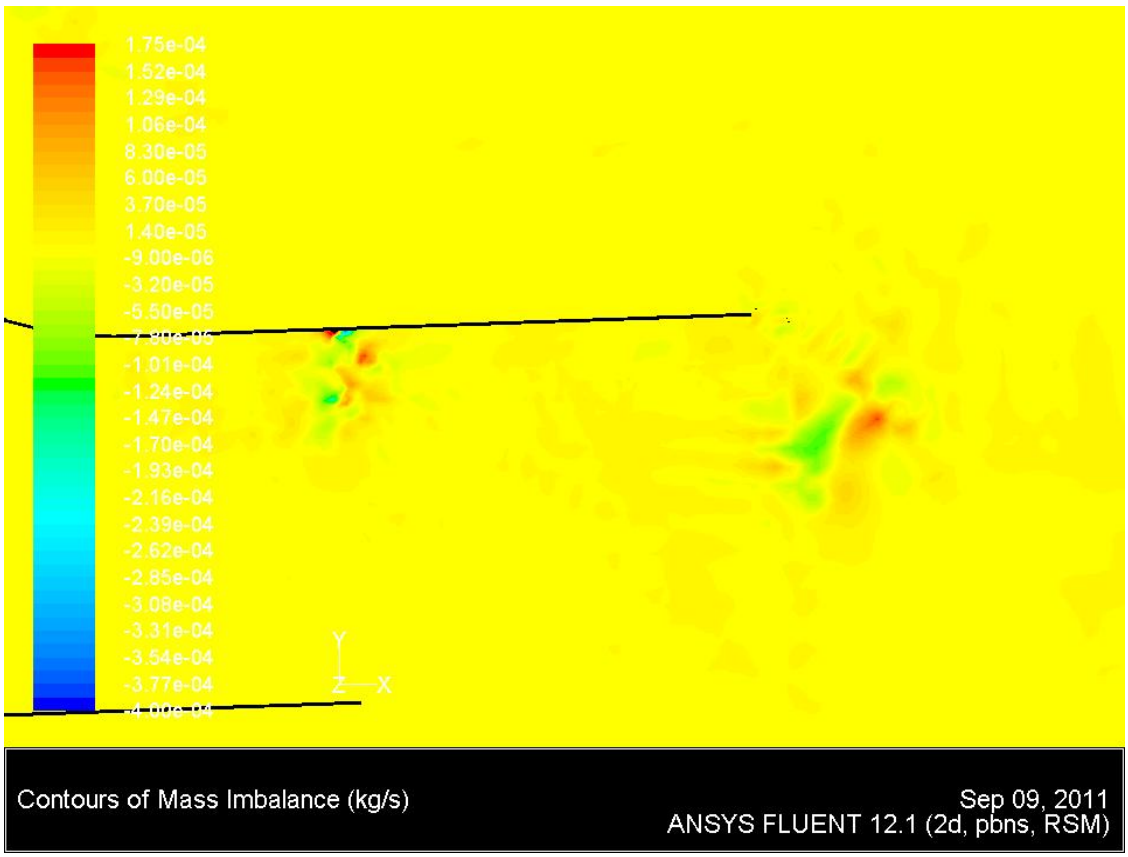

Figure 100 Mass Imbalance around the Uppermost Turning-Vane in the 1800mm TE Length Solution

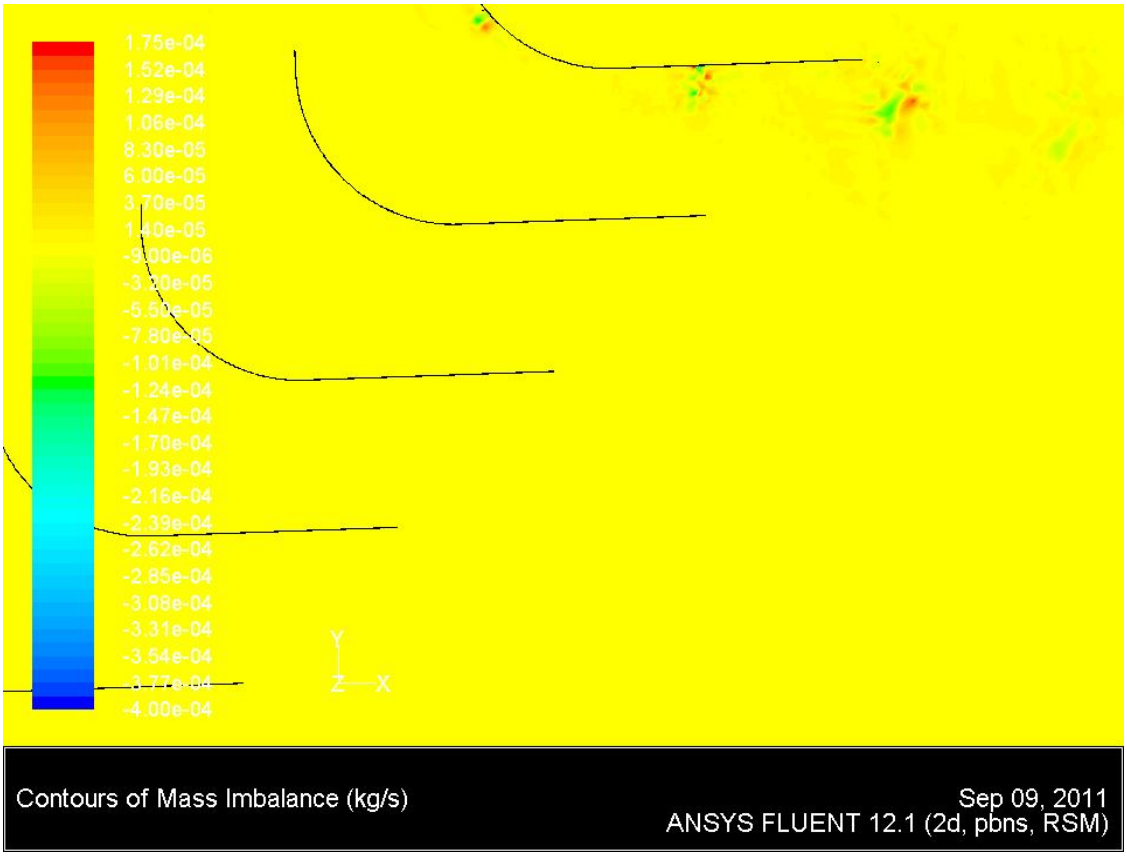

Figure 101 Mass Imbalance through the Turning-Vane Arrangement in the 1800mm TE Length Solution

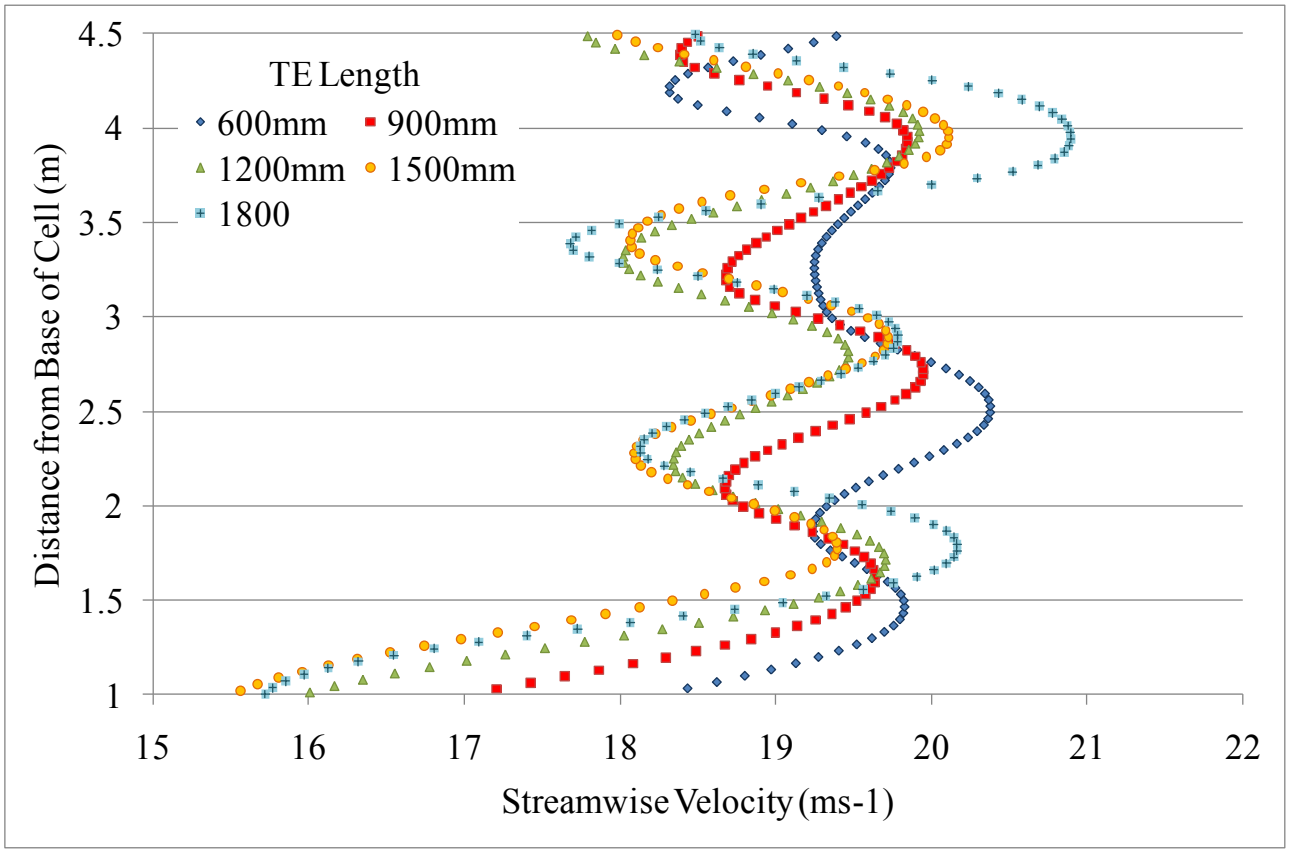

Figure 102 Comparison of Stream-Wise Velocity Profiles along a Limited Velocity Distortion Line with a variation in TE Length

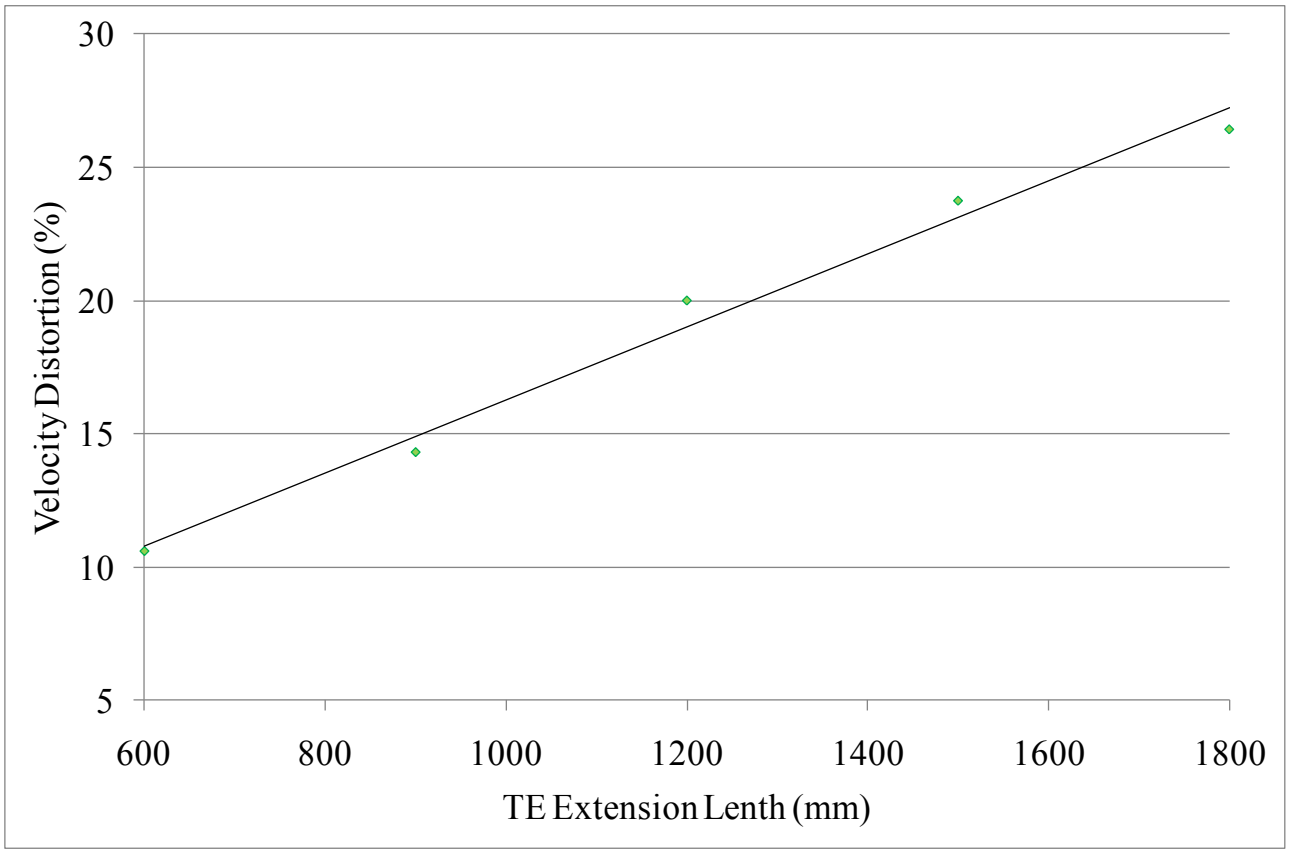

Figure 103 Velocity Distortion Variation with TE Length along Limited Velocity Distortion Line

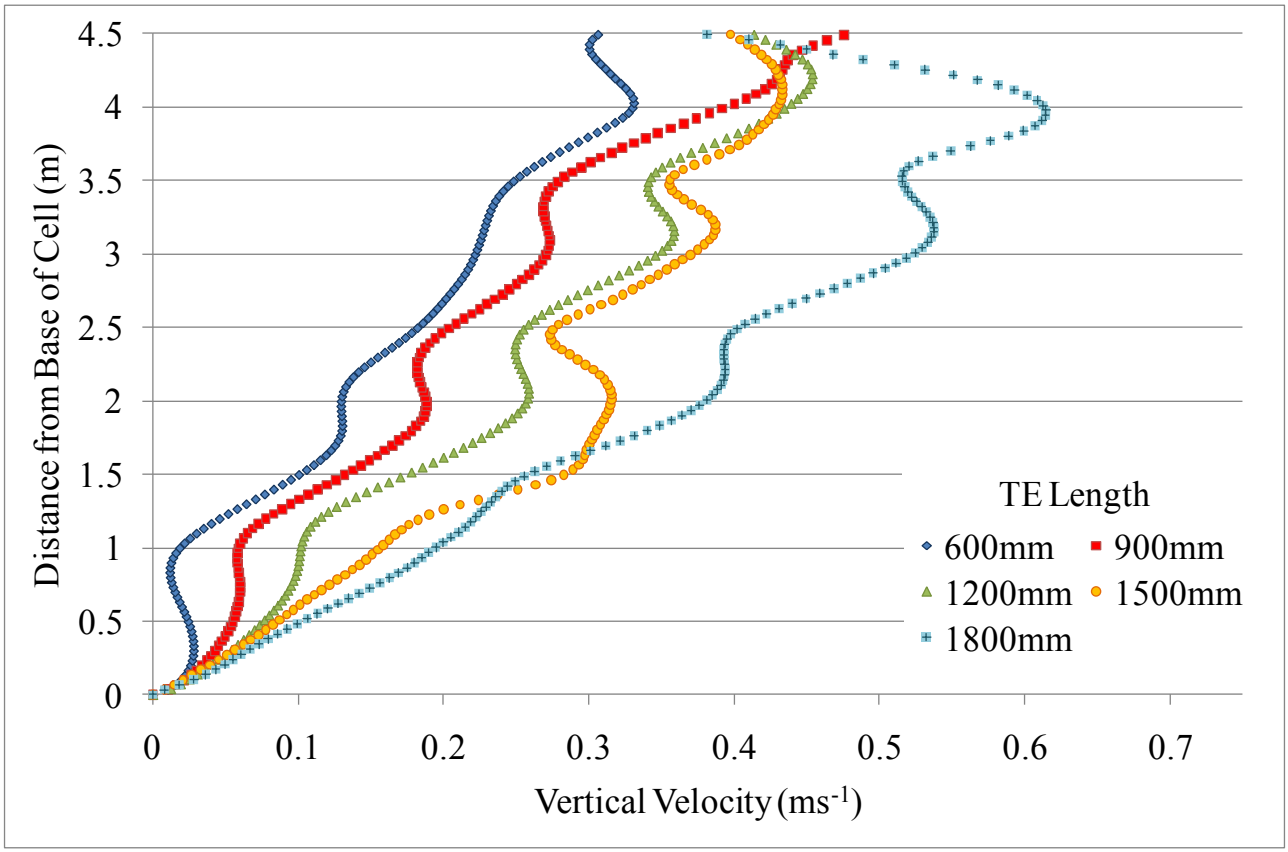

Figure 104 Comparison of Vertical Velocity Profiles along a Limited Velocity Distortion Line with variation in TE Length

4.3.5 Inner Corner Modification

Section 4.3.1 discussed the implications of a low velocity region along the roof of the working section. Section 4.3.1 also showed that in the baseline solution the low velocity was a result of the upstream separation flow feature. As such, a solution was sought to reduce and/or remove the upstream separation zone.

An investigation was firstly performed to determine the influence of the inner corner radius on the separation behaviour. The inner corner radius was seen in Section 4.3.1 to contribute to the adverse pressure gradient along the inner corner through two mechanisms. The first was the change in direction of the solid surface that the inner corner represents. The second was in the formation of a second flow channel expansion between the inner corner itself, and the uppermost vane.

To determine the influence of an inner corner radius modification, the domain of the baseline arrangement was modified to create four additional domains. These domains incorporated inner corner radii of 800mm, 1000mm, 1153mm (matching that of the turning-vane radius), and 1200mm

respectively. Figure 105 compares the geometry of the domains with inner corner radii or 600mm and 1200mm.

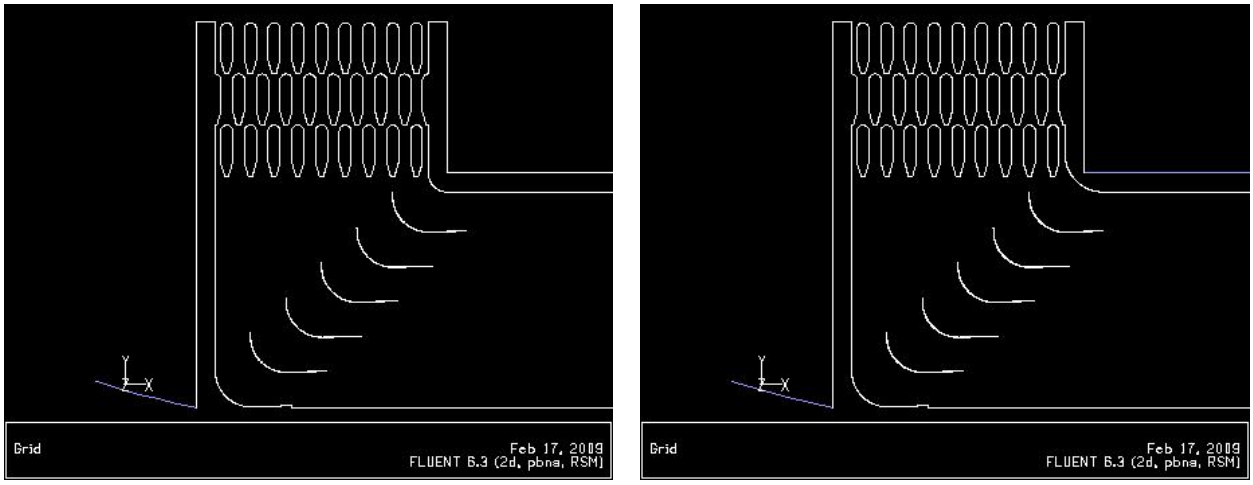

Figure 105 Computation Domains using a 600mm (left) and 1200mm (right) Inner Corner Radius

A solution for each of the four domains was generated. Figure 106 compares the inner corner flow pattern of the baseline solution with that using a 1200mm radius. Contrary to prediction, Figure 106 shows the inner corner flow detached further upstream in the 1200mm solution. It was expected that the reduction in severity of the change in direction would delay the separation point.

Closer observation of Figure 105 shows that the increase in inner corner radius has resulted in aligning the curve of the inner corner nearer to the downstream face of the innermost baffle. The downstream face itself tapers away from the curve of the inner radius, creating a more exaggerated channel expansion scenario. The upstream relocation of the adverse pressure gradient, show in Figure 107, at this expansion created the conditions required for separation to occur.

Increasing the inner corner radius to 1200mm did reduce the degree of diffusion between the inner corner and the uppermost vane, the site of the second channel expansion in the baseline arrangement. This very marginally reduced the downstream extent of the separations zone. This is shown in Figure 108. The findings of this section suggest that solely increasing the inner corner radius is inadequate as a means of reducing inner corner separation, and therefore reducing the downstream low velocity region.

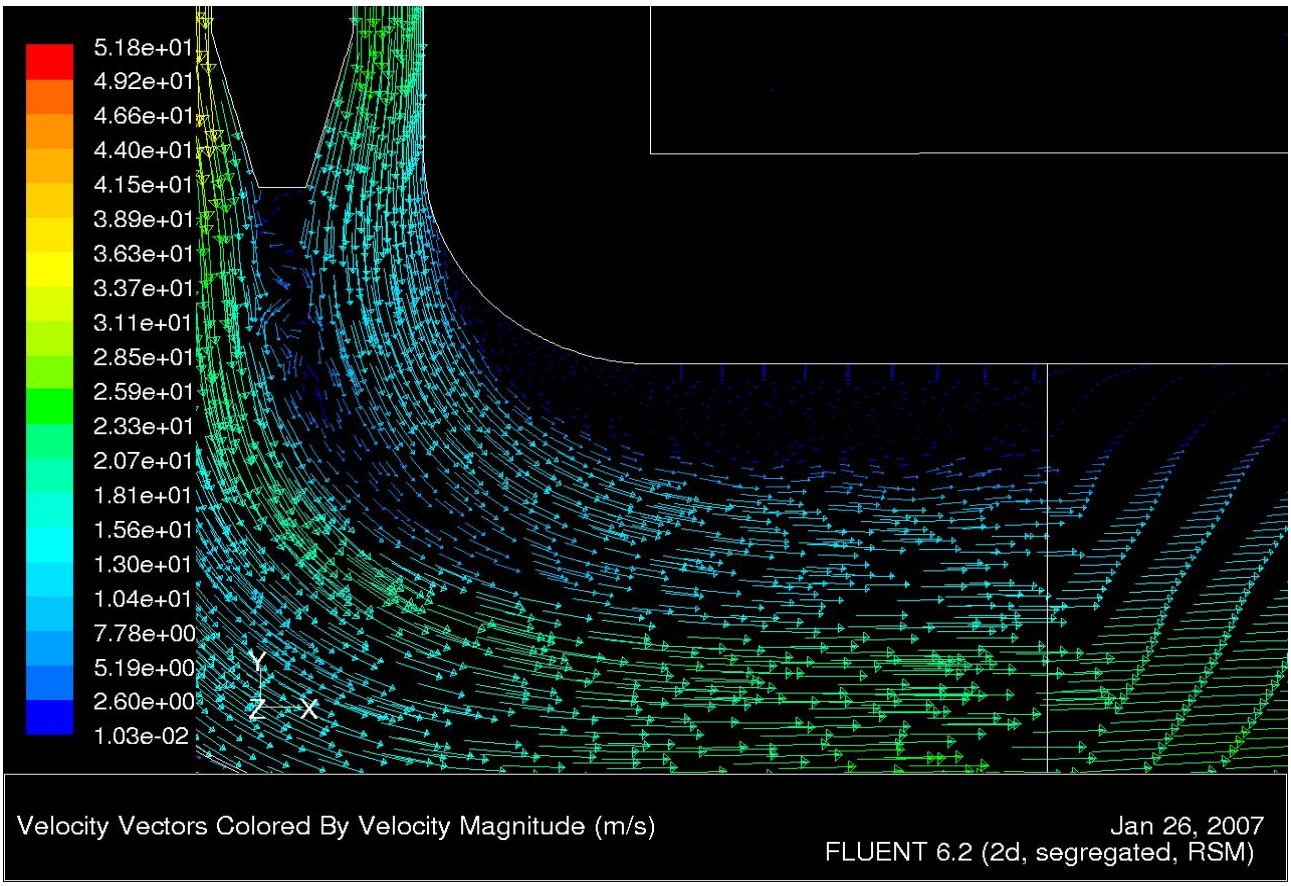

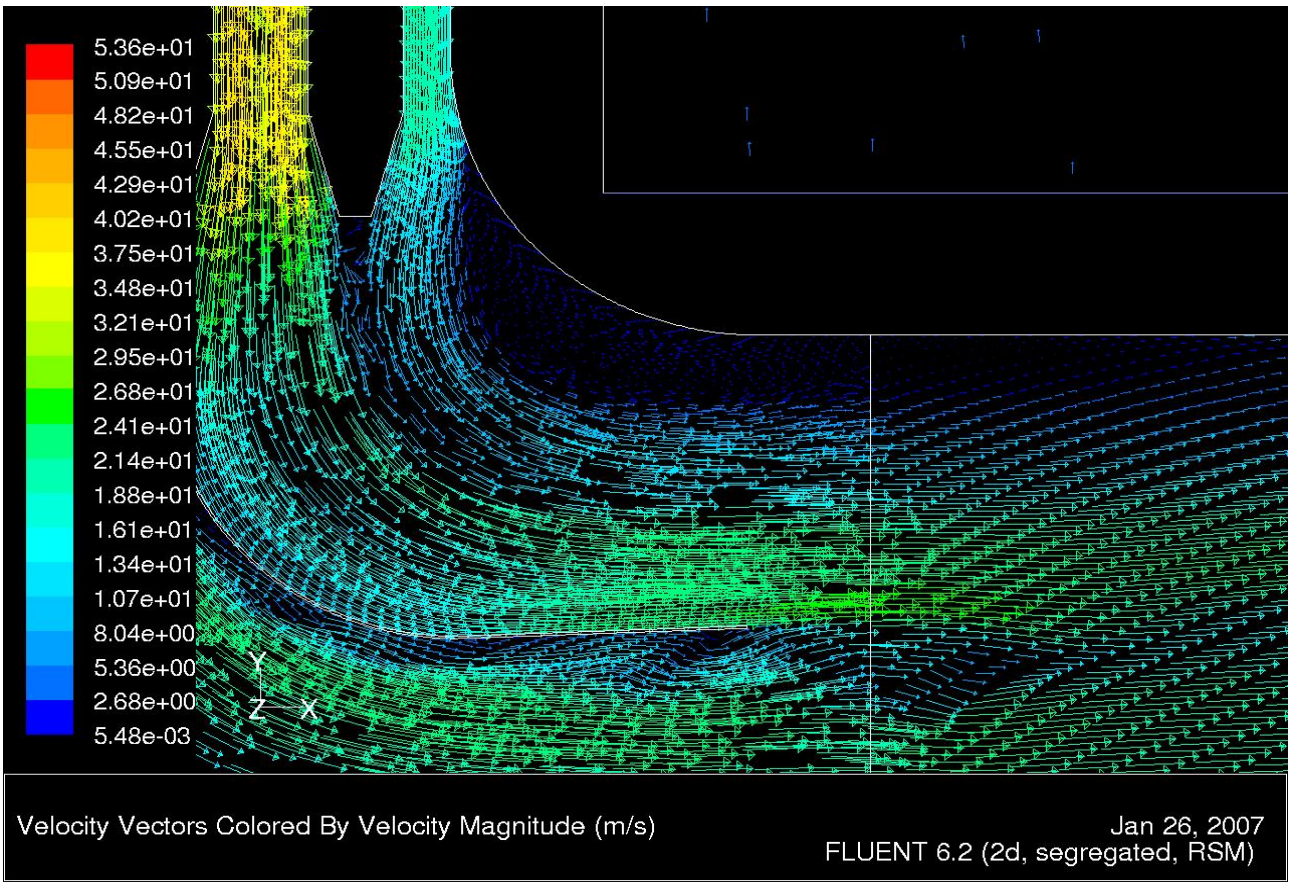

Figure 106 Point of Separation at the Inner Corner with a radius of 600mm (top) and 1200mm (bottom)

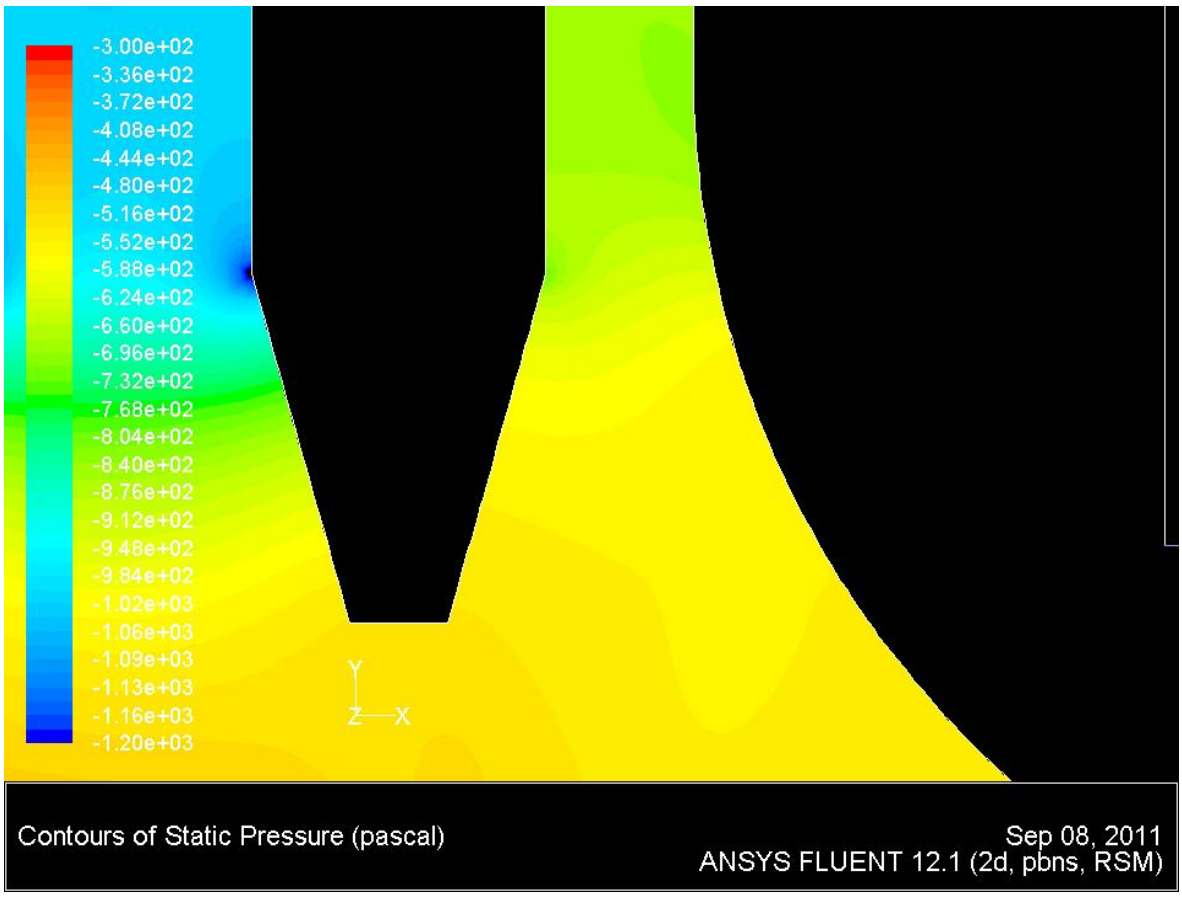

Figure 107 Static Pressure Variation at the Inner Corner with a 1200mm Radius

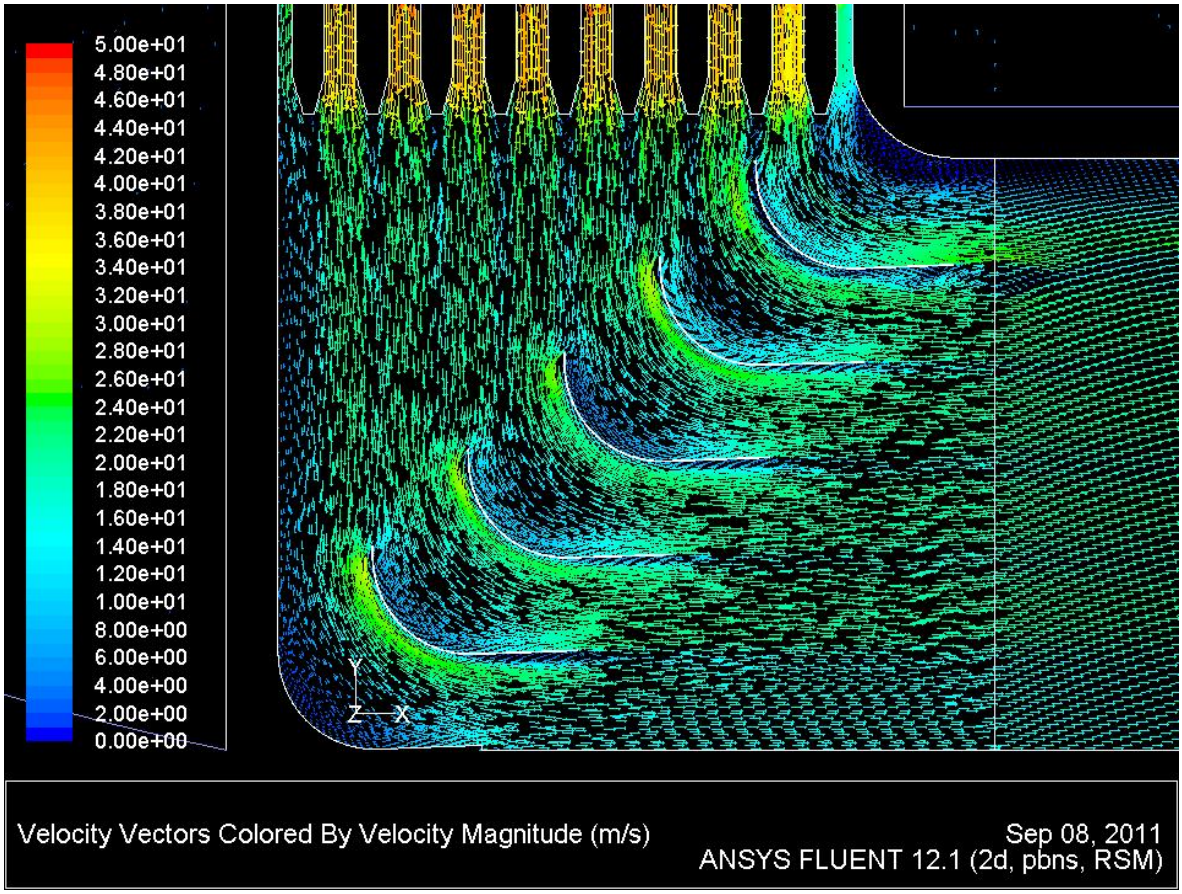

Figure 108 Flow Patterns in the Turning-Vane Arrangement with a 1200mm Inner Corner Radius

4.3.6 Intersecting Baffle-Vane Arrangement

Throughout the previous vane investigations significant inner corner separation has been detected in all solutions. Section 4.3.5 showed that modification of the inner corner radius alone could not decrease the separation patterns. This section aims to reduce the inner corner separation through modification of the vane arrangement itself.

The discussion presented in Section 4.3.1 suggested that the inner corner separation is created as a result of an adverse pressure gradient. Section 4.3.5 discussed that the adverse pressure gradient itself was created by a combination of three factors. The three factors are the flow channel expansion between the cell wall and the tapering downstream face of the innermost baffle, the relatively rapid change in direction of the boundary at the inner corner radius, and the initial flow channel expansion created between the uppermost turning-vane and the inner corner (of mismatched radius).

Focus in the investigation of this section was placed on augmenting the flow channel between the uppermost vane and inner corner. The baseline design was used as a starting point, and the lean angle was altered to reposition the LE of the uppermost vane to intersect with the axis of the second innermost baffle at its TE. In doing so, a closed converging passage between the uppermost vane and the inner corner was created.

The position of the lowermost vane was left adjacent to the inlet stack wall, and the four intermediate vanes were located at equidistant intervals between the upper and lower vanes. Incorporating the baffle-vane intersection with a wall-adjacent lowermost vane meant that consistent baffle vane spacing was unable to be achieved whilst retaining the six-vane arrangement of the baseline domain. Figure 109 shows the computational domain developed.

The solution to the design of Figure 109 is presented in Figure 110 through Figure 113. Inner corner separation was removed entirely. Figure 110 shows a more detailed vector plot in the inner corner region.

Figure 112 can be compared with Figure 77, showing the static pressure variation at the inner corner of the baffle intersecting arrangement and the baseline arrangement. By re-aligning the vane arrangement the profile of the static pressure contours has been significantly augmented. In Figure 77 the static pressure contours mostly run perpendicular to the cell wall near the inner corner.

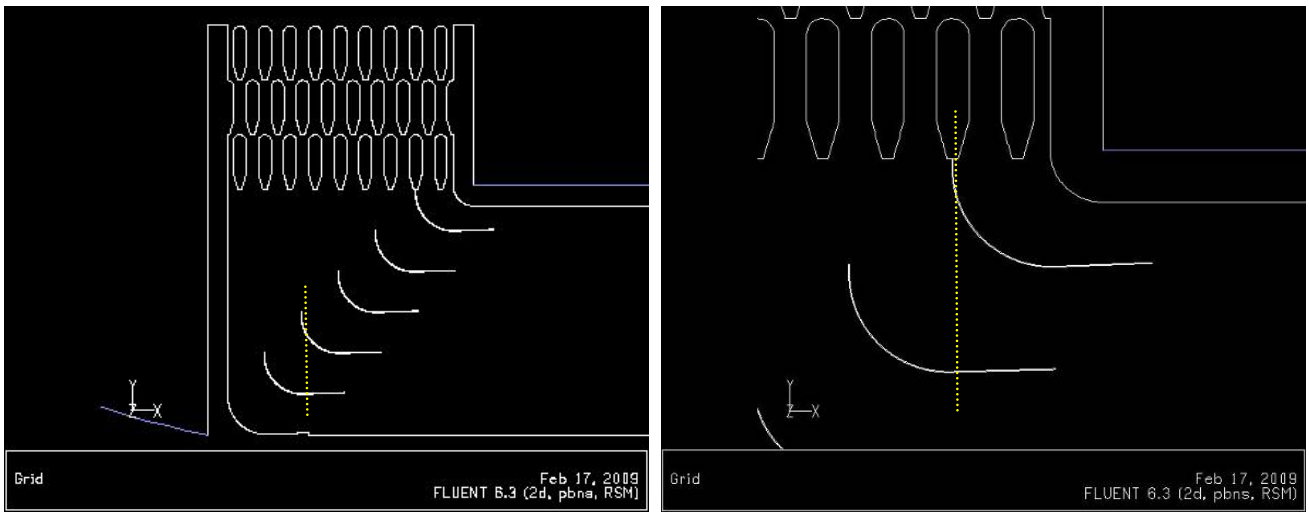

Figure 109 Computation Domain with Uppermost Turning-Vane Intersecting the Second Innermost Baffle on the Lowermost Row

In Figure 112 the contours run near parallel to the cell wall in the same region near the inner corner. As such, the static pressure no longer increase in the direction of the flow near the inner corner, and by definition, an adverse pressure gradient condition is avoided, along with separation (Wilcox, 1997).

Velocity distortion was calculated at 19.5%, a decrease from 23.6% in the baseline arrangement. Figure 113 shows the vertical velocity component along the velocity distortion line with the vane realignment. Comparing this with Figure 83, which presents the same flow parameter for the baseline arrangement, it can be seen that the vane realignment significantly reduced the over-rotation of flow. When compared with the baseline solution, it can also be seen that more severe under-vane low velocity regions are present throughout the arrangement.

The likely cause of both of these features can be found by comparing the geometry of the baseline arrangement (Figure 59) with that of the realigned arrangement (Figure 109). The overlaid yellow lines of Figure 109 show that when the angle of the vane arrangement was steepened, the curvature of adjacent vanes slightly overlapped.

This resulted in each vane (other than the uppermost vane) presenting slightly less of a curved surface to force a directional change to the upstream flow. The overlapping of vanes would likely reduce flow efficiency through the arrangement.

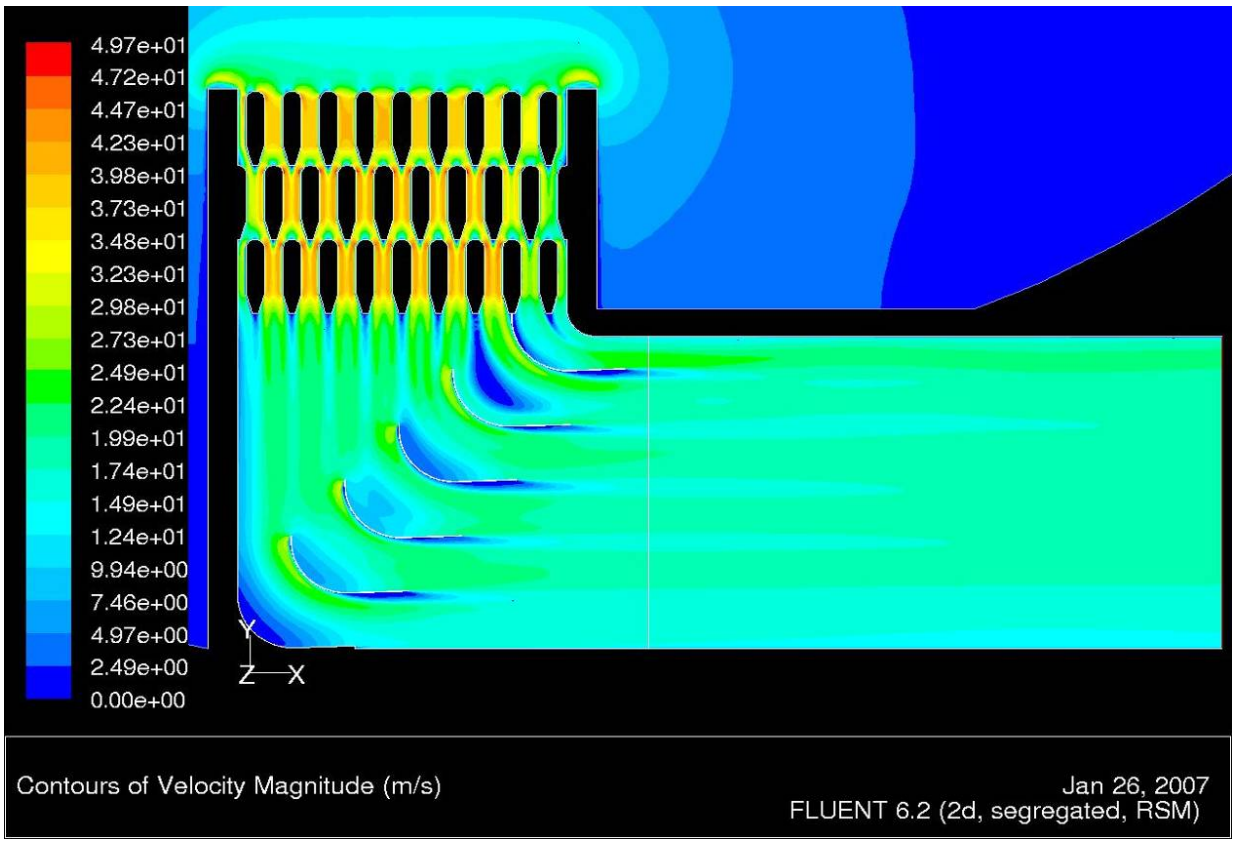

Figure 110 Velocity Magnitude in the Intersecting Baffle-Vane Arrangement

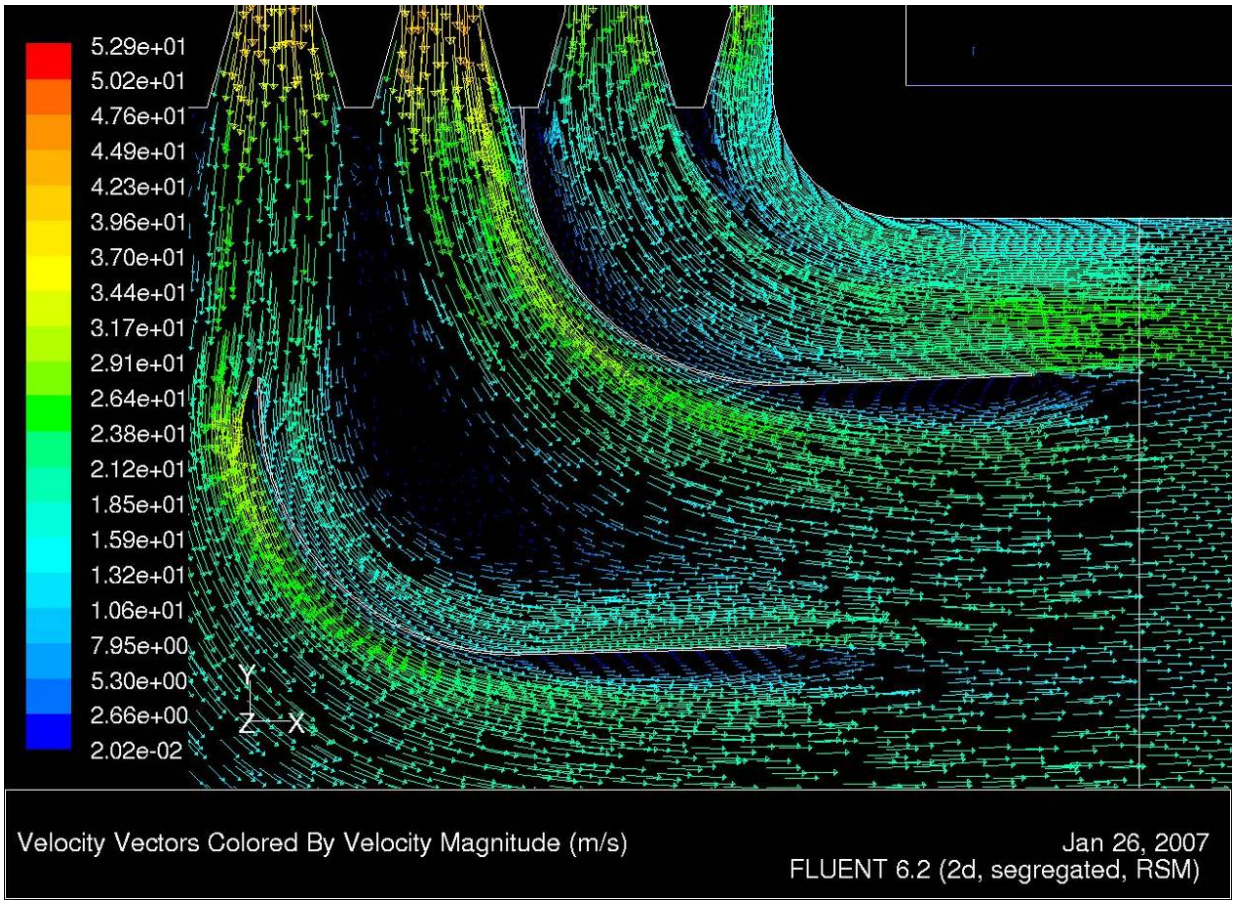

Figure 111 Flow Pattern around Uppermost Turing-Vanes in the Intersecting Baffle-Vane Arrangement

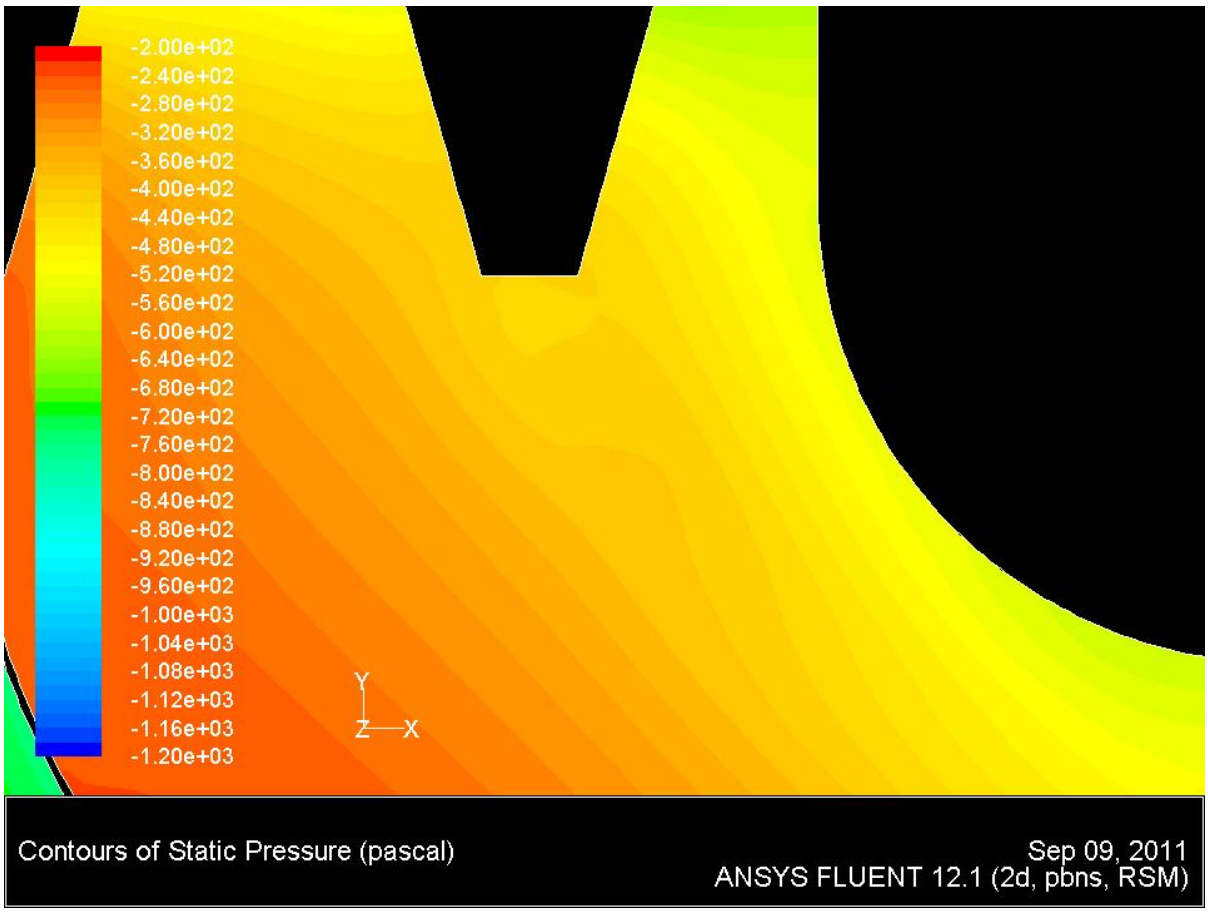

Figure 112 Static Pressure Variation at the Inner Corner of the Intersecting Baffle-Vane Arrangement

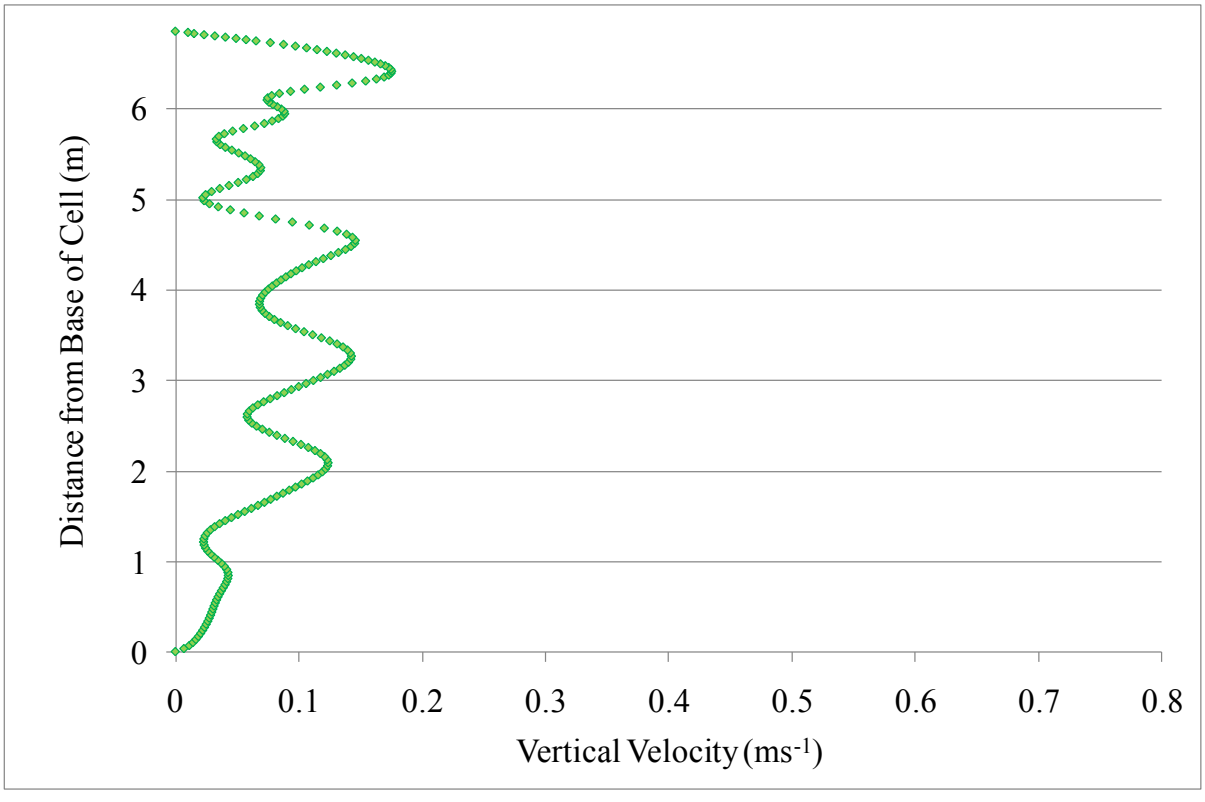

Figure 113 Vertical Velocity Profile along an Extended Velocity Distortion Line in the Intersecting Baffle-Vane Arrangement

4.3.7 Combined Inner Corner and Mid-Baffle-Aligned Arrangement

The arrangement analysed in Section 4.3.6 successfully managed to remove inner corner separation by realigning of the vane arrangement. This was achieved through creating a sizable contraction in the flow channel adjacent to the inner corner. The flow channel between the inner corner and the uppermost vane was inconsistent in size compared to the other flow channels in the arrangement as a result. This can be seen in Figure 109. A brief analysis is performed in this section with the goal of retaining the separation free flow around the inner corner, whilst providing more consistent flow channels throughout the arrangement, and therefore a lower level of velocity distortion.

The nine-vane mid-baffle-aligned arrangement was used as a starting point to develop the domain. The angle of this arrangement was increased so that the LE of the uppermost vane was vertically level with the TE of the lower row of baffles. This was combined with an inner corner radius of 1153mm to give a more even flow channel distribution across the corner representing the intersection of the inlet stack and working section. This is shown in Figure 114.

A solution for the domain was produced and is shown as Figure 115. Compared with the baseline arrangement (Figure 75), inner corner separation is significantly reduced. The separation region is shown in Figure 116.

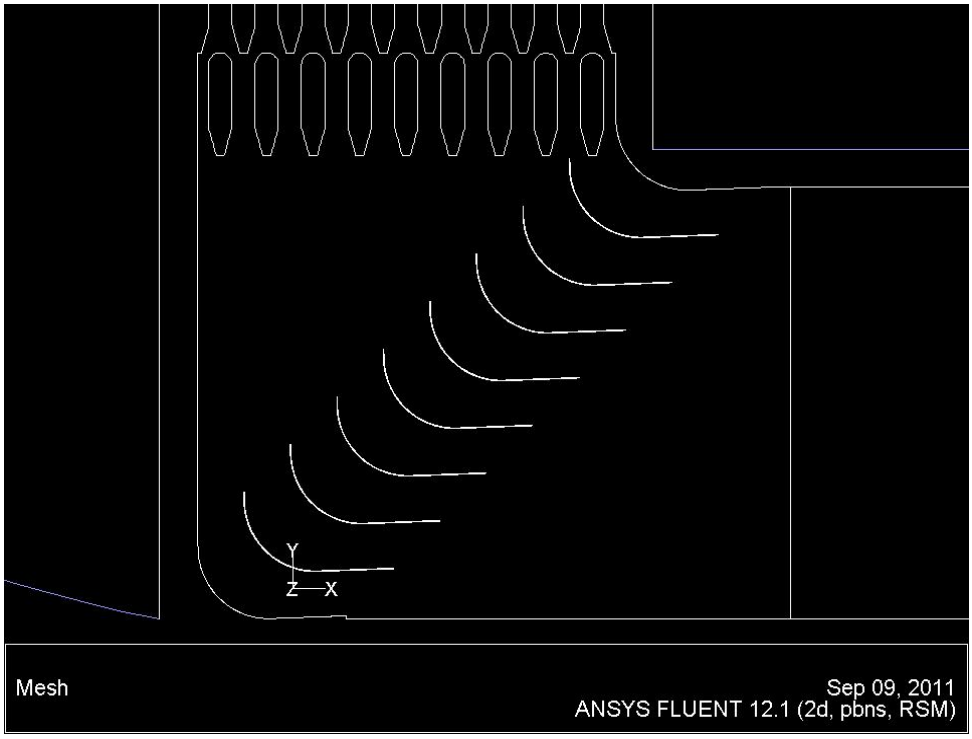

Figure 114 Computation Domain of a Mid-Baffle-Aligned Nine-Vane Arrangement with a Modified Lean Angle and 1153mm Inner Corner Radius

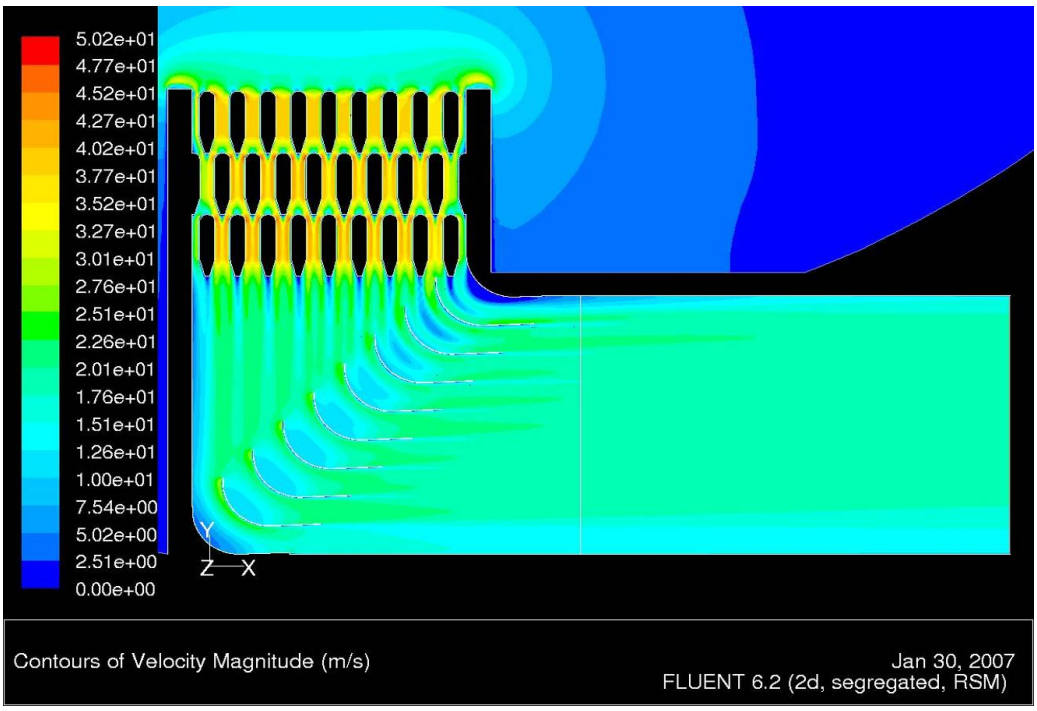

Figure 115 Velocity Magnitude in the Mid-Baffle-Aligned Nine-Vane Arrangement with a Modified Lean Angle and 1153mm Inner Corner Radius

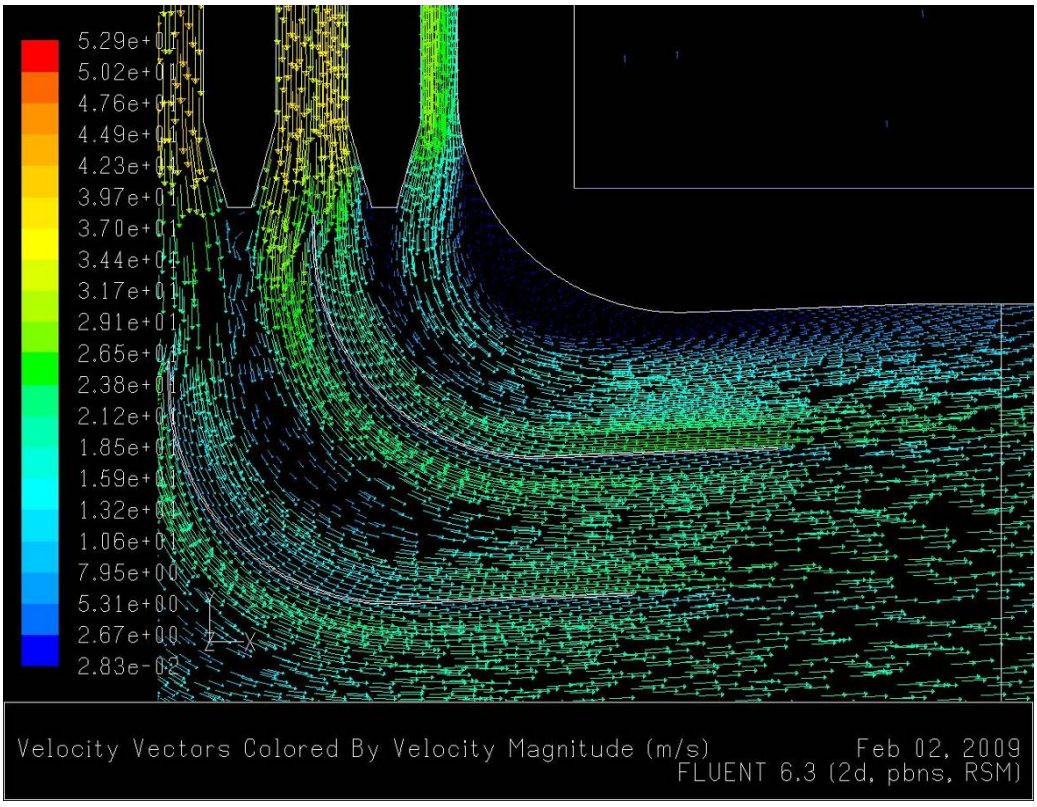

Figure 116 Flow Patterns around the Uppermost Turing-Vanes in the Mid-Baffle-Aligned Nine-Vane Arrangement with a Modified Lean Angle and 1153mm Inner Corner Radius

Figure 116 shows however, that separation was not entirely removed as in the design presented in Section 4.3.6. Figure 117 presents the static pressure distribution for comparison with the baseline solution, Figure 107, and Figure 112. Velocity distortion was calculated at 16.6% - an absolute

reduction of 14.8% over the arrangement of Section 4.3.5, and 29.7% over the baseline arrangement.

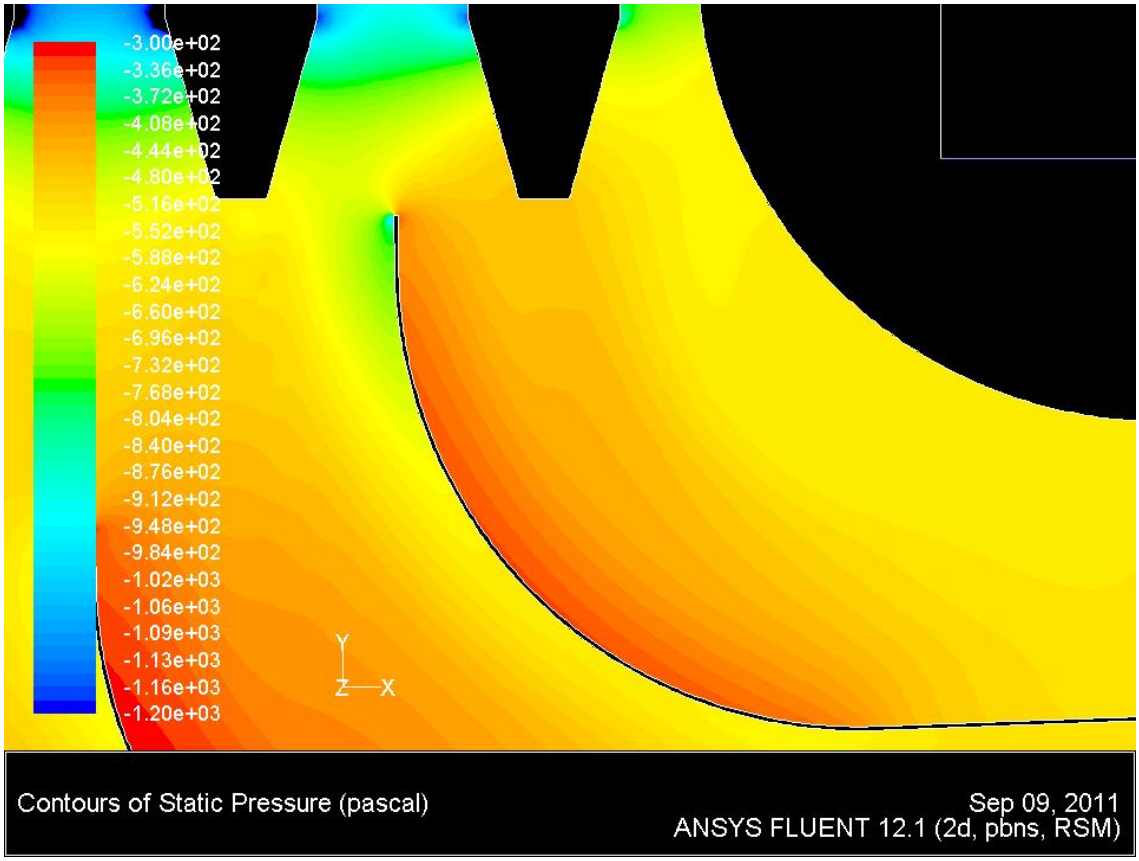

Figure 117 Static Pressure Variation at the Inner Corner of the Mid-Baffle-Aligned Nine-Vane Arrangement with a Modified Lean Angle and 1153mm Inner Corner Radius

4.3.8 Combination of Positive Design Elements

Two individual domains were then developed in an attempt to combine the positive findings found through the investigations of Section 4.3.1 through Section 4.3.7. The aim in combining the designs was to create a single design that would provide maximum reduction in both inner corner separation and velocity distortion simultaneously.

The first domain retained the consistently vane and inner corner combination of Section 4.3.7 that provided a heightened level of flow quality and consistency, whilst also significantly reducing inner corner separation. The original baffle arrangement was then modified. The distribution of the baffles on the middle row was applied on both the bottom and top rows, and vice-versa, as shown in Figure 118a. The two half-baffles adjacent to the walls on the lower row were removed.

This combination allowed consistent spacing of the flow channels within the vane arrangement to be combined with a contacting inner corner flow channel, which was shown to successfully remove inner corner separation in Section 4.3.6. The removal of the outermost half-baffle on the outer wall allowed symmetry about the vertical axis of the baffle arrangement to be maintained. This was deemed important in retaining a higher level of flow uniformity at the velocity distortion plane. The first combined element design is shown in Figure 118a.

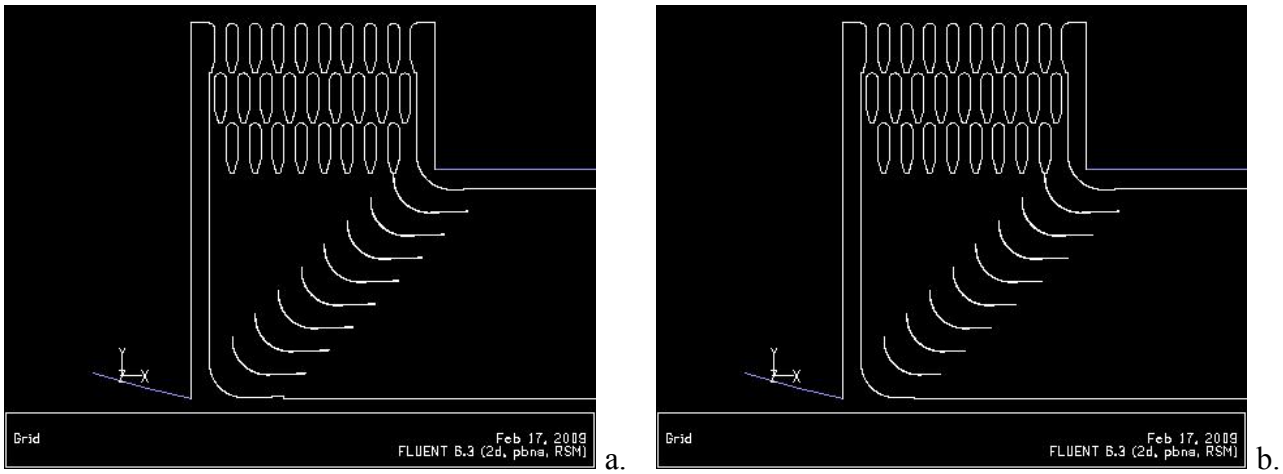

a. b.

Figure 118 Computation Domains using a Combination of Design Features with 1200mm (a), and Tapering (b) TE Length Extensions

The results of the first combined element solution are shown in Figure 119 through Figure 124. A significant reduction of inner corner separation is shown in Figure 120. Although a complete removal of separation has not been achieved, a significant advancement has been made in comparison with the baseline solution. The driving force behind the decrease in separation behaviour can be seen in Figure 121 that shows the static pressure variation at the inner corner. The augmentation in the static pressure field though the design changes made can be seen to substantially decrease the adverse pressure gradient when compared to that of the baseline solution, shown in Figure 77.

An adverse baffle-vane interaction around the second uppermost vane, seen in Figure 119, is shown in more detail in Figure 122. A low velocity ‘pocket’ was seen to develop on the inner side of the vane as a result of the limited baffle-vane spacing.

Velocity distortion was calculated at 9.3%, and reflected a substantial increase in flow quality downstream of the vane arrangement compared to the baseline solution (23.6%). The velocity profile along the distortion line is shown in Figure 123.

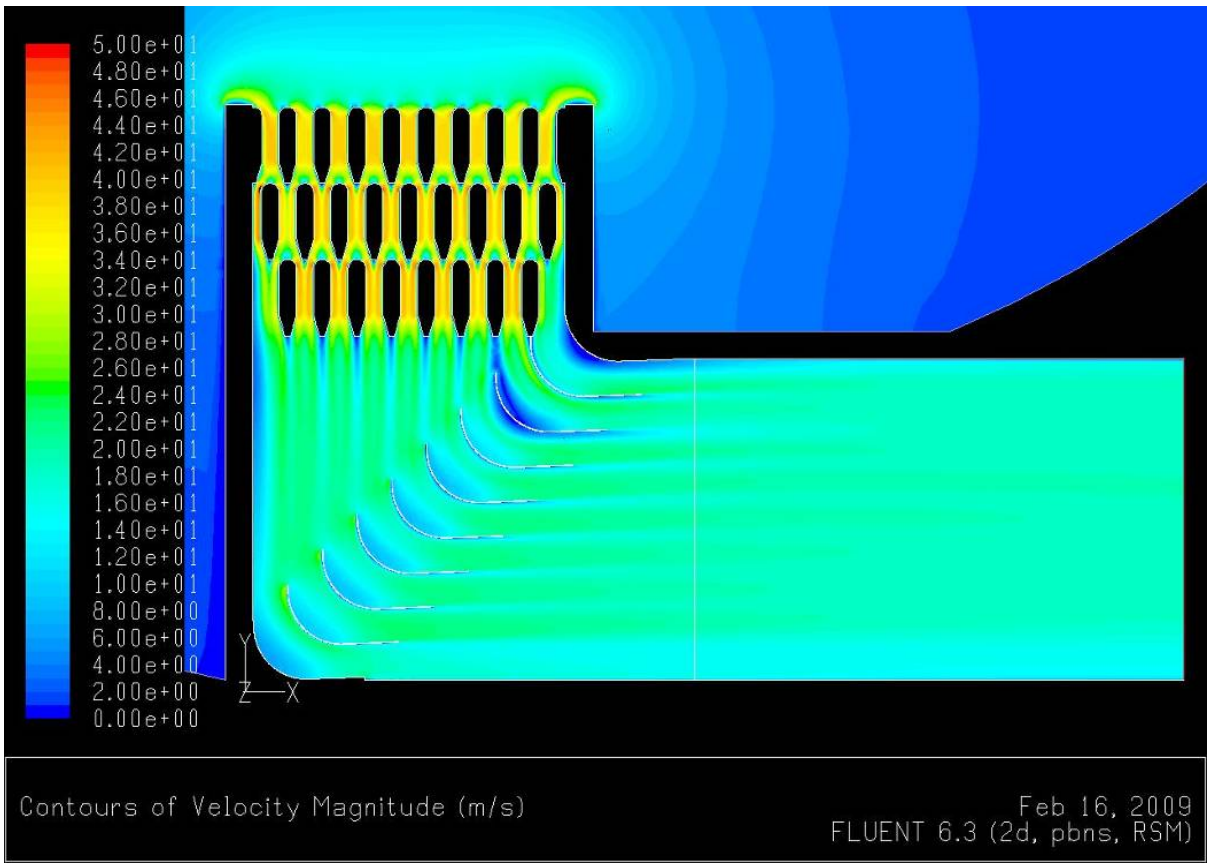

Figure 119 Velocity Magnitude in the Design of Figure 118a

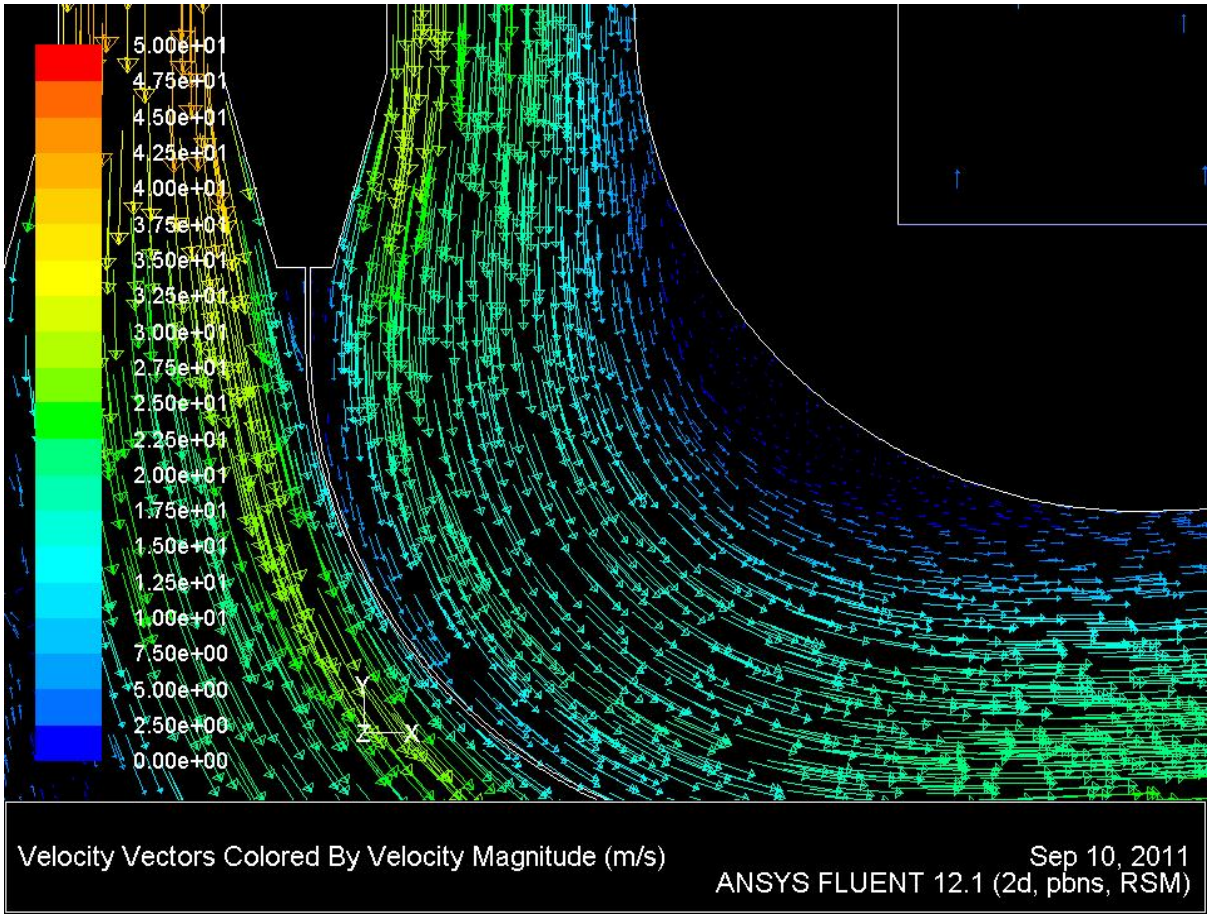

Figure 120 Separation Point at Inner Corner of the Design of Figure 118a

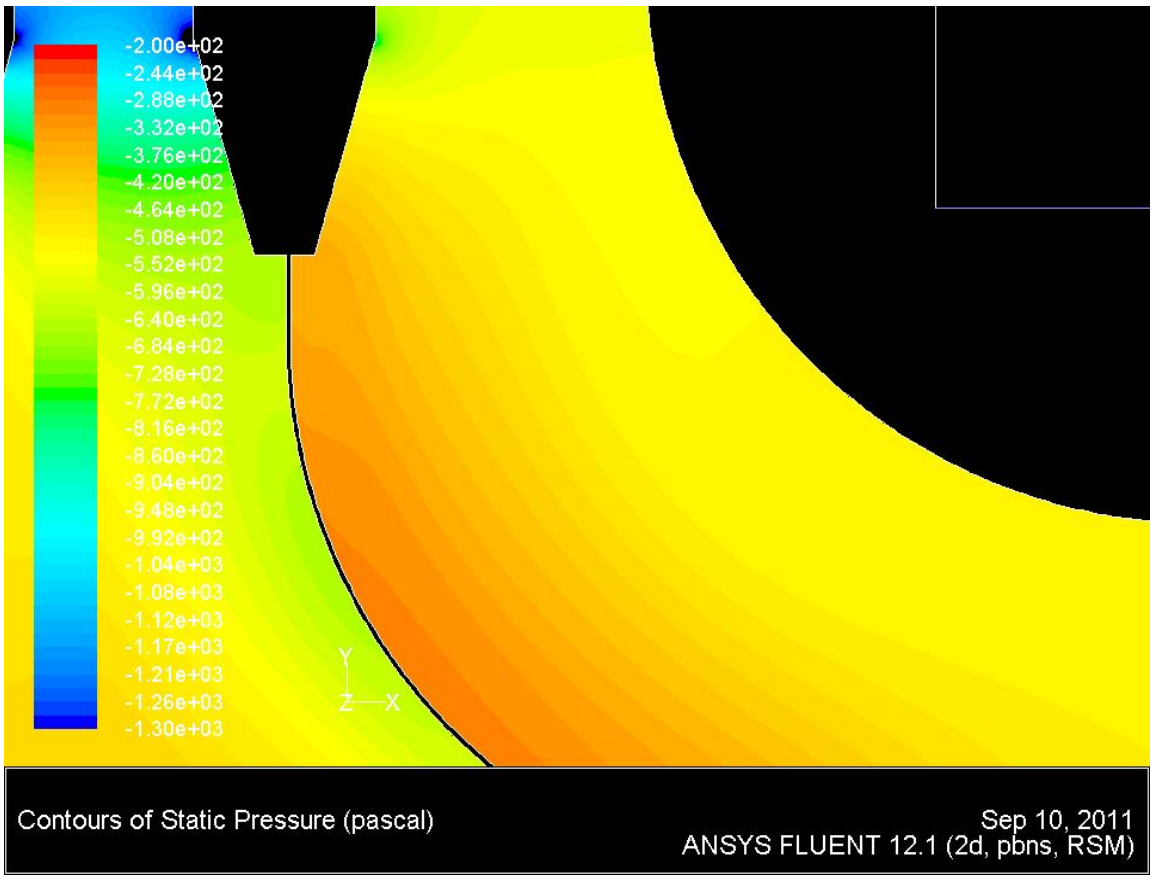

Figure 121 Static Pressure Variation at the Inner Corner of the Design of Figure 118a

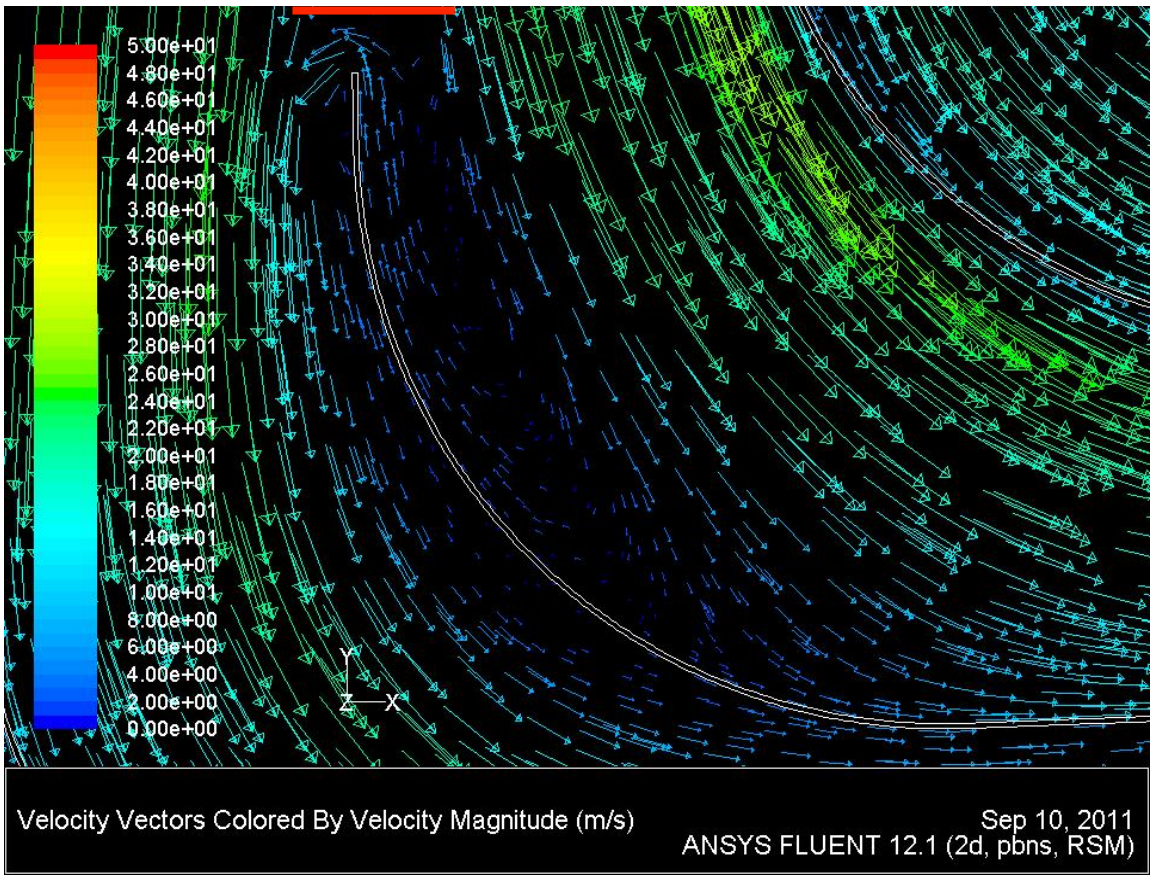

Figure 122 Low Velocity 'Pocket' Adjacent to Second Uppermost Turning-Vane in the Design of Figure 118a

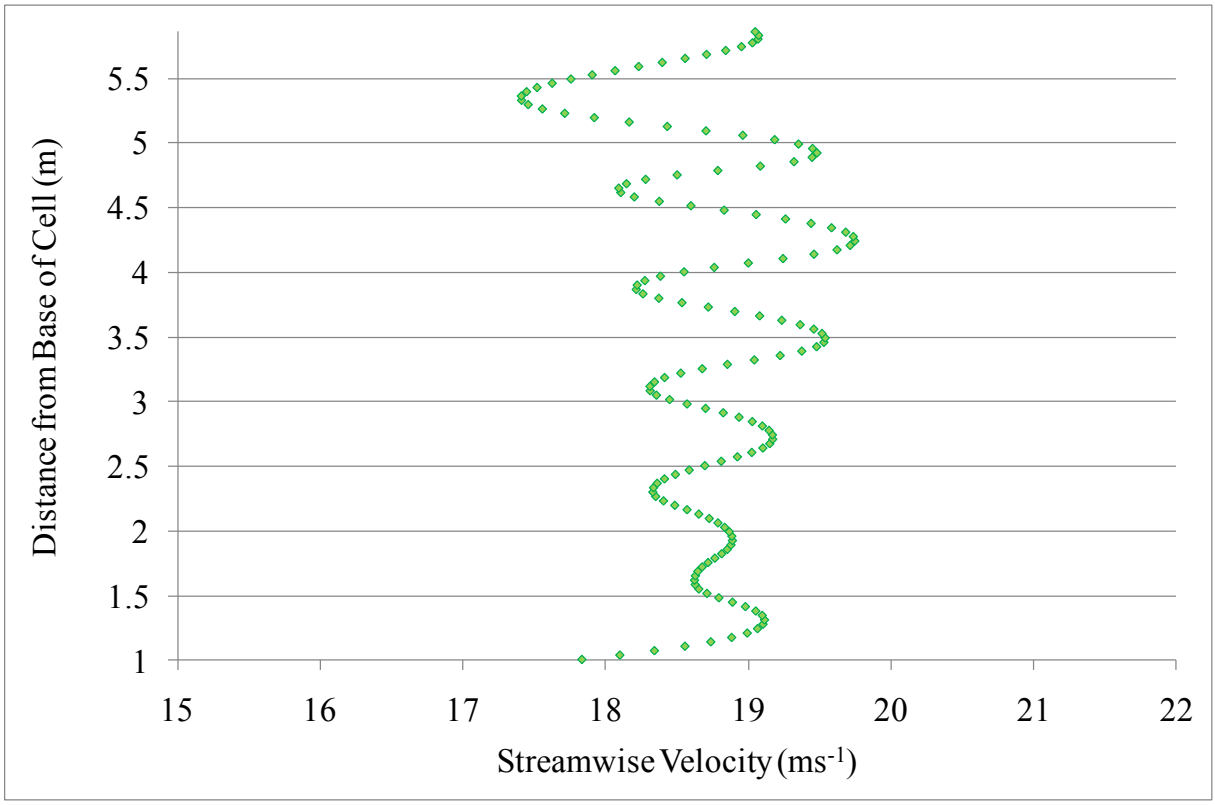

Figure 123 Stream-Wise Velocity Profile in the Design of Figure 118a

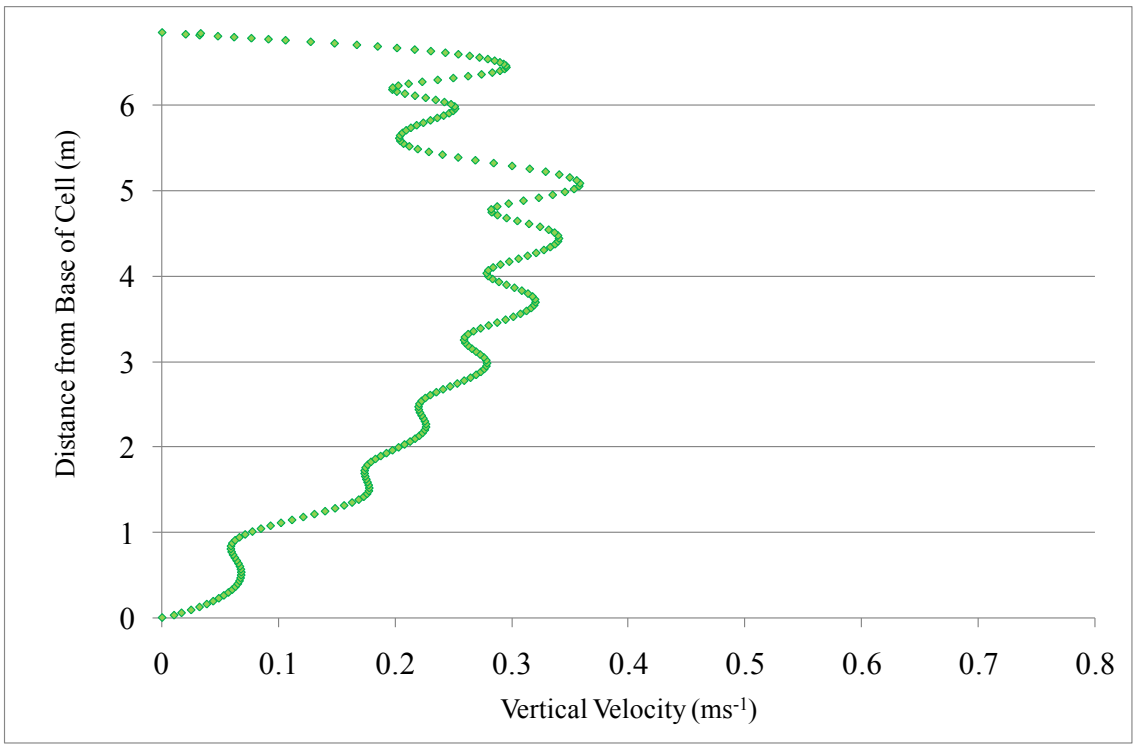

Figure 124 Vertical Velocity Profile along Extended Velocity Distortion Line in the Design of Figure 118a

The vertical velocity along an extended velocity distortion line is shown in Figure 124. Compared with the baseline solution (Figure 83) vertical velocity in the lower 75% has not been significantly

affected. However, due to the significant reduction of inner corner separation, a significant reduction in vertical velocity in the upper 25% of the cell is present.

Although not one of the objectives of the investigation of this section, it should be noted that cell efficiency was increased over the baseline solution. This was indicated by a 3.2% increase in average velocity at the 'Working Section Outlet' using the design of Figure 118a.

The successfully tested design of Figure 118a was altered slightly further to the form of Figure 118b. The design of Figure 118b introduced a staggering of the vane TE extension lengths. The extensions were reduced in equal increments from 1200mm on the uppermost vane, to 600mm on the lowermost vane. The use of staggered extensions was employed in an attempt to remove vane material, and therefore cost, from the arrangement without detrimental effects on flow quality. The findings of Section 4.3.4 suggested this could be successfully achieved.

A velocity contour plot of the solution to the domain of Figure 118b is presented in Figure 125. Velocity distortion remained unchanged at 9.3%, achieving the aim set. Figure 126 and Figure 127 compare the stream-wise and vertical velocity profiles along the velocity distortion plane for the domains of Figure 118a and Figure 118b.

Figure 126 shows that by staggering the TE lengths, the velocity distortion in the lower 50% of the cell, where the TE lengths were more significantly reduced, was improved marginally. In order not to disrupt the inner corner improvements made over the baseline design, further reduction in the length of the upper vanes in the arrangement was not performed, although it is believed there is scope for further 'fine-tuning' of the design to achieve further limited gains. Figure 127 shows that over-rotation was also marginally reduced by the staggering of the TE extensions.

Although only achieving marginal gains in flow quality over the design presented in Figure 118a, the design of Figure 118b did manage to do so with a lower material investment. A marginal 0.5% increase in average velocity (flow efficiency) at the 'Working Section Outlet' was also observed.

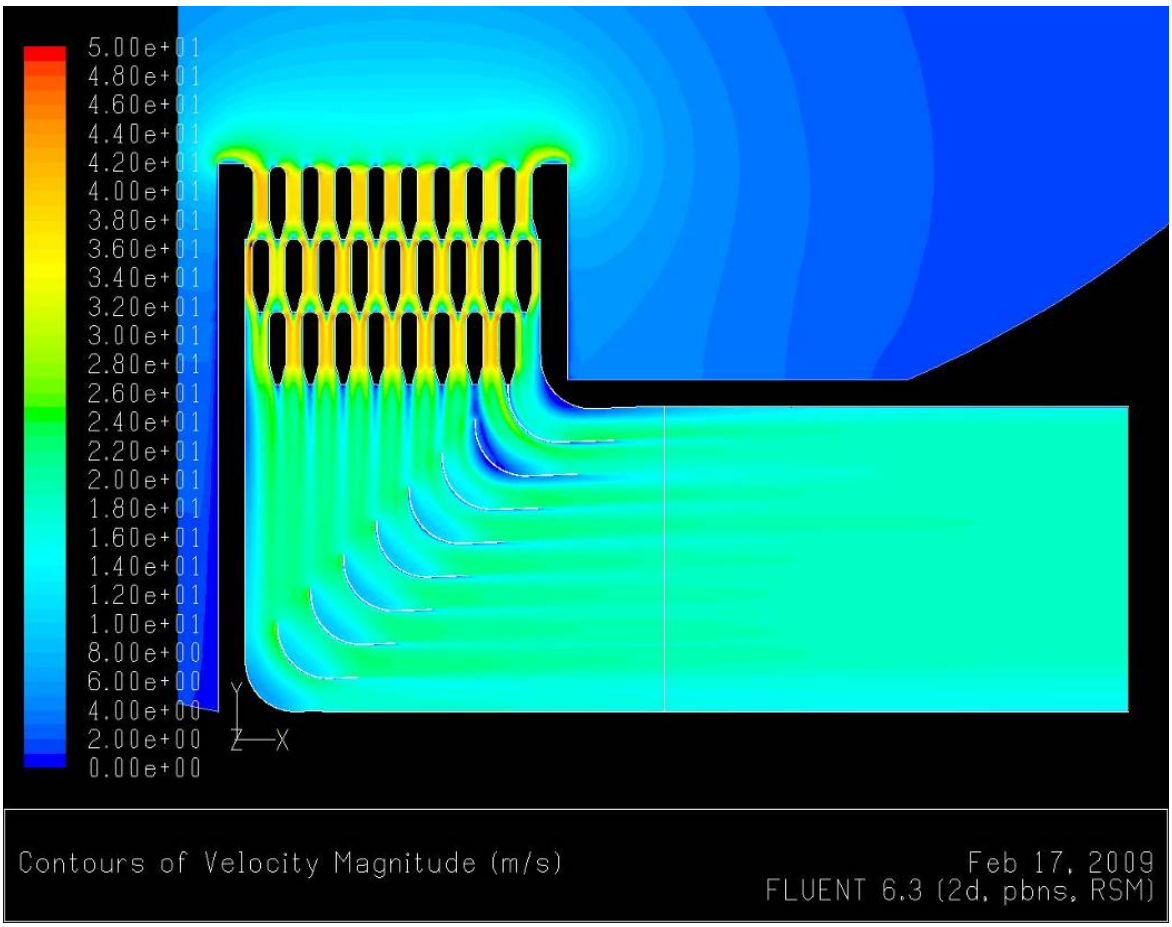

Figure 125 Velocity Magnitude in the Design of Figure 118b

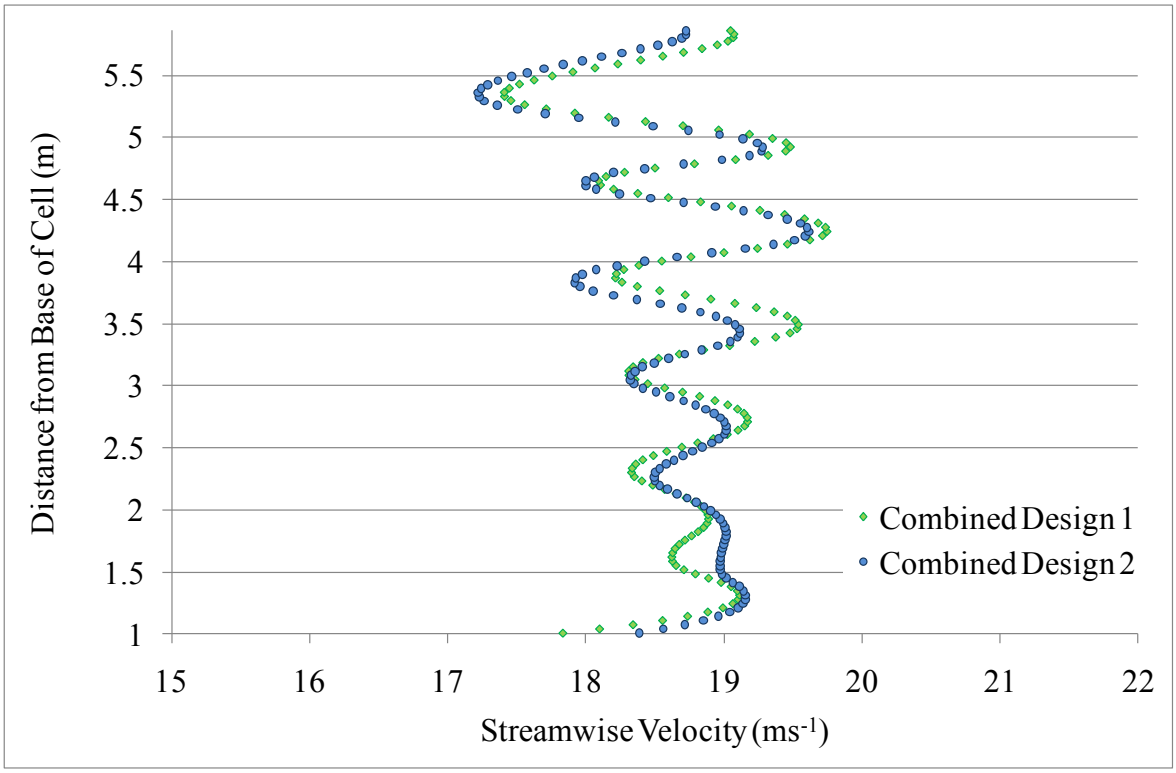

Figure 126 Comparison of Stream-Wise Velocity Profiles for the Designs of Figure 118a (green) and Figure 118b (blue)

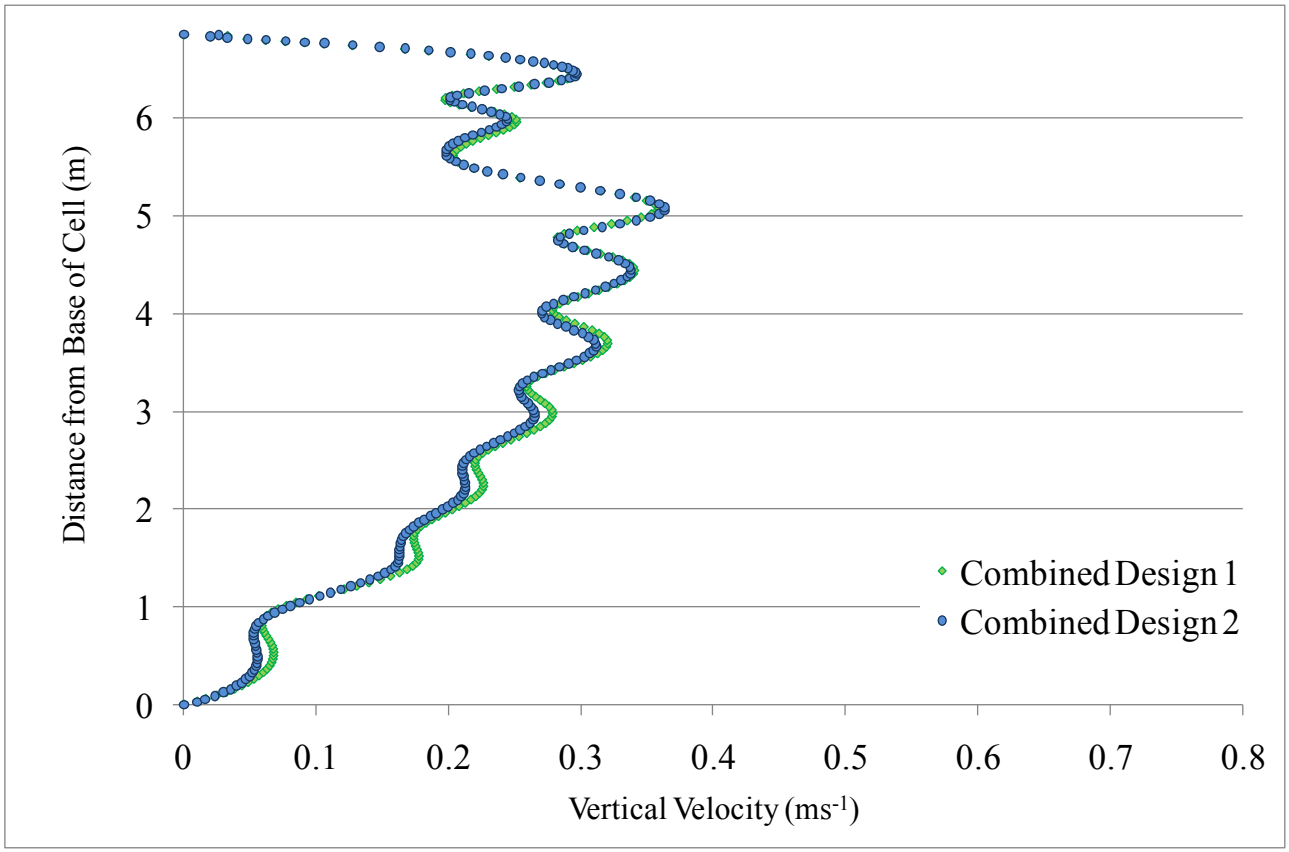

Figure 127 Comparison of Vertical Velocity Profiles along an Extended Velocity Distortion Line for the Designs of Figure 118a (green) and Figure 118b (blue)

4.4 Summary of Findings

A CFD analysis was performed on a JETC turning-vane arrangement in this section. As part of this analysis, validation was sought for the CFD techniques employed by (Agmen et al., 2005) in their analysis of the CHCEC turning-vane arrangement.

A computational domain was created to replicate the experimental setup of (Johl et al., 2007) in two dimensions. The settings of (Agmen et al., 2005) were then used in generating a computation solution for comparison with the experimental results of (Johl et al., 2007). The computational-experimental comparison was made between velocity profiles downstream of three- and four-vane arrangements within a test module containing a 90° corner.

Overall, a good level of agreement between the computational results and the experimental work was achieved. The highest levels of computational accuracy were achieved near the inner bend of the test module corner. In locating the vane wakes, in a direction perpendicular to the mainstream flow, the computational model managed to do so in all cases to within 2.2% of the test module width.

The rate of wake recovery appeared to be slightly over-predicted by the computational model. The largest deviation from the experimental results in prediction of the wake velocity magnitude occurred downstream of the outermost vane in the four-vane solution. In this case, 25mm downstream of the vane cascade, the velocity was experimentally measured to have recovered to 90% of the free-stream value. Computationally, this value was predicted to be 96%.

Therefore, both strong qualitatively and quantitatively comparative conclusions could be made using the solver settings of (Agmen et al., 2005) in a turning-vane analysis. However, it was felt that strict quantitative values would need to be extracted from the solutions with some caution.

The solver settings of (Agmen et al., 2005) were retained for the main body of the investigation. The CHCEC geometry was used to create a baseline turning-vane arrangement. This baseline arrangement was used to develop an understanding of the flow patterns present through and downstream of the cell component.

The main feature of the baseline solution was a large separation region at the inner corner. Three factors were determined as being responsible for the creation of this separation; (i) a flow channel expansion created between the stack wall and the innermost baffle on the lowermost row, (ii) a change in direction of the bounding surface at the inner corner, and (iii) a second flow channel expansion between the uppermost vane and the inner corner.

These factors all contributed to a substantial adverse pressure gradient at the inner corner, which led to the separation occurring. Downstream of the separation zone, a region of low velocity flow was created along the roof of the cell. This was identified as being a potentially dangerous sign in terms of aiding inlet vortex formation.

Separation/low velocity regions were observed along the underside of all vanes within the arrangement. These regions propagated downstream, and contributed to the 23.6% velocity distortion calculated. Qualitatively, the velocity profile exiting the arrangement was comparable to that presented by (Johl et al., 2007).

However, in making this comparison, it was found that the velocities at the base of the stack were lower than would be expected if the vanes had turned the flow by 90°. A plot of vertical velocity showed a positive upward component to the flow throughout the height of the cell. This indicated a flow over-rotation by the baseline arrangement.

An undesirable interaction between the baffle and vane arrangements was seen in the solutions as the baffle wakes propagated downstream. Due to the variation in spacing between the baffle and vanes, the greatest impact was observed in the upper portion of the vane arrangement.

An investigation was performed to gain a greater understanding of the baffle-vane interaction. The baseline six-vane arrangement had an inconsistent alignment with the lower row of baffles. This meant that the wakes from the baffles impacted each vane within the arrangement in an inconsistent manner.

Two domains were created to give vertical alignment between each vane and an overhead baffle. To do so, the number of the vanes in the arrangement was altered. The baseline arrangement was replaced with five- and nine- vane designs, respectively. The five-vane arrangement aligned a vane with every second baffle overhead. The nine-vane arrangement aligned a vane with every successive baffle overhead.

The five-vane design performed poorly in comparison with the baseline arrangement in four areas; (i) an exaggerated diffuser scenario was created at the inner corner, leading to an increase in inner corner separation, (ii) the outer corner became exposed, creating inefficient flow patterns, (iii) a significant low velocity ‘pocket’ was generated on the inner side of the second uppermost vane, and (iv) the size of the low velocity region on the underside of each vane was increased.

In combination, these four factors resulted in a significant jump in velocity distortion to 69.2%. Of the poorly performing aspects of the five-vane design, only the under-vane low-velocity regions were improved upon in the nine-vane arrangement.

The five- and nine-vane designs were then realigned. The realignment placed each vane in the arrangement vertically between adjacent baffles in the lowermost baffle row. This was termed ‘mid-baffle’ alignment. The five-vane domain produced comparable inner corner separation to the baseline solution. The improvement in flow quality, when compared with the baffle-aligned solution, was a result of; (i) reduction in inner corner separation, (ii) a significant reduction in the magnitude of the under-vane low velocity regions, and (iii) an isolation of the outer corner.

The reduction in the under-vane low velocity was directly a result of the improved baffle-vane interaction. This improvement was evident in comparison with both the baseline and baffle-aligned

solutions. An improvement in velocity distortion to 16.7% in the five-vane arrangement provided quantitative affirmation of this observation.

The solution to the nine-vane mid-baffle-aligned arrangement qualitatively showed similar improvements over its baffle-aligned counterpart. A velocity distortion of 12.3% was calculated. (Pope & Rae, 1984) discusses that the flow quality downstream of a vane arrangement can be achieved by improving the gap-chord ratio. This appears to have occurred through a reduction of the ratio from 0.59 in the five-vane case, to 0.32 in the nine-vane case.

Over-rotation of the flow was observed in the baseline solution. An investigation was performed to determine whether a decrease in the length of the TE extensions would reduce this over-rotation. Of additional interest during the investigation was the effect of the extensions on flow quality. Specifically, it was of interest to determine whether the same flow quality could be retained with a lower material investment in the arrangement.

A transient flow pattern was seen to develop from the underside of the uppermost vane as the TE length was increased. The transient nature of the solutions led to inconsistencies in quantitative comparisons over the original velocity distortion line. Velocity distortion was calculated over a limited line, where steady state behaviour was shown to be present. Over this limited line, a steady decrease in distortion was seen with a reduction in TE length. With a length of 1800mm, distortion of 26.4% was calculated. This compared to a distortion of 10.6% with a 600mm length.

The over-rotation of flow was reduced significantly with the reduction in TE length. However, this had an unforeseen negative side effect. When the TE length was reduced on the upper vanes, the reduction in over-rotation meant the low velocity zone downstream of the inner corner separation, became larger. This was a result of less mixing between with the higher velocity over-rotated flow when the TE lengths were shortened. The shorter TE length solutions also showed more concentrated regions of low velocity forming on the underside of the vanes.
Focus was then placed on reducing the separation region at the inner corner. The implications of varying the inner corner radius were investigated. The radius was increased in a number of 200mm increments, from its baseline value of 600mm, up to 1200mm. In theory, the increase in radius was applied to reduce the severity of the change in direction at the inner corner, thus reducing the adverse pressure gradient.

However, as the radius was increased, separation occurred further upstream along the inner corner. This was found to be a result of the upper portion of the inner corner becoming more closely aligned with the innermost baffle when the radius was increased. In doing this, the tapering downstream face of the innermost baffle combined with the inner corner curvature to create an increase in the severity of the diffuser geometry adjacent to the baffle.

Whilst increasing the radius did result in earlier and more significant separation, a marginal reduction in the downstream extent of the associated low velocity zone was detected. The reason for this was thought to be the geometry change in the channel between the upper-vane and the inner corner. With an upper-vane radius of 1153mm, the channel created between the vane and the upper corner expanded with a 600mm inner corner radius. With a 1200mm radius, the channel became mildly contracting.

With a lack of success found by modifying the inner corner, the design of the vane arrangement was altered to reduce inner corner separation. The lean angle of the baseline vane arrangement was modified to intersect the LE of the upper-vane with the second innermost baffle. This created a contracting channel between the upper-vane and the inner corner.

The adverse pressure gradient was removed, along with all separation behaviour at the inner corner. An unforeseen by-product of the realignment was a reduction in the over-rotation of the flow. Close analysis of the refined geometry found that a slight overlap was created between successive curved vane rows. Therefore, less ‘turning-power’ was provided by the arrangement. Also as a result, the under-vane low velocity was more significant than in the baseline solution. A velocity distortion of 19.5% was achieved.

As mentioned above, the removal of inner corner separation was achieved by creating a sizable contraction through the inner corner flow channel. The result of this was an inconsistency of the flow channels throughout the vane arrangement as a whole. This led to the introduction of flow features that negatively affected velocity distortion. To retain the contraction at the inner corner, whilst providing consistent flow channels, the following design was developed. A nine-vane mid-baffle-aligned arrangement was combined with an increase in vane angle, and an increase in inner corner radius to 1153mm.

A significant reduction of inner corner separation over the baseline solution was achieved. However, separation was not entirely removed. The more consistent spacing of the flow channels and the increased 'turning power' of the arrangement reduced distortion to 16.6%.

The positive findings of the investigations performed prior to this point were combined into a single domain. A nine-vane, mid-baffle-aligned arrangement, with an increased vane angle was used. The original baffle arrangement was then modified to swap the layout of the inner row with that of the outer rows, and vice-versa. On the new lower row, the outermost half-baffles were removed. The inner corner radius was also increased to 1153mm. This created a sizable inner corner flow channel contraction, along with consistent vane channels throughout the arrangement.

Minimal inner corner separation was achieved with this combined element design. This, combined with the consistency of the flow channels, reduced velocity distortion to 9.3%: the lowest value calculated in the investigation. A second combined element design, based on the first, reduced the length of the TEs in a staggered manner. The TE lengths were staggered from 1200mm on the uppermost vane, to 600mm on the lowermost vane. The reduction in material investment this modification would allow did not detrimentally affect flow quality in any manner. On the contrary, a velocity distortion of 9.3% was retained from the previous design, whilst a slight reduction in over-rotation was achieved along with a slight increase in flow efficiency.

The main findings of the turning-vane investigation were that the baffle-vane interaction significantly contributes to velocity distortion downstream of the vane arrangement. When the baffle and vane arrangements were designed in consideration of one another, significant reductions in velocity distortion and flow patterns that could lead to vortex formation were made. A mid-baffle-aligned arrangement provided more consistent flow patterns than a baffle-aligned arrangement. This, in turn, led to increased flow quality.

5 Working Section and Augmenter Transition – Cell Efficiency

5.1 Background Information

5.1.1 Working Section and Engine Mounting

The working section of a JETC in most cases consists of a rectangular cross-sectioned concrete shell housing engine support, maintenance, control, and DACQ components. The downstream end of the working section terminates with a wall containing the augmenter tube entrance. Figure 128 shows the structure of the working section in the CHCEC cell.

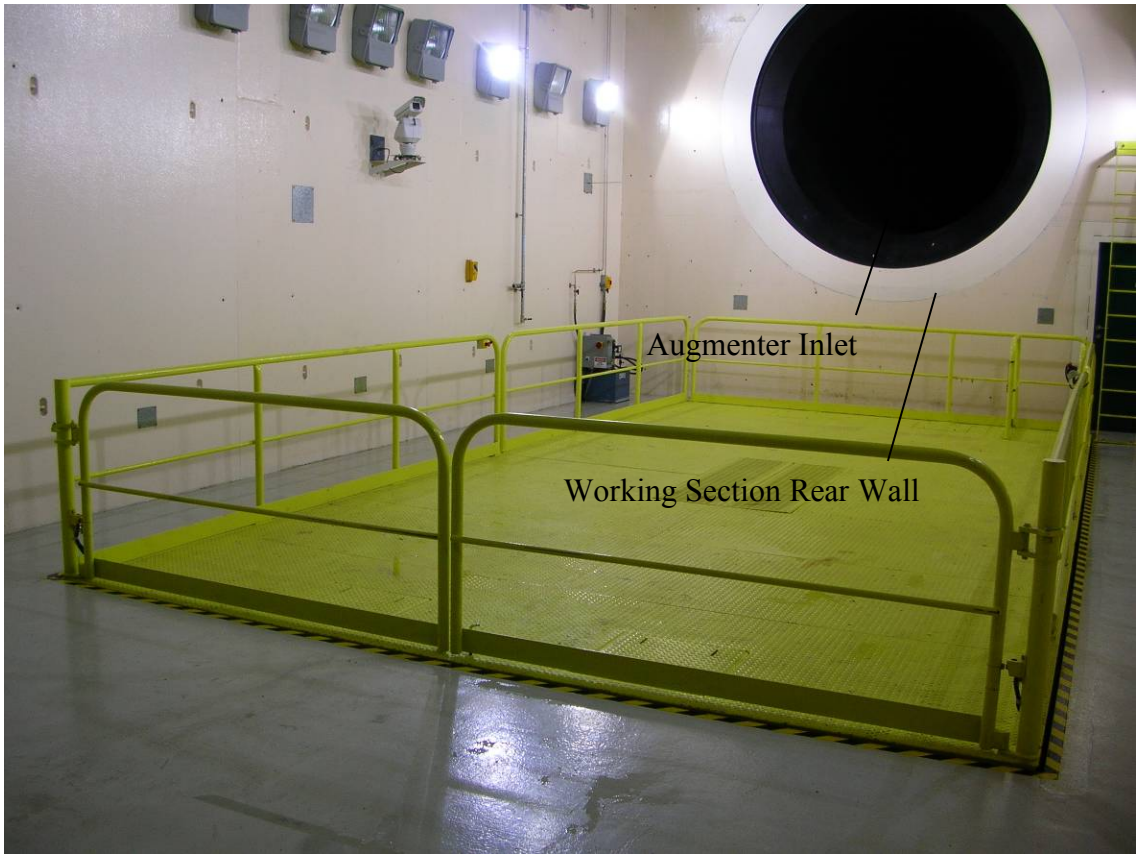

Figure 128 Downstream End of the CHCEC Working Section

A thrust-bed and engine adapter, shown in Figure 129 and Figure 130 respectively, support and locate the engine within the cell. Engine adapters are used as an interface between the engine and thrust-bed. Engine adapters are individually designed for each specific test cell and engine make and model combination. As a result variation exists in the stream-wise mounting position between the range of engines tested within a given cell. Figure 8 showed the thrust-bed, engine adapter, and engine (with dress kit) supported in the CHCEC working section during testing.

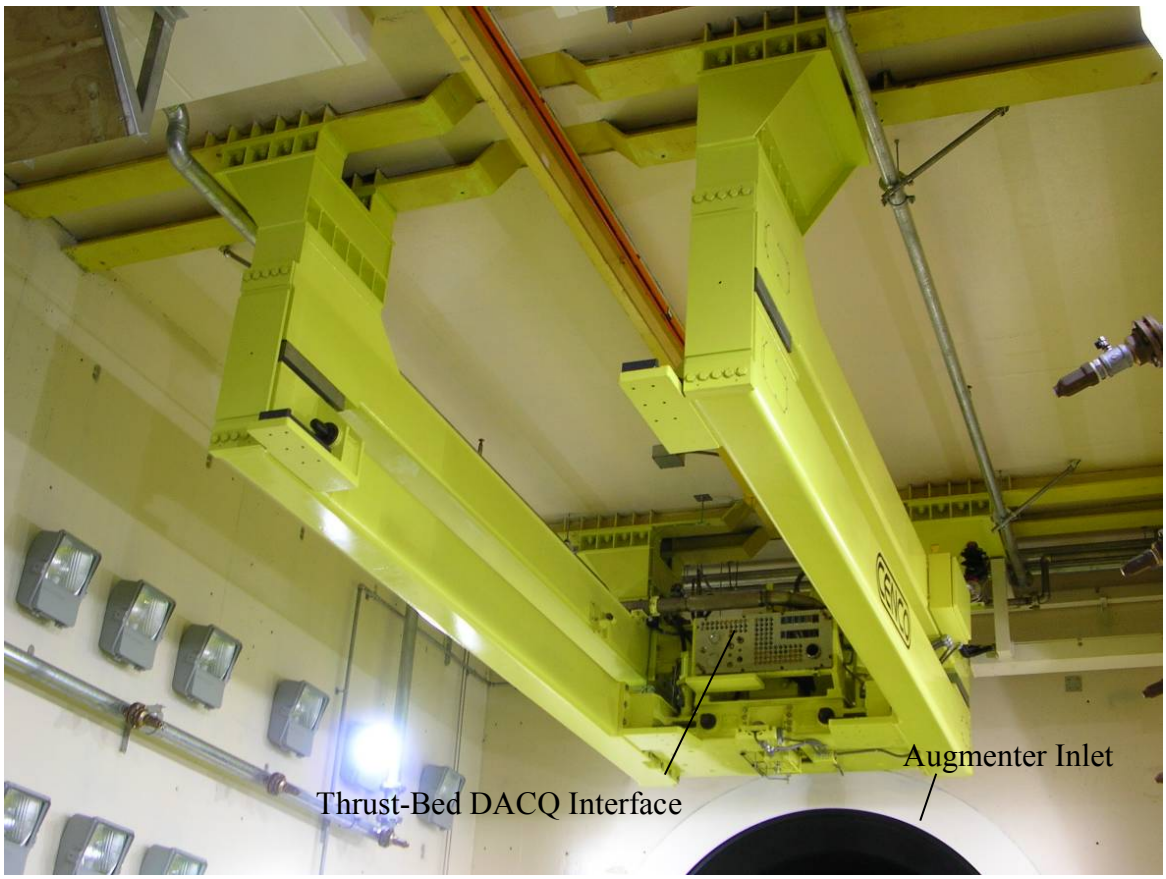

Figure 129 Roof-Mounted Thrust-Bed in the CHCEC Working Section

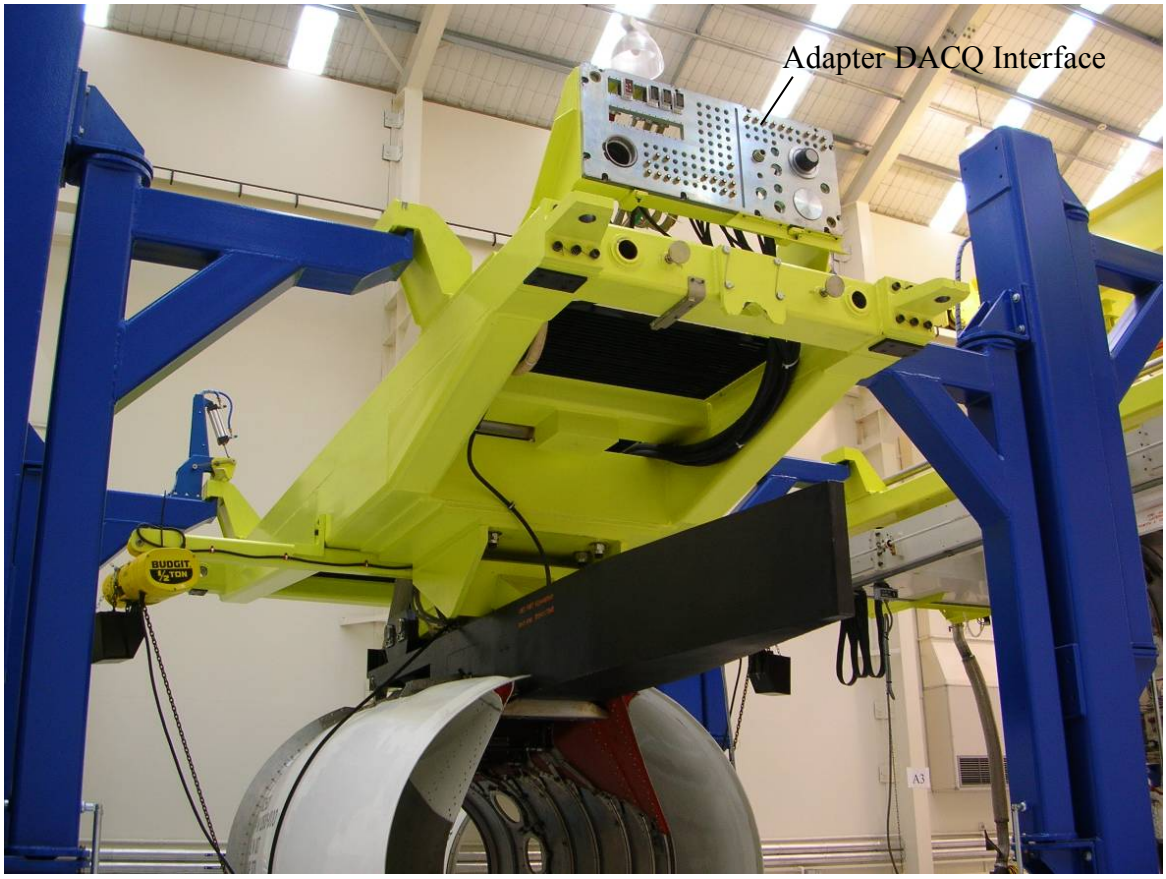

Figure 130 A CHCEC Maintenance Stand (blue) supporting an Engine Adapter (yellow) connected to an Engine Dress-Kit (white and black)

5.1.2 Working Section and Augmenter Transition Flow

The working section of a test cell is essentially a large rectangular duct. The flow and pressure losses through a rectangular duct are well understood in the literature. (Idelchik & Fried, 1986) provides comprehensive tabulated pressure loss coefficients for duct flows of varying Re, flow profile, wall roughness and cross-section.

The transition between the working section and augmenter tube (called the 'augmenter transition' from this point on) is essentially an abruptly contracting duct. Again, the literature provides a good understanding of contracting ducts, and (Idelchik & Fried, 1986) provides tabulated pressure loss coefficients for a selection of contracting duct cases. However, most of the literature focuses on contractions between identical cross-sectional profiles. Comparatively little is presented in relation to square ducts contracting into circular ducts, particularly in an abrupt manner, as is the case in a test cell.

Both (Idelchik & Fried, 1986) and (Massey, 2001) discuss the phenomenon of a sudden contraction in a pipe or circular duct as being similar to that observed when shock losses occur during a sudden expansion. As illustrated in Figure 131, a vena-contracta is formed downstream of the contraction junction. Eddies form between the vena-contracta and the wall of the pipe, downstream of which the stream widens again to fill the cross-section. Both (Idelchik & Fried, 1986) and (Massey, 2001) also state that significant reductions in pressure loss at the contraction can be achieved through the use of a tapered or bell-mouth entry in which the energy-dissipating eddies of the vena-contracta become removed and/or reduced.

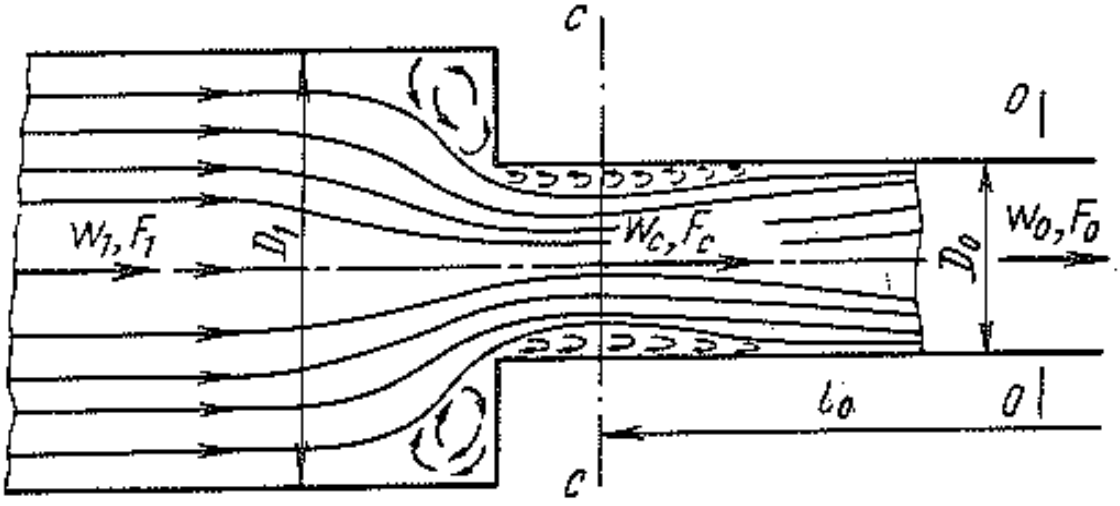

Figure 131 Flow Pattern in a Abruptly Contracting Circular Duct (Source: (Idelchik & Fried, 1986))

Although the flow in ducts and through contractions is relatively well understood, the scenario when a flow driving jet engine is placed immediately upstream of a flow contraction is not so well understood.

5.2 Working Section Analysis Methodology

As discussed above, little understanding is available of a jet engine placed in a ducted flow immediately upstream of an abrupt contraction. An investigation into the flow patterns in rear of a JETC working section was performed in order to generate some understanding. The broader aim of the investigation was to analyse the application of CFD techniques to a region of JETC geometry under operational conditions. More specifically, the investigation sought to:

- Apply recommendations from the literature along with sound reasoning to set up and generate a CFD solution;
- Gain an understanding of the flow patterns and features in the rear of a typical JETC working section;
- Provide computational solutions to contribute one of the two parts (the other being experimental data) required for a problem-specific validation of the CFD techniques used;
- Qualitatively assess the accuracy of computational solutions produced for physical realism;
- Conduct a CFD-aided design process as an assessment of capability of CFD as a design and problem solving tool; and
- Use increased cell efficiency, and the associated benefits it brings, as the driving force behind the design process.

The remainder of this section discusses the methodology employed in performing this investigation.

To gain a basic understanding of the flow features present in an operational working section and augmenter transition, a baseline computational domain was created. The domain was designed to represent a simplified working section, upon which a CFD investigation could be performed upon. The design of the baseline domain is discussed in Section 5.2.1.1. The computational settings used to perform the analysis were then selected. These are presented in Section 5.2.1.2 and Section 5.2.1.3. The computational domain was then meshed, and a mesh independence check performed. These processes are discussed in Section 5.2.1.4. A qualitative validation of the computational settings discussed in Section 5.2.1 is then presented in Section 5.2.1.5.

A solution to the baseline domain was generated and analysed. These results are presented in Section 5.3.1. A CFD-aided investigation and design process was then performed with the aim of improving the flow efficiency in the rear of the working section. Section 5.3.2 and Section 5.3.3 present investigations looking at the interaction of the working section components in terms of contribution to cell efficiency. Section 5.3.4 then evaluates a 'retrofitable' solution for improving airflow efficiency within the working section and augmenter transition.

5.2.1 Computational Settings

This section discusses the computational settings used in the working section analysis.

5.2.1.1 Computational Domain

A three-dimensional computational domain was used, as a square-to-circular transition could not be accurately replicated in two dimensions. The computational domain used a working section 10m wide and of square cross-section. The 10m width was set to maintain comparability with the analysis of Section 3, and represented a 'mid-sized' test cell by industry standards. Section 3 discussed the selection of a 'mid-sized' cell in more detail.

The computational domain was extended from a 'Cell Inlet' BC through to an 'Augmenter Outlet' BC as shown in Figure 132. The working section contained a Rolls-Royce Trent 500 engine, the dimensions of which are shown in Figure 133. As discussed in section 3, a Trent 500 engine represents a 'mid-sized' jet engine, and was chosen for this as it is the likely-sized engine to be tested in a 10m wide cell. The engine inlet face was aligned with the horizontal and vertical midpoints of the cell.

As stated earlier in this section, the rear of the working section, and its transition to the augmenter tube, was the area of interest for the investigation. It was felt these features could be analysed more accurately when isolated from other features that could potentially affect the flow pattern. Therefore, no influences from upstream cell components were included, nor were any wall mounted working section components. These model simplifications also allowed a more general applicability of the results, as many cell components vary in design and integration throughout the industry.

The working section length was set at 20m to allow stream-wise variation of the engine position throughout the investigation. The solutions of (Agmen et al., 2005) suggested that the engine inlet

stream-tube would have an adequate length to develop between the 'Working Section Inlet' and engine inlet with this length of working section.

The augmenter diameter was set at 3.75m to maintain comparability with the CHCEC ratio of cell height (6.858m) to augmenter diameter (2.951m). The entrance to the augmenter was set 4.15m downstream of the engine core exhaust face. This maintained approximate comparability with the ratio of augmenter diameter to engine-augmenter spacing in the CHCEC cell with an IAE V2500 installed. Also, as per the CHCEC cell, a two-stage tapering lip was used around the perimeter of the augmenter entrance.

In setting the length of the augmenter tube, (Idelchik & Fried, 1986) and (Francis, 1975) were referred to. The major flow inefficiency in an abruptly contracting duct scenario is discussed as being the vena-contracta. Therefore, it was important that the length of the augmenter tube in the computational domain would allow a vena-contracta to form if the correct geometry and flow conditions were applied. The augmenter tube was set at a length of 10m, 2.7 augmenter diameters downstream. This was predicted to be an adequate length to contain the significant augmenter entrance flow patterns. This prediction was checked in Section 5.2.1.5.

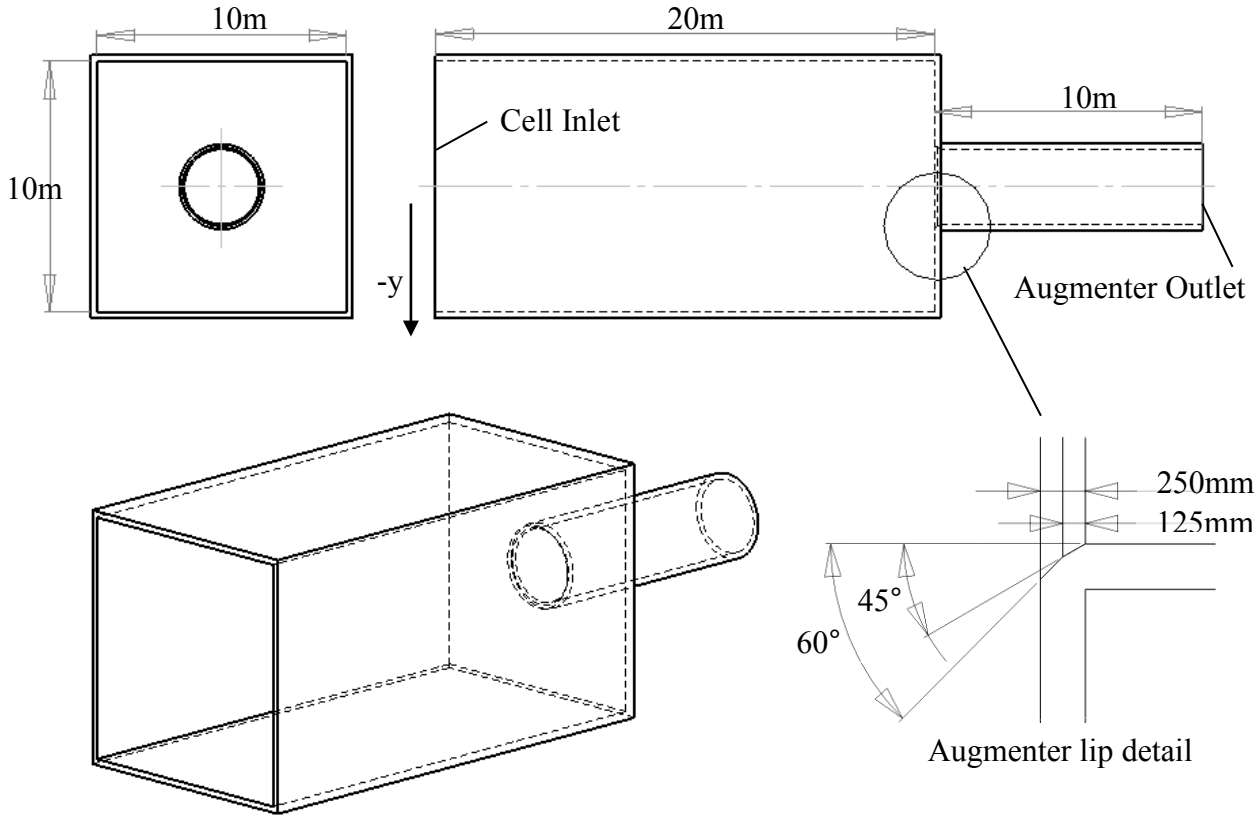

Figure 132 Computational Domain of the Rear of the Working Section

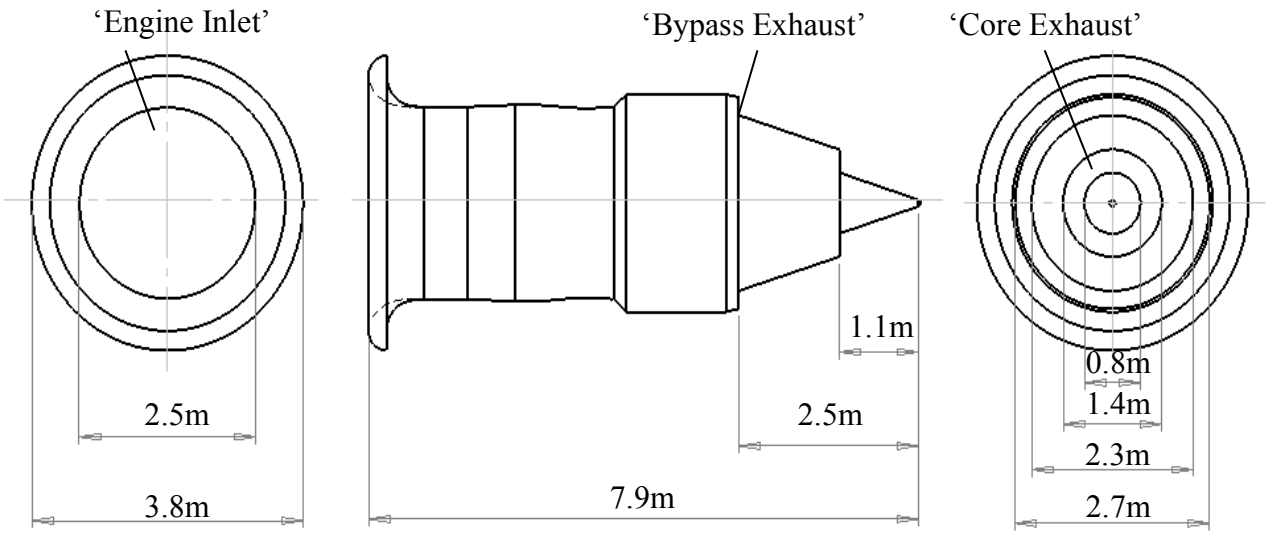

Figure 133 Geometry of a Rolls-Royce Trent 500 with Bell-Mouth and Engine Testing Dress-Kit

The computational domain was dissected along a vertical stream-wise plane running through the centre of the cell. Half of the cell was removed and a symmetry plane placed across the dissection face. Taking advantage of the symmetry of the solution enabled greater mesh density in the remainder of the computational domain and a decrease in solution time.

5.2.1.2 Solver Settings

The fluid modelled within the computational domain was selected to be air. Based on the MFR and geometry of the engine, the velocity at the 'Bypass Exhaust' was expected to reach a Mach number of between 0.8 and 0.9. Therefore, compressibility effects needed to be accounted for. Therefore, air density was modelled by the ideal gas equation, and viscosity using the Sutherland three-coefficient model. Both of these are discussed in (Fluent, 2006). Accounting for compressibility meant the energy equation was used. This required additional thermal BCs to be accounted for, which are discussed in Section 5.2.1.3.

The materials used in the CHCEC working section were the same as those discussed in Section 3, relating to the inlet stack. A K_S of 0m was retained for all working section walls. The engine bell-mouth and cowlings were also modelled as smoothed surface, with a K_S of 0m. This decision was based on similar bell-mouths and cowlings observed at the CHCEC. Augmenter tubes are generally constructed of a round steel tube, with no surface treatment that would add any additional texture or wall roughness features. For this investigation, the augmenter surface was also modelled with a K_S of 0m.

A first-order spatial discretisation scheme and SIMPLE pressure-velocity coupling was chosen. The decision to use these was based on the same arguments presented in Section 3. A steady-state solver was used as no areas of transient flow were predicted. This was based on the intended application of steady state BCs, and the lack of features in the computational domain that would likely create vortex shedding, or similar time dependent flow patterns.

As in Section 3, the k-ω SST turbulence model was used in the working section analysis. The main determining factor in the selection of the k-ω SST model, over the other two-equation models, was the more general applicability of the solution. This was deemed important due to the number of flow features predicted to be generated. Of particular importance to solution accuracy was the prediction of separation at the augmenter entrance, a flow pattern well predicted by the k-ω SST model. In addition, both two-equation models contributing to the k-ω SST model have had proven success in the prediction of jet expansions (Fluent, 2006; Wilcox, 1988).

Of the other options available, the SA model was discarded as it has been specifically proven as a poor performer in the spreading rate of jets. The RSM was discounted based on the three factors discussed in Section 2.4; (i) the comparative lack of validation, (ii) the lack of improved performance over the k-ε model in the prediction of jets and spreading rates, and (iii) the substantial increase in computational expense over the two-equation models. Given that improved accuracy was unlikely to be obtained, the additional computational expense was not justified.

To assess solution convergence, the residuals of continuity, x, y, and z velocity, k, ω, and energy were monitored. The convergence criterion for the solution was based on the reduction of these residuals, scaled in relation to those produced in the first-solution iteration. For all but the energy residual, the criterion was 1.0E-04. For the energy residual, the criterion was decreased to 1.0E-06 as per the recommendations of (Fluent, 2006).

The MFRs at all BCs were also monitored throughout the solution process. A further convergence criterion applied was that these MFRs needed to be seen to be oscillating within 0.001kgs^{-1} about a constant value to ensure solution iteration independence and that a steady-state solution had been reached.

5.2.1.3 Boundary Conditions

BCs were applied at the 'Working Section Inlet', 'Engine Inlet', 'Bypass Exhaust', 'Core Exhaust' and the 'Augmenter Outlet' as shown in Figure 132 and Figure 133. The driving force of the flow through the domain was the engine.

The 'Engine Inlet' was modelled as a pressure outlet with a target MFR. The static pressure at 'Engine Inlet' was initially estimated at -70000Pa based on the work of (Agmen et al., 2005). A target MFR was set at 860kgs^{-1} (Rolls-Royce, 2009). The pressure initially approximated at the 'Engine Inlet' adjusted itself each iteration to meet a target MFR during the solution process.

Being a high bypass engine, the Trent 500 has both bypass and core exhaust faces. The engine BPR of 7.6 was used to calculate the MFR for the 'Bypass Exhaust' and 'Core Exhaust' at 760kgs^{-1} and 100kgs^{-1} respectively (Rolls-Royce, 2009). Turbulence BCs were approximated as data relating to the turbulence of the engine outlet flow were unable to be obtained. The initial goal of this project planned to gather such data for the setting of BCs, but due to withdrawal of interest and support from the CHCEC this goal could not be met.

The flow exiting the engine was thought likely to be of high turbulence due to the mixing and interaction with internal engine components. The recommendations of (Fluent, 2006) were used, and TI set at 10% for both the 'Bypass Exhaust' and 'Core Exhaust' as a reflection of 'high' turbulence.

The TLSs were approximated based on the sizes of respective 'Bypass Exhaust' and 'Core Exhaust' faces. (Fluent, 2006) suggests that the maximum length scale cannot be any larger than the duct itself. The 'Bypass Exhaust' and 'Core Exhaust' are shown in Figure 133, and effectively represent rings with a width of 0.2m and 0.3m respectively. Due to the predicted highly turbulent state, the TLSs were set at the maximum achievable values of 0.4m and 0.9m for the 'Bypass Exhaust' and 'Core Exhaust'.

Thermal BCs at the 'Bypass Exhaust' and 'Core Exhaust' also required approximation. The 'Core Exhaust' was predicted to be of high relative temperature due to being immediately downstream of a combustion process. The 'Core Exhaust' temperature was set using the data obtained by (Agmen et al., 2005) for the exhaust temperature of an IAE V2500 during operation, 475K.

The ‘Bypass Exhaust’ was expected to be of substantially lower temperature than the ‘Core Exhaust’ as the flow upstream had not gone through a combustion process. However, the temperature was expected to be greater than that of the flow entering the engine due to heat exchange occurring inside the engine cowlings. The flow entering the engine was estimated as being equivalent to that of the surrounding atmosphere, and was approximated as 288K, to align with the ICAO standard day parameters. Thus, the ‘Bypass Exhaust’ was estimated to be 310K in temperature.

The ‘Working Section Inlet’ and ‘Augmenter Outlet’ were set as a pressure inlet and pressure outlet respectively. The levels of pressure were set so as to represent the drop in pressure between the inlet BC and the outlet BC. As the other BCs were MFR driven, it was deemed the pressure difference between the two BCs would be of importance, as opposed to the absolute pressure values. The ‘Working Section Inlet’ was set at a total pressure of 1000Pa, and the ‘Augmenter Outlet’ as a static pressure of 0Pa in an attempt to represent this pressure drop. Retrospectively, this pressure drop appears to have been too low, and thus became a limiting factor in the investigation, as discussed in Section 5.3.2.

As discussed in Section 5.2.1.1, it was intended that the working section be analysed in isolation from the remainder of upstream cell features. Therefore the turbulence levels at the ‘Working Section Inlet’ were set to reflect such a scenario. The TLS at the ‘Working Section Inlet’ was based on a fully developed duct flow being present. The recommendation of (Fluent, 2006) was used, and the TLS was assigned a value 7% of the duct width, 0.7m. The TI was also set at a low level, 1%, to reflect a fully developed duct flow being present upstream. The temperature at the ‘Working Section Inlet’ was set to represent an ICAO standard day condition of 288K.

5.2.1.4 Mesh and Mesh Independence Check

The computational domain was broken into zones so that a variety of element types could be utilised. The zones were divided as shown in Figure 134. The density of mesh elements was increased in the areas surrounding the smaller geometries of the engine, and along the borders of the predicted stream-tubes of the core and bypass exhausts. Sizing functions were used to blend the areas of high element density with those of lower mesh density in the upstream region of the working section and the downstream region of the augmenter tube.

In the upstream region of the working section, and along the working section borders, hexagonal elements were used. These areas were predicted to contain flow of low complexity that was aligned with the working section walls. Hexagonal elements perform well when aligned with the flow and combine efficiently to minimise element numbers and computational storage expense (Fluent, 2006).

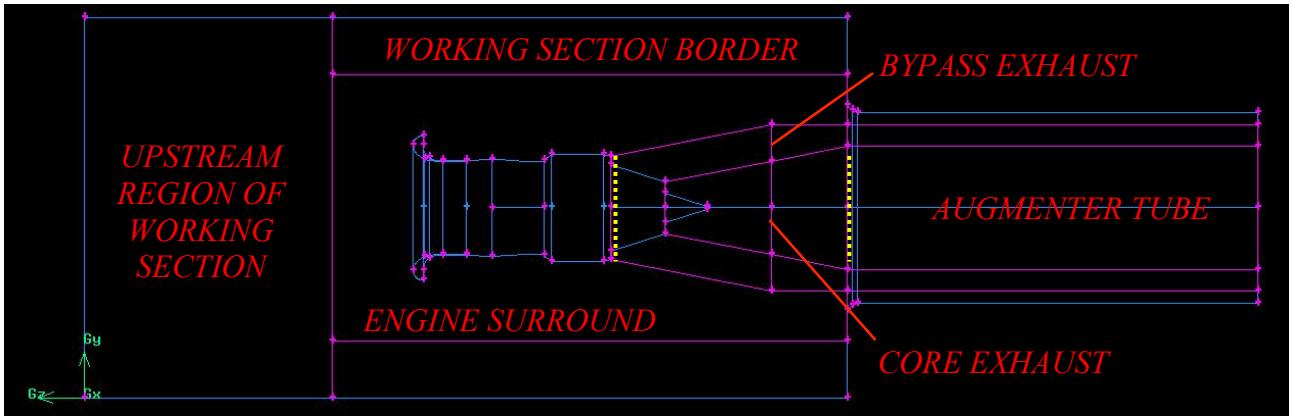

Figure 134 Zones of the Computational Domain used for Mesh Control

The engine surround, core exhaust and bypass exhaust zones were meshed with tetrahedral elements due to the complexity of the geometry and flow near the engine (Fluent, 2006). The augmenter zone was meshed with wedge elements. Wedge elements were used as they were able to be aligned with the flow in the augmenter tube whilst providing a satisfactory interface with the upstream zones. Figure 135 shows the distribution of the mesh density and the element types used.

An initial mesh using 3.49E05 elements was developed. A computational solution was generated using the BCs and solver settings described in Section 5.2.1.3 and Section 5.2.1.2. To perform a check of mesh independence, the mesh density was retained and successive mesh iterations using 5.07E05, 6.52E05, and 8.14E05 elements were created and solutions produced for each. A number of the objectives of the investigation in this section were based around determining cell efficiency. Therefore, as a commonly used industry measure of cell efficiency, cell BPR was used for a quantitative check of mesh independence. The BPRs for each solution are shown in Figure 136.

A mesh of 8.14E05 elements was deemed to be of adequate density, based on the quantitative values of Figure 136, as the absolute variation in cell BPR from the previous iteration was less than 0.1%. The 6.52E05 and 8.14E05 element solutions were then analysed to confirm qualitative independence. Figure 137 shows the comparison of the solutions.

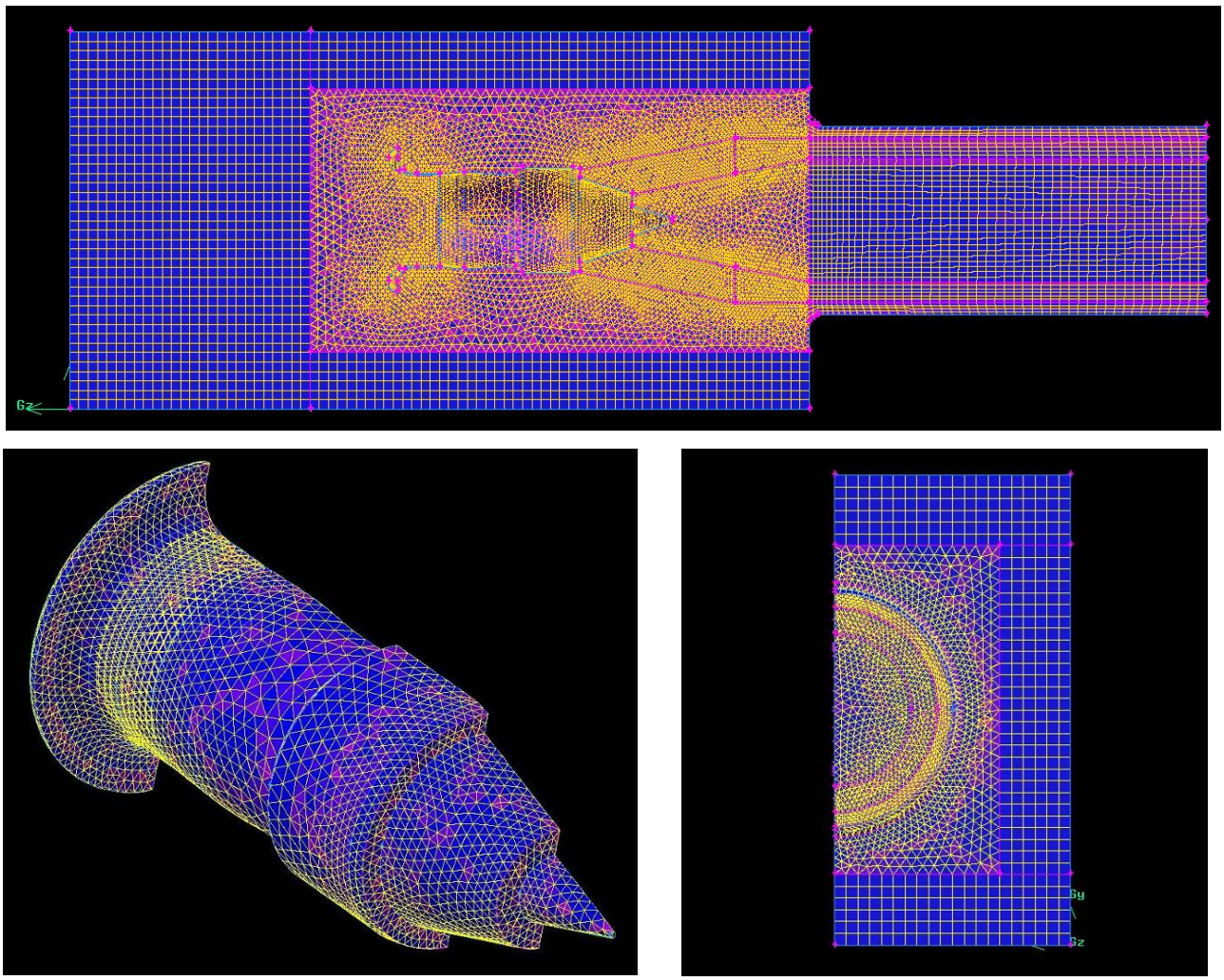

Figure 135 Element Types and Element Density used in the Computational Domain

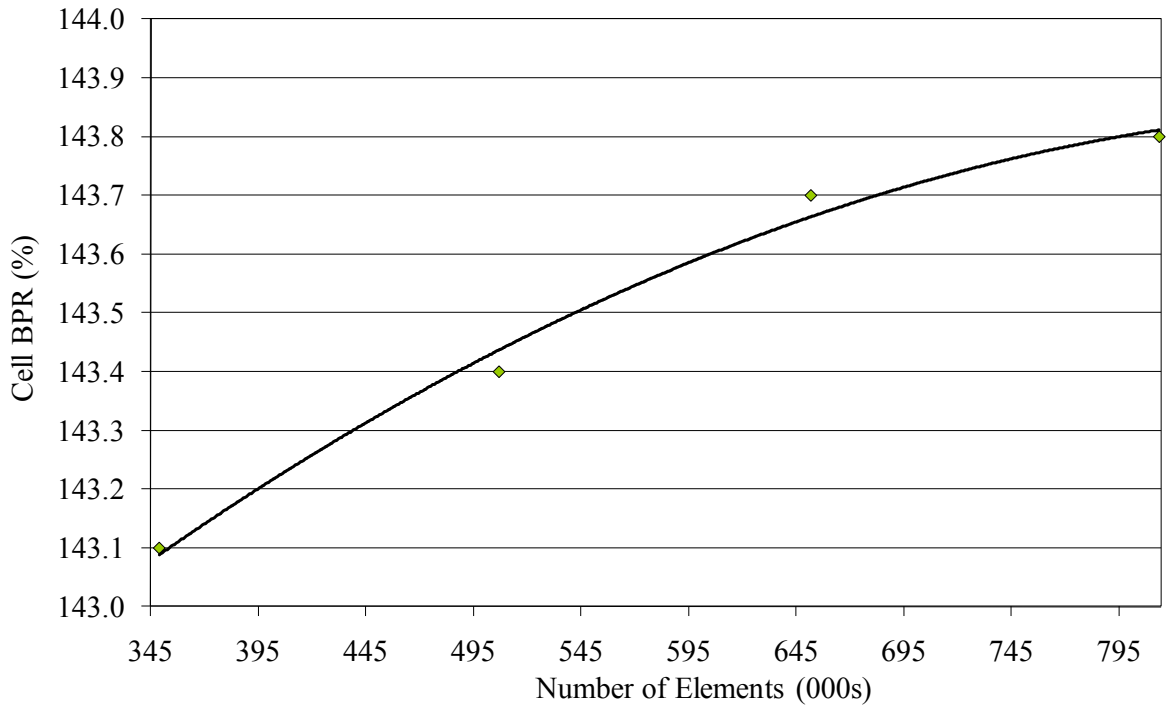

Figure 136 Cell BPR Variation with Number of Mesh Elements in Baseline Arrangement

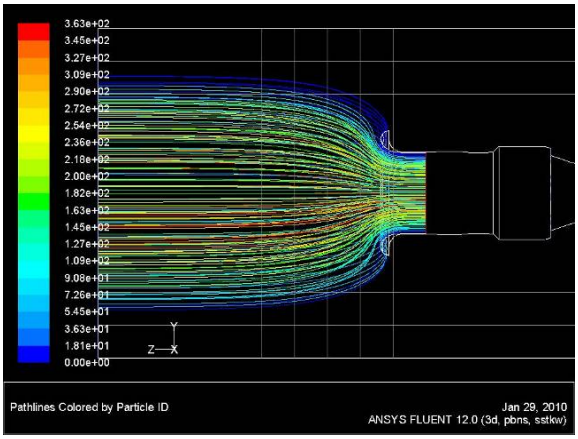

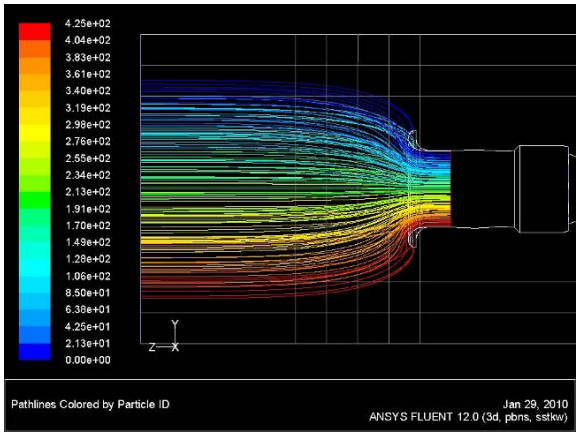

a.

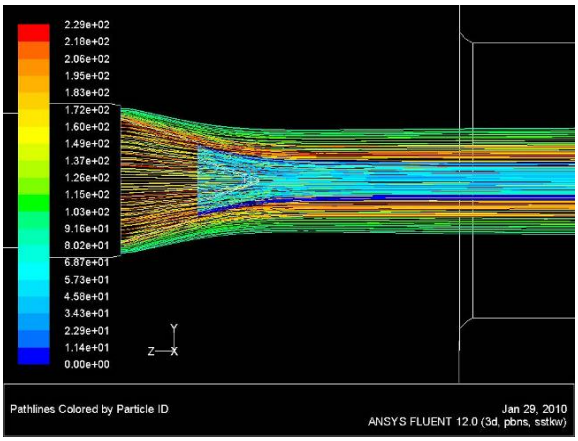

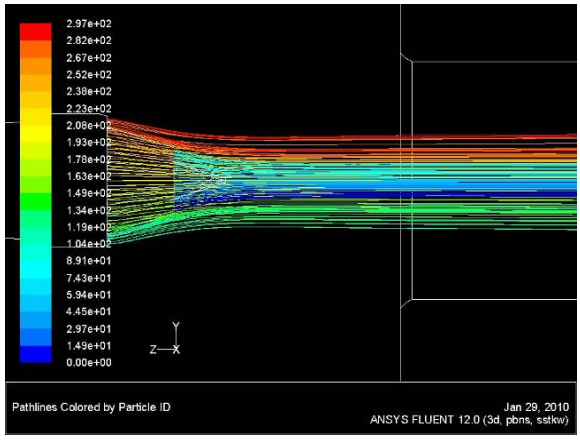

b.

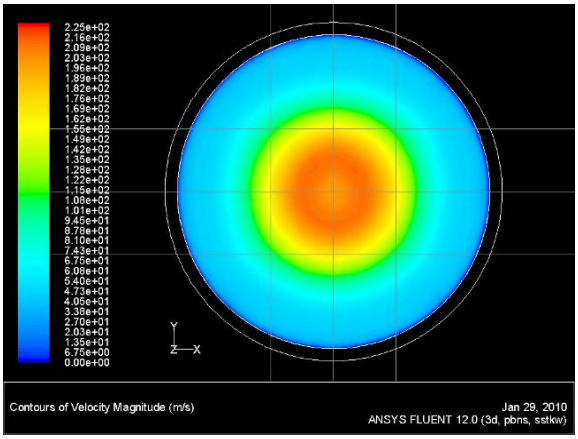

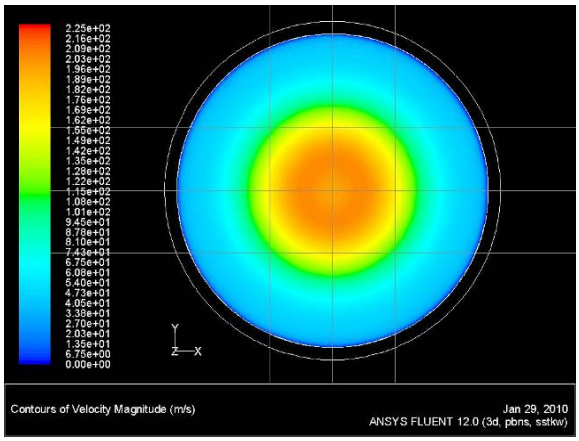

c.

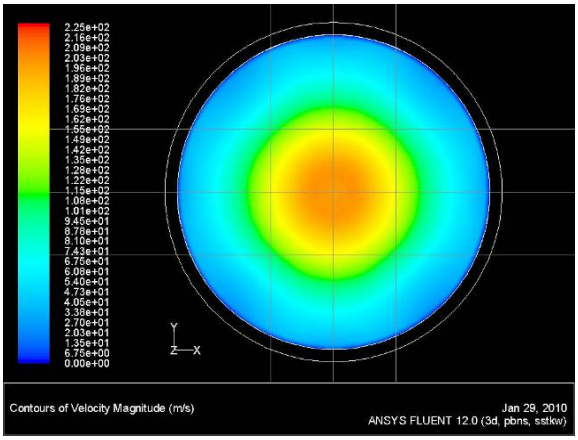

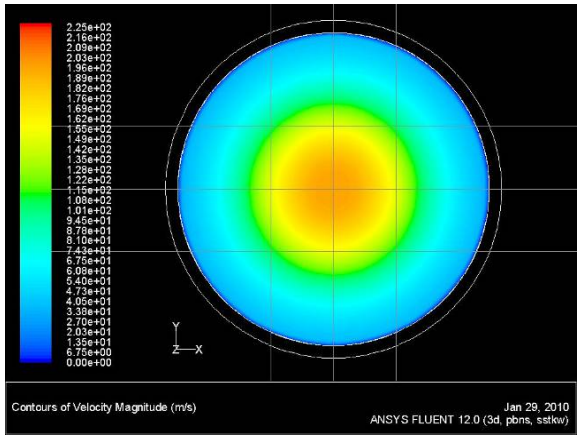

d.

Figure 137 Flow Patterns Upstream of the Engine Inlet (a), in the Exhaust-Bypass Mixing Area (b), 1.0m Downstream of the Augmenter Entrance (c), and 9.0m Downstream of the Augmenter Entrance (d) generated with Meshes of 6.52E05 Elements (left) and 8.14E05 Elements (right)

Figure 137 shows that no discernable qualitative differences were present between the solutions produced with meshes of 6.52E05 and 8.14E05 elements. The following parameters were noted as being identical in both solutions.

- The engine inlet stream-tube extends to within 1.45m of the working section walls (Figure 137a);
- The bypass exhaust stream-tube narrows by approximately 0.75m at a point 1.0m downstream of the exhaust cone tip (Figure 137b);
- 1.0m downstream of the augmenter entrance the core exhaust stream-tube expanded to a diameter of 1.50m (Figure 137c); and
- 9.0m downstream of the augmenter entrance the bypass exhaust stream-tube expanded to a diameter of 2.50m (Figure 137d).

These observations, combined with the agreement between the cell BPRs, indicated that momentum transfer at the exhaust-bypass interface was mesh independent. Therefore, the meshing approach of the 8.14E05 element baseline domain was retained for the investigations of this section.

5.2.1.5 Validation of Computational Settings

A brief validation analysis was performed on the computational settings discussed in Section 5.2.1.1 through Section 5.2.1.4. Because full-scale or scale model data to compare computational solutions of a similar scenario could not be obtained, a qualitative validation was performed.

As discussed in Section 5.1.2, the main energy dissipating process in a sharp-edged abrupt contraction is the formation of eddies between the vena-contracta and wall immediately downstream of the contraction. Figure 131, and the associated discussion of (Idelchik & Fried, 1986), also indicate the presence of circulation in the sharp outer corner of the larger diameter upstream duct immediately adjacent to the contraction. It was deemed that if these two flow features could be reproduced in a computational solution, using the solver settings discussed in Section 5.2.1.1 through Section 5.2.1.4, the same solver settings would be adequate to allow the objectives of the main body of the investigation to be achieved.

Therefore, the next step involved the computational domain discussed in Section 5.2.1.1 being modified to remove the two-stage tapering lip, and developing a solution. Figure 138 and Figure

139 show the flow patterns downstream of the augmenter entrance, and near the downstream wall of the working section.

Figure 138 shows that the vena-contracta and separation at the augmenter inlet is produced in the computational model. Likewise, Figure 139 shows circulation in the outer corners of the working section, representing the larger diameter upstream duct, in Figure 131.

The computational settings of Section 5.2.1.1 through Section 5.2.1.4 were deemed adequate for the analysis of this section, and both qualitative and comparative analyses could be performed confidently.

5.3 Results

The findings of the working section analysis are presented in this section. Section 5.3.1 first presents the findings of the baseline solution. Section 5.3.2 and Section 5.3.3 then present the findings of investigations carried out to gain a greater understanding of the working section and augmenter transition flow. Section 5.3.4 follows with a brief analysis of a proposed retrofit solution aimed to improve airflow efficiency in the augmenter transition region.

The underlying focus of the analysis in this section was to produce greater aerodynamic efficiency within the working section and augmenter transition regions. Cell BPR, a widely used measure of cell efficiency in the JETC industry, is regularly referred to throughout this section as a measure of design performance. The definition and equation for cell BPR was presented in Section 1.4.2.

5.3.1 Baseline Design

A solution to the domain of the baseline working section was generated using the computational settings discussed in Section 5.2.1. Figure 140 through Figure 153 present the solution. Figure 140 shows the variation in velocity along the vertical axis of the cell. From the ‘Cell Inlet’ BC, the flow is accelerated as it nears the entrance with the engine bell-mouth. At a plane aligned with upstream edge of the bell-mouth, and running perpendicular to the mainstream of flow, the airflow is split into two streams. The two streams are the cell bypass flow and the engine flow as discussed in 1.3.3.1. Figure 141, showing streamlines released from the ‘Cell Inlet’, illustrates the paths of the two streams.

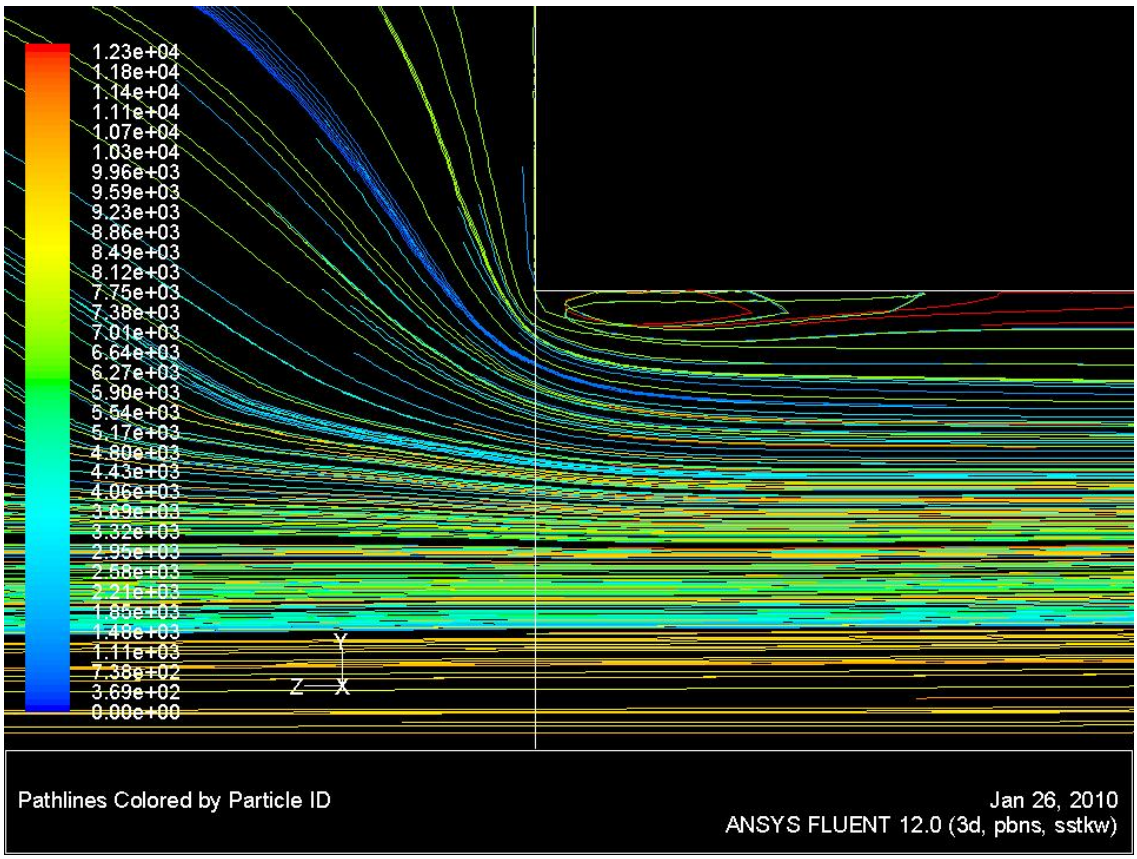

Figure 138 Formation of a Vena-Contracta Immediately Upstream of the Contraction with a Sharp-Edged Augmenter Entrance Lip

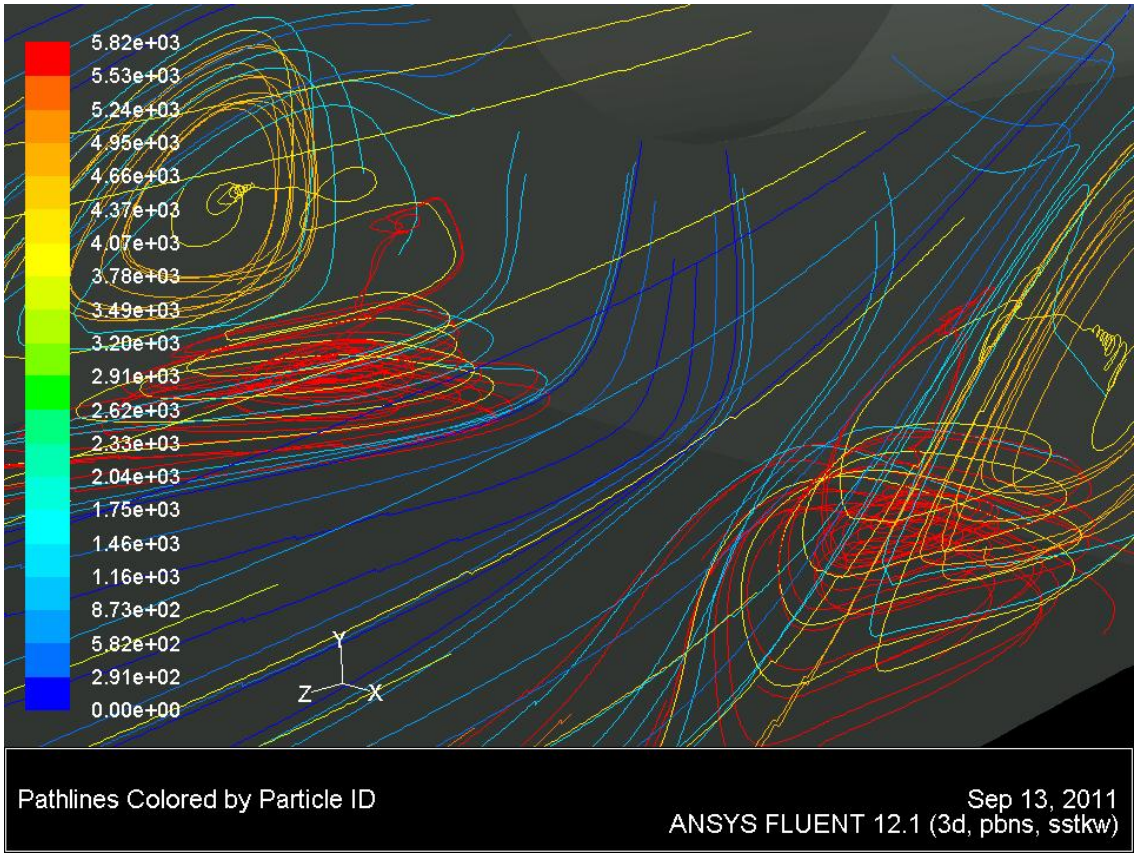

Figure 139 Flow Circulation in the Downstream Corners of the Working Section with a Sharp-Edged Augmenter Entrance Lip

Figure 142 shows the isolated streamlines forming the inlet stream-tube. An important observation is that the stream-tube does not intersect the working section walls at any point, suggesting the solution is representative of a safe engine testing environment.

Figure 141 shows that the engine flow is accelerated significantly between the bell-mouth entrance and the engine inlet face. Figure 140 shows that the bypass flow retains its velocity as it passed between the engine and the cell walls. The effect driving the bypass flow at this point is entrainment, as discussed in Section 1.3.3.1. Momentum is transferred from the high velocity flow of the engine exhausts to the comparatively low velocity of the bypass flow. The transfer of momentum occurs as a result of turbulent mixing (Massey, 2001). The area where turbulent mixing takes place is illustrated in Figure 143 by areas of high k.

Figure 144 shows that in the corners at the rear of the cell circulation regions develop. Figure 145 shows the streamlines of flow entering the augmenter tube from the working section. Figure 144 and Figure 145 viewed in combination show that a vast majority of the circulating corner flow remains isolated in the circulation zone. Figure 146 shows that, compared to the other regions of flow, the circulating pockets rotate at a substantially lower velocity.

The recombined flow streams enter the augmenter tube, which exits the downstream wall of the working section as an abrupt contraction. Figure 147 shows the path of streamlines entering the contraction on a plane running along the axis of the cell. No vena-contracta is seen to form immediately downstream of the augmenter transition as was seen when the tapered augmenter lip was removed in the validation analysis of Section 5.2.1.5. Therefore, the tapered lip at the augmenter entrance has removed the energy-dissipating eddies detected in Section 5.2.1.5.

The BPR of the baseline working section was calculated at 95.8%. This is an improvement of 3.8% over the domain of Section 5.2.1.5. This finding is supported by the discussion of (Idelchik & Fried, 1986) and (Massey, 2001) who both suggest that any form of taper or rounding on the lip of an abrupt contraction will reduce losses and improve efficiency. An alternative method of pressure loss reduction in an abruptly contracting pipe is presented in (Ando & Shakouchi, 2004), in which a small obstacle upstream of the contraction is seen to reduce the separation downstream of the contraction as shown in Figure 148. The contraction at the augmenter entrance varies from the work presented in (Ando & Shakouchi, 2004), as the upstream pipe/duct is square, as opposed to circular. The work presented in (Ando, Shakouchi, Yamamoto, & Tsujimoto, 2009), that looks at the effects

of placing a similar obstacle upstream of a pipe inlet, suggests that other contracting geometries, such as that of the augmenter entrance, would also benefit from such treatments.

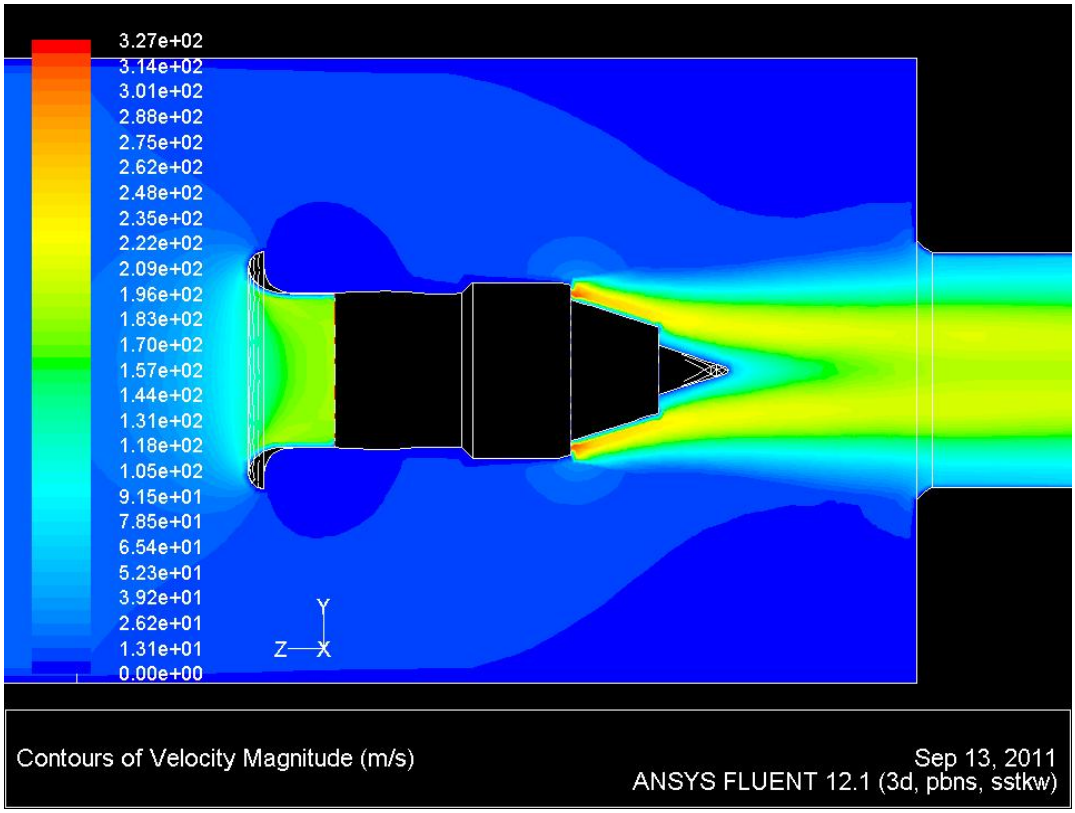

Figure 140 Velocity Magnitude on the Vertical Cell Axis of the Baseline Arrangement

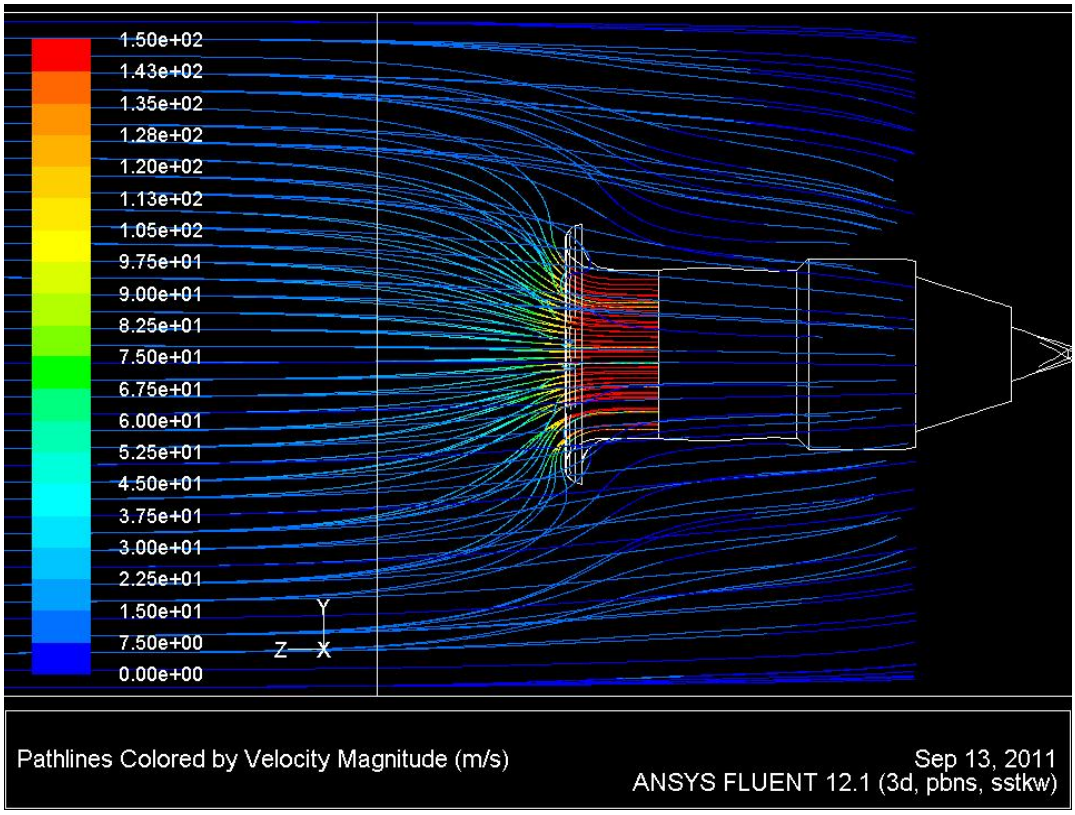

Figure 141 Streamlines released from the 'Cell Inlet' BC in the Baseline Arrangement

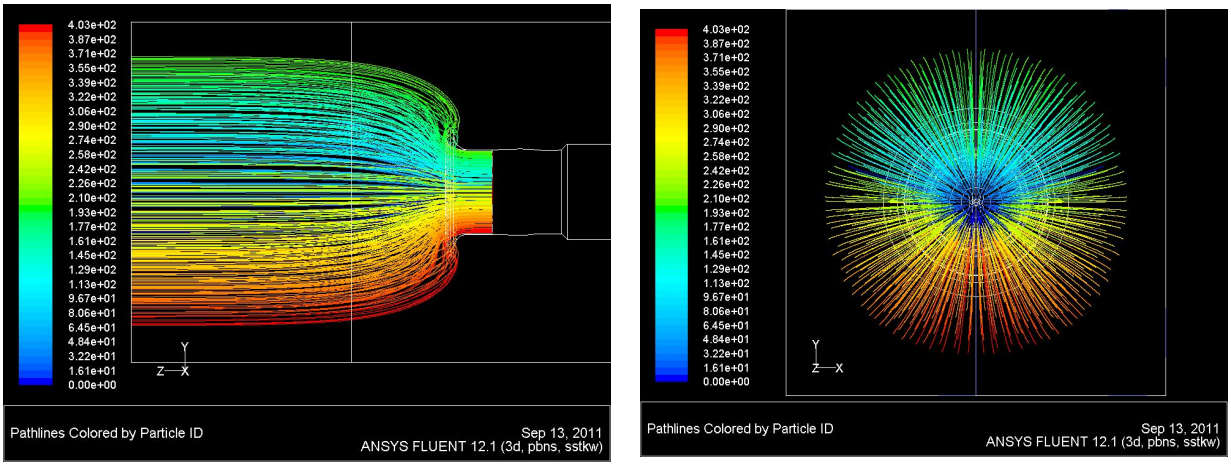

Figure 142 Contraction of the Engine Inlet Stream-Tube in the Baseline Arrangement

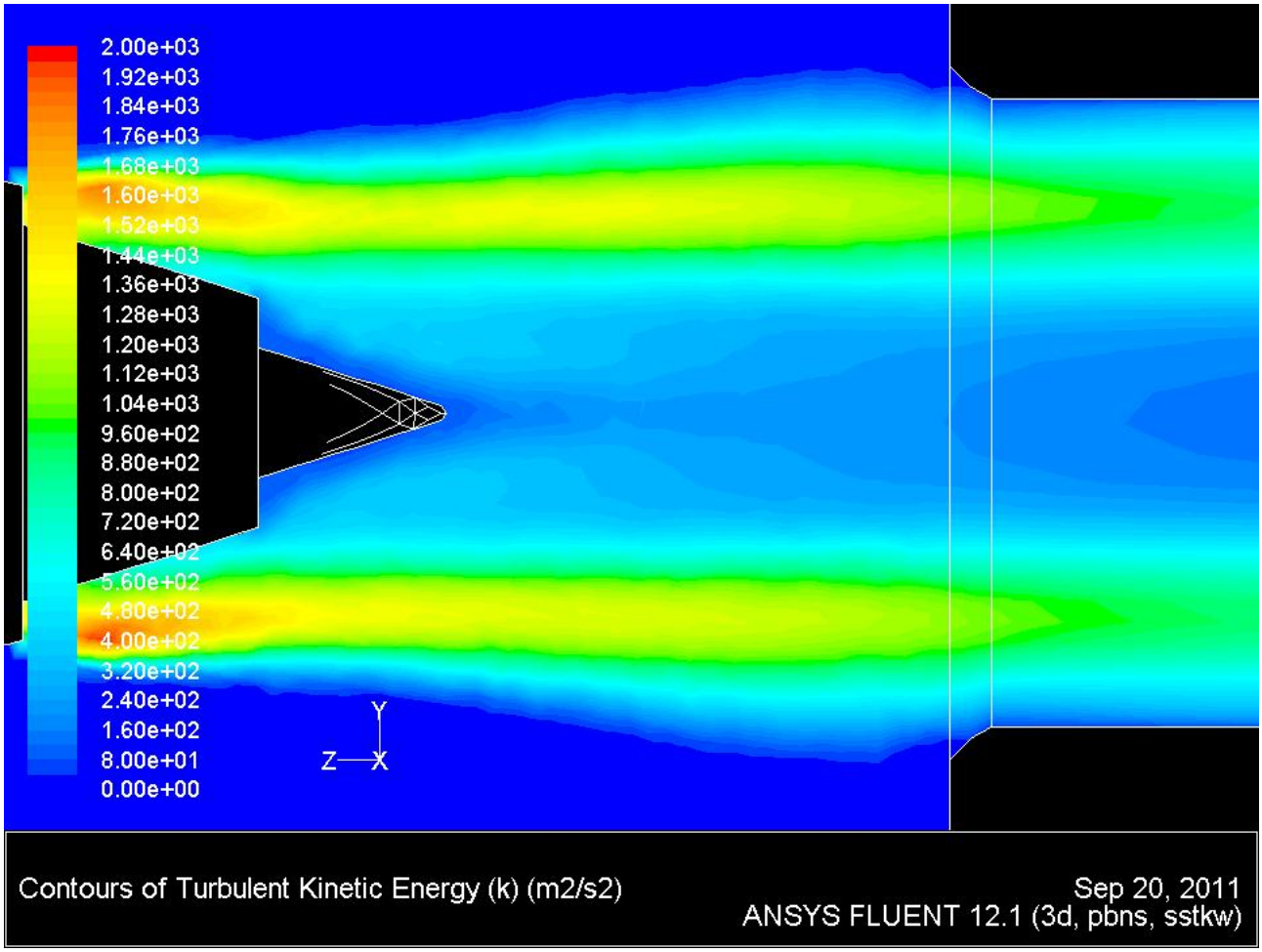

Figure 143 *k* on the Vertical Cell Axis of the Baseline Arrangement

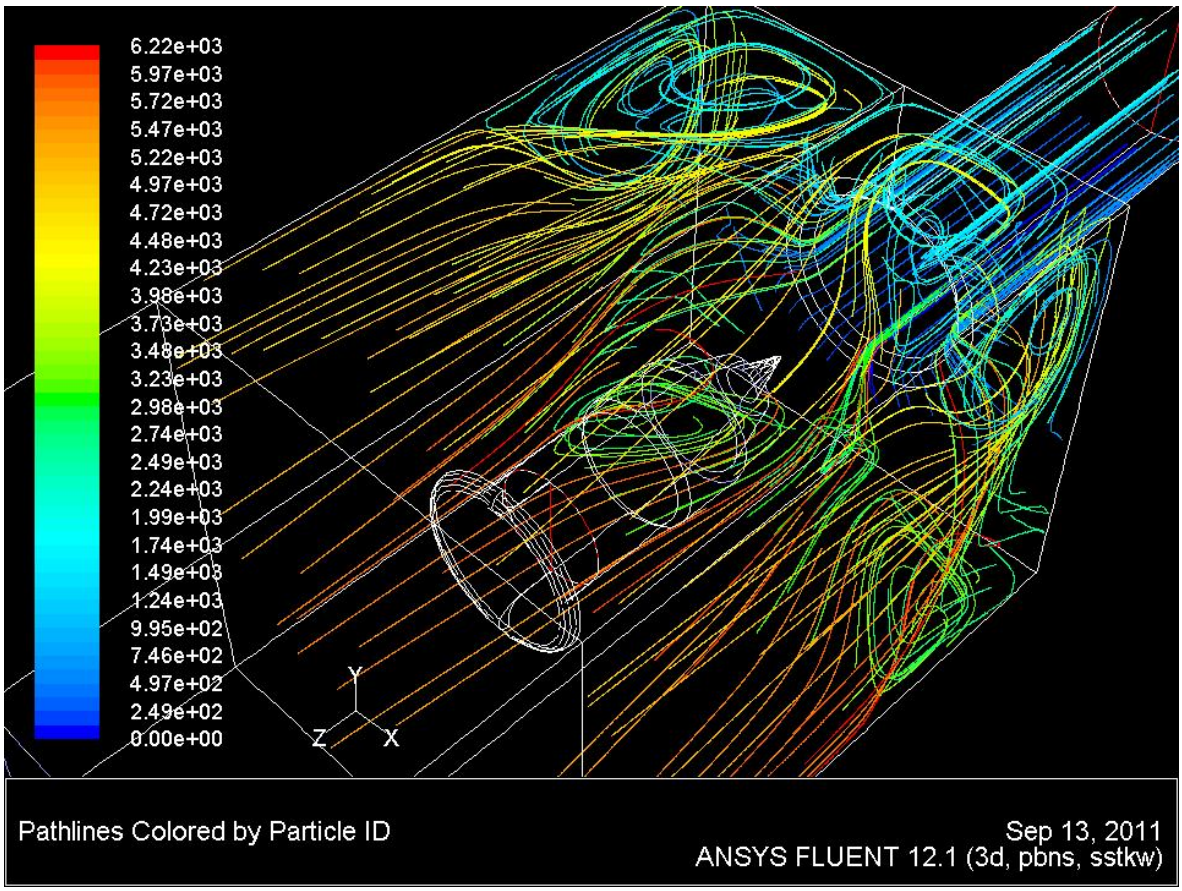

Figure 144 Streamlines of Flow Patterns in the Working Section of the Baseline Arrangement

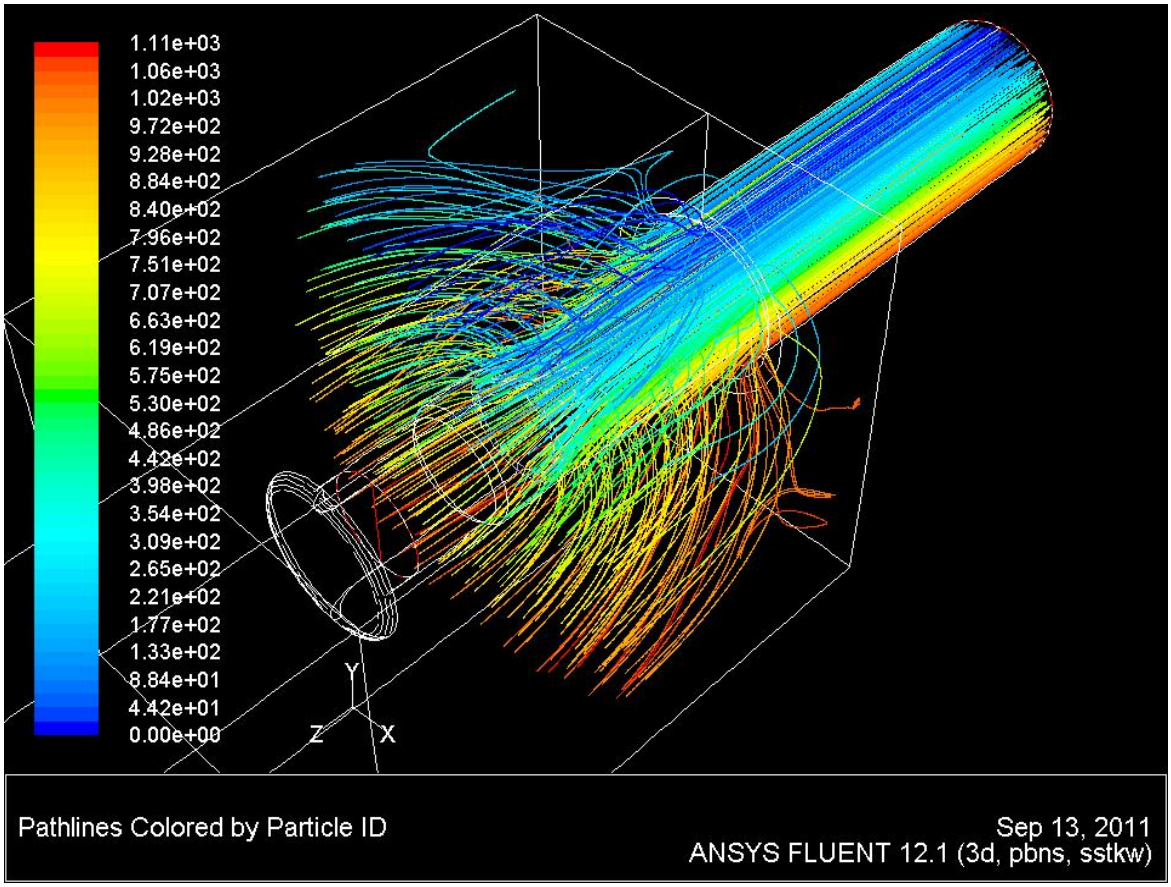

Figure 145 Streamlines Exiting via the 'Augmenter Outlet' BC in the Baseline Arrangement

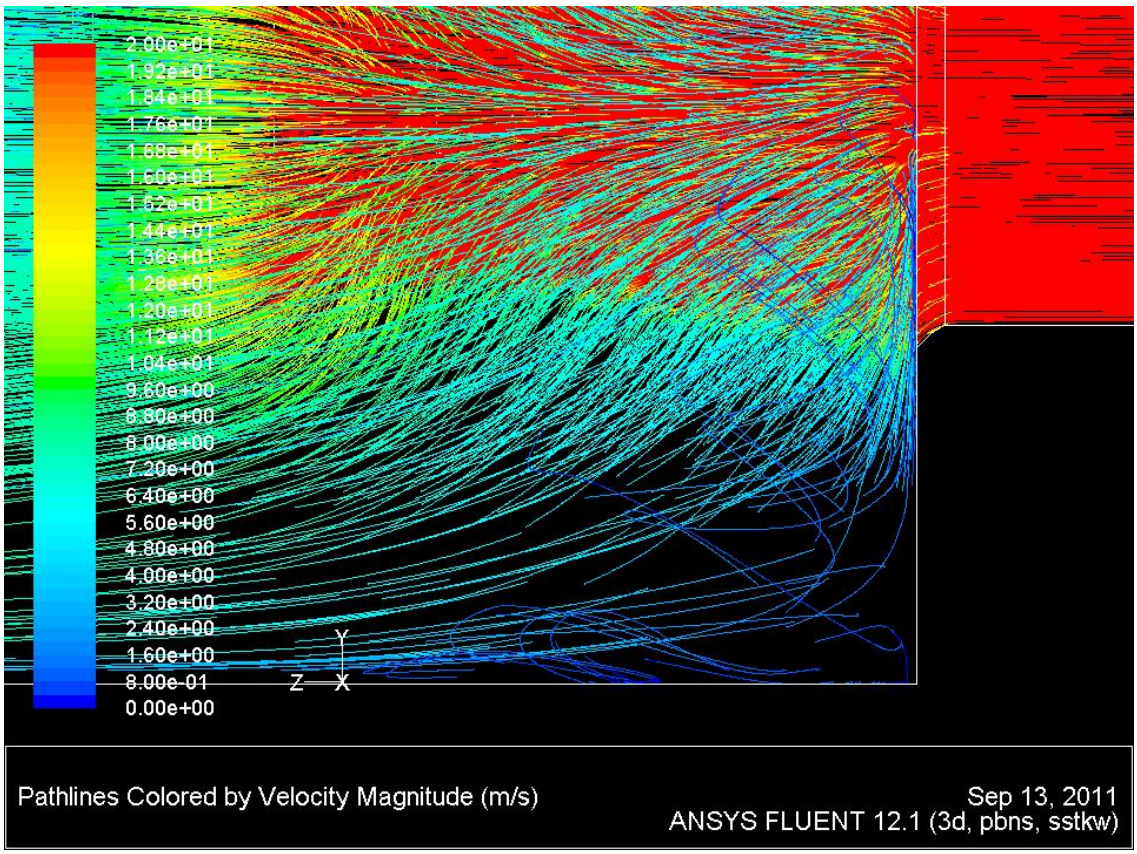

Figure 146 Streamlines in Lower Downstream Corner of the Working Section in the Baseline Arrangement

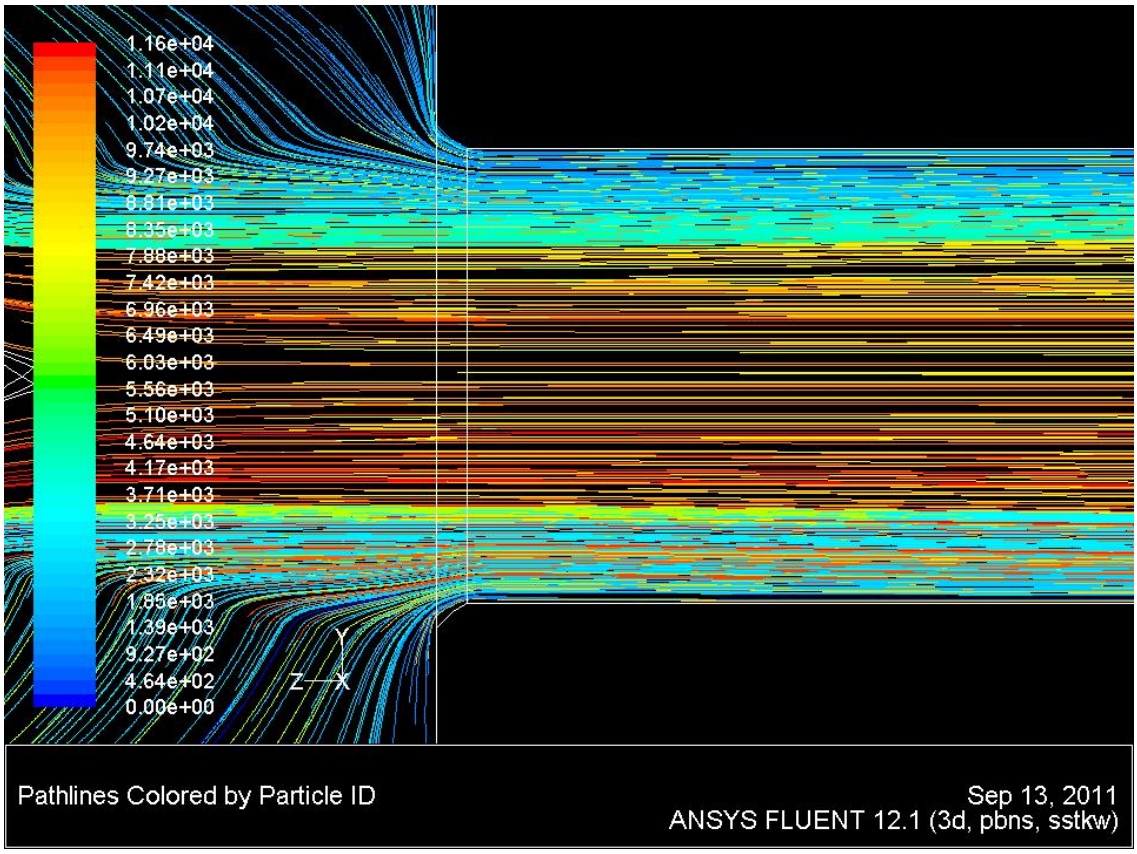

Figure 147 Streamlines on the Vertical Cell Axis around the Augmenter Entrance in the Baseline Arrangement

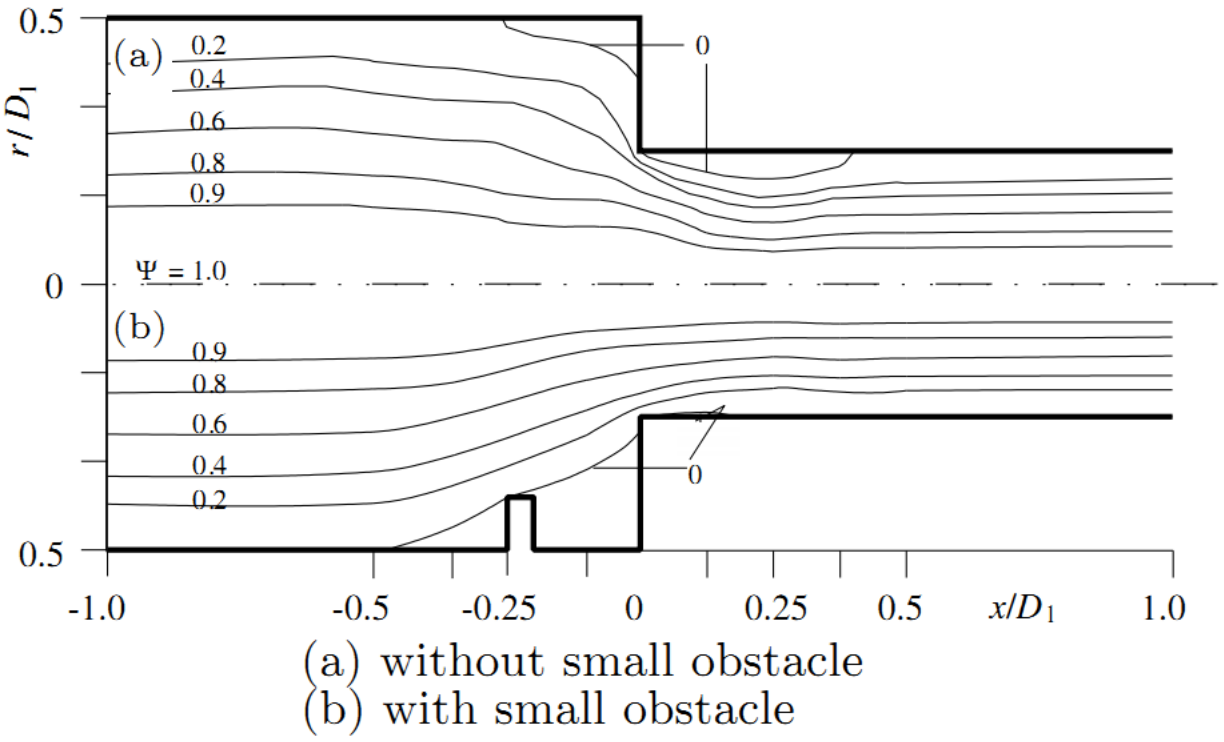

Figure 148 Reduction of Separation Upstream of Abrupt Pipe Contraction through Application of a Small Obstacle Downstream of the Contraction (Source: (Ando & Shakouchi, 2004))

Figure 149 and Figure 150 show the rapid drop in static pressure at the inlet to the augmenter tube. No immediately comparable data from the literature is available to evaluate this finding. However (J. Schmidt & Friedel, 1997) presents Figure 151 in a discussion of a single-phase abruptly contracting flow. Comparison of Figure 149 with Figure 151 shows that the static pressure drop along in the baseline solution qualitatively shares two of the same characteristics. Firstly, the sudden drop in static pressure starts a short distance upstream of the contraction lip. Secondly, the rapid decrease in static pressure continues to a short distance downstream of the contraction.

At this point, Figure 149 and Figure 151 show a variation in characteristics. Figure 151 shows a rapid increase in pressure over the length of the vena-contracta before a slow linear decrease occurs. The slow linear decrease occurs as a result of wall friction once a fully developed flow is re-established. Figure 149 shows a more gradual and continual increase in pressure along the augmenter tube. It is thought that this is a result of the continual transfer of momentum and energy throughout the augmenter tube between the exhaust and cell bypass flows.

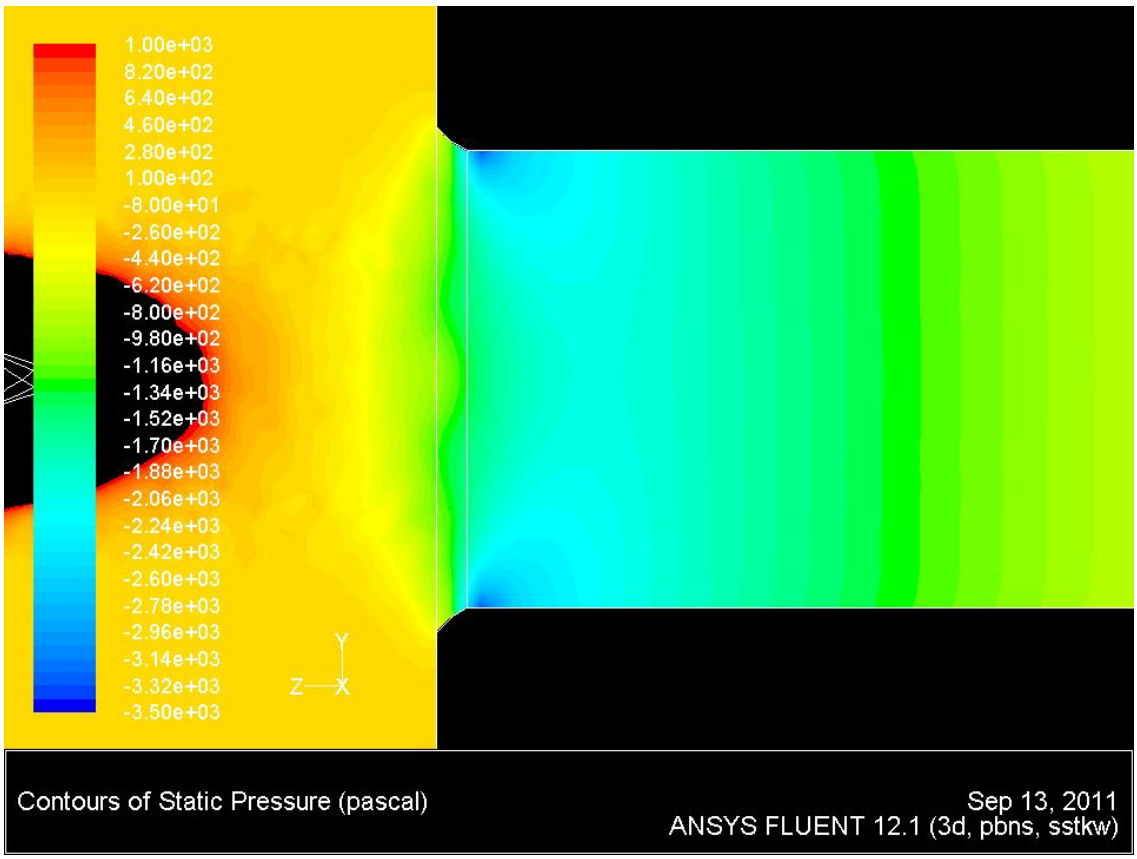

Figure 149 Static Pressure Variation on the Vertical Cell Axis around the Augmenter Entrance in the Baseline Arrangement

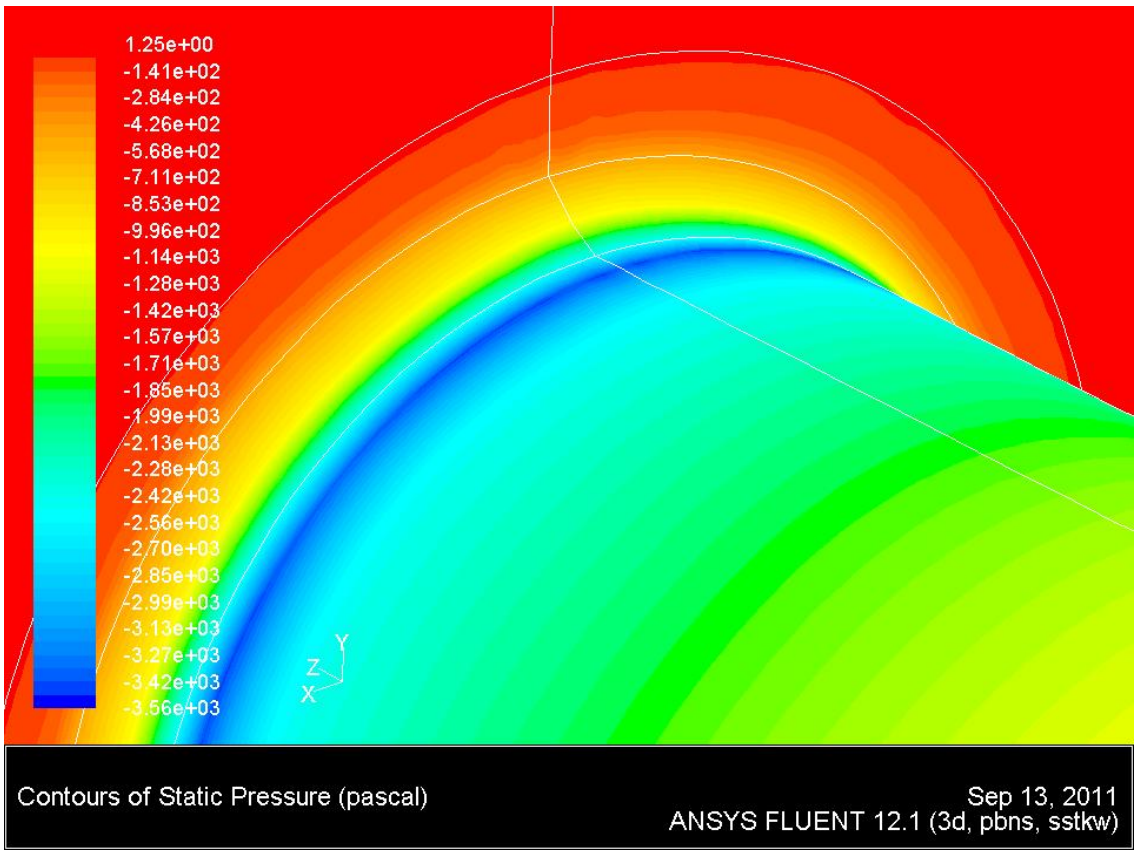

Figure 150 Static Pressure Variation on the Working Section and Augmenter Walls around the Augmenter Entrance in the Baseline Arrangement

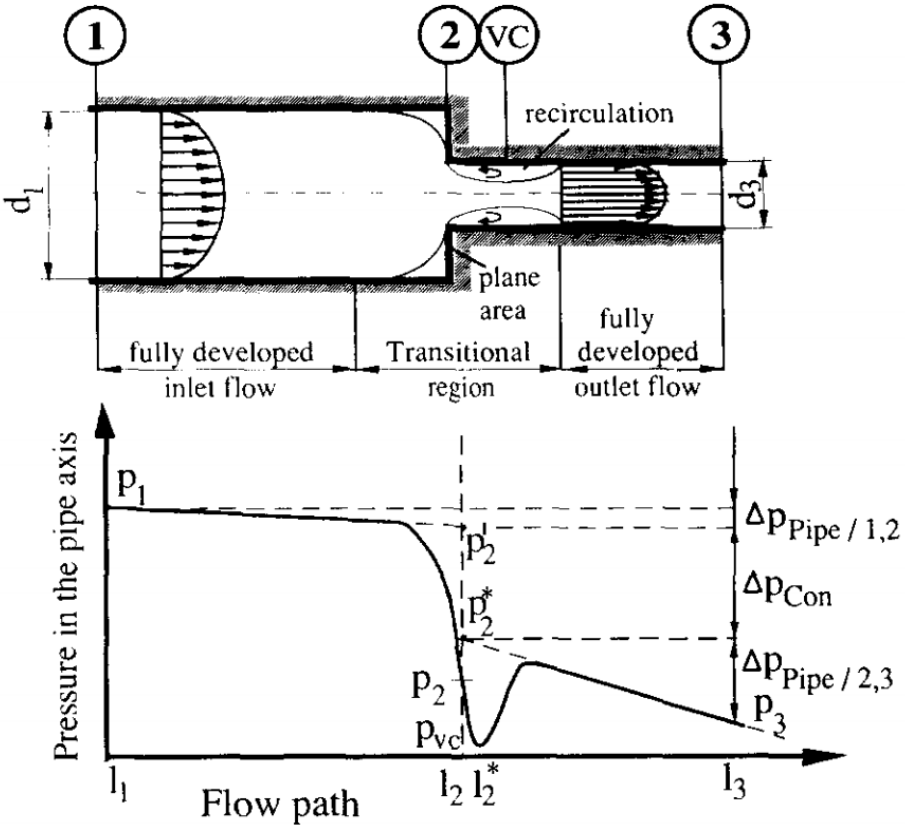

Figure 151 Static Pressure Variation along the Centreline of an Abruptly Contracting Pipe Section (Source: (J. Schmidt & Friedel, 1997))

Figure 152 and Figure 153 show the contours of velocity and *k* throughout the length of the augmenter tube. The velocity profile of Figure 152 shows that two well defined regions of high and low velocity flow exists throughout the length of the augmenter tube. The streams originate from the engine exhaust and cell bypass flows respectively. The slight, but continual reduction in the width of the high velocity flow, and the *k* profile shown in Figure 153, indicates that transfer of momentum between the two streams takes place all the way up to the 'Augmenter Outlet' face.

k can be used as an indicator of momentum transfer in this case when consideration is given to what *k* represents, and the mechanism by which energy and momentum is transferred between air flows of differing velocity. *k* is the turbulent kinetic energy, a measure of the energy contained within the fluctuations prevalent in turbulent flows. When two air flows of differing velocity are adjacent to one another, it is the interaction of these fluctuations that transfer energy and momentum from one flow to the other. Greater transfers of energy and momentum are achieved through greater turbulence fluctuation activity, which has an associated greater kinetic energy. An increase in the value of *k* in the region of between two adjacent flows can therefore be viewed as an indicator of increased energy and momentum transfer.

5.3.2 Engine-Augmenter Spacing

5.3.2.1 Analysis procedure

In Section 5.3.1 it was seen that momentum transfer via entrainment, of the 'jet-pump' effect, was the driving force of the cell bypass flow. The area in the working section over which momentum transfer could take place was limited by the engine-augmenter spacing. The transfer of momentum continued throughout the length of the augmenter tube. Within the augmenter tube the amount of low-velocity bypass flow is limited by the augmenter's radial dimension and the effect of the abrupt contraction.

An investigation was performed with the aim of determining the interaction between the engine-augmenter spacing and the augmenter diameter on cell efficiency. To do this, a number of computational domains were created across a range of engine-augmenter spacings and augmenter diameters. Computational solutions were generated for each, and the cell BPR, as a measure of cell efficiency, along with the flow patterns were analysed.

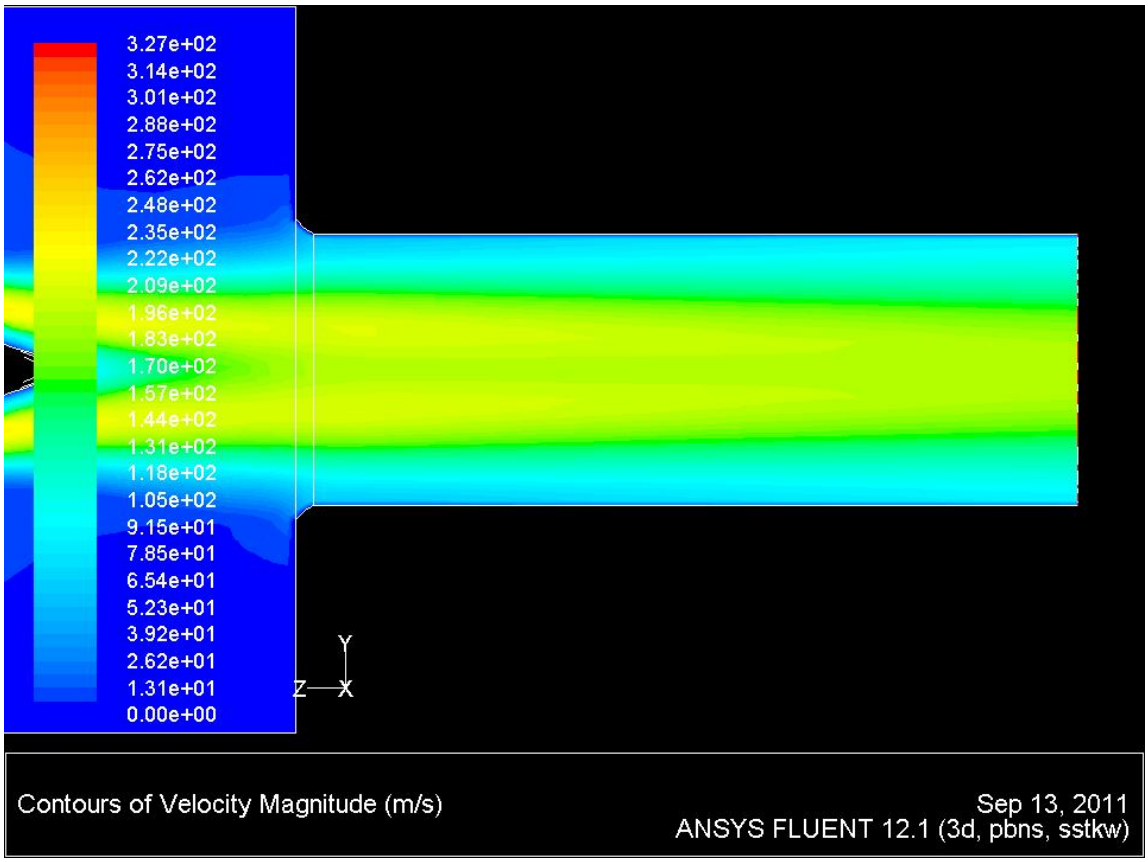

Figure 152 Velocity Magnitude on the Vertical Cell Axis through the Augmenter Tube in the Baseline Arrangement

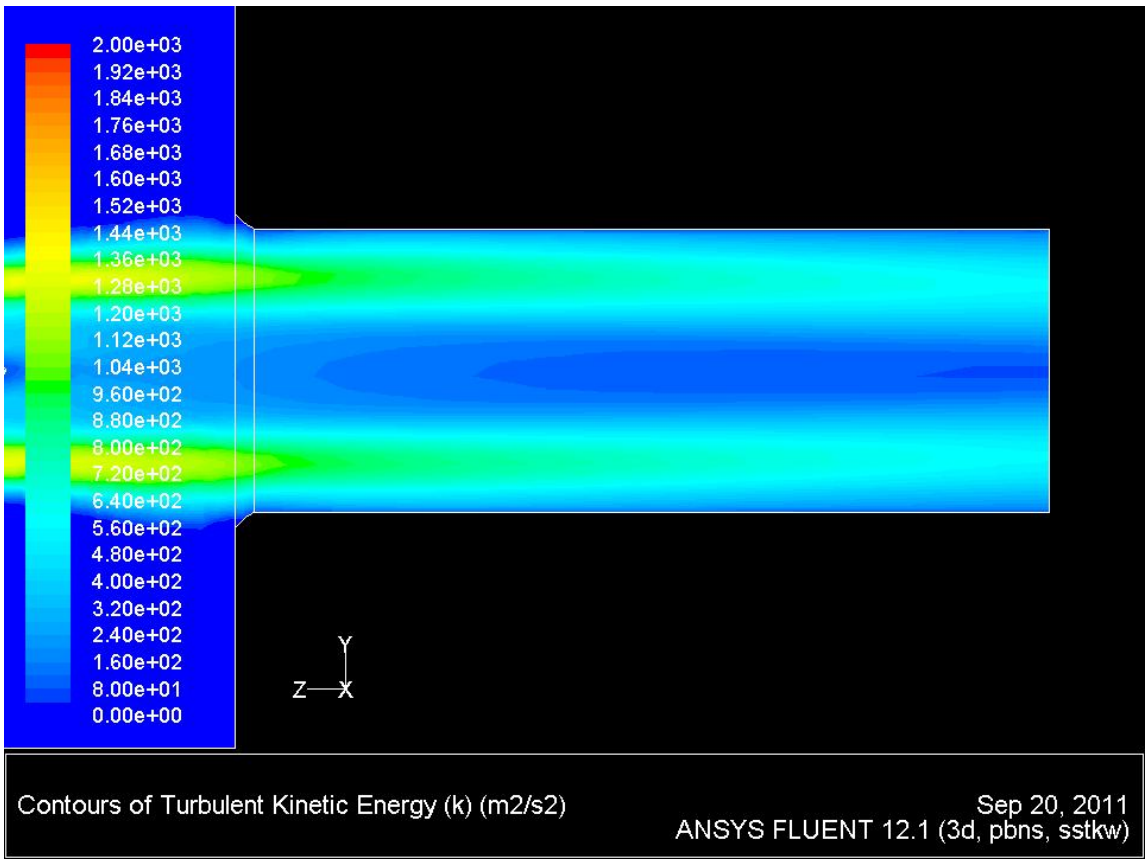

Figure 153 *k* on the Vertical Cell Axis through the Augmenter Tube in the Baseline Arrangement

The engine-augmenter spacing was varied at distances of 2.75, 3.50, 4.15, 4.80 and 5.50m. The engine-augmenter spacing was measured from the bypass exhaust face to the rear cell wall. The two end-points defining this distance are shown as dotted yellow lines in Figure 134. For each engine-augmenter spacing the augmenter diameter was varied at increments between 3.00m and 5.50m. As the investigation developed, additional augmenter diameters of between 6.00m and 7.25m were also investigated. The reasons for doing will become apparent in the discussion of the findings in Section 5.3.2.2.

Table 4 shows the combinations of engine-augmenter spacing and augmenter diameter that were analysed. The baseline domain is noted in bold with a superscript ‘b’.

5.3.2.2 Collated Results

The results of the investigation outlined in Section 5.3.2.1 are presented in this section. Solutions for each of the domains presented in Table 4 were generated. Cell BPR was calculated for each solution produced. The cell BPR for each of the engine-augmenter spacings is presented as a function of augmenter diameter in Figure 154.

Table 4 Augmenter Diameters at which each Engine-Augmenter Spacing was Analysed at in Section 5.3

Engine-Augmenter Spacing (m)	Augmenter Diameter (m)												
2.75	3.00	3.50	3.75	4.00	4.25	4.50	4.75	5.00	5.50	6.00	6.25		
3.50	3.00	3.50	3.75	4.00	4.25	4.50	4.75	5.00	5.50	6.00	6.25		
4.15	3.00	3.50	**3.75**[b]	4.00	4.25	4.50	4.75	5.00	5.50	6.00	6.25		
4.80	3.00	3.50	3.75	4.00	4.25	4.50	4.75	5.00	5.50		6.25	6.75	
5.50	3.00	3.50	3.75	4.00	4.25	4.50	4.75	5.00	5.50		6.25	6.75	7.25

Figure 154 shows that for each engine-augmenter spacing, a common trend of increased cell BPR with increased augmenter diameter exists up to a given point. When the augmenter diameter is increased beyond the given point, a gradual decrease in BPR is evident. The trend observed means a well-defined engine-augmenter spacing for maximum efficiency of a given augmenter diameter is seen. These are discussed further in Section 5.3.2.5. The results presented in Figure 154 are broken down in to three specific regions for the purposes of discussion:

1. Augmenters less than 3.50m in diameter;
2. Augmenters of between 3.50m and 4.25m in diameter; and
3. Augmenters greater than 4.25m in diameter.

Section 5.3.2.3, Section 5.3.2.4 and Section 5.3.2.5 discuss each of these regions respectively.

5.3.2.3 Augmenter Diameter Less than 3.50m

In Figure 154, cell BPR in those solutions produced using an augmenter diameter less than 3.50m (130% of engine bypass exhaust diameter) was found to be a function of both augmenter diameter and flow dynamics. When the engine-augmenter spacing was small, the engine exhaust had less distance over which to spread before entering the augmenter tube. Less spread of the exhaust resulted in a greater portion of the augmenter entrance face being available for entrained bypass flow to enter. Figure 155 and Figure 156 illustrate this point. Figure 155 and Figure 156 were created using reverse streamlines that were seeded from the Augmenter Outlet BC. The seeding process that was used was identical in both cases. The same spatial density of seed particles was spread across the Augmenter Outlet face to produce both graphics. An identical number of identically sized time-steps were used in both reverse streamlining procedures, meaning a direct visual comparison of Figure 155 and Figure 156 can be performed.

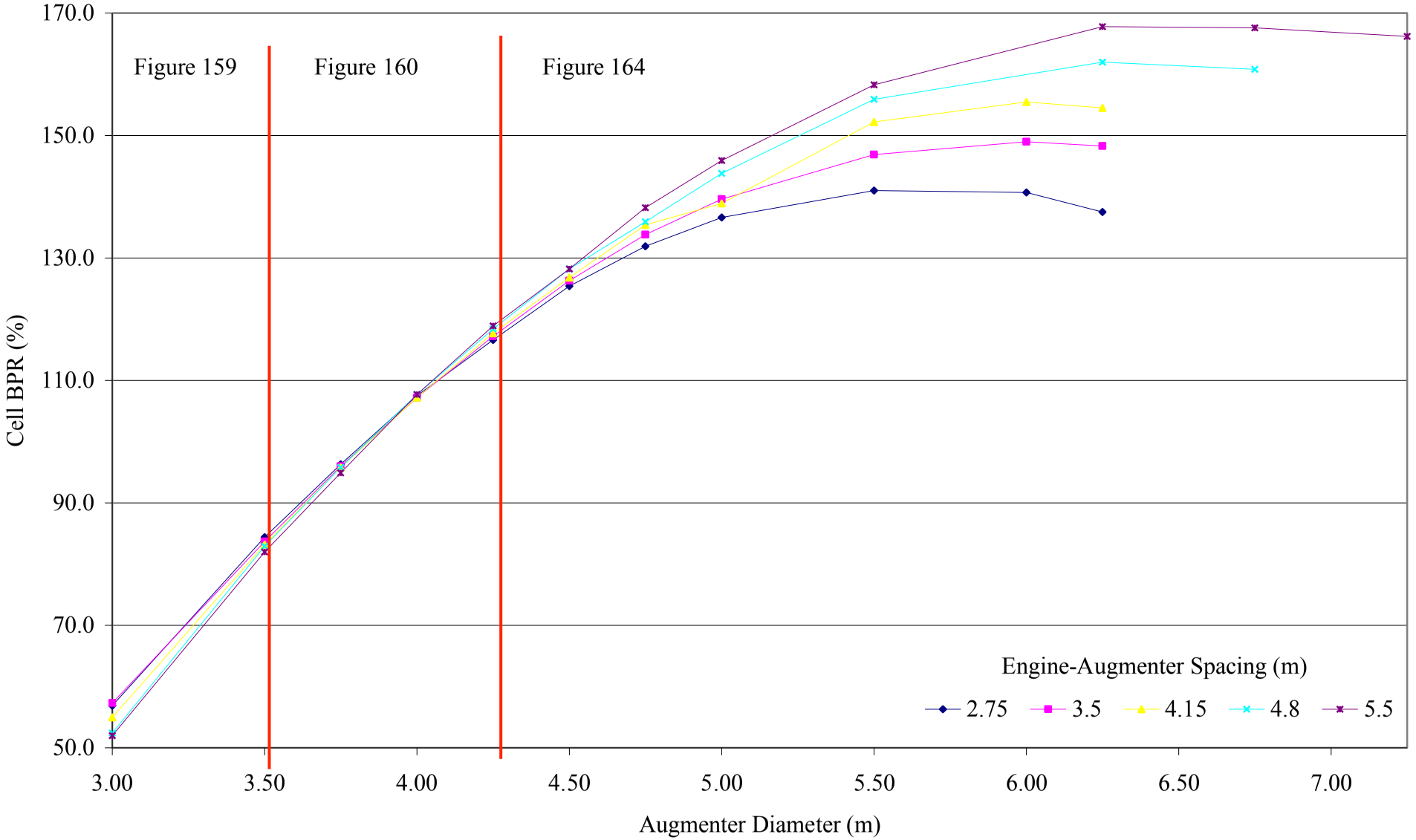

Figure 154 Comparison of Cell BPR Variation with Augmenter Diameter for given Engine-Augmenter Spacings

Figure 157 shows that as a result of this, *k*, as an indication of momentum transfer between the high and low velocity streams, is substantially reduced throughout the length of the augmenter tube when larger engine-augmenter spacings are used.

With an augmenter diameter of 3.00m, the stream-wise forces on the working section walls increased by 7.6% when the engine-augmenter spacing was increased from 2.75m to 5.50m. Figure 158 shows a comparison of static pressure build-up on the cell walls of these two solutions. The region immediately surrounding the augmenter lip is seen to be the cause of the increased stream-wise forces.

Figure 159 presents an isolated region of Figure 154, showing the results obtained using augmenter diameters of less than 3.50m. Figure 159 shows that for augmenter diameters less than 3.50m, smaller engine-augmenter spacings resulted in greater cell efficiency. This is illustrated by looking at the 3.00m augmenter diameter example.

The cell BPR varied from 56.9%, with an engine-augmenter spacing of 2.75m, to 52.0%, with a spacing of 5.50m. This corresponded to an absolute drop of 8.6% in cell BPR. Figure 154 also shows that as augmenter diameter was increased, the variation in the cell efficiency across the engine-augmenter spacing range also decreased.

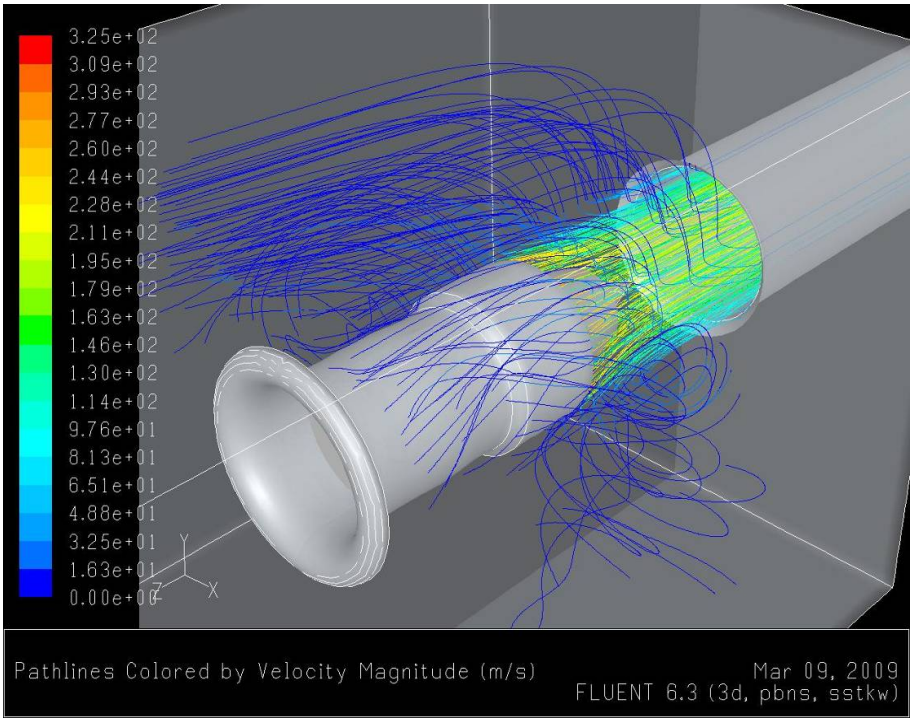

Figure 155 Entrained Streamlines in the Working Section with an Augmenter Diameter of 3.00m and an Engine-Augmenter Spacing of 2.75m

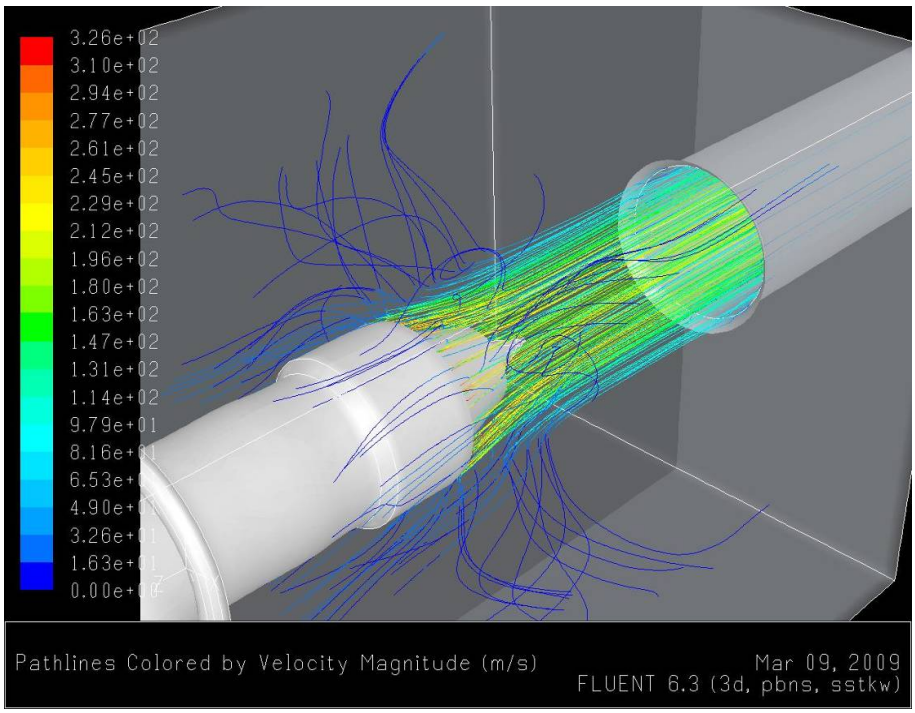

Figure 156 Entrained Streamlines in the Working Section with an Augmenter Diameter of 3.00m and an Engine-Augmenter Spacing of 5.50m

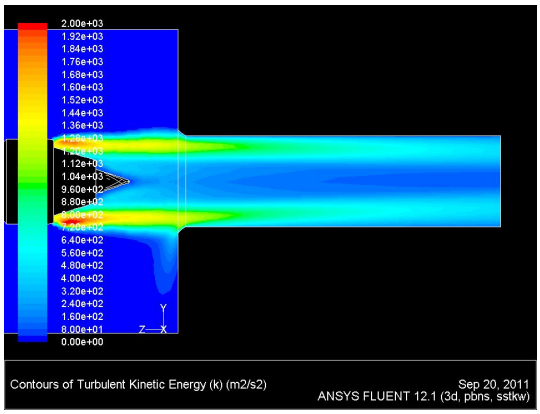

a.

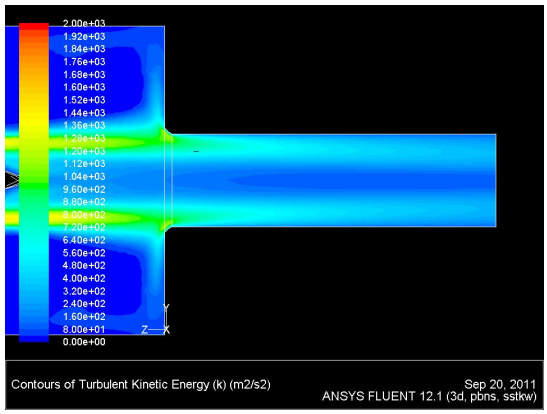

b.

Figure 157 *k* on the Vertical Cell Axis through the Rear of the Working Section and 3.00m Diameter Augmenter Tube with an Engine-Augmenter Spacing of 2.75m (a), and 5.50m (b)

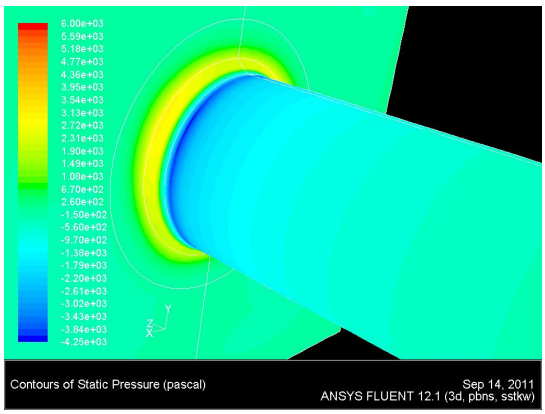

a.

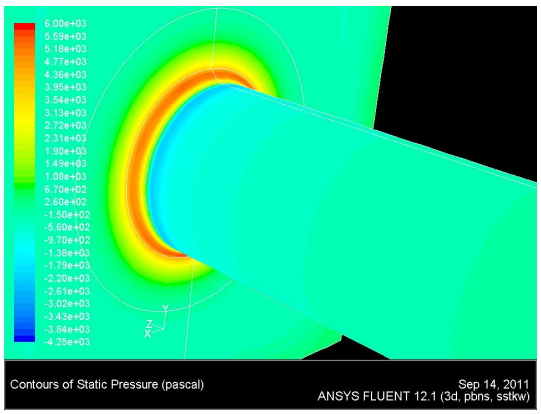

b.

Figure 158 Static Pressure Variation on the Working Section and Augmenter Walls around the 3.00m Diameter Augmenter Entrance with an Engine-Augmenter Spacing of 2.75m (a), and 5.50m (b)

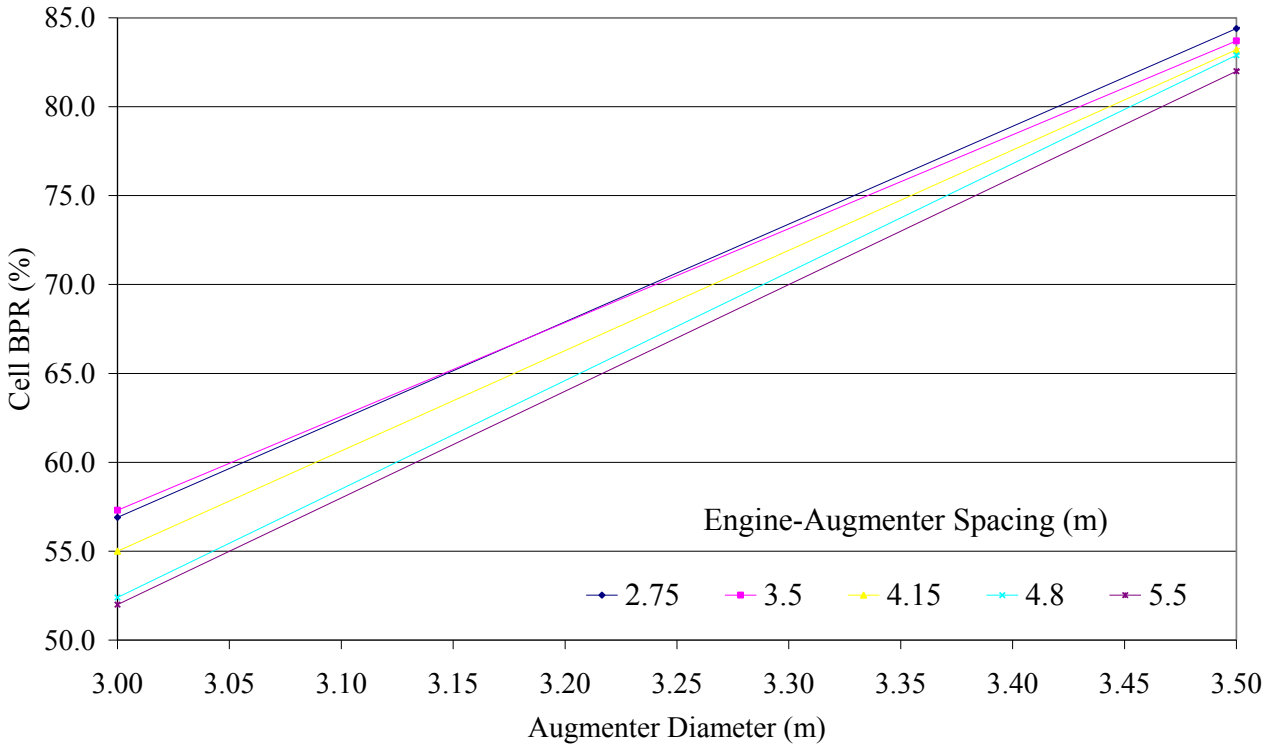

Figure 159 Comparison of Cell BPR Variation with Augmenter Diameter (less than 3.50m) for given Engine-Augmenter Spacings

5.3.2.4 Augmenters Diameters between 3.50m and 4.25m

With augmenter diameters of between 3.50m and 4.25m (130% and 157% of engine bypass exhaust diameter respectively), the variation in cell BPR across the range of engine-augmenter spacings was minimal. Figure 160 presents an isolated region of Figure 154, showing the results obtained using augmenter diameters between 3.50m and 4.25m. With an augmenter diameter of 3.50m, cell BPRs of 84.4% and 82.0% were observed with engine-augmenter spacings of 2.75m and 5.50m respectively. With an augmenter diameter of 4.25m, cell BPRs of 116.6% and 118.9% were observed with an engine-augmenter spacing of 2.75m and 5.50m respectively.

Figure 161 through Figure 163 present a selection of flow parameters using an augmenter diameter of 4.25m and engine-augmenter spacings of 2.75m and 5.50m respectively. Figure 161 through Figure 163 are comparable with Figure 155 through Figure 158 in Section 5.3.2.3. For the augmenter diameter range of 3.50m to 4.25m, the variation in flow parameters between the solutions with engine-augmenter spacings of 2.75m and 5.50m is far less than that seen when the augmenter diameter was less than 3.50m. This is in agreement with Figure 160, and indicates that with an increase in augmenter diameter, the cell efficiency has become less sensitive to changes in engine-augmenter spacing.

Figure 161 shows that the augmenter entrance stream-tube contracts slightly more rapidly when the engine-augmenter spacing is small. Figure 162 shows that, a slight increase in static pressure around the augmenter entrance is the result of the more rapid flow contraction. A drop in stream wise forces along the working section walls reflects this. Figure 162, in which contours are coloured using the same scale as Figure 158, also shows that a significant decrease in static pressure around the augmenter entrance is created as a result of the increase in augmenter diameter.

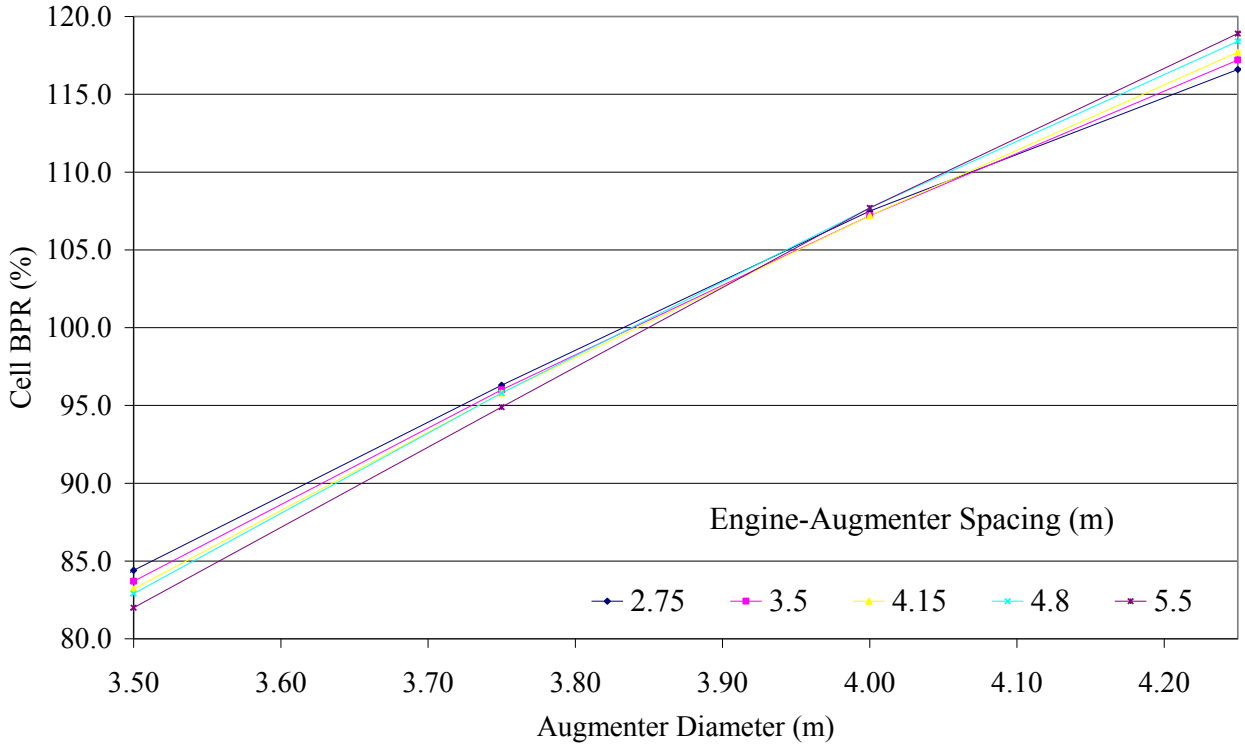

Figure 160 Comparison of Cell BPR Variation with Augmenter Diameter (between 3.50m and 4.25m) for given Engine-Augmenter Spacings

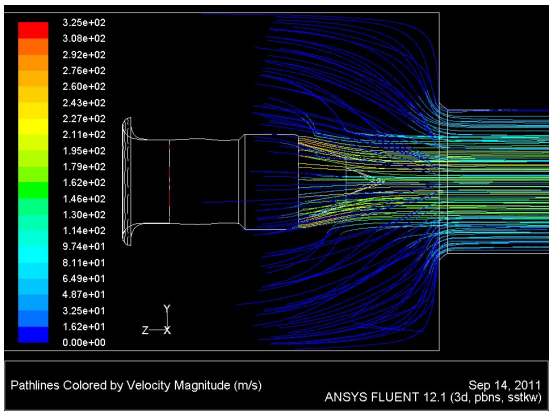

a.

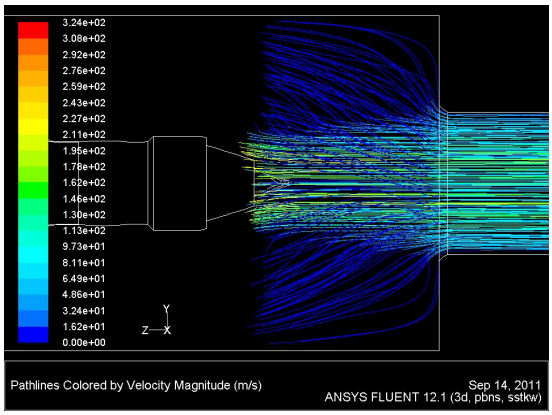

b.

Figure 161 4.25m Diameter Augmenter Entrance Stream-Tubes with an Engine-Augmenter Spacing of 2.75m (a), and 5.50m (b)

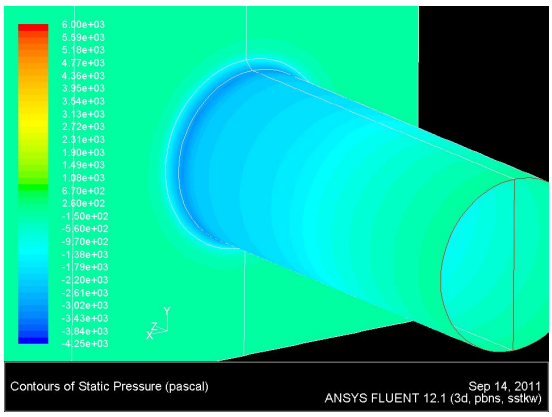

a.
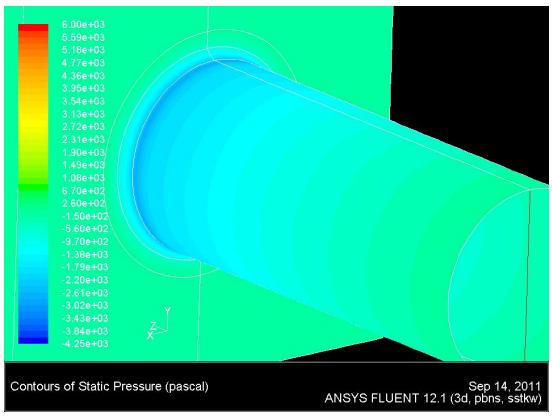

b.

Figure 162 Static Pressure Variation on the Working Section and Augmenter around the 4.25m Diameter Augmenter Entrance and with an Engine-Augmenter Spacing of 2.75m (a), and 5.50m (b)

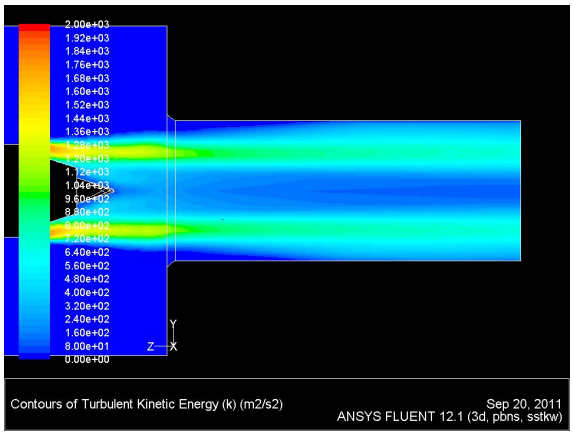

a.
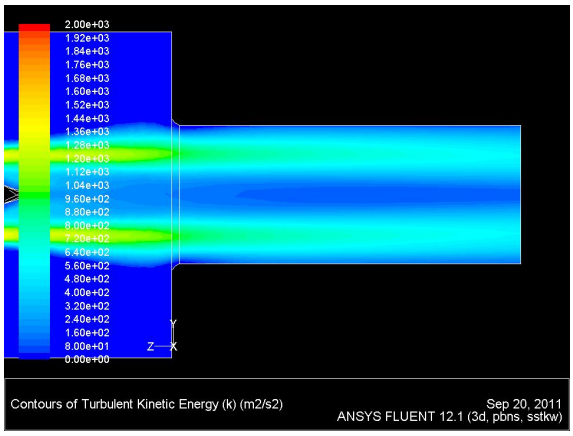

b.

Figure 163 *k* on the Vertical Cell Axis through the Rear of the Working Section and 4.25m Diameter Augmenter Tube with an Engine-Augmenter Spacing of 2.75m (a), and 5.50m (b)

Figure 163 shows that *k* throughout the length of the augmenter tube is similar in both the 2.75m and 5.50m engine-augmenter spacing solutions, meaning similar levels of momentum are transferred to the low velocity bypass flow. A small variation is *k* is seen upstream of the augmenter entrance. As a result of the increased spread of the engine exhaust prior to the augmenter entrance, and with an increase in engine-augmenter spacing, *k* is seen to slightly build-up around the augmenter lip in Figure 163b.

5.3.2.5 Augmenter Diameters Greater than 4.25m

Figure 160 presents an isolated region of Figure 154, showing the results obtained using augmenter diameters between 3.50m and 4.25m. With augmenter diameters greater than 4.25m (157% of engine bypass exhaust diameter), the BPRs produced with all engine-augmenter spacings were seen to increase to a peak value before a gradual decline (Figure 164).

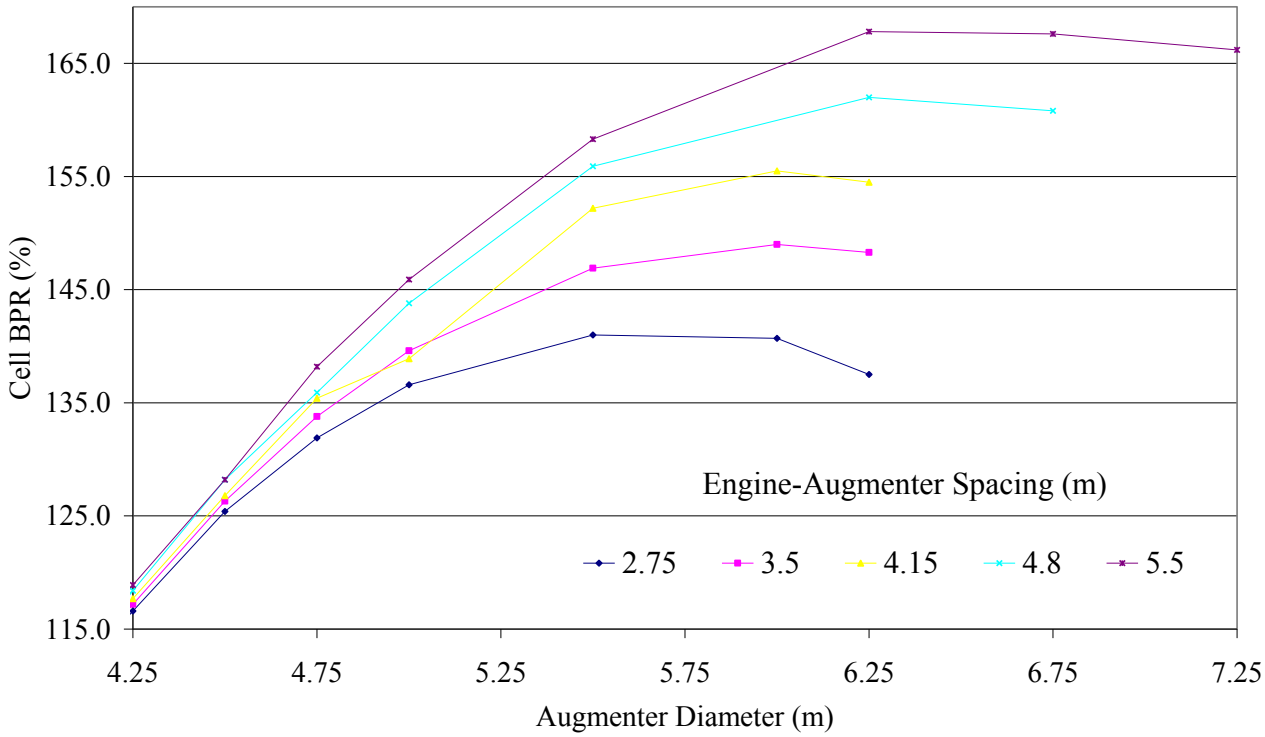

Figure 164 Comparison of Cell BPR Variation with Augmenter Diameter (greater than 4.25m) for given Engine-Augmenter Spacings

In contrast to the results seen at augmenter diameters below 4.00m, greater cell BPRs were achieved with greater engine-augmenter spacings. With an augmenter diameter of 6.00m, cell BPR ranged from 140.7% to 164.0% with engine-augmenter spacings of 2.75m and 5.50m. This corresponded to an absolute increase in cell BPR of 16.6%, a much greater range than seen with smaller augmenter diameters.

To generate the streamline graphics in this section, all solutions were seeded at a constant spatial density at the cell outlet. 'Reverse' streamlines were then propagated into the computational domain from their seeding point. As the seeding density was comparable in each of the solutions generated, comparative comments can be made in relation to the quantity of streamlines as an indication of flow rate between solutions. Figure 165 (cell BPR of 167.8%), produced using an engine augmenter spacing of 5.50m and augmenter diameter of 6.25m, clearly shows the increased bypass flow entering the augmenter when compared with the 3.00m augmenter diameter result of Figure 156 (cell BPR of 52.0%).

Figure 166 shows minimal variation in static pressure between solutions developed using a 5.50m diameter augmenter with engine-augmenter spacing of 2.75m and 5.50m respectively. Comparison the 2.75m and 5.50m spacing solutions showed that stream-wise forces decreased by 5.9%. The

augmenter entrance stream-tube of the larger engine-augmenter spacing is seen to contract slightly less rapidly near the rear working section wall. This trend in stream-wise force reduction with increased engine-augmenter spacing matches that discussed in Section 5.3.2.4, but is the reverse of that seen in Section 5.3.2.3 with augmenter diameters under 3.50m.

The likely contradiction in trends between Section 5.3.2.3 and the two following sections can seen through comparison of Figure 155, Figure 156, Figure 161, and Figure 167. All solutions compared in Figure 161 and Figure 167 show streamlines entering the augmenter entrance have been entrained along the entire length of the exhaust stream-tube between the engine exhaust and the augmenter entrance.

This is also the case seen in Figure 155. However, in Figure 156 only streamlines entrained near the engine exhaust enter the augmenter further downstream. The remainder of the exhaust stream-tube still transfers momentum to the bypass flow. However, that flow is forced into the rear wall. Some of the momentum transferred is then transferred onward to the working section walls by way of a force. This likely causes the mismatching trends between Section 5.3.2.3 and the two following sections.

Despite the mismatching trends, the solutions with augmenter diameters greater than 4.25m show significantly less stream-wise force placed upon the working section walls than those with augmenter diameters less than 3.50m. With an engine-augmenter spacing of 5.50m, the drop in stream-wise force between solutions using augmenter diameters of 3.00m and 5.50m was nearly 50%. This indicates two points. Firstly, the augmenter entrance losses are reduced with a reduction in the ratio of working section cross-sectional area to augmenter tube cross-sectional area. This is a trend that is evident in the tabulated loss coefficients for abruptly contracting pipes in (Idelchik & Fried, 1986). Secondly, the variation in cell BPR across the engine-augmenter spacings at larger augmenter diameters is a result of a different flow phenomenon. This is most likely due to the increase in entrainment surface between the engine exhaust and the augmenter termination when the engine-augmenter spacing is increased.

Figure 164 shows that, across all engine-augmenter spacings, cell BPR increased with augmenter diameter until a peak was reached before a gradual decline in cell efficiency. A number of solutions in and around the cell BPR peak were qualitatively analysed to determine the reason of the peaking behaviour. Figure 169, produced from solutions using an engine-augmenter spacing of 2.75m, and

an augmenter diameter of 5.0m, shows a sequence of solutions produced pre-cell BPR peak, near-cell BPR peak, and post-cell BPR peak.

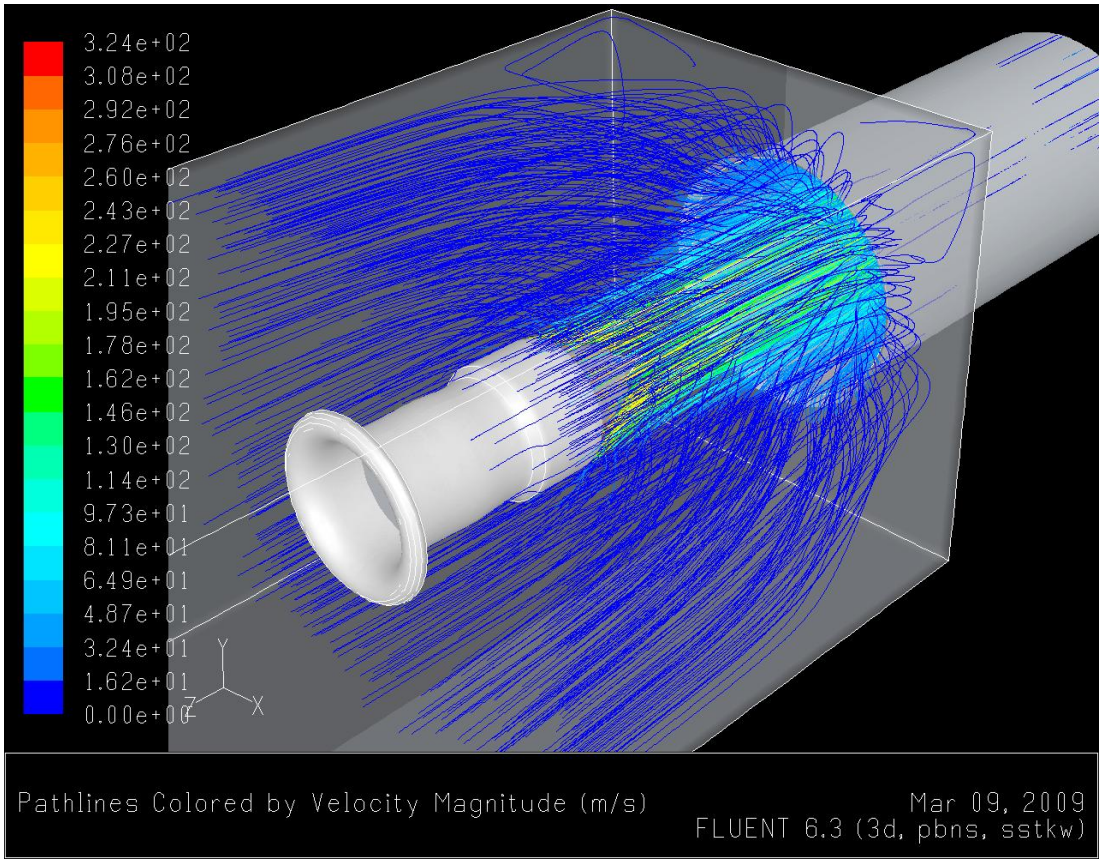

Figure 165 Entrained Streamlines in the Working Section with an Augmenter Diameter of 6.25m and an Engine-Augmenter Spacing of 5.50m

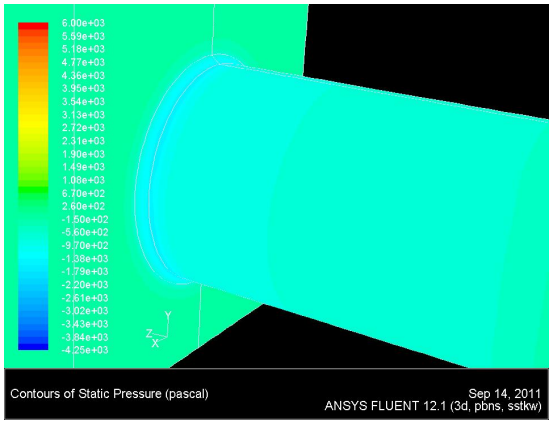

a.

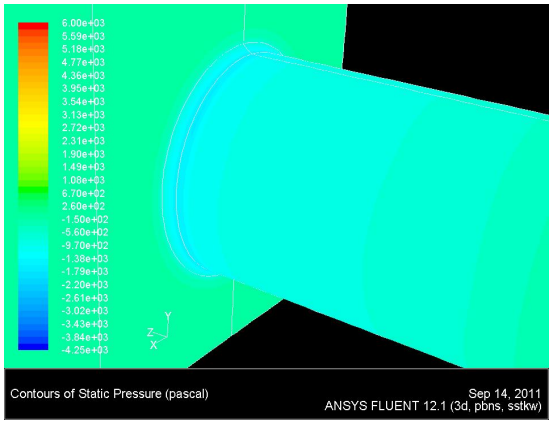

b.

Figure 166 Static Pressure Variation on the Working Section and Augmenter Walls around the 5.50m Diameter Augmenter Entrance with an Engine-Augmenter Spacing of 2.75m (a), and 5.50m (b)

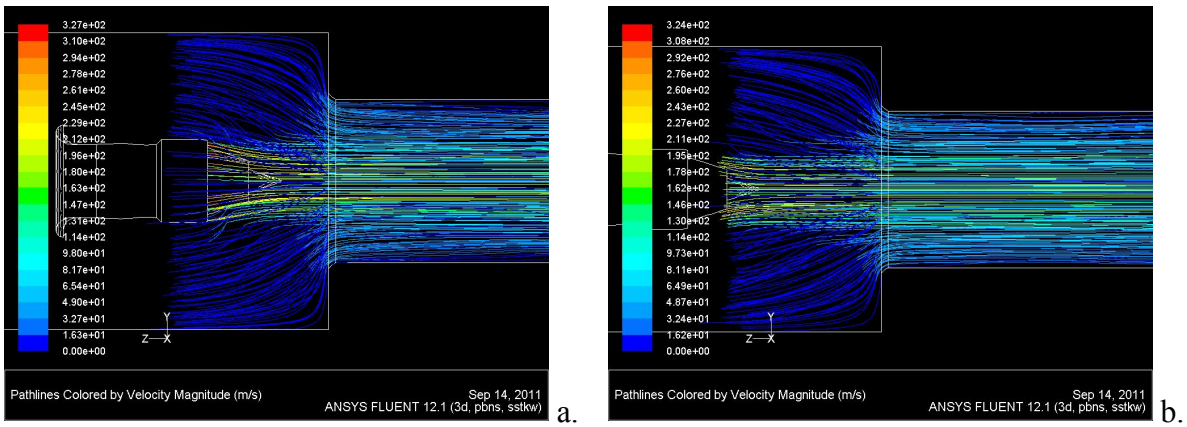

a. b.

Figure 167 5.50m Diameter Augmenter Entrance Stream-Tubes with an Engine-Augmenter Spacing of 2.75m (a), and 5.50m (b)

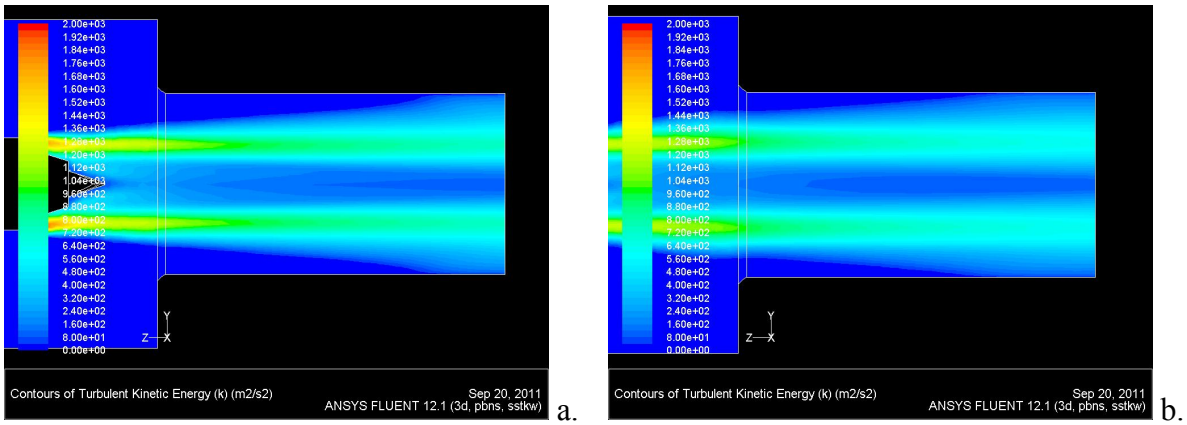

a. b.

Figure 168 *k* on the Vertical Cell Axis through the Rear of the Working Section and 5.50m Diameter Augmenter Tube with an Engine-Augmenter Spacing of 2.75m (a), and 5.50m (b)

Figure 169a shows the pre-cell BPR peak solution using an augmenter diameter of 4.75m. The cell BPR calculated with this arrangement was 133.8%. The augmenter flow remains aligned with the augmenter walls throughout the length of the augmenter tube. When the augmenter diameter was increased to 5.50m (Figure 169b), a near-peak state, separation near the end of the augmenter tube can be seen to begin to develop. Increasing the augmenter diameter further to 6.25m (Figure 169c), took the solution to a post-peak state. Significant separation can be seen near the 'Augmenter Outlet' BC. The cell BPR decreased by 5.0% from the peak solution as a result.

Within the literature there is no suggestion of why this type of flow separation would occur due to realistic phenomena. Therefore, it is believed that the separation is a result of the 'Augmenter Outlet' BC. As the augmenter was increased beyond the peak diameter, the solutions became BC dependent, and therefore did not reflect a true airflow condition. Therefore post-peak conditions above an augmenter diameter of 5.50m are not discussed further in this section.

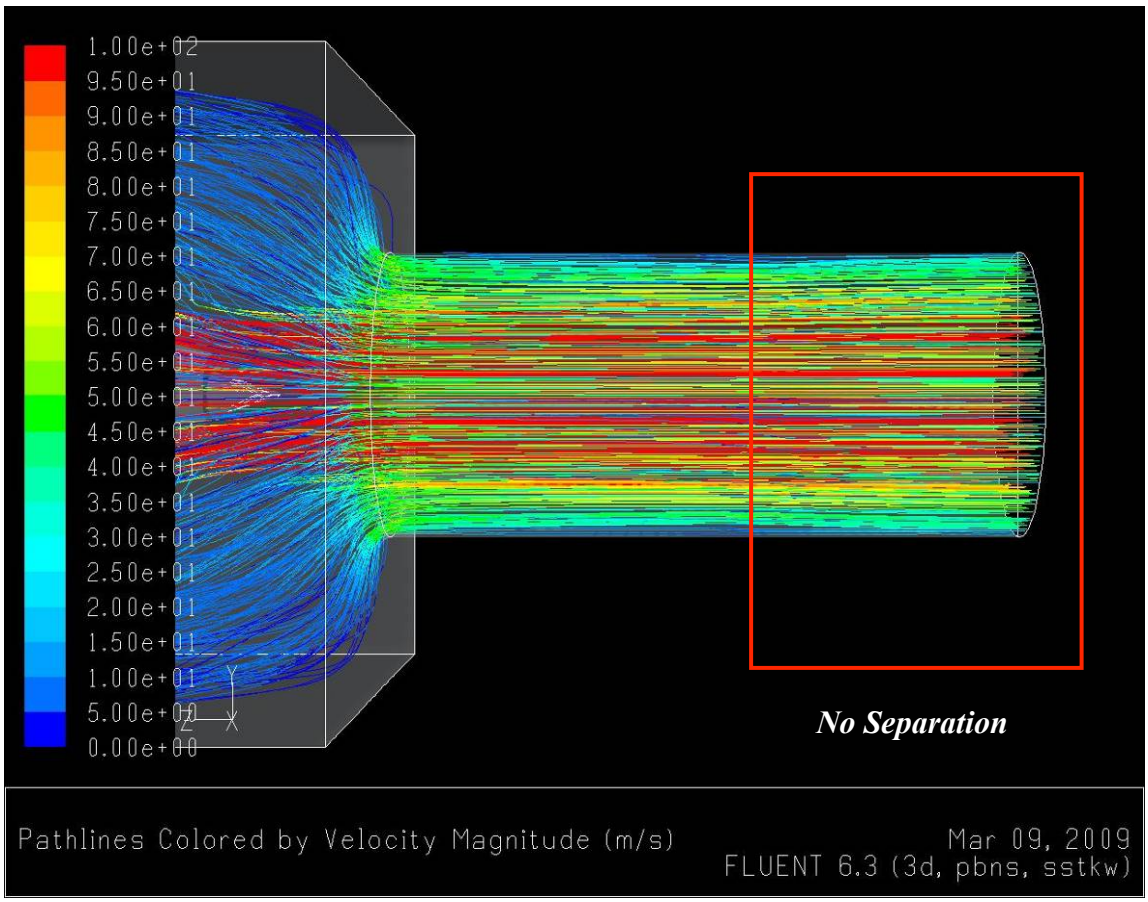
1.00e+02
9.50e+01
9.00e+01
8.50e+01
8.00e+01
7.50e+01
7.00e+01
6.50e+01
6.00e+01
5.50e+01
5.00e+01
4.50e+01
4.00e+01
3.50e+01
3.00e+01
2.50e+01
2.00e+01
1.50e+01
1.00e+01
5.00e+00
0.00e+00
No Separation
Pathlines Colored by Velocity Magnitude (m/s)
Mar 09, 2009
FLUENT 6.3 (3d, pbns, sstkw)

a.

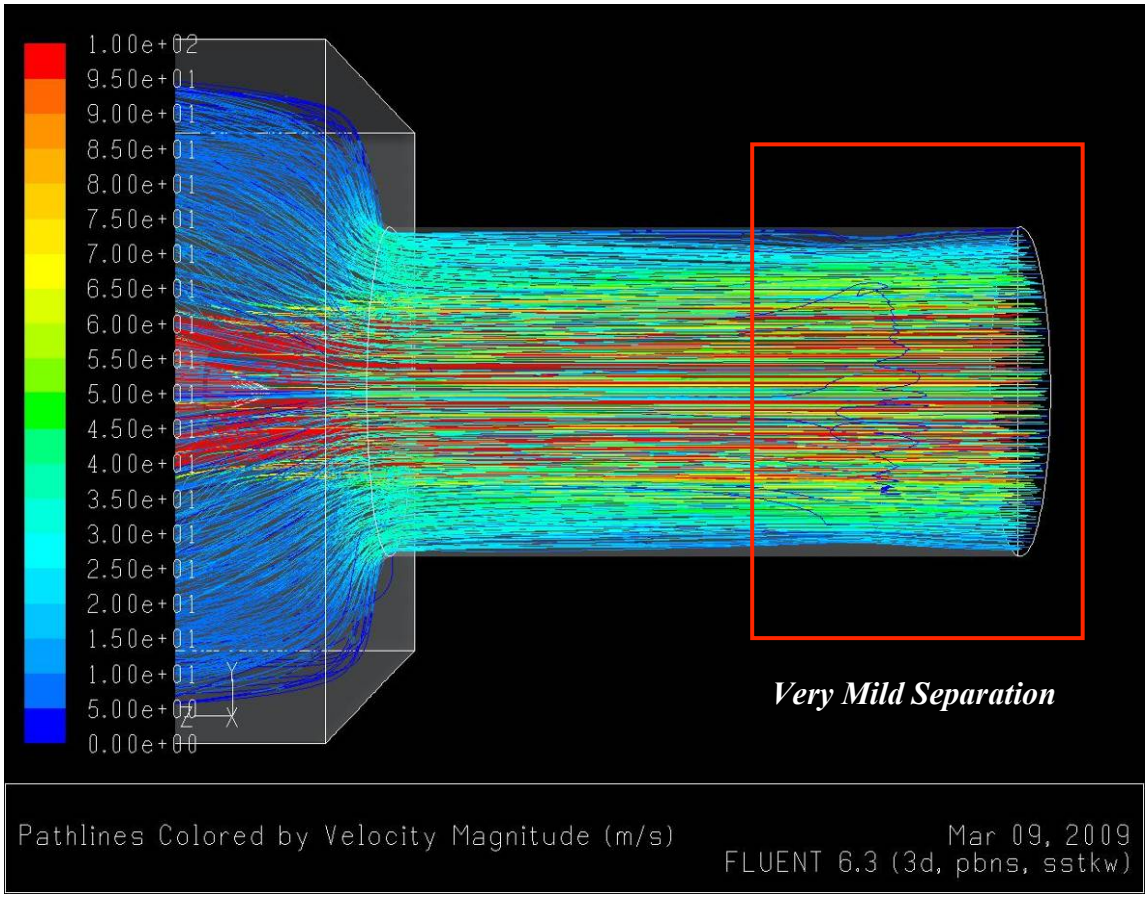
1.00e+02
9.50e+01
9.00e+01
8.50e+01
8.00e+01
7.50e+01
7.00e+01
6.50e+01
6.00e+01
5.50e+01
5.00e+01
4.50e+01
4.00e+01
3.50e+01
3.00e+01
2.50e+01
2.00e+01
1.50e+01
1.00e+01
5.00e+00
0.00e+00
Very Mild Separation
Pathlines Colored by Velocity Magnitude (m/s)
Mar 09, 2009
FLUENT 6.3 (3d, pbns, sstkw)

b.

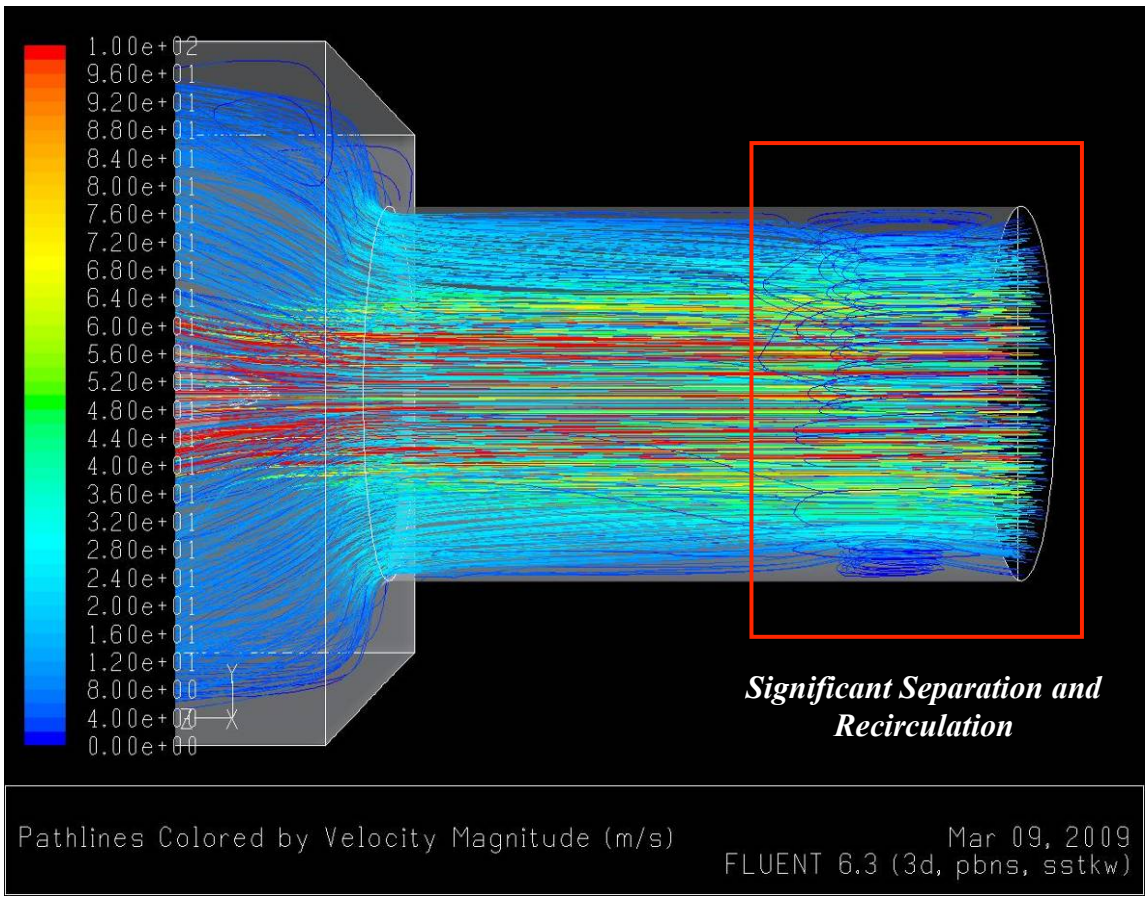

c.

Figure 169 Sequence of Pre- (a), Near- (b), and Post-Peak (c) Cell BPR Solutions with an Engine-Augmenter Spacing of 2.75m

Considering only pre-cell BPR peak solutions, the optimal augmenter diameter, giving maximum cell BPR, for each engine-augmenter spacing can be calculated. A second-order polynomial was fitted to the pre peak solutions in Figure 164. Table 5 presents the polynomials calculating cell BPR in kgs^{-1} for a given engine-augmenter spacing (BPR) as a function of augmenter diameter (Φ). Table 5 also presents the level of fitment between the polynomial and the data of Figure 164, the calculated augmenter diameter of optimal flow efficiency, and the maximum achievable cell BPR. Confirmation of the optimal augmenter diameters were solely based on the polynomial produced from the pre-5.50m Figure 164.

Figure 170 presents the relationship between engine-augmenter spacing and the augmenter diameter of maximum efficiency. A linear trend line was fitted to Figure 170, with the equation $\Phi_{MAX} = 0.346d + 4.857$. The d and Φ_{MAX} components correspond to engine-augmenter spacing and 'augmenter diameter of maximum efficiency' respectively. The R^2 agreement between the data and the trend line was 0.9659.

Table 5 Formulas describing Trend Lines Calculating
Optimum Augmenter Diameter for a given Engine-Augmenter Spacing

Engine-Augmenter Spacing (m)	Polynomial of Trend Line	R^2	Φ_{MAX} (m)	BPR_{MAX} (%)
2.75	$BPR = -11.532\Phi^2 + 132.19\Phi - 236.52$	0.9995	5.73	142.3
3.50	$BPR = -9.737\Phi^2 + 119.2\Phi - 213.43$	0.9995	6.12	151.4
4.15	$BPR = -9.032\Phi^2 + 115.34\Phi - 209.67$	0.9990	6.39	158.6
4.80	$BPR = -9.105\Phi^2 + 118.46\Phi - 220.63$	0.9999	6.51	164.7
5.50	$BPR = -8.644\Phi^2 + 116.05\Phi - 218.39$	0.9990	6.71	171.2

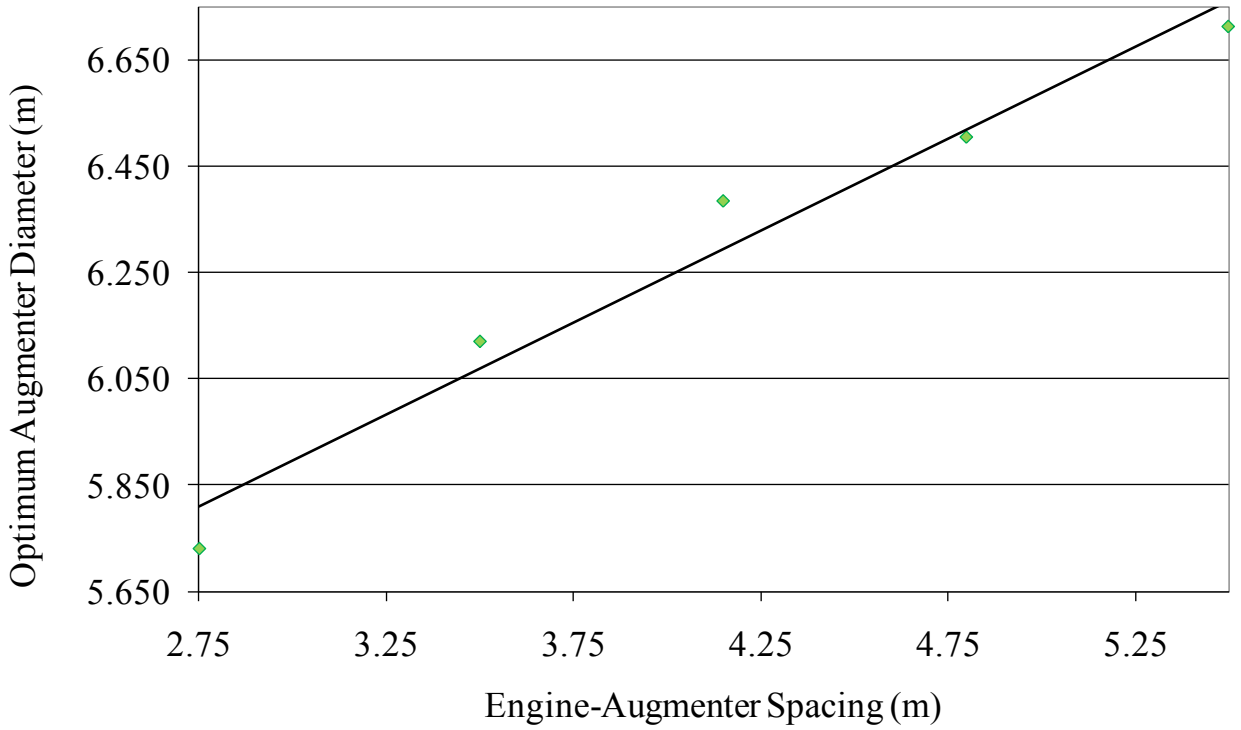

Figure 170 Augmenter Diameter for Optimum Flow Efficiency for a given Engine-Augmenter Spacing

Figure 171 shows the relation between engine-augmenter spacing and maximum achievable cell BPR. Again, a linear trend line was fitted, and could be described by the equation $BPR_{MAX} = 10.4538d + 114.34$. d and BPR_{MAX} correspond to the engine-augmenter spacing and maximum achievable cell BPR in this case. The R^2 agreement between the data and the trend line was 0.9960. The equations of the fitted trend lines are only applicable to the tested engine-cell combination.

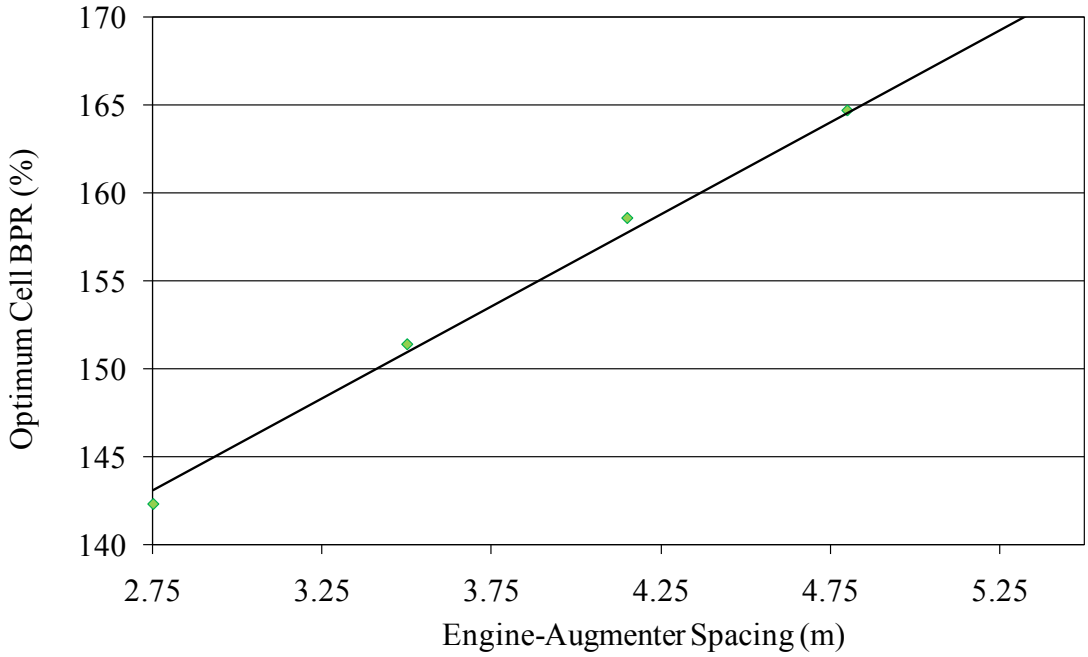

Figure 171 Optimum Cell BPR for a given Engine-Augmenter Spacing

5.3.3 Working Section Cross-Sectional Size and Shape

In the JETC industry the majority of working sections are square or rectangular in shape. The most obvious reasons for this seem to be the ease and cost of constructing them in comparison to more complex geometries. In addition, up until this point, scaling of the proven rectangular and square designs has sufficed.

In Section 5.3.1, that presented the baseline working section results, the square to circular abrupt contraction was seen to create pockets of circulation adjacent to the rear wall of the working section. The discussions of (Idelchik & Fried, 1986), (Massey, 2001), and (Ando & Shakouchi, 2004) all suggest that similar circulation is produced in circular to circular abrupt contraction. However, the circulation in this case is present around the entire perimeter of the contraction entrance.

5.3.3.1 Analysis Procedure

This section investigates whether significant differences in cell efficiency are present when a square to circular contraction is replaced with a circular to circular contraction, in the presence of an upstream jet. For a comprehensive comparison, two domains were created using the circular cross-sectional area. The first one retained the cross-sectional area of the baseline working section, and

the second one retained the perimeter of the baseline working section. The diameters of the circular working sections were set at 11.28m (to retain cross-sectional area) and 12.73m (to retain cross-sectional perimeter length) respectively.

One parameter of the working section and augmenter arrangement that was left un-investigated in Section 5.3.2 was the effect of the working section side length. With the variation in round working section diameters being performed in this section, an appropriate opportunity to integrate a side length investigation on cell efficiency for a square cell was created. As such, three additional domains including square cross-sectioned working sections of 7.5m, 12.5m, and 15.0m side lengths were created.

In all domains the engine-augmenter spacing was set at 4.8m, and the augmenter diameter at 5.0m. To ensure that the findings made were independent of the augmenter diameter used, the 11.28m diameter working section was also matched with augmenter diameters of 4.5m and 5.5m. Table 6 summarises the working section-augmenter combinations that are compared in this section. Those presented in bold, and with a 'p' in superscript, indicate solutions that were produced in previous sections, but are involved in the discussion of this section.

Table 6 Augmenter Diameters at which each Working Section was Analysed at in Section 5.3.3

Working Section Cross-Sectional Shape	Working Section Side Length or Diameter (m)	Augmenter Diameter (m)		
Square	7.5		5.00	
	10.0	**4.50^{p}**	**5.00^{p}**	**5.50^{p}**
	12.5		5.00	
	15.0		5.00	
Circular	11.28	4.50	5.00	5.50
	12.73		5.00	

5.3.3.2 Results

Figure 172 presents the cell BPRs from the solutions generated using a square cross-section working section of varying side length. Figure 172 shows that cell efficiency decreased with an increase in side length. An absolute drop in cell BPR of 3.0% is seen across the 7.5m to 15.0m side length range.

When analysing the working section in isolation the geometry is identical to a standard square duct. In such a case it would be expected that the smoothness of the duct surface would determine whether an increase in side length, and therefore wall area, would increase or decrease the frictional pressure losses. (Idelchik & Fried, 1986) shows that in a smooth surfaced duct, frictional losses decrease with an increase in Re in the region of interest (~2.0E07). Likewise, (Idelchik & Fried, 1986) shows that in a uniformly rough surfaced duct the opposite trend occurs.

The Re has been previously defined as Eq. 3.1. For a duct of square cross-section the duct side length is used for the hydraulic diameter (which was denoted w_b in Eq. 3.1). To maintain the same MFR in a square duct when the side length is increased by 'x' times, the velocity in the duct decreases by x^{-2}. If the flow retains the same temperature, and if we apply the fair assumption that the density of the flow is negligibly affected by the velocity increase, the Re of the flow decreases with an increase in side length.

As the working section walls were modelled with negligible roughness, the trend observed in this section, of an efficiency decrease with an increase in side length are in agreement with (Idelchik & Fried, 1986) when the duct is considered in isolation.

When considering the observed trend in relation to the isolated working section acting as a duct, two factors are balancing against one another. First is the increased surface area if the working section walls. Second is the decrease in flow velocity as the working section cross-section is increased and the MFR retained.

When the size of the working section sides is increased there is an increase in the working section surface area coming in contact with the flow. Doubling the working section side length doubles the contact area between the working section walls and the flow. An increase in contact area between the working section walls and the flow leads to a larger potential area where losses may occur. This potential for increased losses is countered in by the decrease in flow velocity which comes with the increased wall area, and therefore increased cell cross-section. With a lower flow velocity, despite having a larger contact area between the working section and the flow, the losses per unit area of working section wall are decreased.

The second area in the computational domain studied where the flow is affected by an increase in working section wall size, is in the area of the sudden contraction between the working section and augmenter tube. In a similar abruptly contracting pipe scenario, (Idelchik & Fried, 1986) have

tabulated results showing the variation in pressure loss in relation to the ratio of post-contraction (augmenter tube) cross-sectional area to pre-contraction (working section) cross-sectional area. In (Idelchik & Fried, 1986) it is shown that an increase in working section side length, which leads to a decrease in augmenter tube to working section area ratio, pressure losses are increased. This is again in line with the findings in this section.

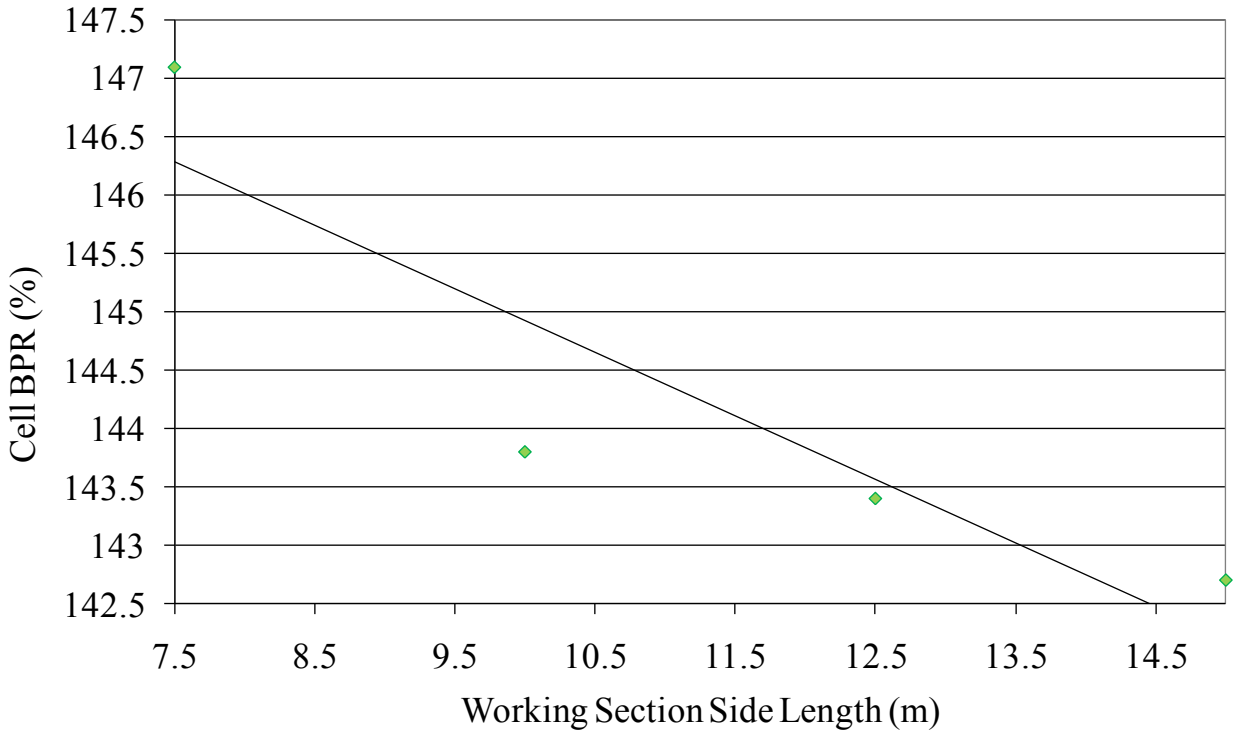

Figure 172 Variation in Cell BPR with Working Section Side Length

Figure 173 compares the flow patterns in the rear of the 7.5m and 15.0m width working section solutions. The 15.0m side length solution shows significant circulation present in the corners of the working section adjacent to the rear wall. The 7.5m diameter cell showed a similar pattern of circulation but of a significantly smaller magnitude. Energy from the mainstream flow is spent creating and maintaining the circulation, thus reducing cell BPR and efficiency. However, as the discussion of Section 5.3.1 indicated, due to the circulation being at a low velocity the losses although present, will only be limited.

Figure 174 presents the cell BPRs for the circular and square working sections of matching cross-sectional area ($100m^2$). Solutions are presented for both cross-sectional shapes for augmenter diameters of 4.5m, 5.0m, and 5.5m as a check of solution independence from augmenter diameter. For all three augmenter diameters analysed, the circular cross-section provided a marginal increase

in cell efficiency in comparison with the square cross-section. Across the range analysed, the absolute variation between the square and circular cross-sections was less than 0.5%.

(Idelchik & Fried, 1986), who reference the findings of (Altshul, 1970), describe the losses in non-circular ducts as the losses in a circular duct multiplied by a correction factor for flows of the same Re. The correction factor for a square duct is 1.0. In relation to the findings of this section, this means the small increase in efficiency when moving to a circular cross-section is solely a function of the contraction between the working section and the augmenter tube.

Figure 175 compares the flow pattern in the rear of the working section for the square and circular cross-sectioned solutions. Rear cell circulation was evident in both arrangements. A consistent pattern in the circular cell was present around the cell perimeter. The circulation regions in the square cell were comparatively large, but isolated to the corners adjacent to the rear wall.

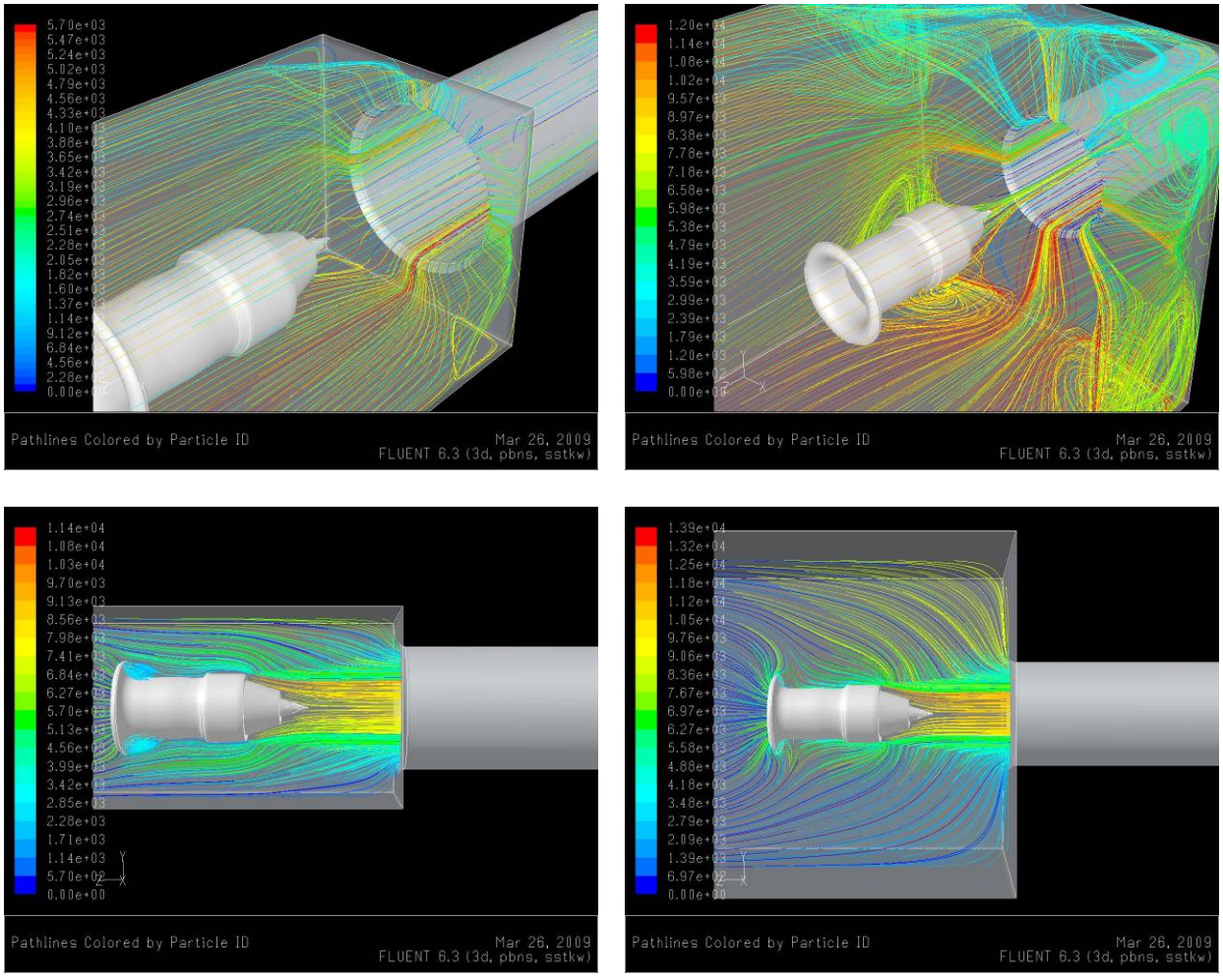

Figure 173 Streamlines in the Rear of the Working Section in 7.5m (left) and 15.0m (right) Width Cells

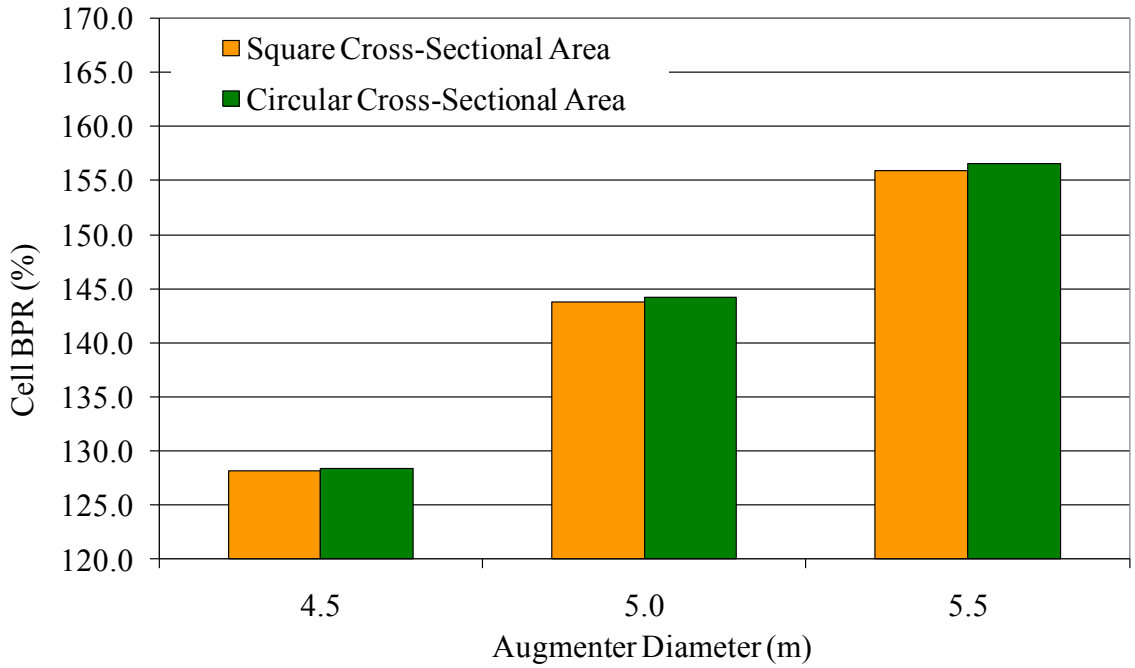

Figure 174 Comparison of Working Section Cross-Sectional Shapes with a 100m^2 Area

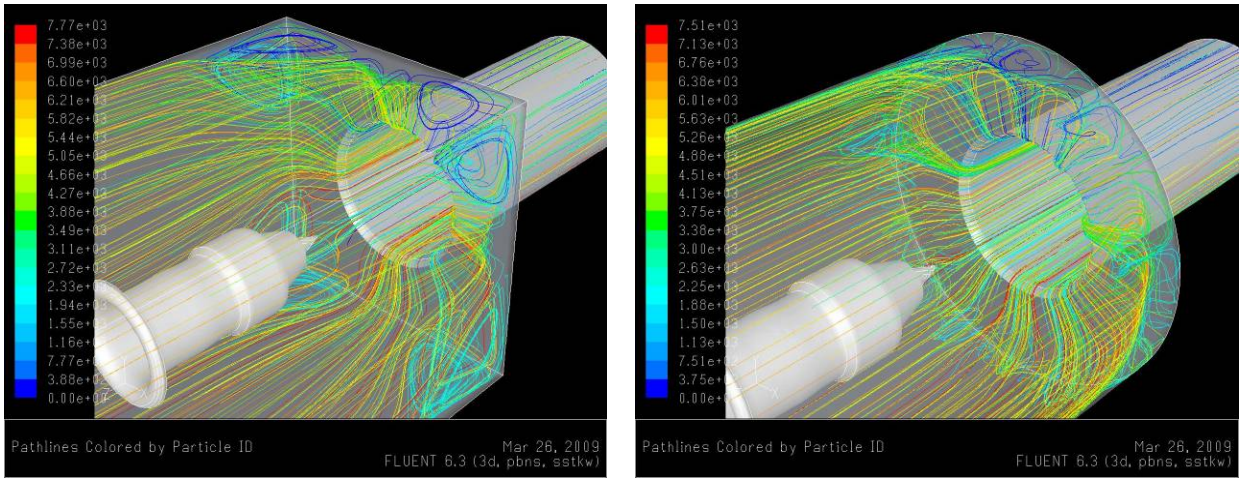

Figure 175 Streamlines in the Rear of the Working Section in a
10.0m Wide Square Cell (left), and a 11.28m Diameter Circular Cell (right)

5.3.4 Working Section-Augmenter Transition

The downstream end of most test cell working sections are capped with flat featureless walls. The working section and end wall intersect perpendicular to one another. A 90° corner is created along the perimeter. As well as capping the working section, the end wall acts to support the entrance of the augmenter tube.

The discussion of Section 5.3.1 showed that the inclusion of a two-stage tapered augmenter lip provided an absolute increase in cell BPR of 3.8% in the baseline domain. Section 5.3.1 also showed that the vena-contracta and associated energy absorbing eddies were removed with the inclusion of the lip treatment.

The typical augmenter tube design at the CHCEC cell is constructed of 12mm thick steel. The augmenter entrance is flush mounted on the cast concrete wall that also provides structural support to the building. Such construction does not lend itself well to retrofit adjustments to the augmenter entrance without a significant financial investment. Therefore, an alternative to improving working section efficiency is sought that can be more easily implemented retrospective of initial construction.

Through the investigations of Section 5.3.1 through Section 5.3.3 the efficiency losses in relation to rear cell circulation have not been easily quantifiable. It was noted in Section 5.3.1 that losses due to this flow feature would likely be low due to the low velocity of the circulation. This claim, which has not up until this point been able to be quantified, still does indicate an area of flow inefficiency.

5.3.4.1 Analysis Procedure

The investigation of this section has two main aims. The first aim is to provide a more quantifiable understanding of circulation in the rear of a JETC working section. The second is to test a potential retrofit solution to improve cell efficiency. It was felt that these aims could be achieved through a simultaneous analysis. To do so, a design process was performed in which the amount of rear cell circulation would be reduced, and eventually removed by incorporating a retrofit solution into the cell. Any modification to the lip profile such as a bell-mouth, which would require modification to the augmenter tube and/or rear wall construction, were not included due to the significant modifications the cell would require to implement in reality.

(Ando & Shakouchi, 2004) showed that a ‘small obstacle’ placed a short distance downstream of an abruptly contracting pipe provided efficiency gains by reducing circulation regions both upstream and downstream of the contraction. With the upstream circulation removed by a two-stage tapered lip, this section investigates the use of more substantial ‘obstacles’ downstream of the contraction. The most intuitive ‘obstacle’ to remove the rear cell circulation by simply filling the space it occupies, was a form of rear cell ramp.

As a ‘ramp-less’ baseline arrangement, the solution generated in Section 5.3.2 that utilised a 5.0m diameter augmenter tube and 4.8m engine-augmenter spacing was used. With consideration for simplicity of construction and cost, a basic ‘picture frame’ ramp was added to the rear of the cell as shown in Figure 176, with a Ω of 45°. A solution was developed using the computational settings discussed in Section 5.2.1.

The analysis of this solution and the continuation of the design process are presented in Section 5.3.4.2 through Section 5.3.4.5. As in Section 3 and Section 4, the analysis of CFD as a design tool was also performed, supplementary to the main objectives of this section.

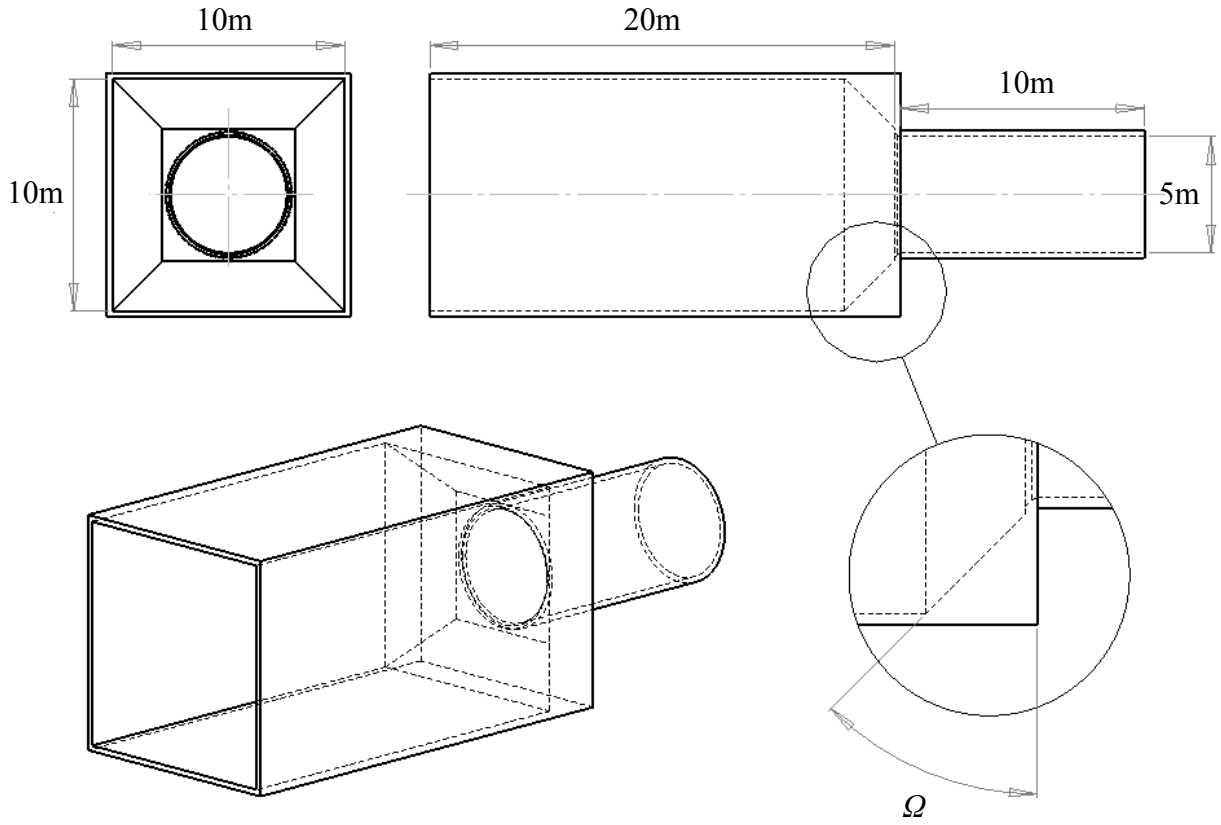

Figure 176 ‘Square’ Ramp Design in the Downstream Corner of the Working Section

5.3.4.2 Results - 45° ‘Picture Frame’ Ramp

As a starting point, and for later comparison, the ‘ramp-less’ baseline solution produced a cell BPR of 143.8%. A streamline plot of this solution is shown in Figure 177.

With the inclusion of the ramp discussed in Section 5.3.4.1, cell BPR improved to 145.9%, an absolute increase of 1.5%. A streamline plot in the rear of the working section for this solution is

shown as Figure 178. A clear reduction in the amount of circulation can be seen, but not a complete removal.

The variation in static pressure build-up between the 'ramp-less' and 'ramped' designs is shown in Figure 179. The maximum static pressure in both solutions is similar. Along the working section walls the build-up in pressure is more sudden in the 'ramped' solution. The inclusion of the ramp distributes the rear wall pressure differently than in the 'ramp-less' solution. Without a ramp, the areas of static pressure are concentrated at the intersection of the sidewalls with the rear wall around both the vertical and horizontal cell axes.

The inclusion of the ramp distributes these areas more evenly around the downstream ramp intersection with the working section walls. Small peaks of static pressure are also seen at the intersection of the ramp with the rear working section wall. The area of low static pressure around downstream of the augmenter entrance, and the pressure distribution through the augmenter tube, were unaffected by the inclusion of the ramp as shown in Figure 180.

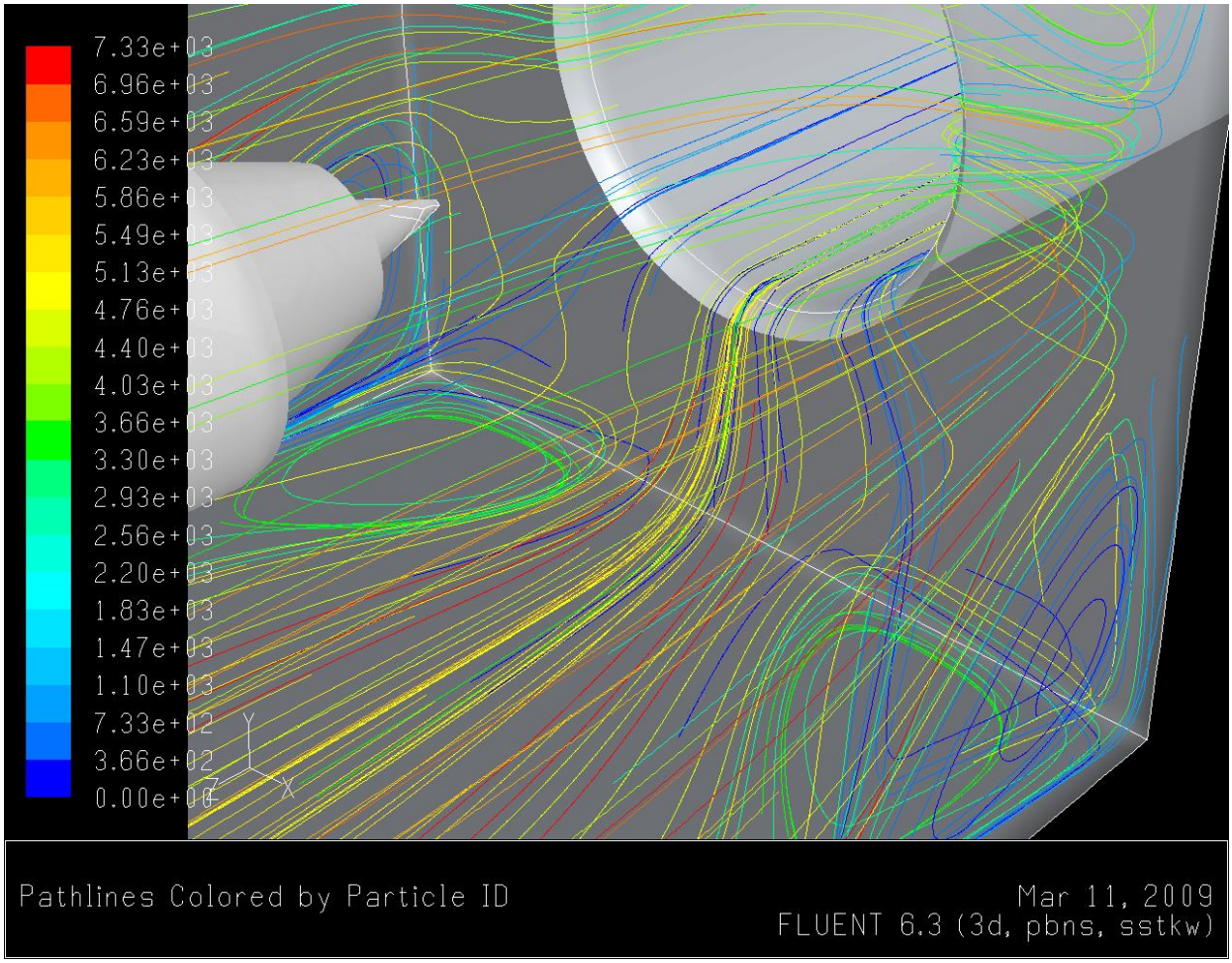

Figure 177 Streamlines in the Rear of the Working Section and 5.00m Diameter Augmenter Entrance with an Engine-Augmenter Spacing of 4.80m

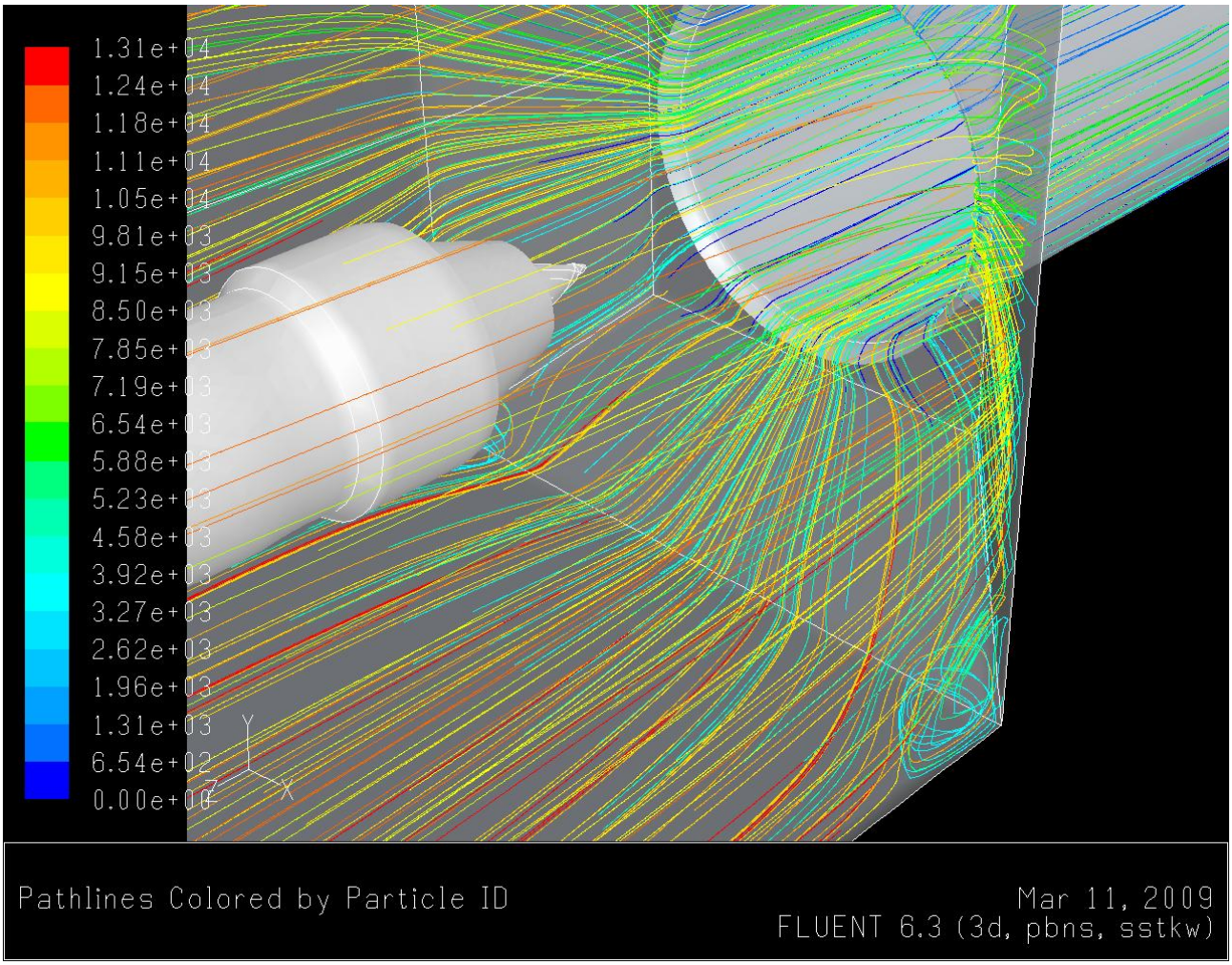

Figure 178 Streamlines in the Rear of the Working Section and Augmenter Entrance with the inclusion of a Square Ramp ($\Omega = 45°$)

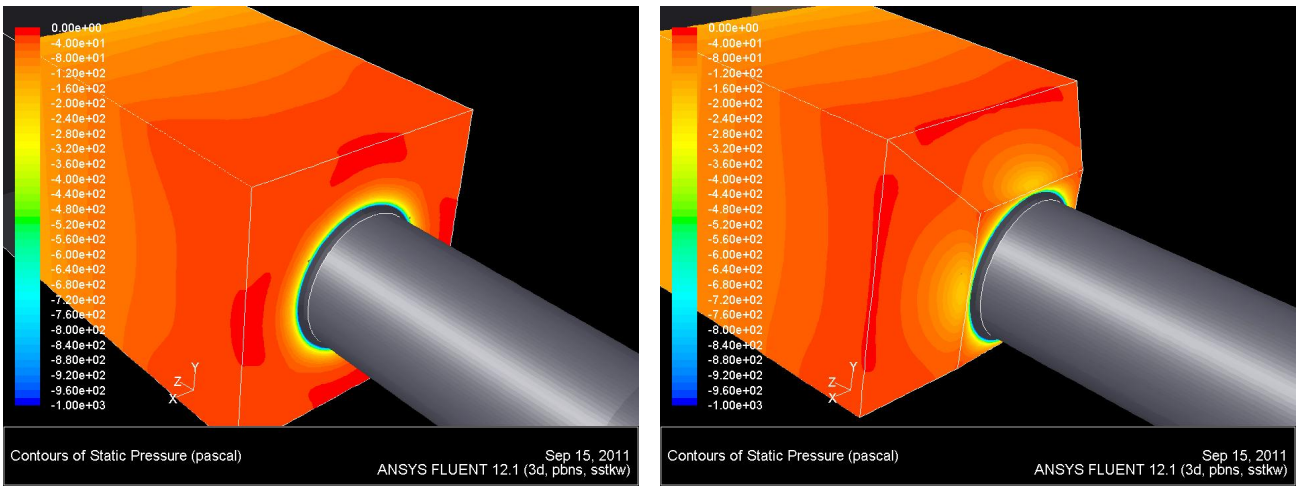

Figure 179 Static Pressure Variation on the Working Section Walls of the 'Rampless' (left) and 'Ramped' (right) Solutions

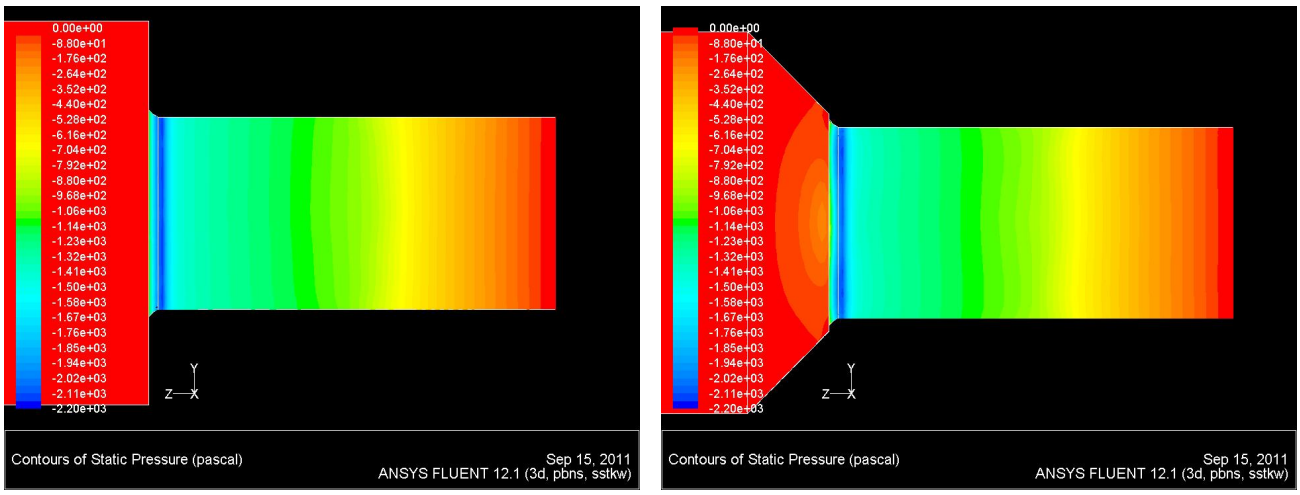

Figure 180 Static Pressure Variation along the Augmenter Tube Walls in the 'Rampless' (left) and 'Ramped' (right) Solutions

5.3.4.3 Results - 60° 'Picture Frame' Ramp

The ramp design discussed in Section 5.3.4.2 was modified in an attempt to completely remove the rear cell circulation, and reduce the static pressure build-up at the downstream intersection of the ramp with the working section walls. To do so Ω, from Figure 176, was increased to 60° and a solution generated. The result was a further increase in cell BPR to 146.4%, an absolute increase of 1.8% over the 'ramp-less' solution.

Figure 181 shows that rear cell circulation was removed by increasing Ω. Comparison of the cell BPRs produced in this section and Section 5.3.4.2 suggest that the rear cell circulation in the 'ramp-less' solution produced between a 1.5% and 1.8% decrease in cell BPR. This is approximately 40% of the improvement made when the two-stage lip was introduced to a sharp-lipped augmenter entrance in Section 5.3.1. It should be noted that a slightly different augmenter diameter and engine-augmenter spacing was used for the generation of the solution in Section 5.3.1, thus the 40% is termed 'approximate'.

Figure 182 can be compared with Figure 179 to see that the high static pressure build-up at the downstream intersection of the ramp with the working section walls has been marginally reduced by the Ω increase. The reduction of static throughout the rear of the working section is lower than in both the domains shown in Figure 179. The small pressure build-up at the intersection of the ramp with the rear cell wall remains present from the design discussed in Section 5.3.4.2.

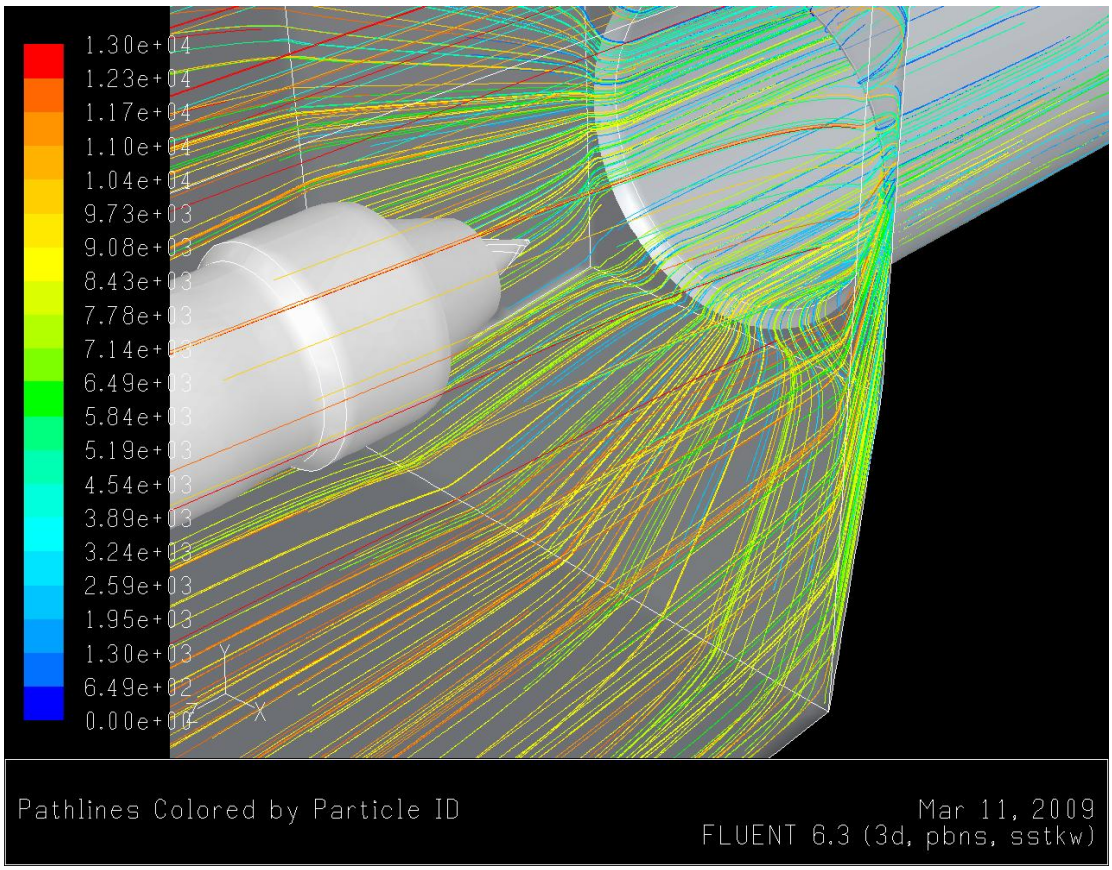

Figure 181 Streamlines in the Rear of the Working Section and Augmenter Entrance with the inclusion of a Square Ramp (with $\Omega = 60°$)

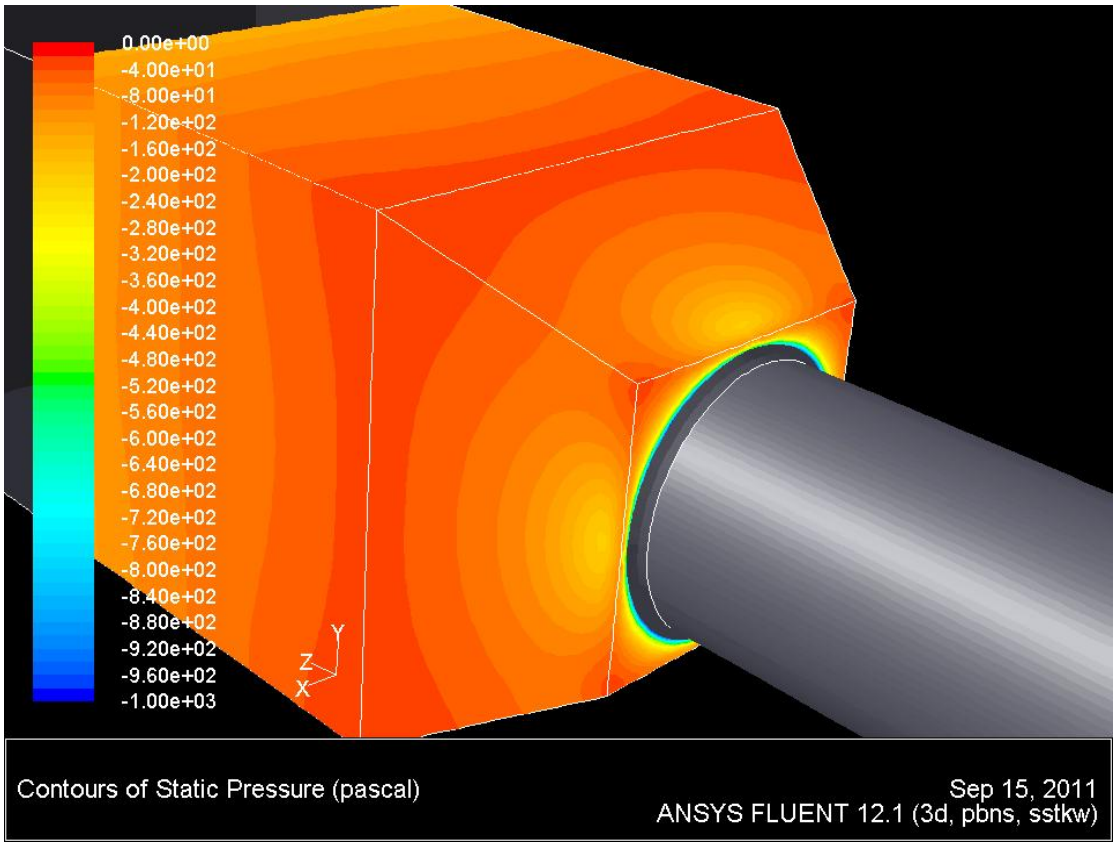

Figure 182 Static Pressure Variation on the Working Section Walls with the inclusion of a Square Ramp (with $\Omega = 60°$)

5.3.4.4 Results - 45° ‘Round’ Ramp

In an effort to remove the pressure build-up at the intersection of the ramp with the rear cell wall, a further design iteration was developed. To eliminate the sudden intersection at the downstream ramp-termination, a ‘round’ ramp of the design shown in Figure 183, with β of 45°, was incorporated into the ‘ramp-less’ domain, and a solution developed.

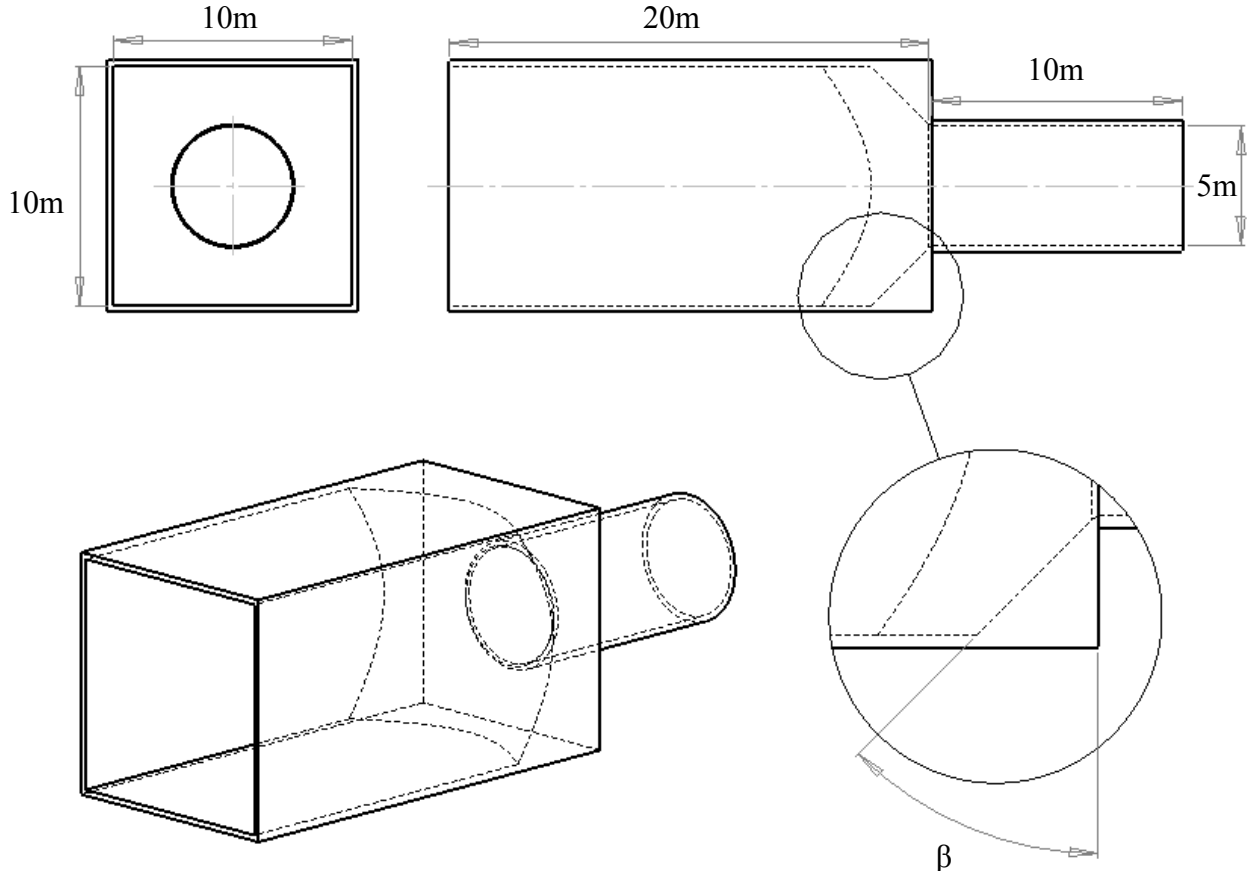

Figure 183 ‘Round’ Ramp Design in the Downstream Corner of the Working Section

With a ‘round’ ramp using a β value of 45° a cell BPR of 148.0% was produced. This was a 2.9% increase over the ‘ramp-less’ solution. Figure 184 and Figure 185 show the streamlines and static pressure distribution in the rear of the working section for this solution. When Figure 185 is compared with Figure 182 the static pressure along the length of the ramp can be seen to be reduced, and is distributed more consistently around the perimeter of the augmenter entrance. The ‘round’ ramp has retained the quality of both ‘picture frame’ ramps in removing the rear cell circulation.

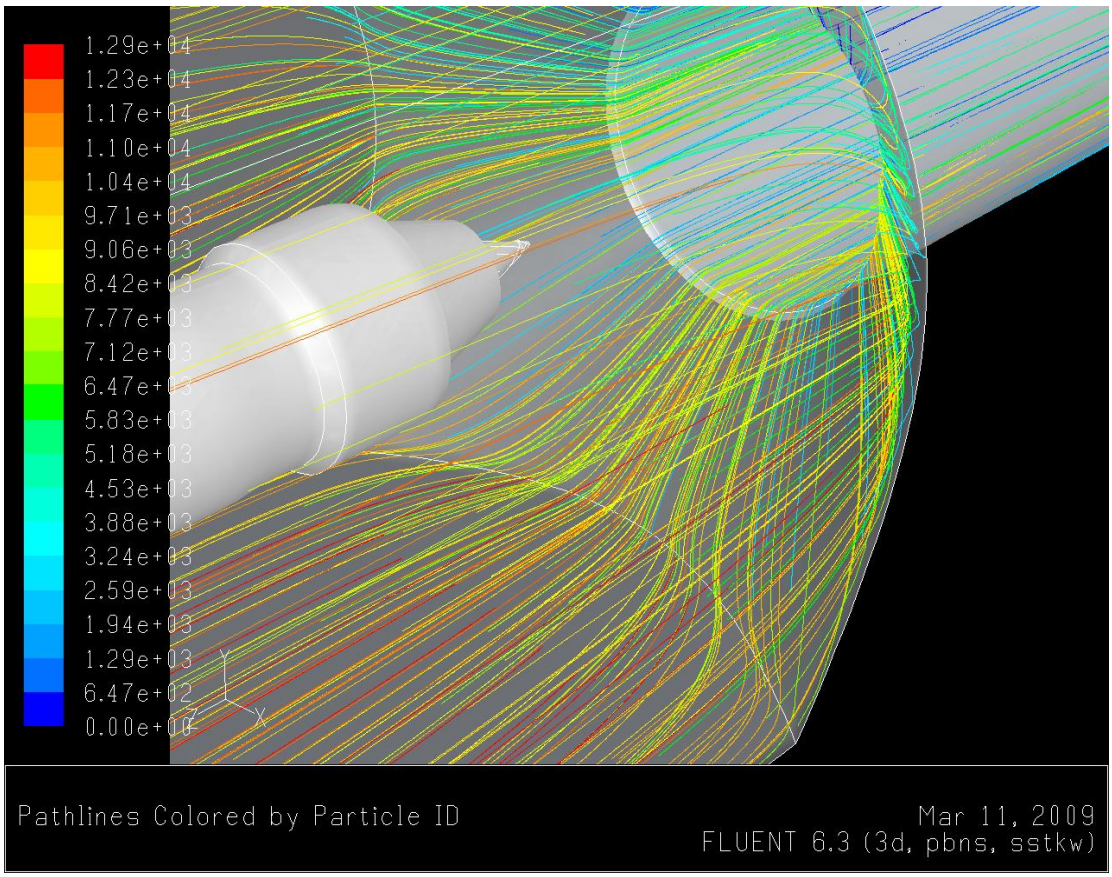

Figure 184 Streamlines in the Rear of the Working Section and Augmenter Entrance with the inclusion of a Round Ramp (with β = 45°)

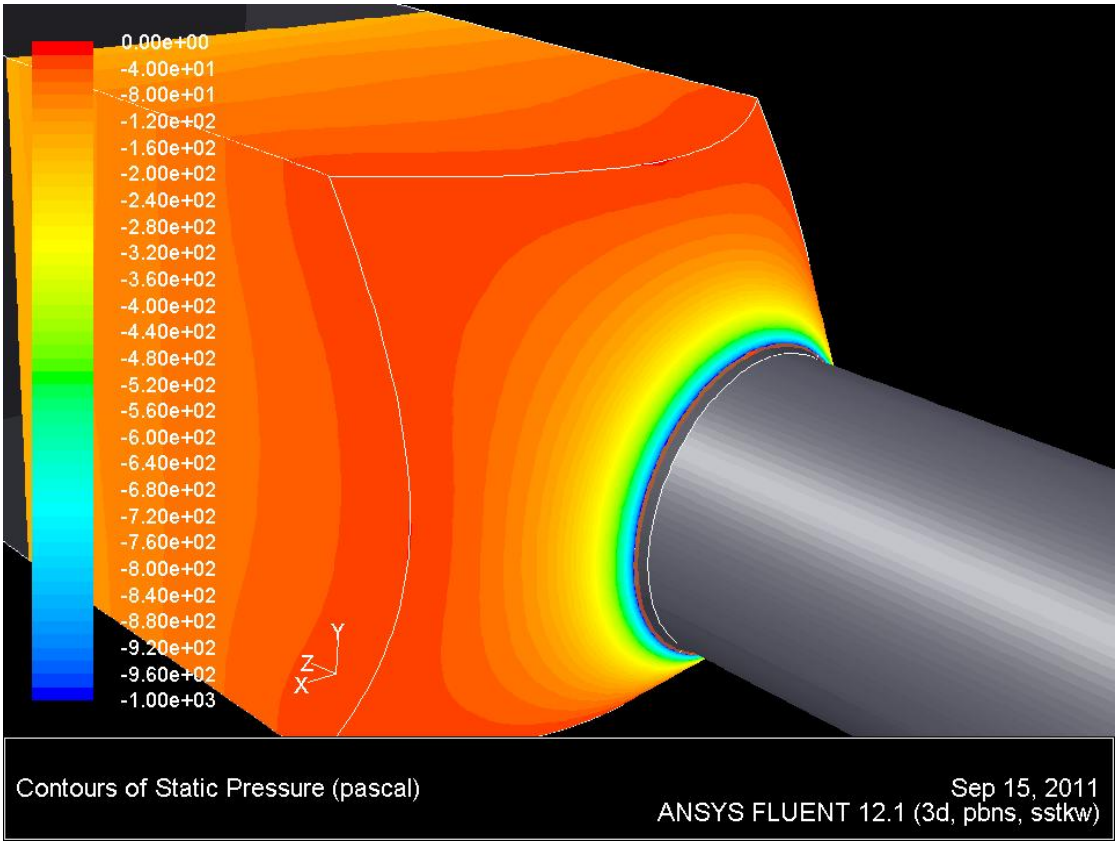

Figure 185 Static Pressure Variation on the Working Section Walls with the inclusion of a Round Ramp (with β = 45°)

5.3.4.5 Results - 60° 'Round' Ramp

Due to the improvements made to cell efficiency with an increase in Ω between Section 5.3.4.2 and Section 5.3.4.3, the 'round' ramp design of Section 5.3.4.4 was altered by increasing β to 60°. A solution was produced, and found to increase cell BPR marginally over the solution of Section 5.3.4.3 to 149.0%. Figure 186 and Figure 187 present the streamline and static pressure at the rear of the working section respectively. When compared with Figure 185, Figure 187 shows that static pressure at the rear of the working section, and along the length of the ramp is again marginally reduced, producing the slight increase in cell efficiency.

5.4 Summary of Findings

This section summarises the findings of each of the three investigations performed on the rear of a JETC working section related to (i) the engine augmenter spacing, (ii) the cross-sectional size and shape, and (iii) the working section-augmenter transition. Portions of the work carried out in this section was included in the paper of (Wei Hua Ho, Gilmore, & Jermy, 2011), which used some of the flow rate findings which provided a base for a further acoustic analysis.

5.4.1 Engine Augmenter Spacing

A CFD analysis was performed on the rear of a JETC working section. Through a computational investigation using a 10m wide square cell, in combination with a Rolls-Royce Trent 500 engine, it was found that cell efficiency was dependent on both the engine-augmenter spacing and augmenter diameter. The flow features determining efficiency varied across the range of solutions analysed. The results produced were broken down and discussed in relation to three cases: those with (i) augmenters less than 3.50m in diameter, (ii) augmenters of between 3.50m and 4.25m in diameter, and (iii) augmenters greater than 4.25m in diameter.

In the case of augmenters less than 3.50m in diameter, cell efficiency was found to be a function of both augmenter diameter and flow dynamics. When the engine-augmenter spacing was increased, the spread of the engine exhaust, prior to the augmenter entrance, was greater. This meant less of the augmenter entrance was available for bypass flow to enter. k, used as a measure of turbulent momentum transfer, was substantially decreased along the length of the augmenter tube as a result.

The restricted augmenter entrance area for bypass flow also resulted in a build-up in static pressure around the augmenter entrance. In such cases the level of rear cell circulation also increased.

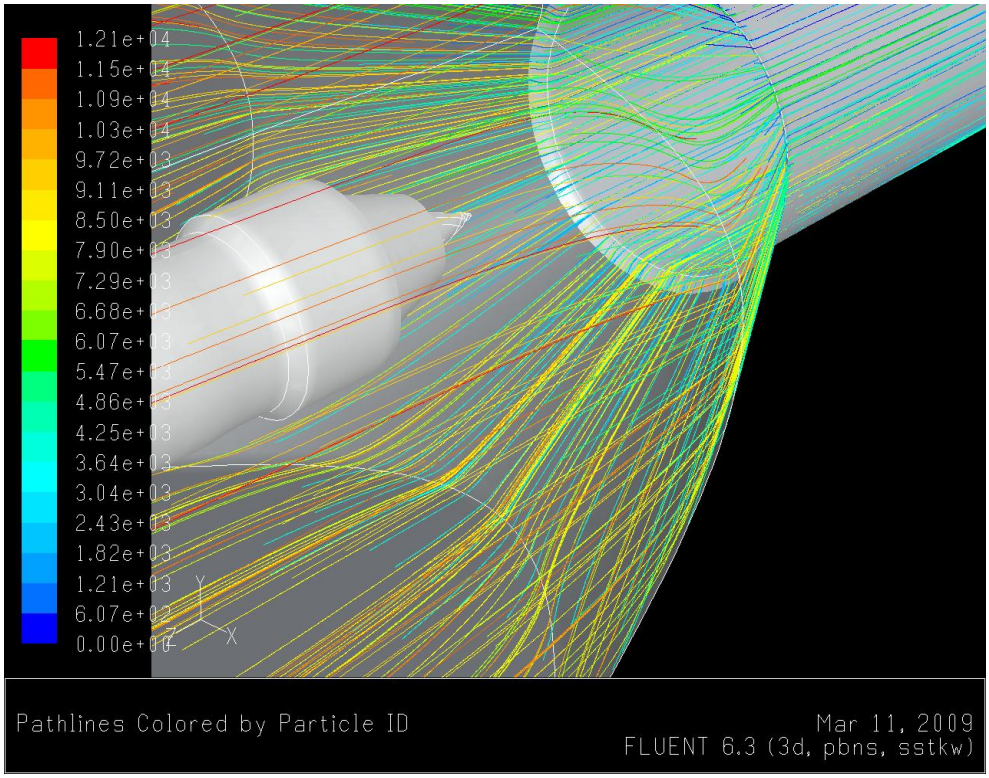

Figure 186 Streamlines in the Rear of the Working Section and Augmenter Entrance with the inclusion of a Round Ramp (with β = 60°)

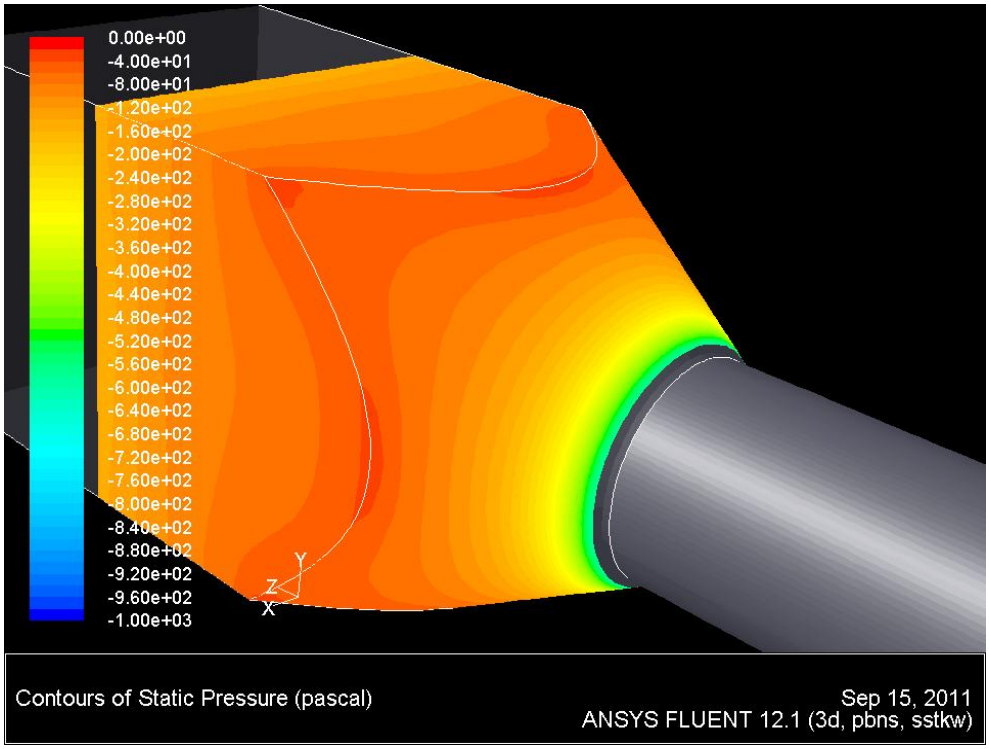

Figure 187 Static Pressure Variation on the Working Section Walls with the inclusion of a Round Ramp (with β = 60°)

Cell efficiency decreased with an increase in engine-augmenter spacing as a result of the above-mentioned energy-wasting flow patterns and restriction to momentum transfer between the exhaust and bypass streams.

The increase in energy losses, with an increase in engine-augmenter spacing, was also observed by comparing stream-wise forces imparted on the working section walls. When using a 3.00m augmenter diameter stream-wise forces from the airflow increased by 7.5% when the engine-augmenter spacing was increased from 2.75m to 5.50m.

In cases with augmenter diameters between 3.50m and 4.25m, the augmenter entrance stream-tube profiles varied minimally across the engine-augmenter spacing range tested. This was in contrast to the findings for augmenters less than 3.50m in diameter, in which the profiles varied significantly.

However, with a reduction in engine-augmenter spacing, the augmenter stream-tubes were found to contract slightly more rapidly. The result of this was a slightly larger build-up of static pressure around the augmenter entrance.

Compared to cases with augmenters less than 3.50m in diameter, the variation in k through the augmenter tube was minimal across the range of solutions produced. This showed that comparable levels of momentum transfer were occurring. As a result of these factors, cell efficiency varied minimally for each augmenter between 3.50m and 4.25m in diameter, when tested across a range of engine-augmenter spacings.

With augmenter diameters greater than 4.25m, cell efficiency was found to be predominantly a function of flow dynamics. The opposite trend, in relation to cell efficiency, was observed when compared to cases using augmenters less than 3.50m in diameter. Cell efficiency was seen to increase, with an increase in engine-augmenter spacing.

An investigation of this trend mismatch was performed. It was found that in cases with small augmenter diameters, and large engine-augmenter spacings, greater energy losses were incurred as a result of momentum being transferred to bypass flow that was unable to enter the augmenter tube. When the augmenter diameters were increased in size, this mechanism of energy loss was removed from all solutions.

Cell efficiency peaked and then declined for each engine-augmenter spacing investigated. This peak occurred when the augmenter diameters were increased over 4.25m. The optimum augmenter diameter (representing maximum flow efficiency) for a given engine-augmenter spacing, increased with an increase in engine-augmenter spacing. The decline in efficiency, following the peak, was thought to be a function of BC dependence in the solution.

Using the data obtained prior to the efficiency peak, an optimum augmenter diameter was found for each engine-augmenter spacing investigated. A polynomial of $y = 0.346x + 4.857$ was found to determine the augmenter diameter of maximum efficiency (y), for a given engine-augmenter spacing (x). A polynomial of the form $y = 10.4538x + 114.34$ was found to give the maximum achievable cell BPR (y), for a given engine-augmenter spacing (x). These results are applicable specifically to the engine-cell combination used in this investigation.

The most significant application of the findings made in this investigation, is thought to be in relation to the design of engine adapters. In most JETCs, a number of engine makes and models are tested. Each engine make and model will have varying dimensions and performance (MFR) capabilities. The individual engine adapters that are used for each engine make and model could be designed to optimise stream-wise engine placement for optimal cell efficiency, and the benefits that are associated with it.

5.4.2 Working Section Cross-Sectional Size and Shape

An increase in the side length in a square working section decreased cell efficiency over the 7.5m to 12.5m range investigated. An increase in stream-wise forces with an increase in working section side length was observed. This contributed to a decrease in cell efficiency, along with a significant increase in circulation adjacent to the rear cell wall. This finding is in alignment with the loss coefficients presented in (Idelchik & Fried, 1986), relating pressure loss to the ratio of pre-contraction duct area to post-contraction duct area.

There was no evidence of a significant effect from the reduction in the blockage ratio (with the blockage being the engine within the working section) created with an increase in cross-sectional working section area.

When the working section was altered from a square to circular cross-section, of the same cross-sectional area, only a marginal increase in cell BPR was observed. This was found to be a result of

the reduction in working section wall area that was associated with the change in cross-sectional shape. This was confirmed when the circular working section was increased in diameter to match the perimeter length of a square working section with a 10m side length. The cell BPR dropped from the previous circular cell solution to equalise with the square cross-sectioned solution.

5.4.3 Working Section-Augmenter Transition

Through a reduction and removal process, it was determined that cell BPR was decreased by between 1.5% and 1.8% in the baseline domain through the presence of rear cell circulation. The inclusion of a ramp increased cell efficiency in all cases. 'Round' ramps provided greater efficiency than 'square' ramps of equivalent lean angles. Both the 'square' and 'round' ramps gave an increase in efficiency with an increase in angle. Both these trends in increased efficiency were mirrored through an observed reduction in static pressure build-up at the rear of the cell.

The greatest absolute gain in efficiency was 3.6% over the 'ramp-less' solution, achieved using a 'round' ramp with a β value of 60°. Compared with the removal of the two-stage lip, all 'ramped' solutions provided a lower gain in flow efficiency, but did show that some gains could be made through an easily installed retrofit solution.

6 Lower Exhaust Stack - Cell Efficiency

6.1 Background Information

In a U-shaped cell the second of two flow re-orientations occurs downstream of the working section, in the lower exhaust stack. The main feature of the lower exhaust stack is the BB, which is located at the downstream end of the augmenter tube. BBs are cylindrical in shape, with a diameter closely matching that of the attached augmenter tube.

A BB is made up of two components; the body, and the forward-facing-cone. The body consists of a perforated cylinder. From cell to cell the length of the perforated area, the porosity level, and the pore distribution within each BB body will vary. The perforated area of the BB is generally made up of a structured series of circular holes 20mm to 40mm in diameter. It is most often the case that the perforations cover the entire perimeter and length of the BB body. Figure 188 shows a standard BB design.

A forward-facing-cone forms the downstream termination of a BB, and aids in dispersing flow through the perforated body. Combined with the lower exhaust stack geometry and the geometry of the BB body, the forward-facing-cone dictates the flow patterns within the lower exhaust stack.

Through a set of flow paths in the lower exhaust stack, the flow exhausted from the BB passes vertically through the remaining height of the exhaust stack before being emitted into the atmosphere. The efficiency of the flow in the lower exhaust stack influences overall cell efficiency, and therefore capacity. This being the case, it is important to understand the flow features present, yet they still remain relatively unknown.

6.2 Lower Exhaust Stack Analysis Methodology

This section performs a CFD investigation into the flow patterns in the lower exhaust stack. The broader aim of the investigation was to analyse the application of CFD techniques to a region of JETC geometry under engine testing conditions. This aimed to more specifically achieve the following:

- Apply recommendations and sound reasoning to set up and generate a CFD solution;

- Gain an understanding of the flow patterns and features at the base of a typical JETC exhaust stack;
- Provide computational solutions to contribute one of the two parts (the other being experimental data) required for a problem-specific validation of the CFD techniques used;
- Qualitatively assess the accuracy of computational solutions produced for physical realism;
- Conduct a CFD-aided design process as an assessment of the capability of CFD as a design and problem solving tool; and
- Use increased cell efficiency, and the associated benefits it brings, as the driving force behind the design process.

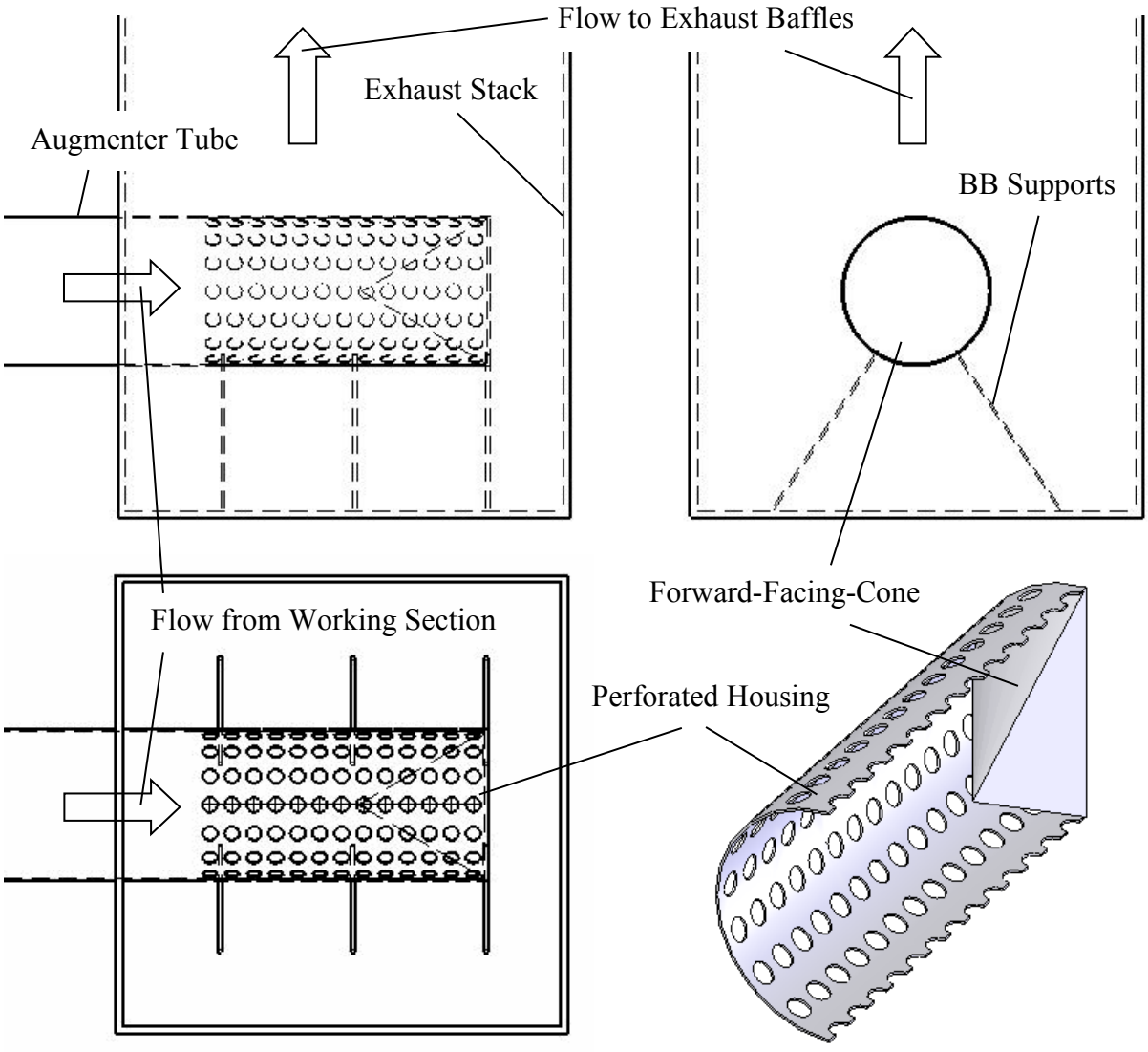

Figure 188 Lower Exhaust Stack Arrangement with the inclusion of a BB

The remainder of this section discusses the methodology employed in performing this investigation. As mentioned above, the flow patterns within a lower exhaust stack (other than in an acoustic

sense) are not well understood and/or documented in the literature. Therefore, reference to other authors work in the findings of this section is very limited. This investigation into the lower exhaust stack flow patterns was therefore viewed by the author as a 'first attempt' at gaining a general understanding of what happens between emission of flow from the BB and exhaustion from the exhaust stack. Without references to compare findings with, an extra effort is made to assess the physical realism of the flow patterns and pressure distributions developed throughout the investigation.

The first step to gaining an understanding of the flow patterns in a 'typical' lower exhaust stack was the creation of baseline lower exhaust stack arrangement. The design and selection of the baseline arrangement is discussed in Section 6.2.1. A computational domain of the baseline arrangement was generated so a CFD analysis of the flow scenario could be performed, and this is discussed in Section 6.2.2.1. Solver settings and BCs were then selected as discussed in Section 6.2.2.2 and Section 6.2.2.3. Next the baseline computational domain was meshed, and a mesh independence check performed. These processes are presented in Section 6.2.2.4.

The main flow patterns and features of the baseline arrangement were analysed by generating a three-dimensional computational solution. This is discussed in Section 6.2.3.1. A CFD-aided investigation and design process was then performed with the aim of improving cell airflow efficiency. The investigation and design process is presented in Section 6.2.3.2 though Section 6.2.3.7. Section 0 then concludes this section with a summary of the findings.

6.2.1 Baseline Design

The first step to generating an understanding of the flow features present in a lower exhaust stack was to design a baseline arrangement. A square cross-section stack was used as it is a common industry design. The width of the exhaust stack was selected to be 10m. As discussed in Section 3, this is representative of a 'mid-sized' JETC by industry standards. Using a 10m wide stack also allowed continuity to be maintained between the investigation of this section and the investigations of Section 3 and Section 5.

The exhaust stack height was set at 30m, giving a 3:1 height to width ratio. At the CENCO cell in Hanover and at the CHCEC cell, the comparative ratios are approximately 2:1 and 2.7:1. By using a greater height to width ratio, a fuller development of the flow patterns was expected to be achieved, leading to a better understanding and more thorough analysis.

An augmenter diameter of 5.0m was used; a 2:1 ratio of stack to augmenter width. This was chosen to maintain comparability with industry examples at the CHCEC, CENCO Hanover, and GE Peebles, who use ratios within a range of 1.95-2.50:1. The BB diameter was set to match that of the augmenter.

The downstream end of the BB was set 2.25m from the downstream wall of the exhaust stack, with a perforated area of 5.50m, comparable with industry examples. In alignment with the CHCEC cell, the BB was capped with a forward-facing-cone with of 110° tip angle. The full geometry of the baseline stack is shown in Figure 189. Figure 189 uses labelling that is referred to in later sections.

It was decided to not include the exhaust stack baffles in the baseline arrangement in order to isolate the effects of the BB flow, and perform a more focused study on the lower exhaust stack region.

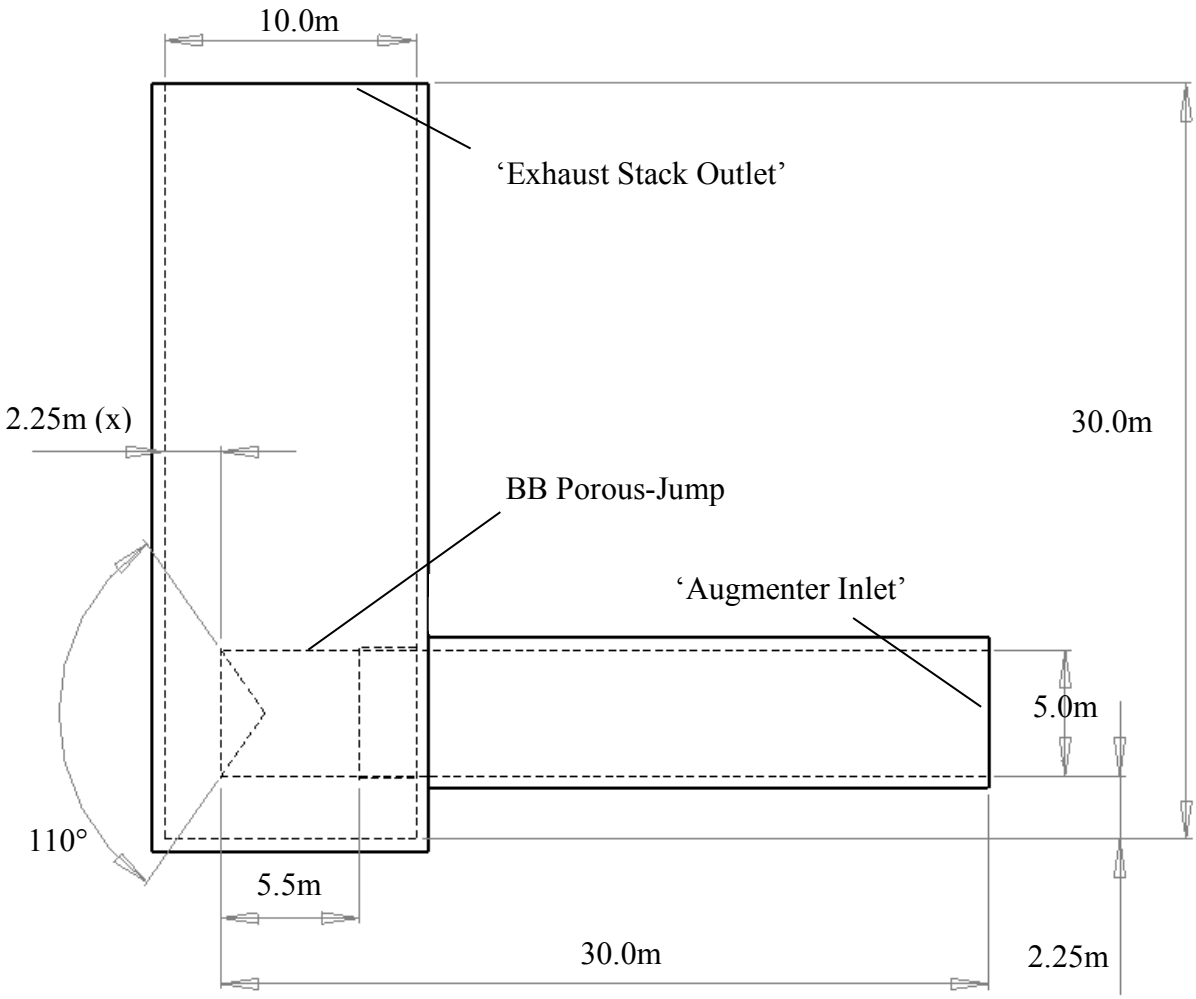

Figure 189 Geometry of Baseline Lower Exhaust Stack Arrangement

6.2.2 Computational Settings

This section discusses the computational settings used in the BB analysis.

6.2.2.1 Computational Domain

The geometry of the baseline lower exhaust stack, discussed in Section 6.2.1, was used in the creation of a three-dimensional computational domain. The outlet BC for the domain was set to align with the top of the exhaust stack. The plane representing the outlet BC is labelled 'Exhaust Stack Outlet' in Figure 189.

The augmenter tube was extended 30m upstream of the downstream end of the BB. An inlet BC was assigned at the upstream end of the augmenter, and is labelled 'Augmenter Inlet' in Figure 189. The length of the augmenter was assigned such a length to ensure that the effects of pressure build-up across the BB would not interact with the upstream BC. The perforated region of BB was modelled as a porous jump, and therefore had no physical thickness in the computational domain.

6.2.2.2 Solver Settings

The fluid modelled within the computational domain was selected to be air. It was predicted that high velocities would be generated in modelling a realistic MFR through the domain, so compressibility effects were accounted for. To do so, the energy equation was activated, and density was modelled via the ideal gas equation. Viscosity was modelled by the Sutherland three-coefficient method. These models are both discussed in (Fluent, 2006).

The construction material of the augmenter tube is discussed in Section 5.2.1.2, and a K_S of 0m was retained for this analysis. The forward-facing-cone was assumed to be constructed in the same material as the augmenter tube, as is the case in the CHCEC cell. The same K_S value of 0m was applied. In the CHCEC cell the construction of the exhaust stack is the same as that of the inlet stack and the working section, smoothed concrete. A K_S value of 0m was also assigned to the stack walls represented in the domain.

A first-order spatial discretisation scheme and SIMPLE pressure-velocity coupling was chosen, both based on the arguments and discussions presented in Section 3. A steady-state solver was used as no areas of transient flow were predicted. This prediction was based on the intention to apply

steady state BCs, and that there was no flow features in the domain that was likely to generate vortex shedding behaviour.

The standard k-ε model was chosen to account for turbulence effects in the computational domain. This was based on the proven performance of the k-ε model in abrupt pipe expansions and scenarios involving side discharge into channels (discussed in Section 2.4), both of relevance to the current investigation (Abbott & Dasco, 1989). Also as discussed in Section 2.4, the k-ε model, although not accepted as being as widely applicable as the k-ω SST model, has still been proven an excellent performer in a wide range of industrial flow problems.

The SA model was again rejected due to its lack of ability in complex flows, as predicted in the lower exhaust stack. The RSM was considered due to its claimed superior performance in wall jet scenarios, which was thought have some applicability in the current case. However, was deemed too computationally expensive to be applied in the sizable three-dimensional domain of this investigation.

6.2.2.3 Boundary Conditions

Due to the lack of test cell data from the intended validation testing, 'artificial' inlet and outlet BCs were applied to represent a realistic MFR through the domain. In a real JETC scenario, the driving force between the surfaces, represented by the 'Augmenter Inlet' and 'Stack Exit', would be a pressure difference. To replicate this, a combination of pressure inlet and pressure outlet BCs were assigned at the 'Augmenter Inlet' and 'Stack Exit' respectively.

Focus was then placed on generating a cell MFR comparable to that that would be expected in a 10m wide cell. As per the discussion of Section 3, a 10m wide exhaust stack represents a 'mid-sized' cell by JETC industry standards. As a 'mid-sized' engine, the Rolls-Royce Trent 500 was deemed to be a likely choice of engine tested in the size of cell represented in the computational domain.

The Trent 500 produces an air MFR of approximately 860kgs^{-1} (Rolls-Royce, 2009). A realistic cell BPR of 150% was then selected (Clarke, 2000). Combining these figures allowed a goal cell MFR to be calculated, 2150kgs^{-1}, from which the inlet and outlet BCs would need to approximately replicate.

The ‘Stack Exit’ BC was initially considered. As it represented an exhaustion to the atmosphere, a static gauge pressure of 0Pa (atmospheric pressure in the domain) was selected. The total pressure at the ‘Augmenter Inlet’ was then set through an iterative process immediately prior to the main body of the investigation. The total pressure was set at 2000Pa and a solution produced. The solution generated a MFR well below 2150kgs^{-1}. The pressure at the BC was incrementally increased in 500Pa steps, until a solution approximating the desired 2150kgs^{-1} cell MFR was achieved. This method led to the ‘Augmenter Inlet’ being assigned a total pressure of 4500Pa for the main body of the investigation.

The use of a uniform pressure BC at the ‘Augmenter Inlet’ meant a near fully developed flow condition would be present. This was deemed ideal, as it would allow the BB and lower exhaust stack to be analysed in isolation from the upstream cell components. To reflect this scenario the TI at the ‘Augmenter Inlet’ was set at a low level of 1%, and the TLS at 0.35m, as per the recommendations of (Fluent, 2006).

The best source of information for the thermal BC at the ‘Augmenter Inlet’ was thought to be the solutions produced in Section 5. Although not validated to the level desired, it was felt it provided the best approximation available, reflecting the thermal interactions of the respective cell bypass, engine bypass, and engine core flows. Figure 190 presents a plot of temperature at the ‘Augmenter Outlet’ in a solution produced in Section 5 using an augmenter diameter of 5.0m, and an engine-augmenter spacing of 3.5m. The average temperature across the face was calculated at just below 300K. This value was assigned at the ‘Augmenter Inlet’ BC.

Figure 191, shows a case considered by (Idelchik & Fried, 1986), in which *K* was calculated to be 0.9 across a comparable BB type structure. The case considered in Figure 191 uses a modified geometry to that in the current scenario being investigated. Compared to the example of the CHCEC the porosity was much greater, at 82.5%, giving a much more open structure. As a result *K* in the case tested by (Idelchik & Fried, 1986) is much lower than that in place at the CHCEC. The (Idelchik & Fried, 1986) case also uses a forward-facing-cone that is slightly elongated from the CHCEC example. As can be calculated from Figure 191, the cone tip angle is 42°, sharper than the CHCEC equivalent.

Despite the above-mentioned differences in the CHCEC and (Idelchik & Fried, 1986) BB examples, at the same time, it was not felt that the correlations for a flat perforated plate presented by (Brundrett, 1993) and (Idelchik & Fried, 1986) in Section 2.3.2.3 could accurately be used to

predict the BB scenario. The reason for this was due to the presence of the forward-facing-cone, and the predicted variation in angle of incidence across the perforated area it would produce. As such, as the best source of approximation, that presented in Figure 191 was used. C_2 and Δm were set at $100m^{-1}$ and 0.009m respectively. Via the relation discussed in Section 2.3.2.3, these values combined to generate a value of 0.9 for K across the 'BB Porous Jump'.

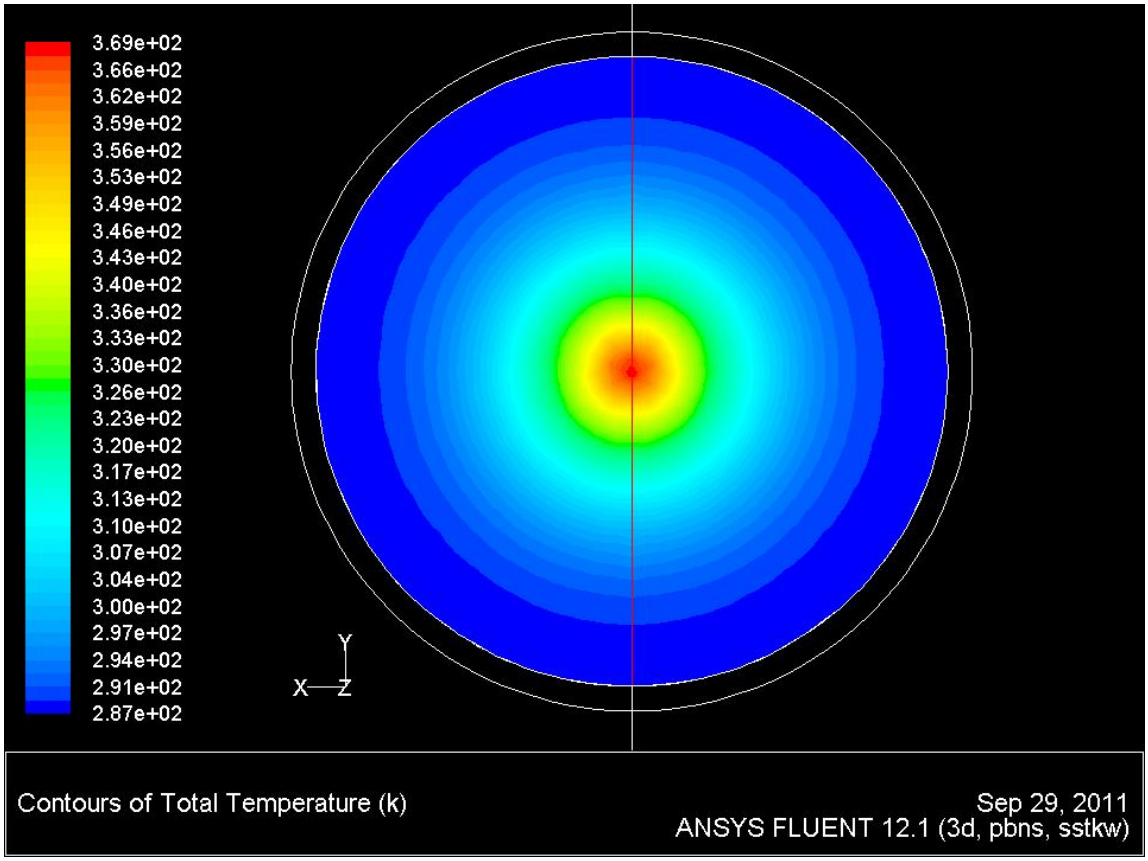

Figure 190 Variation in Temperature on 'Augmenter Outlet' BC Face (Source: Section 5)

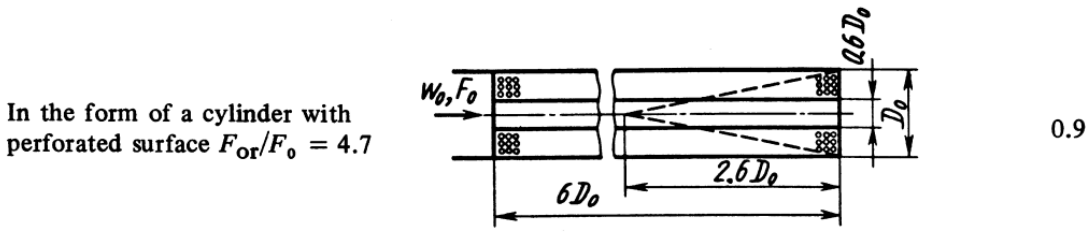

Figure 191 Geometry used by (Idelchik & Fried, 1986) in calculation of a Pressure Loss Coefficient through a Perforated Blast Basket (Source: (Idelchik & Fried, 1986))

6.2.2.4 Mesh and Mesh Independence

The computational domain described in Section 6.2.2.1 was broken into zones for the purpose of controlling the mesh density. The four zones used are shown in Figure 192.

The most complex flow was predicted to be in the BB and the lower exhaust stack. Therefore, a high relative mesh density was used in these areas. The highest density of mesh elements was concentrated on the forward-facing-cone. Since the flow patterns were not well understood prior to solution, but predicted to be complex, tetrahedral elements were used in these areas (Fluent, 2006).

In the augmenter tube, wedge elements were used. This allowed a structured mesh development along the length of the tube, where the flow was expected to be boundary aligned, along with compatibility with the tetrahedral elements in the downstream BB zone.

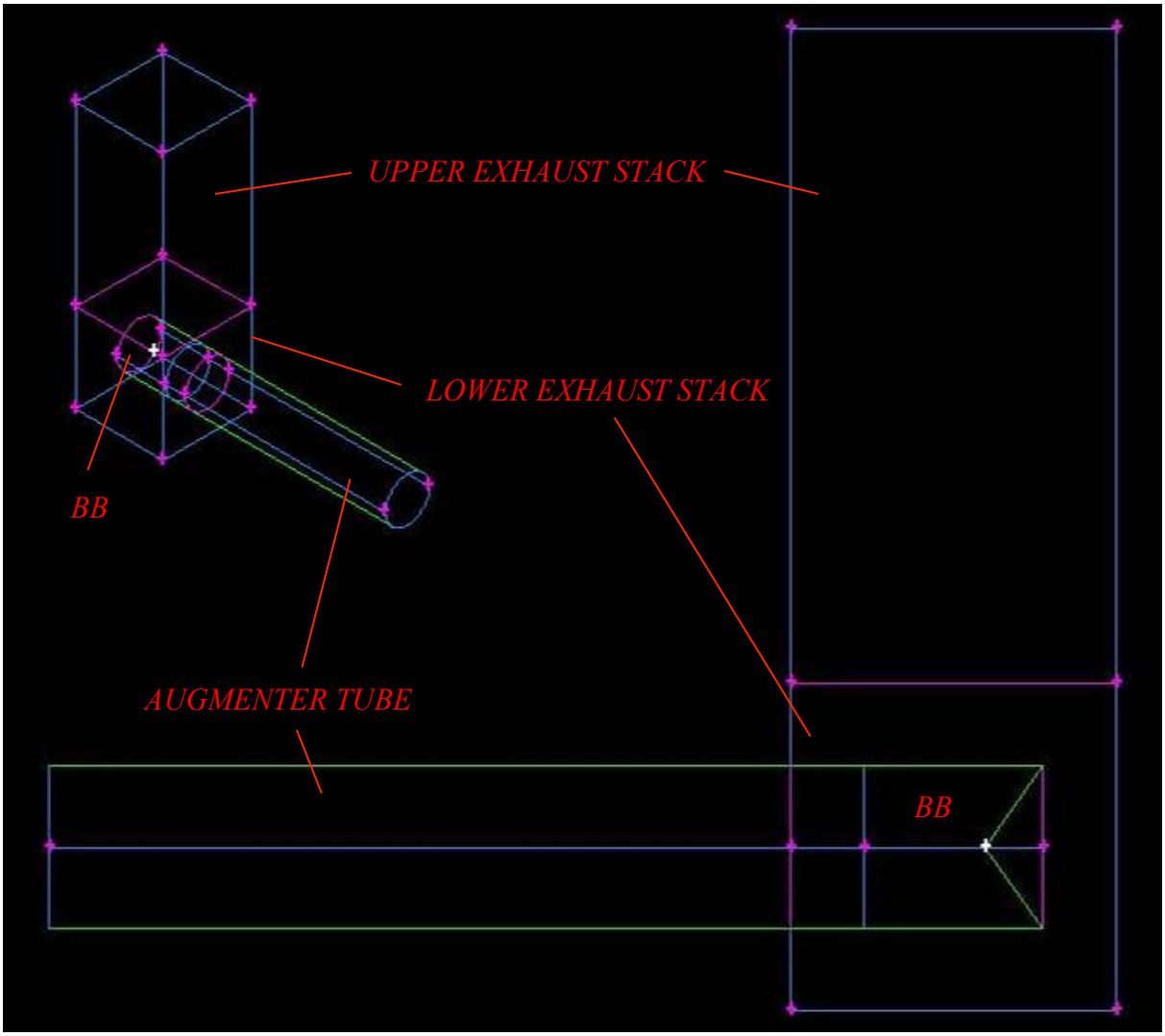

Figure 192 Zones of the Computational Domain used for Mesh Control

In the upper exhaust stack, flow patterns were predicted to simplify and become mostly aligned with the exhaust stack walls. Hexagonal elements were used in this area as they perform well in such conditions and stack efficiently (Fluent, 2006). The mesh density and element types used in the computational domain are shown in Figure 193.

An initial mesh iteration containing 8.56E05 elements was developed. A solution was generated using the solver settings and BCs described in Section 6.2.2.2 and Section 6.2.2.3. The density distribution was retained, and subsequent meshes containing 1.06E06, 1.44E06, and 1.95E06 elements were developed. Solutions were generated for each and then compared.

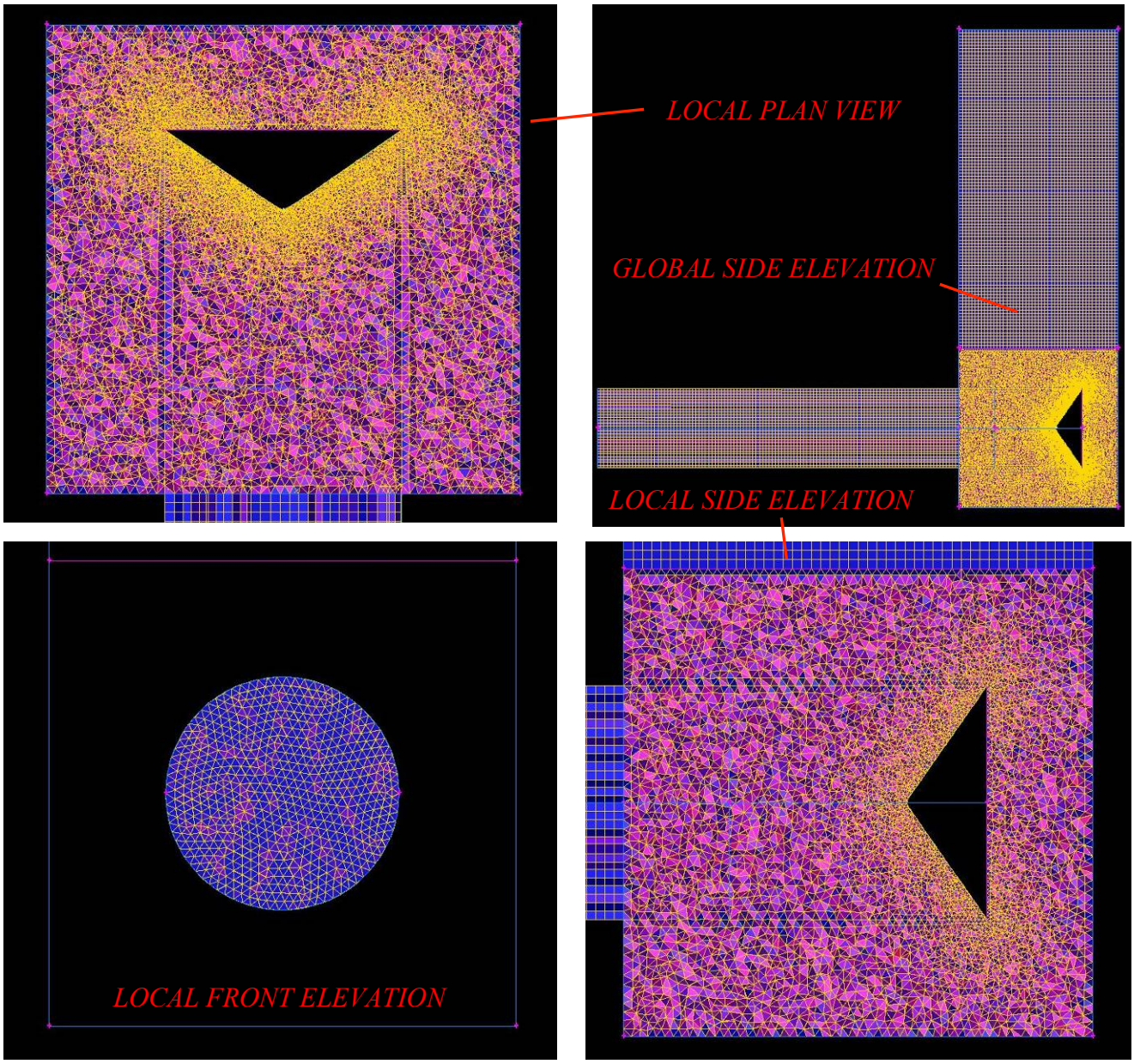

Figure 193 Element Types and Element Density Distribution in the Computational Domain

As a standard industry measure cell efficiency, cell BPR was used as the determining parameter in mesh independence. The BPRs for all mesh iterations fell within the range of 138.0% to 139.2%, representing an absolute variation of 0.87%.

A qualitative analysis of the flow patterns between the BB and exhaust stack exit was performed. Figure 194 presents the flow patterns for solutions developed with meshes of 1.44E06 and 1.95E06 elements respectively.

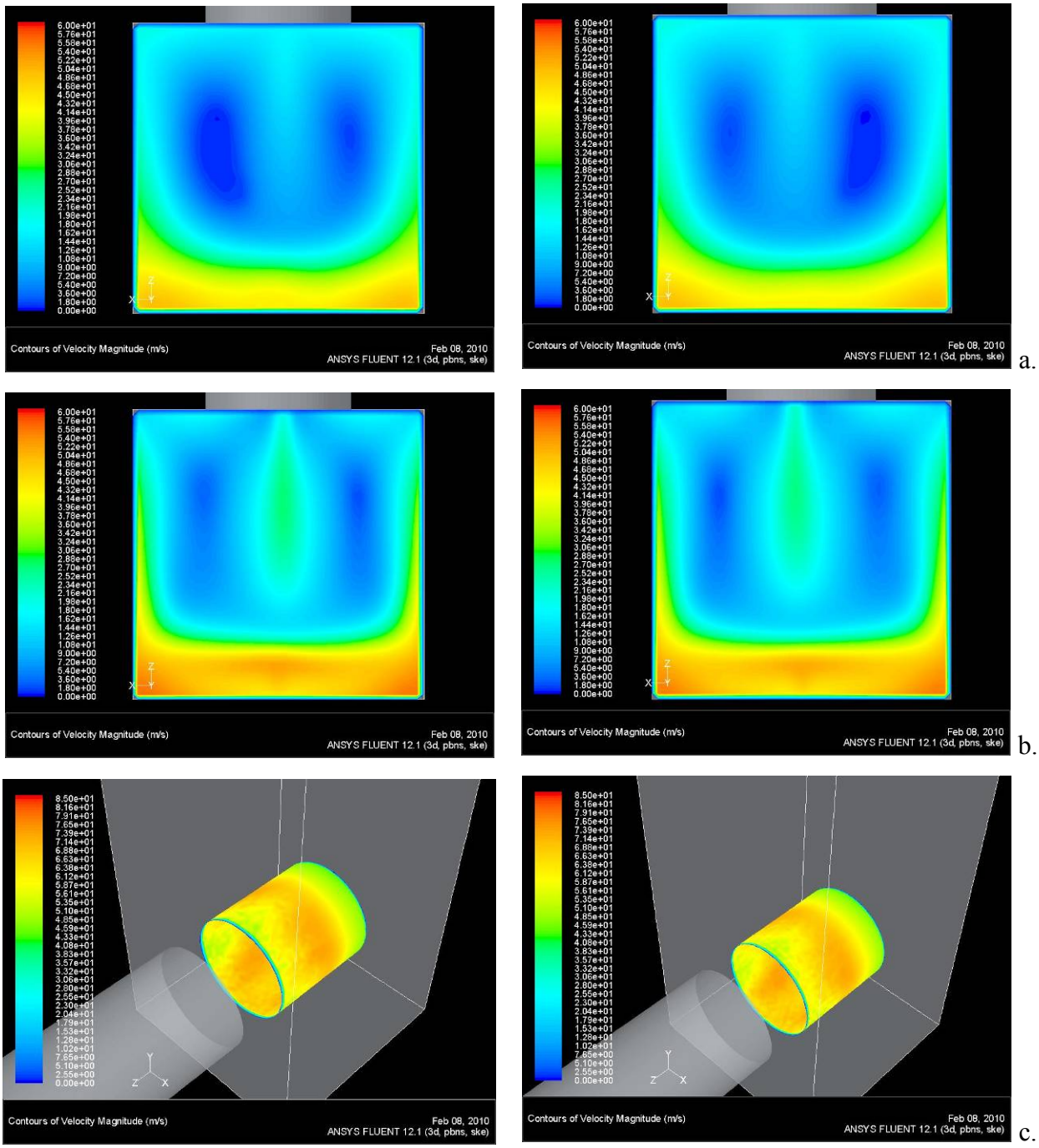

Figure 194 Velocity Magnitude at Exhaust Stack Mid Height (a), Exhaust Stack Exit (b), and BB exit (c), generated from Solutions using 1.44E06 (left) and 1.95E06 Mesh Elements (right)

Figure 194 shows there are no significant qualitative differences between the solutions produced with 1.44E06 and 1.95E06 elements. The velocity distribution at the exhaust stack mid-height and exit, shown in Figure 194a and Figure 194b, show the only visible variation, which is marginal. A

slight horizontal asymmetry is seen consistently across both solutions. Consequently, a mesh of 1.95E06 elements was deemed appropriate for the aims of the analysis in this section.

6.2.3 Results

The findings of the lower exhaust stack investigation are presented in this section. The baseline stack is initially discussed in Section 6.2.3.1. An investigation and design process is then presented in Section 6.2.3.2 through 6.2.3.7. Throughout this section cell MFR was used as the determining parameter in cell efficiency.

6.2.3.1 Baseline Design

A computational solution to the baseline domain described in Section 6.2.1, using the computational settings of Section 6.2.2, was generated. Figure 195 through Figure 204 show the flow patterns generated within the baseline arrangement. A MFR of 2052kgs^{-1} was achieved.

In Figure 195 and Figure 196 the forward-facing-cone can be seen to distribute the flow at a relatively even velocity throughout the entire 360° perimeter of the BB body. This is reflected by a fairly even static pressure distribution on forward-facing-cone face, as seen in Figure 197. A majority of the flow can be seen to exit via the downstream 50% of the BB body, as seen in Figure 198 and Figure 199.

Figure 199 also shows two regions of rotation have developed, with the centre of rotation running perpendicular to the augmenter flow. The centres of rotation are marked with res crosses in Figure 199. One occurs downstream of the lower edge of the forward-facing-cone, and the other adjacent to the base of the stack towards the rear of the BB body. Figure 200 shows the pressure build-up in the BB structure, and is used for reference in later sections.

The flow exiting above the BB centreline can be seen to separate into mirrored streams to the left and right of the forward-facing-cone. This is evident in Figure 201 and Figure 202. Each stream is turned perpendicular to augmenter flow, through interaction with the downstream stack wall. This leads to a build-up of static pressure on the downstream wall as seen in Figure 203. Through a further interaction with the downstream stack sidewalls, a rotational flow component is developed, as seen in Figure 201. In Figure 201 this region of rotation is marked with a red oval, and is confined to the downstream portion of the exhaust stack.

Flow exiting below the BB centreline is also turned adjacent to the downstream stack walls in two separate streams. The streams form large rotational regions in the base of the exhaust stack as seen in Figure 202. The region of the exhaust stack occupied by the streams exiting below the BB centreline is marked in yellow in both Figure 201 and Figure 202.

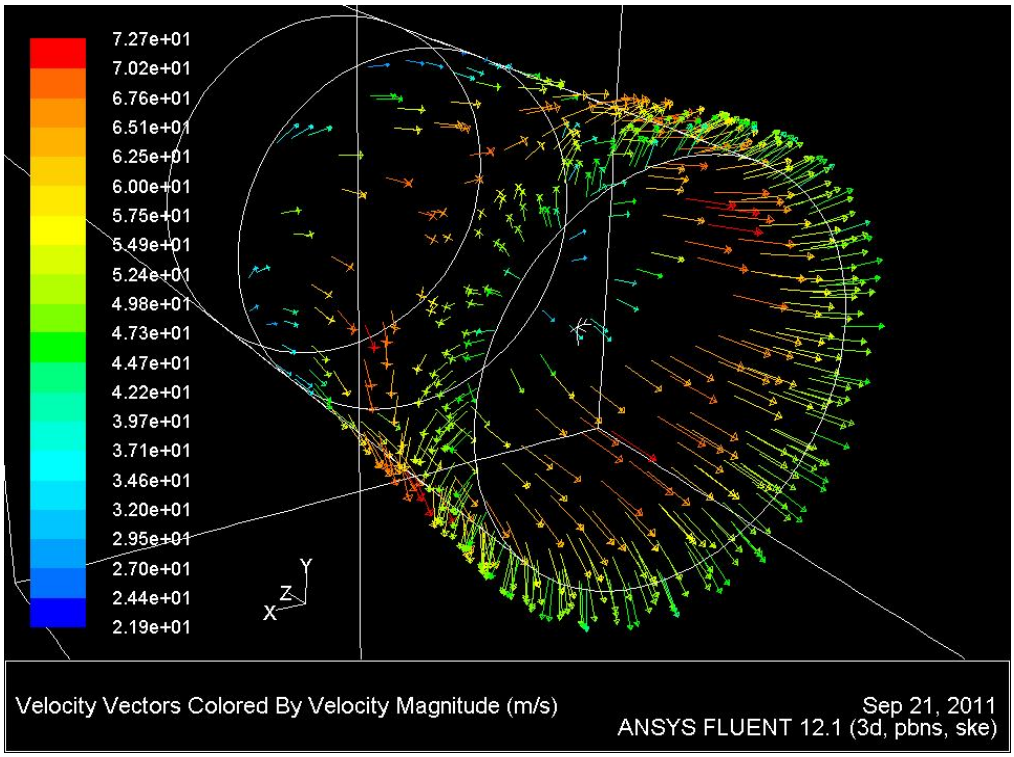

Figure 195 Direction and Velocity of Flow Exiting the BB in the Baseline Arrangement

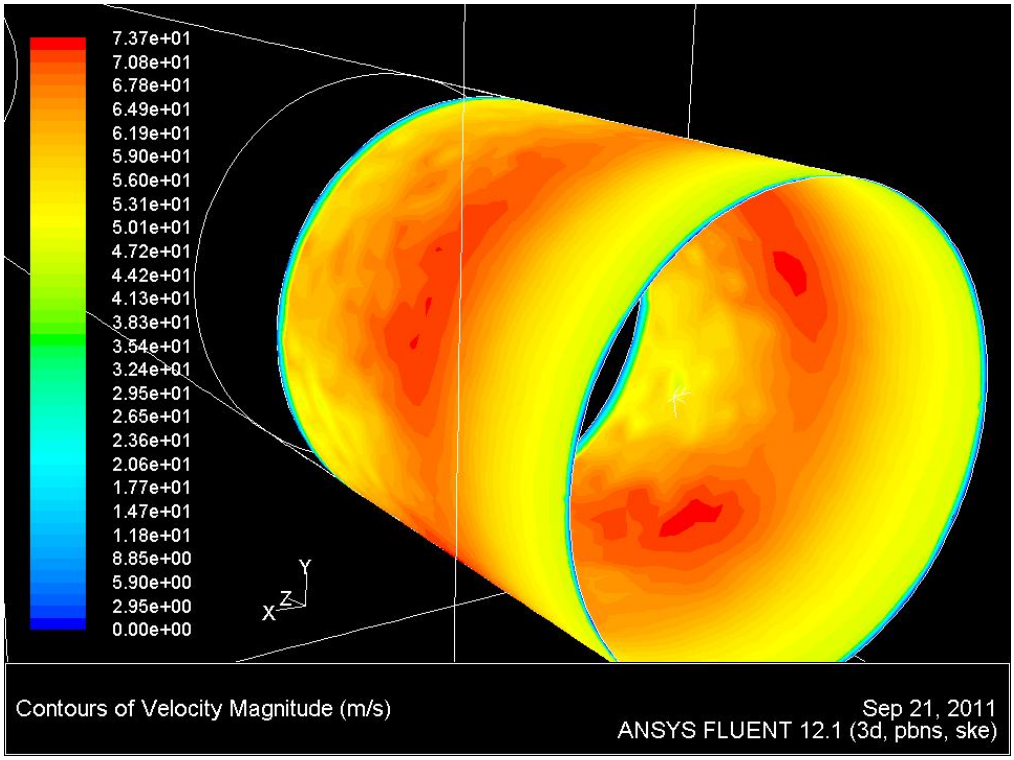

Figure 196 Velocity Magnitude on the BB Face in the Baseline Arrangement

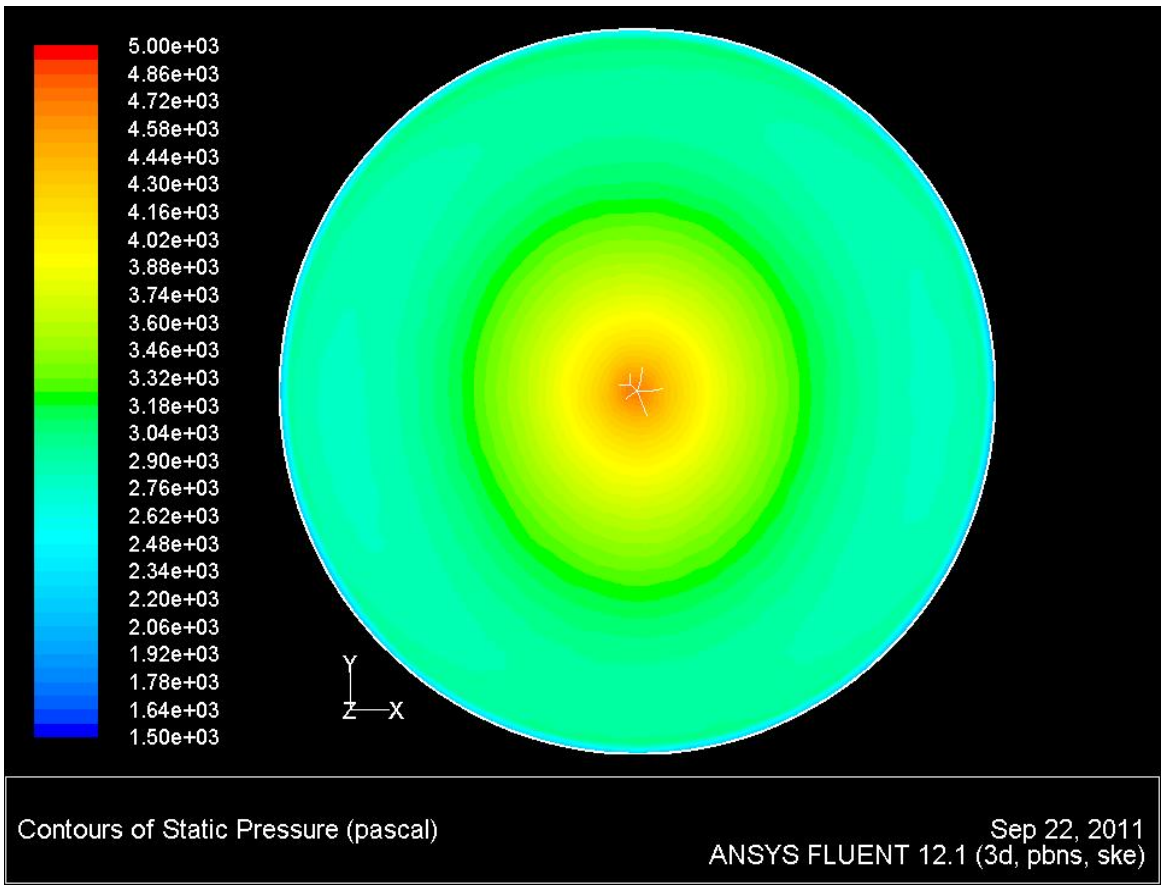

Figure 197 Static Pressure Distribution on the Forward-Facing-Cone in the Baseline Arrangement

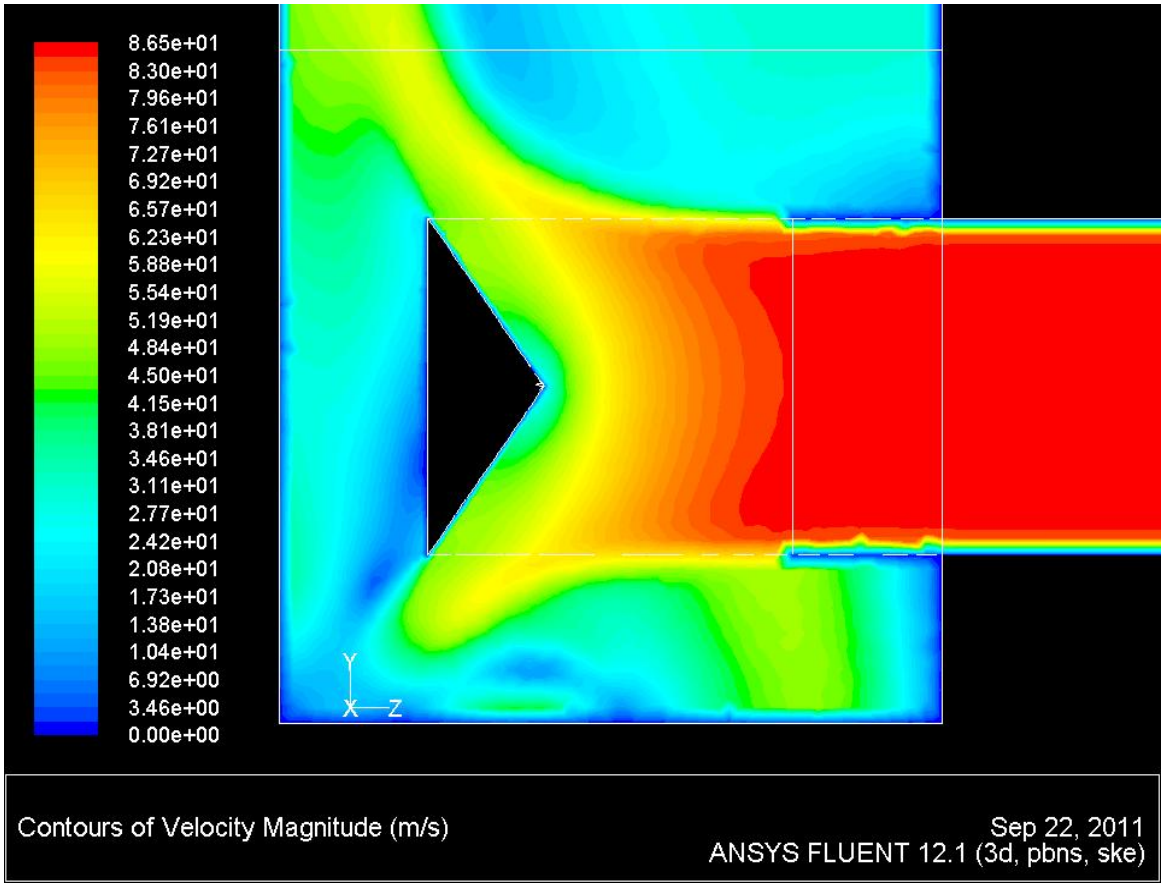

Figure 198 Velocity Magnitude on the Vertical BB Axis in the Baseline Arrangement

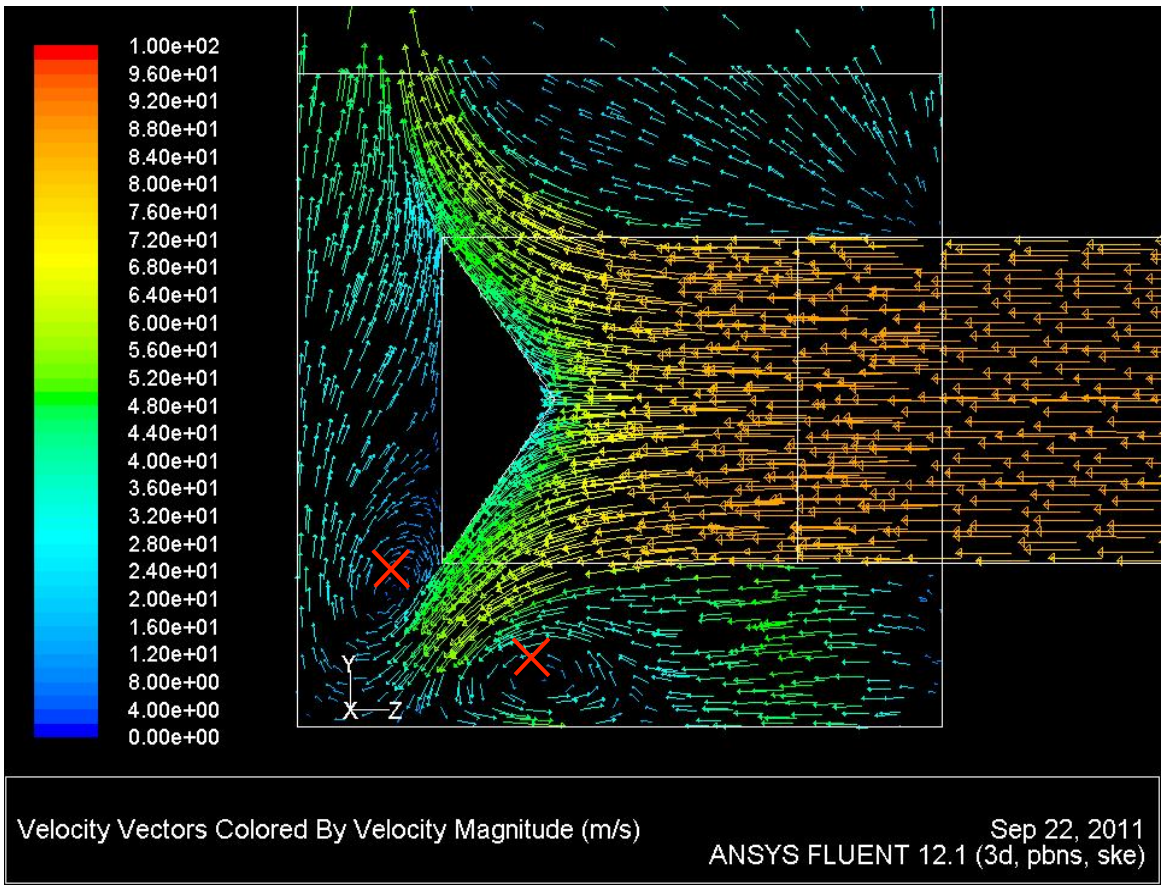

Figure 199 Velocity Magnitude on the Vertical BB Axis in the Baseline Arrangement

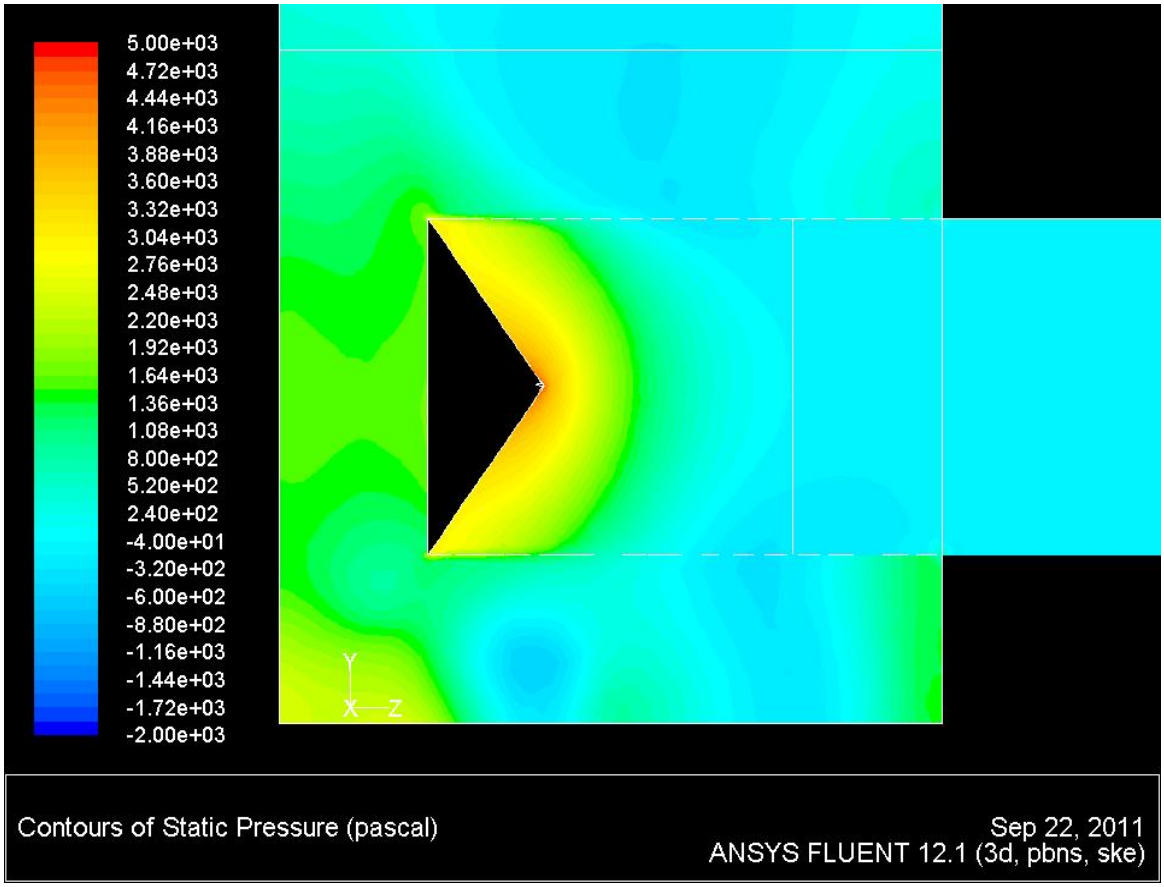

Figure 200 Static Pressure Distribution on the Vertical BB Axis in the Baseline Arrangement

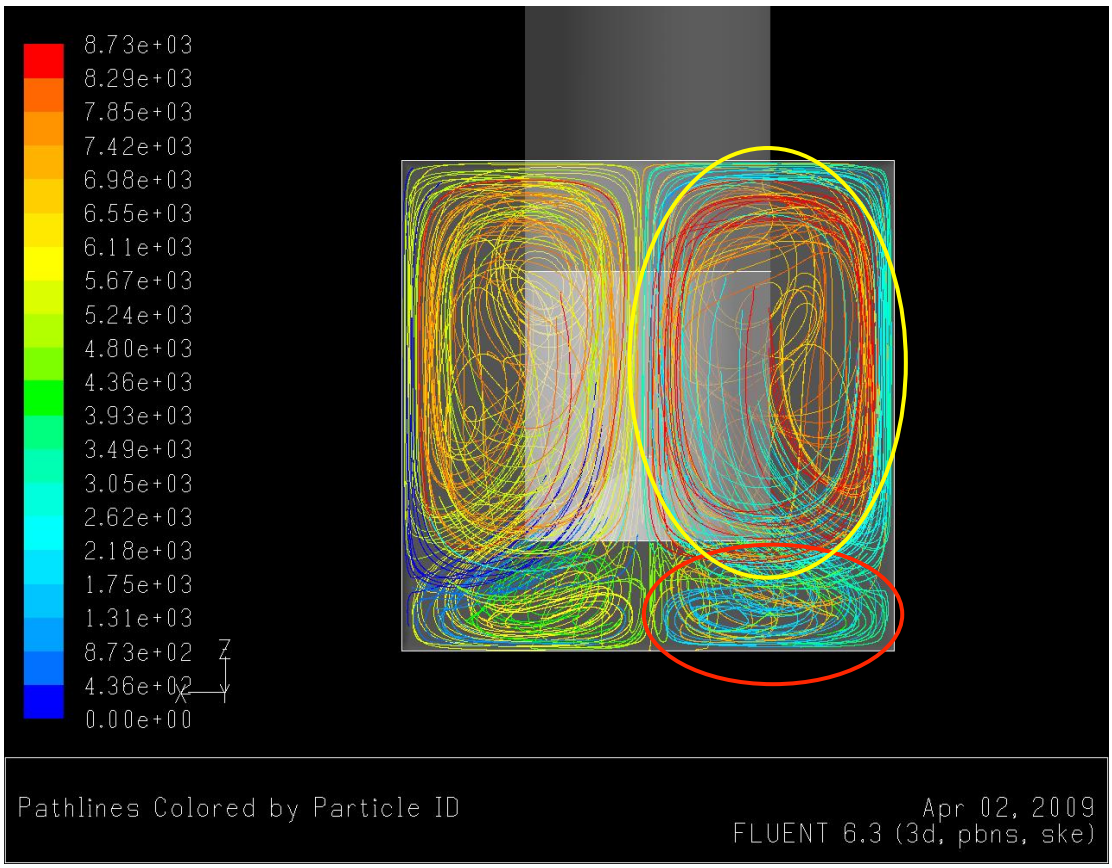

Figure 201 Streamlines Emitted from the BB Face in the Baseline Arrangement (viewed from above the 'Stack Exit' BC)

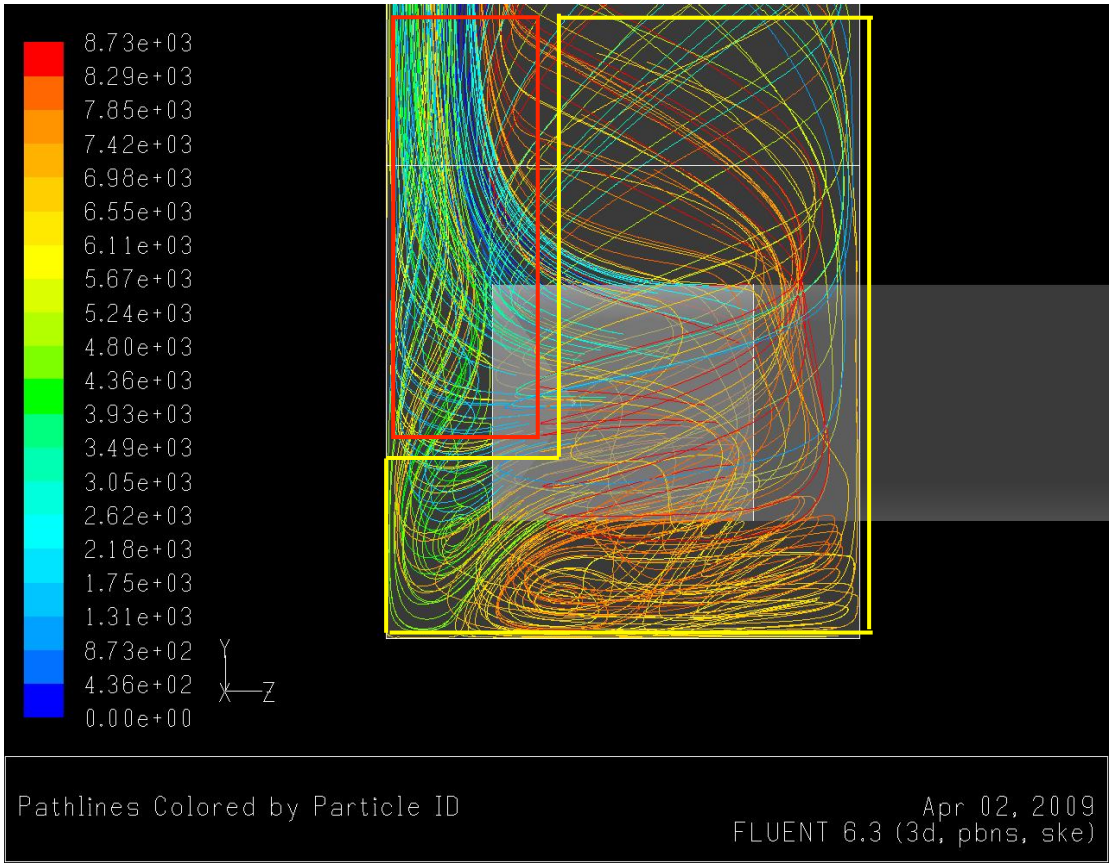

Figure 202 Streamlines Emitted from the BB Face in the Baseline Arrangement (viewed from the exhaust stack sidewall)

Substantial areas of high static pressure are seen to build-up at the base of the exhaust stack walls are seen in Figure 203 as flow was continually driven into this region. Comparison of the graphics in Figure 204 show that flow exiting above the BB centreline leaves the exhaust stack at velocities between 40ms^{-1} and 60ms^{-1}. Flow exiting below the centreline retains a proportionally higher rotational component, and exits at a comparatively low velocity. This point is also well illustrated in Figure 205.

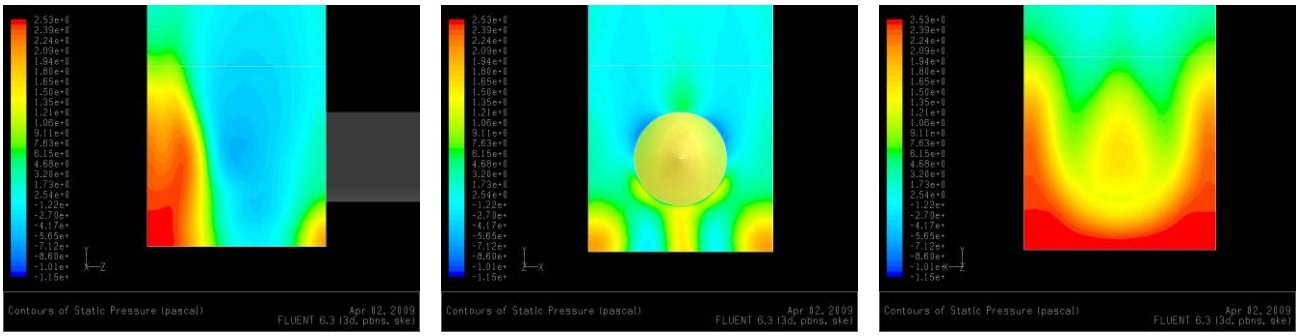

Figure 203 Static Pressure Variation on the Side (left), Upstream (centre), and Downstream (right) Walls of the Exhaust Stack in the Baseline Arrangement

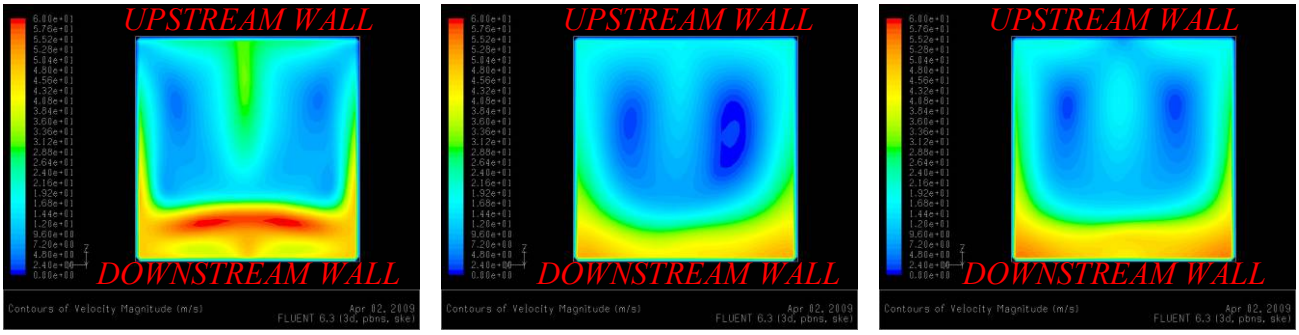

Figure 204 Velocity Magnitude at heights of 10m (left), 20m (centre), and 30m (right) above the Base of the Exhaust Stack in the Baseline Arrangement

6.2.3.2 Forward-Facing-Cone Tip Angle

In the baseline solution the distribution of flow throughout the exhaust stack was heavily weighted towards the downstream wall. A possible option to even out the distribution was to make an adjustment to the tip angle of the forward-facing-cone. It was anticipated that if the tip angle was increased, a build-up in static pressure on the cone-face would force a more even distribution of flow out of the BB body.

Through increasing the tip angle an increase in losses associated with the static pressure build-up was also anticipated.

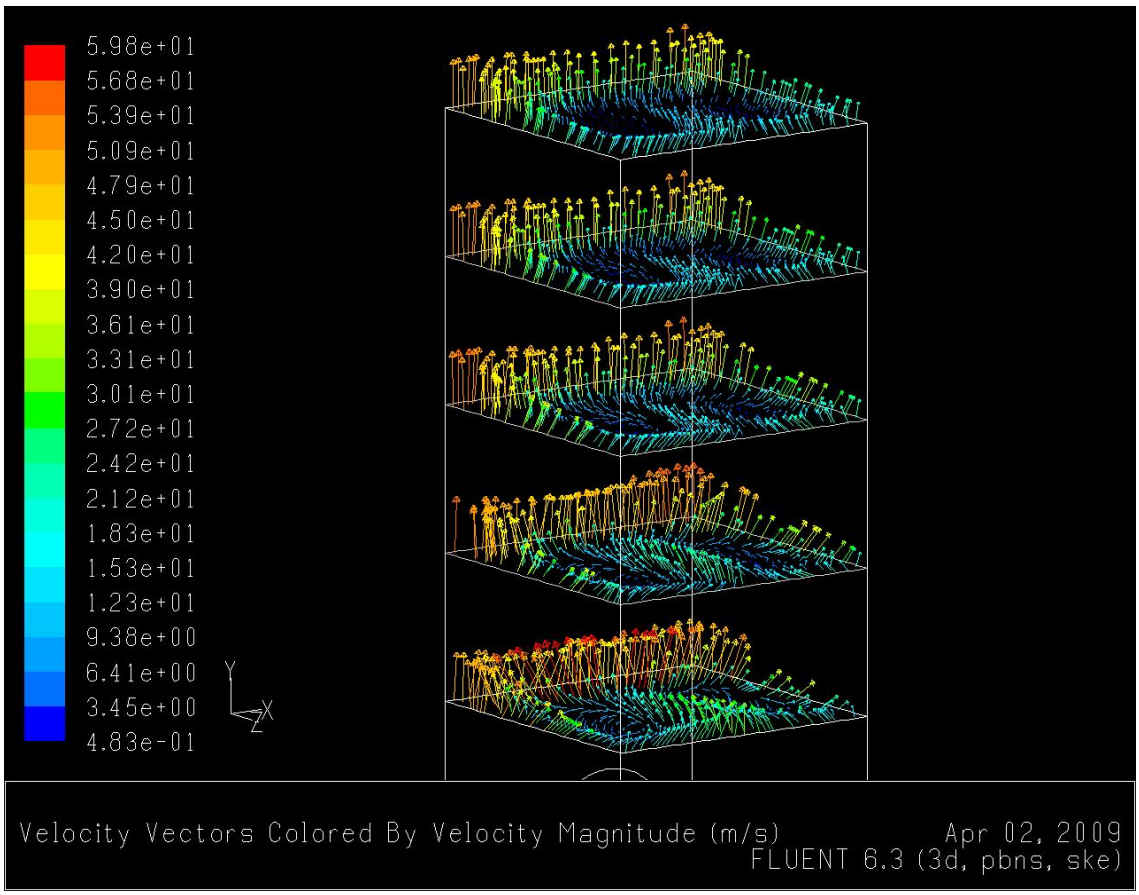

Figure 205 Development of the Flow Direction and Velocity through the Exhaust Stack in the Baseline Arrangement

Therefore, it was deemed necessary to get an understanding of how the tip angle would affect the flow distribution, and how any effect on flow distribution would improve or harm cell efficiency solutions. This was achieved through analysing a range of tip angles. The baseline domain was altered to create three additional domains using tip angles 70°, 90° and 130°. This produced a set of data from which quantitative values could be comparatively analysed, and a qualitative analysis could be performed.

When the tip angle was reduced to 70°, the MFR in the solution produced an insignificant drop to 2043.4kgs^{-1}. Likewise, an insignificant increase in MFR, to 2052.7kgs^{-1}, was observed with a tip angle increase to 130°. A significant increase in pressure can be seen with the increase in tip angle. A comparison of cone-face static pressure is made in Figure 206.

Figure 207 shows that a more even distribution of flow throughout the stack cross-section was achieved through an increase in tip angle. Comparison of these qualitative observations with the MFRs achieved showed that this did not equate to an increase in cell efficiency.

Figure 208 shows that the flow patterns were slightly altered with tip angle variation. In both the 70° and 130° cases, similar circulation zones (with an axis perpendicular to the augmenter flow) were present at the rear and base of the stack. The marked location of the centre of circulation is seen to vary slightly between solutions.

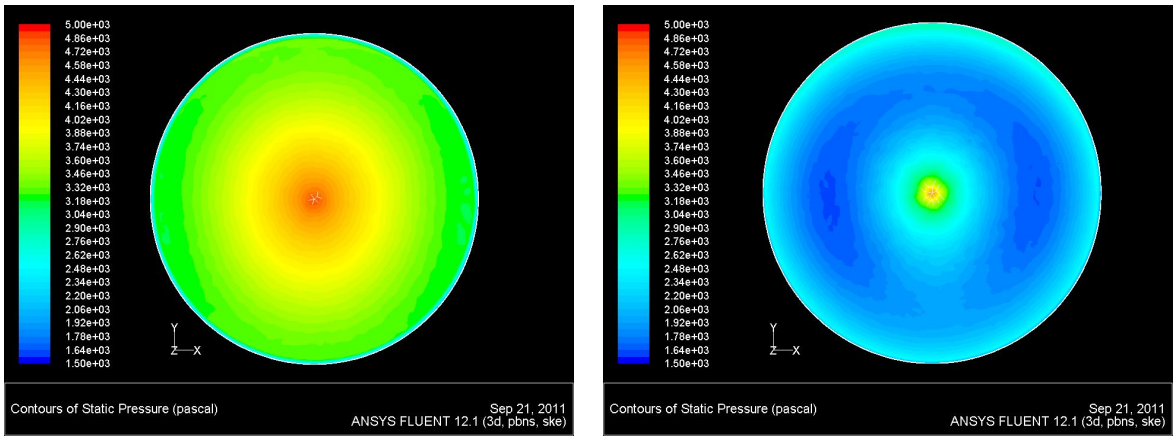

Figure 206 Static Pressure Distribution on the Forward-Facing-Cone with a 70° (left) and 130° (right) Tip Angle

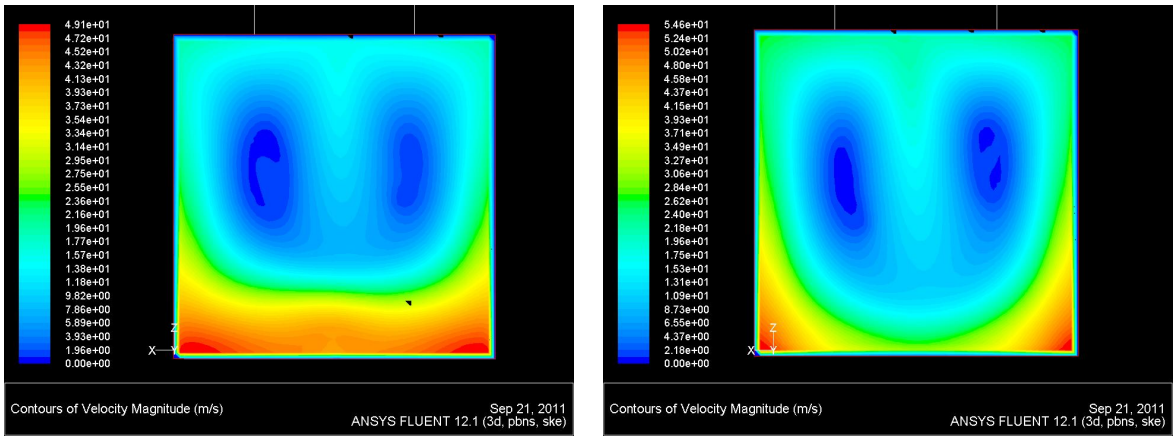

Figure 207 Velocity Magnitude at the 'Stack Exit' with a with a 70° (left) and 130° (right) Forward-Facing-Cone Tip Angle

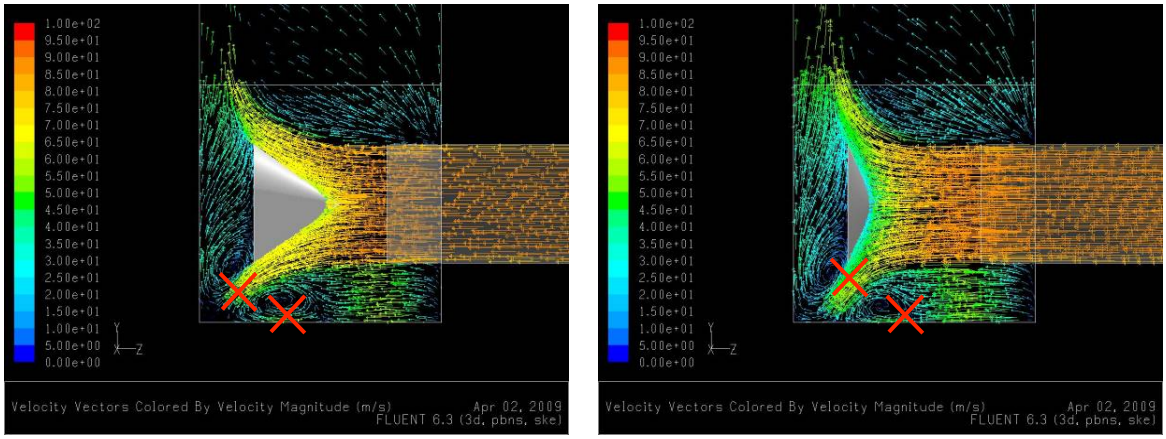

Figure 208 Velocity Magnitude on the Vertical BB Axis with a 70° (left) and 130° (right) Forward-Facing-Cone Tip Angle

6.2.3.3 Blast Basket Relocation

Section 6.2.3.1 showed that the flow patterns developed in the lower exhaust stack were significantly affected by the interaction of the flow exiting the BB with the downstream wall of the stack. Section 6.2.3.2 showed that the flow patterns in the lower exhaust stack were to some degree affected by altering the angle of flow exiting the BB.

To gain a further understanding of how the BB and exhaust stack interact to form the flow patterns observed the BB location within the stack was altered. Starting from the baseline arrangement, the BB was shifted fore and aft of its original stream-wise position in a number of steps. These steps were made to alter the distance marked 'x' in Figure 189 to values of 0.25m, 1.25m, 3.25m, and 4.25m in four new domains. Solutions for each domain were generated, and are discussed below.

MFR gains were made when moving the BB nearer the downstream stack wall (reducing x in Figure 189). With x = 4.25m, a MFR of 1981.7kgs^{-1} was calculated, 3.4% lower than the baseline solution, and 6.0% lower than the x = 0.25m solution.

Figure 209 through Figure 213 compare the flow patterns and parameters of the x = 0.25m and x = 4.25m solutions. By reducing x to 0.25m the flow pattern in the exhaust stack was altered significantly. This can be seen when comparing Figure 209 with Figure 199 and Figure 208 from previous sections. The two centres of rotation present in Figure 199 and Figure 208, and the x = 4.25m solution of Figure 209, have been reduced to one in the 0.25m solution.

Figure 210 through Figure 212 show further indications of flow pattern augmentation when compared with Figure 201 and Figure 202 of the baseline solution. Figure 210 shows that much more significant distribution changes are achieved when altering the BB stream-wise location compared with altering the cone tip angle, discussed in Section 6.2.3.2.

The x = 4.25m solution of Figure 210 shows similarities with that of the baseline solution in Figure 204. The flow is heavily orientated towards the downstream stack face in both solutions. The x = 0.25m solution of Figure 210 shows a more even distribution of the flow across the stack cross-section, although still concentrated near the stack walls.

The x = 0.25m solution of, Figure 211 and Figure 212, show that the two distinct streams, exiting each side of the BB vertical axis in the baseline and x = 4.25m solutions, have been replaced by a larger singular stream.

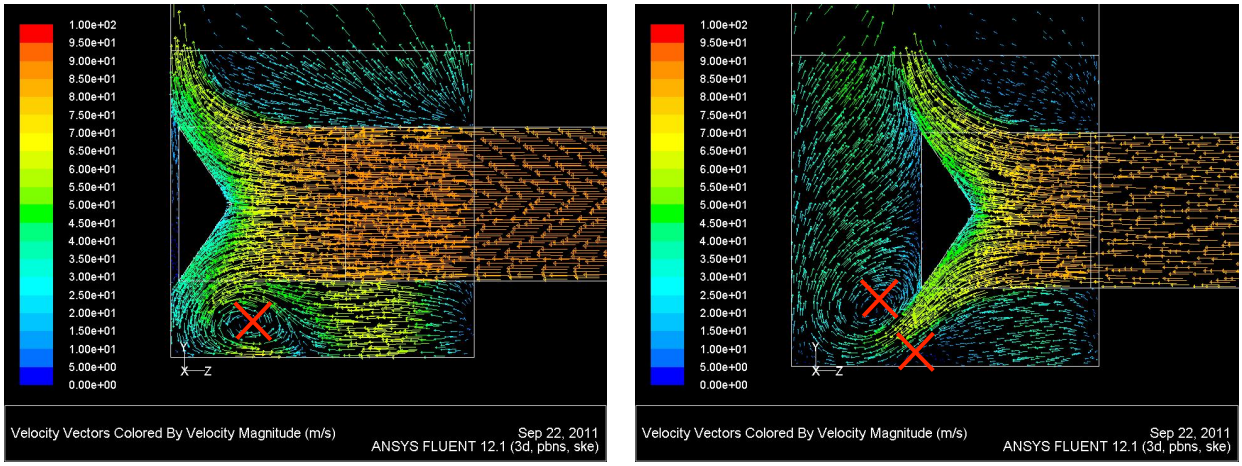

Figure 209 Velocity Magnitude on the Vertical BB Axis with x = 0.25m (left) and x = 4.25m (right)

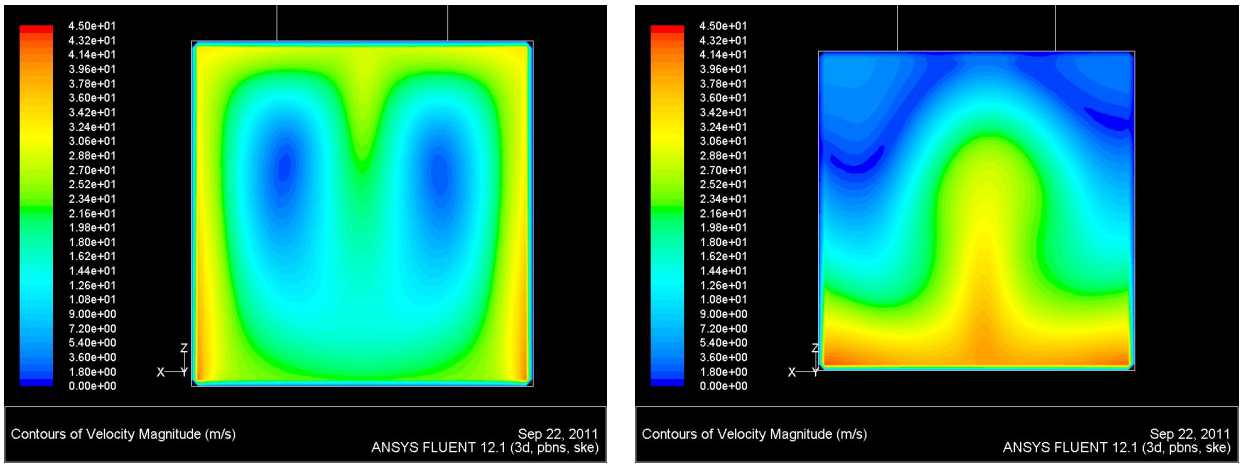

Figure 210 Velocity Magnitude at the 'Stack Exit' with x = 0.25m (left) and x = 4.25m (right)

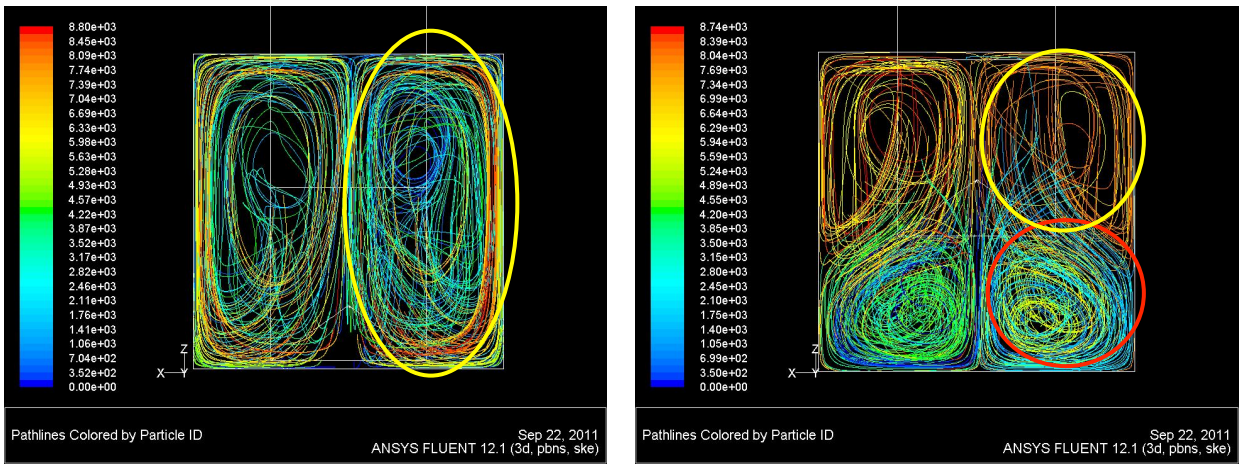

Figure 211 Streamlines Emitted from the BB Face with x = 0.25m (left) and x = 4.25m (right) (viewed from the 'Stack Exit' BC)

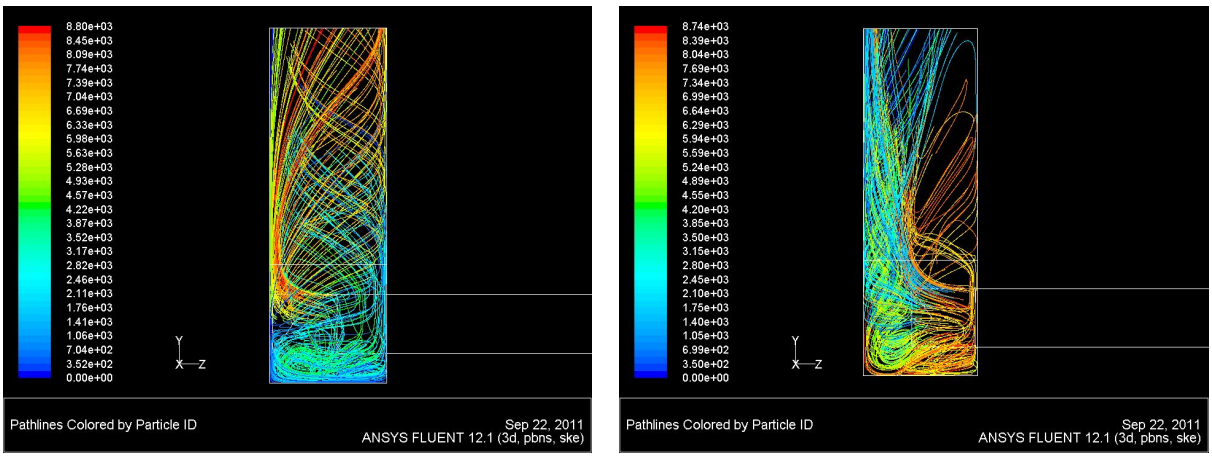

Figure 212 Streamlines Emitted from the BB Face with x = 0.25m (left) and x = 4.25m (right) (viewed from the exhaust stack sidewall)

Figure 213 suggests that by more closely aligning the cone and rear stack wall (by reducing x) a singular, but larger, area of high static pressure is formed near the downstream wall of the stack. This in turn appears to have resulted in a reduction of flow complexity and the formation a singular stream of flow forming each side of the BB vertical axis in the x = 0.25m solution. The MFRs calculated suggest that this has resulted in improved flow efficiency.

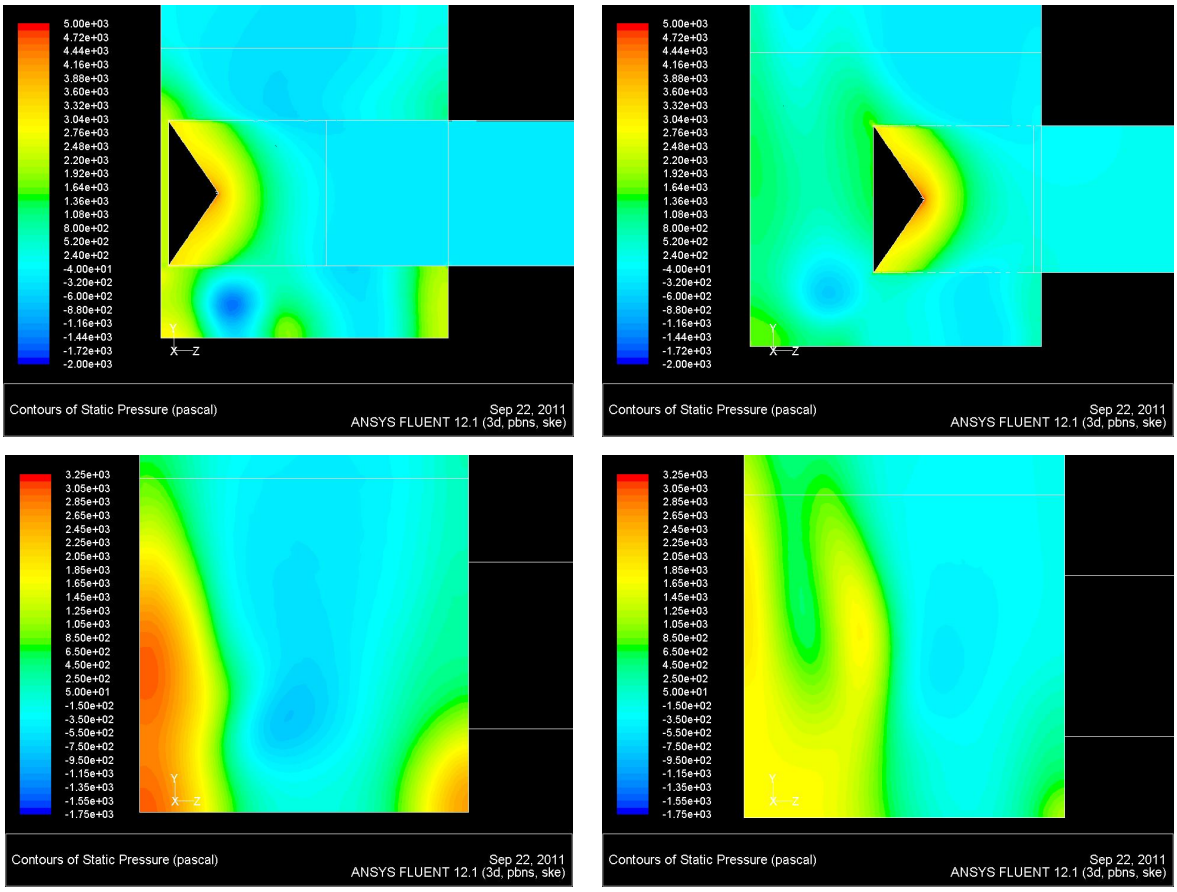

Figure 213 Static Pressure Distribution on the Vertical BB Axis (top) and the Exhaust Stack Sidewall (bottom) with x = 0.25m (left) and x = 4.25m (right)

6.2.3.4 Forward-Facing-Cone Extension

Section 6.2.3.3 showed that by relocating the BB nearer the downstream wall of the stack, a more structured and efficient flow pattern could be developed. However, to implement such a change in a currently in-service cell would likely be prohibitively expensive because the augmenter and BB in a constructed cell are relatively inaccessible. Therefore, to investigate whether the same simplification of the flow patterns in the base of the exhaust stack could be achieved through a retrofit solution, a cone extension was investigated.

A cone extension, of the design shown in Figure 214, was incorporated into the baseline computational domain, discussed in Section 6.2.2.1. Through incorporating the cone extension it was hoped the multiple areas of pressure build-up, seen in the above solutions when the BB was well spaced from the downstream stack wall, would be concentrated into a single area as seen in the x = 0.25m solution of Section 6.2.3.3. A solution was generated for the modified domain and the results are discussed below.

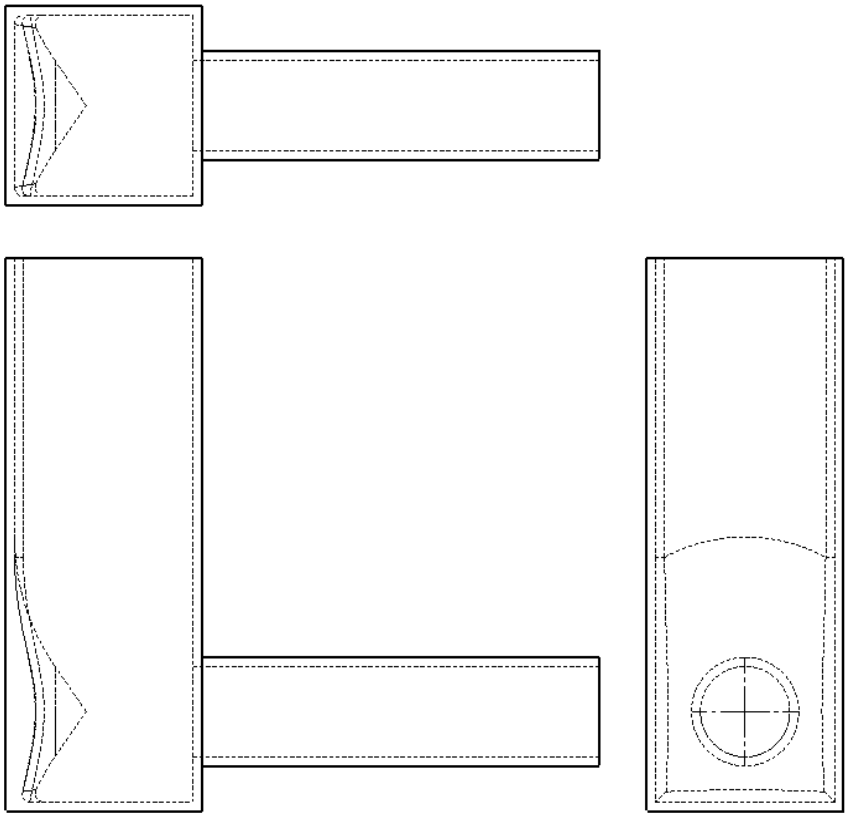

Figure 214 Design of the Forward-Facing-Cone Extension

The addition of the cone extension only provided a marginal 0.8% increase in MFR over the baseline solution. The flow patterns and parameters in the lower exhaust are show in Figure 215 through Figure 220. In Figure 215 the singular centre of rotation (perpendicular to the augmenter flow) has been retained for the x = 0.25m solution of Section 6.2.3.3. Figure 216 and Figure 217 show that the more even distribution of flow throughout the stack is maintained as a result. Figure 218 and Figure 219 show that the successful combination of the BB and stack wall into a single surface has assembled the area of low static pressure into a single region. This has allowed this pattern of flow with a single centre of rotations to be retained as per the design theory.

Compared with the baseline solution of Figure 200, Figure 218 shows an increase in the magnitude of the static pressure build-up in the corner between the stack base and the downstream wall/cone extension. In the design shown in Figure 214, the tightening of this corner, which effectively bends at 55° in comparison with the 90° of the baseline solution, is seen to be the likely cause.

Figure 220 shows a slight asymmetry of static pressure on the cone face, with a lower pressure on the upper portion of the face. This appears to be a result of the pressure build-up in the above-mentioned corner of the stack. Figure 221 and Figure 222 show that the distribution of velocity contours is affected by this pressure variation. The flow exiting above the BB centreline is a notably higher velocity than that seen in the baseline solution (Figure 196 and Figure 198), and shows more variation around the perimeter of the BB body.

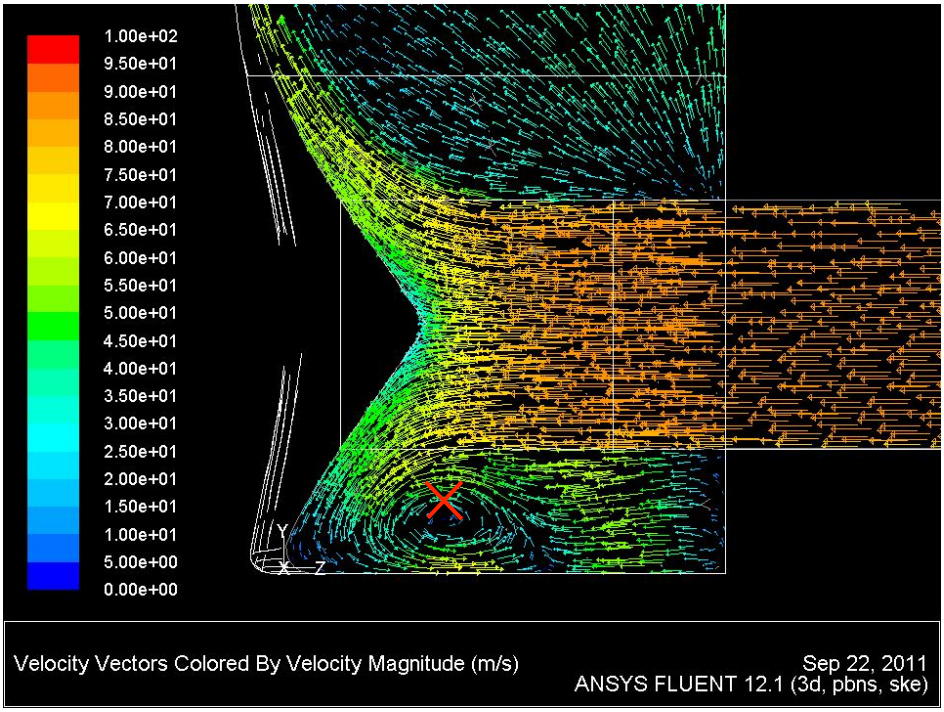

Figure 215 Velocity Magnitude on the Vertical BB Axis with a Forward-Facing-Cone Extension

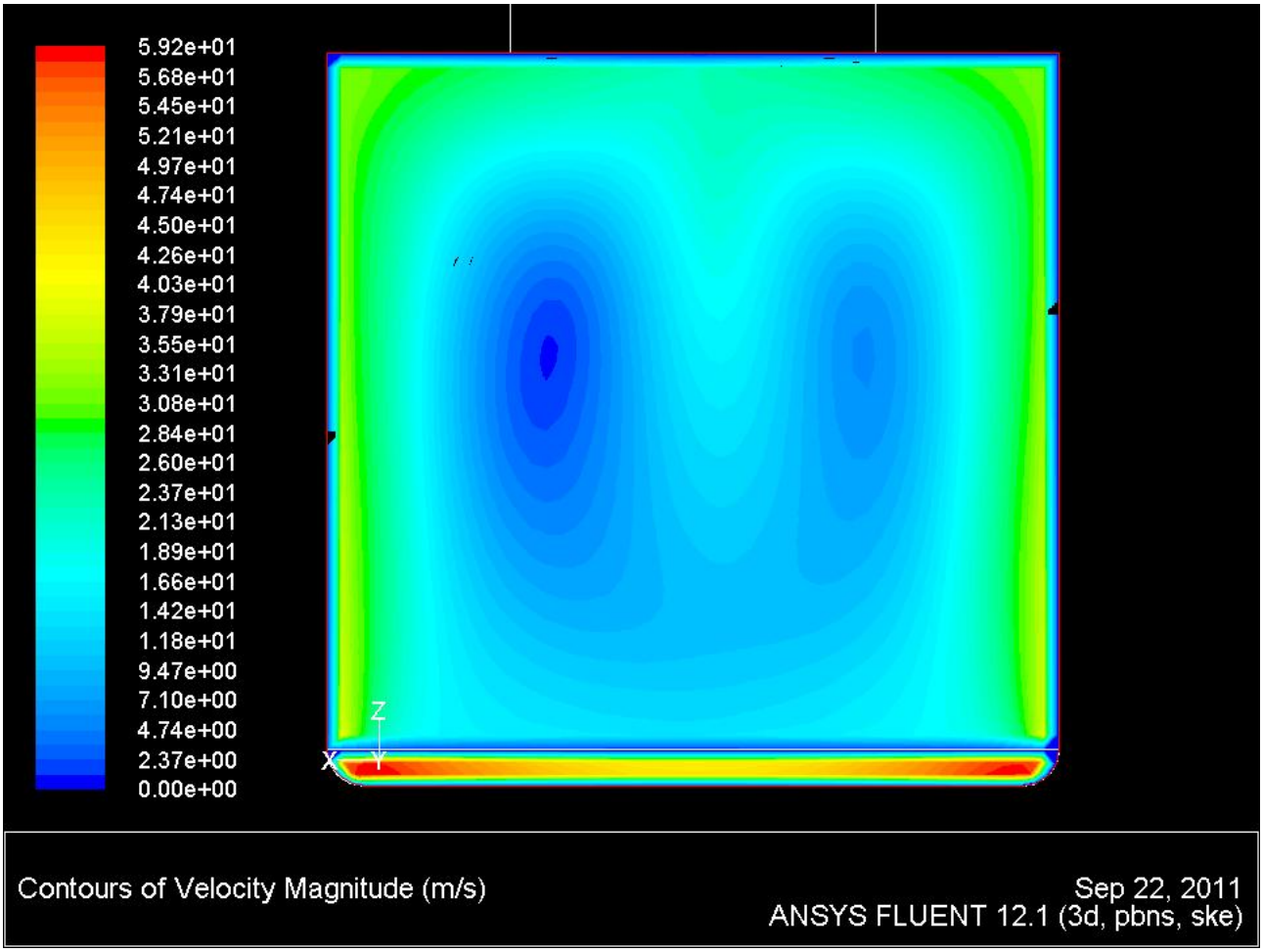

Figure 216 Velocity Magnitude at the 'Stack Exit' BC with a Forward-Facing-Cone Extension

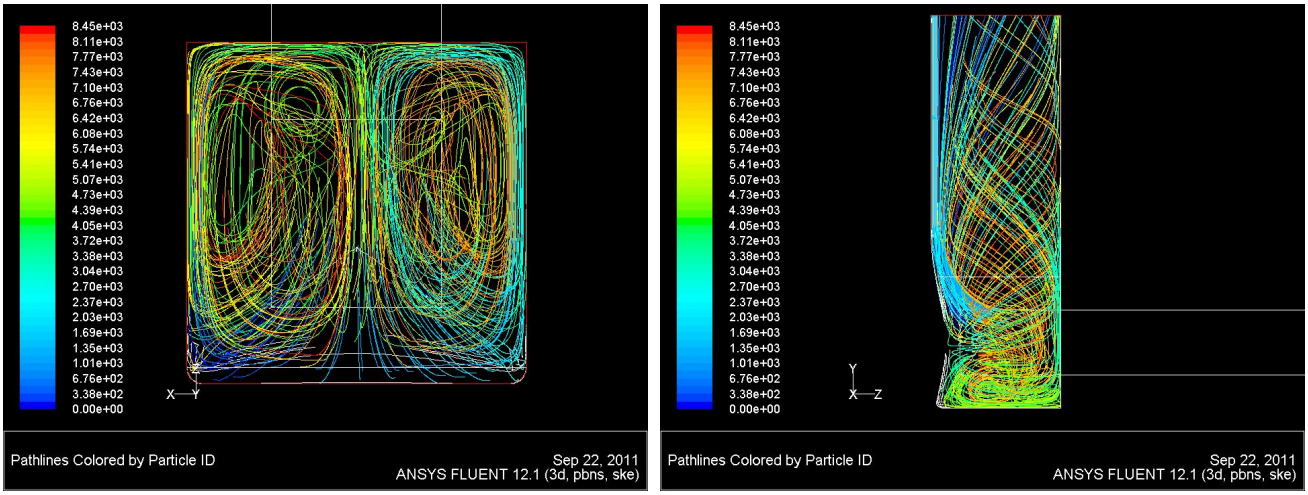

Figure 217 Streamlines Emitted from the BB Face with a Forward-Facing-Cone Extension (viewed from the 'Stack Exit' BC (left), and exhaust stack sidewall (right))

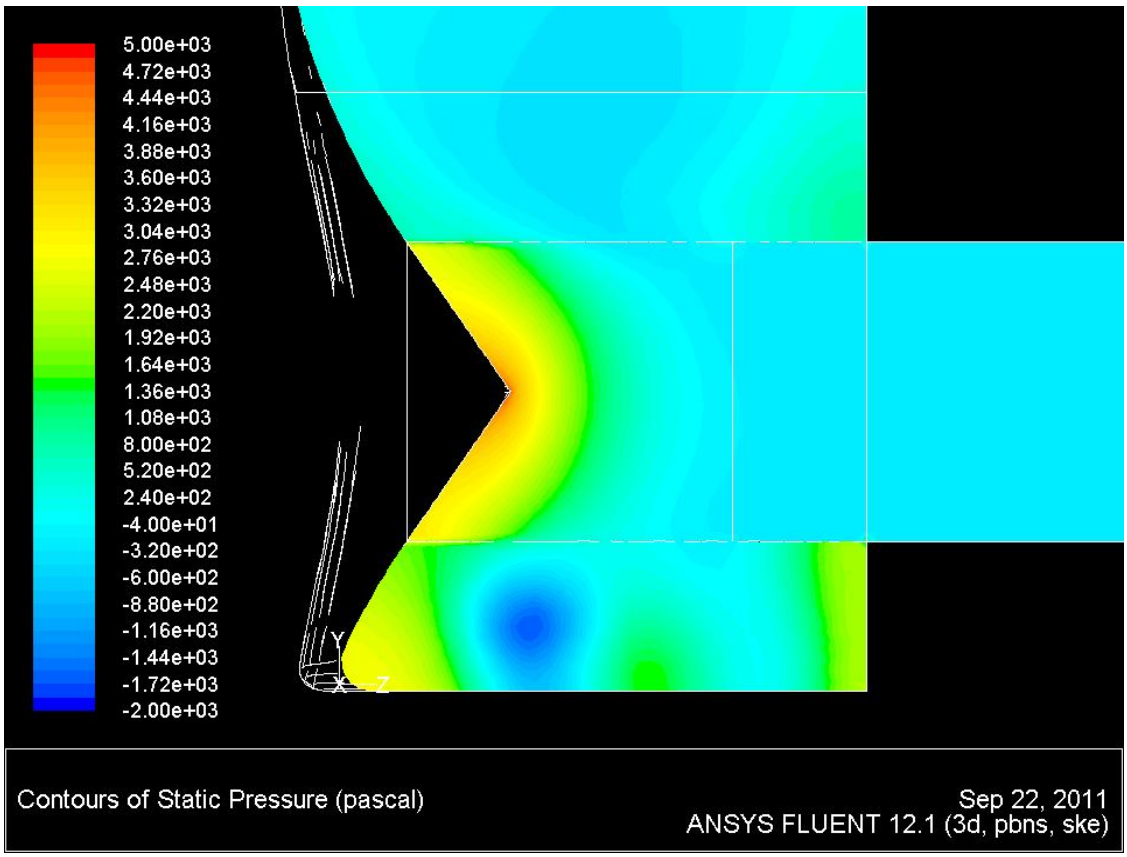

Figure 218 Static Pressure Distribution on the Vertical BB Axis with a Forward-Facing-Cone Extension

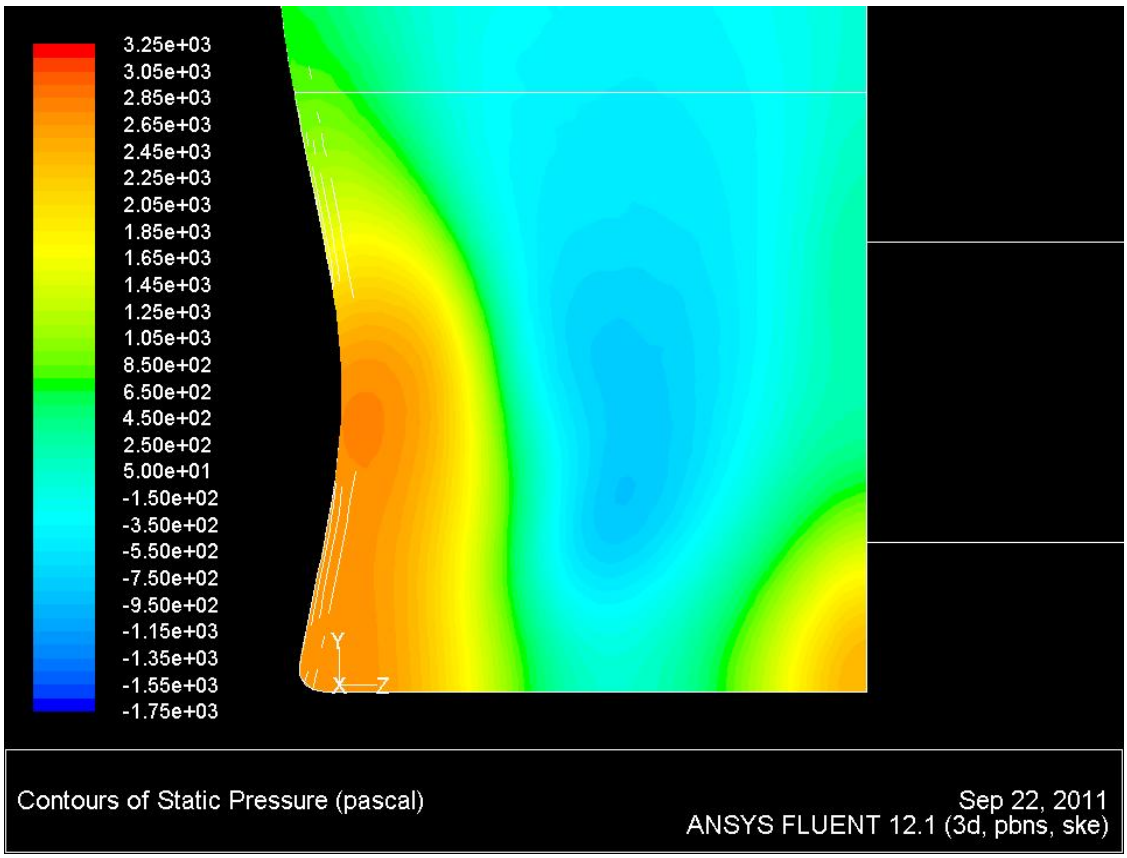

Figure 219 Static Pressure Distribution on the Exhaust Stack Sidewall with a Forward-Facing-Cone Extension

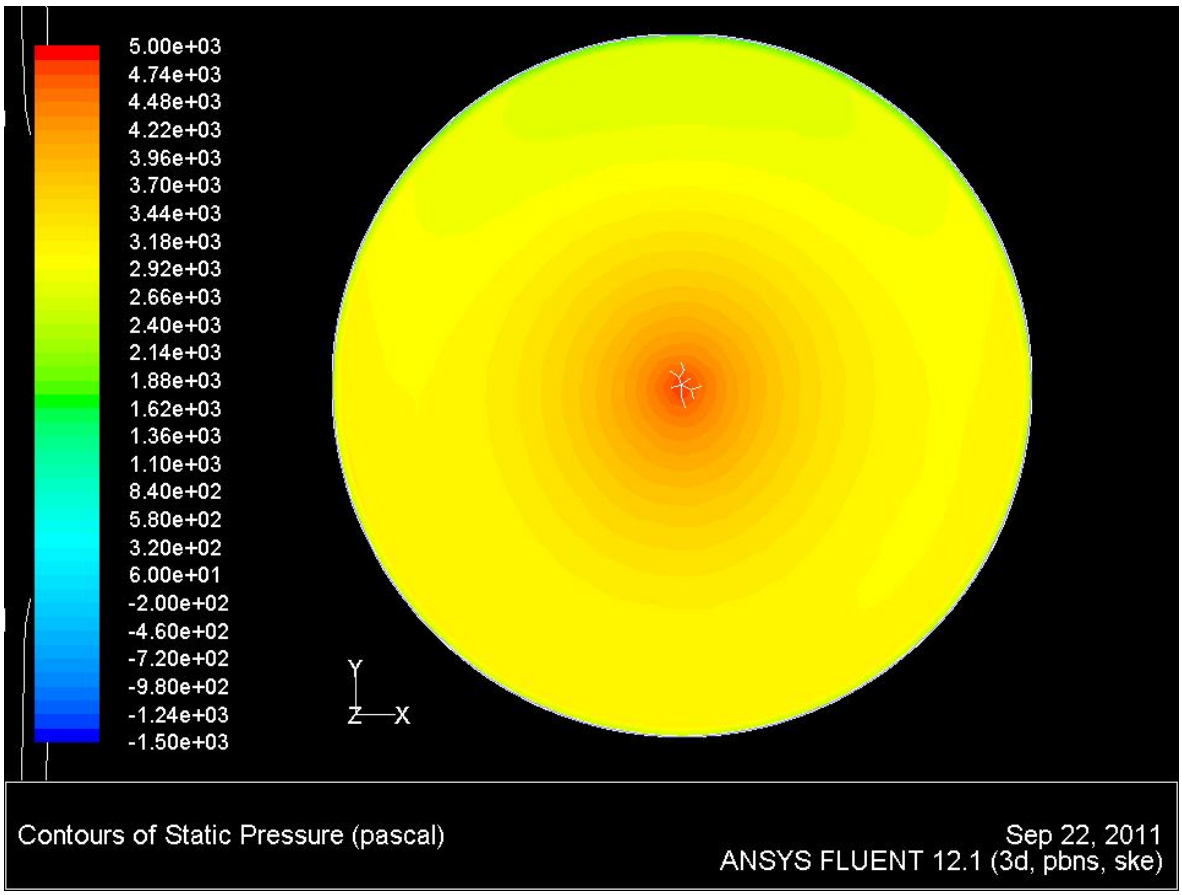

Figure 220 Static Pressure Distribution on the Forward-Facing-Cone with Extension (not shown)

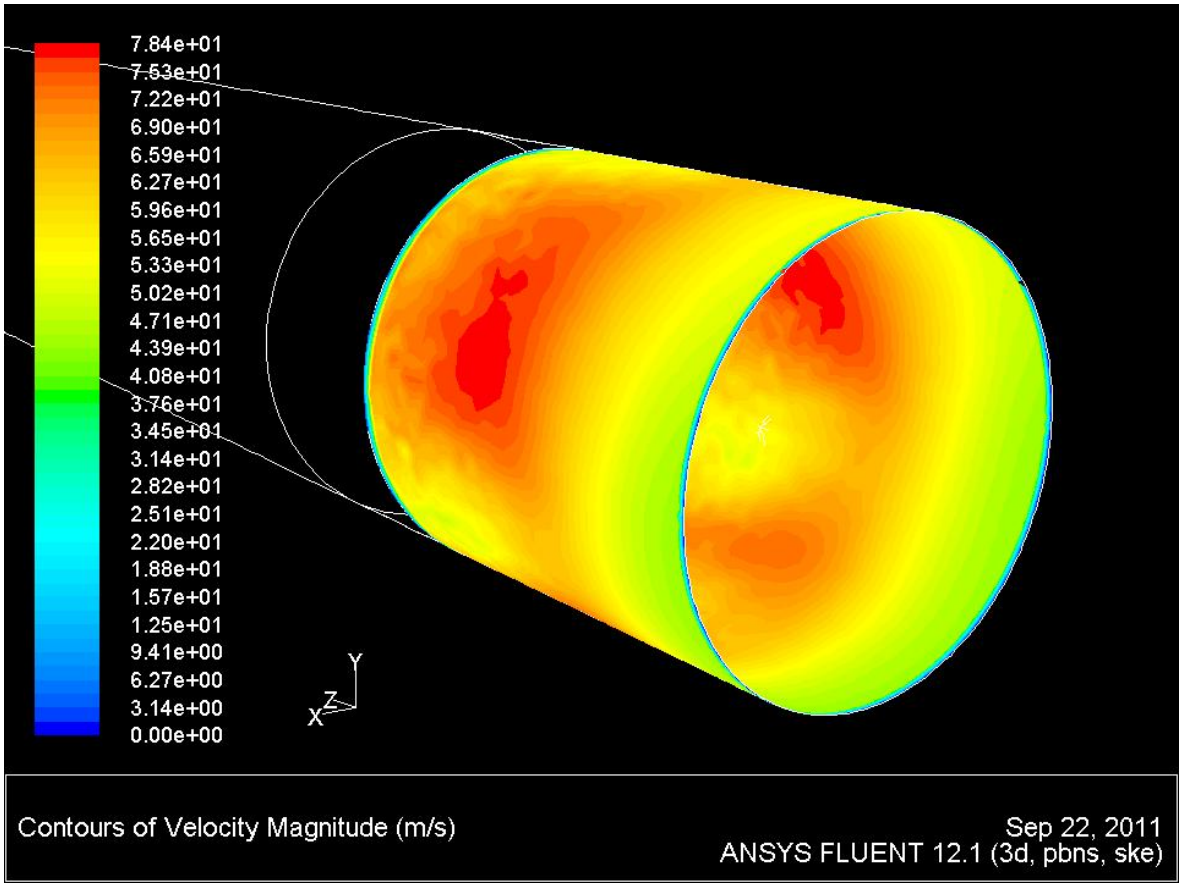

Figure 221 Velocity Magnitude on the BB Face with a Forward-Facing-Cone Extension

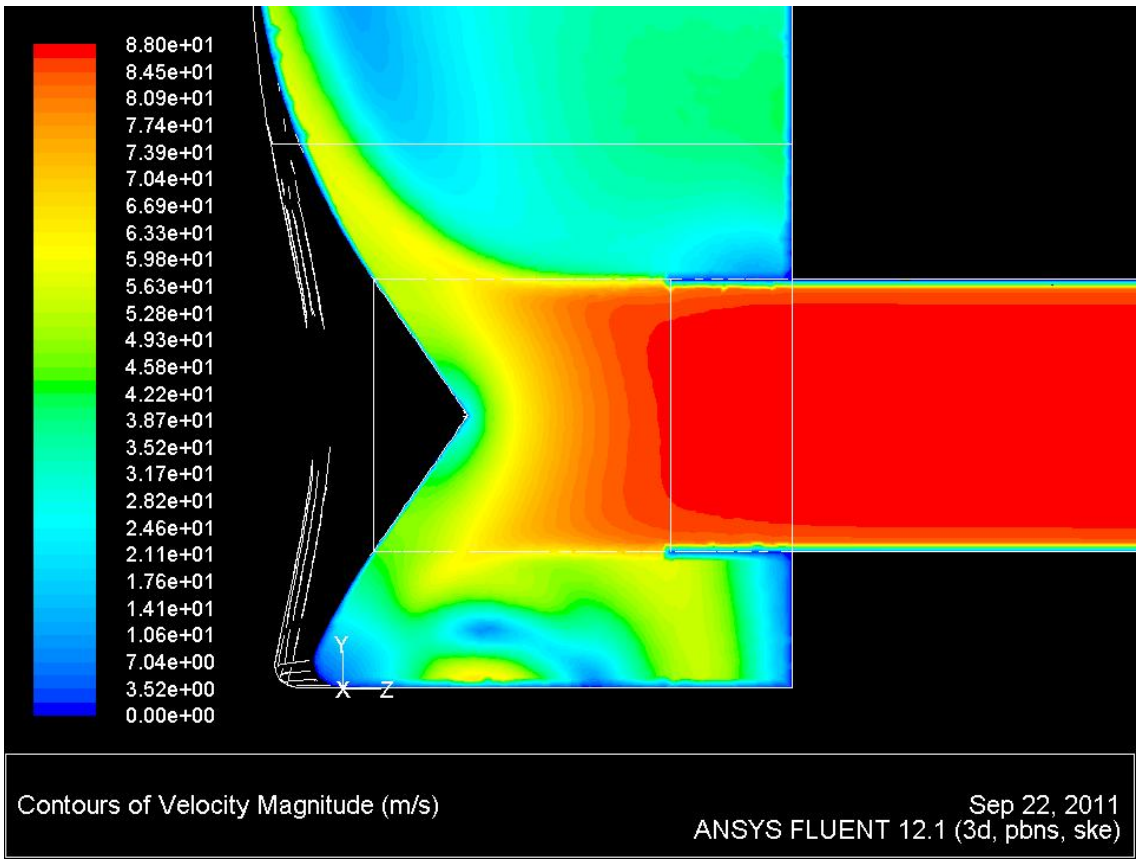

Figure 222 Velocity Magnitude on the Vertical BB Axis with a Forward-Facing-Cone Extension

6.2.3.5 Extruded Spine

Section 6.2.3.4 showed that more structured flow patterns of the x = 0.25m solution could be achieved in a retrofit solution to a current test cell. However, the increase in cell efficiency of the x = 0.25m solution could not be replicated through the use of a cone extension due to the inefficiencies created in the lower exhaust stack.

An alternate retrofit approach to that of the cone extension was developed in the form of an extruded spine secured running across the width of the exhaust stack adjacent to the downstream stack wall. The cross section of the spine is shown in Figure 223. The spines cross section was constant across the entire width of the exhaust stack. The extruded spine design was intended to generate the efficient 'single circulation zone' flow pattern of the x = 0.25m solution, whilst reducing the static pressure build-up in the corner between the stack base and downstream wall as seen in Figure 214.

A solution was generated, and Figure 224 presents the flow pattern along the vertical BB axis. The incorporation of the extruded spine did not enhance the structure of flow in the lower exhaust stack

as per the design intention, which is overlaid in the figure with yellow arrows. Two centres of rotation perpendicular to the centre of rotation were seen as per the baseline solution.

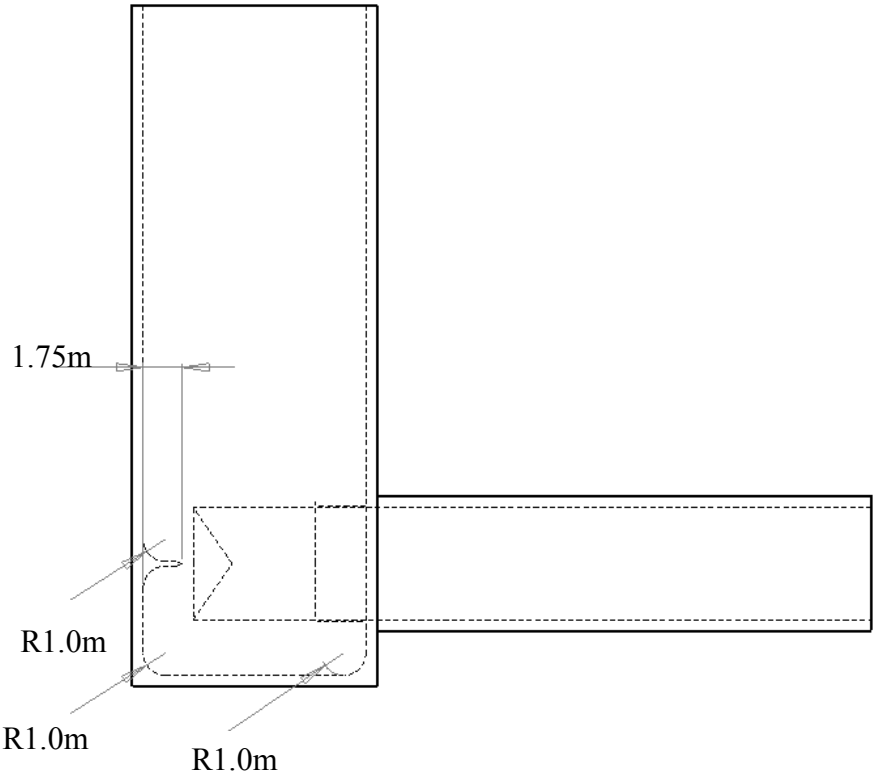

Figure 223 Design of the Downstream Wall Extruded Spine

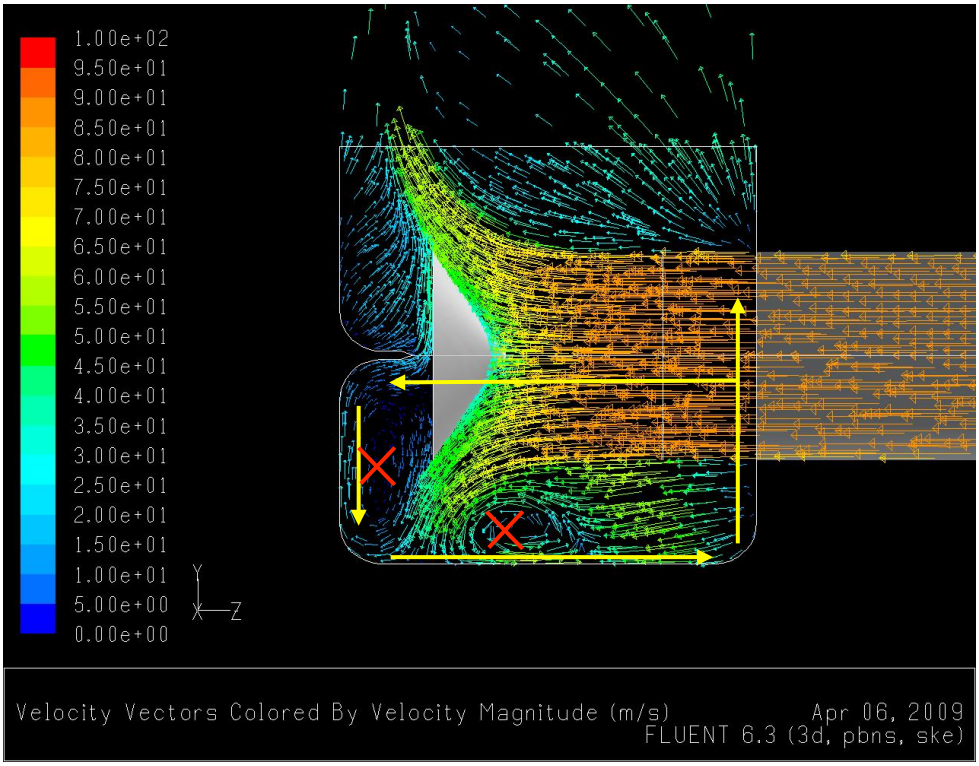

Figure 224 Velocity Magnitude on the Vertical BB Axis with an Extruded Spine Design

Figure 225 showed only marginal variation in the flow distribution at the stack exit when compared with the baseline solution. A negligible change in MFR was the result.

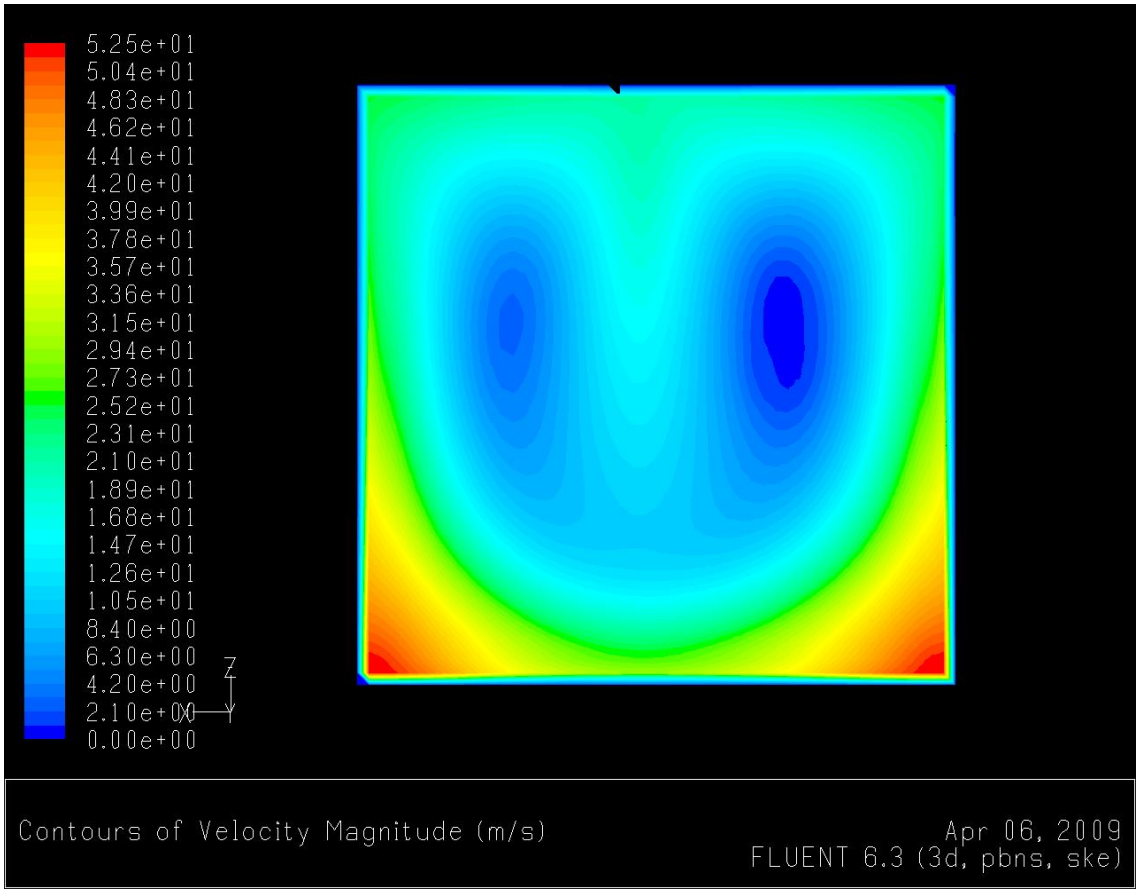

Figure 225 Velocity Magnitude at the 'Stack Exit' BC with an Extruded Spine Design

6.2.3.6 Asymmetric Forward-Facing-Cone

Section 6.2.3.1 showed that a near even proportion of flow exited the BB around the entire perimeter of its body. Therefore, nearly 50% of the flow exited below the BB centreline. As was seen in Figure 195, the flow exiting the BB below the centreline has a downward velocity component due to its interaction with the forward-facing-cone. The downward vertical component of this flow needs to be re-orientated by between 90° and 180° in order for it to be exhausted through the stack exit, counteracting the initial reorientation in the BB.

Figure 203 together with Figure 226 of the baseline solution show that the interaction of the flow with the downstream end of the stack base and the lower downstream stack wall perform the upward reorientation. In all solutions produced in Section 6.2.3.1 through Section 6.2.3.5 a messy flow in the lower stack has been observed. These two patterns suggest that the flow that exits the BB below the centreline, exits via an inefficient path.

Using the baseline BB geometry, a method was sought to increase the proportion of flow exiting above the BB centreline. With the constraints of the BB geometry, the proposed solution was to incorporate an asymmetrical forward-facing-cone as shown in Figure 227.

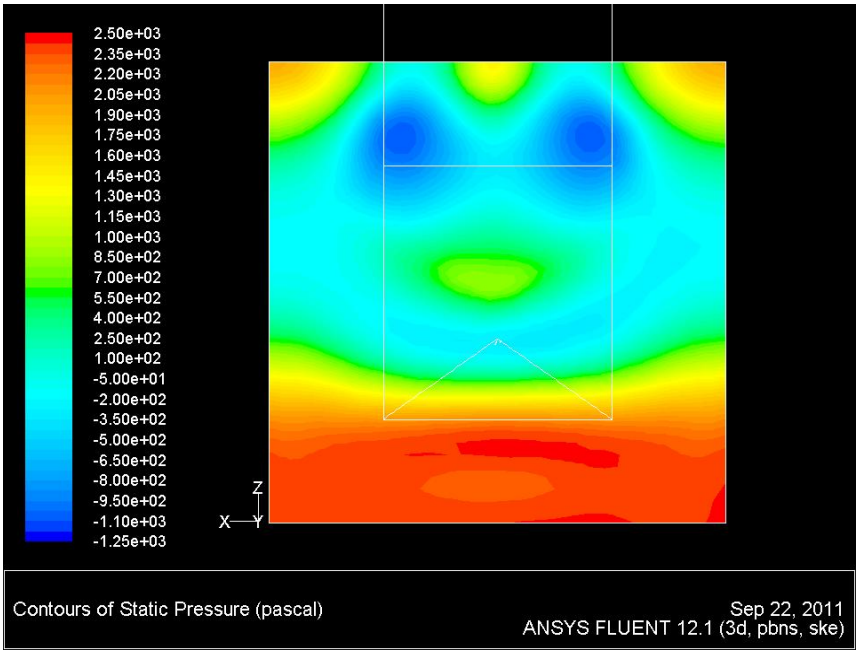

Figure 226 Static Pressure Distribution on the Base of the Exhaust Stack in the Baseline Arrangement

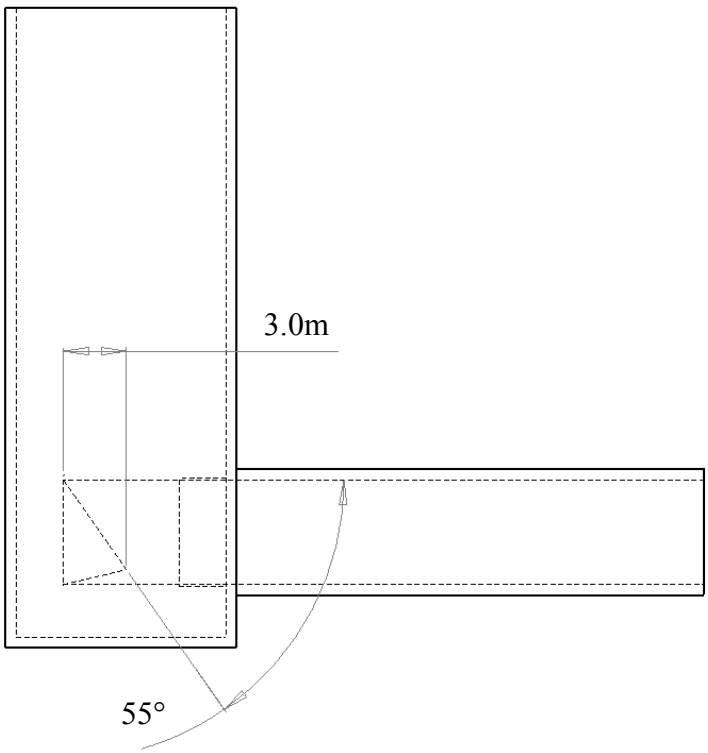

Figure 227 Design of the Asymmetric Forward-Facing-Cone

The 55° cone tip half-angle was retained from the baseline design, but the tip of the cone was extended to be 3.0m (arbitrarily chosen) upstream of the rear of the cone. This had the effect of lowering the cone tip below the centreline of the BB, and thus presenting a greater upward facing portion of the cone to the oncoming flow. A solution for this domain was generated and the results are discussed below.

Figure 228 compares the streamlines emitted from the augmenter in the baseline and asymmetric cone designs. The asymmetry introduced to the cone has successfully managed to exhaust a greater portion of the augmenter flow with an upward vertical velocity component.

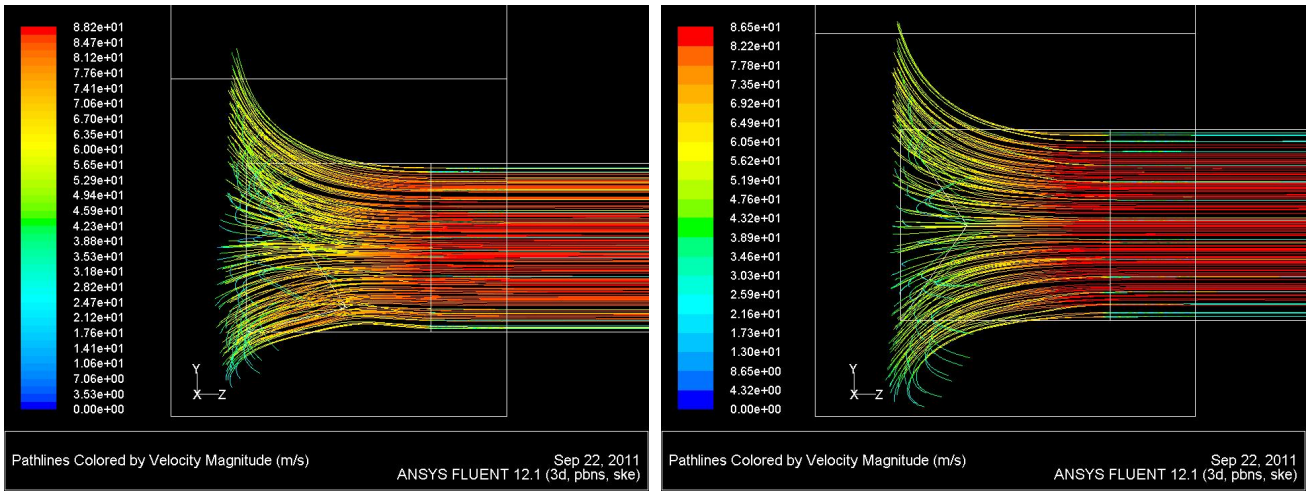

Figure 228 Streamlines Emitted from the 'Augmenter Inlet' BC with an Asymmetric Forward-Facing-Cone (left) and in the Baseline Solution (right)

Figure 229 shows the much greater static pressure variation on the cone face when compared with the baseline solution, shown in Figure 197. Originating at the cone tip, a region of high pressure is formed on the upward facing side of the asymmetric cone. The magnitude of this highest pressure point is comparable with that of the baseline solution.

On the downward facing portion of the asymmetric cone, a significantly lower minimum pressure is created in comparison with the baseline design. Figure 230 and Figure 231 show that this region of low static pressure is a result of a centre of circulation, perpendicular to the augmenter flow, being created adjacent to the lower boundary of the BB.

Figure 232 shows that the flow that does exit the BB with a downward velocity component still gets captured in a messy rotation at the base of the stack. However, Figure 232 also emphasises the greater proportion of flow exiting above the BB centreline, with the greater density of streamlines seen adjacent to the downstream stack wall. Figure 233 shows agreement, with a significant

concentration of the flow exiting the stack along the downstream face. A negligible drop in MFR was observed when compared to the baseline solution.

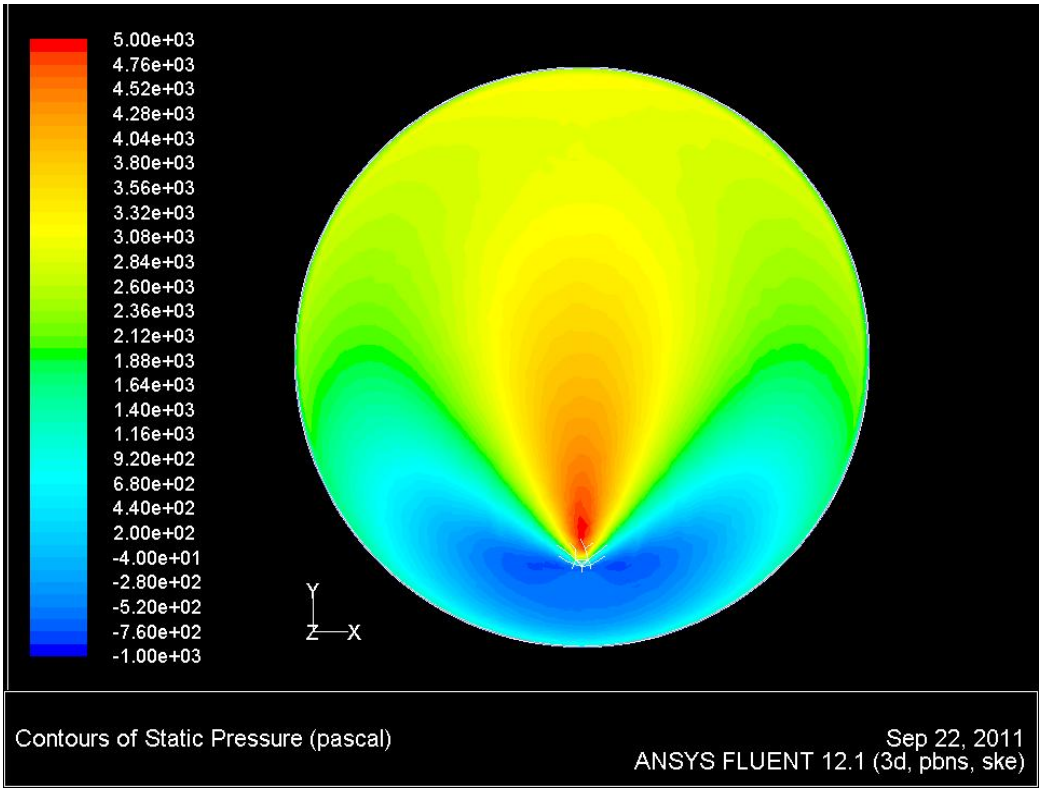

Figure 229 Static Pressure Distribution on the Asymmetric Forward-Facing-Cone

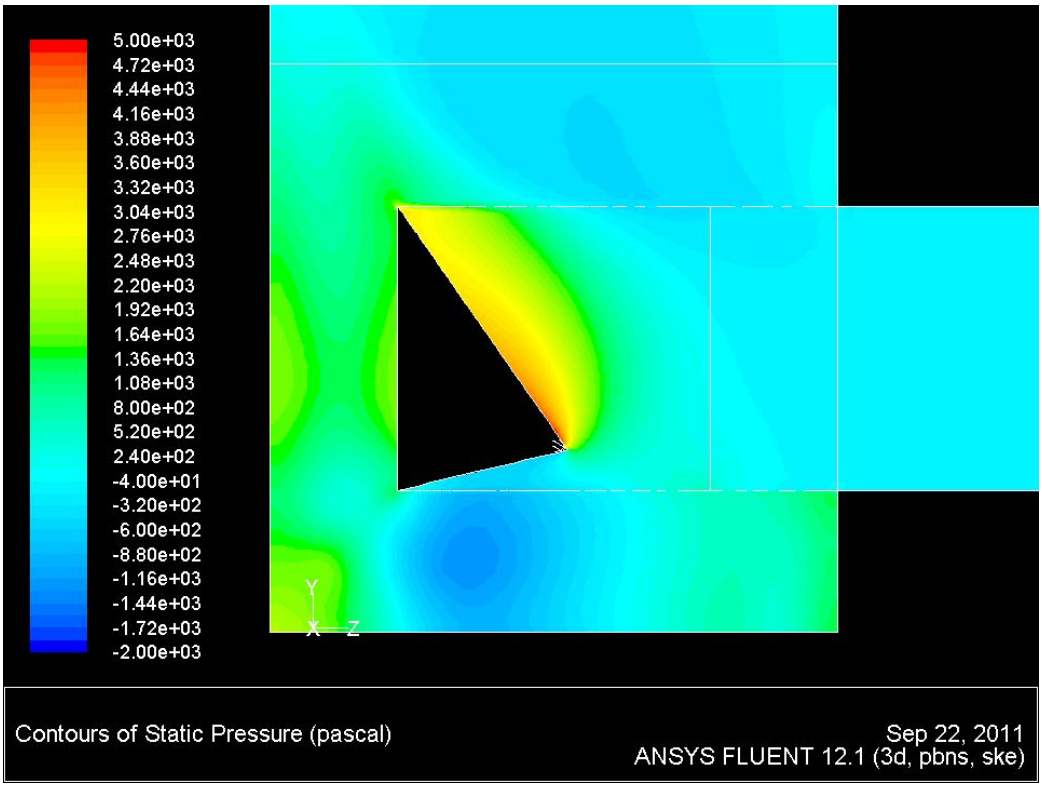

Figure 230 Static Pressure Distribution on the Vertical BB Axis with an Asymmetric Forward-Facing-Cone

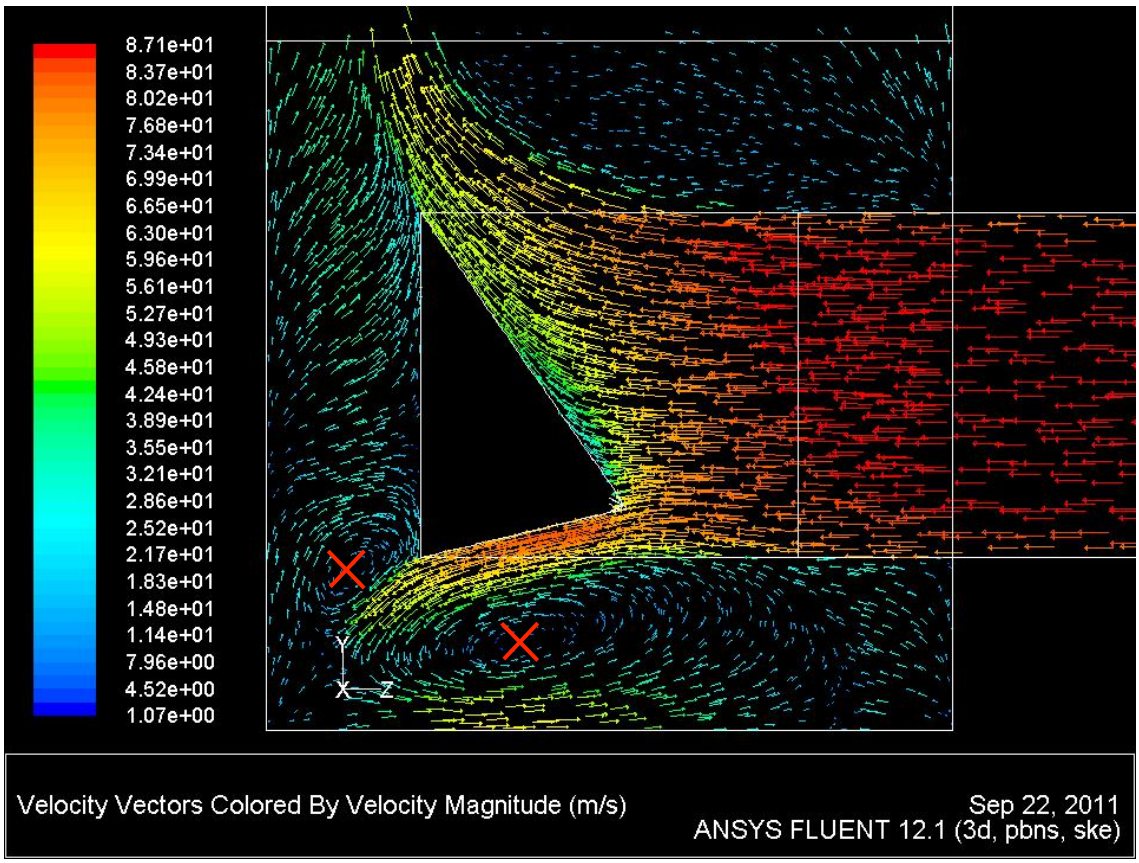

Figure 231 Velocity Magnitude on the Vertical BB Axis with an Asymmetric Forward-Facing-Cone

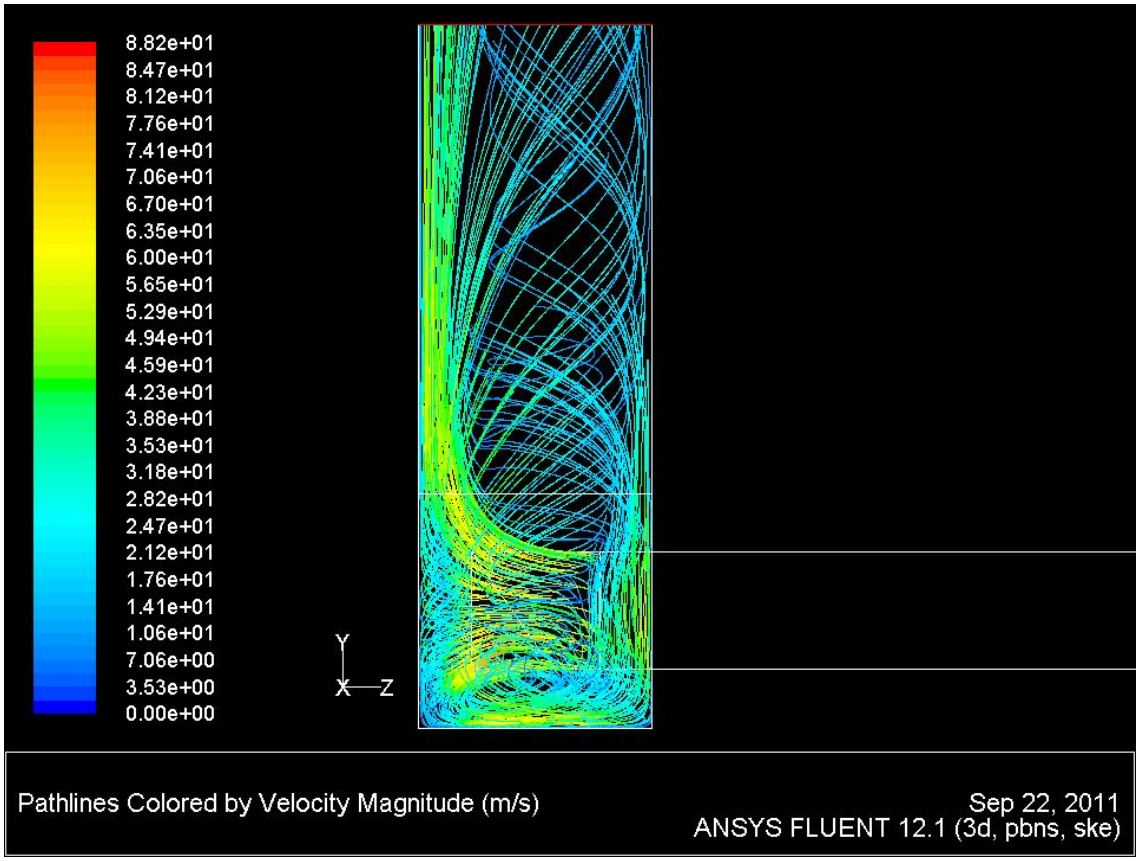

Figure 232 Streamlines Emitted from the BB Face with an Asymmetric Forward-Facing-Cone (viewed from the exhaust stack sidewall)

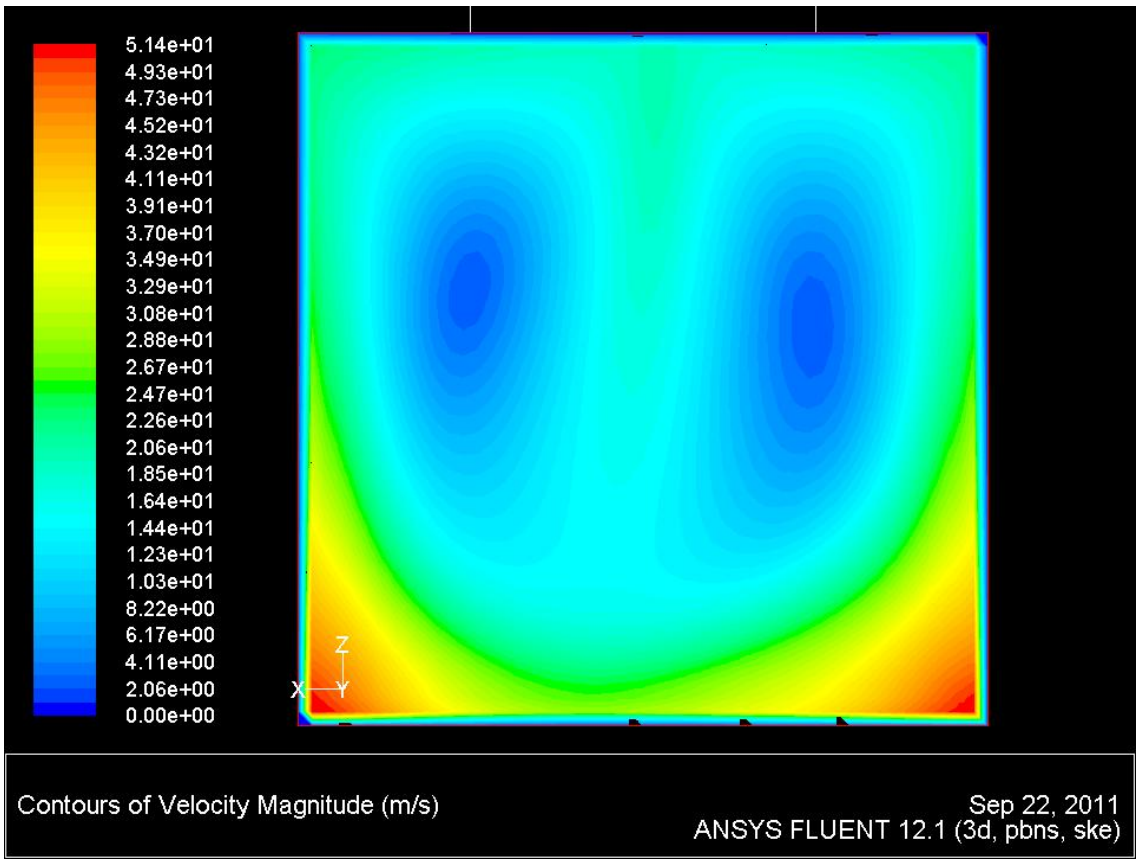

Figure 233 Velocity Magnitude at the 'Stack Exit' BC with an Asymmetric Forward-Facing-Cone

6.2.3.7 Ramp-Terminating Blast Basket

Section 6.2.3.6 showed that an asymmetric forward-facing-cone directed a greater proportion of the augmenter flow in an upward direction from the BB body. However, a significant portion of the augmenter flow still passed through the messy flow paths in the base of the stack. To entirely eliminate flow in the base of the stack, whilst retaining the baseline BB geometry, the forward-facing-cone termination was replaced with a ramp-termination as shown in Figure 234.

The ramp was designed with a 5.0m radius, as shown in Figure 234. This allowed a full 90° sweep of the ramp within the confines of the 5.0m diameter BB geometry. The dimensions of the ramp perpendicular to the augmenter flow were trimmed to fit within the baseline BB geometry. A solution was produced using the ramp-termination, and the results are discussed below.

Figure 235 shows that a far greater proportion of the flow exiting the BB was isolated from the lower exhaust stack. Figure 236 shows similarities with the solution of Section 6.2.3.6, with a large proportion of flow exiting the stack via a path adjacent to the downstream stack wall. However, Figure 237 shows a slightly better distribution of velocity at the stack exit in comparison with Figure 233.

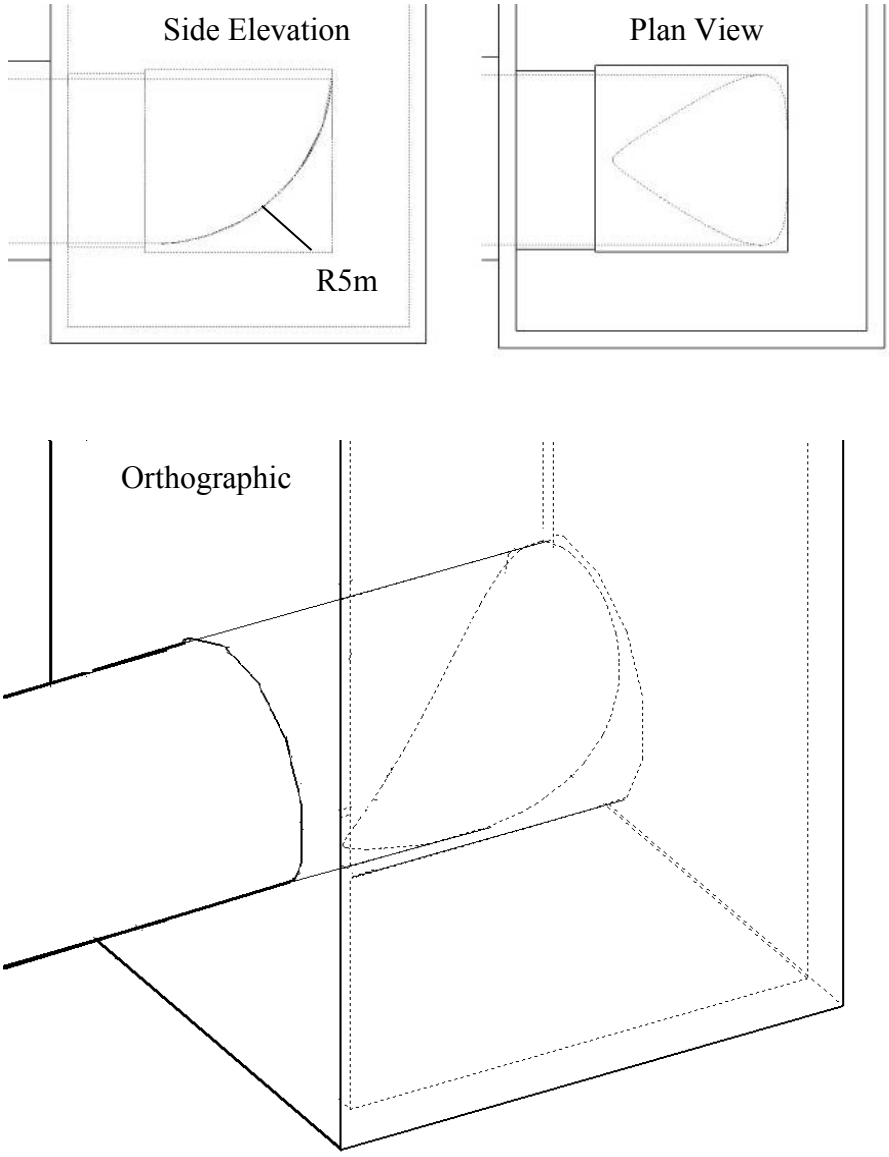

Figure 234 Design of the Ramp-Terminating BB

Figure 238 shows that there is some static pressure variation on the face of the ramp-termination of the BB. When viewed from an upstream position there is an area of comparatively high static pressure on the lower and central sections of the ramp, with low areas of static pressure at the upper corners. This pressure distribution suggests that the flow is driven outwards from the centre of the ramp. Figure 239, which shows the orientation of velocity vectors one mesh element away from the ramp surface, supports this.

Figure 239 also supports the above-mentioned point, in that it shows that by replacing the forward-facing-cone with a ramp, the orientation of the flow exiting through a majority of the BB has an upward vertical velocity component. The line overlaid in Figure 239 roughly indicates the boundary

between flow that exits the BB with an upward vertical component, and that with a downward vertical component.

Figure 240 and Figure 241 show the flow pattern in the lower stack, and how the pressure build-up on the ramp encourages the flow in an upward orientation. In order to fit a constant radius ramp in the cell with a 90° sweep, a 0.5m gap along the base of the BB resulted due to the combination of a 5.0m diameter BB and a 5.5m long perforated BB body. Figure 240 shows that a very small portion of flow finds its way through this perforated region, and drives a recirculation region with a centre of rotation perpendicular to the augmenter flow.

Due to the inclusion of the ramp, the perforated area of the BB body was significantly reduced, with a 20.5% reduction in open area for the flow to exit the BB. As such, direct comparisons of the calculated MFR in relation to the other solutions cannot be fairly made. The MFR produced of 1927.5kgs^{-1} was 6.1% lower than the baseline solution.

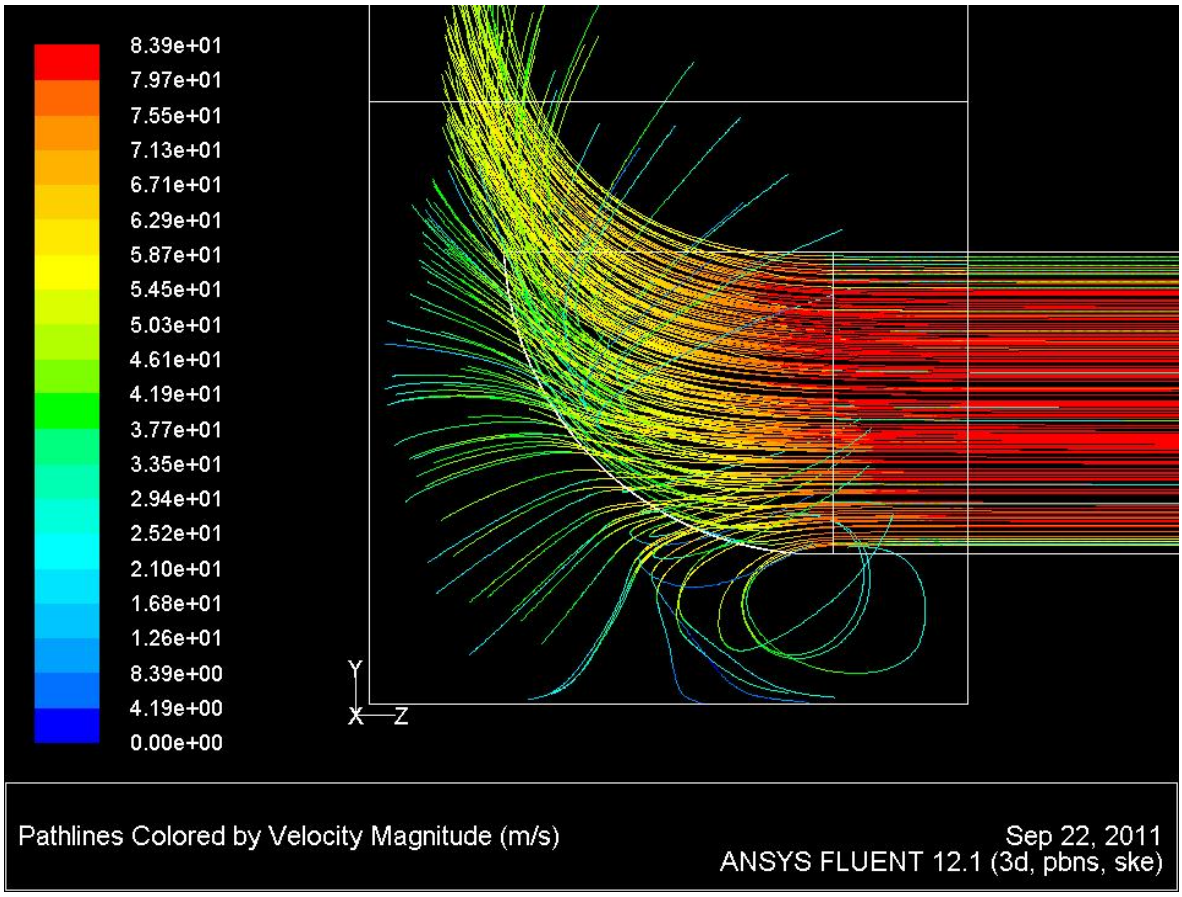

Figure 235 Streamlines Emitted from 'Augmenter Inlet' BC with a Ramp-Terminating BB

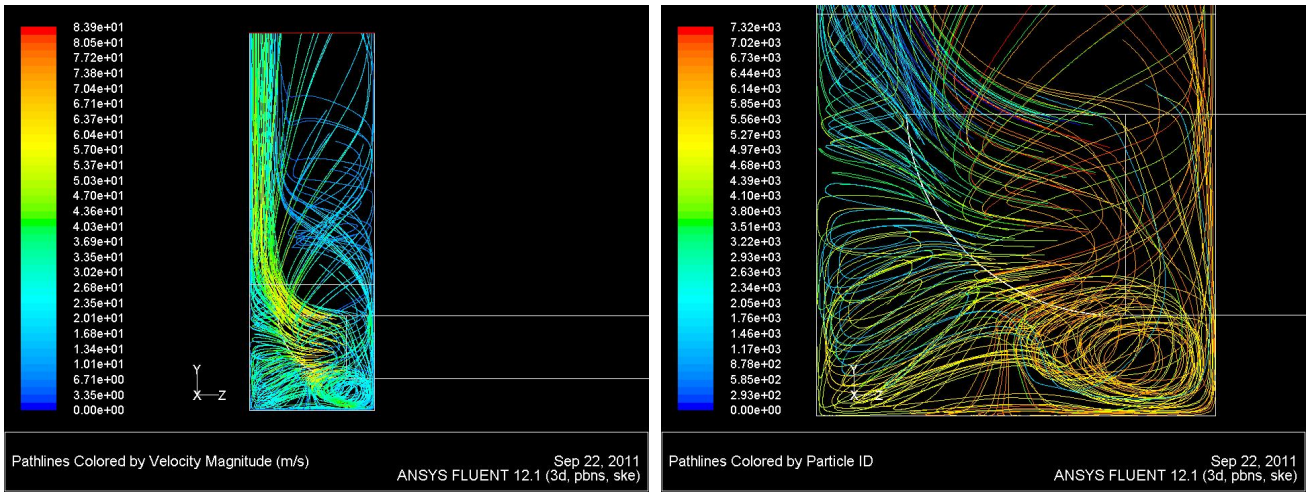

Figure 236 Streamlines Emitted from the BB Face with a Ramp-Terminating BB
(viewed from the exhaust stack sidewall)

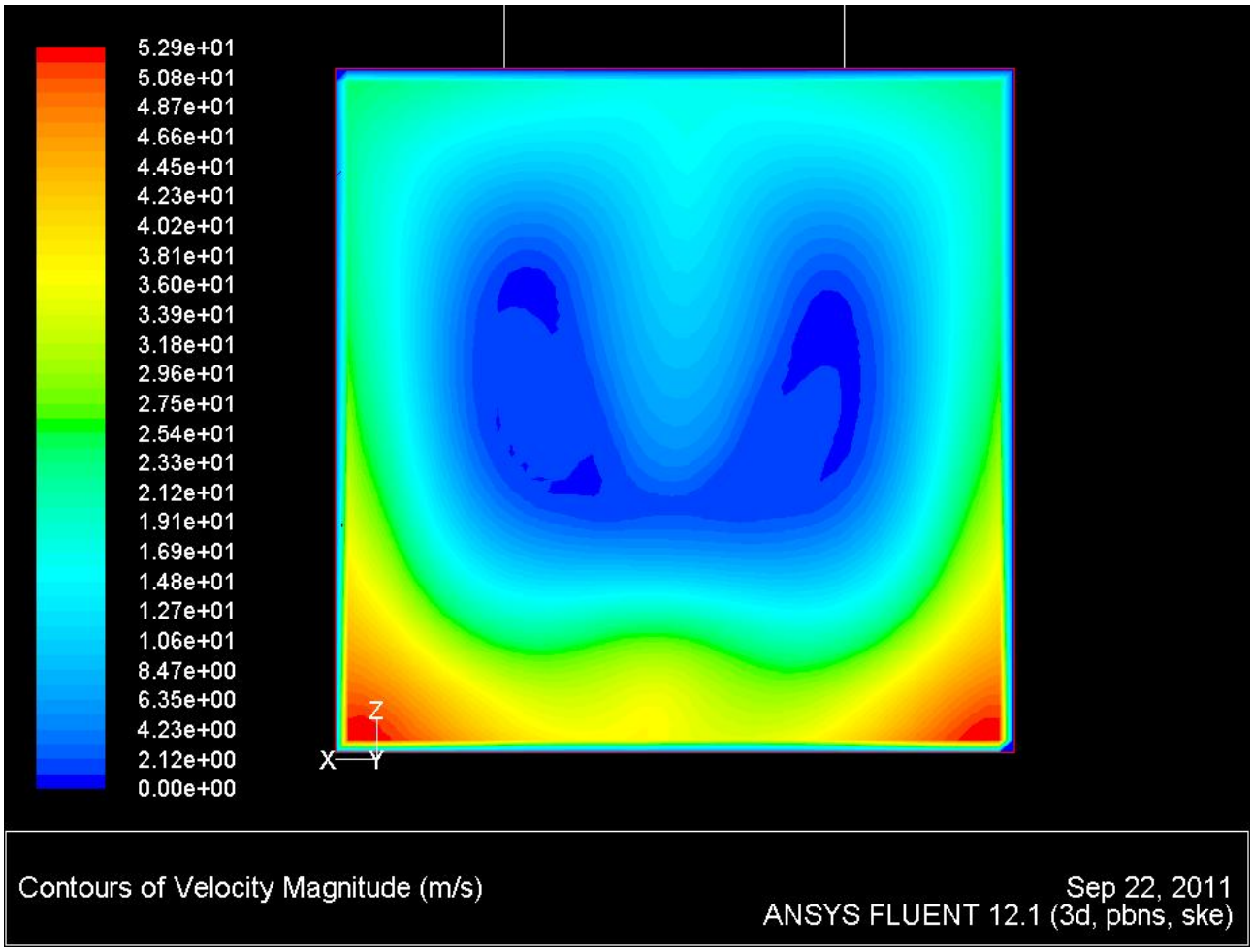

Figure 237 Velocity Magnitude at the 'Stack Exit' BC with a Ramp-Terminating BB

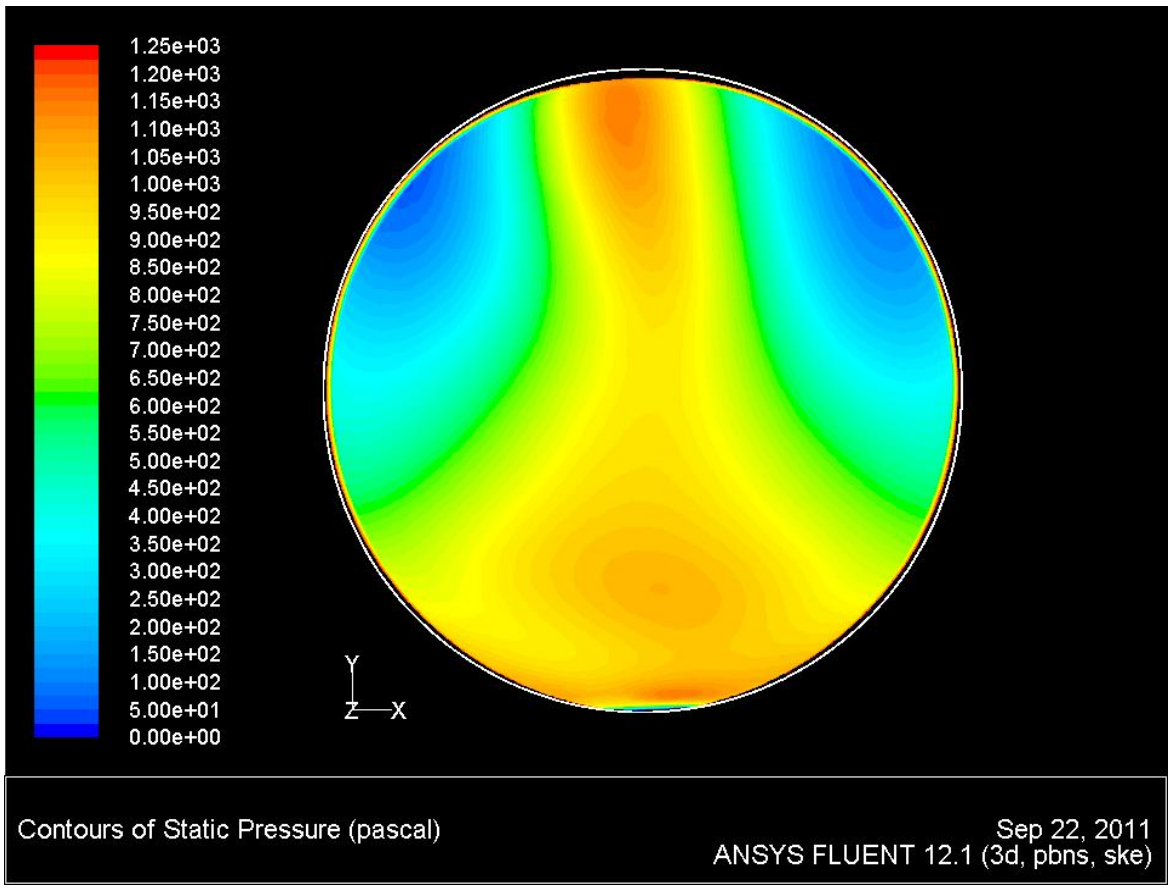

Figure 238 Static Pressure Distribution on the Ramp-Termination of the BB

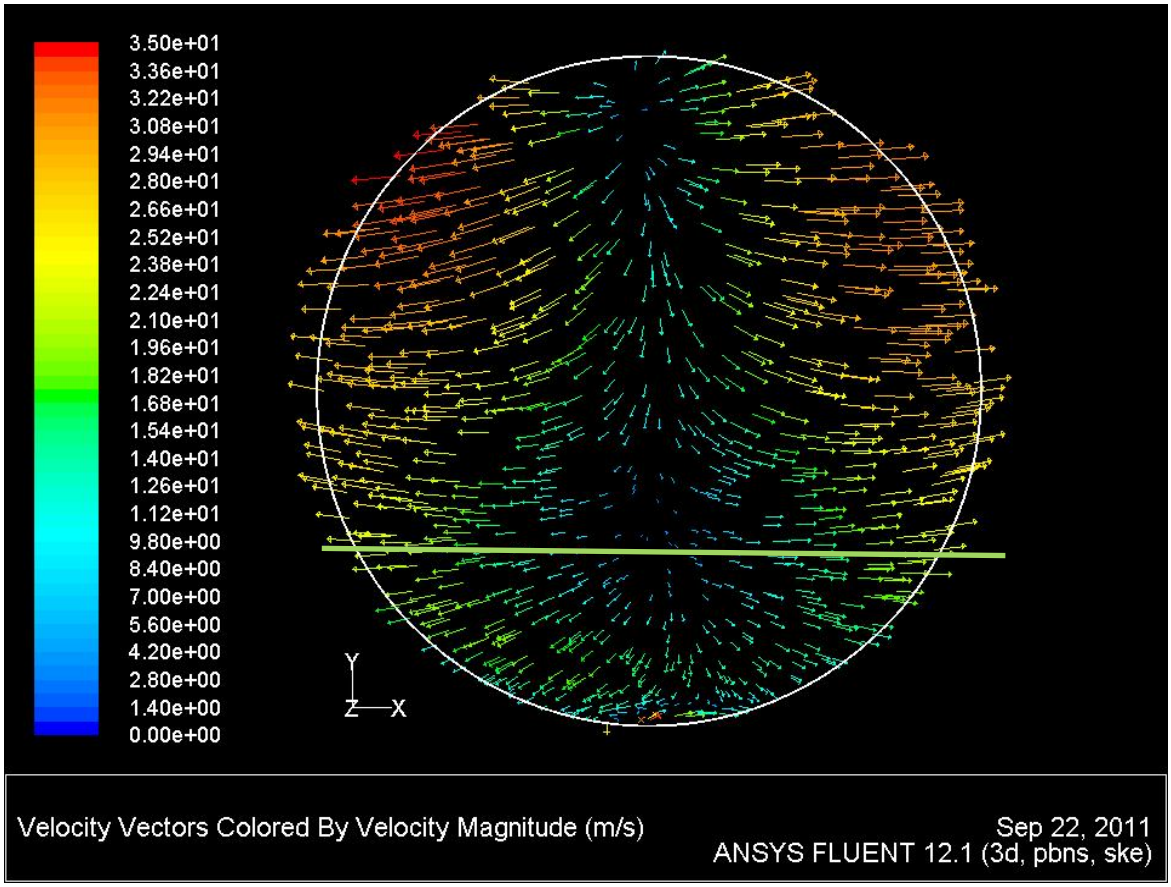

Figure 239 Flow Direction and Velocity Immediately Upstream of the Ramp-Termination of the BB

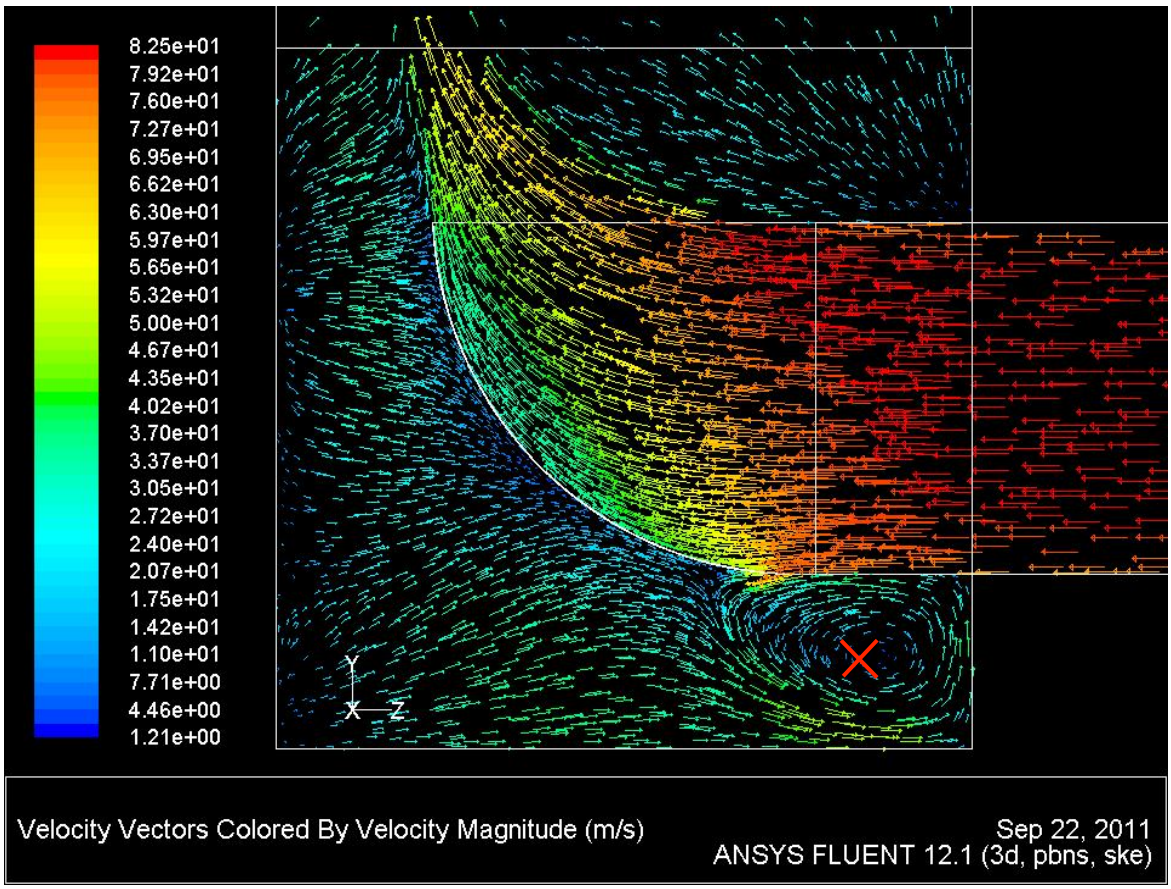

Figure 240 Velocity Magnitude on the Vertical BB Axis with a Ramp-Terminating BB

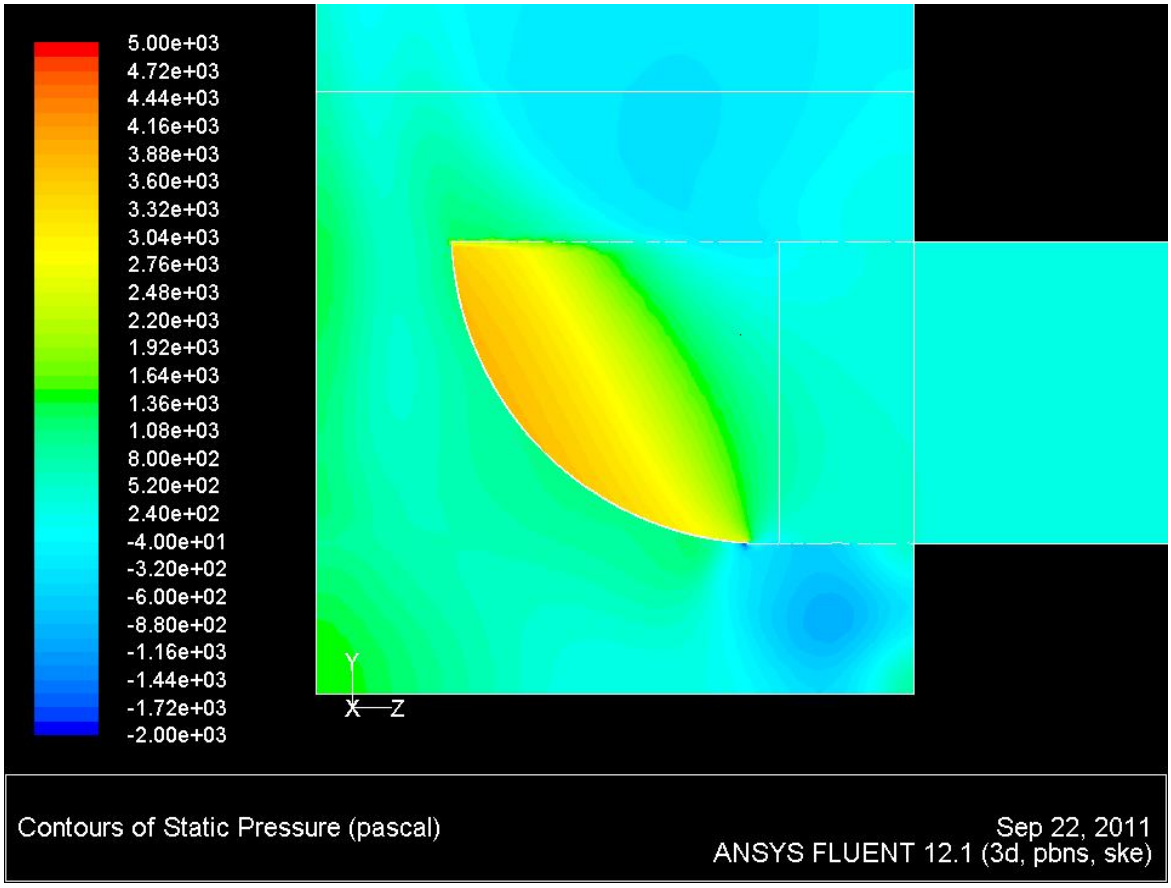

Figure 241 Static Pressure Distribution on the Vertical BB Axis with a Ramp-Terminating BB

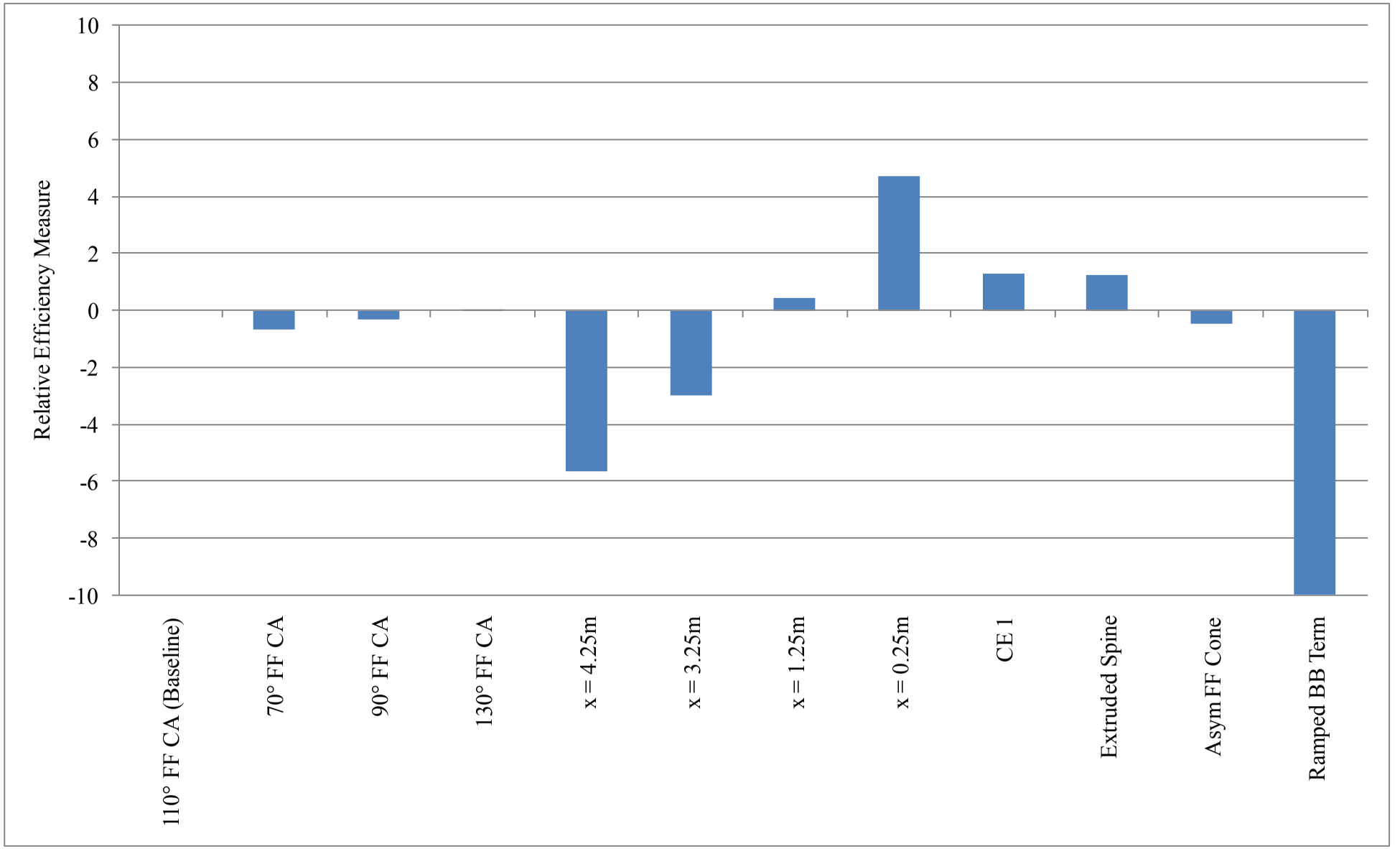

Figure 242 Airflow Efficiency (Scaled to Baseline Arrangement) for BB Analysis

6.3 Summary of Findings

In this section a CFD analysis of the lower exhaust stack of a JETC was performed. The solution to the baseline stack arrangement showed that flow exited evenly around the perimeter of the BB. However, a majority of the flow exited via the downstream 50% of the perforated area.

Analysing a vertical plane aligned with the augmenter flow, and with the stack axis, showed that two areas of circulation formed in the lower stack with axes of rotation about a line perpendicular to the augmenter flow. Both centres of circulation were located below the BB centreline, and in the downstream half of the stack.

The flow exiting the BB took one of two specific paths, determined by whether it exited the BB above or below the vertical centreline. The flow exiting above the vertical centreline split into two moderately counter-rotating streams through interaction with the forward-facing-cone and the downstream stack wall. These streams exited the exhaust stack at a comparative high velocity adjacent to the downstream stack wall.

The flow exiting below the BB centreline also split into two streams, mirrored about the augmenter's stream-wise centreline. These streams formed large circulating regions in the lower exhaust stack. A large rotational component was retained in these streams as the flow moved up the exhaust stack and was expelled. The exiting velocity of these streams was comparatively low, and occupied a significant portion of the exhaust stack exit face.

Overall, the distribution of flow in the exhaust stack was heavily weighted towards the downstream wall. Areas of large static pressure build-up were observed on the forward-facing-cone and on the downstream wall and base of the stack.

The baseline forward-facing-cone tip angle was varied through a structured range of values between 70° and 130° to determine any influence on flow distribution in the stack and flow efficiency. Overall, a negligible variation in flow efficiency was observed across the solutions produced.

The structure of the flow in the lower stack was augmented slightly through modification of the tip angle. A decrease in tip angle moved the above-mentioned centres of rotation, perpendicular to the augmenter flow, further downstream. At the exhaust stack exit this equated to a slightly more evenly distributed flow, although still heavily weighted towards the downstream stack wall.

To gain an understanding of the way the BB and stack walls interacted to form the flow patterns that had been observed, the stream-wise location of the BB was altered. Solutions were produced with the BB both 1m and 2m upstream and downstream of its location in the baseline arrangement. From the extreme upstream position to the extreme downstream position, a drop in cell efficiency of 6% was calculated.

The most notable qualitative observations were made when the BB was placed 2m downstream of its baseline location. In this scenario, one of the circulation zones, with a centre of rotation perpendicular to the stream-wise flow, was removed. This resulted in a flow efficiency increase over the baseline solution, and significantly altered the flow distribution at the exhaust stack exit.

The exhaust exit flow was more evenly distributed across the stack exit face, with high velocity flow exiting along a majority of all four stack sidewalls, and along a line representing the augmenter's stream-wise axis. The change in flow distribution at the exit was found to be a result of a singular distinct stream of flow exiting from either side of the BB. A comparison of static pressure contours showed that by aligning the BB nearer the downstream stack wall, the build-up in static pressure was concentrated to a single continuous area. This was in contrast to solutions produced with the BB placed further upstream.

The promising increase in cell efficiency produced by relocating the BB downstream was attempted to be replicated through the use of a retrofit design that could be incorporated into current cells. A cone extension was added to physically link the forward-facing-cone and the downstream stack wall in the baseline domain. The extended cone successfully managed to replicate the single centre of rotation flow pattern produced by moving the BB downstream. However, the increase in cell efficiency was only marginal over the baseline solution.

This was deemed to be a result of increased static pressure build-up due to the sharpening of the corner between the stack base and the downstream wall as a result of the cone extension inclusion. The increase in static pressure in this area resulted in a larger proportion of the flow exiting above the centreline than in the baseline solution.

A spine extruded from the downstream wall of the working section was added to the baseline domain in an attempt to retain the flow pattern of the extended cone design, but remove the high static pressure build-up. The intent of the extruded spine was not realised when employed, and a flow state very similar to the baseline solution was observed.

Throughout the designs investigated up to this point, flow exiting below the centreline of the BB was seen to be contained in inefficient patterns that involved multiple vertical and horizontal redirections. This was illustrated through the previously mentioned build-up of static pressure. An asymmetric forward-facing-cone, with a tip lowered below the vertical centreline of the BB, was incorporated into the baseline domain in an effort to reduce the proportion of flow exiting below the BB centreline.

The asymmetric cone was successful in increasing the proportion of flow exiting above the BB centreline, and with an upward vertical velocity component. This was illustrated by the significant modification to the static pressure profile on the cone face. However, this was detrimental to the distribution of flow at the exhaust stack face, with the exiting flow more heavily concentrated towards the downstream stack wall than in the baseline solution. A slight decrease in flow efficiency resulted.

A ramp-terminating BB was investigated as a more definite means of reducing flow passing into the lower portions of the exhaust stack. Flow was still seen to dissipate throughout a significant portion of the perforated area of the BB, despite the removal of the ‘directional’ aid of the cone. The static pressure and velocity contours near the ramp face showed that flow near the rear of the BB still exited via the perforated side regions. Flow distribution at the stack exit was comparable with that of the asymmetric cone, with a very heavy weighting towards the downstream stack wall. With the inclusion of the ramp, the perforated area of the BB was reduced by 20.5%. Cell efficiency decreased 6.1% from the baseline solution.

7 Conclusions

This section collates and synthesises the findings of the investigations undertaken in this research, links the findings to the research objectives, and considers the implications of the findings for future research.

This study sought to generate an understanding of flow patterns throughout a JETC, and investigate ways to improve the airflow efficiency and velocity distortion. CFD was established as an investigative technique that, whilst not able to provide direct numerical solutions, produces computational solutions within acceptable margins of error.

CFD techniques were applied in a systematic series of investigations focussed around different sections of the JETC: namely the inlet and exhaust stack baffle arrangements; the turning-vane arrangement; the rear of the working section; and the lower exhaust stack. Discussions from the literature were used to set up the CFD analyses and provide validation for the choices made.

Baseline arrangements were used to generate an understanding of the flow patterns in each of the above-mentioned areas. The CFD solutions to these baseline arrangements were then used for comparisons during investigation and design analyses. A number of parameters were varied in a structured series of analyses to determine their influence on cell airflow efficiency and velocity distortion. For each series of investigations, the solutions produced provided computational data for problem-specific validation of the techniques used.

The selection of an appropriate model to describe turbulence and/or its effects was identified as being an important decision when approaching a CFD analysis. In this thesis, two-equation models were predominantly adopted because in complex and large computational domains they represent the upper limit of computational expense that can be afforded for turbulence consideration.

Through analysis of a baffle baseline arrangement, a number of flow features were identified. The most significant flow feature present in the baffle arrangement structure was separation adjacent to the downstream face of each individual baffle. The profile and magnitude of the separation regions were significantly dependent on both the immediate upstream and downstream geometries within the arrangement.

A CFD-aided design process was performed, and showed the ability of CFD as an investigative and design tool. A number of design iterations were readily replicated, analysed, and adjusted in a computational manner. The design process found that significant decreases in static pressure loss across the baffle arrangement could be made through modification of the upstream and downstream baffle faces.

The most effective modifications to the baseline design, in terms of gain compared to investment, were thought to be the addition of a semi-circular upstream face, and a decrease in downstream taper angle to 30°. These modifications were shown to give a 58% decrease in static pressure loss across the baffle arrangement when compared to the baseline design. The design process also found that by 'clipping' the TE of individual baffles, as seen in the inlet stack of the CHCEC, airflow efficiency was poor compared to other designs tested.

In investigating the turning-vane arrangement, the settings used in the CFD investigation of (Agmen et al., 2005) were retained for the purpose of validation. The experimental work of (Johl et al., 2007) was used to determine that the settings applied in the work of (Agmen et al., 2005) were valid for qualitative and quantitatively comparative analyses. It was suggested that strict quantitative values extracted from solutions developed using the settings of (Agmen et al., 2005) should be taken with caution, and in acknowledgement of the margins of error that were present.

The geometry of the CHCEC cell was used for the analysis of a baseline turning-vane arrangement. The resultant CFD solution provided a computational comparison for problem-specific validation. In the solution produced, inner corner separation, under-vane separation/low velocity, and baffle-vane interaction were all identified as flow patterns that detrimentally affected downstream velocity distortion.

An adverse pressure gradient caused by the combining geometry of the baffle arrangement, cell walls, and the turning-vane arrangement was determined to be the source of the inner corner separation. In addition, a low velocity region was produced downstream of the inner corner separation. This was identified as being a potentially dangerous flow feature in terms of inlet vortex creation.

A CFD-aided investigation process allowed a number of parameters within the turning-vane arrangement to be individually analysed. Mid-baffle alignment of the turning-vanes was found to produce a substantially more consistent flow than a baffle alignment. The decrease in gap-chord

ratio, created by introducing more vanes into the arrangement, decreased downstream distortion by reducing the size of the under-vane low velocity regions. A decrease in TE length was found to significantly decrease the flow over-rotation and velocity distortion. Transient flow was seen, originating from the uppermost vane when the TEs were lengthened.

An increase in inner corner radius provided no reduction in inner corner separation. To remove inner corner separation, a significant realignment of the vane arrangement was identified as being required. Moderate vane arrangement realignment, combined with a baffle arrangement modification and an inner corner radius increase, was required to create a significant reduction in separation whilst retaining consistency in the turning-vane flow channels. This finding highlighted the need for cell designers to consider the interaction of respective components during the design process. Through implementing the findings of the individual parameter investigations, velocity distortion was reduced from 23.6% in the baseline solution to below 10%.

To investigate the rear of a JETC working section CFD solutions were produced. These solutions also provided a validation comparison for experimental work. A number of findings were made in relation to the rear working section flow patterns and how the combination of working section components interacted to create optimal airflow efficiency.

It was found that cell efficiency was a function of both engine-augmenter spacing and the augmenter diameter. Trends were identified between flow efficiency and the cell parameters of augmenter diameter and engine-augmenter spacing. The factors that generated the observed trends varied across the augmenter diameter range analysed.

These trends showed a general growth in cell efficiency with augmenter diameter until a peak value was reached. The subsequent observed decline in cell efficiency, after the peak, was found to be a function of BC dependence, and was deemed not to be a 'realistic' phenomenon. For the engine-cell combination investigated, a polynomial of $\Phi_{MAX} = 0.346d + 4.857$ was found to determine the augmenter diameter of maximum efficiency (Φ_{MAX}), for a given engine-augmenter spacing (d).

An investigation of the influence of augmenter size and shape on flow efficiency revealed that the (engine) blockage ratio had no significant effect on airflow efficiency. On the contrary, cell efficiency decreased with an increase in cell width. Investigations showed that shifting from a conventional square cross-section cell to a circular cross-sectioned cell provided no appreciable gains in airflow efficiency.

A CFD solution was produced to determine the flow features within the lower exhaust stack of a JETC, and to provide the computational contribution to a problem-specific validation process. The most notable features in the baseline solution were an even distribution of flow around the perimeter of the BB, an uneven flow distribution at the stack exit, and the defined difference in flow streams present throughout the height of the exhaust stack.

It was found that variations in the forward-facing-cone angle provided no significant effect on airflow efficiency. The relocation of the BB towards the downstream wall of the stack provided a notable gain in flow efficiency, and substantially affected the flow patterns observed. A cone-extension was found to be a suitable retrofit solution for current cells to replicate the more structured flow patterns observed when relocating the BB downstream. Both an asymmetric forward-facing-cone and a ramp-terminating BB provided some isolation of the flow from the lower exhaust stack, but it was not associated with substantial gains in airflow efficiency.

This thesis has provided a thorough understanding of flow patterns present throughout a JETC. In doing so, a number of computational solutions suitable for problem-specific validation were produced. A number of individual parameters throughout a JETC were analysed in a structured manner. The findings made have provided recommendations for improvements to cell design to increase cell efficiency and reduce velocity distortion.

Overall, the findings suggest that aerodynamic optimisation of the baffle arrangements would provide the greatest gains to cell efficiency. As some cells contain as many as three baffle arrangements, increases made to cell BPR and capacity could be sizable.

For low levels of velocity distortion, the need to design the inlet stack baffles in consideration of the turning-vane arrangement was highlighted. Mid-baffle vane alignment, consistent flow channels, and sufficiently low chord to gap ratios should be incorporated into a turning-vane design to maximise flow uniformity. These baffle and vane components need to combine with the geometry of the cell to limit adverse pressure gradients at the inner corner to minimise separation and the downstream threat it creates to a safe testing environment.

7.1 Suggestions for Future Research

This section outlines a number of areas worthy of future research. The first area relates to the collection of problem-specific experimental data from a JETC. The subsequent areas relate to

advancements that may be achieved within the specific sections of the test cell that were investigated.

The collection of problem-specific experimental data from a JETC would substantially advance the findings of this thesis in two ways. Firstly, problem-specific BC parameters could be more accurately set. Secondly, and more importantly, a problem-specific validation of the CFD techniques employed could be performed. This would allow firmer quantitative assessments to be made from the computational solutions generated. The strength of CFD as a design tool throughout the JETC industry would be significantly enhanced as a result.

As an acknowledgement of the enhancements that problem-specific validation would add to the findings of this thesis, a section discussing the original validation testing plan of this project has been included as Appendix A.

7.1.1 Baffle Analysis

Whilst a thorough aerodynamic analysis was performed on the baffle arrangement, an acoustic assessment was not performed in combination. An analogous acoustic investigation of the designs proposed in this section would give a greater overall understanding of the interaction between aerodynamics and acoustics in a baffle arrangement.

The investigations reported in this section looked at the baffle arrangement in isolation. The baffle design process could potentially be performed with consideration of the functionality of other cell components. For example, some asymmetry could be incorporated into an inlet stack baffle design to assist in the downstream turning process performed by the turning-vane arrangement. Likewise, an exhaust stack specific baffle design could be developed to enhance the aerodynamic flow emitted from the lower exhaust stack.

7.1.2 Turning-Vanes

The focus of the turning-vane investigation was limited to the case where the baffle arrangement was aligned perpendicular to the flow in the working section. A similarly structured analysis for the parallel alignment case would add to the findings made in this investigation by providing a more comprehensive view on baffle-vane interaction.

It would be ideal to analyse every aspect of turning-vane design so that a structured design procedure could be developed for test cell engineers. The application of validated CFD techniques to create such a tool would be valuable. This is due to the number of designs that could be tested within a given time frame and budget that CFD allows. There are a substantial number of areas where further research would contribute towards a structured design procedure being developed. Some of these areas include:

- A more in-depth investigation of the impacts of staggering vane radii, LE/TE angles, and extension lengths across a vane arrangement;
- An investigation on the effect of variations in the baffle-vane spacing in relation to the downstream benefits for velocity distortion levels; and
- The development of a mathematical relation for velocity distortion as a function of cell MFR, cross-sectional cell geometry, vane radii, number of vane rows, and chord to gap ratio, and velocity distortion etc.

As briefly alluded to in Section 7.1.1, it would also be of interest to investigate if the functions of the vane and baffle arrangements could be combined. Currently the baffle and vane arrangements perform individual and specific tasks. As such, the merits of providing acoustic suppression through a turning-vane type arrangement would prove an interesting investigation. Would it be possible to effectively combine the functionality of the two components into one? Whilst an immediate solution is not evident, baffle and vane arrangements do share some features. One such feature is the repetitive individual geometries within a larger arrangement.

7.1.3 Working Section

In this working section investigation, an engine-cell specific correlation was found between engine-augmenter-spacing and optimum augmenter diameter. Comparable analyses with other cell widths, rectangular cell cross-sections, and other engine makes and models would expand the applicability of the findings made. A comprehensive range of analyses would allow the creation of a more comprehensive and usable reference tool for cell designers.

There is a significant amount of tabulated data in the literature for loss factors and flow patterns for circular-to-circular contractions. There is a comparative lack of information relating to abrupt contractions between ducts with non-matching cross-sections. Therefore, future work in this area would fill a current void. Particularly constructive developments could be made in the determining

correction factors, which would relate the losses incurred in contracting ducts of non-matching cross-sections, to those in the well-tabulated circular-to-circular contractions.

7.1.4 Lower Exhaust Stack

The investigation of the aerodynamic patterns in the lower exhaust stack of a JETC reported in this thesis is new to this field. No research literature that deals with experimental or computational aerodynamic studies of similar geometries was identified. An expansion of the work presented in (Idelchik & Fried, 1986) in relation to pressure loss in a BB geometry would be valuable. Such work would allow a more accurate representation of 'real-world' BB pressure losses through a porous jump BC.

Alternatively, the work of (Brundrett, 1993), which was developed by (Groth & Johanssson, 1988; Munson, 1988; Shubauer et al., 1948), provides a pressure loss correlation for a perforated plate with flow normal to the surface. This work also provides a correction for the correlation, which allows for variations in angle of incidence. Prior to this analysis, the angle of incidence in relation to the given BB perforated area was unknown. It was also unknown if the angle of incidence varied substantially across the BB perforations. The findings of this investigation provide indicative answers to these questions. Further concentrated analyses of the solutions produced in this thesis would generate more specific and definitive answers.

Further work, utilising these answers in addition to other research, could provide a correction to the correlation for BB geometries. An accurate correction of this type would form a tool with very wide applications for test cell designers and other investigations of this sort.

The focus of the investigations in this section was solely on flow patterns and flow efficiency. A comparative acoustic analysis, particularly in the case of the asymmetric cone and ramp-terminating BB, would add a useful dimension to the findings made.

The simplified lower exhaust stack case considered in this investigation did not account for velocity or turbulence profiles at the inlet BC. The use of experimental JETC data for setting this BC would enhance the analysis. However, further useful developments could be made in the absence of data. A comparative study to that performed, applying non-uniform inlet BCs, would show how sensitive the findings of this investigation are to the upstream flow profile.

A number of areas of lower exhaust stack performance investigated in this section, however a number of areas where future contributions would be valuable additions (in the authors opinion) have been included in this section. These have been presented as a series of questions below.

The area where the findings of greatest interest would likely come from would be in the construction and dimensions of the BB itself (and the augmenter tube by association). In the investigations presented in this section, the construction of the perforated area was not a variable investigated. The areas where future efforts spent on investigating traits of the BB specifically are posed below in the form of questions.

- What would the impact be on the flow patterns and efficiency if the perforated area were to be increased or decreased?
- How would a change to the percentage of open area of the BB affect the efficiency of flow and the evenness of flow distribution through the exhaust stack?
- What sort of gains could be made by putting additional manufacturing effort into amending the cross-sectional profile of the individual perforations?
- Would rounding or tapering the profile of the perforation lips provide notable performance effects?
- For the type of flow scenario present in the lower exhaust stack what, what are the optimal individual perforation sizes for a given BB open area?
- Is there an optimal BB (and associated augmenter tube) cross-sectional area to open area percentage ratio?
- Is there an optimal BB (and associated augmenter tube) cross-sectional area to perforated length ratio?

References

Abbott, M. B., & Dasco, D. R. (1989). *Computational Fluid Dynamics - An Introduction for Engineers*. New York: Wiley.

Agmen, K., Bosworth, S., Gilmore, J., & Hager, F. (2005). Christchurch Engine Centre - Aerodynamic Jet Engine Test Cell Analysis - Group Report.

Altshul, A. D. (1970). *Hydraulic resistance*. Moscow: Nedra Press.

Ando, T., & Shakouchi, T. (2004). Flow Characteristics over Forward Facing Step and through Abrupt Contraction Pipe and Drag Reduction. *Res. Rep. Fac. Eng. Mie Univ., 29*, 1-8.

Ando, T., Shakouchi, T., Yamamoto, H., & Tsujimoto, K. (2009). Effects of Side Walls on Pipe Inlet Flow (Drag Reduction by Separated Flow Control Using Ring Shaped Small Obstacle). *Journal of Fluid Science and Technology, 2*(Special Issue on Jets, Wakes and Seperated Flows No. 2), 468-478.

Ballough, J. (2002). Correlation, Operation, Design, and Modification of Turbofan/Jet Engine Test Cells *FAA Advisory Circular*.

Bosworth, S. (2005). Christchurch Engine Centre - Aerodynamic Jet Engine Test Cell Analysis.

Brundrett, E. (1993). Prediction of Pressure Drop for Incompressible Flow through Screens. *Transactions of the ASME. Journal of Fluids Engineering, 115*(2), 239-242.

Buice, C. B., & Eaton, J. K. (2000). Experimental Investigation of Flow Through an Asymmetric Plane Diffuser. *Journal of Fluids Engineering, 122*(2), 433–435.

Caldarelli, D., & Campanella, R. (2003). Ear

Cantwell, B. (2011 - Downloaded). The GE90 - An Introduction (Stanford University Referenced Course Notes). Retrieved from

CFD-Online. (2011). *SST k-omega Model.*

Cherry, E. M., Elkins, C. J., & Eaton, J. K. (2008). Geometric Sensitivity of Three-Dimensional Separated Fows. *International Journal of Heat and Fluid Flow, 29*(3), 803-811.

Chung, T. J. (2002). *Computational Fluid Dynamics*. Cambridge ; New York: Cambridge University Press.

Clarke, T. (2000). Inlet Airflow Ramps for Gas Turbine Engine Test Cells. In S. AIR5306 (Ed.), *SAE AIR5306*: Society of Automotive Engineers.

Clarke, T. (2005). [Private Communication].

Corce, D. (1990). Feasibility Study for Utilizing Sawtooth Noise Reduction Device wit Type T-10 Turbofan/Jet Engine Test Cells. *Naval Air Engineering Centre Design Data Report*.

Currie, I. G. (2003). *Fundamental Mechanics of Fluids*: CRC Press.

Daly, B. J., & Harlow, F. H. (1970). Transport Equations in Turbulence. *Phys. Fluids, 13*, 2634-2649.

Davidson, P. A. (2004). *Turbulence: An Introduction for Scientists and Engineers*: Oxford University Press.

De Siervi, F., Viguer, H. C., Greitzer, E. M., & Tan, C. S. (1982). Mechanisms of Inlet-Vortex Formation. *Journal of Fluid Mechanics, 124*, 173-207.

Dickman, R. A., Hehlnann, H. W., Hoelmert, W., & Freuler, R. J. (1984). A solution for aero-acoustic induced vibrations originating in a turbofan engine test cell. *AIAA 84-0594*.

Doelling, N., & Bolt, R. H. (1961). Noise Control for Aircraft Engine Test Cells and Ground Run-Up Suppressors. Volume 2: Design and Planning for Noise Control. *DTIC Document*.

El-Behery, S. M., & Hamed, M. H. (2011). A comparative study of turbulence models performance for separating flow in a planar asymmetric diffuser. *Computers & Fluids, 44*(1), 248-257.

Fluent. (2006). *Fluent v6.3.26 Help Files*.

Flynn, P. (2008). [Private Communication].

Francis, J. R. D. (1975). *Fluid Mechanics for Engineering Students*. London: Arnold.

Fu, S., Launder, B. E., & Leschziner, M. A. (1987). Modeling Strongly Swirling Recirculating Jet Flow with Reynolds-Stress Transport Closures. *Sixth Symposium on Turbulent Shear Flows*.

Germano, M., Piomelli, U., Moin, P., & Cabot, W. H. (1991). A dynamic subgrid-scale eddy viscosity model. *Physics of Fluids A (Fluid Dynamics), 3*(7), 1760-1765.

Gibson, M. M., & Launder, B. E. (1978). Ground Effects on Pressure Fluctuations in the Atmospheric Boundary Layer. *Journal of Fluid Mechanics, 86*.

Glenny, D. E., & Pyestock, N. G. T. E. (1970). Ingestion of Debris into Intakes by Vortex Action: Ministry of Technology, Aeronautical Research Council.

Groth, J., & Johanssson, A. V. (1988). Turbulence Reduction by Screens. *Journal of Fluid Mechanics, 197*, 139-155.

Ho, W. H. (2009). *Investigation into the Vortex Formation Threshold and Infrasound Generation in a Jet Engine Test Cell.* PhD, University of Canterbury, Christchurch.

Ho, W. H., Gilmore, J., & Jermy, M. (2011). Reduction of engine exhaust noise in a jet engine test cell. *Noise Control Engineering Journal, 59*(2), 194-201.

Huff, D. L. (2007). *Noise Reduction Technologies for Turbofan Engines.*

IAE. (2011). V2500 Fact Sheet - The Power of Superior Technology.

Idelchik, I. E., & Fried, I. (1986). *Handbook of Hydraulic Resistance* (2nd , rev. and augm. ed.). New York: Hemisphere Pub. Corp.

Jermy, M., & Ho, W. H. (2008). Location of the Vortex Formation Threshold at Suction Inlets Near Ground Planes by Computational Fluid Dynamics Simulation. *Proceedings of the Institution of Mechanical Engineers, Part G: Journal of Aerospace Engineering, 222*(3), 393-402.

Johl, G., Passmore, M. A., & Render, P. M. (2007). Design and Performance of Thin, Circular Arc, Wind-Tunnel Turning Vanes. *The Aeronautical Journal, 111*.

Kennedy, L. (2008). [Private Communication].

Kline, H. (1953). Small Scale Tests on Jet Engine Pebble Aspiration Tests. *Douglas AircraftCompany, Report SM-14885*.

Kodres, C. A. (2000). Jet Engine Test Cell Noise Reduction. *Naval Facilities Engineering Command Technical Review TR-2118-ENV*.

Launder, B. E. (1989a). *Second-moment closure and its use in modelling turbulent industrial flows*, UK.

Launder, B. E. (1989b). Second-Moment Closure: Present... and Future? . *International Journal of Heat Fluid Flow, 10*(4).

Launder, B. E., G. J. Reece, G. J., & Rodi, W. (1975). Progress in the Development of a Reynolds-Stress Turbulence Closure. *Journal of Fluid Mechanics, 68*(3).

Launder, B. E., & Spalding, D. B. (1972). *Lectures in Mathematical Models of Turbulence*. London ; New York: Academic Press.

Lein, F. S., & Leschziner, M. A. (1994). Assessment of Turbulent Transport Models Including Non-Linear RNG Eddy-Viscosity Formulation and Second-Moment Closure. *Computers and Fluids, 23*(8), 983-1004.

Lilly, D. K. (1992). A proposed modification of the Germano subgrid-scale closure method. *Physics of Fluids A (Fluid Dynamics), 4*(3), 633-635.

Liu, W., Greitzer, E. M., & Tan, C. S. (1985). Surface Static Pressures in an Inlet Vortex Flow Field. *Journal of Engineering for Gas Turbines and Power, 107*, 387-393.

Mankbadi, R. R., Habashi, W. G., & Hafez, M. M. (1995). *Computational Fluid Dynamics Techniques*. Australia: Gordon and Breach.

Massey, B. (2001). *Mechanics of Fluids (7th Edition)*.

Meneveau, C., Lund, T. S., & Cabot, W. H. (1996). A Lagrangian dynamic subgrid-scale model of turbulence. *Journal of Fluid Mechanics, 319*, 353-385.

Menter, F. R. (1993). Zonal Two-Equation k-ω Turbulence Model for Aerodynamic Flows. *AIAA Paper 1993-2906*.

Menter, F. R. (1994). Two-Equation Eddy-Viscosity Turbulence Models for Engineering Applications. *AIAA Journal, 32*, 1598-1605.

Menter, F. R., Kuntz, M., & Langtry, R. (2003). Ten Years of Industrial Experience with the SST Turbulence Model. *Turbulence, Heat and Mass Transfer 4*.

Moller, H., & Pedersen, C. S. (2004). Hearing at Low and Infrasonic Frequencies. *Noise Health, 6*, 37 – 57.

Motycka, D. L., & Walter, W. A. (1975). *An Experimental Investigation of Ground Vortex Formation During Reverse Engine Operation.* Paper presented at the AIAA/SAE 11th Propulsion Conference, Anaheim, California.

MTU, A. E. (2011). V2500 Turbofan Engine - The Innovative Power.

Munson, B. R. (1988). Very Low Reynolds Number Flow through Screens. *Transactions of the ASME. Journal of Fluids Engineering, 110*(4), 462-463.

Nakayama, A., & Jones, J. R. (1996). Vortex Formation in Inlet Flow Near a Wall *34th Aerospace and Sciences Meeting and Exhibit*: AIAA 96-0803.

Nijdam, J. (2007). *Lecture Notes ENGR401 - Introduction to Computational Fluid Dynamics*. Department of Chemical and Process Engineering, University of Canterbury.

Obi, S., Aoki, K., & Masuda, S. (1993). Experimental and Computational Study of Turbulent Separating Flow in and Asymmetric Plane Diffuser. *Proceedings 9th Symposium of Turbulent Shear Flow*.

Pankhurst, R. C., & Holder, D. W. (1952). *Wind-tunnel Technique : An account of Experimental Methods in Low- and High-speed Wind Tunnels*. London: Pitman.

Pope, A., & Rae, W. H. (1984). *Low-speed Wind Tunnel Testing* (2nd / ed.). New York: Wiley.

Raithby, G. D., & Van Doormaal, J. P. (1984). Enhancements of the SIMPLE Method for Predicting Incompressible Fluid Flows. *Numerical Heat Transfer, 7*.

Ridder, S. O., & Samuelsson, I. (1982). An Experimental Study of Strength and Existance Domain of Ground-to-Air Inlet Vortices by Ground Board Static Pressure Measurements. *Stockholm Royal Insitute of Technolgy*(KTH AERO TN 62).

Rolls-Royce. (2009). Trent 500 - Optimised for the Airbus A340 Family.

Roth, M. (2000). Review of Atmospheric Turbulence over Cities. *Quarterly Journal of the Royal Meteorological Society, 126*.

Ruehr, W. C. (1975). General Electric Technical Information Series Report. *R75AEG384*.

Sagaut, P. (2006). *Large Eddy Simulation for Incompressible Flows (Third ed.)*: Springer.

Salter, C. (1952). Experiments on Thin Turning Vanes. *Aeronautical Research Council Reports and Memoranda*.

Sapp, C. N. (1978). Experimental Investigation of Turbojet Test Cell Augmentors. *DTIC Document*.

Sarkar, S., & Balakrishnan, L. (1990). Application of a Reynolds-Stress Turbulence Model to the Compressible Shear Layer. *ICASE Report 90-18*.

Schmidt, D. R. (1987). Noise Levels of the NAS Cubi Point, T. P., TIO Test Cell During J52, J52/P408, F404, TF30/P414, and TF41 Engine Runups. *Naval Ocean Systems Center Technical Note 1501*.

Schmidt, J., & Friedel, L. (1997). Two-phase pressure drop across sudden contractions in duct areas. *International Journal of Multiphase Flow, 23*(2), 283-299.

Shin, H. W., Cheng, W. K., Greitzer, E. M., & Tan, C. S. (1986). Inlet Vortex Formation due to Ambient Vorticity Intensification. *AIAA Journal, 24*(4), 687-689.

Shin, H. W., Greitzer, E. M., Cheng, W. K., Tan, C. S., & Shippee, C. L. (1986). Circulation Measurements and Vortical Structure in an Inlet-Vortex Flow Field. *Journal of Fluid Mechanics, 162*, 463-487.

Shubauer, G. B., Spangenburg, W. G., & Klebanoff, P. S. (1948). Aerodynamic Characteristics of Damping Screens.

Smagorinsky, J. (1963). General Circulation Experiments with the Primitive Equations. *Monthly Weather Review 91*(3).

Spalart, P. R. (1992). A One-Equation Turbulence Model for Aerodynamic Flows. *AIAA Paper 92-0439*.

Speziale, C. G. (1990). A Critical Evaluation of Two-Equation Models for Near Wall Turbulence *NASA Contractor Report 182068*.

STAR-CCM. (2011). *STAR-CCM Help Files*.

Torblom, O., Lindgren, B., & Johansson, A. V. (2009). The separating flow in a plane asymmetric diffuser with 8.5 opening angle: Mean flow and turbulence statistics, temporal behaviour and flow structures. *Journal of Fluid Mechanics, 636*, 337-370.

Tu, J., Yeoh, G. H., & Liu, C. (2008). *Computational Fluid Dynamics : A Practical Approach* (1st ed.). Amsterdam ; Boston: Butterworth-Heinemann.

Versteeg, H. K., & Malalasekera, W. (2007). *An Introduction to Computational Fluid Dynamics : The Finite Volume Method* (2nd ed.). Harlow, England ; New York: Pearson Education.

Wesseling, P. (2001). *Principles of Computational Fluid Dynamics* (Vol. 29). Berlin: Springer.

Wilcox, D. C. (1988). Reassessment of the Scale-Determining Equation for Advanced Turbulence Models. *AIAA Journal, 26*(11).

Wilcox, D. C. (1997). *Basic Fluid Mechanics*: DCW Industries.

Wilcox, D. C. (1998). *Turbulence Modeling for CFD*.

Wilcox, D. C., & Rubesin, M. W. (1980). Progress in Turbulence Modeling for Complex Flow Fields including Effects of Compressibility. In N. T. Paper (Ed.).

Yakhot, V., Thangam, S., Gatski, T. B., Orszag, S. A., & Speziale, C. G. (1991). Development of Turbulence Models for Shear Flows by a Double Expansion Technique. *NASA Contractor Report 187611*.

Appendix A: Future Work – Collection of Test Cell Validation Data

This section is included to provide a very brief overview of the validation testing plans that were formulated with the initial development of the project. The validation testing plans were designed to be implemented at the CHCEC, with supplementary scale modelling to be performed utilising the facilities of the mechanical engineering department at the UoC. The discussion of the testing plans relate to the structure and facilities available at these two locations.

A.1 Objectives of the Validation Testing Process

The problem-specific validation testing process is used to enhance confidence in the qualitative and quantitative solutions produced in CFD calculations. As such, a testing plan was developed that covered areas where experimental data was to be collected, collated, and compared to the computational CFD solutions.

A.2 Overall Testing Process

Validation testing was to be performed in relation to each major element affecting airflow in the test cell to provide points of reference from which the CFD solutions could be compared. In a U-shaped JETC these areas were identified as:

- Pre-inlet stack baffles;
- Post-inlet stack baffles/Pre-turning-vanes;
- Post-turning-vanes/Pre-FOD and turbulence screens;
- Post-FOD and turbulence screens;
- Surrounding the features used for engine transport (monorail, trough etc.);
- Along the profile of the engine inlet stream-tube;
- Through the entrainment mixing plane, where momentum is transferred from the exhaust to the bypass air;
- At distances along the augmenter tube pre-BB;
- In the lower exhaust stack, slightly elevated above the BB;
- Pre-exhaust stack baffles;
- Post exhaust stack baffles; and

- Within the exhaust plume at an elevated height above the stacks exit (although outside the scope of this project).

The feasibility of testing at all locations within a 'real-world' JETC is limited by engine safety, rigging, testing cost, and thermal considerations. Through consultation with CHCEC staff it was deemed that in some specific areas of the cell, scale model testing would be sufficient to accompany full-scale testing. The areas identified as being appropriate for full-scale testing were:

- Post-inlet stack baffles/Pre-turning-vanes;
- Post-turning-vanes/Pre-FOD and turbulence screens;
- Post-FOD and turbulence screens;
- Pre-exhaust stack baffles;
- Post-exhaust stack baffles;
- Surrounding the features used for engine transport (monorail, trough etc.);
- The far to moderate upstream profile of the engine inlet stream-tube; and
- The pre- and post-BB structure.

The areas identified where supplementary scale model testing was deemed to be more appropriate were:

- The immediate upstream profile of the engine inlet stream-tube;
- Through the entrainment mixing plane; and
- Immediately pre- and post-BB structure.

Full-scale testing would have been limited to pressure and temperature measurements. Scale modelling was deemed an adequate supplement to full-scale testing as it allowed measurements to be taken utilising experimental techniques not practical within a full-scale cell.

The use of PIV techniques, which are available at the UoC, lends itself well to taking 'slices' of velocity planes through scale modelled JETC sections. The output data of PIV is also easily comparable to that of CFD calculations. With PIV, the density of data gathered at each plane is also significantly higher than can be gathered through the likes of pressure probes. As such, more complex flow features could have been isolated and tested to a higher degree. Flow visualisations, such as smoke injections and tufting, also lend themselves well to scale model testing of JETCs.

Below are the areas which were deemed ideal for gathering scale model validation data via PIV and flow visualisations respectively.

- Surrounding the turning-vane and monorail section;
- Defining the profile of the engine inlet stream-tube;
- Through the entrainment mixing planes of the engine exhaust and cell bypass airflow;
- Along the length of the augmenter tube to determine the flow profile development; and
- Through the exhaust stack dissipation plume (although outside the scope of this project).

A.3 Full-Scale Testing Methodology

The following are a selection of the regions that were identified as being appropriate for testing in the full-scale CHCEC cell. Each of these selected regions is discussed as an example of the objectives that validation testing throughout the cell would achieve. Similar objectives would be sought for the remaining regions listed above as being appropriate for validation testing.

A.3.1 Post-Inlet Baffles and Pre-Turning-Vanes

Testing at this plane, when combined with data obtained at the post turning-vane location, would have provided validation data in the area of turning and circulating flow that occurs between the entrance and exit of the turning-vane structure. Testing at this plane was to be carried out over 25 point equi-spaced pitot probe grid. The data obtained would have shown the flow distribution across the inlet stack cross-section post-baffle arrangement. This, when compared to the cross-sectional flow distribution post-turning-vanes, would provide information on the effectiveness of the turning-vane arrangement, and experimental data for validation of the comparable CFD calculations performed.

A.3.2 Post-Turning-Vanes

A single cell cross-sectional test plane was to be used to look at flow in the post-turning-vane cell cross-section. Testing at this plane was to be carried out over 25 point equi-spaced pitot probe grid. As discussed in the above, comparison of the results of the pre- and post-turning-vane planes would have provided both effective information regarding the turning-vanes, and CFD validation data.

Multiple spacing arrangements were to be used when gathering data on the post turning-vane plane. An equi-spaced arrangement that would look at the overall cell flow, and a modified arrangement, would gather data to be used in conjunction with that gathered from the post FOD screen region.

The latter of the two arrangements would focus on looking at the pressure drops across the combined FOD and turbulence screens. Within the CHCEC inlet screen's arrangement there are two combinations of screen make-up. The inner portion of the screen arrangement is covered by a combination of both finely spaced FOD mesh, and a more coarsely spaced turbulence screen. The outer portion of the screen section, including the access door, is covered solely by the turbulence screen mesh. As such, the probe grid arrangement would be modified to gather the pressure data, in areas free of obstruction, and to cover both screen combinations.

The data gathered pre-FOD screen would be combined with the data post-FOD screen. This would enable the pressure drop to be measured for both screen combinations. The pressure drop data would provide a validation tool for the porous jump portion of the CFD calculation performed. More specifically it would allow the process and methods of calculating the porous jump BCs to be assessed, and if necessary, modified to increase accuracy.

A.3.3 Post-Foreign Object Damage and Turbulence Screens

As in the previous section, two grid arrangements would be used in analysis at this plane. The first would analyse the uniformity of flow throughout the cell. The second would analyse the pressure drop across the porous media immediately upstream. This would allow analysis of the flow development between the two respective planes, and give an insight into test cell design requirements for 'settling chamber' length prior to the engine inlet.

A.4 Full-Scale Test Rig Design

For testing within a full-scale JETC, pressure measurements using pitot and combination probes was decided upon as the most appropriate method data collection. This method is already used for cell certification by test cell manufacturers and operators within the industry. This is also the only quantitative method that was identified as being able to gather data over such a large test area.

In order to distribute the probes throughout the JETC in a number of arrangements, and in a number of cells, the test apparatus needed to be flexible in its application. The design of the test rig was

separated into two components; (i) probes and data acquisition (DACQ), and (ii) the supporting structure.

A.4.1 Probe Type

A number of probe options were available to be employed in the probe grid arrangement. Amongst them are the standard pitot-probe and the pitot static probes. The choice of pitot static over standard pitot-probes would not have warranted the extra expense, as a single (possibly centrally located) static pressure or pitot static probe would have been sufficient as the static pressure was not predicted to vary greatly in the planes of interest in this validation process.

Yaw and pitch angle data can be attained with the implementation of flow direction and combination probes. These come in a number of configurations depending on the nature of the flow and the desired data output. It is of interest, particularly in relation to the turning-vane validation data, to determine the flow direction, and thus the yaw and pitch angles. As the flow is three dimensional in nature, four- to seven-hole combination probes were thought to be the most appropriate for the task. There are a large number of combination probe variations including, wedge, conical, and pyramid shaped options. These alternatives all rely on having multiple pressure taps lying on a plane rotated about the respective yaw, and/or pitch axis. In addition, a centrally located forward facing total pressure tap is often present.

A truncated five-hole pyramid probe is displayed in Figure 242. The conical variation is very similar. The nose angles are typically varied between 60° and 120° degrees depending on application. As the velocity profile, measured through dynamic pressure readings, was of primary importance in the validation analysis, an angle of between 90° and 120° was thought to be most appropriate for this application.

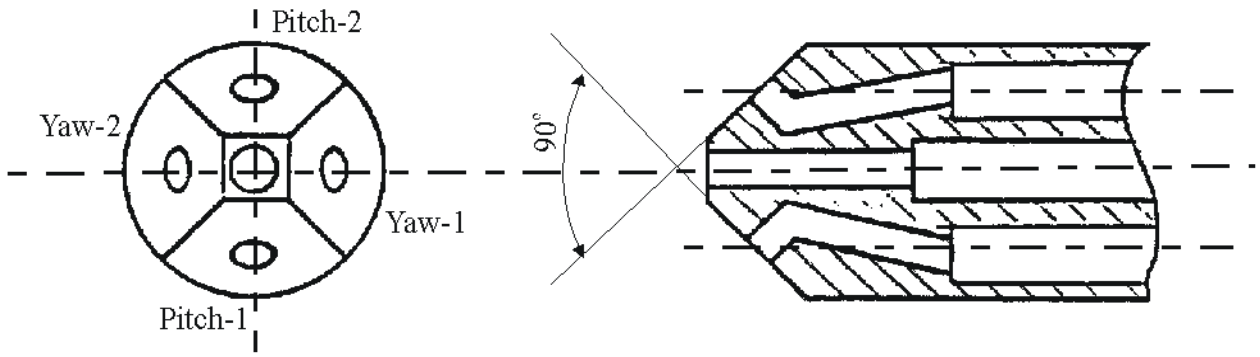

Figure 242 Truncated Five-Hole Pyramid Probe (Source: Whittle Lab, Cambridge University)

A.4.2 Supporting Framework

Consultation with CENCO cell engineers resulted in the design of the supporting probe-grid framework presented in Figure 243. Important features of the frame were identified as flexible application in both location throughout the cell, and distribution of the probes throughout the grid. The latter was of importance when higher density data are required. A tensioned cable supporting frame was to be utilised to support five double rows of probe supporting cables as shown Figure 243.

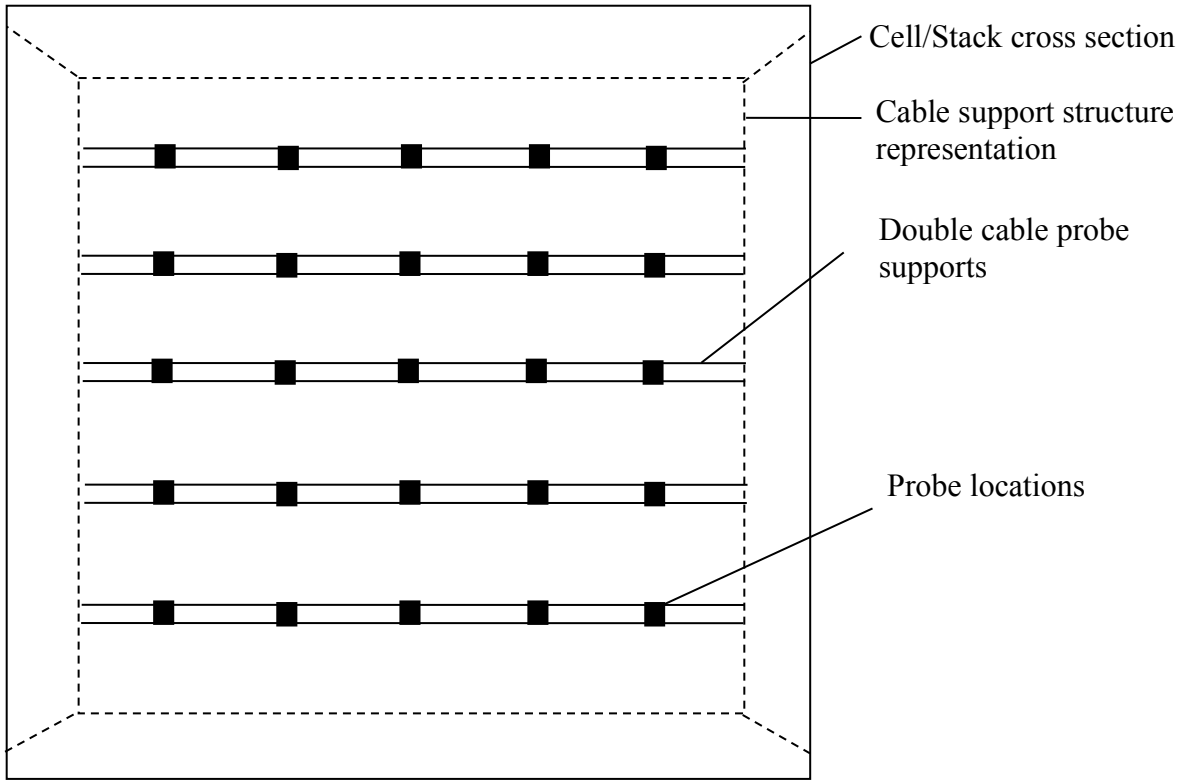

Figure 243 Proposed Supporting Arrangement for Probe Grid

In Figure 243 the double rows of probe supporting cables would be tensioned to limit displacement in the stream-wise flow direction. Throughout the CHCEC, a number of re-bar tapping points are in place as a result of the cell construction process. The support arrangement design proposed to utilise these points for the supporting frame as shown in Figure 244.

The supporting cable structure was to have the form as shown in Figure 245. Depending on the spacing of the re-bar tapping points, each wire section spanning the wall anchor points would support either one or two probe support rows. To space the rows of probe supporting cables, hollow aluminium piping with flanged ends were to be used. These spacing pipes are shown in Figure 246.

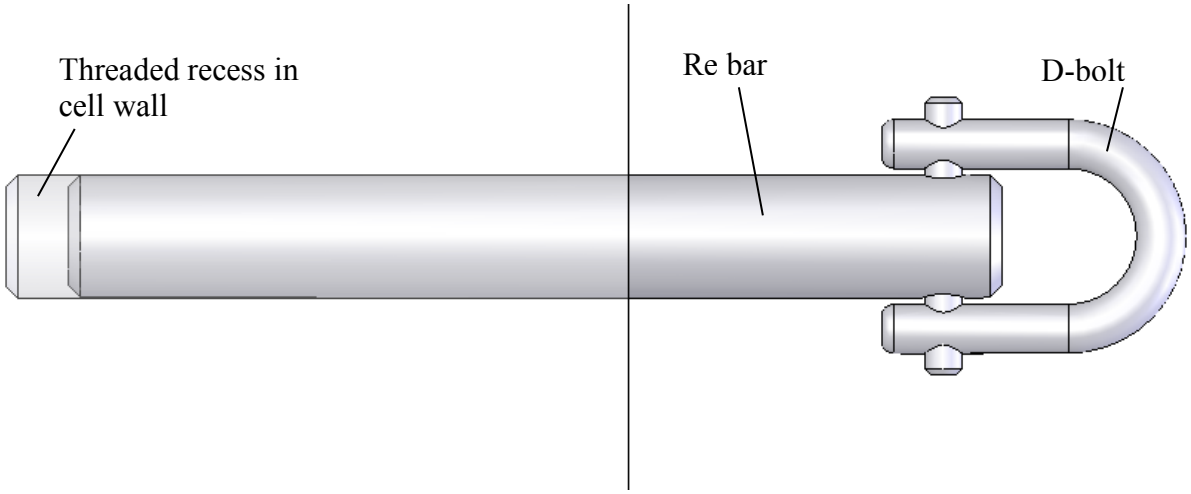

Figure 244 Test Cell Wall Attachment and D-Bolt Interface

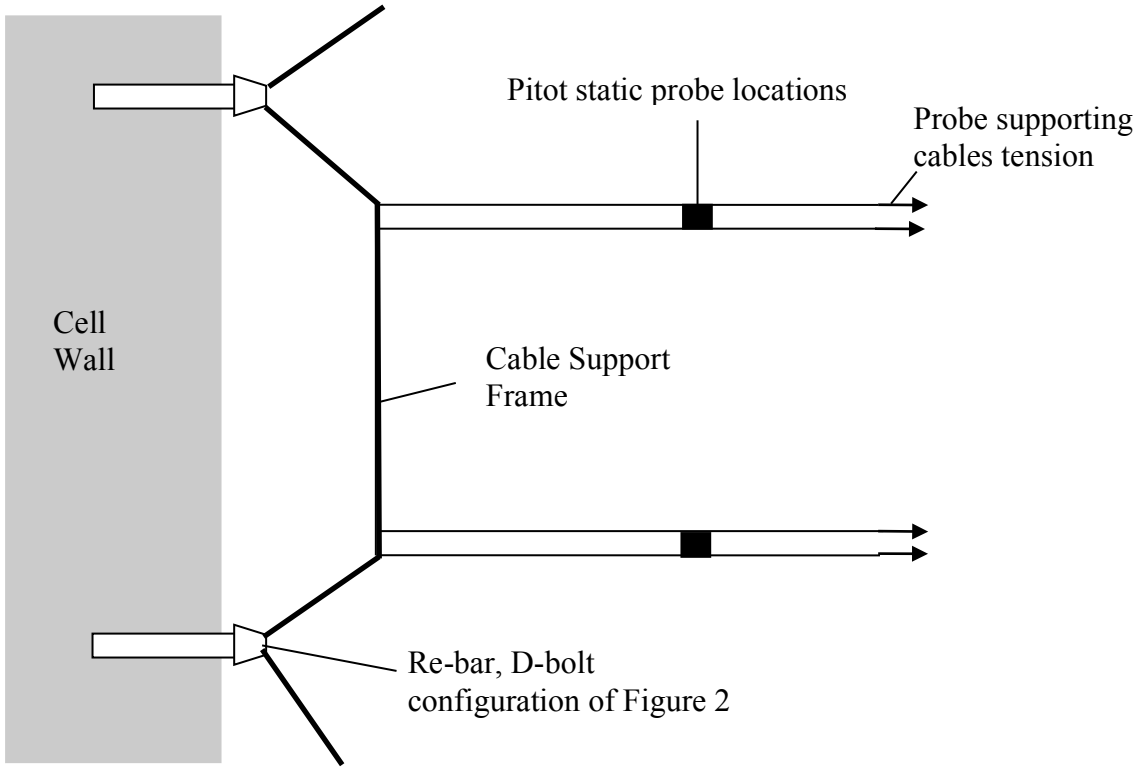

Figure 245 Proposed Structure of the Supporting Frame

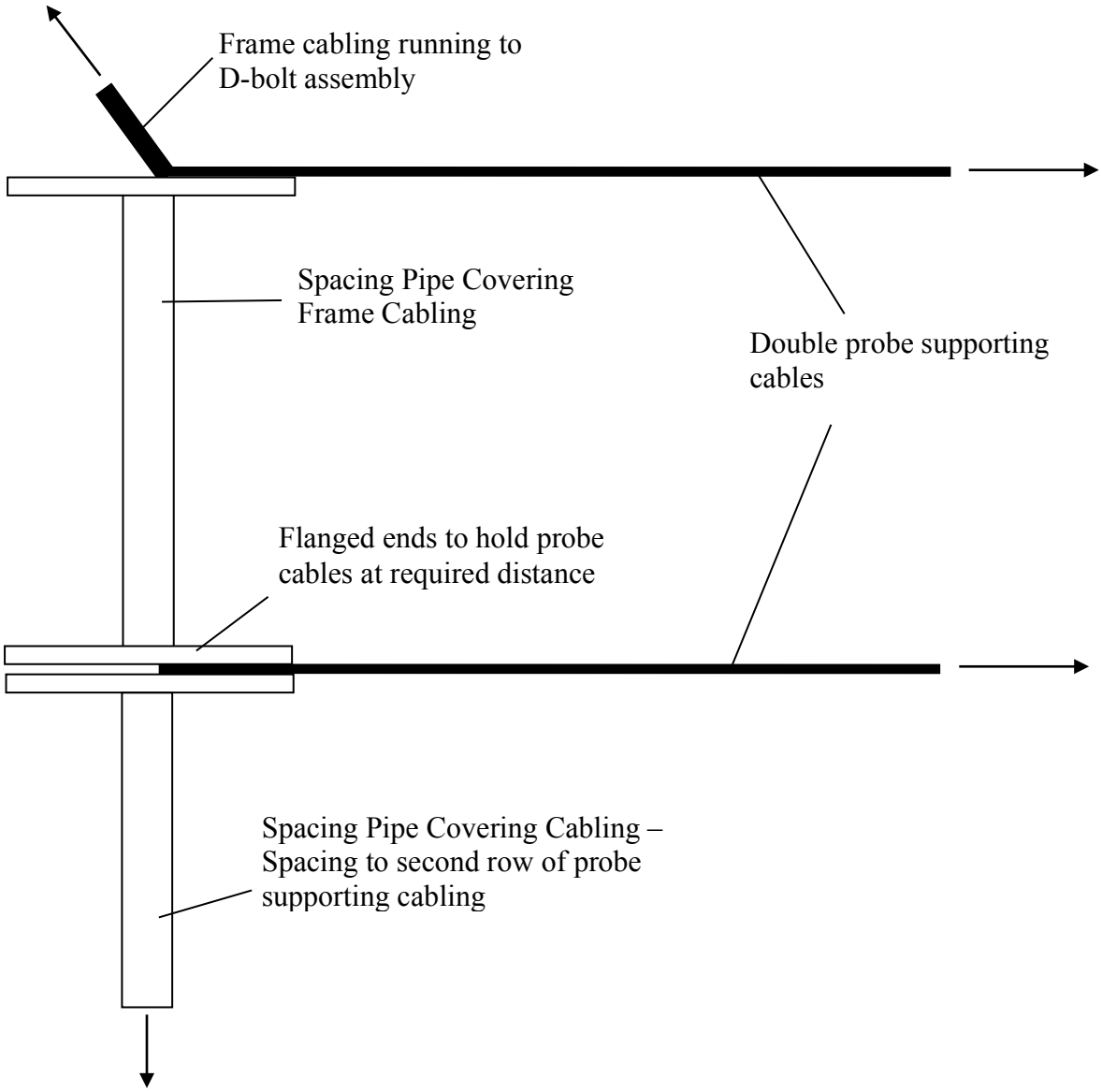

Figure 246 Proposed Cable Spacing Arrangement

A.4.3 Probe Mounting Cables

The cables the probes were to be mounted on would be held by the supporting framework from both sides of the cell. Probe support cabling would run in parallel pairs to support each probe at two points to avoid rotation under the loading imposed by the cells airflow. One end of the probe support cabling would be attached via a cable loop created by a crimped ferrule that would thread over the supporting frame. The other end would connect to the framework via a turnbuckle in conjunction with a sprung tension indicator. The turnbuckle and tension indicator would be used to set the appropriate tension to limit the deflection created as a result of wind loading on the cables.

The shape of the probe supporting cables under wind loading could likely have been described by the catenary equation. The catenary shape is generally applied to the deflection experienced by chain or cable section that is sagging under its own (uniformly applied) self-weight. With a uniform wind loading applied across the cabling in the cell, the catenary equations were to be applied to set the required tension to limit displacement in the stream-wise direction.

A.4.4 Probe Mounting

The probes were to be mounted between two parallel cables running between the two sides of the cell. This mounting arrangement would eliminate the possibility of rotation. The probes would have two small plates soldered to the downwind side to reduce rotation about a floor to ceiling axis.

This arrangement is shown in Figure 247. Due to the number of locations, and the desired flexibility required in the design, plastic zip fasteners would be used to secure the probes to the supporting cabling. This would avoid additional bolt/clamping arrangements that would result in increased flow disturbances.

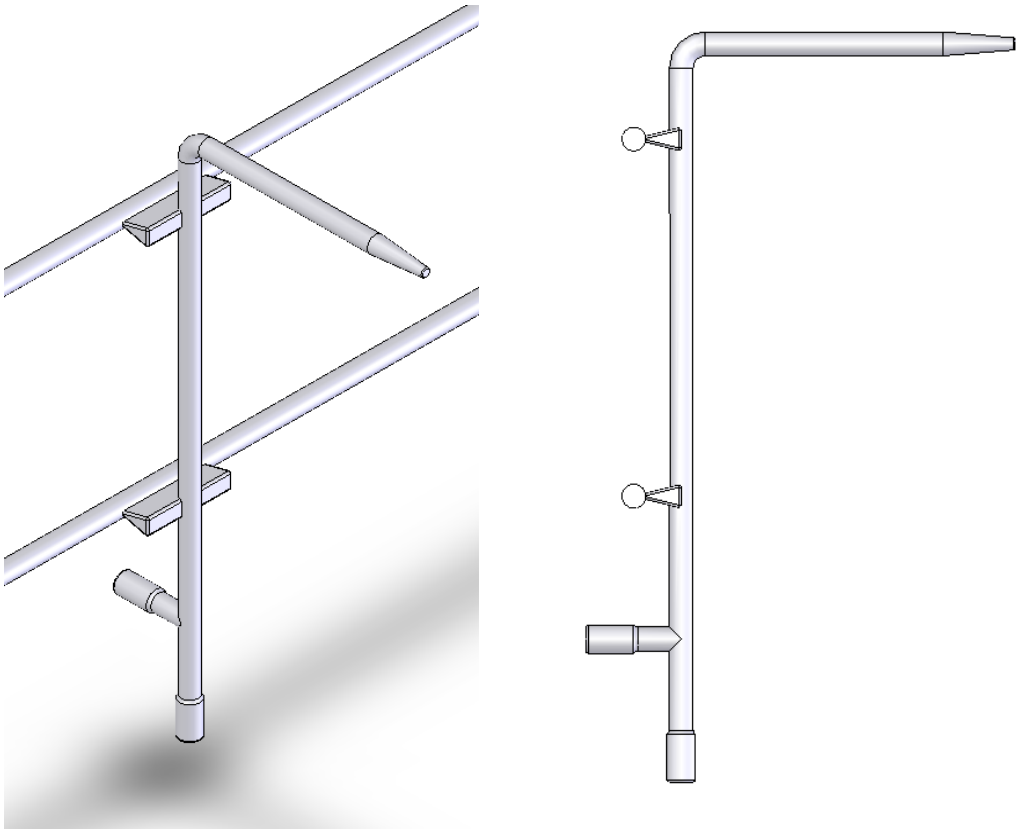

Figure 247 Proposed Pitot-Probe Mounting Arrangement